Mixed-Phase Ice-Particle Growth Mechanisms in Mesoscale Model Simulations of Northeast U.S. Extratropical Cyclones

A thesis submitted to the University of Manchester for the degree of
Doctor of Philosophy
in the Faculty of Science and Engineering

2023

Joshua J. Carter

School of Natural Sciences
Department of Earth and Environmental Sciences

Contents

Contents **2**

List of Figures **7**

List of Tables **28**

Terms and Abbreviations **30**

Declaration of Originality **40**

Copyright Statement **41**

Acknowledgements **42**

Abstract **43**

Lay Abstract **44**

I Review and Methodology **45**

1 Literature Review **46**

2 Case Studies **75**

2.1 Part II: February 2013 Storm 75
    2.1.1 Phase 1: 2000–2300 UTC 78
    2.1.2 Phase 2: 2300–0200 UTC 81
    2.1.3 Phase 3: 0200–0800 UTC 82
2.2 Part III: January and February 2020 IMPACTS Storms 83
    2.2.1 CASE 1: 18th January 2020 Storm 85
    2.2.2 CASE 2: 25th February 2020 89

3 Methods **95**

3.1 WRF Initialisation and Usage 95
    3.1.1 Model setup: Part II - 2013 Winter Storm 95
    3.1.2 Model setup: Part III - Two Winter Storms in 2020 97

3.2 Microphysics Schemes Used During Case Studies 99
  3.2.1 ISHMAEL Microphysics Scheme 99
  3.2.2 Morrison Microphysics Scheme 100
  3.2.3 P3 Microphysics Scheme 101
3.3 IMPACTS Instruments 102
  3.3.1 CPI 102
  3.3.2 Fast Cloud Droplet Probe (FastCDP) 102
  3.3.3 The Particle Habit Imaging and Polar Scattering Probe (PHIPS) 103
3.4 Mathematical Methods 103
  3.4.1 Generalised-Ice Category Partitions 103
  3.4.2 Mass Weighting of Variables 111
  3.4.3 Isolated-Active-Deposition Cell Analysis 111

II Riming, Snowfall and Reflectivity in a North-East US Winter Storm. 118

4 Simulated Precipitation Fields 119
4.1 Simulated Precipitation Type and Spatial Distribution 119
4.2 Comparison to Habit Observations Taken at Stony Brook, NY 122

5 Riming 133
5.1 Rimed Precipitation and Riming Rates 133
5.2 Riming-Rates and Graupel Production in the Morrison Scheme 137
5.3 Relating Rimed Particle Growth to Riming Rate in P3 and ISHMAEL 141

6 Reflectivity Simulated by Three Microphysics Schemes 151
6.1 Comparison of Simulated Reflectivity to Observations 151
  6.1.1 Observed and Simulated Spatial Distribution of Radar Reflectivity . . 151
  6.1.2 Observed and Simulated Vertical Distribution of Radar Reflectivity . . 155
  6.1.3 Simulated and Observed Reflectivity Maxima 158
  6.1.4 Re-examination of the Spatial Distribution Below 4 km 164
6.2 Precipitation Associated with High Reflectivity 165
  6.2.1 Precipitation Coincident with High Reflectivity Cells 167
  6.2.2 Collocation of Multiple Precipitation Types within High Reflectivity Cells 169
  6.2.3 Precipitation Coincident with the Melting Layer Aloft 171
  6.2.4 Density of Precipitation Coincident with High Reflectivity Cells . . . 174
6.3 Analysis of Reflectivity Parameterisations 176
  6.3.1 Radar Reflectivity Parameterisations per Microphysics Scheme 177
  6.3.2 More Detailed Analysis of the ISHMAEL Reflectivity Equation 179

6.3.3 Application of a Liquid-Skin Parameterisation to the Morrison Simulated Reflectivity Field 195
6.3.4 Comparison to Observations 198
6.3.5 Discussion 205
6.4 Conclusions on the Simulated Reflectivity 207

7 Snow Depth, SLR and Density 209
7.1 Preliminary Results 210
7.2 Overview of Snow Depth Parameterisation 218
7.2.1 Frozen Fraction of Precipitation 218
7.2.2 Density of Precipitation 223
7.3 Toward an Improved Snow Depth Parameterisation 228

8 Predicted Density and Snow-to-Liquid Ratio 236
8.1 Simulated Snow Depth Qualities at Stony Brook 237
8.1.1 Sources of Change in Density Predicting Schemes 243
8.2 Analysis of Density Formulations 247
8.2.1 Density Formulation per Scheme 248

III Deposition and Riming in Two North-East US Winter Storms Captured by IMPACTS 258

9 Introduction 259
9.1 Motivation from a Previous Study 260
9.2 Investigation 261

10 Preliminary Results 266
10.1 Broad-scale Analysis of Cloud Ice 266
10.2 Vapour Deposition to Cloud Ice 273
10.2.1 Consequences of Elevated Vapour Deposition for Riming 277

11 Cloud Overview 283
11.1 Cloud Top 284
11.2 On The Effects of Nucleation 286
11.3 Analysis of Deposition in Isolation 290
11.4 Impacts for the Cloud Droplet Field 294

12 Capacitance Investigation 303
12.1 Overview of Spheroid Approximations 304
12.1.1 Differences in Volume and Surface Area 307
12.2 Two Cases of Capacitance in the Literature 310

12.2.1 Theoretical Capacitance of Spheroids 310
12.2.2 Computed Capacitance of Ice Crystal Geometries 312
12.3 Box-Model Setup 314
12.3.1 Particle Distributions 314
12.3.2 Morrison Solution 315
12.3.3 ISHMAEL Solution 316
12.3.4 Comparison to the Literature 318
12.3.5 Mean Particle Size 319
12.4 Deposition Frameworks per Scheme 321
12.4.1 Morrison Deposition Framework 322
12.4.2 ISHMAEL Deposition Framework 325
12.5 Capacitance Function 328
12.6 Capacitance Testing 329
12.7 Box-Model Testing 332
12.7.1 Initialisation of Environmental Variables 332
12.7.2 Initialisation of Ice Variables 337
12.7.3 Progression of Variables per Time Step 338
12.8 Box-Model Results 339

IV Discussion and Conclusions **348**

13 Summary and Conclusions **349**
13.1 Conclusions 350

References **357**

Appendices **378**

A Phase Relaxation Time Scale **379**

B Proof: Moments of the Gamma Distribution **381**

C Aspect Ratio and Inherent Growth Ratio **386**

D Limits to the `getvar` Reflectivity Routine **390**

E ISHMAEL Reflectivity Parameterisation **394**

F Conventional Parameterisation of Reflectivity **397**

G WRF-python Reflectivity Parameterisation **399**

H Three Component form of the Mixed Phase Reflectivity Component **401**

I P3 Reflectivity Formulation **403**

J Mixed-Phase Reflectivity Enhancement by a Liquid Skin **406**

K Review of Nucleation and Ice Field Initialisation **408**

L Morrison and ISHMAEL Microphysics Tendency Formulations **414**

M Figures of Reflectivity Components in the ISHMAEL scheme **432**

N Total Reflectivity Analysis for Unrimed and Partially Rimed Crystals **435**

O PHIPS Algorithm for the Analysis of Ice Habit Imagery **438**

P Initialisation and Operation of the WRF Model **448**

Q Comparison of Loading Efficiency for WRF Analysis **463**

R Determination of Mass Weighted Variables **476**

S Evaluation of IMPACTS Data Sets **479**

Word Count: 81411

List of Figures

1.1 Sketch of a human-powered weather forecasting computer as hypothesised by Richardson (1922) . A conductor organises with a light the symposium of human computers who sit in many rows (Courtesy A. Lannerback, Dagens Nyheter, Stockholm). 47

1.2 Schematic of cloud microphysical processes for the NDW6 scheme adapted from Satoh et al. (2018). Categorised hydrometeor types are shown in boxes. Arrows indicate the exchange of mass (blue) or mass and number concentration (black) between hydrometeor types. Hom: homogenous, het: heterogenous 51

1.3 The large range of habits distributed by temperature and saturation (Bailey and Hallett 2009). Top shows distribution in text format, bottom shows pictorial format. The large variety of habits adds considerable complexity to computational models. Explicitly representing each habit costs additional computational time, and amplifies the error by autoconversion. Instead, a unified habit building scheme that utilises environmental conditions to build unique structures provides a uniform basis that may make riming autoconversion redundant 53

1.4 Graph of crystal density changing with temperature, (Fukuta and Tsuneya Takahashi 1999). Large fluctuations occur at changing periods of efficient geometrical growth, which are then opposed by periods of *fill-in* mass growth, which exhibit limited geometric modification. *m-D* relationships cannot account for inconsistent fluctuations in density originating from dynamic environmental effects. 54

1.5 Drag coefficients and Best numbers for crystals as functions of Reynolds number, (List and Schemenauer 1971). Numbers 1-6 indicate: 1. Disc, 2. Hexagonal plate, 3. Broad Branched Crystal, 4.Stellar Crystal with Plates, 5. Dendrite, 6. Stellar Crystal. Hence increasing numbers generally indicate increasing porosity and complexity of structure. 56

1.6 Difference in vapour pressure over water and ice from Storelvmo and Tan (2015). Left: saturation vapour pressure over bulk liquid (e_l) and bulk ice (e_i). Right: absolute (red) and relative (black) difference between e_i and e_l. 61

1.7 The hexagonal structure of the ice lattice projected onto the basal plane from Lamb and Verlinde (2011). The unit cell of water is shown by black solid lines. Cutting the lattice along the fewest bonds produces a hexagonal structure (grey line). 64

1.8 The Nakaya (1954) ice crystal habit diagram adapted by Libbrecht (2001). Crystal images indicate the type of ice habit found for a given supersaturation and temperature. General classifications of habit are attributed to broad temperature ranges (top). Intricate structural patterns are found above the water saturation curve. 66

1.9 Ice particle in a vapour field as imagined by the electrostatic analogy adapted from Lamb and Verlinde (2011). Lines of constant vapour density are indicated by field lines, and the vapour deposition net tendency is indicated by black arrows. Ice particle is an approximate flat plate indicated by grey shading. A cross section in the near field is shown in close proximity to the crystal surface. 68

2.1 Map of mainland United States of America (U.S.), Alaska omitted. Relevant states to this study are indicated with a two-letter state abbreviation. The approximate location of accumulated snow depth measurements shown in Figure 2.2 are overlaid. 76

2.2 Accumulated snow depths for the 8–9th February winter storm adapted from Griffin et al. (2014) and provided by the National Weather Service (NWS) Forecast Office in Raleigh. Approximate location of this region in the larger U.S. context is shown in Figure 2.1 77

2.3 Radar Plan Position Indicators (PPI) adapted from Picca et al. (2014) for times 2129 UTC (a), 0042 UTC (b), and 0340 UTC (c) representative of phases 1–3, respectively. Top: Reflectivity (at horizontal polarisation) Z_H. Middle: differential reflectivity Z_{DR}. Bottom: correlation coefficient CC. Radar data was retrieved from the National Weather Service (NWS) radar site based at Upton, New York with code-name KOKX (black dot). Yellow star shows the location of Stony Brook University. Media and mPING reports are indicated by bold lettering: S-Snow, W-Wet Snow, R-Rain, ZR-Freezing Rain, ○ -Sleet. mixed-phase precipitation areas shown by 1 (white dashed) and 2 (black dashed). 78

2.4 Observed precipitation type provided by community mPING reports adapted from Griffin et al. (2014) between times; 1200–1800 UTC (a), 1800–0000 UTC (b), and 0000–0600 UTC (c) on 8–9th February. 79

2.5 Images of ice particles sampled at Stony Brook adapted from Picca et al. (2014) (their Figure 8). (a) irregular sleet that infers wet growth and refreezing were present at 0043. (b) lightly rimed plate with dendritic extensions taken at 0415 UTC February 9th. 82

2.6 Instantaneous precipitation rate (mm hr^{-1}) and pressure (hPa) for 18th Jan 2100 UTC forecast by the NAM model (a) and WRF model with Morrison microphysics (b). Precipitation type indicated by colour: snow (blue), rain (green) and likely mixed-phase (purple) are shown across eastern PA and Jersey. WRF domains 2 and 3 are indicated with dashed lines. Parent domain is indicated by the Figure border. 86

2.7 500-hPa Geopotential heights (contoured), winds, and absolute vorticity for left: WRF simulation, right: GFS model. 87

2.8 Time series of reflectivity above SBNY. Increased reflectivity and cloud depth present from 1800 UTC. 88

2.9 Example domains and measurement data coordinates for Case 1. Nested Domains 1-3 are shown by black dotted rectangles. In (a), ASOS (Automated Surface Observing Systems), SBU (Disdrometer) and 2DVD (Two-Dimensional Video Disdrometer) points are shown with coloured shapes indicated in legend. In (b), sites of release of sounding balloons measuring thermodynamic data. Green line shows flight path of P-3 and ER-2 aircraft for 18th January. Course is a bow tie flown at different altitudes and overlapped by both aircraft simultaneously on the long lengths. 88

2.10 Skew T-log p diagram of the observed sounding at Buffalo, NY (BUF) 1800 UTC 18 January 2020. Left: IMPACTS observed sounding. Right-top: WRF simulated sounding for ISHMAEL microphysics. Right-bottom: WRF simulated sounding for Morrison microphysics. 89

2.11 Observed and simulated meteogram qualities for Stony Brook University (SBU). Note that observations at this station only span 20 hours from 17/01/2020 0000 UTC. Top: Temperature (°C) and Dew-point. Middle-upper: Wind speed (kt). Middle-lower: Wind direction (degrees from north). Bottom: mean sea level pressure (hPa) 90

2.12 GFS forecast Geopotential Height (dam), cyclonic vorticity (10^1 s^{-1}) and wind (kt). Top left: 1200 UTC February 24. Top right: 0000 UTC February 25. Bottom left: 1200 UTC February 25. Bottom right: 0000 UTC February 26. 91

2.13 NEXRAD radar reflectivity mosaic (dBZ) valid at 2200 UTC 25th February. Overlaid P-3 flight track is shown in red. 92

2.14 Heavily rimed crystals photographed by PHIPS and CPI at approximately 0100 UTC on 26th February from onboard the NASA P-3 aircraft. Left: columnar crystals with varying degrees of rime. Right: Stellars, dendrites and aggregates with surface rime. 94

3.1 WRF domain location and scale for the winter storm simulated in Part II. Domains one (blue), and nested domains two (black) and three (red) are indicated by coloured and labelled boxes. 96

3.2 WRF domain layout for a) Case 1: 17–19th January 2020 b) Case 2: 24–26th February 2020. Domain 1 (black), domain 2 (yellow), domain 3 (red). . . . 98

3.3 Partitioning flowchart for the retrieval of precipitation types (orange) from the P3 generalised-ice category. In this study, only one generalised ice category is simulated for the P3 scheme. Precipitation type is determined by partitioning ice-particle characteristic variables (diamonds); density $\bar{\rho}$, rime fraction F_r and diameter D. Flowchart format ensures that no ice remains uncharacterised. All precipitation types are mutually exclusive such that only one precipitation type can exist per cell 114

3.4 Partitioning flowchart for the retrieval of precipitation types (orange) from the ISHMAEL generalised-ice categories. Precipitation type is determined by partitioning ice-particle characteristic variables (diamonds); density $\bar{\rho}$, aspect ratio ϕ and diameter D. Flowchart format ensures that no ice remains uncharacterised. Ice category 3 is an aggregate-only ice category, so is held separate to general ice categories 1 (planar-nucleated) and 2 (prolate-nucleated). All precipitation types are mutually exclusive such that only one precipitation type per ice category can exist per cell 115

3.5 Normalised histograms of precipitation density (left), fall speed (middle), and diameter (right), for precipitation types; sleet (row 1), ice (row 2), pristine ice (row 3), hail (row 4), graupel (row 5), snow (row 6) in the ISHMAEL scheme. Precipitation types are extracted according to boundary conditions of the ice particle properties $\bar{\rho}$ (kg m^{-3}, ϕ and D (m) (see Figure 3.4). 116

3.6 Normalised histograms of precipitation density (left), fall speed (middle), and diameter (right), for precipitation types; sleet (row 1), ice (row 2), rimed ice (row 3), hail (row 4), graupel (row 5), rimed snow (row 6), and unrimed snow (row 7) in the P3 scheme. Precipitation types are extracted according to boundary conditions of the ice particle properties $\bar{\rho}$, F_r and D (see Figure 3.3) 117

4.1 Shaded contour plot of dominant precipitation-type per surface grid cell per phase: phase one (left), phase two (middle) and phase three (right) simulated by the Morrison (a), ISHMAEL (b), and P3 (c) microphysics schemes. Dominant precipitation type is determined by the largest overall accumulated mass over the course of the phase. Precipitation type is given in the panel legend for each scheme. 123

4.2 Shaded contour plot of all predicted precipitation types per surface-level grid cell during phase one (left), phase two (middle) and phase three (right) simulated by the Morrison (a), ISHMAEL (b), and P3 (c) microphysics schemes. Precipitation types (given in the panel legend per scheme) are independent, that is they do not indicate co-location, but simply the presence of the precipitation in that grid cell at some time during the phase. 124

4.3 Observations of ice habit and degree of rime adapted from Ganetis and Colle (2015) for the period 1830–1030 UTC. Shaded vertical bars indicate the types and relative proportions of sampled precipitation given in the legend. Degree of riming is shown in black for the high (dotted-dashed), low (dashed), and mean (solid) riming. 125

4.4 Precipitation type at Stony Brook as a percentage of the total precipitation mass received at the surface (vertical shaded bars) predicted by the ISHMAEL (a), P3 (b), and Morrison (c) microphysics schemes between 1800–1100 UTC 8–9th February. Precipitation type is indicated by shading detailed in the subfigure legend. Data is a mass-weighted average over all surface level cells within a 20 km by 20 km area centred over Stony Brook. . 126

4.5 Histograms of ice-particle aspect ratios throughout domain 3 for all grid points (row 1), bottom layer (*surface*) points (row 2), grids including, and in close proximity to, SBNY (row 3), SBNY grid cell only. Bars are shaded according to the habit-type associated with each aspect ratio, oblate (ϕ < 0.8, dark blue), spherical ($0.8 < \phi < 1.2$, light blue), and prolate (ϕ > 1.2, purple) 128

4.6 Aspect ratio of ice observed at SBNY (top) and simulated by the ISHMAEL scheme at three points in proximity to SBNY (shown in Figure 4.7). Observational data derives directly from a re-categorisation of precipitation type as shown in Figure 4.3. Aspect ratios are grouped into plates (dark blue), columns (light blue), and spherical (purple). The observed high, low and mean riming rate 4.3 is shown for observations (top). A proxy to the degree of riming, the rime mass tendency is shown for the ISHMAEL scheme in (black, solid) 129

4.7 Grid-cell frequency of prolate crystals simulated at the surface by ISHMAEL between 2300–0430 UTC. Frequency is defined as number of times present per time step, and the domain 3 time step was 15 minutes (4 per hour). The location of Stony Brook is shown with a red cross. The location of three sample points for aspect ratio analysis (see Figure 4.6) are shown in black and given by the Figure legend. 130

4.8 Vertical distribution and characteristics of the melting layer (T > 0°C) aloft of Stony Brook for phase one (blue shading), phase two (red shading), and phase three (green shading) simulated by the ISHMAEL (top), Morrison (middle), and P3 (bottom) microphysics schemes. Column 1; elevation of the melting layer top (green dotted), bottom (blue dotted), and maximum temperature (red, solid). Column 2; descent rate (m 15 min^{-1}) of the melting layer top (green, dotted) and bottom (blue, dotted). Column 3; melting layer width (top layer elevation minus bottom layer elevation). 132

5.1 Time series of total rimed-particle mass (kg, left) and total riming rate (kg s^{-1}, right) per microphysics scheme in domain 3. Quantities associated with the ISHMAEL, Morrison and P3 microphysics schemes are shown in blue, red and green, respectively. Blue, orange and green backgrounds span phases one, two and three, respectively. Rimed-particles are graupel (solid) in the ISHMAEL, Morrison and P3 schemes, and also partially rimed ice (dashed) in the P3 scheme only. 134

5.2 Time series of percentage rimed particle mass (%) applied to each hydrometeor category at the end of the model time step, simulated by Morrison microphysics in WRF domain 3. Left: cloud droplet riming. Right: raindrop riming. Three hydrometeor categories are considered; Graupel (green), Snow (orange), and Ice (blue). For rain droplet riming, rimed cloud ice mass that is subsequently added to snow mass (auto-converted) is also shown (red). Blue, orange and green backgrounds span phases one, two and three, respectively. 137

5.3 Percentage of mass accreted to snow that is transferred to the graupel category (x-axis) as a percentage of the total number of autoconversion cases (y-axis) in the Morrison scheme. Left: the proportion of converted mass owed to cloud droplet riming. Right: the proportion of converted mass owed to rain droplet riming. 139

5.4 Visual aid for the development of rimed particles in the ISHMAEL and P3 schemes. The P3 scheme (left, blue) tracks the rime fraction F_r and density ρ (kg m^3) of the precipitation field. The ISHMAEL scheme (right) tracks the aspect ratio ϕ and density ρ (kg m^3) of the precipitation field. Precipitation type is indicated by the sub range of each variable; graupel (green) and rimed snow (yellow) are considered here. Note that graupel occurs when the criteria for both variables is met simultaneously 142

5.5 Time series of average change in characteristic density in the ISHMAEL and P3 microphysics schemes across all riming cells per time step. Average change is split between sub ranges of density (see Figure 5.4). Column 1: $\rho < 300$ kg m^3. Column 2: ρ in graupel range, Column 3: $\rho > 700$ kg m^3. Note that ISHMAEL ice-types are distinguished ice-type 1 (orange), ice-type 2 (green), ice-type 3 (red) 144

5.6 Time series of average change in characteristic variable: rime fraction F_r (P3, blue) and ϕ (ISHMAEL) within riming cells per time step. Average change is split between sub ranges of each characteristic variable (see Figure 5.4). Row 1: $F_r < 0.1$, $\phi > 1.2$. Row 2: $0.1 < F_r < 0.6$, $0.8 < \phi$. Row 3: $0.6 < F_r < 0.1$, $0.8 < \phi < 1.2$. Note that ISHMAEL ice-types are distinguished ice-type 1 (orange), ice-type 2 (green), ice-type 3 (red) 146

5.7 Rate of change of characteristic variables F_r, ρ in the P3 scheme (left) and ϕ, ρ in the ISHMAEL scheme (right). Each characteristic variable is depicted as a scale of possible values (increasing from left to right), wherein sub ranges of each scale determine a precipitation type, denoted above the sub range and indicated by a double-headed arrow. The rate of change of each characteristic variable for particles within a sub range, is shown above the respective sub range. The residency time proportional to the inverse of the rate of change is given below the respective sub range. 150

6.1 Contours of simulated maximum reflectivity factor Z_H (dBZ) at times 2130 UTC (column 1), 0045 UTC (column 2), 0345 UTC (column 3), for microphysics schemes ISHMAEL (row 1), Morrison (row 2) and P3 (row 3) up to a maximum elevation of 1.5 km (replicating the observed shallow layer). Observations of KOKX radar reflectivity (dBZ) adapted from Ganetis and Colle (2015) (see their Figure 4) shown in row 4 for comparison at times: 2129 UTC (column 1), 0042 UTC (column 2), 0340 UTC (column 3). Contours shaded according to scale. 153

6.2 Latitudinal-Longitudinal position of vertical cross section chosen for horizontal interpolation. Left: position adapted from Ganetis and Colle (2015) (see their Figure 4 Panel i) for their vertical interpolation of observed radar reflectivity shown in Figure 6.3 (column 4). Right: position of horizontal interpolation used for simulated microphysics schemes shown in Figure 6.3 rows 1–3. Position of KOKX radar shown by black plus + marker. Position of Stony Brook University shown by blue dot · 156

6.3 Contours of simulated reflectivity factor Z_H (dBZ) in vertical cross section along line A to A' (see Figure 6.2) at times 2130 UTC (column 1), 0045 UTC (column 2), 0345 UTC (column 3), for microphysics schemes ISHMAEL (row 1), P3 (row 2) and Morrison (row 3). Observations of KOKX radar reflectivity (dBZ) adapted from Ganetis and Colle (2015) (see their Figure 5) shown in row 4 for comparison at times: 2129 UTC (column 1), 0042 UTC (column 2), 0340 UTC (column 3). Contours shaded according to scale. Hatched area indicates radar cone of silence. Position of SBNY along the cross section is indicated by black arrow below the x-axis. 159

6.4 Time series of the maximum simulated reflectivity (dBZ) per microphysics scheme: ISHMAEL (blue), Morrison (orange), and P3 (green). Time series is separated into three columns for phases one, two, and three, respectively. Row 1: maximum reflectivity is determined throughout all vertical levels of domain 3. Row 2: maximum reflectivity determined from within a 1.5 km surface layer only. 160

6.5 Histograms of simulated reflectivity factor frequency for microphysics schemes ISHMAEL (row 1), Morrison (row 2), and P3 (row 3) and phases 1–3 (columns 1–3, respectively) for all cells in domain 3. 162

6.6 Scatter plot time series of the height (km) at which maximum reflectivity occurs in domain three for microphysics schemes: ISHMAEL (blue), Morrison (orange) and P3 (green). Height of the shallow 1.5 km layer is indicated with a red line. 163

6.7 Contours of simulated maximum reflectivity factor Z_H (dBZ) at times 2130 UTC (column 1), 0045 UTC (column 2), 0345 UTC (column 3), for microphysics schemes ISHMAEL (row 1), Morrison (row 2) and P3 (row 3) as in Figure 6.1 but up to an altitude of 4 km. Observations of KOKX radar reflectivity (dBZ) adapted from Ganetis and Colle (2015) (see their Figure 4) shown in row 4 for comparison at times: 2129 UTC (column 1), 0042 UTC (column 2), 0340 UTC (column 3). Contours shaded according to scale. . . 166

6.8 Percentage (%) of high reflectivity grid cells (99th percentile of reflectivity per scheme) containing precipitation type for microphysics schemes ISHMAEL (top), Morrison (middle), and P3 (bottom). Phases one to three are separate and percentages are calculated per phase only. Precipitation type indicated by Figure legend. 168

6.9 Percentage (%) of high reflectivity grid cells (99th percentile of reflectivity per scheme) containing specified collocated precipitation types for microphysics schemes ISHMAEL (top), Morrison (middle), and P3 (bottom). Percentage is calculated across all three phases. Bars are vertically stacked and ordered by number of precipitation types per mixture in increasing number from left to right. Precipitation type combination is indicated by Figure legend. 170

6.10 Time series of the percentage of high reflectivity grid cells (99th percentile of reflectivity per scheme) coincident with the melting layer (T ≥0°C) at time T. Time range spans phases 1–3 for the duration of the melting layer lifespan. Shown for schemes ISHMAEL (top), Morrison (Middle) and P3 (Bottom). Red dashed line indicates 40% for comparison. 172

6.11 Comparison of average mass-weighted ice density present within 99th percentile high reflectivity grid cells (orange), to average mass-weighted ice density within background cells (blue). Average density is determined for all non-zero mass valued cells present in all domain three grid cells, per phase (columns 1–3) and per microphysics scheme: ISHMAEL (top), Morrison (Middle) and P3 (Bottom) 175

6.12 ISHMAEL ice-reflectivity component to the total reflectivity calculation (see Equation 6.8 versus ice number concentration n_{ice}. Three example precipitation types are considered; Dendrites (left), Graupel (middle), and Prolates (right). Four values of the ice characteristic radius a_{ni} are shown by coloured lines given in the Figure legend. 181

6.13 Plot of factor F (see Equation 6.9) versus characteristic ice radius for three values of the inherent growth ratio δ_* that are indicative of oblate (blue), spherical (orange), and prolate (green) ice crystals. Black dots indicate the characteristic radius of each example precipitation type; dendrites, graupel, prolate ice. Blue crosses adjoined by red dashes correspond to the inverse square density associated with each precipitation type (blue axis, right). . . 184

6.14 Distributions of γ_n, the ratio of rain to ice number concentration (orange, left) and average crystal mass m_i (green, right) simulated by ISHMAEL during case one for precipitation classed as dendrites (row 1), graupel (row 2), and prolates (row 3). 185

6.15 Plot of the ratio of reflectivity components in ISHMAEL $\varepsilon = Z_{\text{rain}}/Z_{\text{ice}}$. The log (base 10) of the summation of components $Z_{\text{rain}} + Z_{\text{ice}}$ is equal to the reflectivity on the dBZ scale. ε is plotted versus the ratio of raindrop number to ice crystal number, across three scenarios: Dendrites ($\delta_* = 0.6$, $\bar{\rho} = 100$), Graupel ($\delta_* = 1$, $\bar{\rho} = 400$) and needles ($\delta_* = 1.3$, $\bar{\rho} = 900$) in columns 1–3, respectively. In each case, the ratio ε is plotted for several values of its parameters rain mass mixing ratio q_r (kg kg^{-1}) and ice characteristic radius a_{ni} (m) specified in the Figure legend. Inflection points of the y and x-axis ratios are shown with grey lines. 186

6.16 Reflectivity components A and B (see Equation 6.8) and their summation (multiplied by 10) the total reflectivity Z_{total} (dBZ) versus the average rain droplet mass m_r (kg) for prolates ($\delta_* = 1.3$, $\bar{\rho} = 900$. Terms A, B and the total are shown by dashed, dotted, and translucent lines. Components are plotted for three values of the ice number concentration n_i (kg^{-1}): 1×10^5, 1×10^2, 1×10^{-1} in columns 1–3, respectively, and three values of ice mass mixing ratio q_r (kg kg^{-1}): 1×10^{-8}, 1×10^{-4}, 1×10^{-2} in rows 1–3, respectively. 189

6.17 Histograms of reflectivity dependencies in the ISHMAEL scheme. Each dependency type is titled per panel 190

6.18 Plots of the P3 ε function versus ice particle radius r for three hydrometeor types: unrimed snow ($F_r = 0$, $\rho = 100$), rimed snow ($F_r = 0.667$, $\rho = 400$), and graupel ($F_r = 1$, $\rho = 600$) (rows 1–3) and three ice mass m_i values 1×10^{-10}, 1×10^{-8}, 1×10^{-6} (columns 1–3). ε is shown for four average rain mass (m_r) values; 1×10^{-4} (yellow), 1×10^{-6} (green), 1×10^{-8} (red), 1×10^{-10} (blue). Three fixed values of ice mass and rain mass are considered; base state $q_i = 1 \times 10^{-5}, q_r = 1 \times 10^{-2}$, decreased ice $q_i = 1\times10^{-6}, q_r = 1\times10^{-2}$ and decreased rain $q_i = 1\times10^{-5}, q_r = 1\times10^{-6}$ shown by solid, dotted, and dashed lines, respectively. 193

6.19 Total reflectivity Z (dBZ, black), ice reflectivity component A (dBZ, blue), and mixed-phase reflectivity component B (dBZ, red) as shown in Equation 6.15 versus average ice particle radius r (m) for graupel (see Table 6.2). Average crystal mass $m_i = 1 \times 10^{-10}$, 1×10^{-8}, 1×10^{-6} kg in columns 1–3, respectively. Average raindrop mass $m_r = 1 \times 10^{-10}$, 1×10^{-6}, 1×10^{-4} kg in rows 1–3, respectively. Three sets of fixed ice mass mixing ratio q_i (kg kg^{-1}) and rain mass mixing ratio q_r (kg kg^{-1}) are shown with differing line styles; base state $q_i = 1 \times 10^{-5}, q_r = 1 \times 10^{-2}$, decreased ice $q_i = 1\times10^{-6}, q_r = 1\times10^{-2}$ and decreased rain $q_i = 1\times10^{-5}, q_r = 1\times10^{-6}$ shown by solid, dashed, and dotted lines, respectively. 194

6.20 Net gain in simulated radar reflectivity factor by inclusion of liquid skin parameterisation over default parameterisation ΔZ. ω is the ratio of rain mass mixing ratio to frozen mass mixing ratio (combined snow and graupel). Plotted for multiple ratios of graupel mass mixing ratio to snow mass mixing ratio δ. i.e. $\delta > 1$ indicates an environment with more graupel mass than snow, $\omega > 1$ indicates an environment with more liquid (rain) mass than frozen mass. 200

6.21 Contours of maximum radar reflectivity factor Z_H (dBZ) at times 2130 UTC (column 1), 0045 UTC (column 2), 0345 UTC (column 3), derived from Morrison simulated precipitation using the wrf-python `getvar` routine (Ladwig 2017). Row 1: Liquid skin calculation turned on. Row 2: Liquid skin calculation turned off (as in Figure 6.1). Row 3: Absolute difference in reflectivity factor between liquid skin options. Contours shaded in rows 1–2 according to top scale. Contours shaded in row 3 according to bottom scale. 202

6.22 Contours of simulated reflectivity factor Z_H (dBZ) in vertical cross section along line A to A' (see Figure 6.2) at times 2130 UTC (column 1), 0045 UTC (column 2), 0345 UTC (column 3), derived from Morrison simulated precipitation using the wrf-python `getvar` routine (Ladwig 2017). Row 1: Liquid skin calculation turned on. Row 2: Liquid skin calculation turned off (as in Figure 6.1). Row 3: Absolute difference in reflectivity factor between liquid skin options. Contours shaded in rows 1–2 according to top scale. Contours shaded in row 3 according to bottom scale. Position of SBNY along the cross section is indicated by black arrow below the x-axis. 206

7.1 Accumulated snow depth (in.) between 0000–0000 UTC 8–9th February. Observed depth adapted from Ganetis and Colle (2015) (row 1, column 1), ISHMAEL simulated depth (row 1, column 2), P3 simulated depth (row 2, column 1) and Morrison simulated depth (row 2, column 2). Contour levels are equivalent in all sub figures. Location of Stony Brook University (SBNY) indicated by yellow star. Location of the maximum simulated snow depth per microphysics scheme indicated by yellow circle. 211

7.2 Contours of accumulated liquid equivalent frozen precipitation (mm) between 0000–0000 UTC 8–10th February simulated by ISHMAEL (top left), P3 (top right) and Morrison (bottom) microphysics schemes. Location of Stony Brook University (SBNY) indicated by yellow star. Location of the maximum simulated liquid equivalent per microphysics scheme indicated by yellow circle. 214

7.3 Total accumulated liquid equivalent frozen precipitation (mm) on Long Island between 0000–0000 UTC 8–9th February simulated by ISHMAEL (left), P3 (middle) and Morrison microphysics schemes (right). 215

7.4 Average SLR (`SNOWH` [m] $\div$ liquid equivalent [m]) deriving from total snow height and liquid equivalent depth between 0000–0000 UTC 8–10th February simulated by ISHMAEL (top left), P3 (top right) and Morrison microphysics schemes (bottom). 216

7.5 Noah-MP LSM parameterised functions for the determination of the fraction of total precipitated mass arriving at the surface that is frozen. By default the Jordan (1991) parameterisation is used during snow depth calculations (row 1 column 1). The surface temperature method (row 2 column 1) and surface temperature method with BATS adjustment (row 1 column 2) are non-default options. 221

7.6 Scatter diagram of simulated frozen fraction at the surface in ISHMAEL (left, red), P3 (middle, green), and Morrison (right, blue) versus surface temperature. Scattered points are a randomly sampled subset ($\sim$ 1000) of the frozen fraction data set. Parameterised frozen fraction is overlaid for comparison, and the parameterisation type is indicated in the Figure legend (see Figure 7.5 “Combined”) 222

7.7 Parameterisation of density versus surface temperature in the Noah-MP land surface scheme given by the Hedstrom and Pomeroy method (left) and the weighted-precipitation method (right). For the weighted method, three example weightings are shown; snow dominated (dashed), graupel dominated (dotted), and equivalent (solid). 224

7.8 Scatter diagram of simulated precipitation density at the surface in ISHMAEL (left, red), Morrison (middle, blue), and P3 (right, green), versus surface temperature. Scattered points are a randomly sampled subset ($\sim$ 1000) of the entire simulated density data set. Parameterised density is overlaid for comparison; the weighted precipitation method (orange) is given for several values of snow to graupel mass ratio (see Figure legend). As graupel mass approaches zero, the weighted method approaches the original Hedstrom and Pomeroy (1998) method (red). 227

7.9 Comparison of the accumulated snow depth (in.) between 0000–0000 UTC 8–9th February. Top: observations of accumulated snow depth adapted from Ganetis and Colle (2015). Row 2: accumulated snow depth derived directly from microphysics scheme output variables. Row 3: accumulated snow depth parameterised by the Noah-MP land-surface model i.e. variable `SNOWH`. Columns 1–3: Morrison, P3 and ISHMAEL microphysics schemes, respectively. Contours of the observed > 12 inch snow depth (dark blue), and > 24 inch snow depth (light pink) are approximately modelled by dashed and dotted ovals respectively. The ovals are overlaid on simulated snow depths for comparison. 232

8.1 Phase-averaged density and microphysical process rate with elevation at SBNY for the ISHMAEL microphysics scheme. Values averaged per vertical layer in a column with 20 km^2 base centred on SBNY. Average density in each vertical layer (White line). Average microphysical process mass tendency rate as a fraction of the total microphysical process mass tendency rates per vertical layer (see legend). Phase averaged number aggregation rate per vertical layer given in side plot per phase with symmetric logarithmic scale. 246

8.2 As in Figure 8.1 but for the P3 microphysics scheme. 246

8.3 Change in microphysical process rate and density with height aloft of Stony Brook for phase one. Left: change [kg kg s^{-1}] in cloud droplet mass mixing ratio (blue), riming mass tendency (black, dotted) and melting mass tendency (black, dashed). Right: average density (green) [kg m^{-3}]. Temperature (K) overlaid for both panels in red. 252

8.4 Density evolution during melting and wet growth for switched mass tendency rates. 253

8.5 As in Figure 8.3 for phase 2. 254

8.6 Time series of dependencies for the mass-melting process in a shallow layer aloft of Stony Brook during phases one and two; ice crystal number concentration (kg^{-1}) (left), temperature (K) (column 2), vapour mixing ratio (kg kg^{-1}) (column 3), and rain ice collision term (kg kg^{-1} s^{-1}) (column 4). . . 255

8.7 Tendency of melting for the ISHMAEL and P3 schemes during phases one and two in a shallow vertical layer aloft of Stony Brook. 256

9.1 Cloud ice qualities as determined in a previous simulation of a north-east winter storm using WRF. Left column: Total summed mass and number concentration timeseries. Right column: variables as in left but averaged amongst non-zero valued cells. Bottom: mass divided by number indicating the average crystal mass. Background shading indicates phases of precipitation: Blue: mixed-phase and snow. Orange: mixed-phase and graupel. Green: Snow. 262

9.2 Time series of total vapour deposition mass tendency to graupel as determined in a previous simulation of a north-east winter storm using WRF for domains 1–3. 263

10.1 Time series of total cloud ice mass (kg) (row 1), total crystal number (dimensionless) (row 2), and total deposition mass tendency (kg s^{-1}) (row 3) simulated by ISHMAEL (blue, yellow) and Morrison (Black) during cases one (left) and two (right). ISHMAEL ice-type 1 (oblate-nucleated) and ice-type 2 (prolate-nucleated) are blue and orange, respectively. The x-axis is given in time steps, which are hourly from midnight. 269

10.2 Average vertical distribution of total vapour depositional mass (kg)(left), cloud ice mass (kg) (middle), and crystal number (right) over the duration of the simulation for Case 1. ISHMAEL ice-types one (blue) and two (orange) are shown in rows 1–2, respectively. Morrison is shown in row 3 (black). Area of maximum deposition per scheme and ice-type is highlighted with coloured rectangle per row. 272

10.3 Vertical Distribution of total cloud ice mass (kg) and total cloud ice number (dimensionless) in the ISHMAEL (light blue) and Morrison (black) schemes (as in Figure 10.2 but overlaid). Overlapping ice mass is shown in dark blue. 273

10.4 Mass tendency components for microphysical processes in cases one (a) and two (b). Left; the percentage of the total mass tendency to cloud ice that derives from the deposition process for ISHMAEL ice-type 1 (blue), ice-type 2 (orange), and Morrison (black). Right; timeseries of total mass tendency to cloud ice for microphysics processes (see Figure legend) for ISHMAEL ice-type 1 (column 2), ISHMAEL ice-type 2 (column 3), and Morrison (column 4). 275

10.5 Time series of the mass-weighted average vertical elevation (km) of cloud ice, deposition to cloud ice, and riming of cloud ice in cases one (a) and two (b). ISHMAEL ice-type 1 (red), ice-type 2 (green), and Morrison (black) are shown with circles and triangles for each respective scheme. Deposition (dashed) and riming (dotted) are coloured with respect to each ice-type. . . 277

10.6 Time series of average, per-grid cell vapour deposition rate kg kg^{-1} s^{-1} for domain 1 in cases one (a) and two (b) simulated by Morrison (black) and ISHMAEL ice-types 1 (red) and 2 (green). Vertical bars (coloured according to scheme) indicate the (non-zero) minimum and maximum deposition rate simulated by the respective scheme in the time step. 277

10.7 Time series of average, mass-weighted fall speed (m s^{-1}) of cloud ice particles simulated by Morrison (green) and ISHMAEL ice-types 1 (blue) and 2 (orange), for cases one (a) and two (b). 278

10.8 Scatter-density plot of ice fall speed (m s^{-1}) versus average crystal mass (kg) per cell in domain 1 for ISHMAEL ice-type 1 (left) and ice-type 2 (middle), and the Morrison scheme (right) during cases one (top) and two (bottom). Density colour mapping is per graph-pixel. 280

10.9 Scatter-density plot of ice riming mass tendency (kg kg^{-1} s^{-1}) versus ice mass mixing ratio (kg kg^{-1}) per cell in domain 1 for ISHMAEL ice-type 1 (left) and ice-type 2 (right) during cases one (top) and two (bottom). Density colour mapping is per graph-pixel. 282

11.1 Time series of sum-total cloud ice mass concentration (kg m^{-3}, top) and number concentration (m^{-3}, bottom) per time step for Case one (left) and Case two (right) as simulated by ISHMAEL (red) and Morrison (black) at the cloud top.. Vertical bars indicate the maximum and minimum value of mass or number concentration produced at the cloud top by each scheme (colour) during the time step 287

11.2 Time series of average crystal mass (kg) (left), average deposition mass tendency per cell (kg s^{-1}) (centre), and total deposition mass tendency (kg s^{-1}) (right) in domain 1 per time step during case one (a) and case two (b). Vertical bars indicate the maximum and (non-zero) minimum value of each variable produced during the time step (coloured with respect to scheme). . 288

11.3 Example of the deposition “zone” criteria (left) for a latitude-longitude slice of the domain and the corresponding binary mask associated with these criteria being fulfilled (right). Blue boxes indicate deposition is non zero. Orange boxes indicate that a non-depositional process is non-zero. Green boxes highlight the cloud top as defined in the cloud top analysis. Grey box highlights where cloud ice mass >0 but no process is taking place. 292

11.4 Simulation-averaged vertical distribution (m) of deposition layer height for ISHMAEL ice-type 1 (blue, left) and ice-type 2 (yellow, middle), and Morrison (black). 292

11.5 Example time series of mass mixing ratio (kg kg^{-1}) and number mixing ratio (kg^{-1}) of cloud ice obtained per vertical level when considering ice that is within the depositional zone. ISHMAEL shown in blue, Morrison in orange. Each subfigure represents a vertical height indicated by respective axis title. The tendency of increase or decrease with cloud depth is shown by large arrows (coloured according to scheme). Arrow gradient indicates the rate of change of each variable with height due to deposition only. . . . 295

11.6 Average, in-deposition layer mass mixing ratio (kg kg^{-1}) (left), ice number (kg^{-1}) (centre) and average crystal mass (kg) (right) with cloud depth for cloud ice meeting the deposition zone criteria in ISHMAEL (ice-type 1, blue) and Morrison (yellow). Results are for Case 1 only but Case 2 average crystal mass is shown in subfigure of panel 3. For average crystal mass an exponential fit has been produced for each case with good agreement. . . . 296

11.7 Vapour and cloud droplet total mass (kg) for the whole of domain 1 (a) and inside the deposition zone (b) for case 1. Left; histograms of mass distribution for vapour (top) and cloud droplet (bottom) mass for entire simulation in the ISHMAEL (dark blue) and Morrison (clear, orange border) schemes. Overlap indicated by purple shading. Right; timeseries of sum-total vapour mass (kg) (top) and droplet mass (kg) (bottom) for domain 1 in ISHMAEL (blue) and Morrison (yellow, dashed) 298

11.8 As in Figure 11.7 for case two. 299

11.9 Total vapour mass (kg) distribution versus vertical elevation (km) for ISHMAEL (blue) and Morrison (yellow) schemes in case one. Green shaded region indicates deviation of the deposition mass tendency between schemes. 301

11.10 Total vapour mass (kg) (solid) and cloud droplet mass (kg) (dashed) distribution versus vertical elevation (km) for ISHMAEL (blue) and Morrison (yellow) schemes in cases one (a) and two (b). Shaded region indicates deviation of the deposition mass tendency between schemes per respective case. 302

12.1 A standard ellipse. The semi-minor and semi-major radii are shown in orange. The axes of rotation are the minor and major axes which extend beyond the ellipse. 304

12.2 Oblate (left) and Prolate (right) spheroids adapted from Wikimedia Commons (2015). The spheroid a and c axes are related to the Cartesian coordinate system. The spheroid is formed by rotating a two-dimensional ellipse by π. 305

12.3 Ice particle geometries adapted from Ding and Liu (2020). Plate (left), Column (left-centre), sector-like plate (right centre), branched stellar (right). Maximum crystal dimension D and side length a indicated. 306

12.4 Schematic of prolate (a) and oblate (b) spheroids (light blue) encapsulated within a crystal with equivalent radial lengths. 307

12.5 The ratio of volume and surface area of spheroids to their equivalent hexagonal prisms. 311

12.6 Capacitance of spheroid types with fixed semi-minor axis versus semi-major axis. The semi-major axis is an indication of the extremity of prolate or oblate crystals. Right: as in left but re-parameterised for aspect ratio. . . 312

12.7 Functions for the capacitance of ice crystals as determined by Westbrook et al. (2008) and McDonald (1963) (left) and the ratio of capacitance derived in the McDonald (1963) equation set to that derived by Westbrook et al. (2008) (right) 313

12.8 Relationship between the ice particle aspect ratio ϕ and the inherent growth ratio δ_* for differing values of the spheroid a-axis relative growth factor R . 317

12.9 Ratio of the distribution average radius between the ISHMAEL and Morrison microphysics schemes versus the inherent growth ratio δ_*. When $\delta_* = 1$ both distributions simulate spherical particles. The ratio is plot for several values of the average ice-mass K shown in the Figure legend. . . 321

12.10 Visual schematic of how the ice maximum dimension `DCS` parameter partitions the particle distribution such that large ice particles enter into the snow category. 323

12.11 Distribution averaged capacitance (left), ratio of capacitance between ISHMAEL and Morrison (middle) and value of the distribution averaged shape factor (right) versus inherent growth ratio δ_* for varying average crystal mass K (kg) (see Figure legend) 330

12.12 Simulated distribution of average crystal mass K in the ISHMAEL (left) and Morrison (right) microphysics schemes across cases one (top) and two (bottom) 333

12.13 Scatter density plot of average crystal mass value K versus the ambient temperature in the ISHMAEL (top, middle) and Morrison (bottom) microphysics schemes. Density of points is indicated by color mapping, and is determined by the local pixel density. 334

12.14 Scatter plot of pressure versus temperature in the ISHMAEL (top) and Morrison (bottom) microphysics schemes. Each panel (left to right) indicates a new average crystal mass (titled). Data point colouring is in accordance with the vapour mass mixing ratio. 336

12.15 Scatter density plot of mass mixing ratio (kg kg^{-1}) for ice in Morrison (left) and ISHMAEL (right). Points chosen as Representative of the microphysics scheme are shown in coloured dots (see Figure legend) 338

12.16 Time series of Temperature (K), Pressure (hPa), Vapour mass mixing ratio (kg kg^{-1} and frozen mass mixing ratio in an idealised deposition box model (columns 1–4, respectively). Results are obtained for multiple initial temperatures (shaded, see Figure legend). In this analysis, box model thermodynamic option two was chosen (pressure and temperature held constant). Average ice mass was fixed at 1×10^{-9} kg. 342

12.17 Ratio of ice mass mixing ratio produced by the ISHMAEL scheme and Morrison scheme (ISHMAEL:Morrison) for a 60 minute simulation using an idealised box model. Columns 1–4 vary with initial average ice mass. Each time series is shown for several initialisation temperatures (shaded), which remain constant. The parity value of 1 is indicated with a grey dashed line. 344

12.18 Ratio of the ice mass mixing ratio produced by the ISHMAEL scheme when capacitance is predicted, to the ice mass mixing ratio produced by ISHMAEL when capacitance is constant. Columns 1–4 vary with initial average ice mass. Each time series is shown for several initialisation temperatures (shaded), which remain constant. The parity value of 1 is indicated with a grey dashed line. 345

12.19 Graph of the inherent growth ratio (IGR) used in the ISHMAEL scheme, versus temperature (K). The form of the IGR function used for simulations in this study is shown in black (solid). The extended form that was not used is shown in black (dashed). 346

12.20 Time series of influential terms for the calculation of deposition rate in the ISHMAEL scheme. Left: the difference between initial and final ice particle radius (m) during deposition. Middle; the deposition density (kg m^{-3}). Right the combination of these terms as calculated in the deposition rate equation. Each variable is shown for a 60 minute simulation using an idealised box model with fixed average ice mass of 1×10^{-9} kg. Each time series is shown for several initialisation temperatures (shaded), which remain constant. 347

K.1 Deposition rates (L^{-1}) compared for Cooper curve (Morrison, red) and DeMott curve (ISHMAEL, blue). Y axis is $\log_{10}$ scale. Analysis produced via the Desmos Studio (2023) graphing calculator. 411

K.2 Number of contact nuclei (L^{-1}) used in Morrison (Meyers curve). Y axis is $\log_{10}$ scale.Analysis produced courtesy of the Desmos Studio (2023) graphing calculator. 412

M.1 Reflectivity components A and B (see Equation 6.8) and their summation (multiplied by 10) the total reflectivity Z_{total} (dBZ) versus the average rain droplet mass m_r (kg) for dendrites ($\delta_* = 0.6$, $\bar{\rho} = 100$). Terms A, B and the total are shown by dashed, dotted, and translucent lines. Components are plotted for three values of the ice number concentration n_i (kg^{-1}): 1×10^5, 1×10^2, 1×10^{-1} in columns 1–3, respectively, and three values of ice mass mixing ratio q_r (kg kg^{-1}): 1×10^{-8}, 1×10^{-4}, 1×10^{-2} in rows 1–3, respectively. 433

M.2 Reflectivity components, and the total reflectivity Z_{total} (dBZ) versus the average rain droplet mass m_r (kg) ($\delta_* = 1$, $\bar{\rho} = 400$) as in Figure M.1 for graupel hydrometeors. 434

N.1 Total reflectivity Z (dBZ, black), ice reflectivity component A (dBZ, blue), and mixed-phase reflectivity component B (dBZ, red) as shown in Equation 6.15 versus average ice particle radius r (m) for unrimed snow. Average crystal mass $m_i = 1 \times 10^{-10}$, 1×10^{-8}, 1×10^{-6} kg in columns 1–3, respectively. Average raindrop mass $m_r = 1 \times 10^{-10}$, 1×10^{-6}, 1×10^{-4} kg in rows 1–3, respectively. Three sets of fixed ice mass mixing ratio q_i and rain mass mixing ratio q_r are shown with differing line styles; base state $q_i = 1 \times 10^{-5}, q_r = 1 \times 10^{-2}$, decreased ice $q_i = 1 \times 10^{-6}, q_r = 1 \times 10^{-2}$ and decreased rain $q_i = 1 \times 10^{-5}, q_r = 1 \times 10^{-6}$ shown by solid, dashed, and dotted lines, respectively. 436

N.2 Total reflectivity Z (dBZ, black), ice reflectivity component A (dBZ, blue), and mixed-phase reflectivity component B (dBZ, red) as shown in Equation 6.15 versus average ice particle radius r (m) for partially rimed snow. See Figure N.1 for description. 437

O.1 Two PHIPS images (one image pair) of a single ice crystal (dark) from two lenses separated by an angle of 120°. 438

O.2 Example image-pair read in by the post processing script during Step 1. The crystal image may contain artefacts or other unwanted features at this stage. The crystal is identifiable by a near-opaque silhouette but exhibits blurring and intersection with the image boundary. 440

O.3 Example image-pair as in Figure O.2 after crystal-surface mapping has been applied (Step 2). The output data-field is a binary array (i.e. crystal=1, background =0) plotted here where the crystal area is mapped in yellow. . . 441

O.4 The boundary of the crystal edge is established in Step 3 from the predetermined crystal surface area (Step 2). The computed crystal borders are shown in green. 443

O.5 Example crystal with previously computed boundary (green). The maximum dimension of the boundary and its normal length are used to compute an ellipse (red) that conserves these quantities. The ellipse axes can be used to approximate the maximum dimension. 444

O.6 Three dimensional inferred properties of two 2-dimensional images separated by an angle of 120 degrees in the third dimension. (a) Two ellipsoids based on the boundary contours of the 2-dimensional images are represented at their relative angle. (b) identical ellipsoids as in (a) but with the viewing plane reoriented to the X-Y plane. (c) The projection of the ellipsoids in (b) against a two-dimensional plane (the projected area) 445

O.7 Height, width and aspect ratio variations of the two-dimensional projected area of a prolate ellipsoid during rotation. In panel (a) the prolate ellipsoid has z-parallel axis length equal to 2. In panel (b) the z-parallel axis length is equal to 8. In both cases the x and y-parallel axes have unit length. 447

P.1 Spatial locations of two WRF domains set up as detailed in the test run example. Domain 1 (D01, parent) indicated by white bounding box. Domain 2 (D02, nested) indicated by yellow box. Plotted variable is elevation (m) of the terrain within the domains. 460

Q.1 Graphical aid for the interpretation of NetCDF file structures adapted from Russell (2018). Single variables within a NetCDF data mirror the three-dimensional WRF domain structure which is compared to a Rubiks cube. Multiple Rubiks cubes represent the compartmentalisation of spatial data across the fourth time dimension at time step t_x. 465

Q.2 Comparison of loading times (s) for left: NetCDF files and right: NetCDF variables, of multiple file size. Loaded files correspond to Part II case one simulated domains one (green, 20 km), two (blue, 4 km), and three (red, 800 m). An exponential function with form shown in Figure legend is fit to NetCDF variables (blue, right) 469

Q.3 Load time (s, shaded) for a NetCDF file (left) and QRAIN variable (right) as a function of the loaded file or variable size (y-axis) and the system memory (Bytes) already in use during loading (x-axis). 469

Q.4 Variation of NetCDF variable system memory usage (MB) versus a variety of common datatype formats. As standard, variables are loaded as int64 type (orange) but can be converted to less precise data types (blue) during analysis. The function $y = \frac{A_0}{8}x$ is given in black, where x is the size of the datatype precision in bits (i.e. the suffix). A_0 is the total number of data points in the input array. 472

Q.5 Time saved (s) when using a late-stage concatenation method on NetCDF variables. Domains 1–3 (i.e. d01–do3) represent increasing array sizes in system memory. Left: variables loaded from Part II case study. Right: variables loaded from Part III case study one. 474

List of Tables

1 Units of measurement for quantities used in this thesis. 38

2 Metric prefixes relevant to the units used in this thesis. 39

1.1 The extent of the inclusion of capacitance as a term in the vapour deposition framework of microphysics schemes. The precipitation types that the capacitance term applies to are given under *Hydrometeors* 72

2.1 Review of measurement data obtained for each storm during the IMPACTS 2020 campaign. Crosses indicate that the data was obtained but not that the data was available for use at the time of writing. 84

2.2 Review of features and qualities found in storms during the IMPACTS 2020 campaign that were found to have the most comprehensive data sets (see Table 2.1). Cell shading indicates the suitability for this storm as a case study from most suitable (dark green) to least suitable (yellow). 84

3.1 Observations of precipitation type characteristics used for justification of the partition choices for P3 and ISHMAEL post-processing. Citations are [1]: Locatelli and Hobbs (1974), [2]:AMS (2020), [3]: Organization (1975), [4]: Prodi (1970), [5]:Knight (1986), [6]:Knight and Heymsfield (1983), [7]:Heymsfield et al. (2018), [8]:Heymsfield and Kajikawa (1987), [9]:Pruppacher and Klett (2010), [10]:Garrett et al. (2015), [11]:Westbrook (2008), [12]:Yagi (1970), [13]:Kneifel and Moisseev (2020), [14]:Sterzinger and Igel (2021), [15]:Nagumo and Fujiyoshi (2015), [16]:Braham (1963), [17]:Mosimann et al. (1994), [18]:Dowling and Radke (1990), [19]:Korolev and Isaac (2003), [20]:Gibson et al. (2009), [21]:Ishizaka (1993) 106

6.1 Characteristic density (kg m^3), Inherent Growth Ratio (IGR) and radius (m) for three characteristic precipitation-type profiles in the ISHMAEL scheme. 180

6.2 Characteristic density (kg m^3) and rime fraction F_r for three characteristic precipitation-type profiles in the P3 scheme. 191

8.1 Observed and simulated snow depth parameters in the ISHMAEL and Morrison schemes. Parentheses indicate values owed to snow only. Square brackets indicate values owed to ice components only. 240

12.1 Relationship between spheroid axes a and c and the axes of a governing ellipse 306
12.2 Theoretical Capacitance of spheroids adapted from McDonald (1963) . . . 311
12.3 Functions for the capacitance of ice crystals as determined by Westbrook et al. (2008). The capacitance is a function of the maximum crystal dimension D, the length of the basal face a, and the aspect ratio $\mathcal{A}$. 313
12.4 Power law parameters for oblate and prolate crystals adapted from Harrington et al. (2013). 328
12.5 Variable values and ranges for a capacitance-testing box-model. Average crystal mass K (kg), Ambient Temperature T (K), Ambient pressure P (Pa), and vapour mass mixing ratio q_v (kg kg^{-1}). 337
12.6 List of simulated qualities output by the idealised box model for the ISHMAEL microphysics scheme. 340
12.7 List of simulated qualities output by the idealised box model for the Morrison microphysics scheme. 340
12.8 Initial conditions for the box model as tested in this chapter. 341

L.1 Parameterised relationship between temperature (°C) and cloud-ice rime density (kg m^{-3}) featured in the ISHMAEL scheme, described by (Jensen et al. 2017) and adapted from measurement by Macklin (1962). The parameter β_{T_l} is a function of temperature shown in Equation L.2.2. 425

P.1 Useful links and resources for users of the WRF model or the University of Manchester CSF 449

S.1 Review of available measurement data products for an IMPACTS storm (see Table 2.1). Information pertains to storm case one (Part III). Data product indicates the equipment used to retrieve measurement data. Full data product names can be found in the abbreviations and acronyms section. Available indicates whether the data was available to download at the onset of Part III analysis. Type lists the variables obtained by the measurement equipment. 479

Terms and Abbreviations

Abbreviations and Acronyms

2DVD	Two-Dimensional Video Disdrometer (Kruger and Krajewski 2002)
AHAB	Adaptive-habit framework (J.-P. Chen and Lamb 1994)
AMPR	Advanced Microwave Precipitation Radiometer
APU	Autonomous Parsivel Unit
ASOS	Automated Surface Observing Systems
AVAPS	Advanced Vertical Atmospheric Profiling System
BATS	Biosphere-Atmosphere Transfer Scheme (Yang and Dickinson 1996)
CC	Correlation Coefficient of reflectivity field
CCD	Charge-coupled device
CCMEP	Canadian Centre for Meteorological and Environmental Prediction
CCN	Cloud-condensation-nuclei
CONUS	Contiguous United States (WRF physics-suite option)
CoSMIR	Conical Scanning Millimetre-wave Imaging Radiometer
CPI	Cloud Particle Imager
CPL	Cloud Physics Lidar
CRS	Cloud Radar System
CSF3	Computational Shared Facility v.3 (Manchester Research IT 2023)
DGZ	Dendritic Growth Zone
DVN	National Weather Service Office based at Davenport, Iowa
ECMWF	European Centre for Medium-Range Weather Forecasts
ERA5	ECMWF Global Reanalysis Data Set (Hersbach et al. 2020)
EXRAD	ER-2 X-band Doppler Radar
Fast-CDP	Fast Cloud Droplet Probe
FEMA	Federal Emergency Management Agency (U.S.)
GFDL-CM3	Geophysical Fluid Dynamics Laboratory Climate Model (Donner et al. 2011)
GFS	Global Forecast System (NOAA/NCEP)
GOES	Geostationary Operational Environmental Satellite
GPU	Graphics Processing Unit
GYX	National Weather Service Office based at Gray/Portland, Maine
HadGEM2	Hadley Centre Global Environment Model (Martin et al. 2011)

HIWRAP	High-Altitude Wind and Rain Airborne Profiler
HPC	High Performance Computer
ILX	National Weather Service Office based at Lincoln, IL
IMPACTS	Investigation of Microphysics and Precipitation for Atlantic Coast-Threatening Snowstorms
ISHMAEL	Ice-Spheroids Habit Model with Aspect-Ratio Evolution (Jensen et al. 2017)
KALB	NWS Radar site based at Albany
KASPR	Ka-band Scanning Polarimetric Cloud Radar based at Stony Brook University, Long Island, NY
KBUF	NWS WSR-88D Radar site based at Buffalo, New York
KGYX	NWS WSR-88D Radar site based at Portland
KOKX	NWS WSR-88D Radar based at Upton, New York
LIP	Lightning Instrument Package
LSM	Land Surface Model
LWC	Liquid Water content
m-D	Mass-Dimension distribution hypothesis
Morrison	Morrison Two-Moment Microphysics Scheme (Morrison et al. 2005)
MP	Microphysics-derived (snow depth)
mPING	Meteorological Phenomena Identification Near the Ground (Elmore et al. 2014)
MRR2	Micro Rain Radar 2
MWR	Microwave Radiometer
NAM	North American Mesoscale Forecast System
NASA	National Aeronautics and Space Administration (U.S.)
NCAR	US National Center for Atmospheric Research
NCEP	National Centers for Environmental Prediction
NCSU	North Carolina State University
NEXRAD	NWS Next-Generation Doppler Radar, technical name WSR-88D
NOAA	National Oceanic and Atmospheric Administration
NOAH-MP	National Centers for Environmental Prediction, Oregon State University (Department of Atmospheric Sciences), Air Force, NWS Hydrology Lab with Multi-Physics options
NPOL	NASA S-band Dual Polarimetric Radar
NWS	National Weather Service
P3	Predicted Particle Properties microphysics scheme (Morrison and Milbrandt 2015)
P-3	NASA Observation Aircraft
PBL	Planetary Boundary Layer
PDS	Particle detection system
PHIPS	Particle Habit Imaging and Polar Scattering (Abdelmonem et al. 2016a)
PPI	Plan Position Indicator
PSD	Particle Size Distribution

RGEM	Regional Global Environmental Multiscale Model developed by CCMEP (Mohammadlou et al. 2022)
RHI	Range-Height Indicator
SBNY	Stony Brook University, New York
SBU	Stony Brook University, New York (IMPACTS Data set)
SLR	Snow-to-Liquid Ratio
SO	Southern Ocean
TAMMS	Turbulent Air Motion Measurement System
U.S.	United States of America
UAlbany	University at Albany
UIUC	University of Illinois Urbana-Champaign
UND	University of North Dakota
WBF	Wegener–Bergeron–Findeisen process
WRF	The Weather Research and Forecasting model version 4.3 (Skamarock et al. 2019)
WSM6	WRF Single-Moment 6-class Microphysics scheme (Song-You Hong and Lim 2006)
WSR-88D	Weather Surveillance Radar 1988 Doppler operated by NWS
YSU	Yonsei University PBL (Song-You Hong et al. 2006)
Z	Radar reflectivity factor
Z_{DR}	Differential radar reflectivity factor

Relevant States and Territories of the U.S.

CT	Connecticut
FL	Florida
ID	Idaho
IL	Illinois
IN	Indiana
KS	Kansas
MA	Massachusetts
ME	Maine
MI	Michigan
MO	Missouri
MT	Montana
NC	North Carolina
NH	New Hampshire
NJ	New Jersey
NY	New York
OK	Oklahoma
PA	Pennsylvania
TX	Texas
VT	Vermont
WA	Washington State

Terms Derived From Source-Codes

ISHMAEL

`AFN`	Combined heating and ventilation term
`IWCF`	Ice water content after deposition
`IWCI`	Ice water content prior to deposition
`QSMALL`	Small ice mass mixing ratio limit
`NU`	Shape parameter in particle size distribution
`PRD`	Mass tendency due to deposition
`PRDR`	Mass tendency due to riming
`varcheck`	Variable checking routine
`IGR`	Inherent growth ratio due to ambient temperature at time step start

Morrison

`ABI`	Latent heating term correction to deposition rate
`CPM`	Specific heat capacity of moist air at constant pressure
`DCS`	Cloud ice maximum diameter / threshold for autoconversion to snow
`DV`	Diffusivity of water vapour in air
`EPSI`	Inverse phase relaxation time for ice hydrometeor category
`EPSS`	Inverse phase relaxation time for snow hydrometeor category
`F1S`	Ventilation parameter for snow
`F2S`	Ventilation parameter for snow
`GAMMA(x)`	Euler gamma function of parameter x
`LAMI`	Slope parameter for ice hydrometeor category
`LAMS`	Slope parameter for snow hydrometeor category
`LAMG`	Slope parameter for graupel hydrometeor category
`NOI`	Intercept parameter for the ice hydrometeor category
`NOS`	Intercept parameter for the snow hydrometeor category
`OPT_SNF`	LSM namelist option for the parameterisation of frozen fraction
`PI`	Mathematical constant π
`PRD`	Mass deposition tendency to the ice hydrometeor category
`PRDG`	Mass deposition tendency to the graupel hydrometeor category
`PRDS`	Mass deposition tendency to the snow hydrometeor category
`QSMALL`	Small ice mass mixing ratio limit
`QV3D`	Water vapour mixing ratio
`QVI`	Ice saturation mixing ratio
`QVS`	Saturation mixing ratio
`RHO`	Air density
`RHOI`	Bulk density of ice
`SNOWH`	Accumulated snow depth
`T3D`	Temperature (K)
`XXLS`	Latent heat of sublimation

Mathematical Terms and Constants

General / Shared

$\odot$	Hadamard product
α	Shape parameter in the general form of the gamma distribution
$\alpha_{\odot}$	Constant that accounts for the phase of water in the Stoelinga (2005) reflectivity equation
β	Rate parameter in the general form of the gamma distribution
Γ	Euler Gamma function
λ	Size distribution slope parameter of general hydrometeor
λ_g	Size distribution slope parameter of graupel hydrometeor category
λ_i	Size distribution slope parameter of ice hydrometeor category
λ_r	Size distribution slope parameter of rain hydrometeor category
λ_s	Size distribution slope parameter of snow hydrometeor category
ϕ	Aspect ratio of a spheroid
ρ_a	Density of air
ρ_g	Density of graupel
ρ_h	Density of hail
ρ_i	Density of ice (general)
ρ_l	Density of liquid water
ρ_r	Density of rain
ρ_s	Density of snow
μ_a	Viscosity of air
η_0	Permittivity of free space
A	Area
A_{hp}	Surface area of a hexagonal prism
A_{ob}	Surface area of an oblate spheroid
A_{pr}	Surface area of a prolate spheroid
a	Spheroid a-axis radial length
C	Crystal capacitance
C_0	Dimensionless Capacitance
C_{pw}	Heat capacity of water
c	Spheroid c-axis radial length
c_p	Specific heat of dry air at constant pressure
D_c	Hexagonal crystal principle axis length
D_G	Diameter of Graupel
D_m	Maximum particle dimension
D_T	Total accumulated snow depth
$\bar{D}(t)$	Accumulated snow depth across the time interval t
D_v	Diffusivity of water vapour in air
e_o	Eccentricity of oblate spheroid
e_p	Eccentricity of prolate spheroid

F_{ice}	Fraction of precipitation that is frozen
$f(x)$	Probability density function of the gamma distributed variable x
f_h	Particle size ventilation coefficient (see Lamb and Verlinde (2011) Eq. 8.85)
f_v	Particle size ventilation coefficient (see Lamb and Verlinde (2011) Eq. 8.85)
h	Hexagonal crystal height
J	Total mass flux of frozen precipitation reaching the surface over time period T
j	Mass flux of frozen precipitation reaching the surface per second
K	Ratio of crystal mass to number concentration (or mixing ratio), analogous to average crystal mass
k_t	Thermal conductivity
L_{total}	Combined liquid equivalent precipitation across a time step
l_f	Enthalpy of fusion
l_v	Enthalpy of vaporisation
m_I	Total mass of ice
m_{dep}	Mass of ice gained or lost due to deposition
m_{melt}	Mass of ice gained or lost due to melting
m_{nuc}	Mass of ice gained or lost due to nucleation
m_{rime}	Mass of ice gained or lost due to riming
N	Total number concentration of general gamma distributed hydrometeor
N_0	Intercept of the gamma distribution
n_x	Number mixing ratio of general gamma distributed hydrometeor x
$O(f)$	Omit the contributions of function f (*Big O'* notation)
Q	Total mass concentration of general gamma distributed hydrometeor
q	Mass mixing ratio of general gamma distributed hydrometeor
r	Hexagonal crystal basal length radius
S_c	Schmidt Number
s	Hexagonal crystal side length
s_i	Supersaturation over ice
Δt_h	WRF history interval time period
T	Temperature (K)
T_{fz}	Freezing temperature (K)
T_s	Surface temperature (K)
T_R	Residency time of prognostic variable (see section 5.3
V	Volume
V_{hp}	Volume of hexagonal prism
V_{sph}	Volume of spheroid
v_{i}	Fall speed of ice
z	Liquid equivalent depth of frozen precipitation
Z_g	Radar reflectivity component of graupel
Z_r	Radar reflectivity component of rain
Z_s	Radar reflectivity component of snow

ISHMAEL

α_*	Shorthand for factor $a_0^{1-\delta_*}$
α_a	Mass growth efficiency for the spheroid a-axis length
α_c	Mass growth efficiency for the spheroid c-axis length
α_{nr}	Mass growth efficiency for the equivalent spheroid radius r
α_{cap}	Factor in relation of capacitance and a-axis length
$\bar{\rho}$	Average ice density
ρ_{dep}	Density of new ice mass gained by deposition
ρ_{rime}	Density of new ice mass gained by riming
φ	Aspect ratio
δ	Inherent growth ratio
δ_*	Average inherent growth ratio of all processes
δ_x	Inherent growth ratio for process x
δ_{cap}	Average inherent growth ratio for capacitance relation
δ_{dep}	Average inherent growth ratio during deposition
δ_{rime}	Average inherent growth ratio during riming
δ_{melt}	Average inherent growth ratio during melting
ν	Shape parameter in particle size distribution
ϵ	Exponent including the artificially bound inherent growth ratio (see Eq. C.5)
ε	Ratio of liquid-phase reflectivity component to solid phase reflectivity component (mixed-phase contribution)
γ_n	The ratio of raindrop number mixing ratio to ice number mixing ratio
γ_{r_i}	ratio of initial equivalent spheroid axis to initial a-axis
κ_{r}	Ratio of final to initial equivalent spherical radius
A	Solid phase component of total reflectivity factor
$\bar{a}$	Average a-axis size
a_0	Initial spheroid a-axis size
a_1	Coefficient in power law relation of shape factor and aspect ratio
a_2	Coefficient in power law relation of shape factor and aspect ratio
a_i	Ice a-axis mixing ratio
a_n	Characteristic a-axis length
a_{ni}	Initial characteristic a-axis length prior to microphysical process
a_{nf}	Final characteristic a-axis length after microphysical process
B	Mixed phase component of total reflectivity factor
b_1	Coefficient in power law relation of shape factor and aspect ratio
b_2	Coefficient in power law relation of shape factor and aspect ratio
C_I	Distribution averaged capacitance
C_i	Single crystal capacitance
c_1	Coefficient in power law relation of capacitance and a-axis length
c_2	Coefficient in power law relation of capacitance and a-axis length
c_i	Ice c-axis size at time t
d_1	Coefficient in power law relation of capacitance and a-axis length
d_2	Coefficient in power law relation of capacitance and a-axis length

$\bar{f}_s$	Shape factor of spheroidal ice for equivalent volume sphere
G_i	Effective diffusion coefficient (see Lamb and Verlinde 2011 p. 343, Equation 8.41)
m_r	Average raindrop mass
q_{s0}	Saturation vapour mixing ratio at 0°C
R	Ratio of a_i to a_0
r_n	Characteristic r-axis length
r_{ni}	Initial characteristic r-axis length prior to deposition
r_{nf}	Final characteristic r-axis length after deposition
$Z_{\text{i1/2/3}}$	Radar reflectivity component of ice-types 1–3, respectively

Morrison

δ_0	Ice supersaturation at the beginning of the time step
τ	Phase relaxation time
τ_i	Phase relaxation time of ice hydrometeor category
τ_s	Phase relaxation time of snow hydrometeor category
τ_g	Phase relaxation time of graupel hydrometeor category
ρ	Density of general hydrometeor category
ω	Ratio of liquid to solid precipitation mass
A_s	Constant in the fall-speed-diameter relation for snow
a_f	Parameter in the mass-fall speed relation
B_s	Constant in the fall-speed-diameter relation for snow
b_f	Parameter in the mass-fall speed relation
c_m	Constant in mass dimensional relationship
c_p	Specific heat at constant pressure for moist air
$\bar{D}$	Mean diameter length
D	Hydrometeor Particle diameter in mass-diameter and particle size distribution relationships
E_{II}	Collection efficiency of ice-ice collisions
f_1	Ventilation Coefficient 1c (see Pruppacher and Klett (2010))
f_2	Ventilation Coefficient 2 (see Pruppacher and Klett (2010))
L_s	Latent heat of sublimation
N_0	Intercept of gamma distribution for general hydrometeor
N_{0i}	Intercept of gamma distribution for ice hydrometeor class
N_{0s}	Intercept of gamma distribution for snow hydrometeor class
P_c	Spectral parameter in size distribution relation
Q_2	Latent heating term correction to deposition rate (see `ABI`)
q_{si}	Ice saturation mixing ratio
q_{sw}	Water vapour mixing ratio at saturation

P3

ε	Ratio of liquid-phase reflectivity component to solid phase reflectivity component (mixed-phase contribution)
γ_n	The ratio of raindrop number mixing ratio to ice number mixing ratio
ρ_r	Density of accreted rime
ρ_v	Volume of accreted rime
μ	Particle size distribution shape parameter
χ_ρ	Fall speed density correction term in melting equation
A	Solid phase component of total reflectivity factor
B	Mixed phase component of total reflectivity factor
F_5	Fall speed related variable (see Eq. 8.12)
F_{14}	Fall speed related variable (see Eq. 8.12)
F_r	Rime fraction
m_r	Average raindrop mass
q_sat0	Saturation vapour mixing ratio at 0°C

Units of Measure and Prefixes

Symbol	Name
atm	Standard Atmosphere
B	bel
b	bar
°C	degree Celsius
ft	feet
g	gram
Hz	Hertz
in.	inches
K	Kelvin
m	metre
min	minute
Pa	Pascal
s	second
UTC	Coordinated Universal Time

Table 1. Units of measurement for quantities used in this thesis.

Symbol	Name	Base 10
G	Giga	10^9
M	Mega	10^6
k	Kilo	10^3
h	Hecto	10^2
da	Deca	10^1
d	Deci	10^{-1}
c	Centi	10^{-2}
m	Milli	10^{-3}
μ	Micro	10^{-6}
n	Nano	10^{-9}
p	Pico	10^{-12}

Table 2. Metric prefixes relevant to the units used in this thesis.

Declaration of Originality

The University of Manchester
PhD by Monograph: Candidate Declaration

Candidate Name: Joshua J. Carter

Faculty: Science and Engineering

School: Natural Sciences

Department: Earth and Environmental Sciences

Thesis Title: Mixed-Phase Ice-Particle Growth Mechanisms in Mesoscale Model Simulations of Northeast U.S. Extratropical Cyclones

Declaration to be completed by the candidate:

I hereby confirm that no portion of the work referred to in the thesis has been submitted in support of an application for another degree or qualification of this or any other university or other institute of learning.

Signed:

Date: 8/09/2023

Copyright Statement

i The author of this thesis (including any appendices and/or schedules to this thesis) owns certain copyright or related rights in it (the “Copyright”) and s/he has given The University of Manchester certain rights to use such Copyright, including for administrative purposes.

ii Copies of this thesis, either in full or in extracts and whether in hard or electronic copy, may be made *only* in accordance with the Copyright, Designs and Patents Act 1988 (as amended) and regulations issued under it or, where appropriate, in accordance with licensing agreements which the University has from time to time. This page must form part of any such copies made.

iii The ownership of certain Copyright, patents, designs, trademarks and other intellectual property (the “Intellectual Property”) and any reproductions of copyright works in the thesis, for example graphs and tables (“Reproductions”), which may be described in this thesis, may not be owned by the author and may be owned by third parties. Such Intellectual Property and Reproductions cannot and must not be made available for use without the prior written permission of the owner(s) of the relevant Intellectual Property and/or Reproductions.

iv Further information on the conditions under which disclosure, publication and commercialisation of this thesis, the Copyright and any Intellectual Property and/or Reproductions described in it may take place is available in the University IP Policy (see `http://documents.manchester.ac.uk/DocuInfo.aspx?DocID=24420`), in any relevant Thesis restriction declarations deposited in the University Library, The University Library’s regulations (see `http://www.library.manchester.ac.uk/about/regulations/`) and in The University’s policy on Presentation of Theses.

Acknowledgements

To my family, who didn't really know where I was, what I was doing, or even why I was doing it but supported me nonetheless. You accepted my absence without complaint and greeted me on my return as if I had never left. I am so thankful for your unwavering encouragement and the refuge you provided from the demands of my PhD. Thank you most of all to my Mom and Julian who have provided unconditional support over many difficult years. I couldn't have reached this point without you, this is as much your achievement as mine.

I extend heartfelt thanks to Dave, who has guided me through this daunting process and has always made me feel as though my thoughts had value and merit. You have supported me through difficult times and reminded me what science is truly all about. Your feedback has kept me grounded and I'm all the better for it.

I'm deeply appreciative of the NCAS group at the University of Manchester particularly Geraint Vaughan, Paul Connolly and Douglas Lowe, who have each provided excellent advice and world-class expertise. I must also thank my viva examiners Hugh Coe and Chris Westbrook for generously dedicating their time and providing a thought-provoking discussion.

A special tribute goes to my *Leeds-Family* who have shaped the person I've become. Your kindness and success inspire me endlessly. I cherish the brief moments we steal together on the all-too-few occasions that they arrive.

Of course, I must pay tribute to Jack and James with whom I weathered four years of doctoral studies, three Prime Ministers, two barely liveable flats, and one global pandemic. It worked well because we understood what each other was going through. I have loved living with you these past few years and I can't imagine Manchester without you.

Finally, to Natalie. You are an endless source of motivation, happiness and comfort. Your understanding has been unwavering throughout this process, I hope I have done you proud. Thank you for everything

This project was sponsored a NERC funded doctoral studentship. The author would like to acknowledge and thank NERC for their support throughout the doctoral programme.

Abstract

Weather predictions from bulk numerical models can be sensitive to how cloud microphysical processes are parameterised, especially in mixed-phase scenarios involving vapour deposition, riming, and melting. Conventional microphysics schemes represent these processes as transfers of mass or number between fixed precipitation categories, but they struggle to capture the nuanced qualities of ice particles, such as density or habit. To address this, a new mathematical framework of free-ice categorisation has been developed to continuously track and evolve ice particle qualities, allowing for a wider range of characteristics.

New microphysics schemes; P3 and ISHMAEL have been designed to improve predictions of riming, a crucial process for precipitation growth. P3 tracks rimed density, while ISHMAEL tracks ice geometry. These schemes remain relatively untested and may introduce uncertainties to riming and other mixed-phase processes. The question remains whether these schemes enhance microphysical process predictions and precipitation forecasts. To answer this, ISHMAEL, P3, and a conventional scheme; Morrison, were tested in two northeast U.S. snowstorm case studies simulated by the Weather Research and Forecasting model (WRF). The storms exhibited extremely high (> 50 dBZ) radar reflectivity, heavy snowfall and mixed-phase periods, and were supported by various measurements including radar and IMPACTS campaign data products.

Predicted precipitation was remarkably diverse amongst the simulations. All schemes underestimated observed snowfall depth, particularly density-predicting schemes. ISHMAEL's inclusion of ice habit parameterisation generated more ice mass and graupel compared to P3 and Morrison and radar reflectivity predictions were strongly dependent on the rates of riming and wet growth aloft supported by ice habit evolution. Increased vapour deposition to ISHMAEL ice habits indirectly influenced accretion, resulting in higher ice and water mass mixing ratios than the other schemes. It was identified that geometric capacitance was a source of divergence between conventional and habit-diagnosing schemes. However, a small study of isolated vapour deposition in a box model showed that differences in the vapour depositional framework related to the mass-distribution hypothesis artificially increased deposition rates more significantly than capacitance and should also be investigated in future schemes. Further work is required to standardise emerging schemes and recommendations are made to improve these schemes in the immediate future.

Lay Abstract

Computational models are used to predict and study weather events by incorporating real-world measurements into mathematical equations representing atmospheric mechanics. To handle complex interactions between numerous particles in some atmospheric processes, simplification, or *parameterisation*, using a small number of equations becomes necessary. While predicting interactions in bulk introduces uncertainty, it is necessary to manage computational complexity. These parameterisations are grouped into microphysics schemes, which are the subject of ongoing research and debate

A key source of uncertainty are particle interactions between solid and liquid water, the *mixed-phase*, where interaction processes and the method of representing particles have been called into doubt. Novel microphysics schemes aim to provide new methods of particle representation that better capture interactions in the mixed-phase; ISHMAEL captures the geometry of ice as it gains mass, and P3 determines the density. However, these schemes have not undergone rigorous testing, and it is not known how these representations may affect the vast array of microphysical processes.

In this study, we evaluated the performance of ISHMAEL, P3, and the conventional Morrison scheme in two case studies of north-east U.S. Winter Storms simulated by the WRF model. We focused on how each scheme's mathematical underpinnings influenced their ability to replicate observed precipitation qualities such as radar reflectivity signature, snow depth and density, precipitation type and amount, amongst others. To support our findings, we utilised observational data sets including the findings of the IMPACTS campaign, encompassing radar and both on-ground and aerial *in situ* ice geometry sampling.

It was determined that the introduction of ice geometry can drastically alter the amount and type of precipitation that is forecast at the ground. Whereas, the unconstrained prediction of ice density causes inconsistent predictions of snow depth. While conventional ice frameworks provided moderate and reliable predictions, they fell short in predicting extreme phenomena. Notably, conventional frameworks benefit from wide compatibility with other areas of the model. Adapting emerging ice particle representations into the broader model poses a formidable challenge, despite their potential to enhance forecasting capabilities. Considerable work is required to adapt emerging ice particle representations if these schemes are to become a mainstay in the arsenal of forecasters.

Part I

Review and Methodology

Chapter 1

Literature Review

Within the field of atmospheric science, weather encompasses a spectrum of short-term atmospheric conditions, giving rise to a diverse array of meteorological phenomena ranging from overcast skies to hurricanes. The weather at its most extreme can be destructive to property, infrastructure and livelihoods, even causing fatalities, but even in more modest conditions, the weather can be surprisingly impactful. Predicting, or *forecasting* the weather is therefore a valuable tool providing multiple benefits to individuals and businesses alike.

In the early twentieth century Bjerknes (1904) had established weather predication as an initial value problem of mathematics, identifying two requirements: sufficiently accurate physical equations of the atmosphere, and sufficient observations of atmospheric conditions to initialise them. Iterative integration of the equations at a rate faster than real-time could thus enable a forecast. However, a third, more practical requirement emerged: achieving the great many necessary calculations at speed. Famously, Richardson (1922) posed that 64,000 human-computers could process the data in unison (Figure 1.1) but completing the task quickly enough remained unlikely. Reviewing Richardson, Woolard (1922) captured the exasperation of their contemporaries;

> *“What satisfaction is there in being able to calculate to-morrow’s weather if it takes us a year to do it?”.*

With remarkable foresight, Bjerknes signalled his faith in science to achieve a solution in the future (Schultz and Lynch 2022). By the end of the twentieth century, exponential advances in technology and our understanding of atmospheric physics have more than satisfied Bjerknes’ conjectures. In addition, modern computers have enabled the rapid integration of physical equations faster than real-time at small spatial and temporal scales or high resolution. As of the time of writing, modern supercomputers have reached exascale computation; at least 10^{18} 64-bit Double Precision operations per second, which is approximately equal to a hundred million earth populations working in unison at the rate of one calculation per second.

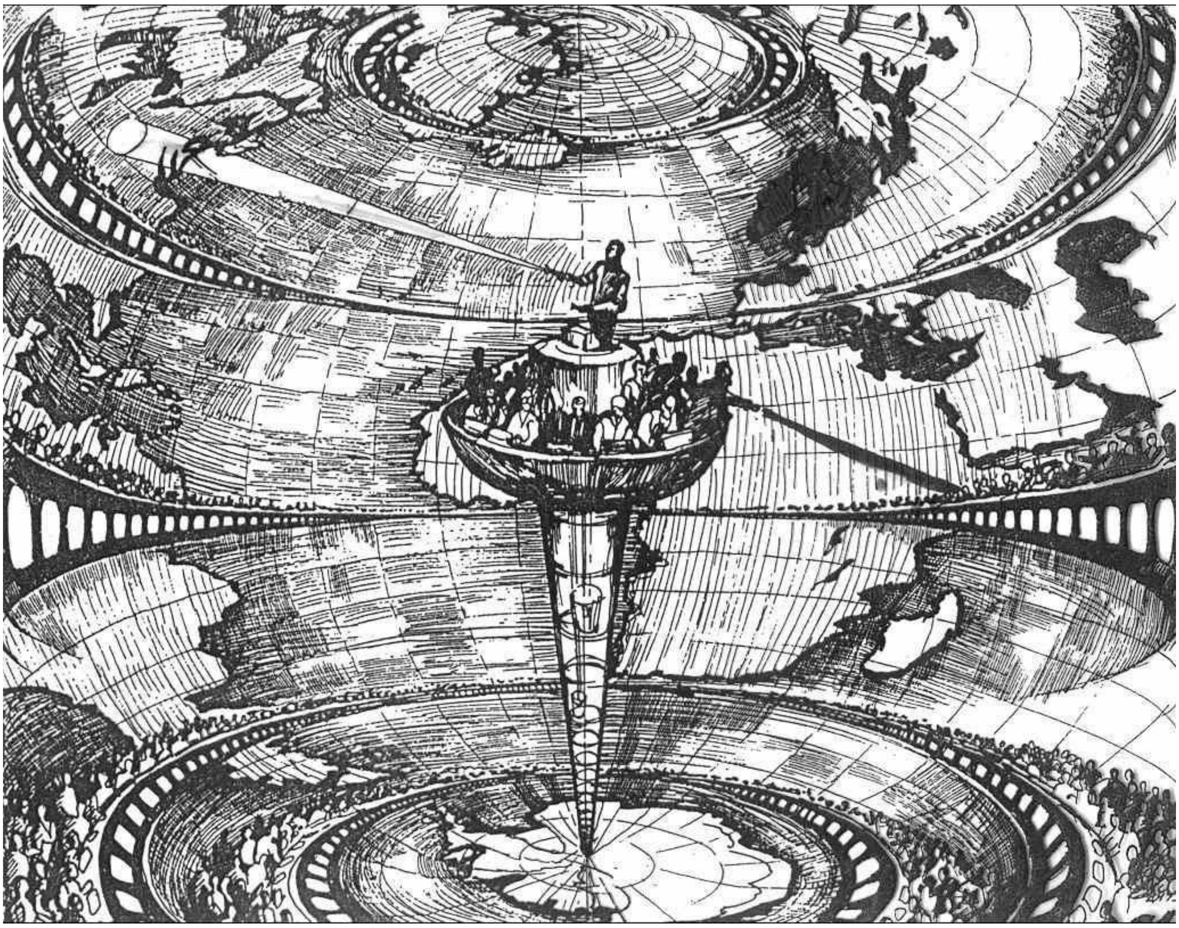

Figure 1.1. Sketch of a human-powered weather forecasting computer as hypothesised by Richardson (1922) . A conductor organises with a light the symposium of human computers who sit in many rows (Courtesy A. Lannerback, Dagens Nyheter, Stockholm).

Modern numerical models aren't dissimilar to Richardson's original model. The region to be studied is divided into three dimensional grid cells that span the atmospheric extent. The governing equations are applied to the grid and integrated forwards in time by a single time step, with the results shared to neighbouring cells. Once all grid cells have been integrated the future state of the atmosphere has been forecast by a single time step. If required, this process can be repeated iteratively to obtain an atmospheric state any number of time steps into the future, although it is widely regarded that the limitations of computational precision and chaotic nature of the atmosphere place the upper limit of predictability at two weeks (Lorenz 1963). The accuracy of the forecast is dependent upon several factors, primarily the reliability of the governing equations, the precision and extent of the initialising measurements, and the spatial (grid length) and temporal (time step) resolution of the model. In general, the latter two factors evolve with the pace of technology, whereas considerable debate surrounds the ideal formulation of equations to represent complex atmospheric processes.

The mathematical representation of clouds is a key source of uncertainty in numerical models for weather and climate (Morrison et al. 2020; Schneider et al. 2017; Zelinka et al. 2016). On the climate scale, clouds absorb and reflect energy which is significant for the retention of heat. The frequency and distribution of clouds are therefore important to capture for reliable climate projections. Whereas on the weather scale, clouds are harbingers of precipitation, so the ability to accurately represent the mathematics of clouds or *cloud microphysics* is essential to the accurate prediction of precipitation at the surface. Much uncertainty in modern day weather forecasts derives from the small (10^{-7}–10^{-1} m) scale of cloud particles and microphysical processes that do not generalise well to the much larger scale of resolutions used in numerical models (10^{1}–10^{5} m) or climate forecasting (10^{5}–10^{7} m). To understand the complexities of clouds across scales it is first important to understand the constituent particles and their microphysical interactions.

Cloud particles or *hydrometeors*, are water-based structures formed within the cloud structure that collectively with water vapour distinguish the cloud from typical atmosphere. Numerous hydrometeor types have been classified according to their method of formation, phase or combination of phases. For example, solid phase hydrometeors include suspended ice crystals, snow and hail, whereas liquid phase hydrometeors include micrometre scale droplets, drizzle and raindrops. Further classification exists based on particle temperature such as supercooled droplets that remain liquid below 0 °C, or so-called liquid skin ice that melts from outside to inside. Where discernible variation in precipitation structure or development presents itself to human eyes, a new class of hydrometeor has shortly followed. This is perhaps no more true than with the identification and classification of an ice crystal's shape or geometry, known as the crystal *habit*.

In general, habit refers to vapour-grown ice crystals that exhibit distinct, hexagonal structures and consequently they lie within the definition of ice crystal or snow crystal hydrometeors. At the most rudimentary level, ice habits mirror the hexagonal structure of the H_20 lattice to form plates or columns, depending on the ratio of the crystal lengths along its principal axis and basal plane. More complex habits are usually structural variations or combinations of these geometries. For example, sectored plates and dendrites exhibit branching at the plate corner, and capped-columns result from plate like growth at the edge of pre-formed columns. A multitude of crystal habits have been catalogued and organised, however creating a comprehensive catalogue of ice habits is difficult simply due to the large number of possible geometries that can occur. For example, Magono (1962) formulated 27 types of snow crystals alone, and Bailey and Hallett (2004) has highlighted the fine-scale differences across even singular categories of habit, of which a subsection are shown in Figure 1.3. Ultimately, the habit is an important feature of precipitation because it can modify the rates and efficiencies of various microphysical processes.

Interactions that occur between hydrometeors causing the transfer of mass, particle number, or any other quality are termed microphysical processes. Figure 1.2 provides an example of some of the possible processes that exist in reality and that are represented in a two-moment numerical model. Note that the majority of interactions are mixed-phase (operating between hydrometeors that occupy different phases of water), which proves a significant barrier to forecasts given that mixed phase processes are notoriously difficult to accurately represent (Grabowski et al. 2018). These mixed phase processes are important to the development of the cloud structure and the precipitation field. Nucleation of crystals and water droplets from vapour is integral to the correct partitioning of water and the subsequent development of precipitation. Similarly, deposition and condensation form primary hydrometeor growth processes at an early stage. The rate at which these processes take place is important for the correct partitioning of mass and number concentrations in numerical models, which has long been a focus of conventional two moment microphysics schemes. However, for the ice phase there are other substantial characteristics to be considered. The aforementioned habit is intricately related to the deposition process, though the growth of any one habit is highly sensitive to the ambient environmental conditions (see Figure 1.8). Another example is the formation of graupel by the process of accretion.

The accretion process concerns the growth of a hydrometeor by the collection of solids or liquids, the former producing aggregated structures and the latter forming surface layers of varying density. The growth of ice by the accretion of liquid droplets is termed either dry or wet growth, depending on the phase of droplets immediately after accretion. The wet growth regime considers the accretion of droplets that remain in a liquid state immediately after accretion (Phillips et al. 2014). This may occur if the accretion intensity is sufficiently high that the latent heat of freezing droplets raises the ice surface to near 0°C (Ludlam 1951). During wet growth a liquid-skin coating distributes evenly across the ice surface causing smooth surface geometries that may subsequently refreeze, or exhibit shedding into water droplets, which is an important secondary ice mechanism (Pruppacher and Klett 2010). However, in most instances the impact of a supercooled water droplet to an ice crystal surface is sufficient to instantaneously freeze it at the ice surface, preserving its geometry and modifying that of its host. Thus, the geometrical modification incurred by the dry growth regime is radically different to that in the wet growth regime. Dry growth or *riming* is an important pathway for ice habit modification.

Riming is commonplace in mixed phase clouds and requires only the presence of the constituent particles and a difference in relative fall speeds, which is readily obtainable by sedimentation of particles or forcing of particles in updrafts. Once heavily rimed, the resulting graupel particle is near spherical and resembles soft hail. However, partially rimed particles are much more geometrically complex due to the combined geometries of the initial habit and the random nature of riming collisions. These partial, or transitional states of riming are significant because riming is an efficient and fast paced method of ice growth in clouds

(Ávila et al. 2009). The riming process has implications for ice density and geometry, fall velocities, droplet depletion, liquid water content (LWC) and cloud longevity; it is a key precursor to precipitation (Harimaya 1975) and vital for electrification (Tsutomu Takahashi 1978) and snow density predictions (Roebber et al. 2003).

Harimaya (1975) and Ono (1969) were amongst the first to complete comprehensive measurements of riming. Their studies spanned several ice habits, of many size distributions, and the interaction of these crystals with a drop spectrum. The habit of a crystal could determine its ability to rime, with generally more porous crystals requiring a larger crystal size to initiate riming (Harimaya 1975); columns accrete at smaller sizes than plates, branch thickness was also an important riming parameter. Ono (1969) found that crystals rimed along a certain axis of preference, which depended on temperature. Even in these early studies, the complexity of collection efficiencies was well demonstrated, and many of the criteria listed remain absent in current cloud models. The effect of crystal re-orientation along its largest dimension is crucial to the parameterisation of fall speeds (Erfani and Mitchell 2017; Ono 1969); deducing the orientation and projected area effects upon riming, are still ongoing (Dunnavan and Jiang 2019; Erfani and Mitchell 2017). It was well noted that the collection efficiency may be of secondary importance to the habit formation region, as crystals forming higher up would have a longer collisional path which was the overall determinant for the amount rime accreted (Harimaya 1975; Ono 1969). While the differing origins of habits are often featured in microphysics schemes, the associated link between mass growth and fall velocity is not (Fan et al. 2016; Y. Lin et al. 2011).

The onset of riming is an important determinant, as this factor controls when riming can begin to convert droplets and so has implications for cloud LWC and the rate of precipitation development. Harimaya (1975) found that the riming onset was habit and size dependent. It was determined that small droplets cannot accrete to crystals, primarily due to the ventilation effect which diverts small droplets around the crystal's flow field. Recent studies have provided evidence that indicates small droplets may actually be accreted with similar efficiency to other droplet sizes. Ávila et al. (2009) conducted a study using cloud chamber measurements and compared the distribution of surface accreted droplets to the distribution of the droplet field, finding that there were not significant differences between the rimed particles and the cloud droplet distribution. This indicated that all sizes of particles were rimed in fairly equal manner, and below the riming onset as determined by earlier studies. The findings reiterated that habit was still a key factor for collection, as the overall number of rimed droplets varied between different habits. The authors note that more work must be done to determine the effect of small droplet accretion, and state that the collection efficiency of models was likely not suited to these riming cases.Unfortunately, it is difficult to make progress on these areas within the established hydrometeor categorisation system of conventional numerical models.

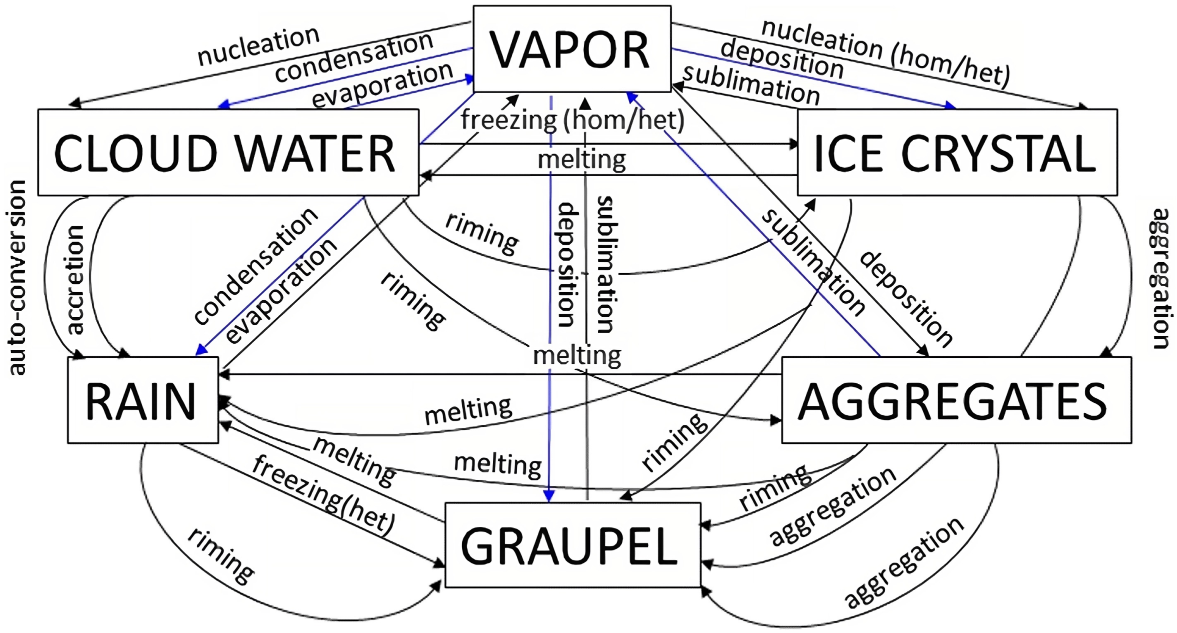
VAPOR
CLOUD WATER
ICE CRYSTAL
RAIN
AGGREGATES
GRAUPEL
nucleation
condensation
evaporation
nucleation (hom/het)
deposition
sublimation
freezing (hom/het)
melting
auto-conversion
accretion
condensation
evaporation
riming
riming
deposition
sublimation
sublimation
deposition
aggregation
melting
melting
melting
melting
freezing(het)
riming
riming
riming
aggregation
aggregation
riming

Figure 1.2. Schematic of cloud microphysical processes for the NDW6 scheme adapted from Satoh et al. (2018). Categorised hydrometeor types are shown in boxes. Arrows indicate the exchange of mass (blue) or mass and number concentration (black) between hydrometeor types. Hom: homogenous, het: heterogenous

In conventional, bulk microphysics schemes such as in Figure 1.2, the precipitation field is represented by a small group of predefined hydrometeor categories, namely ice, snow, cloud water and rain that follow from classical observations prior to computer modelling (Magono 1962; Nakaya 1954). These categories have characteristics such as density defined *a priori*, which makes them inflexible to variation but has the benefit of constraining the precipitation to a physically reasonable representation. Categorisation of hydrometeors in this manner has occurred in examinations of secondary ice production (Sullivan et al. 2018), riming (Milbrandt and Morrison 2013; Morrison and Milbrandt 2015; Satoh et al. 2010), habit (Erfani and Mitchell 2017; Jensen et al. 2017; Praz et al. 2017) and cloud-condensation-nuclei (CCN) (B. Chen and Xiao 2010; Stevens et al. 2018). Each category is represented by a log-normal, or more commonly, gamma distribution that enables a spectrum of particle sizes within a category as is often observed in reality (Adirosi et al. 2015; Marshall and Palmer 1948; Morrison and Grabowski 2008; Shan et al. 2020). The moment of each distribution, a statistical quantity that relates the integration of the gamma distribution to a power of the diameter, can be determined with each time step (Molthan 2011). Single-moment schemes use a mass distribution hypothesis or mass-diameter relation (*m*-*D*) to prognose the total hydrometeor mass. Thus, the transfer of mass by microphysical processes can be achieved by modifying the distribution parameters. As computational power increases, more moments of the distribution can be integrated and retrieved, enabling the number concentration to be tracked in double-moment schemes and even more properties, such as the radar reflectivity to be obtained in emerging triple-moment schemes (Loftus et al. 2014; Milbrandt et al. 2021). A significant advantage of this methodology is that hydrometeor populations are represented by analytical functions, which are less computationally expensive than binned schemes, and are much more realistic than the intractable problem of exact particle representation (Straka and Mansell 2005). However, strictly defining the precipitation field into a handful of discrete categories is associated with several problems in cloud models.

Hydrometeor categories may be distinguished from each other by their qualities or the processes they undergo. For example, in the Morrison scheme snow and graupel have different densities (100 kg m^{-3} and 400 kg m^{-3}, respectively) and experience differing growth paths (aggregation and riming, respectively) but this is by virtue of model design rather than physical law. For example, the density of rimed supercooled droplets can range from 50–900 kg m^{-3} providing considerable change in the overall crystal density (Milbrandt and Morrison 2013). Figure 1.4 highlights the wide variety of densities that occur in ice crystals with variation in temperature. The value of these fixed properties are important because they're used to feed physical equations and parameterise process rates, which in turn decide the evolution of the cloud and the forecast precipitation. One such case is the aforementioned mass-moment of the hydrometeor distribution, which requires an *m-D* relation. Commonly, hydrometeors are represented as constant-density spheres, enabling a convenient and simple cubic *m-D* relation that neglects variation in density or geometry. This may result in inflexible predictions of fall velocity, the speed at which hydrometeors fall within and outside the cloud, and may affect microphysical processes that have fall velocity dependencies, such as riming and coalescence.

To overcome the limitations of fixed density and geometry, relationships such as the fall velocity diameter (*v-D*) relation are parameterised by measurements. Such relationships are useful for defining the very different dynamics of each hydrometeor, but do not allow flexibility of these dynamics for differing environments. (Jensen and Harrington 2015a) argues that the inflexibility of these parameters make particle growth a predetermined process, rather than a consequence of environmental conditions. Ices are nearly isometric at nucleation, and go on to form a variety of shapes over time, but *m-D* relationships don't allow natural growth; a branched dendrite is always branched (Jensen and Harrington 2015a). Under the riming process, supercooled water droplets have been shown to primarily *fill-in* crystals, causing a mass increase which does not necessarily increase dimension (Heymsfield 1982), this is in disagreement with *m-D* relationships that associate an increase in mass with a corresponding dimensional increase (Jensen et al. 2017). Specific habits may also have an axial preference for riming that promotes an uneven dimensional gain and affects the fall speed parameterisation (Ávila et al. 2009; Fukuta and Tsuneya Takahashi 1999; Pitter and Pruppacher 1974). Where habit is absent or fixed, these effects are entirely ignored.

In addition to the unreliability of fixed-quality categories for the dynamics of single hydro-

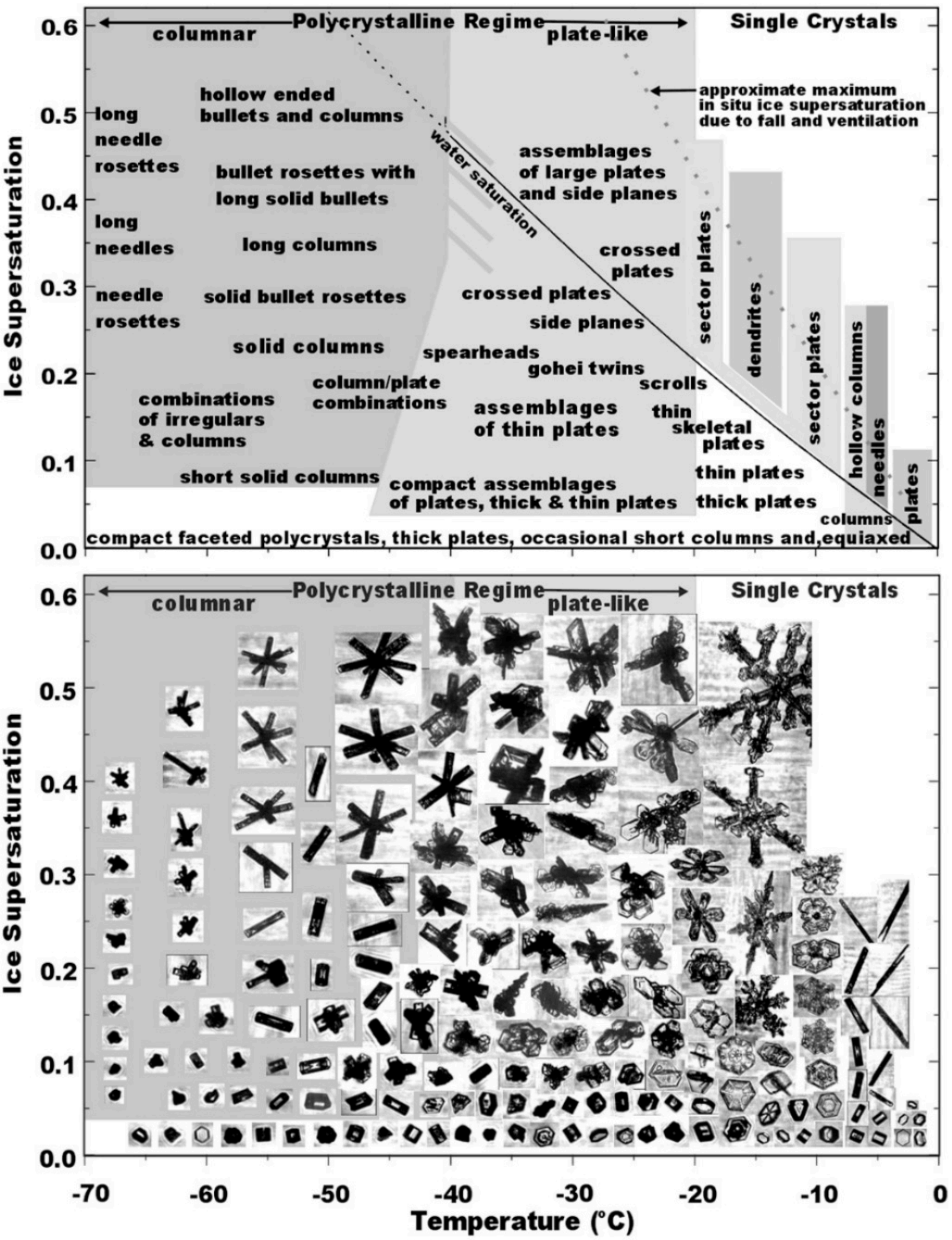

Figure 1.3. The large range of habits distributed by temperature and saturation (Bailey and Hallett 2009). Top shows distribution in text format, bottom shows pictorial format. The large variety of habits adds considerable complexity to computational models. Explicitly representing each habit costs additional computational time, and amplifies the error by autoconversion. Instead, a unified habit building scheme that utilises environmental conditions to build unique structures provides a uniform basis that may make riming autoconversion redundant

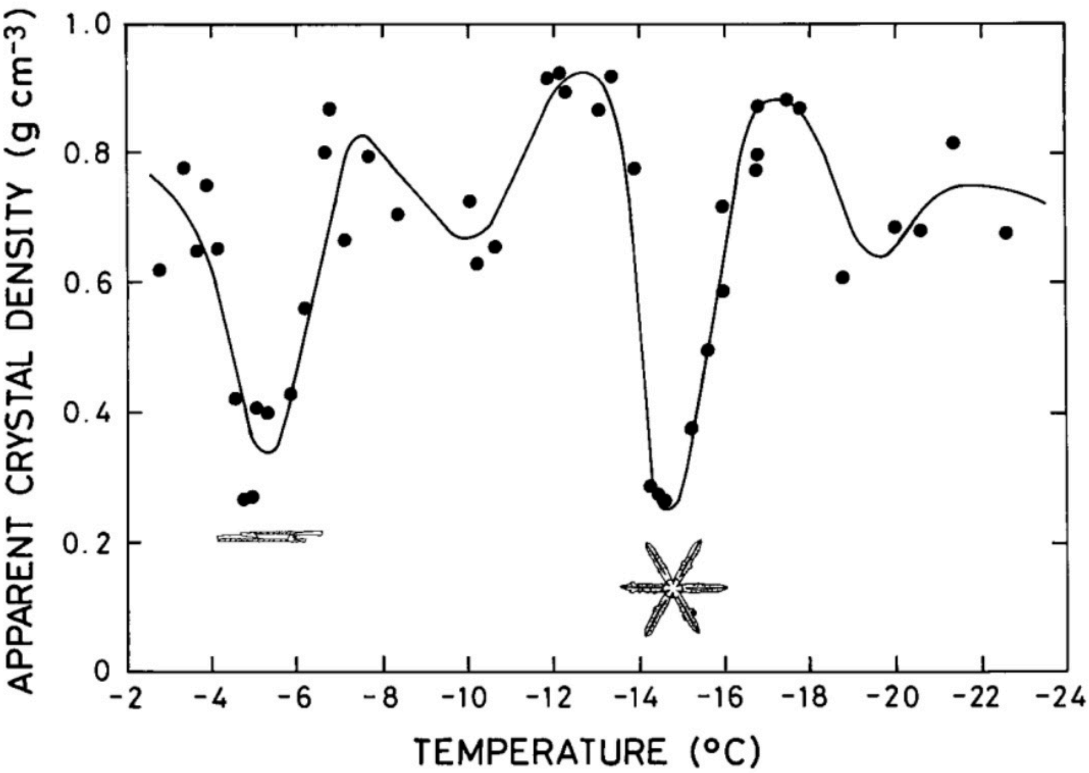

Figure 1.4. Graph of crystal density changing with temperature, (Fukuta and Tsuneya Takahashi 1999). Large fluctuations occur at changing periods of efficient geometrical growth, which are then opposed by periods of *fill-in* mass growth, which exhibit limited geometric modification. *m-D* relationships cannot account for inconsistent fluctuations in density originating from dynamic environmental effects.

meteors, further problems arise when converting mass or number between hydrometeor categories, known as the autoconversion process. As autoconversion operates between hydrometeor categories it is strongly associated with cloud microphysical processes, which are responsible for interacting hydrometeors in reality. For example, the autoconversion of cloud droplets to rainwater that reflects the coalescence process, or the autoconversion between snow and graupel that mirrors riming (Lee and Baik 2017). The autoconversion process diverges from reality where it considers physical processes that are gradual in reality to be discrete and instantaneous. The accretion of droplets to snow causes a smooth transition to rimed crystals over time, whereas autoconversion processes define a threshold droplet count that, when met, immediately converts mass from the snow category to the graupel category. Autoconversion of snow to graupel is over-reliant on *m-D* and *v-D* relationships, which relate mass or velocity to particle dimension (Jensen et al. 2017).

In the liquid phase, autoconversion of droplets to greater sizes; drizzle or rain, contributes to high sensitivities in cloud optical thickness, with significant consequences for global net cloud radiative forcing of up to 10 W m^{-2} (Michibata and Takemura 2015). The choice of autoconversion scheme determines the rate of rain formation. Beheng (1994) showed that the popular Kessler scheme forms rain too early in cloud simulations, and that, as opposed to the Kessler scheme, parameterisations with at least two droplet spectrum parameters are needed to reliably simulate the coagulation process. Even so, the scheme is still regularly used in models, and is present in the Hadley Centre Global Environment Model (HadGEM2) and the Geophysical Fluid Dynamics Laboratory Climate Model (GFDL-CM3) (Cheng and Xu 2009; Colle and Zeng 2004; Michibata and Takemura 2015; Yamasaki 2013). Michibata and Takemura (2015) demonstrated that Kessler-type schemes may underestimate the accretion-autoconversion ratio, a key parameter for the conversion of cloud and rainwater, and traced the source of error to the conversion threshold.

Attempts to overcome the autoconversion problems try to reduce the effect of jumps between categories. Creating more hydrometeor intermediary classes was attempted, to minimise the gap made between categories during large jumps. This method has been applied to the problematic autoconversion of snow to graupel (Straka and Mansell 2005). By introducing partially-rimed hydrometeor categories it was hoped that effects due to large mass jumps would be dampened. Though, with added hydrometeor types, additional complexity comes with an additional computational cost (Jensen et al. 2018). Furthermore, the addition of more autoconversion occurrences in a model run does not resolve the inherent problems of autoconversion, but increases the possible number of opportunities for these errors to occur. The faulty *m-D* relationships remain unchanged for any number of intermediary categories (Jensen et al. 2017).Innovative methods have emerged in recent years that aim to build hydrometeor states in a more continuous way, which is particularly beneficial to mixed phase processes and of these, the accretion processes such as riming, have received particular attention in the field of model development.

Continuous droplet accretion during riming is at odds with strictly defined *v-D* relationships. The fall speeds of partially rimed snow remain the same as unrimed snow despite the possibility of ongoing accretion, only changing in value after meeting the autoconversion threshold for graupel (Jensen and Harrington 2015a). The effect of predefined *v-D* relationships is to create stepwise fall velocities with unnatural jumps in speed (Grabowski et al. 2018). Poor representation of riming in this manner has been linked to decreased confidence precipitation forecasting, and inter-model precipitation variability (Colle et al. 2005; Y. Lin et al. 2011; Morrison and Grabowski 2008). Colle and Zeng (2004) noted that by slight changes to the fall speeds can contribute surface precipitation variations of between 10–30%.

The amount of droplets and their size has been shown to be a factor in riming collection efficiency, and in a similar vein, the introduction of aerosols which mediate these cloud qualities can also affect riming. Borys et al. (2000) hypothesised that riming would be less efficient when high concentrations of CCN were introduced to a cloud, as CCN increases make droplets more populous but smaller. The decreased droplet sizes would be too small to rime

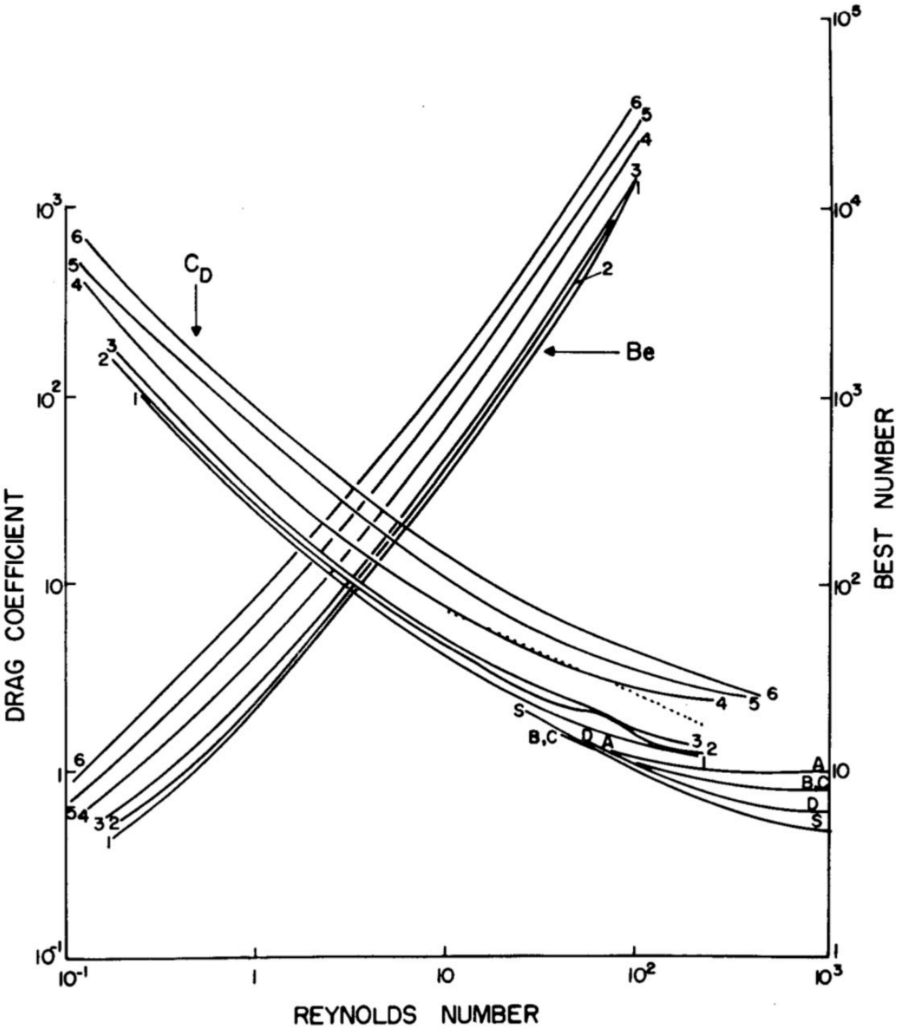

Figure 1.5. Drag coefficients and Best numbers for crystals as functions of Reynolds number, (List and Schemenauer 1971). Numbers 1-6 indicate: 1. Disc, 2. Hexagonal plate, 3. Broad Branched Crystal, 4.Stellar Crystal with Plates, 5. Dendrite, 6. Stellar Crystal. Hence increasing numbers generally indicate increasing porosity and complexity of structure.

and thus reduce the riming effect, decreasing the snow precipitation. This general method of riming suppression is supported by Colle and Zeng (2004) who found that higher CCN concentrations promoted the amount of retained cloud water in small droplets, which did not promote riming. However, the reduced conversion of snow to graupel meant that snow output actually increased. These indirect effects of graupel on precipitation were found to be important, with a graupel formation having a weighted importance of 35% on final precipitation output (Colle and Zeng 2004). Some studies have pointed to the opposite effect, whereby the benefit of increased number density outweighs the cost of droplet size reduction (Fan et al. 2016; Lohmann et al. 2003). The addition of CCN may change the qualities of the cloud which determine habit production, and therefore modify the habits produced. These habits have different riming qualities, including variable collection efficiencies across droplet sizes. Consequently, riming benefitted from an increased density of riming particles. The introduction of CCN, and subsequent effects upon the riming rate, often leads to reduced cloud lifetime (Colle and Zeng 2004; Lohmann et al. 2003). Fan et al. (2016) stated that the uncertainty around riming rates for different habits and droplets is an area of uncertainty for aerosol modelling.

The amount of radiative forcing due to cloud water retainment is a large area of uncertainty (Fan et al. 2016; IPCC 2013; Y. Lin et al. 2011). Investigations into the southern ocean (SO) radiative bias have indicated that riming has a substantial effect on the droplet population, and cloud lifetime (Vergara-Temprado et al. 2018). Too much ice in the initial stages of simulations can cause clouds to rapidly glaciate and disperse the water content to fewer larger ices. This riming dominance then contributes to a shortening of cloud lifetime and encourages a lower albedo. This contributes to more short wave radiation reaching the surface of the ocean, contributing to the SO radiative bias (Vergara-Temprado et al. 2018). Similarly Furtado and Field (2017) examined the SO radiative bias, and determined that models were sensitive to ice content in the early stages of model runs. They found that the inclusion of non spherical ice particles, a step toward habit representation, allowed for a more dynamic riming representation which increased the LWC retainment in comparison to models with less riming consideration, and affected the radiation output.

In a study of glaciated winter cumulus over the UK, Crawford et al. (2012) found that models were sensitive to the initial ice formation and the amount of ices present at early stages. Increased ice early on enhanced the riming process, exhausting the liquid content of the cloud and causing a reduction in cloud lifetime. Instead, cloud glaciation was not due to the production of more initial ices, but due to an enhanced Hallett and Mossop (1974) process in which riming of ice crystals in the vicinity of $-5^{\circ}\mathrm{C}$ can produce copious secondary ices by rime splintering, with the process active in the range $-8^{\circ}\mathrm{C} < \mathrm{T} < -3^{\circ}\mathrm{C}$. The effective representation of this glaciation mechanism was very sensitive to the representation of riming (Crawford et al. 2012). The poor representation of riming in global climate models has been isolated as a key to cloud lifetime and radiative bias. In some models, fall speed is not adaptive to the growing mass of rimed particles. By modifying the representation to include a mass weighted fall speed component, (Y. Lin and Colle 2011) determined that there was an increase in ice aloft, which contributes more outgoing long wave radiation as well as a slight precipitation decrease.

Representation of riming in models is particularly problematic and it can make evolving ice properties that depend on riming, such as habit and fall speed, more uncertain (Erfani and Mitchell 2017; Fan et al. 2016; Grabowski et al. 2018; Milbrandt and Morrison 2013). Some models have begun to use convenient power law relations for axial growth, which can circumvent some of the autoconversion problems (Erfani and Mitchell 2017). However, even in these cases, the riming collection efficiency is treated as constant and determined *a* *priori*. Y. Lin and Colle (2011) used an adaptive scheme which included rime intensity, allowing a singular rime category to grow in size more dynamically so that particle growth could be determined by LWC and temperature. This method allowed secondary effects, such as cross section and fall velocity to be implicitly modelled and particle growth utilised local environmental conditions, enabling it to adapt in real time. The results included a reduced computational time, and increased riming rates (Y. Lin and Colle 2011). To focus on adaptive growth, Lagrangian schemes which are particle focused, have been identified as well suited to the riming problem rather than traditional bin schemes (Grabowski et al. 2018). Further developments and innovations in this area are expected in the coming years (Grabowski et al. 2018).

Linking mass and dimensional growth due to riming, with fall speeds that are mass and area dependent, seems a very natural aim for models. However, many models do not effectively link riming and fall speeds. This was highlighted by Milbrandt and Morrison (2013), who developed an adaptive scheme allowing for rimed particle growth of variable rime density within a single category, thus increasing the degree of freedom for a category rather than including more partially rimed stages. This free-ice or generalised-ice approach allows precipitation to drift according to physical principles rather than catering to pre-defined precipitation types. The representation of riming in this model highlighted the effects upon the graupel spatial distributions, which could subsequently affect fall speeds (Milbrandt and Morrison 2013). For example, changes to the rime density enhanced graupel found in the convective regions which raised the precipitation output. The advent of prognosed density provides multiple opportunities to improve precipitation forecasts, not least for extreme snow depth events in which the density of snow relative to water, termed the snow-to-liquid ratio (SLR) is an influential factor in the calculation of snow height. Despite these advantages, prognosing density or other variables in a free ice category framework presents numerous practical problems. For example, the Milbrandt and Morrison (2013) scheme could not represent different rime densities at the same point; which deterred the authors from suggesting a possible unified ice category encompassing both graupel and hail. The authors remarked that “adding complexity can solve problems but generate new ones”.

Users of microphysics schemes based upon the free-ice categorisation framework may find that retrieving precipitation forecasts from the model output is significantly more complex. Modern bulk-microphysics schemes typically contain the four conventional categories; cloud droplets, rain, ice and snow, and in some schemes an additional mixed-phase category such as graupel or hail. The presence of these hydrometeor categories has negated the requirement for an end user to define precipitation, either mathematically or conceptually. Instead, the end user simply retrieves the moments of one of the predetermined hydrometeor-categories. In many respects this is advantageous, as precipitation types are readily available from the model output requiring less work by the end-user in post processing. However, the end-user is also limited to only the precipitation types chosen by the model developer, and the qualities of the precipitation field remains relatively inaccessible.

By shifting the focus of microphysics schemes away from strictly defined precipitation categories, microphysical processes can be viewed more so as a function of fundamental ice characteristics, rather than discrete constituents. A caveat of using this methodology in microphysics schemes is that the qualities of the precipitation field are not categorised into precipitation types in the output, likely to minimise computation time and conserve memory. Instead, the determination of precipitation type is left to the end user. This poses several challenges to the end-user and to the wider scientific community, as precipitation type definitions are not standardised and so the definition of precipitation type may vary from user to user. For example, ice pellets in the Commonwealth are referred to as sleet, and in the United States of America (U.S. hereafter), *snow* may refer to aggregated ice in some cases, but in other cases may refer to unaggregated but large crystals, such as dendrites and stellars. Graupel and hailstones have also been historically used interchangeably, and similar complications arise in several other precipitation types. Defining the precipitation type can therefore have interesting cultural and historical discrepancies.

Defining precipitation is further complicated by the wide array of physical characteristics used to describe precipitation-type in reality, but the comparatively small set of simulated precipitation variables handled by a microphysics scheme. In some instances, there is considerable overlap in the precipitation definitions from the available variables. For example, cloud ice and ice-pellets can share similar density and size ranges, but are visually dissimilar in reality. Their difference arises from vastly different growth histories, but several, key historical prognostic variables are not tracked in free-ice microphysics schemes. For example, cloud ice may grow by deposition, and ice pellets may undergo melting and refreezing, but this important historical-contextual information is often absent. Instead, the density is evolved and tracked regardless of microphysical process, so similar density particles provide no contextual information regarding the processes that led to that value. While the effect of microphysical processes on particle growth is certainly included, and arguably in a more consistent fashion than categorised schemes, the final prognostic variables don't provide a complete enough picture to accurately distinguish precipitation types with subtle differences. On occasion, this may be made easier by a specifically tracked prognostic variable, but comparison between schemes only becomes more difficult, as the limited prognostic variable set in each scheme may differ, and therefore so to do the criteria which define the precipitation. It is important to consider then that the uptake of free-ice categorisation in emerging microphysics schemes, though it may be beneficial to transitional processes, may be difficult to grasp for forecasters used to the conventional system.

In addition to the uptake of generalised categories, emerging microphysics schemes are simultaneously incorporating predicted particle qualities such as rime density or aspect ratio. Habit determines the mass distribution and surface area of crystals, which are defining features for the calculation of fall speeds (Heymsfield and Westbrook 2010; Westbrook 2008). J.-P. Chen and Lamb (1994) developed the theoretical framework for an adaptive-habit (AHAB) hydrometeor category, which enabled microphysical process rates to directly affect particle habit during growth. In this framework, ice particles were represented as spheroids whose aspect ratios developed continuously according to their local environment. The development of specific habits depends on the availability of vapour for deposition (saturation), temperature, and the mixing ratios of these hydrometeors in the habit's locality (J.-P. Chen and Lamb 1994; Fukuta and Tsuneya Takahashi 1999). These features are implemented through an inherent growth ratio δ_* that relates environmental conditions to axial growth. This concept was implemented in the ISHMAEL bulk microphysics scheme that simulates two generalised ice categories using the J.-P. Chen and Lamb (1994) framework (Harrington et al. 2013; Jensen et al. 2017). The beauty of this method is that transitional ice particle habit can affect process rates and vice versa, enabling more dynamic feedback between the local environment and the development of precipitation. These feedback mechanisms are important to mixed phase processes, which are particularly sensitive to continuous, transitional development (Grabowski et al. 2018). The process of riming produces a continuous transition in a crystals habit and density that lends itself to free-ice categorisation.

Importantly, even these emerging microphysical schemes still do not account for non uniform density effects, such as changing axial preference and fill-in. The use of spheroids does not allow for ice gaps or holes which occur in some porous crystal species, although the introduction of differing axial densities provides an analogue for this (Jensen and Harrington 2015a). The ventilation effects of species with a discontinuous surface area, such as dendrites and stellars, affects accretion rates (Fukuta and Tsuneya Takahashi 1999). Furthermore, porous species experience modified aerodynamics (see Figure 1.5 which lead to differing fall velocities (Heymsfield and Westbrook 2010; List and Schemenauer 1971). There are considerable aerodynamic differences between porous and non-porous crystal types, and even still between types of non-porous crystals (List and Schemenauer 1971). It is not clear that models such as ISHMAEL can dynamically include these effects. Perhaps most notably, and in the vein of (Milbrandt and Morrison 2013), complexity can create as many problems as it solves. Unlike the P3 scheme, which isolates its complexity to the riming process alone, the ISHMAEL parameterised habit has far reaching effects for a whole host of microphysical processes beyond riming. Perhaps the most important of these is the vapour deposition process, which is intricately related to the development of habits and the early growth of cloud ice in general.

At high elevations, the vapour deposition process is likely to be the most efficient growth pathway of ice for several reasons. The character of recently nucleated ice particles have microscale cross-sectional areas and negligible fall speeds, resulting in a reduced likelihood of multi-particle interactions. The most effective transfer of mass in this environment is via ambient water vapour that has comparatively more dynamic freedom to disperse and interact with crystals. Although these crystals typically exist at very cold (< -30 °C) temperatures, droplet formation is constrained by the small concentration of cloud-condensation-nuclei (CCN) available for nucleation at high elevation, and thus the ambient environment is in a saturated state with respect to water. Figure 1.6 highlights the smaller vapour pressure over ice compared to water and the exacerbation of this effect at decreasing temperatures. Temperatures between -10°C and -30°C host ice saturation vapour pressures considerably smaller than that of liquid, resulting in an environment that is saturated over liquid water but is supersaturated with respect to ice crystals. The resulting thermodynamic action is for ice crystals to scavenge vapour by deposition whilst simultaneous droplet evaporation maintains the liquid water saturation level. This *Wergener-Bergeron-Findeison* (WBF) process is a primary method of early ice crystal growth that is essential to the mass gain and resulting sedimentation of ice crystals through the cloud. Given its importance to ice and droplet size distributions during early development, it is essential to accurately parameterise the deposition process in numerical models.

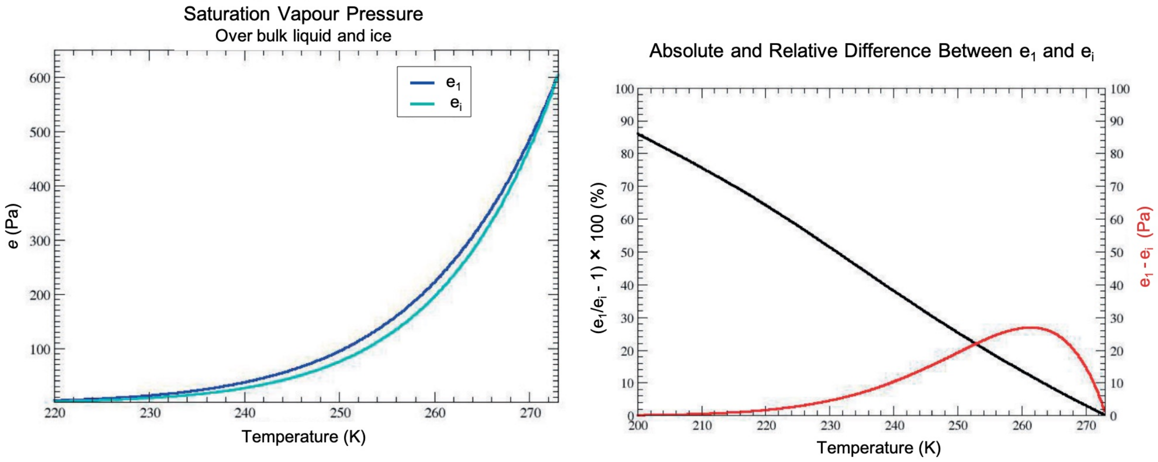

Figure 1.6. Difference in vapour pressure over water and ice from Storelvmo and Tan (2015). Left: saturation vapour pressure over bulk liquid (e_l) and bulk ice (e_i). Right: absolute (red) and relative (black) difference between e_i and e_l.

In numerical models, deposition can be viewed from an ingredients based methodology as a transfer of mass between hydrometeor populations or categories, and at a more rudimentary level a manipulation of the respective particle size distributions (PSD) of each category. Inaccurate calculations of the deposition rate by parameterisation schemes can be expected to produce inaccurate moments of the PSD for each hydrometeor category. During deposition, the mass and number of ice particles are influential to both the supply and scavenging of vapour in a cyclical manner. If poorly captured, this can lead to a cycle of diminishing returns and compounding errors for the PSD during the cloud ice growth stage. Further, second-order consequences can be expected to arise later in the cloud cycle, during the formation of precipitation, if the early growth of cloud ice by deposition is not captured effectively. For example, the mass of a crystal distribution is integral to the accurate computation of ice particle fall speeds, and the collection efficiency of snowflakes is dependent on the number concentration of ice crystals during descent. Thus small errors at the deposition stage may bleed into subsequent microphysical processes, causing them to be inaccurate even if their individual parameterisation is very effective.

The process of riming might be particularly sensitive to the effects of deposition as it operates in the mixed-phase, requiring the accurate formulations of two hydrometeor PSDs and therefore compounding the errors found in the respective PSD of each. This is only more pertinent in the context of the WBF process, as these hydrometeor PSDs are in active competition and so inaccuracies may quickly compound. Furthermore, the riming process is dependent on the ice particle fall speed, number concentration, ice particle size and aspect ratio for the correct determination of riming rates. So, whilst improving the riming parameterisation directly is beneficial, such as by the explicit inclusion of ice geometry, the improvements in captured riming rates must not occur at the expense of other microphysical processes that feed the riming dependencies. It is clear that even the most adept riming parameterisation cannot overcome poorly predicted ingredients data.

Poorly constrained deposition process rates that have consequences for subsequent process such as riming or aggregation might inhibit or enhance the onset of precipitation. For example, by the formation of a homogeneously sized droplet field devoid of ice or, at the other extreme, a completely glaciated cloud. These effects may materialise in absent or poorly timed precipitation development, incorrect forecasting of precipitation type, or a combination of both. The size and concentration of droplets and crystals collectively determines the cloud albedo, a significant factor on the meteorological time scale but perhaps even more so on that of the climate. The scale of the potential problems becomes apparent when considering the proportion of clouds that contain ice. A study of satellite data by Lau and Wu (2003) found that 70% of tropical precipitation events begin in the ice phase. By extension, these cases will feature deposition during the formation of precipitation. Understanding deposition is therefore an important feat not only to improve accuracy on the microscale, but in order to improve macro-scale properties with wider utility, from cloud lifetime to precipitation forecasting.

Deposition from the perspective of thermodynamics is a straightforward process that should be possible to capture in microphysical parameterisations analytically, but a closer look at ice crystals in reality reveals a complex myriad of factors to be considered that seem to almost-deliberately evade computationally simplistic parameterisation. Perhaps the most obvious and famous feature is the geometry of ice, or habit.

Ice crystal shapes have been recorded by observers for hundreds if not thousands of years i.e. Han Yin (200 B.C.) but formal classifications began perhaps as early as the 1600s in Europe with the likes of Descartes (i.e. *Discours de la Méthode Pour bien conduire sa raison, et chercher la vérité dans les sciences*). In 1837 Suzuki Bokushi published *Hokeutsu Seppu* containing sketches of 86 snow crystal types (later 97 with the addition of *Doi Toshitsura*) in the Echigo province of Japan, famous for its snowy winters. Almost 100 years later, Ukichiro Nakaya, a scientist born in the same region, produced the first artificially grown crystals using rabbit hair and documented his findings. *Snow Crystals* by Nakaya (1954) produced a scientific classification of habits numbering forty-one types, thirty-one more than the system proposed by the International Commission on Snow and Ice only three years prior. A subsequent classification by Magono (1962) categorised 80 crystals of unique habit. This work had remained the definitive guide, until an updated classification in 2013 expanded the count to 121 types Kikuchi et al. (2013). Indeed there may be more forms as the features of complex crystals are identified and categorised even further.

The existence of these varied and numerous ice crystal geometries does not necessitate their need in numerical models. However, the motivation for their inclusion can be found in their effects upon a wide array of microphysical processes. For example, vapour deposition, accretion, fall speed and aggregation are all dependent on ice habit. The question of how impactful is its inclusion in numerical models remains open, primarily due to the absence of habit in almost all microphysical schemes used to date. The next generation of microphysics schemes face a barrage of competing variables that also command attention, for example rime density, but the narrow focus of these variables may limit their perceived importance as opposed to the far reaching effects of ice habit. Certainly, the results obtained in Part II show that the inclusion of ice habit in the ISHMAEL scheme has a multitude of impacts across processes.

Understanding deposition on the molecular scale is required to understand the development of macro-scale habits. The prevalence of so many differing types of habit indicates that deposition is not as simple as the thermodynamic picture, or the Bergeron process, would imply. First we must understand how vapour molecules attach to the surface and how that surface is ordered. By definition, ice exhibits an ordered crystalline structure with rigid bonds. The unit cell of solid water is well known and its repetition by stacking is a good approximation of the structure of recently nucleated ice particles, though defects can and do exist to great importance that will not be mentioned here. Stacking the unit cell creates a tetrahedral lattice and projections of this lattice onto a basal plane can illuminate the familiar hexagonal shape with which snow crystals are synonymous on the macro-scale. Thus the intrinsic structure of ice is hexagonal, providing a basis, but not an explanation, for the macro-scale hexagonal structure easily identified by eye. The axes of growth are divided between the basal or prism faces, effectively compounding the hexagonal structure in width or height. Habits are combinations of uniform or localised depositional growth across the crystal faces.

Given this simple ice structure to build upon, deposition as a simple addition of molecules from the gas phase to the ice surface can explain axial growth. Given that a gas has negligible collective structure and a statistically even distribution of molecules, ambient vapour levels are, over the growth period of a crystal, practically uniform on all surfaces of the crystal at any instant, leading to symmetric growth to the human eye. The freedom provided to vapour molecules by their gaseous state allows molecules to take on a position and orientation favourable to the pre-existing crystalline structure of the solid in a way that perpetuates the tetrahedral geometry of the ice lattice, preserving the six-fold symmetry. Such an effect cannot readily occur from ice-liquid interactions, for example, as the water molecules are themselves loosely bound and unlike the uniform vapour field, droplets coat only localised areas of the crystal. The method of depositional growth is therefore clear, water vapour will bind molecules to the ice structure in a way that perpetuates the lattice.

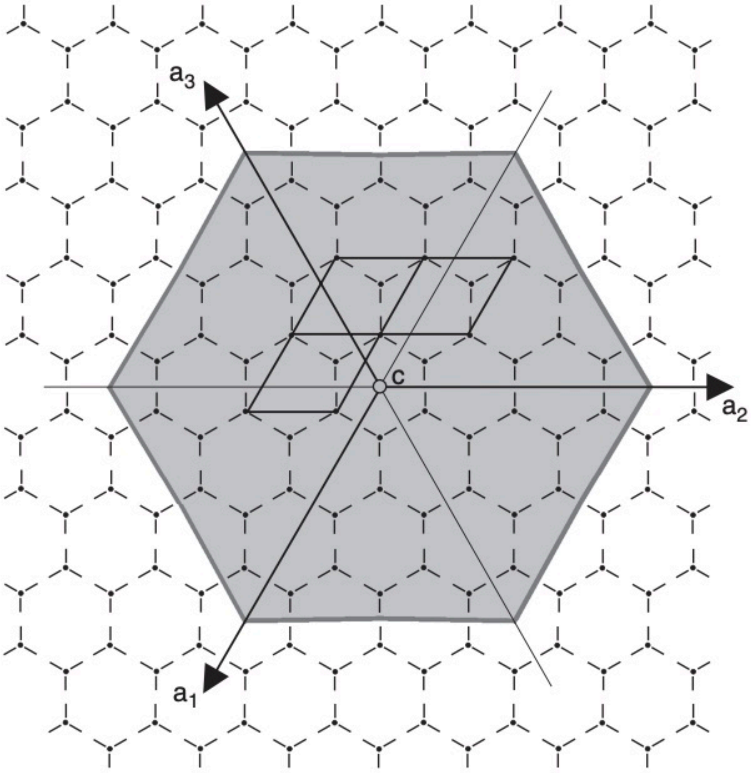

Figure 1.7. The hexagonal structure of the ice lattice projected onto the basal plane from Lamb and Verlinde (2011). The unit cell of water is shown by black solid lines. Cutting the lattice along the fewest bonds produces a hexagonal structure (grey line).

Facets, or faces, of the crystal develop naturally as a consequence of the lattice. A slice of the lattice that produces the fewest free or dangling bonds produce a hexagon, as shown in

Figure 1.7. Indeed, the number of available bonds is important to the growth rate. So called *rough* surfaces have lots of available bonds and so grow more quickly in the presence of vapour than facets, which are comparatively smooth and have few free bonds. As the rough areas grow they too develop into facets and their growth rate reduces. Over time the tendency is for rough edges to fill out quickly and for facets to do so slowly, thus after considerable vapour growth the hexagonal structure of ice becomes apparent.

Branching is the growth of ice at the apex of two facets, a mechanism that occurs as crystals grow larger beyond the facet growth stage. This is caused by the additional length an apex extends into the vapour field compared to the facets. Branching is the first of two ice crystal instabilities, so called because the effect is self compounding. Branching begins slowly, but as the branch itself extends further from the crystal, it more rapidly grows, accelerating from the facets. At the leading edges of the branch further branching can occur and so on creating fractals or repeating branches that define the iconic image of a characteristic snowflake.

A second instability is similarly present during ice crystal development, the sharpening instability. In nature snow crystals are often thin and flat, an extreme shape for an apparently random process. Moreover, the thin facet is almost always the prism face, not the basal. The development of such an extreme shape is accounted for by the uncanny attraction of molecules to small facets. As the ice facets grow they do so in terraces or layers that overlay the facet surface. Larger facets have typically slower growth than their smaller counterparts, so newly developed terraces themselves develop terraces more rapidly than their larger counterparts. This leads to accelerating facet growth across thin layers extending outward of the prism face, with facet fill-in occurring over longer time periods.

Possibly the most interesting question of how do conditions manipulate the ice geometry, was the subject of the earliest studies into ice habit. During Nakaya’s studies into artificial and natural crystals he developed his famous ice diagram (Figure 1.8), the first of its kind to relate ambient supersaturation and temperature to ice habit formation. In his diagram, it is shown that crystals transition from plates to columns and back again as temperature decreases, whereas increases in supersaturation lead to more elaborate and detailed shapes at all temperatures. Ice crystals that traverse multiple temperatures or supersaturation levels could be expected to form in a predictable way. For example, with supersaturation held constant, columns would require only a few degrees of temperature difference to develop plates or *caps* at their basal faces. Many implementations of ice habit in modern microphysics schemes derive from this diagram, for example the conditions of the dendritic zone are used to determine when snow production occurs.

Clearly, the scale and complexity of surface processes that occur during deposition on the microscale are far beyond the reach of bulk microphysics schemes. However, it is important

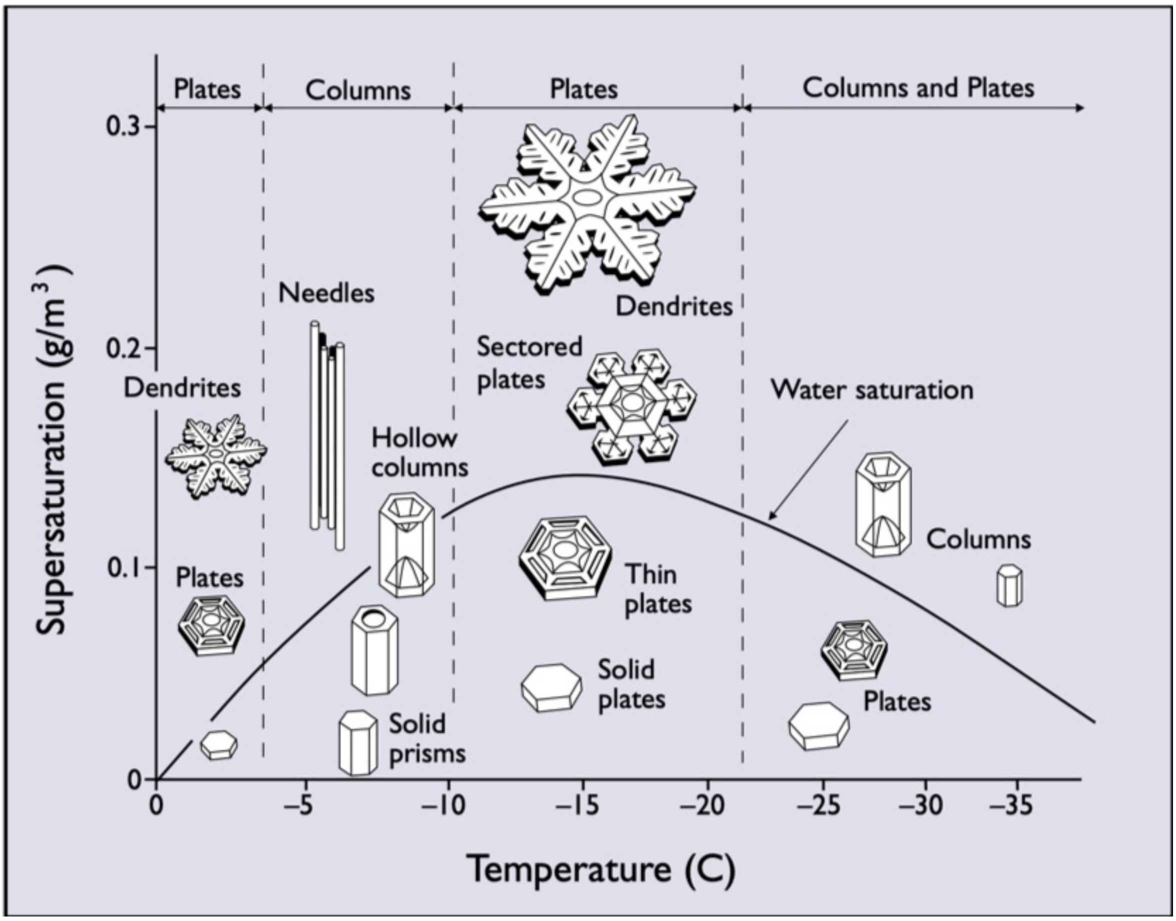

Figure 1.8. The Nakaya (1954) ice crystal habit diagram adapted by Libbrecht (2001). Crystal images indicate the type of ice habit found for a given supersaturation and temperature. General classifications of habit are attributed to broad temperature ranges (top). Intricate structural patterns are found above the water saturation curve.

to appreciate the origins of these processes to ensure that they are consistent with coarse-scaled parameterisations schemes. One of the simplest and earliest methods of incorporating shape to the deposition formulation used in droplets was to use the electrostatic analogy.

The growth of ice at the molecular level is complex and discrete, and far beyond the scope of microphysics schemes. A simpler and more commonly used approximation is to draw comparison with electrostatics, namely a conductor in an electric field. This analogy is justified because the action of an electric charge in a changing electric potential is similar to water vapour with varying vapour concentration (Lamb and Verlinde 2011). Simplifying the many vapour molecules in the gas by approximation of a continuous field allows for efficient analytical expressions of the deposition process that are convenient for numerical models. Solutions for vapour deposition can therefore be taken directly from electrostatics: the flux of vapour to ice is directly proportional to the field's gradient, resulting in a Maxwell-like growth law (and with Maxwell this analogy possibly originated). As in electrostatics, each ice habit has an analogous "capacitance" that determines the relationship between the concentration of the ambient vapour field and the consumption of vapour molecules by the ice particle. The capacitance of crystal habits in electrostatics is directly ported to the vapour deposition model.

A common choice when approximating the deposition process of a single ice crystal is to draw comparison with the well established field of electrostatics, namely to make an analogy between the capacitance of a conductor in an electric field with the depositional potential of an ice crystal in a vapour filled environment. Figure 1.9 adapted from Lamb and Verlinde (2011) shows how an ice particle in this framework might be imagined. The ice particle with flat, disc-like shape (shaded grey) is resident in a continuous vapour *field* indicated by field lines extending radially from the ice particle centre. The net flux of the theoretical vapour field is towards the ice particle. The area occupied by the ice crystal is a fixed boundary, that perturbs the vapour field in its vicinity. For example, circular lines of constant vapour density tend to be increasingly perturbed as they approach the crystal surface resulting in more oblate field lines. The vapour density increases in proximity to the ice surface (indicated by increasingly dense field lines) implying that vapour in the near-field experiences a greater pull toward the ice than vapour that is further away. A cut out of the near field, shown in Figure 1.9 highlights that the capacitance analogy identifies areas of very high net flux near to the crystal prism face, which is far more narrow than the basal face. This increased flux at the sharp edges of ice crystals is related to branching and preferential axial growth during deposition that leads to more and more oblate (flat) crystals, such as plates and stellars.

The electrostatic analogy applied to the vapour deposition process is typically justified by recognising similarities between how an ice particle attracts and collects ambient vapour molecules, and how a capacitor attracts and stores charged particles. For example, a capacitor's potential difference affects its ability to store additional charge in a similar way to how the amount of vapour mass collected by ice will reduce the vapour mass accordingly, resulting in a less dense field and a reduced net tendency to ice with time. The action of a vapour molecule in a varying vapour concentration is also similar to that of an electric charge in a changing electric potential (Lamb and Verlinde 2011). The near-surface field experience a greater pull and more influence over the ongoing exchange process than more distant sections of the field. In the deposition process, this allows the exchange of vapour mass to be closely tied to the geometry of ice in the near-field whilst distant vapour experiences negligible pull toward the ice crystal.

With several similarities between these two frameworks identified, one may be satisfied that this analogy holds for the vapour process, whilst acknowledging that some modifications will be required to fully translate it to the deposition process observed in reality. One of the most useful features of the capacitance analogy is that the well-established Maxwell equa-

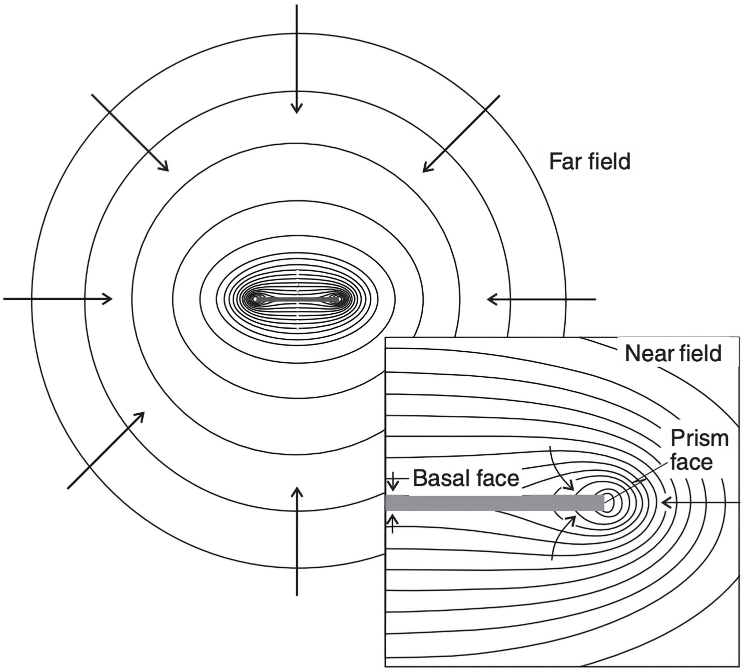

Figure 1.9. Ice particle in a vapour field as imagined by the electrostatic analogy adapted from Lamb and Verlinde (2011). Lines of constant vapour density are indicated by field lines, and the vapour deposition net tendency is indicated by black arrows. Ice particle is an approximate flat plate indicated by grey shading. A cross section in the near field is shown in close proximity to the crystal surface.

tions can be lifted directly from electrostatics and applied to the deposition. For example, assuming that the flux of vapour to ice is directly proportional to the vapour-field gradient, a Maxwell-like growth law can be established.

To fully utilise the electrostatic framework in a microphysics scheme, the value of the analogous capacitance must be determined for ice crystals. One may begin with the electrostatic capacitance of a conductor, which is a function of only geometry and determines its ability to both collect and store charge. Thus, by analogy, the capacitance of an ice crystal is also a function of geometry and determines the particle's ability to collect and store deposited vapour molecules. However, this is difficult to implement across bulk microphysics schemes that simulate particle size distributions (PSD), and which often do not consider the geometry of ice crystals as a factor in microphysical process rates.

An review of several bulk microphysics schemes was performed to determine the prevalence of capacitance as term in the vapour deposition process parameterisation. The schemes, shown in Table 1.1 were chosen for examination because they span a variety of frameworks and are commonly used. For example, the ISHMAEL and P3 schemes belong to an emerging branch of bulk microphysics schemes that track particle properties, and the Morrison scheme uses a conventional binned hydrometeor framework. The Thompson and WSM6 schemes are commonly used in the literature, but also receive increased exposure due to their use in WRF *physics-suite* options; `CONUS` (contiguous United States) and `TROPICAL` (Song-You Hong and Lim 2006; Thompson et al. 2008). The *physics-suite* is a user-selected option in the WRF namelist file that was devised to provide reliable combinations of namelist options for a given scenario, i.e. the WSM6 is the recommended microphysics option for `TROPICAL` storms (Skamarock et al. 2019). Given that the *physics suite* parameter is likely to be used by those unfamiliar with the details of microphysics schemes, it is reasonable to assume that the capacitance formulation is likely to not be considered.

The capacitance term is a factor in the deposition formulation of all schemes considered in Table 1.1 and is generally used during the solving of the supersaturation equation. In Morrison and P3, the supersaturation is determined over the hydrometeor population using the average capacitance of each hydrometeor type and their specific phase relaxation time τ (see Appendix A). The resulting supersaturation difference drives the deposition mass tendency, with the mass redistributed over the PSD. In other schemes such as ISHMAEL and WSM6, the capacitance is a component in the deposition mass tendency equation. The deposition process redistributes vapour and ice mass, and this drives the resulting supersaturation level. Importantly, in most bulk schemes the capacitance as it appears in the electrostatic analogy is not fully realised due to geometrical constraints. Most microphysics schemes lack the ability to fully represent ice particle geometry and so will often represent ice according to a single dimension, such as the radius or diameter, which forms the gamma distributed variable in the particle size distribution. The geometry of ice can be inferred by the mass distribution (*m-D*) hypothesis and in nearly all cases, hydrometeor geometry is determined by a spherical *m-D* relation. Consequently, all ice particles are assumed to be spherical and this makes determining the capacitance for a range of possible ice particle habits difficult.

For most bulk schemes a simple choice is to make the capacitance proportional to the diameter, and to use a fixed value as a constant of proportionality, which enables relatively easy integration of capacitance throughout the PSD. For example, in WSM6 the capacitance is used only for graupel with $C = 2\eta_0 \pi D_G$, where D_G is the diameter of graupel and η_0 the permittivity of free space and in Morrison (Morrison et al. 2005) particles are treated as spheres with C_0 the *dimensionless capacitance*, set to 1 such that $C = C_0 D$. This method is the least complex way of including the capacitance because the constant of proportionality does not need to be considered during integration of the PSD and it does not need to be calculated based on any dependencies. However, this formulation does not consider three dimensional variability as in the original analogy. By parameterising capacitance in this way, the deposition process assumes that all particles are spherical and accumulate vapour molecules as a sphere would, which negates the more complex variations in capacitance that occur in reality. The one-dimensional capacitance faces an uphill battle to accurately forecast deposition rates because, for a given diameter, particles may exhibit a range of geometries and therefore a one-to-one capacitance-diameter relationship cannot accurately reflect the possible range of possible capacitances that might occur.

An attempt to improve the one dimensional capacitance was made in some bulk microphysics schemes by allowing the constant value of dimensionless capacitance to take on more values. This flexibility was introduced by determining the upper and lower limits of C_0 for a given hydrometeor category and interpolating between these limits based on a secondary variable that evolved more naturally. For example in P3, small spherical ice and graupel are treated as spheres with $C_0 = 1$, whereas unrimed non-spherical ice has $C_0 = 0.48$. Linear interpolation takes place between 0.48 and 1 according to the particle's mass. In Thompson microphysics, linear interpolation occurs for snow crystals between the values of 0.3 and 0.5 but interpolation is according to temperature. Reasoning for this choice originates in first principles derivation with steady state assumption (Srivastava and Coen 1992). Whilst interpolation can account for the variety of possible capacitance values that might occur for a given diameter, the choice of interpolation method is highly varied amongst schemes and no consensus on an ideal method has been identified. Each method also amounts to a parameterisation of a parameterisation, which may produce small improvements but cannot bypass the fundamental constraint at the heart of this problem; these methods are attempting to improve a one-dimensional parameterisation of an innately higher-dimensional problem. We argue that only a three-dimensional parameterisation can fully realise the capacitance as intended in the original analogy.

Of the schemes reviewed in Table 1.1, only the ISHMAEL scheme considers higher dimensions of ice particle radii. Notably, ISHMAEL does not stray significantly from other bulk schemes in that, the ice particle population is still approximated analytically (bulk) and gamma distributed along one dimension, so it is reasonable to assume that it too should face a dimensionality problem when calculating capacitance. However, unlike other schemes, the one dimensional gamma distributed variable is a function of the spheroidal a-axis length, which is intrinsically related to the spheroidal c-axis length by a a function of the inherent growth ratio δ_* determined by the combined action of microphysical processes. The a-axis and c-axis lengths are conserved and advected by two prognostic volume-dimensioned mixing ratios. This method enables a two-dimensional appreciation of ice to be computed explicitly during microphysical processes, and by extension a three dimensional appreciation assuming that the three dimensional spheroid is simply a rotation of 2π of the ellipse given by both axis lengths. Spheroids provide a good geometric approximation of plate-like or column-like ice crystals, and these geometries are easily obtained by modifying the aspect ratio of the a and c-axes. Most importantly, the capacitance of a spheroid is known theoretically i.e. Snow (1954), enabling direct calculation of the three dimensional capacitance for the first time in a bulk microphysics scheme to our knowledge. Of course, the inclusion of ice geometry does not guarantee a more accurate capacitance (and by extension, deposition) calculation but does achieve a methodology that is closer to the true capacitance as intended by the electrostatic analogy.

Scheme	Relevance	Capacitance Used	Hydrometeors	Extent of Inclusion
ISHMAEL (Jensen et al. 2017)	Current study	yes	All	C is a term in the deposition mass tendency that is distribution averaged (Harrington et al. 2013) their Equation B14)
Morrison 2-Moment (Morrison et al. 2005)	Current study	yes	All	C is a term in the phase relaxation time of each hydrometeor. All hydrometeors treated as spheres and $C_0 = 1$ ($C_0 D$ relation).
P3 (Harrington et al. 2013)	Previous Study	yes	All	C is a term in the phase relaxation time of each hydrometeor (Morrison and Grabowski 2008). $C = kC_s$ where C_s is the capacitance of a sphere and k is a constant. $k = 0.48$ for unrimed non-spherical ice as in Field et al. (2008) and $k = 1$ for spheres. C is linearly interpolated based on particle mass.
Thompson (Thompson et al. 2008)	WRF *physics_suite* option: CONUS	yes	Aggregates	Dimensionless capacitance for aggregates and spheres = $0.3, 0.5$ respectively, with intermediate linear interpolation based on temperature (Srivastava and Coen 1992).
WSM6 (Song-You Hong and Lim 2006)	WRF *physics_suite* option: TROPICAL	yes	Graupel only	C is a term in the graupel deposition mass tendency only. Capacitance is in spherical form $C = 2\pi D_G$. Deposition of ice is based on (Song-You Hong et al. 2004).

Table 1.1. The extent of the inclusion of capacitance as a term in the vapour deposition framework of microphysics schemes. The precipitation types that the capacitance term applies to are given under *Hydrometeors*

As an aside, it is important to note the electrostatic analogy is still only an analogy and several problems with this framework may exist that are important to state. First, consider that the application of electrostatic capacitance to ice crystals in a vapour field is not an ideal scenario. For example, ice crystals in reality do not exhibit a natural capacitance in the physical sense, and there is no depositional force of attraction between vapour molecules and the ice surface analogous to the electrostatic force of attraction between oppositely charged bodies. Rather, the attachment of molecules to the ice surface is determined by a series of surface effects, including the growth of facets by terraces and surface-diffusion, which are complex molecular scale interactions that vary simultaneously over different crystal faces. The classical capacitance approximation is therefore not well suited to incorporating these processes, and must be viewed as a statistical simplification of surface processes. That is not to say that the capacitance analogy is incapable of producing physically realistic results, but is instead a useful simplification of the general deposition tendencies of crystals. Indeed, for the accurate prediction of branching and faceting, the capacitance analogy is likely to break down but this is a feature shared with any parameterisation in general.

Measurements of ice capacitance have been performed to try and identify the rates at which an ice crystal might receive vapour. (McDonald 1963) attempted to measure ice crystal capacitance using symmetric brass-model crystals in a Faraday cage. This study had mixed success but has remained a key piece of literature on this topic. By the author's own admission, the capacitance measurements were difficult to obtain accurately due to the act of measurement introducing secondary, additive capacitance. The reliability of these results is therefore dubious and debate on the validity of McDonald's results has remained since the paper was published. (J.-P. Chen and Lamb 1994) stated that the theoretical and measured capacitances in McDonald "agree very well". Whereas (Bailey and Hallett 2006) was far less confident, their comparison showed that measured values were up to half of that predicted theoretically by McDonald. Further work has been done in recent years to improve upon the brass-crystal findings but these have only raised more questions. Measurements of crystal growth rates by (Bailey and Hallett 2004) seem to contradict the theoretical capacitances, returning rates between 3 and 10 times slower than the capacitance model (Bailey and Hallett 2006).

In addition to the contradicting evidence surrounding the findings of McDonald, further issues have been raised regarding the validity of the measured capacitances of symmetric crystals. Ice crystals do not exhibit the convenient shapes used in capacitance calculations or measurements, such as the spheroidal theoretical approximations, or the symmetric brass crystals. Bailey and Hallett (2006) notes that a key failure of the electrostatic analogy is that the theoretical capacitance relies heavily on symmetry in order to produce simple analytical solutions, but ice crystals in nature are rarely symmetric and cannot be accounted for by simple shapes. These factors were considered by McDonald (1963) who measured porous, dendrite-like brass models and found that the resulting differences in crystal surface area could modify the value of capacitance by up to 20%. Bailey and Hallett (2006) noted that asymmetry of structure or facets could result in uneven growth rates and vapour pressure over the surface, as well as mixtures of ice habit in otherwise equivalent conditions. Not only therefore is the use of the capacitance analogy an area of debate, but the theoretical and measured capacitances obtained to date are likely overly simplistic and bear considerable inaccuracies. Combined with the complexity of fine-scale surface processes, it may be important to scrutinise the suitability of this method in bulk schemes and the available data for constraining of the method in future.

In light of the challenges concerning the accurate prediction of mixed-phase processes in numerical models, coupled with the emergence of innovative but largely unverified microphysics schemes that aim to overcome these challenges, an investigation is necessitated to ascertain the viability of these schemes for operational weather models. Can these schemes yield superior representations of mixed-phase processes and can they increase the accuracy of forecast precipitation deriving from mixed-phase environments? Additionally, it is important to assess whether the leap in complexity that these schemes provide is a worthwhile pursuit, or one prone to unforeseen consequences.

To investigate these questions, two studies of north-east U.S. extra-tropical cyclones will be conducted (Parts II and III). The first study concerns a winter storm that produced record breaking snow accumulations in several states, exhibited an unusually high radar reflectivity, and underwent a well defined period of mixed-phase precipitation recorded at the surface. The purpose of this study is to assess the accuracy of several microphysics schemes when reproducing key observational markers of the storm including reflectivity, snow depths, ice habits, precipitation distributions, and mixed phase activity such as riming and melting. Part III examines two further winter storms that each impacted the U.S. and produced mixed-phase precipitation. The purpose of this study is to further investigate interesting results from Part II, including the role of geometric capacitance during deposition, and the artificial enhancement of cloud ice mass by a habit predicting scheme.

The remainder of Part I will provide an in-depth review of the case studies used in Part II and Part III, before detailing the mathematical and computational methodology used in these studies.

Chapter 2

Case Studies

Three case studies of north-east U.S. winter storms will be examined across Parts II and III of this thesis. In this chapter, we will briefly overview the development of each storm, its key features as observed and recorded by various measurement data, and the type of precipitation that were produced.

2.1 Part II: February 2013 Storm

At midday on 7th February 2013, two surface cyclones were present over the north-east United States. The first cyclone was present off the coast of Texas and had developed by 0600 UTC from an upper-level shortwave trough in a southern branch of the polar-front jet stream moving into the Gulf of Mexico. A second low was incident over Montana at approximately 1200 UTC, and had resulted from an upper-level shortwave trough in a northern branch of the jet stream in the Gulf of Alaska. The southernmost cyclone travelled eastward along the North Carolina coast and the northernmost cyclone took a path travelling east across the Midwest (Krekeler 2013). In combination, both lows were typical of a Miller Type-B cyclone track (Miller 1946).

By midday 8th February, both surface cyclones were present in close proximity over the North Carolina coast and over the next 12–18 hours both lows merged and deepened over the coast. The combined low dropped 24 mb from 994 mb to 970 mb between 1200 UTC 8th February to 1200 UTC 9th February or as much as 29 mb between 0600 UTC 8th February and 0600 UTC 9th February (Ganetis and Colle 2015; Krekeler 2013) meeting the criteria for *bomb* or *explosive* cyclogenesis (Sanders and Gyakum 1980). Such severe drops in pressure are not necessarily unusual for the winter storms over the eastern United States but they do bring severe winds and heavier precipitation as was seen in this case.

As the phased low travelled northwards along the coastline it brought sustained and severe precipitation primarily to the coastal regions of the north-eastern states, but precipitation was felt as far west as the Great Lakes region due to the track of the northernmost surface

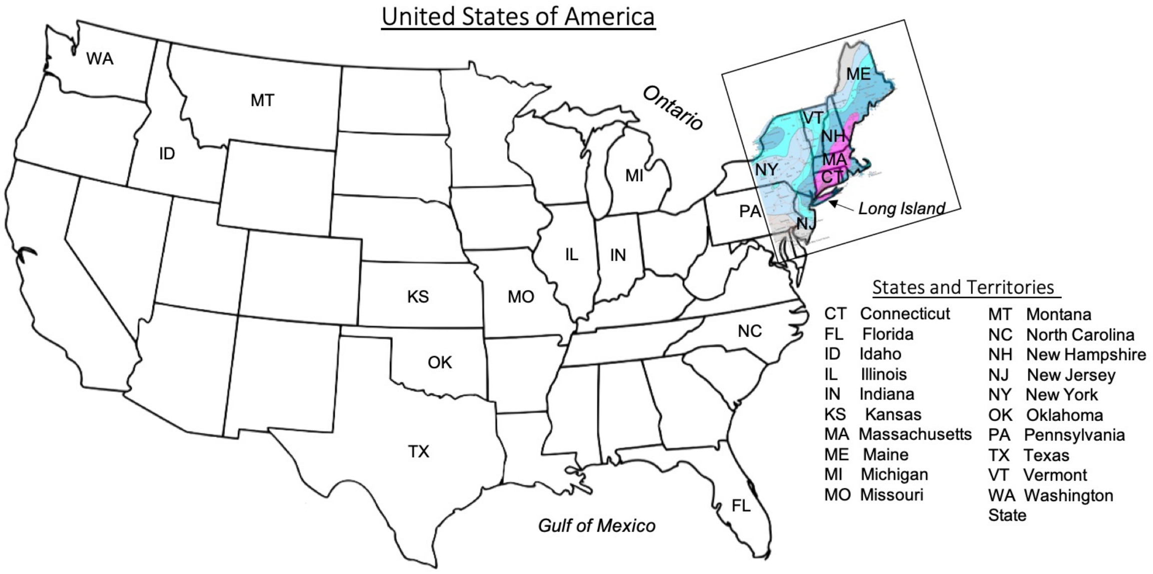
United States of America
WA
MT
ID
Ontario
ME
VT
NH
MA
CT
NY
PA
NJ
Long Island
MI
IL
IN
KS
MO
NC
OK
TX
FL
Gulf of Mexico
States and Territories
CT Connecticut
FL Florida
ID Idaho
IL Illinois
IN Indiana
KS Kansas
MA Massachusetts
ME Maine
MI Michigan
MO Missouri
MT Montana
NC North Carolina
NH New Hampshire
NJ New Jersey
NY New York
OK Oklahoma
PA Pennsylvania
TX Texas
VT Vermont
WA Washington State

Figure 2.1. Map of mainland United States of America (U.S.), Alaska omitted. Relevant states to this study are indicated with a two-letter state abbreviation. The approximate location of accumulated snow depth measurements shown in Figure 2.2 are overlaid.

cyclone. High pressure over Canada allowed subfreezing temperatures to reside over the coastal states which enabled the production of ice and snow hydrometeors that characterised the precipitation felt on the ground. This cold air, in combination with the advection of warm marine air, set up a strong, north-south oriented front along the eastern U.S. coast.

The storm was particularly devastating to the coastal regions in the proximity of its track. Hurricane force winds, extreme snowfall rates, and storm-surge flooding caused considerable damage to infrastructure that resulted in 6000 cancelled flights, 600,000 homes without power and 18 fatalities (Krekeler 2013). Accumulated snow depths shown in Figure 2.2 highlight the broad swathe of impacted areas spanning from Philadelphia Pennsylvania (PA) to the Great Lakes. In particular, a narrow stretch of coastal land in Connecticut, Massachusetts (MA) and New Hampshire (NH), as well as Long Island, were severely impacted by 24–36 in. of snowfall (0.6 m–0.9 m). Hamden, Connecticut (CT) received the highest total amount of snow at 40 in. ($\sim$ 1 m) and Portland, Maine (ME) received 31.9 in. (0.81 m), its highest ever snowfall for a single snowstorm (Krekeler 2013). After the storm, a federal state of emergency was declared for Connecticut and a federal disaster declaration was issued for Connecticut and Long Island at the cost of \$31 million (FEMA 2022; Ganetis and Colle 2015; Picca et al. 2014).

Beside the notable and severe precipitation rates, the storm possessed an abnormally high radar reflectivity factor that exceeded 50 dBZ, far higher than the 40 dBZ maximum reflectivity typically found in north-east U.S. snowbands. Picca et al. (2014) were the first to study the unusual reflectivity found in this storm, focusing on a very high reflectivity

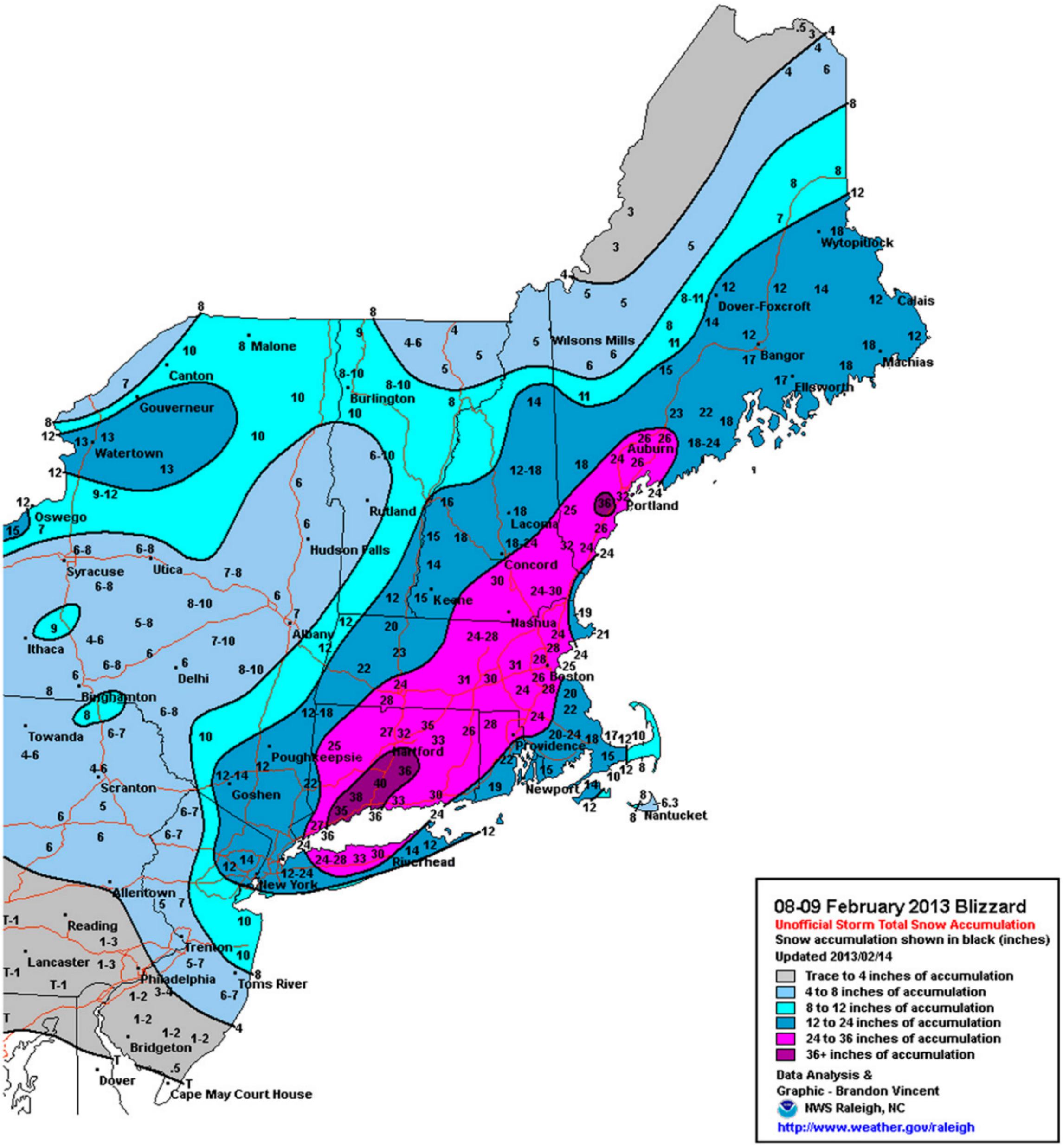
08-09 February 2013 Blizzard
Unofficial Storm Total Snow Accumulation
Snow accumulation shown in black (inches)
Updated 2013/02/14
▨ Trace to 4 inches of accumulation
▨ 4 to 8 inches of accumulation
▨ 8 to 12 inches of accumulation
▨ 12 to 24 inches of accumulation
▨ 24 to 36 inches of accumulation
▨ 36+ inches of accumulation
Data Analysis &
Graphic - Brandon Vincent
NWS Raleigh, NC
http://www.weather.gov/raleigh
Wytopitlock
Calais
Dover-Foxcroft
Bangor
Machias
Ellsworth
Wilsons Mills
Malone
Canton
Gouverneur
Watertown
Oswego
Burlington
Rutland
Hudson Falls
Auburn
Portland
Laconia
Concord
Keene
Nashua
Boston
Syracuse
Utica
Ithaca
Delhi
Albany
Binghamton
Towanda
Scranton
Poughkeepsie
Hartford
Providence
Newport
Nantucket
Goshen
Riverhead
New York
Allentown
Reading
Lancaster
Trenton
Philadelphia
Toms River
Bridgeton
Dover
Cape May Court House

Figure 2.2. Accumulated snow depths for the 8–9th February winter storm adapted from Griffin et al. (2014) and provided by the National Weather Service (NWS) Forecast Office in Raleigh. Approximate location of this region in the larger U.S. context is shown in Figure 2.1

region embedded within the storm's most intense snowband. Here the authors note that the reflectivity reached up to 60 dBZ in localised regions of the band, and underwent a sudden and sharp decline to around 30 dBZ over the course of only one hour. Using dual-polarisation radar products (Reflectivity at horizontal polarisation Z_H, differential reflectivity Z_{DR}, and correlation coefficient CC). Picca et al. (2014) related the peaks and troughs of reflectivity to microphysical processes and changes in precipitation-type within the band. To describe these features over the course of the storm, Picca et al. (2014) ordered their observations of precipitation and reflectivity into three approximate time periods or *phases* motivated by the distinct character of the precipitation and reflectivity produced during

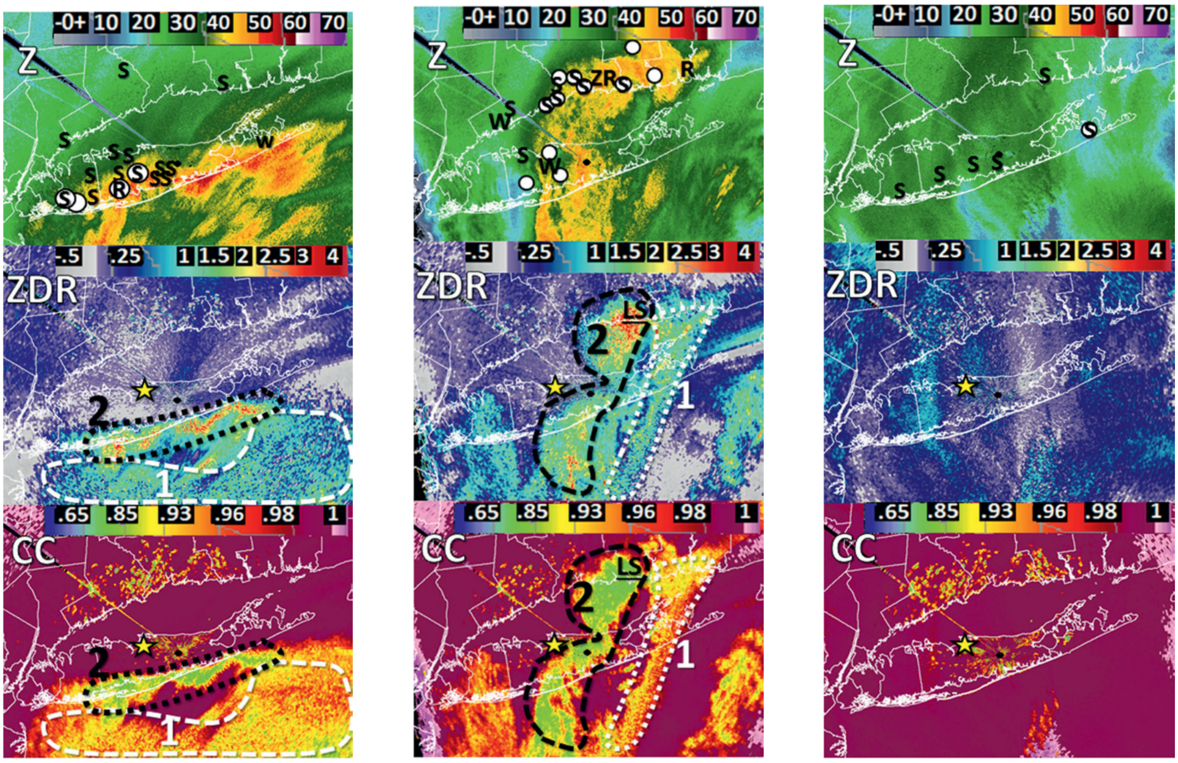

(a) 2129 UTC (b) 0042 UTC (c) 0340 UTC

Figure 2.3. Radar Plan Position Indicators (PPI) adapted from Picca et al. (2014) for times 2129 UTC (a), 0042 UTC (b), and 0340 UTC (c) representative of phases 1–3, respectively. Top: Reflectivity (at horizontal polarisation) Z_H. Middle: differential reflectivity Z_{DR}. Bottom: correlation coefficient CC. Radar data was retrieved from the National Weather Service (NWS) radar site based at Upton, New York with code-name KOKX (black dot). Yellow star shows the location of Stony Brook University. Media and mPING reports are indicated by bold lettering: S-Snow, W-Wet Snow, R-Rain, ZR-Freezing Rain, ○ -Sleet. mixed-phase precipitation areas shown by 1 (white dashed) and 2 (black dashed).

each phase, and the rapid change in these qualities between phases. Subsequent work by Ganetis and Colle (2015) followed a similar framework of phases for their description, noting its utility when describing the microphysical evolution of the storm. Consequently, we will also adapt the phase by phase description of the precipitation and reflectivity during the storm's evolution.

2.1.1 Phase 1: 2000–2300 UTC

Radar reflectivity products; the horizontal reflectivity factor (Z, referred to hereafter as "reflectivity"), differential reflectivity Z_{DR}, and the correlation coefficient CC, are shown for phase one at 2129 UTC in Figure 2.3. Here we associate an elevated region of reflectivity ($>$ 20 dBZ) with a broad, precipitating snowband extending from the comma-head of the storm. Reflectivity levels ranging between 20 and 30 dBZ are characteristic of precipitating snowbands in north-eastern U.S. snowstorms (Picca et al. 2014). This snowband exhibited a west-east orientation, aligned with and parallel to Long Island, NY. At its northernmost, the

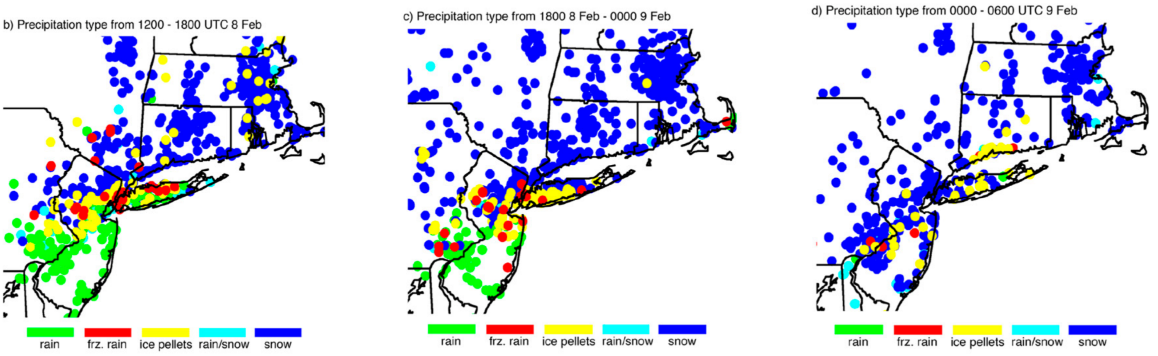
b) Precipitation type from 1200 - 1800 UTC 8 Feb
c) Precipitation type from 1800 8 Feb - 0000 9 Feb
d) Precipitation type from 0000 - 0600 UTC 9 Feb
rain
frz. rain
ice pellets
rain/snow
snow

(a) 1200-1800 UTC (b) 1800–0000 UTC (c) 0000-0600 UTC

Figure 2.4. Observed precipitation type provided by community mPING reports adapted from Griffin et al. (2014) between times; 1200–1800 UTC (a), 1800–0000 UTC (b), and 0000–0600 UTC (c) on 8–9th February.

band reached coastal Connecticut, and its southern extent spanned the entirety of Long Island and further south into the Atlantic. Notably, this snowband displayed a nearly uniform correlation coefficient (CC $\approx$ 1) and differential reflectivity ($Z_{\mathrm{DR}} \approx 0$ dB), collectively indicating a near uniform field of low-density aggregates with minimal riming both at and above this location (Ganetis and Colle 2015). This conclusion is corroborated by ground based reports retrieved from the Meteorological Phenomena Identification Near the Ground (mPING) community programme, which indicated precipitation at this time shown in Figure 2.4 (b) was snow across much of the U.S. coastal mainland and along the northern coast of Long Island. Ground based measurements of precipitation type at Stony Brook (SBNY) record primarily aggregates and heavy snowfall at this time.

A unique feature of this snowband was a collection of high reflectivity bands embedded within it, situated along, and parallel to, the south coast of Long Island and extended southward over the Atlantic ocean. At 2000 UTC the bands exhibited reflectivity in excess of 35 dBZ, with the greatest reflectivity observed along the Long Island coastline. Radar products from the nearby polarimetric WSR-88D S-band radar based at Upton, New York (KOKX) were retrieved and analysed in vertical cross sections by Griffin et al. (2014) who showed that the bands contained localised regions of elevated radar reflectivity that frequently exceeded 55 dBZ but were limited to a shallow, 1.5 km layer near to the surface. Differential radar reflectivity in this layer was high and correlation coefficient low, which Griffin et al. (2014) states indicated a melting layer that likely precipitated wet snowflakes or other melting hydrometeors. Picca et al. (2014) corroborated the presence of a melting layer in the high reflectivity region situated approximately 20 km south-east of SBNY, and also associated it with snow aggregates that had descended into a warm layer and had completely or partially melted. High reflectivity observed at this time was therefore likely due to a combination of both liquid and solid water, likely a mixture of snow, sleet and rain. In addition to the discovery of this melting layer, Picca et al. (2014) also identified a second, more northern area of interest approximately along the south coast of Long Island. This narrow band exhibited the greatest differential reflectivity ($Z_{\mathrm{DR}} > 2$) and a local minima in correlation coefficient $CC < 0.85$ which they determined indicated the refreezing signature that was documented by Andrić et al. (2013). This signature is indicative of refreezing rain and sleet below the melting layer, which is suitably close to the surface that such precipitation is readily observed.

Precipitation across Long Island was spatially segregated between the north and south as Picca et al. (2014) identified using dual-polarisation radar products. Along, and south of, Long Island's southern coast two regions defined by enhanced differential radar reflectivity ($Z_{\mathrm{DR}} >$ 1dB) and reduced correlation coefficient (CC < 0.95 dB) were associated with mixed-phase activity. The southernmost of these two regions indicated the presence of melting, liquid-coated snow as it fell through a warm layer aloft approximately 20 km southeast of Stony Brook. The second, northernmost of these two regions indicated refreezing of partially melted hydrometeors and rain into sleet and ice pellets below a melting layer. Consequently, precipitation in the south of Long Island featured varying combinations of rain, sleet, ice pellets and wet snow. North of the southern shoreline and extending toward the mainland U.S. coast was a large region of $Z_{\mathrm{DR}} \sim$ 0 dB, CC $\sim$1 dB which identified the snowband. Surface reports of precipitation below this area at this time indicate large, dry aggregates of snow with low to moderate surface riming. At the intersection of these two regions, approximately situated over central Long Island, lay a transitional zone that produced combinations of the aforementioned mixed-phase precipitation and dry precipitation. Throughout the phase, this transitional belt moved progressively northward and reorientated to a north-south parallel with the progression of the storm, bringing mixed-phase precipitation types increasingly north across central Long Island.

Snowfall rates for this period spanned 4–8.5 cm hour^{-1} with a snow-to-liquid ratio (SLR) of 10–13:1 near SBNY, which is positioned to the north of central Long Island (Ganetis and Colle 2015; Picca et al. 2014). Surface observations of microphysical habit at this location indicate aggregates composed of colder-type crystals, such as side planes and plates, with reports of aggregates up to 4 cm in diameter with little riming (Ganetis and Colle 2015; Picca et al. 2014). Observations in the south indicate mixed-phase precipitation, rain, and even several inches of sleet accumulation (Picca et al. 2014). As the storm progressed east during the course of this phase, the snowbands and the high reflectivity contained within them, rotated gradually to a more north-south orientation. Cross sections of reflectivity at 2130 UTC in Ganetis and Colle (2015) (their Figure 5), indicate that the melting signature had moved north-west encroaching on SBNY and central Long Island by this time.

Griffin et al. (2014) examined the shape of the melting layer in the vertical and noted a downward protrusion in the reflectivity bright band, indicating descent of the melting layer over the course of the phase. Two causes for this effect were hypothesised, first that localised updrafts enhanced accretion in this area and formed larger, faster falling particles that subsequently melted lower in the warm layer. Polarimetric evidence by Picca et al. (2014) showed that an updraft similar to that found in warm-season convection was present, and may have been responsible for enhanced riming in this area. However, Griffin et al. (2014) also speculates that enhanced latent cooling due to melting of a heavy pocket of precipitation could be the central cause. This would require the emergence of developing isothermal layers below the melting layer.

2.1.2 Phase 2: 2300–0200 UTC

In phase two, the snowband, both mixed-phase regions to the south of Long Island and, consequently, the transition zone all rotated to a southwest to north-east parallel, intersecting central Long Island and extending into the U.S coastline at southern Connecticut. During this phase, the band continued to return high Z_H, reaching a peak intensity of 57.5 dBZ in a region of highly diverse hydrometeors $(CC < 0.85)$ with substantial differential reflectivity $(Z_{\mathrm{DR}} > 3)$ at 0042 UTC. Radar plots show that the refreezing and melting signatures Picca et al. (2014) had identified were still present, and had both shifted to a north south orientation. The refreezing layer was positioned just west of SBNY and east of the melting layer signature. Within the refreezing layer, a local maximum persisted just east of New Haven, CT where large sleet was observed at the surface.

During this phase, a warm layer was collocated with the snowband, bringing considerable mixed-phase precipitation to much of Long Island and the coastal U.S. Picca et al. (2014) identified a decrease in correlation coefficient over this area tied to “heavy snow, raindrops, ice pellets approaching the size of hail, and graupel” and correlated sustained high reflectivity and differential reflectivity with large numbers of liquid coated hydrometeors indicative of melting aloft. This radar-derived characterisation of precipitation agreed with multiple ground level reports of mixed-phase precipitation during this phase. mPING reports of ice pellets at central Long Island and Connecticut in Griffin et al. (2014) (their Figure 2), correspond with the position of the mixed-phase transition line.

Surface observations at Stony Brook recorded a sharp decline in the snowfall rate, which reduced to 1.5–7.6 cm hour^{-1}, and the SLR, which dropped below 8:1 and reached as low as 4:1 by 0000 UTC. During this time, heavy snow was replaced by ice pellets, heavily rimed crystals including graupel, and sleet (Ganetis and Colle 2015). In Connecticut sleet was large enough to be considered pea-size hail (Picca et al. 2014). Observations of habit and degree of rime at SBNY from note that 10–20% of observed hydrometeors were categorised as miscellaneous ice, and the average degree of rime temporarily reached a rating of 4

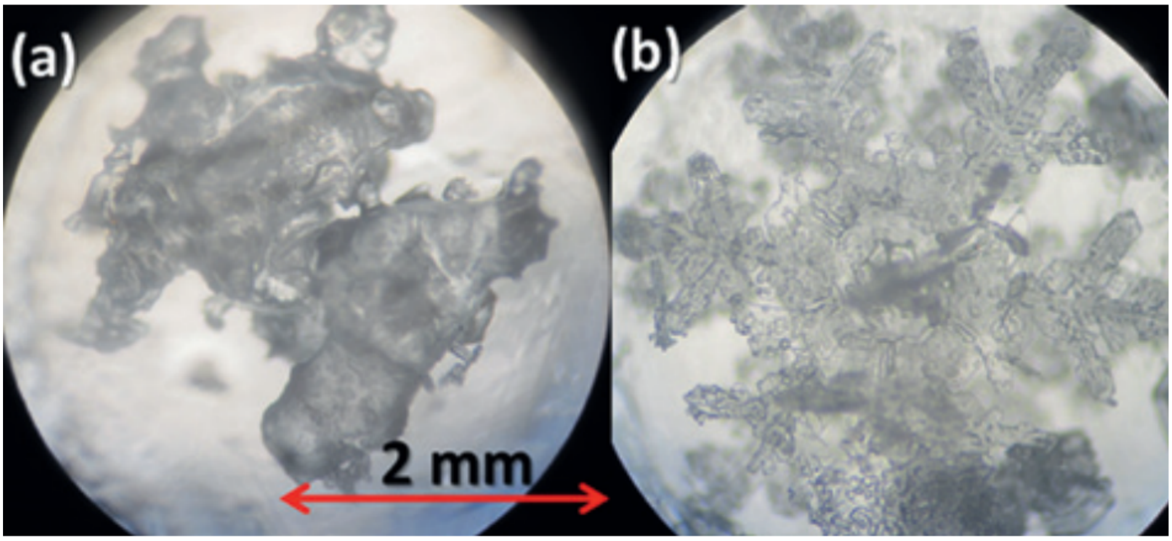

Figure 2.5. Images of ice particles sampled at Stony Brook adapted from Picca et al. (2014) (their Figure 8). (a) irregular sleet that infers wet growth and refreezing were present at 0043. (b) lightly rimed plate with dendritic extensions taken at 0415 UTC February 9th.

(heavy riming or graupel-like) at 0030 UTC at SBNY (Ganetis and Colle 2015). Additionally, the maximum degree of rime reached 5 at 2300 and 0030 UTC indicating the presence of graupel at this location and time. Images of crystals during this phase taken by Picca et al. (2014) and shown in Figure 2.5 provide visual evidence of wet growth, whereby intense accretion of supercooled droplets close to 0°C maintain their liquid state and coat the ice on a smooth liquid-skin. This period of mixed-phase activity slowed at SBNY from approximately 0130 UTC, when there was a significant reduction in sleet and miscellaneous crystals, as well as the degree of riming of crystals (Ganetis and Colle 2015). However, mixed-phase activity continued over Connecticut where R. Hanrahan (Personal communication with Picca et al. (2014)) noted “large sleet” resembling pea-sized hail from 0030 UTC until 0200 UTC.

2.1.3 Phase 3: 0200–0800 UTC

After 0200 UTC, radar reflectivity suddenly decreased across Long Island, marking a shift in the precipitation field away from the mixed-phase and toward dry snow production, though radar reflectivity analysis by Griffin et al. (2014) showed that wet snow and ice pellets were still present at Connecticut as late as 0236 UTC. Analysis of the reflectivity after 0200 UTC shows that the $>$ 50 dBZ reflectivity factor Z_H abruptly stopped at 0230 UTC (Ganetis and Colle 2015) and the entire high-reflectivity banded region saw a rapid decrease in horizontal reflectivity factor to 30 dBZ within an hour. Picca et al. (2014) noted that the reduction in reflectivity was likely the consequence of a shift in hydrometeor density away from high density ices originating from wet growth processes, toward less dense hydrometeors such as aggregates. Indeed, mixed-phase precipitation had reduced and was replaced by dry snow as the lower troposphere cooled, marking a return to similar conditions as in phase one. Consequently, Long Island and much of the coastal mainland remained beneath broad and uniform snowband coverage that remained for several hours after 0200 UTC. The reflectivity for the remainder of the phase spanned 25–35 dBZ and remained elevated over some parts of Connecticut (Griffin et al. 2014).

At the surface, precipitation returned to heavy ($\sim$ 6.5 cm hour^{-1}) bouts of snow that remained steady or even increased in intensity. Traces of melting or riming were greatly reduced and this is mirrored by the corresponding SLR increase to 9–10:1 during this phase (Picca et al. 2014). This is in keeping with the reflectivity aloft, Ganetis and Colle (2015) notes that the reflectivity shift occurred only throughout the lower atmosphere where mixed-phase precipitation had been present and consequently the change in reflectivity indicated a stark reduction in melting, and refreezing but not a cessation of snow production. At SBNY, crystal habit observations showed that snow was formed of aggregates of colder-type crystals, such as stellars. Conditions in this phase remained consistent until 0500–0700 UTC when habit diversity reduced and dendritic observations increased. The snowband persisted until 0800 UTC 9th February before dissipating over Long Island.

2.2 Part III: January and February 2020 IMPACTS Storms

In Part III of this thesis, two further case studies are undertaken to examine the development of cloud ice during deposition and its impact upon the subsequent generation of mixed-phase particles at the surface. This study was designed to expand and elaborate on the findings of Part II so it was important to maintain geographical and synoptic similarity with the previous case. Some additional priorities for the new case studies were the availability of comprehensive precipitation reports, the presence of mixed-phase activity, particle size data such as particle size distributions, and if possible ice habit data, such as imagery.

The required criteria were met by the recently conducted Investigation of Microphysics and Precipitation for Atlantic Coast-Threatening Snowstorms (IMPACTS) field campaign sponsored by the National Aeronautics and Space Administration (NASA) (McMurdie et al. 2022). The IMPACTS campaign was designed to improve the current understanding of snowfall processes within winter storms along the U.S. east coast by uniting and coordinating measurement resources across multiple states and institutions. The campaign captured a variety of data types throughout its course, including ground based measurements and *in situ* data obtained via the P3 and ER-2 aircraft. Importantly, the IMPACTS campaign focused on storms that were similar to the previous case study in Part II, for example these were winter storms that occurred in the U.S., and exhibited snowfall and mixed-phase activ-

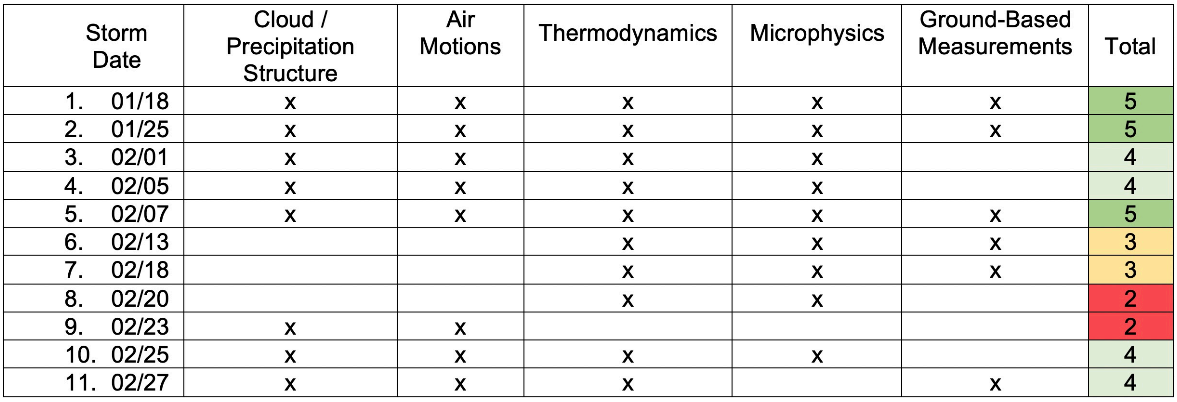

Storm Date	Cloud / Precipitation Structure	Air Motions	Thermodynamics	Microphysics	Ground-Based Measurements	Total
1. 01/18	x	x	x	x	x	5
2. 01/25	x	x	x	x	x	5
3. 02/01	x	x	x	x		4
4. 02/05	x	x	x	x		4
5. 02/07	x	x	x	x	x	5
6. 02/13			x	x	x	3
7. 02/18			x	x	x	3
8. 02/20			x	x		2
9. 02/23	x	x				2
10. 02/25	x	x	x	x		4
11. 02/27	x	x	x		x	4

Table 2.1. Review of measurement data obtained for each storm during the IMPACTS 2020 campaign. Crosses indicate that the data was obtained but not that the data was available for use at the time of writing.

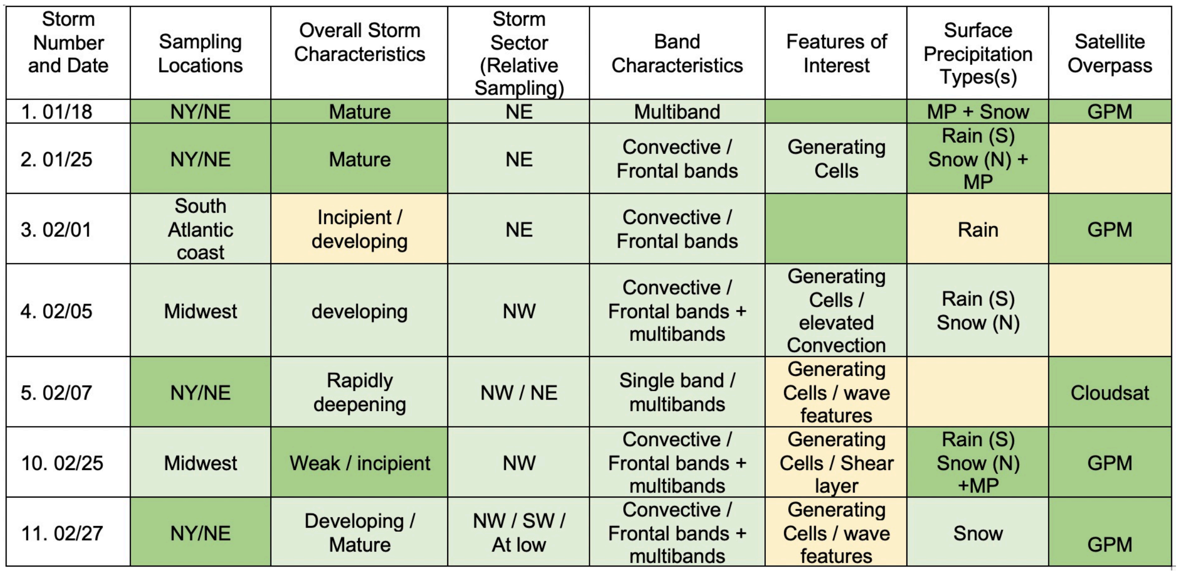

Storm Number and Date	Sampling Locations	Overall Storm Characteristics	Storm Sector (Relative Sampling)	Band Characteristics	Features of Interest	Surface Precipitation Types(s)	Satellite Overpass
1. 01/18	NY/NE	Mature	NE	Multiband		MP + Snow	GPM
2. 01/25	NY/NE	Mature	NE	Convective / Frontal bands	Generating Cells	Rain (S) Snow (N) + MP	
3. 02/01	South Atlantic coast	Incipient / developing	NE	Convective / Frontal bands		Rain	GPM
4. 02/05	Midwest	developing	NW	Convective / Frontal bands + multibands	Generating Cells / elevated Convection	Rain (S) Snow (N)	
5. 02/07	NY/NE	Rapidly deepening	NW / NE	Single band / multibands	Generating Cells / wave features		Cloudsat
10. 02/25	Midwest	Weak / incipient	NW	Convective / Frontal bands + multibands	Generating Cells / Shear layer	Rain (S) Snow (N) +MP	GPM
11. 02/27	NY/NE	Developing / Mature	NW / SW / At low	Convective / Frontal bands + multibands	Generating Cells / wave features	Snow	GPM

Table 2.2. Review of features and qualities found in storms during the IMPACTS 2020 campaign that were found to have the most comprehensive data sets (see Table 2.1). Cell shading indicates the suitability for this storm as a case study from most suitable (dark green) to least suitable (yellow).

ity.

The entire 2020 campaign (the only campaign in which data was available for use) was evaluated to meet the previously outlined criteria and to determine if any storms were suitable for this investigation. Tables 2.1 and 2.2 indicate how each storm was evaluated based on its data availability and similarity to the storm studied in Part II. Storms 1, 2 and 5 had the most comprehensive data sets and storms 3, 4, 10 and 11 were the second-most comprehensive. More in-depth analysis of the available data sets (see Appendix S.1 for an example) indicated that the 18th January 2020 and 25th February 2020 storms ultimately were most suitable for case studies.

2.2.1 CASE 1: 18th January 2020 Storm

A winter storm was forecast to impact the north-eastern U.S. on the 18th and 19th January 2020 providing an ideal first case for the IMPACTS campaign. A low pressure system passed over the upper Midwest and headed towards the north-east over Michigan (MI) and southern Ontario. The Global Forecast System (GFS) model-derived forecasts shown in Figure 2.7 panel (b) at 0600 UTC 18th January indicated a mobile upper-level short wave was situated over Kansas (KS) (McMurdie et al. 2020). Throughout the 18 January the shortwave sharpened and became negatively tilted, and by 1800 UTC the short wave trough was situated over Indiana. At this time, data recording flights took off with the intent to measure precipitation characteristics east of the parent cyclone stationed over Michigan. Subsequently, between 1800 UTC and 0000 UTC, the short-wave broadened enabling mid-level frontogenesis over New York State at 1800 UTC that preceded a warm front over Toronto and Ohio. A warm frontal snowband coincided with low level 850 hPa temperatures of approximately -7 $^\circ$C over New York State causing precipitation to fall as snow. As the warm front progressed north-east, frontogenesis occurred ahead of it, bringing a blanket of snow over Long Island, upstate New York, western Vermont and North Hampshire. By the end of the flight at around 0000 UTC, the trough had broadened and the upper level flow became more zonally orientated resulting in a westerly wind across the Midwest states.

Precipitation was expected to the east of the parent cyclone, across northern New York (NY) and Vermont (VT) where low level (850 hPa) temperatures were below -7 $^\circ$C resulting in snow. From 1800 UTC on the 18th, precipitation built in eastern NY, peaking at 2200 UTC and then waned with the descent of dry air aloft. The rain/snow line then travelled north from south of Pennsylvania (PA) to southern NY around 0400 UTC on the 19th. The 3 km North American Mesoscale Forecast System (NAM) forecast predicted a high likelihood of snow accumulation north of PA, while to the south rain was the predominant precipitation type. In the south and east of PA at the intersection of these precipitation types the NAM forecast predicted mixed-phase precipitation such as sleet and freezing rain.

The coordination of measurements across states and institutions was supported by various forecasts including that by NAM, WRF and GFS models. WRF simulated geopotential shown in Figure 2.7 panel (a) produced a very similar geopotential field to that in the GFS, with vorticity of up to 5×10^{-4} s^{-1} and meridional flow about the low pressure centre. The WRF simulated pressure field evolved a very similar spatial distribution as the GFS model, but experienced a less sharp trough and winds to the west of the low became more zonal but retained a stronger meridional component than in the GFS. Comparison of the WRF simulated fields to meteogram products in Figure 2.11 shows that, at Stony Brook, the WRF model overestimated the temperature, wind speed and mean sea level pressure by

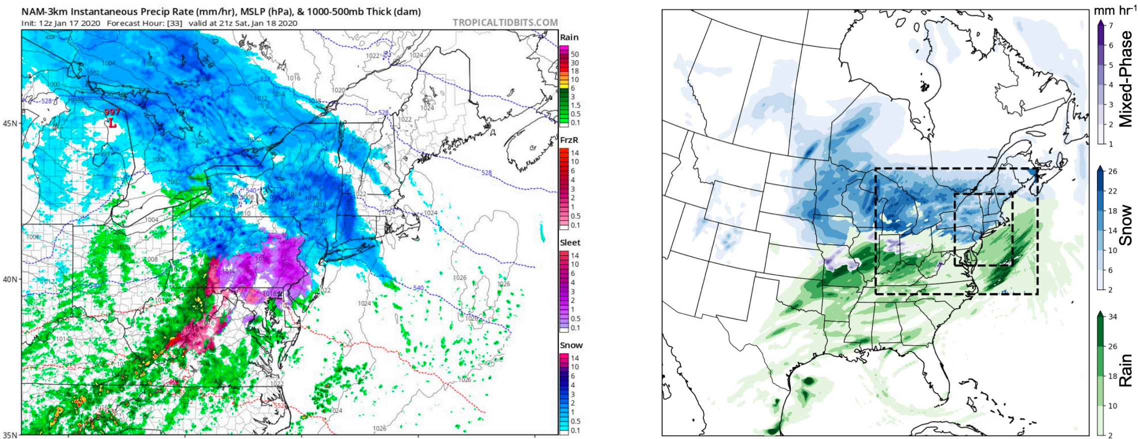
NAM-3km Instantaneous Precip Rate (mm/hr), MSLP (hPa), & 1000-500mb Thick (dam)
Init: 12z Jan 17 2020 Forecast Hour: [33] valid at 21z Sat, Jan 18 2020
TROPICALTIDBITS.COM
Rain
FrzR
Sleet
Snow
45N
40N
35N
85W
80W
75W
70W
65W
mm hr⁻¹
Mixed-Phase
Snow
Rain

(a) Case 1 18/01/2020: NAM 3 km precipitation forecast.

(b) Case 1 18/01/2020: WRF precipitation forecast with Morrison microphysics.

Figure 2.6. Instantaneous precipitation rate (mm hr^{-1}) and pressure (hPa) for 18th Jan 2100 UTC forecast by the NAM model (a) and WRF model with Morrison microphysics (b). Precipitation type indicated by colour: snow (blue), rain (green) and likely mixed-phase (purple) are shown across eastern PA and Jersey. WRF domains 2 and 3 are indicated with dashed lines. Parent domain is indicated by the Figure border.

small amounts.

The cross-model forecasts enabled planning of flight paths for the ER-2 and P-3 aircraft, which aimed to study generating cells in the eastern sector of the low, passing through Michigan and intercepting over New York (McMurdie et al. 2020). The P-3 and ER-2 aircraft flight path is shown in Figure 2.9 panel (b), flying a bow-tie path based at Albany, NY and oriented north-south. This path intersected eastern NY, VT and New Jersey and the bow tie pattern was flown at three altitudes to obtain data relevant to the generating cell top at 5 km, the crystal growth region 3.5 km and a high shear region at 2 km. Take off was at approximately 1700 UTC and 1800 UTC 18 January for ER-2 and P-3, respectively, and the total mission flight time was between 1900 UTC 18th and 0000 UTC 19th January. This time period and path overlapped with areas of NAM predicted snowfall and mixed-phase predictions, which overlap into New Jersey from eastern PA. Additionally the flight takes a route from south to North of Long Island where radar imagery shows melting and or riming were present.

Several soundings were made to sample the thermodynamic environment at approximately 1800 UTC 18 January. KALB (Albany) and KGYX (Portland) experienced dry, low-level air but at KBUF (Buffalo, New York) to the west, the atmosphere was mainly saturated in the whole column. Figure 2.10 indicates the observed saturation as well as reasonable reproductions by the WRF model for the ISHMAEL and Morrison schemes, which are used in this study. All three National Weather service (NWS) locations experienced warm air advection, a stable frontal zone layer at low to mid-levels, a near moist-neutral layer aloft and a high tropopause of around 200 hPa. KALB started to report snow at 1800 UTC and

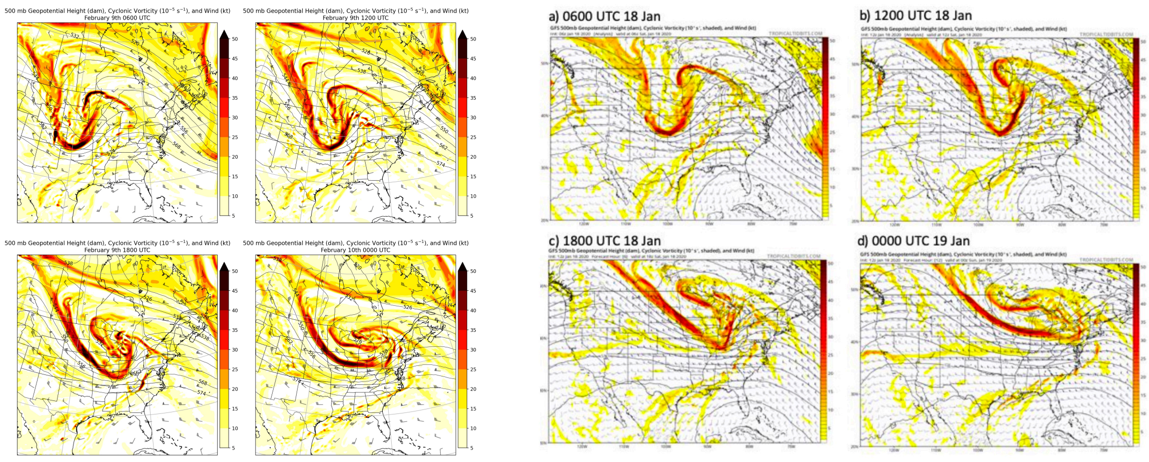

(a) Case 1 18/01/2020: WRF simulation

(b) Case 1 18/01/2020: GFS Model

Figure 2.7. 500-hPa Geopotential heights (contoured), winds, and absolute vorticity for left: WRF simulation, right: GFS model.

by 2100 UTC the column at this location was moist. All three locations showed saturated environments by 0000 UTC. At this time, mid level dry air had begun to intrude at KBUF with IMPACTS sounding teams at Binghamton reporting a similar intrusion albeit slightly later. Mid-level drying was evident in Geostationary Operational Environmental Satellite (GOES) imagery which showed an eastward path across New York state from 2100–0000 UTC. Imagery indicates that the intrusion of cold air may have led to instability as the stratiform deck was replaced by convective cells.

The passage of the front can be described by observations taken at Stony Brook where the warm frontal band approached from 1500 UTC and crossed the site at 1900 UTC. Before and after the band's arrival, wind speed increased and was southerly, whilst during the passage winds were slower and easterly. The microwave radiometer (MWR) present at Stony Brook indicated that dry air was in place until 1800 UTC when snowfall began and the cloud base lowered. Integrated water vapour increased until 0200 UTC. Radar reflectivity shown in Figure 2.8 highlights the rapid (< 1 hour) increase in reflectivity from less than 20 dBZ to between 20 and 30 dBZ at 1900 UTC. Next-Generation Radar (NEXRAD) at KOKX showed a near uniform ρ_{hv} field at 1851 UTC indicating snowfall, but by 2307 UTC two patches of melting or mixed-phase activity or both were present. Interestingly, the Doppler velocity field showed streaks of shear layers that were associated with shallow, turbulent layers.

The aircraft sampled deep low level cloud at 1834 UTC but turned around at 1854 UTC due to mechanical issue. P-3 sampled snow at 1838 UTC just before entering the bow tie pattern near the southern tip of New York state and at an altitude of approximately 5.1 km. A hexagonal plate was imaged at this time (Temperature:-12.2 °C, Dew point: -15.3°C, Pressure: 534.7 hPa). Later at 3 km altitude in northern New York State plates and capped

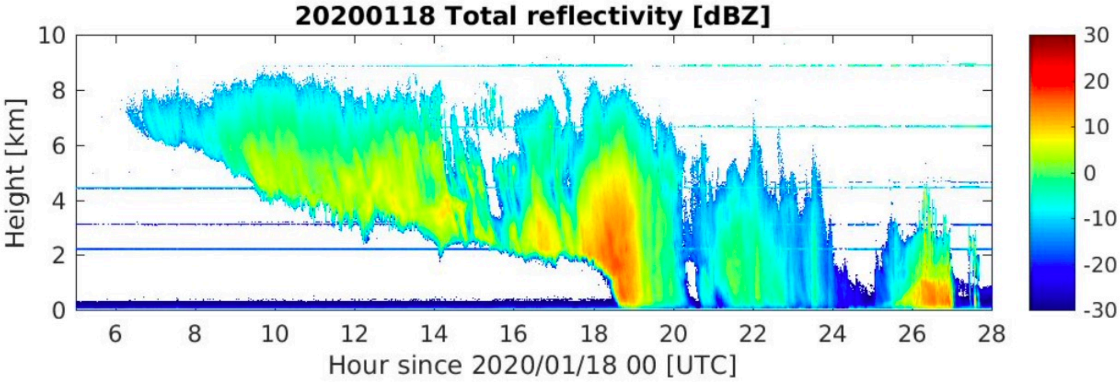

Figure 2.8. Time series of reflectivity above SBNY. Increased reflectivity and cloud depth present from 1800 UTC.

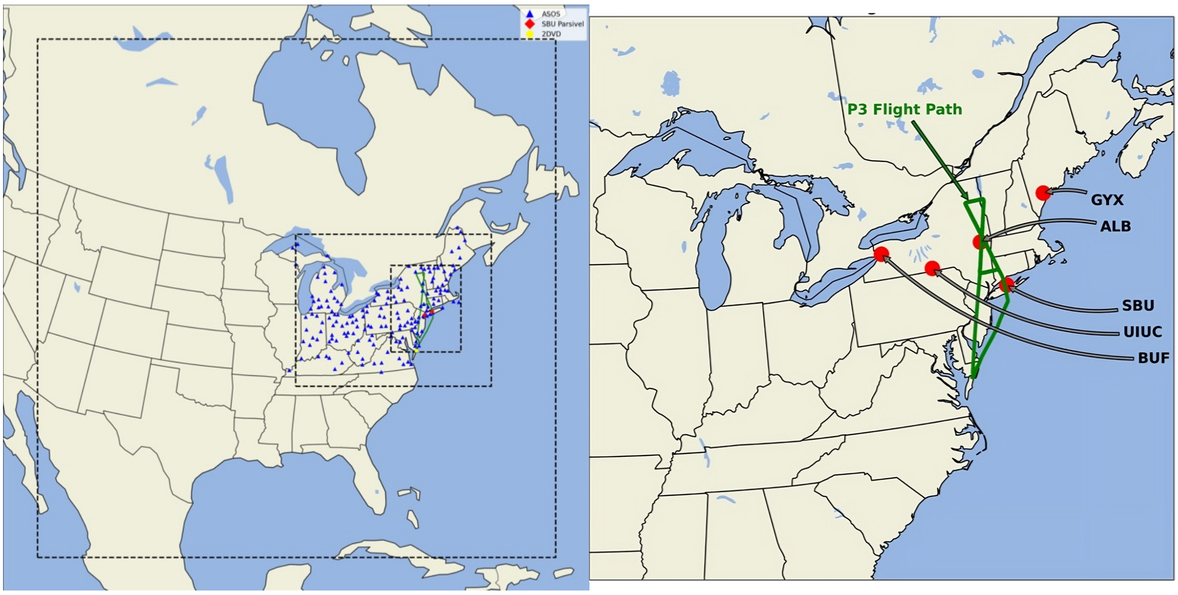

(a) Ground based measurement locations

(b) Sounding locations and P3 flight path

Figure 2.9. Example domains and measurement data coordinates for Case 1. Nested Domains 1-3 are shown by black dotted rectangles. In (a), ASOS (Automated Surface Observing Systems), SBU (Disdrometer) and 2DVD (Two-Dimensional Video Disdrometer) points are shown with coloured shapes indicated in legend. In (b), sites of release of sounding balloons measuring thermodynamic data. Green line shows flight path of P-3 and ER-2 aircraft for 18th January. Course is a bow tie flown at different altitudes and overlapped by both aircraft simultaneously on the long lengths.

columns were imaged (Temperature: -10.0°C, Dew point: -13.6 °C, Pressure: 677.2 hPa). Finally at 2.3 km altitude along eastern New York state and within a higher (25 dBZ) reflectivity region sampled by NEXRAD needles and aggregates were imaged with (Temperature: -4.2 °C, Dew point: -7.0 °C, Pressure: 756.7 hPa). Comparison with familiar ice crystal growth diagrams indicate that supersaturation over ice was likely low.

After the flight, at 2300 UTC, P-3 made an overpass of Stony Brook north of Long Island at an altitude of approximately 3.6 km. At this time, SBNY was experiencing snow but after 0000 UTC radiometer shows that liquid water significantly increased. The Range-Height

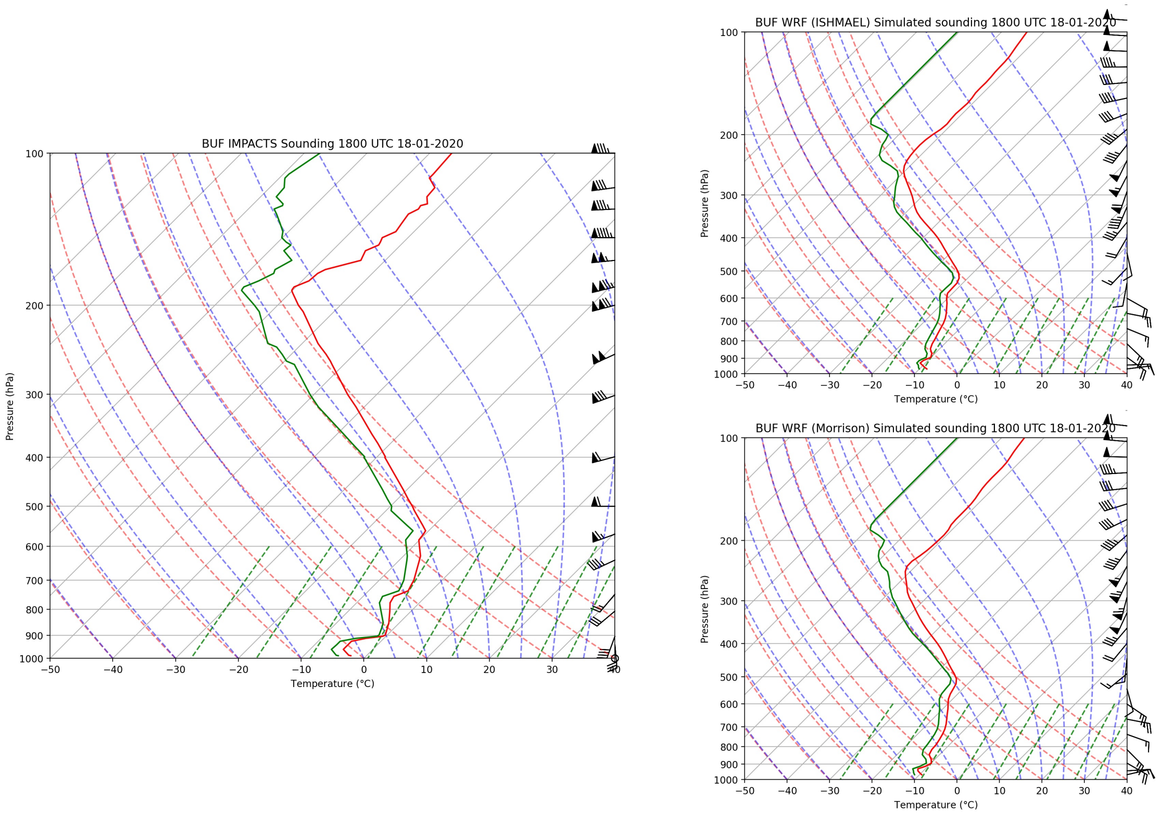

Figure 2.10. Skew T-log p diagram of the observed sounding at Buffalo, NY (BUF) 1800 UTC 18 January 2020. Left: IMPACTS observed sounding. Right-top: WRF simulated sounding for ISHMAEL microphysics. Right-bottom: WRF simulated sounding for Morrison microphysics.

Indicator (RHI) taken at 2300 UTC showed increased numbers of convective generating cells and a decrease in differential reflectivity Z_{DR}, which was likely to be a sign of aggregation and riming.

2.2.2 CASE 2: 25th February 2020 Shallow Precipitation Bands in the North-West Sector of a Low Centre

For the second case, a low pressure system in the Midwest U.S. was forecast to create a narrow snow band from eastern Iowa to southern Michigan. GFS forecasts shown in Figure 2.12 indicated that two upper level troughs merged to create the low pressure system that would track from Oklahoma at 1200 UTC 24th to the Great Lakes 0000 UTC 26th. The resulting snow band was forecast to be narrow due to the prevalence of dry air both north and south of the system. The mission goal was to study the microphysical characteristics of the snowband over central and northern Illinois and to sample the physical characteristics of precipitation in the northwest quadrant of the low.

At 1200 UTC on 24th February, two 500 hPa troughs occurred over the Western U.S. The easternmost trough was situated over Washington state and Idaho, whilst the westernmost

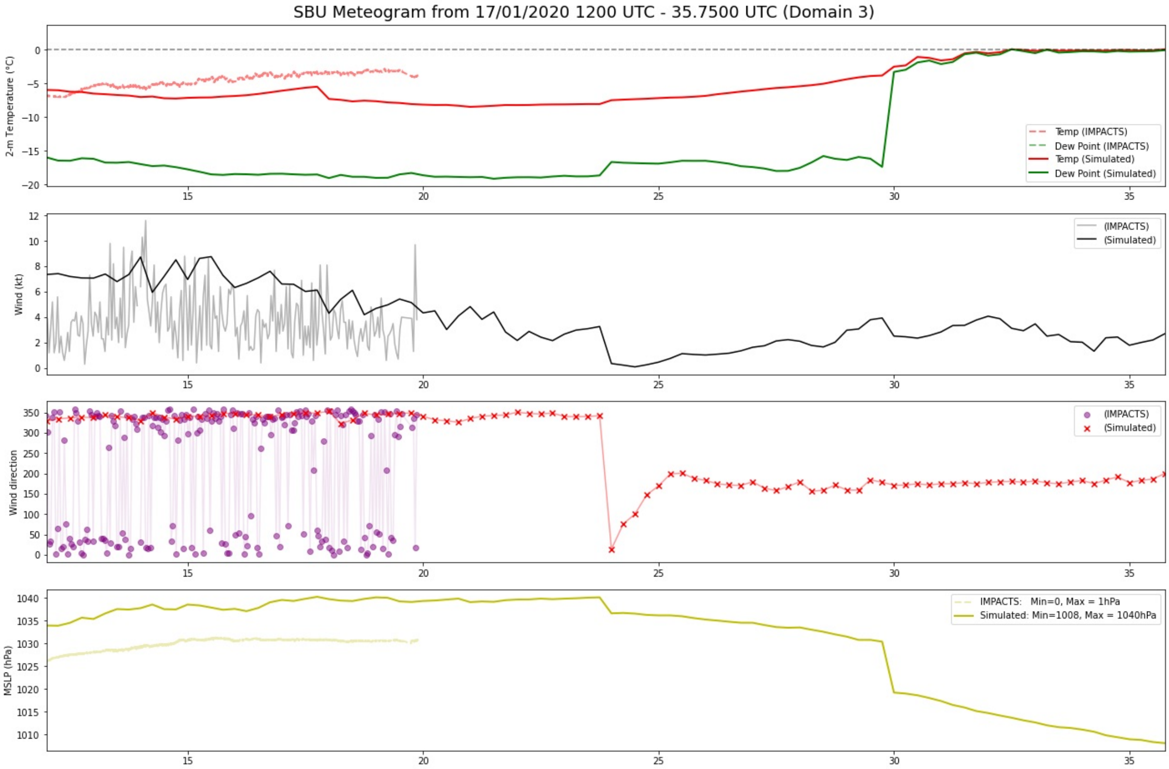

Figure 2.11. Observed and simulated meteogram qualities for Stony Brook University (SBU). Note that observations at this station only span 20 hours from 17/01/2020 0000 UTC. Top: Temperature (°C) and Dew-point. Middle-upper: Wind speed (kt). Middle-lower: Wind direction (degrees from north). Bottom: mean sea level pressure (hPa)

was over Oklahoma where it advected cyclonic vorticity to Missouri and Illinois. At this time, a strong subtropical jet situated across Mexico, Arkansas and Texas in a north-east southwest orientation, drew dry and moist air along its path.

By 0000 UTC 25th February, the eastern trough grew less pronounced and the westernmost trough dug south over northern Texas. Low-level temperatures over the Midwest were anomalously warm, with the 0°C isotherm situated zonally over Illinois, Ohio and Indiana. The primary surface low associated with the 25th February event was situated over southern Missouri by this time. A warm front allowed warm air convection into Tennessee. By 1200 UTC 25th February, the low had moved north-eastward towards the Indiana-Kentucky border and subsequently between 1200 UTC and 0000 UTC, the surface low moved north-eastward and colder air was advected southward over Missouri and Illinois.

At 0000 UTC 26th February (see Figure 2.12 panel d) the troughs had phased and only one trough existed over New Mexico and Texas. At this time, a second dry air stream was present stretching from North Dakota to Texas. The phasing of these jet streams were inconsistently predicted with forecast models and slower phasing affected the low level dynamic support. Cold air advection continued behind the cyclone causing surface temperatures to drop to 0°C for northern Illinois and Indiana by this time. Soundings from Illinois

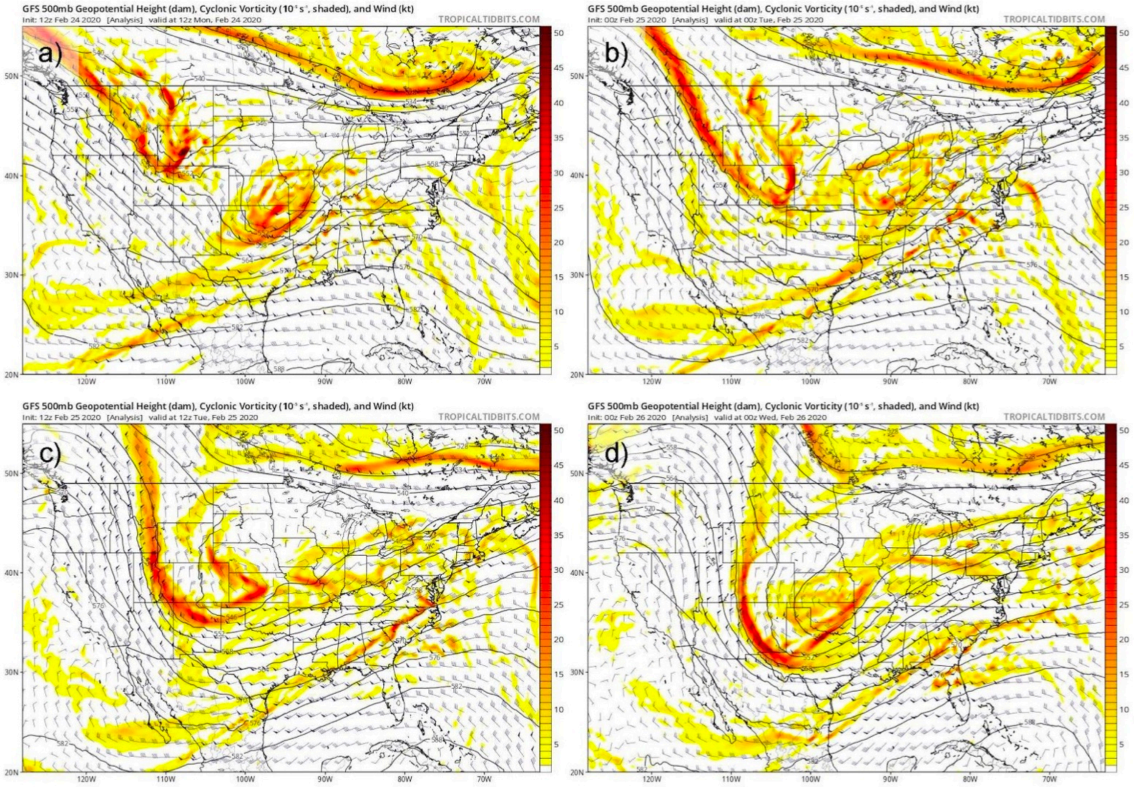
GFS 500mb Geopotential Height (dam), Cyclonic Vorticity (10^{-5} s^{-1}, shaded), and Wind (kt)
Init: 12z Feb 24 2020 [Analysis] valid at 12z Mon, Feb 24 2020
TROPICALTIDBITS.COM
a)
GFS 500mb Geopotential Height (dam), Cyclonic Vorticity (10^{-5} s^{-1}, shaded), and Wind (kt)
Init: 00z Feb 25 2020 [Analysis] valid at 00z Tue, Feb 25 2020
TROPICALTIDBITS.COM
b)
GFS 500mb Geopotential Height (dam), Cyclonic Vorticity (10^{-5} s^{-1}, shaded), and Wind (kt)
Init: 12z Feb 25 2020 [Analysis] valid at 12z Tue, Feb 25 2020
TROPICALTIDBITS.COM
c)
GFS 500mb Geopotential Height (dam), Cyclonic Vorticity (10^{-5} s^{-1}, shaded), and Wind (kt)
Init: 00z Feb 26 2020 [Analysis] valid at 00z Wed, Feb 26 2020
TROPICALTIDBITS.COM
d)
50N
40N
30N
20N
120W
110W
100W
90W
80W
70W
50
45
40
35
30
25
20
15
10
5

Figure 2.12. GFS forecast Geopotential Height (dam), cyclonic vorticity (10^1 s^{-1}) and wind (kt). Top left: 1200 UTC February 24. Top right: 0000 UTC February 25. Bottom left: 1200 UTC February 25. Bottom right: 0000 UTC February 26.

airport (ILX) and the University of Illinois campus (UIUC) show that the air was saturated from the surface up to 650 hPa. Soundings at Davenport, IA (DVN) showed drier air as it was at the edge of the precipitation shield. In all three locations a shear zone was present at 750 hPa (north-east winds below, southwest winds above) and a shallow isothermal layer below 900 hPa (1 km) was present. By 0600 UTC 26th February, the low had progressed east over southern Ohio.

NAM and NWS forecasts predicted that the heaviest snow (> 6 in.) would fall over central Illinois but different models predicted different times of arrival that spanned between 1600 UTC and 2200 UTC, and then continued into the morning. GFS, European Centre for Medium-Range Weather Forecasts (ECMWF) and the Regional Global Environmental Multiscale Model (RGEM) forecast mixed-phase precipitation and rain to the south. Ultimately, the low pressure system over the Midwest produced snow over Missouri, Illinois, Indiana, and Lower Michigan, originating from the northwest sector of the low. The snowband in the wrap-around region of the cyclone produced 2–4 in. across Illinois and parts of Indiana and Michigan with local amounts exceeding 4 in.

The reasonable agreement between forecast models enabled the P-3 and ER-2 aircraft to conduct a racetrack-pattern flight path shown in Figure 2.13, oriented northwest to south-

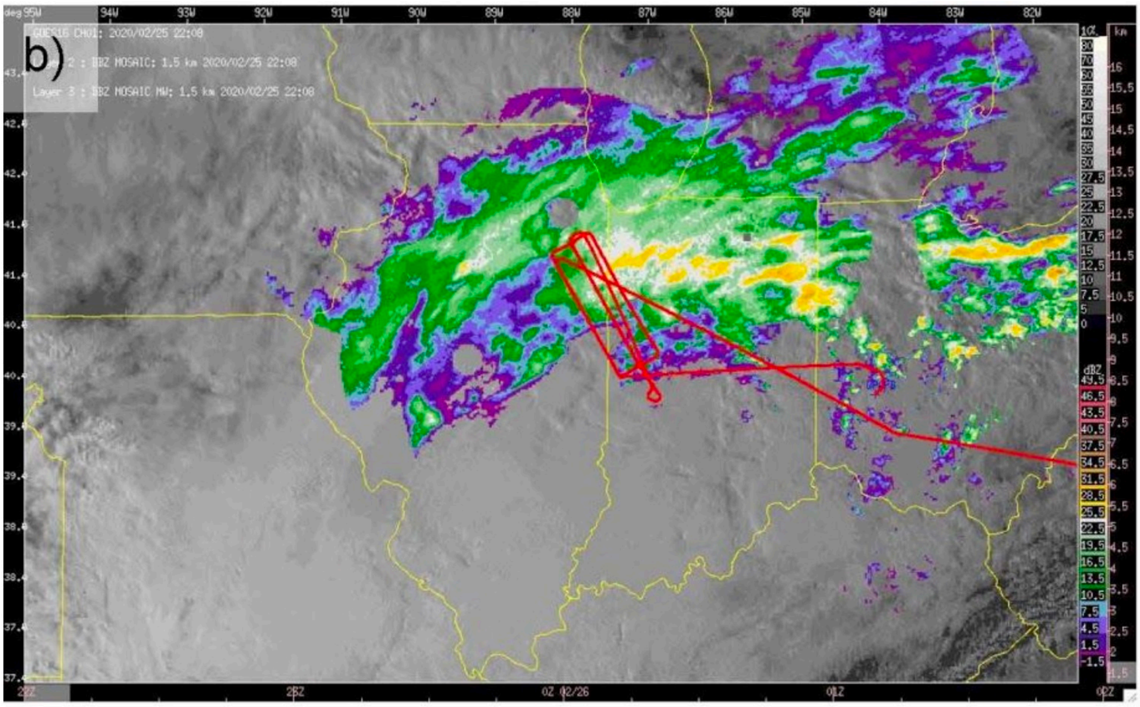
b)
GOES16 CH01: 2020/02/25 22:08
2 : DBZ MOSAIC: 1.5 km 2020/02/25 22:08
Layer 3 : DBZ MOSAIC MW: 1.5 km 2020/02/25 22:08
dBZ
km

Figure 2.13. NEXRAD radar reflectivity mosaic (dBZ) valid at 2200 UTC 25th February. Overlaid P-3 flight track is shown in red.

east and flown at multiple altitudes (3.5 km, 2.5 km and 1.2 km). This path intersected the wraparound region of the cyclone where frontogenesis was predicted to occur. The racetrack legs were approximately 150 km long and 25 km wide for P-3, whilst ER-2 followed the same racetrack but above the storm. The planes had plans for five pre-planned altitudes: (1) dendritic-growth-zone (DGZ) at 600 mb (∼14–15 kft, 4.3–4.6 km), (2) DGZ at 700 mb (∼10–11 kft, 3.0–3.4 km), (3) ground radar altitude of 4–5 kft (1.2–1.5 km) and roughly -4 °C temperature, (4) 6–7 kft (1.8–2.1 km), and (5) 12–13 kft (3.7–4.0 km) with additional legs at the cloud top. The ordering of the flight altitudes was from high to low then low to high. Take off occurred at 2058 UTC, and the first leg of the eastern line started at 2147 UTC. The objective of P-3 was to sample the microphysics in the relatively shallow cloud.

A vertical cross section roughly in the direction of the flight path and normal to the snowband showed modest dynamics, with limited potential for convective instability in the dendritic growth zone and cloud top region. Cloud top imagery from the GOES-E satellite showed a smooth cloud top over eastern Missouri and much of southern Illinois around 2325 UTC 25th February containing small scale wave-like features are present translating in a northeast direction. This cloud deck remained consistent for the duration of the flight and was the main sampled area. Farther north, satellite imagery showed heterogeneous cloud with some tops above the rest of the cloud deck. In northwestern Illinois, gaps in cloud matched closely with absences of snow in the precipitation field. Turbulence was observed by NEXRAD radar (see Figure 2.13) between 2–2.5 km and in the KLOT radar enhancements in Doppler spectrum width were observed at this height. This was co-located with shear in earlier soundings.

The untypically low cloud top height allowed P-3 to make multiple passes through the generating cell layer at an altitude of around 3.5 km and temperature -12 to -10 °C. Generating cells were evident for all leg of the flight and were picked up by the W-band Cloud Radar System. The tops of generating cells contained supercooled liquid water as detected by the Fast Cloud Droplet Probe (Fast-CDP) around 2323 UTC 25th February. Between 0108 and 0125 UTC 26th February, P-3 conducted flight legs at generating cell height, where larger crystals were more common at the northwest end of the flight leg and cloud depth was greater. Dendrites and plate-like crystals were common with some having significant rime, and as P-3 flew south-east towards shallower clouds concentrations and sizes of ice crystals decreased.

Regions of enhanced Z_{DR} were observed below the ER-2 at an altitude of approximately 3.2 km, 500 m below cloud top at 2327 UTC 25th February. P-3 was geographically close at this time and observed plates sectors and dendrites consistent with planar growth at the generating cell level and resulting in the observed increased Z_{DR}. A second series of flight legs were conducted at 2.5 km altitude by P-3 to sample supercooled liquid water and crystal growth below the generating cell level. Temperatures were between -6 °C in the south-east leg and -8 °C in the north-western leg. Fast-CDP observed supercooled droplets between 1×10^{-5}–3×10^{-5} m as well as crystals less than 1 mm in size. Cloud Particle Imager (CPI) images showed riming was present on these crystals. Abundant supercooled liquid water and riming at these temperatures coincided with icing of the plane. As P-3 flew north-east into colder cloud spherical particles were observed as well as heavily rimed crystals and larger dendrite aggregates.

The final flight leg of P-3 flew between 1.2 km and 1.8 km to sample supercooled liquid water and ice within the Hallett-Mossop region and near the melting layer. Temperatures ranged between -3 and 0°C towards the southeast end of the flight legs and -6 to -4°C farther north-west in the wrap-around region. Spherical particles were observed during this leg, mixed with needles and needle aggregates at 0009 UTC 26th February. The large aggregates were near to the cloud top so the crystals had either aggregated below and been raised up or aggregated out of high needle concentrations. A mixture of habits, including feathered columns, irregulars, and other rimed crystals, were observed towards the northwest end of this flight leg. The largest particles briefly approached 1 cm in size.

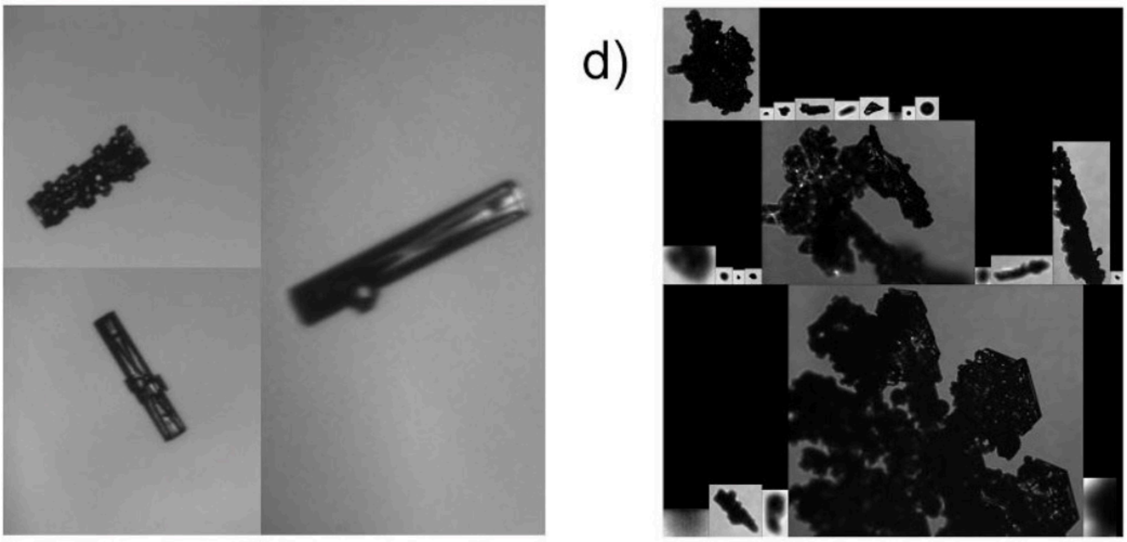

Figure 2.14. Heavily rimed crystals photographed by PHIPS and CPI at approximately 0100 UTC on 26th February from onboard the NASA P-3 aircraft. Left: columnar crystals with varying degrees of rime. Right: Stellars, dendrites and aggregates with surface rime.

Chapter 3

Methods

3.1 WRF Initialisation and Usage

The Weather Research and Forecasting model (WRF-ARW) version 4.3 (Skamarock et al. 2019) was used to simulate all cases discussed in this thesis and outlined in greater detail in Chapter 2. The WRF model has shown suitability in simulations of similar north-east extratropical cyclones and was used by Ganetis and Colle 2015 during their study of thermodynamic evolution for the same storm as is discussed in Part II.

3.1.1 Model setup: Part II - 2013 Winter Storm

Three nested domains with grid-spacing 20 km, 4 km and 800 m (domains 1–3, respectively) were initialised using the European Centre for Medium-Range Weather Forecasts (ECMWF) ERA5 data set (Hersbach et al. 2020). Figure 3.1 shows the positioning of domain 1 over the north-east coast of the United States, extending from the gulf of Mexico to south-eastern Canada, and into the central U.S. mainland in order to capture the passage of both lows observed during this storm. Domains two and three were centred over Long Island where observations of precipitation and reflectivity were recorded. All domains extended 91 vertical levels using a hydrostatic pressure and terrain following vertical coordinate system, with 5000 Pa model top. A 1:5 nested time step ratio was employed for domains 1, 2 and 3 resulting in a 120, 24, 4.8 second time step, per respective domain. Boundary conditions at all domain edges were updated at hourly intervals and two way feedback was turned on for nested domains. The model simulation began at 0000 UTC 8th February 2013 and spanned a 48 hour period ending 0000 UTC 10th February 2013 such that all three phases of the storm were encompassed (see Chapter 2) in addition to a 12 hour initial spin-up period that was sufficient to capture the formation of the band as in (Ganetis and Colle 2015). Note that all data output during the spin-up period is intentionally omitted from further analysis.

The Yonsei University (YSU) planetary boundary layer scheme, and Noah-MP land-surface

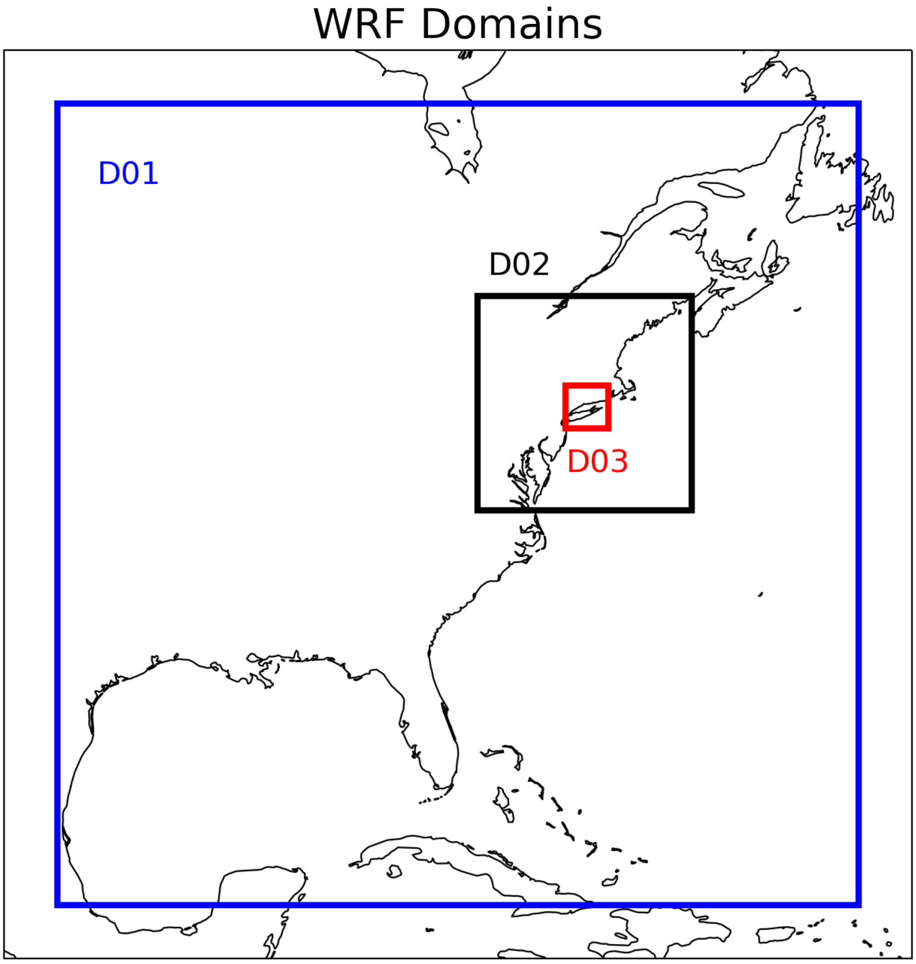

Figure 3.1. WRF domain location and scale for the winter storm simulated in Part II. Domains one (blue), and nested domains two (black) and three (red) are indicated by coloured and labelled boxes.

model were used in all three domains owing to their use in similar storms in the literature. The Betts-Miller-Janjic cumulus scheme was used in the parent domain, whilst convection was resolved in domains 1 and 2. Three different microphysics parameterisations were simulated with otherwise identical settings: the Morrison Two-Moment scheme (Morrison et al. 2005), the Predicted-Particle-Properties scheme (Morrison and Milbrandt 2015) and the Ice-Spheroids Habit Model with Aspect-Ratio Evolution (Jensen et al. 2017), hereafter Morrison, P3 and ISHMAEL. An overview of these schemes and the motivation for their inclusion is given in Section 3.2. WRF output data was retrieved at hourly periods for domains one and two, and per 15 minutes in domain three.

The technical specification of the WRF namelist parameters is provided in each Part of this thesis respectively, and so will not be discussed here. However, several files that were employed to guide the set up and technical details of the model can be found in the appendix, including the overview of model set up and compilation in Appendix P.

3.1.2 Model setup: Part III - Two Winter Storms in 2020

In Part III, the Weather Research and Forecasting model (WRF-ARW) was used to simulate two cases; case one was a warm frontal snowband resident over north-eastern U.S. from 7–9 January 2020, and case 2; a shallow snowband resident over Illinois from 24–26th February 2020.

Three nested domains were used in each case with grid spacing 20 km, 4 km, and 800 m respectively and were each initialised using the European Centre for Medium-Range Weather Forecasts (ECMWF) ERA5 reanalysis data set (Hersbach et al. 2020). All domains extended 91 vertical levels using a hydrostatic-pressure and terrain-following vertical coordinate system, with 5000 Pa model top. A 1:5 nested time step ratio was employed for domains 1, 2 and 3 resulting in a 120, 24, 4.8 second time step, per respective domain. Boundary conditions at all domain edges were updated at hourly intervals and two way feedback was turned on for nested domains. For each case, the simulation was initialised at 0000 UTC on the date specified so that a 12 hour initial spin-up period could be conducted in order to minimise initialisation error. All data output during the spin-up period is intentionally omitted from further analysis.

The geographic location of each domain is shown in Figure 3.2 where panel (a) shows domains for Part III case one and panel (b) for Part III case two. In case 1, the parent domain encompassed central U.S. from Idaho (ID) in the northwest to New England in the east and from Florida to Alberta, Canada. This span was chosen to envelop the developing shortwave upper-level trough resident over northern Montana at 0600 UTC 18th January that extended to Massachusetts by 0000 UTC 19th January. Domain 2 was situated over the Great Lakes region, which received the heaviest snowfall of the storm, and New England. Domain 3 enclosed New York state, Long Island and Vermont, fully containing the bow tie flight path taken by P-3 and ER-2.

In case 2, (Figure 3.2 panel b) the parent domain spanned the breadth of the U.S. as well as the southernmost Canadian states and northern Mexico. This large area captured both 500 hPa troughs that were situated over Washington state (WA) and Oklahoma (OK) before digging south towards Mexico. The domain also captures a stagnant low over Ontario and Quebec and an influential eastern subtropical jet that stretched over North Carolina. Domain 2 is centred over eastern-central U.S. where a shallow front was observed and precipitation was forecast. Domain 3 was situated over Illinois (IL) and Indiana (IN) to fully enclose the flight path of P-3 and ER-2.

Each simulation was performed twice, once with both Morrison and ISHMAEL microphysics (Jensen et al. 2017; Morrison et al. 2005). Otherwise, each simulated storm had identical settings. The model time step of the parent domain was set to 120 s, and a time

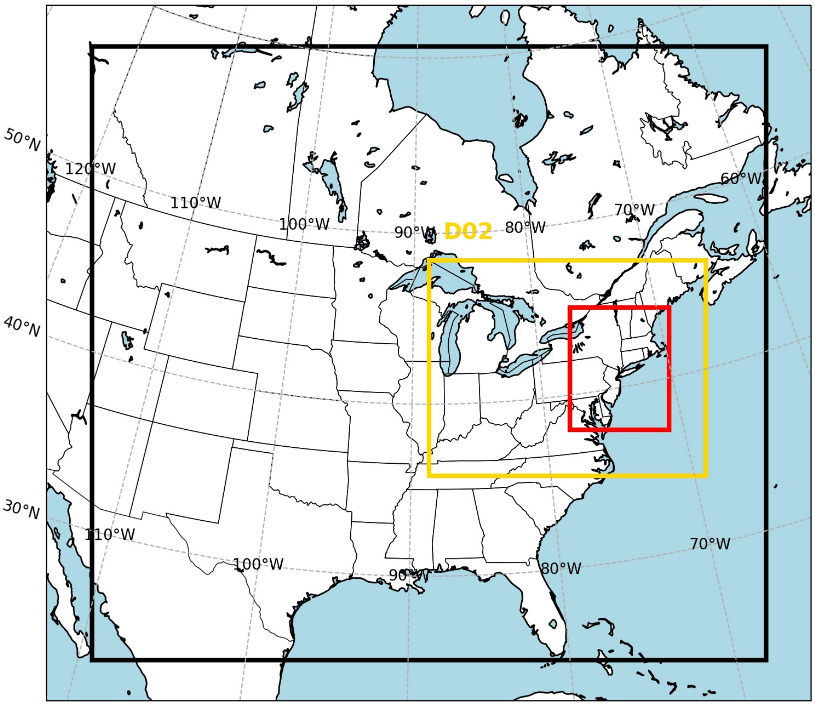
50°N
120°W
110°W
100°W
90°W
D02
80°W
70°W
60°W
40°N
30°N
110°W
100°W
90°W
80°W
70°W

(a) Case 1: 18/01/2020

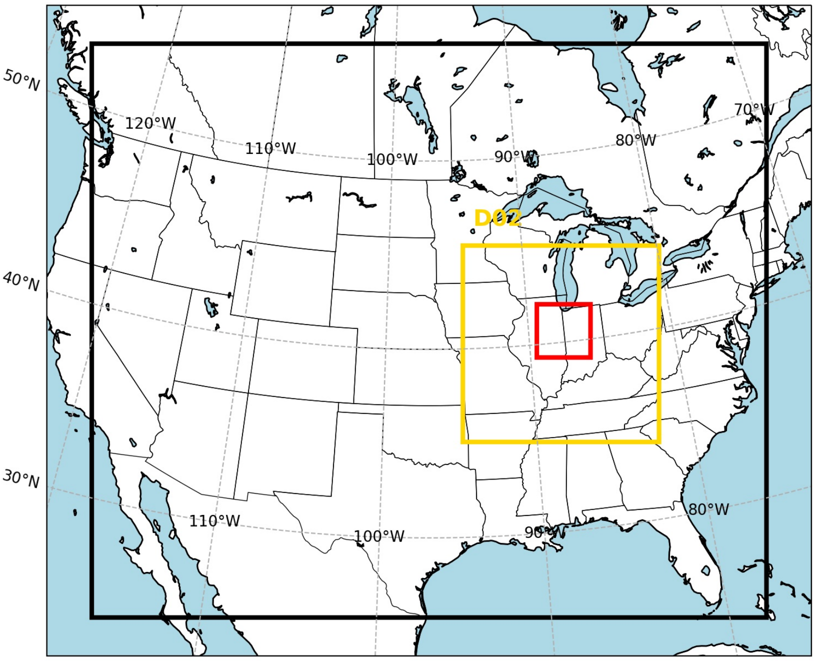
50°N
120°W
110°W
100°W
90°W
80°W
70°W
D02
40°N
30°N
110°W
100°W
90°W
80°W

(b) Case 2: 25/02/2020

Figure 3.2. WRF domain layout for a) Case 1: 17–19th January 2020 b) Case 2: 24–26th February 2020. Domain 1 (black), domain 2 (yellow), domain 3 (red).

step ratio of 1:5 used for each domain thereafter resulting in 24 s and 4.8 s time steps for domains two and three, respectively. The Yonsei University (YSU) planetary boundary layer scheme, and Noah-MP land-surface model were used in all three domains, whereas the Betts-Miller-Janjic cumulus scheme was used in the parent domain only. Domains two and three were assumed to operate at a convection resolving scale and therefore had no cumulus parameterisation. WRF output data was retrieved hourly for domains one and two, and per 15 minutes in domain three.

3.2 Microphysics Schemes Used During Case Studies

Three microphysics schemes are used to parameterise cloud microphysics throughout this thesis; the Ice-Spheroids Habit Model with Aspect-Ratio Evolution (ISHMAEL) (Jensen et al. 2017), the Double-moment bulk microphysics scheme (Morrison) (Morrison and Grabowski 2008), and the Predicted Particle Properties (P3) scheme (Morrison and Milbrandt 2015). All three microphysics schemes are used to simulate a case study of a north-east U.S. snowstorm in Part II, and the ISHMAEL and Morrison microphysics schemes were used in the simulation of a further two case studies outlined in Part III. Each schemes was chosen for its unique mathematical approach to tackling the problem of mixed-phase precipitation prediction, particularly for the riming process. Here we will briefly overview the scheme frameworks, and what new ideas or technical abilities motivated their development, as well as their inclusion in this study.

3.2.1 ISHMAEL Microphysics Scheme

ISHMAEL is a bulk-analytic microphysics scheme that parameterises ice geometry using an idealised spheroid approximation. The ISHMAEL scheme was developed to test the prediction of ice habit evolution, which is an influential factor in the accurate prediction of microphysical process rates in the mixed-phase regime (Jensen et al. 2017). The scheme builds upon the Adaptive Habit (AHAB) approach developed by J.-P. Chen and Lamb (1994) that approximated planar and columnar ice as like-spheroids of differing aspect ratio, which could evolve dynamically over time. The evolution of aspect ratio in the AHAB framework is related to microphysical process rates by the inherent growth ratio (IGR) that is constrained by physical measurement. Theoretically, this enables the ice geometry to grow in accordance with the processes that it is subject to. For example, during depositional growth the IGR is sensitive to saturation and temperature driving geometric evolution in a similar way to the Nakaya ice diagram (see Figure 1.8) and during riming the ice geometry gradually tends toward a spherical graupel particle emulating habit fill-in. The ISHMAEL scheme uses a modified gamma distribution over the spheroid axis length, with a mass-distribution hypothesis derived from the spheroid volume and prognosed density.

The ISHMAEL scheme uses a semi-Lagrangian generalised-ice category framework for frozen particles, whereby multiple types of frozen hydrometeor are defined within a single category. However, the unique qualities of precipitation type remain identifiable by the evolution of prognostic variables derived from moments of the mass-distribution (see Appendix B). The tracked moments of the distribution are ice mass and number mixing ratios (conventional two-moment) as well as two volume-dimensioned mixing ratios that are associated with the parameterised spheroid axes. Additional prognosed quantities include (but are not limited to), ice and rime density, aspect ratio, fall speeds, and maximum diameter. These quantities are used to evolve the ice field gradually over time, as well as to diagnose precipitation in post processing (see Section 3.4.1). The prognosis of rime density is a key improvement for the riming process, and was a motivating factor in the development of the P3 scheme. However, note that in ISHMAEL the rime density is not tracked historically, and only the present density is conserved and advected between cells. Importantly, particle evolution by the IGR is related to all mechanisms of ice growth, including vapour deposition, riming (both dry and wet growth) and melting. This presents a considerable number of model parameterisations that have been modified to include ice habit.

To prevent smoothing of ice qualities during the simulation of competing but dissimilar ices, two free-ice categories are nucleated with planar or columnar-like aspect ratios. These initial aspect ratios help to provide non-uniformity but are otherwise inconsequential as both ice categories are free to evolve in accordance with the local environment. The coexistence of two distinct categories enables multiple precipitation types to be present within the same cell. For similar reasons, a third category is used exclusively for aggregates, though it is important to note that this category follows the conventional framework (i.e. autoconversion of mass). Planar-nucleated, columnar-nucleated, and aggregated ice categories will be referred to as ice-types 1–3, respectively. The liquid prognostic variables used by ISHMAEL include cloud water and rain water mass mixing ratios, as well as rainwater number mixing ratios. The raindrop size distribution follows an inverse-exponential distribution based on Marshall and Palmer (1948). To calculate riming rates, the cloud-droplet size distribution is assumed to be a log-normal distribution, as described in Frisch et al. (2002). A complete breakdown of the parametrisation methods used in this scheme can be found in Jensen et al. (2017) or Appendix L.

3.2.2 Morrison Microphysics Scheme

The Morrison scheme is a two-moment bulk microphysics scheme that relates particle mass and dimension to the filling in of crystals during riming growth (Morrison and Grabowski

2008). This task is enabled by the inclusion of purpose built mass-dimensional (*m-D*) and area-dimensional (*A-D*) relationships for various crystal sizes that used to provide a more natural representation of the gradual conversion of cloud ice into snow. This method was developed to to improve the accuracy of the autoconversion process, which has been problematic in conventional bulk models especially during riming and other mixed-phase processes. The particle size distribution for ice particles takes the form of a generalised gamma distribution (see Appendix B.2), and the mass-dimensional relationship is either a conventional fixed-density sphere, or an empirically derived power law, depending on the type of precipitation category.

The Morrison scheme is a conventional categorised scheme that simulates pre-determined, discrete precipitation categories and transfers mass between these categories based on microphysical process rates. The categories simulated are; cloud droplets, rain drops, ice particles, snow particles, and graupel. This framework is convenient because precipitation types are clearly defined, requiring no post processing to obtain precipitation fields. However, the static qualities of each precipitation category, such as their fixed densities defined *a priori*, provide rigid constraints that are poorly equipped to capture transitional processes in general.

3.2.3 P3 Microphysics Scheme

The P3 scheme is a bulk-analytic, semi-Lagrangian microphysics scheme that can prognose rime density and track rimed-particle extent (Morrison and Milbrandt 2015). P3 uses a conventional modified-gamma distribution (see Appendix B) for all hydrometeors, and is integrated with a mass-diameter (*m-D*) hypothesis that represents particles as spheres, as in Morrison, but that has non-constant density, as in ISHMAEL. This enables the evolution of the particle size distribution to be intrinsically linked to the predicted density evolution during its growth. However, it avoids the additional problem of simultaneously constraining geometry during growth.

P3 prognoses four tracked distribution moments for frozen hydrometeors; the total ice mass and ice number (conventional two-moment) and additionally the mass attributed to rime growth and bulk rime volume (Morrison and Milbrandt 2015). Conservation and advection of the latter two variables are used to determine rime density, and can be used to form a historical knowledge of rimed mass fraction, which is a proxy for the degree of riming. This is especially advantageous as partial riming is a key source of mass transfer in mixed-phase clouds that is incompatible with the categorised framework of many conventional schemes such as Morrison. Additionally, this quantity enables a more powerful method of precipitation diagnosis in post processing. For example, the ISHMAEL scheme can calculate and implements variable rime density during calculation of the riming process but this information is lost at the end of each time step. In this regard, P3 has an advantage during the riming process as the historical rimed mass can be an important source of information to processes as well as fall-speed parameterisations.

The P3 scheme consists of one free-ice category, whereby multiple types of frozen hydrometeor can coexist within a single category. However, unlike the ISHMAEL scheme which employs multiple precipitation categories, the P3 scheme is particularly susceptible to smoothing for significantly dissimilar bulk properties in the same vicinity. Also, without several categories, the P3 scheme cannot simulate multiple frozen precipitation types within the same grid cell. To mitigate distribution smoothing, the current version of the scheme excludes consideration of ice multiplication from rime splintering.

3.3 IMPACTS Instruments

Measurement data from The Investigation of Microphysics and Precipitation for Atlantic Coast-Threatening Snowstorms (IMPACTS) campaign (see Chapter 2) is used in Part III (Bansemer et al. 2019). Here instruments that are relevant to this study are briefly described

.

3.3.1 CPI

The CPI (Cloud Particle Imager) is an unmanned measurement tool developed to capture high-definition (2.3 micron pixel size) digital images of cloud particles (droplets or ice crystals) and measures their size, shape, and concentration (Lawson et al. 2001). The CPI uses a 25 nanosecond pulsed, high-power laser diode to track particle motion and project an image onto a solid-state, charge-coupled device (CCD) camera. Operating at a frequency of 40 Hz, the CPI is capable of imaging a thousand particles per second within a size range of 10×10^{-6} m to 2×10^{-3} m. The CPI includes a particle detection system (PDS) enhanced by AI that ensures particles are in focus at the point of capture (Zavaleta 2022). Additionally, the images undergo processing to reduce errors caused by out-of-focus particles, which had been a limitation in preceding 2-dimensional imaging probes.

3.3.2 Fast Cloud Droplet Probe (FastCDP)

The Fast Cloud Droplet Probe (FastCDP) is a forward-scattering instrument manufactured by SPEC that is designed to measure cloud droplet concentrations and diameters in the range 1.5–50×10^{-6} m at altitudes of up to 70,000 ft (21 km). (Justice 2022; SPEC 2012).

Though not its original purpose, the FastCDP can also measure these quantities for ice crystal populations. Each sampled particle has arrival and transit time, signal and qualifier pulse heights recorded at a resolution of 25 nanoseconds to the system's onboard 16 gigabyte memory. The FastCDP also has the advantage of built-in Linux processor that has enabled multiple electronic upgrades since the probe's inception, further increasing its accuracy and reliability.

3.3.3 The Particle Habit Imaging and Polar Scattering Probe (PHIPS)

The Particle Habit Imaging and Polar Scattering (PHIPS) Probe is a particle imaging probe that was mounted onboard the NASA P3 aircraft during *in situ* measurement runs. The primary function of PHIPS is to determine the geometry and size of ice crystals, which it achieves by capturing stereo images of cloud ice crystals. Simultaneously, PHIPS measures the corresponding angular scattering function, which is used to deduce the thermodynamic phase and the scattering equivalent diameter (Waitz et al. 2021). The 3.3 μm resolution optical cameras are separated in orientation by a fixed angle of between 18 and 170 degrees, which can aid in identification of the three dimensional habit, and an image analysis algorithm has been developed to facilitate this process (Schön et al. 2011). The sensitive area of PHIPS measures approximately 0.7 mm, which makes it unlikely to capture shattering events. This is ideal for the IMPACTS campaign, in which larger ice crystals were the subject of examination. During the campaign, the sampled droplets had a lower limit of 100 μm and for ice this limit was 40 μm. The angular separation of the cameras was fixed at 120 degrees. Per case, each PHIPS output data set consisted of 10^4 image-pairs in **.png** format. Further detail on the PHIPS setup can found in (Abdelmonem et al. 2016b) and (Schnaiter et al. 2018) and a computational method of image analysis to extract particle properties can be found in the Appendix O.

3.4 Mathematical Methods

In this section various mathematical methods used during data analysis are outlined in full. Note that these techniques are assumed to be used in all cases that they apply by default.

3.4.1 Generalised-Ice Category Partitions

An additional step of partitioning or filtering the output data in post-processing is required to obtain the precipitation field in the case of P3 and ISHMAEL, or more generally *free-ice* microphysics schemes, as opposed to conventional categorised frameworks. In order to derive precipitation from the ISHMAEL and P3 output variables, boundary conditions of precipitation qualities are required. Qualities of the precipitation field span moments of the distribution such as mass mixing ratio, number mixing ratio, or distribution reflectivity factor, or prognostic variables that are derived from the distribution, such as the degree of riming or the relative size of ice particle axes. Prognostic variables are generally more useful than distribution moments when it comes to defining precipitation as they are representative of the mass-weighted average ice quality of a single crystal and theoretical descriptions of precipitation type usually refer to the characteristics of a single crystal sample rather than an entire distribution. In the ISHMAEL scheme, the possible prognostic variables that can be used for precipitation definitions are the density of ice ρ_i, the fall speed of ice v_i, the aspect ratio ϕ, and the maximum particle dimension D_m. In the P3 scheme, the possible prognostic variables are the density of ice ρ_i, the fall speed of ice v_i, the maximum particle dimension D_m, and rime fraction F_r.

From the prognostic variables one may derive the likely precipitation in a cell. For example, suppose that a cell contains a mass of ice with mass-weighted prognostic variables $\rho_i = 800$, kg m^{-3} $D_m = 8 \times 10^{-6}$ m. These variables indicate that the mass weighting of the ice distribution exhibits typical density similar to that of bulk ice, and maximum dimension on the microscale. In combination, these features may be associated with cloud ice, and therefore the precipitation mass would be *partitioned* or *filtered* into a cloud ice hydrometeor category during post-processing. In this example:

$$\text{Precipitation type} = \begin{cases} \text{Cloud ice,} & \text{if } \rho = 800 \text{ and } D_m = 8 \times 10^{-6} \\ \text{Not cloud ice,} & \text{otherwise} \end{cases}$$

This method is not well suited to variables that span continuous ranges, but an analogous association between perceived precipitation type and simulated ice variable can be made by formulation of boundary conditions. For example the above is similar to:

$$\text{Precipitation type} = \begin{cases} \text{Cloud ice,} & \text{if } \rho >= 800 \text{ and } D_m <= 8 \times 10^{-6} \\ \text{Not cloud ice,} & \text{otherwise} \end{cases}$$

This method enables cloud ice to be extracted from a precipitation field iteratively. Boundary conditions can be formed for a collection of precipitation types in this manner. For example:

$$\text{Precipitation type} = \begin{cases} \text{Cloud ice,} & \text{if } \rho >= 800 \text{ and } D_m <= 8 \times 10^{-6} \\ \text{Snow,} & \text{if } \rho <= 100 \text{ and } D_m >= 1 \times 10^{-3} \\ \text{Graupel,} & \text{if } 200 < \rho < 600 \text{ and } D_m > 1 \times 10^{-4} \\ \text{Unknown,} & \text{otherwise} \end{cases}$$

This methodology may incur errors if applied inappropriately. The definition of precipitation types and their respective boundaries is done manually by the end-user and so both the range of precipitation types and their boundaries must be empirically based. Additionally, the unknown category becomes increasingly complex as the boundary list grows, even in this simple case the unknown category spans several intervals that do not immediately correspond to a precipitation type. Without properly accounting for this unknown category, a portion of the precipitation field may be lost during analysis (the missing-mass problem).

Two methods were used to limit the extent of inaccuracies due to boundary conditions and to overcome the missing-mass problem. First, to determine physically realistic partitions of the precipitation field, a review of the literature was conducted and the typical ranges of prognostic variables were noted in Table 3.1. Definition of the precipitation boundaries is therefore based on empirical measurement rather than perception. However, we note that there are several caveats to the use of measured data from the literature. Most notably, the boundaries of precipitation types are not wholly precise, and there are considerable overlaps to the prognostic variables at the intersection of precipitation types. For example, the fall speed is a poor predictor of precipitation type, as most precipitation particles span a relatively narrow fall-speed range between 0.1–2 m s^{-1}. There are also cultural or historical ties to certain variable ranges, for example, hail and ice pellets are separated by an arbitrary dimensional value of 5 mm. Whilst this information is important to know when considering the origins of precipitation definitions, it is certainly a motivating factor for the development of more standardised definitions of precipitation type.

Precipitation Type	Density ρ (kg m^{-3})	Rime Fraction F_r	Aspect Ratio ϕ	Maximum Diameter D (m)	Fall Speed v (m s^{-1})
Snow	10–200 [9] < 200 [21]	Nil to light	0.4–0.8 average 0.6 [10]	Densely rimed dendrites 1.8–4.0 mm [1] Unrimed aggregates of dendrites 2–10mm [1] Unrimed aggregates of columns and plates 0.2–3 mm [1] Unrimed aggregates of side planes “most” 2–5mm [9] Aggregates 5–10 mm [9]	Unrimed dendrites 0.5–1.4 [1] Unrimed aggregates of plates, columns, or bullets 0.8–1.4 [1] Densely rimed dendrites 0.7–1.2 [1] Aggregates of unrimed side planes 0.5–1.6 [1] Densely rimed dendrites 0.7–2 [1]
Cloud ice / ice crystals	~ 917	Nil to light	0–1 (inverted for columns) [19]	2×10^{-6}–3×10^{-3} [18]	0.107 when $D < 1$ mm [11][12] < 1 when $D < 1$ mm [13]
Graupel	200–700 [7][8] 50–450 [1] 50–890 [9] < 200 [21]	Heavy	0.8–1.0 [10]	Lump graupel 0.5–3 mm [1] Conical Graupel 0.8–3 mm [1] Hexagonal Graupel 08–3.2mm [1] Graupel-like snow (lump) 0.5–2.2mm [1] Graupel-like snow (hexagonal) 0.8–2.8mm [1]	Graupel-like snow (lump) 0.8–1.6 [1] Graupel-like snow (hexagonal) 0.8–1.9 [1] Hexagonal graupel 0.8–2.7 [1] Conical graupel 0.9–2.9 [1] Lump graupel 0.6–2.7 [1] 0.1–3 [10]
Pellets	160 [15] 870–890 [16]	Heavy	Minority spherical or near-spherical. Majority bulged / aggregates [15][20]	< 5 mm [15]	Two modes observed related to habit and density; fast falling (< 10) and slow falling (< 3) [15]
Hail	820–870 [4] dry 910 [6] 310–610 [6] Average 440 [6]	Heavy	Average 0.8, range 0.6–0.95 [5]	Size convention >5 mm [2][3]	< 10 for small hail when $D < 2cm$ [7]
Pristine Ice	See cloud ice	Nil to light	See cloud ice	Densely rimed columns 0.8–2.0mm [1] Unrimed side planes 0.4–1.2 mm [1] Pristine ice is split from cloud ice by size [14]	Unrimed side planes: 0.6–1 [1] Densely rimed plates 0.7–1.4 [1] Densely rimed columns 0.8–1.9 [1] 0.1–0.8 [9](Figures 10–42)

Table 3.1. Observations of precipitation type characteristics used for justification of the partition choices for P3 and ISHMAEL post-processing. Citations are [1]: Locatelli and Hobbs (1974), [2]:AMS (2020), [3]: Organization (1975), [4]: Prodi (1970), [5]:Knight (1986), [6]:Knight and Heymsfield (1983), [7]:Heymsfield et al. (2018), [8]:Heymsfield and Kajikawa (1987), [9]:Pruppacher and Klett (2010), [10]:Garrett et al. (2015), [11]:Westbrook (2008), [12]:Yagi (1970), [13]:Kneifel and Moisseev (2020), [14]:Sterzinger and Igel (2021), [15]:Nagumo and Fujiyoshi (2015), [16]:Braham (1963), [17]:Mosimann et al. (1994), [18]:Dowling and Radke (1990), [19]:Korolev and Isaac (2003), [20]:Gibson et al. (2009), [21]:Ishizaka (1993)

To avoid the missing-mass problem, the most ideal method for determining a consistent set of precipitation boundaries is to follow a computational `if-else` mechanism, which can be represented visually with a flowchart. This method ensures that all mass is accounted for by default, and simply separated when the conditions are acceptable.

Figure 3.4 and Figure 3.3 show the definitions of precipitation partitions used in this study for the ISHMAEL and P3, schemes respectively. As both schemes output different prognostic variables, the precipitation is partitioned using separate methods but along broadly similar definitions of precipitation type. In P3 the available prognostic variables; rime mass fraction F_r, density ρ and maximum diameter D_m were used to first distinguish between rimed and unrimed hydrometeors, before classifying each precipitation type thereafter in accordance with Table 3.1. In ISHMAEL, riming is implicit and so rimed particles are more difficult to distinguish. Instead, precipitation was first split amongst aggregated and non-aggregated ice, which could be tracked according to the separate aggregated ice category (ice-type 3). Aggregates were considered snow, unless they were of sufficiently high density to have been rimed. Spherical, aggregated ice was then partitioned into graupel or hail by density. Unaggregated ice (ice-types 1 and 2) was determined to only be classified as snow (i.e. snow-crystals) if the density was sufficiently low, with non spherical ice instead making way for pristine or cloud ice dependent on diameter, while spherical ice of low density became graupel, and high density was hail or ice pellets dependent on diameter. For each scheme, care was taken to ensure identical partitions were constructed. However, due to the difference in variable computation some differences remain. This is viewed as a limitation to the comparability of the microphysics schemes.

The computational implementation of the boundary conditions can proceed via binary matrices. For example, consider a vertical column of grid cells positioned at latitude-longitude grid coordinates (x, y) at time t. The column will contain mass-weighted grid cell variable χ with example values:

$$\chi = \begin{pmatrix} 1 \\ 8 \\ 4 \end{pmatrix}$$

A binary conditional array can be determined by iterative evaluation of the column according to a boundary condition and preserving dimensions:

$$B = \begin{cases} 1, & \text{if } \chi >= 4 \\ 0, & \text{otherwise} \end{cases}$$

which yields a column array of identical shape:

$$B = \begin{pmatrix} 0 \\ 1 \\ 1 \end{pmatrix}$$

Evaluating the Hadamard (element-wise) product of the arrays yields:

$$\chi \times B = \begin{pmatrix} 1 \\ 8 \\ 4 \end{pmatrix} \odot \begin{pmatrix} 0 \\ 1 \\ 1 \end{pmatrix} = \begin{pmatrix} 0 \\ 8 \\ 4 \end{pmatrix},$$

thus the result preserves the shape of the initial matrix and accordingly masks the elements that do not meet the criteria defined in B. The Hadamard product is commutative, associative and distributive, which makes it extremely flexible computationally, and enables multiple criteria to be rendered into a single array. For example, suppose that a second condition C was imposed:

$$C = \begin{cases} 1, & \text{if } \chi < 5 \\ 0, & \text{otherwise} \end{cases}, \qquad C = \begin{pmatrix} 1 \\ 0 \\ 1 \end{pmatrix}$$

The conditional statements of B and C may be combined with the Hadamard product:

$$B \odot C = \begin{pmatrix} 0 \\ 1 \\ 1 \end{pmatrix} \odot \begin{pmatrix} 1 \\ 0 \\ 1 \end{pmatrix} = \begin{pmatrix} 0 \\ 0 \\ 1 \end{pmatrix} = C \odot B$$

Therefore, evaluating χ under the condition B then C, is equivalent to evaluating χ under the condition C then B, which is equivalent to evaluating χ under the condition $C \odot B = B \odot C$. This method extends to n-dimensional arrays, enabling the evaluation of model output data in three spatial dimensions and one time dimension.

This method can be used to produce filters or masks of the precipitation field across multiple variables in a computationally efficient manner, as sequential conditional statements require only the simultaneous storage of 2 arrays in system memory. The method can provide considerable improvements to computation speed and memory usage when compared to the simultaneous comparison of multiple arrays using masking functions. Additionally, the product of all conditions (the total mask) can be stored at reduced size by manually selecting a reduced precision data type. For example, by switching from 64 bit float to 8 bit integers. Importantly, there is no loss of precision as the array features only binary elements (0, 1).

A real example of this can be demonstrated using the definition of cloud ice in P3. Following the flowchart in Figure 3.3 cloud ice requires the following conditions:

$$\text{Cloud ice} = \begin{cases} F_r < 0.1 \\ \rho_i > 300 \\ D_m < 2 \times 10^{-3} \end{cases}$$

The column arrays masks for these conditions can be determined by iterative application of the conditions to the respective variable array (e.g. F_r conditions applied to the F_r array). The resulting column arrays are:

$$\gamma_{F_r} = \begin{pmatrix} 1 \\ 1 \\ 1 \end{pmatrix}, \qquad \gamma_{\rho_i} = \begin{pmatrix} 1 \\ 1 \\ 0 \end{pmatrix}, \qquad \gamma_{D_m} = \begin{pmatrix} 1 \\ 0 \\ 0 \end{pmatrix}$$

Individually, the masked arrays γ_x indicate where each condition is true, and therefore reveal some information about the precipitation field. In this case, all ice is unrimed, the two highest cells (assuming the row dimension corresponds to height) exhibit high density, and only the topmost cell contains ice with a very small diameter. The Hadamard product is of γ_x:

$$\gamma_{F_r} \odot \gamma_{\rho_i} \odot \gamma_{D_m} = \begin{pmatrix} 1 \\ 0 \\ 0 \end{pmatrix} = \gamma_{\text{cloud ice}} \tag{3.1}$$

the resulting, combined-conditional array $\gamma_{\text{cloud ice}}$ can be used to retrieve the cloud ice component of any variable from the precipitation field. For example the mass mixing ratio or the number concentration of cloud ice crystals:

$$q_{\text{cloud ice}} = q_i \odot \gamma_{\text{cloud ice}}$$
$$q_{\text{cloud ice}} = \begin{pmatrix} 0.0005 \\ 0.00305 \\ 0.0045 \end{pmatrix} \odot \begin{pmatrix} 1 \\ 0 \\ 0 \end{pmatrix} = \begin{pmatrix} 0.0005 \\ 0 \\ 0 \end{pmatrix}$$

$$n_{\text{cloud ice}} = n_i \odot \gamma_{\text{cloud ice}}$$
$$n_{\text{cloud ice}} = \begin{pmatrix} 1673 \\ 980 \\ 234 \end{pmatrix} \odot \begin{pmatrix} 1 \\ 0 \\ 0 \end{pmatrix} = \begin{pmatrix} 1673 \\ 0 \\ 0 \end{pmatrix}$$

Precipitation-specific variables analysed in the P3 and ISHMAEL schemes are retrieved using this method.

To test the qualities of precipitation types as defined by the partitions in Figures 3.3–3.4, the partitions were applied to the entire precipitation distribution simulated by each scheme during case one. No consideration was given to the location of the ice in the domain or the microphysical processes that were present for this analysis. Histograms of each characteristic variable per scheme were produced for all precipitation types defined in Figures 3.3–3.4. The resulting precipitation qualities are shown in Figures 3.5 and 3.6 for the ISHMAEL and P3 microphysics schemes, respectively. Note that the scale of the y-axis (total grid cell number) is arbitrary, and so we only consider the distribution of each variable.

Comparison of the precipitation qualities indicates that the precipitation types exhibit broadly similar distributions in characteristic variables, though some differences are apparent. One key point of comparison is the density distribution of graupel, which spans a larger total density range in P3 ($\rho < 700$ kg m^{-3}) than in ISHMAEL ($200 < \rho < 700$ kg m^{-3}). This difference originates with the order of application of partitions. In the P3 scheme, graupel is determined primarily from the rime fraction variable, and so any ice that exhibits a large rime fraction will be considered graupel. Whereas in ISHMAEL, low density graupel is explicitly restricted by the snow boundary condition. This is a good example of the small discrepancies in precipitation qualities that can arise when different prognostic variables are calculated. In P3, the rime fraction takes precedence over density, i.e. it is assumed that if rime fraction$\sim$ 1 then the crystal must be heavily rimed and so is considered graupel, regardless of density. In the ISHMAEL scheme, the density takes precedence, because the aspect ratio prognostic variable cannot accurately discern between graupel and snow, i.e. aggregates often exhibit a near-spherical volume.

It is notable, however, that despite lower density graupel existing in P3, the distribution of fall speed and diameter in the P3 scheme are much larger than in ISHMAEL, with fall speeds reaching twice as large, and diameters 5 times as large. This is contradiction with the hail category, which has extremely high fall speeds in ISHMAEL which reach up to 25 m s^{-1}. We note that the hail diameter begins as the graupel diameter ends, and therefore it is likely that hail in ISHMAEL is a continuation of the graupel category at larger sizes.

This is not apparent in P3, where density takes precedence, and graupel can therefore exist at any size range.

3.4.2 Mass Weighting of Variables

The mass-weighting of variables is conducted to ascertain a typical or mean quantity relative to the total mass of the grid cell, for example the mass-weighted fall represents the average fall speed with respect to all mass over the sampled space. Mass weighting is a logical method of ascertaining group characteristics in single (or higher) moment numerical models, which prognose and conserve the mass moment of hydrometeor size distributions. In fact, many precipitation quantities output by microphysics schemes are mass weighted as standard. Therefore, when working with non-standard precipitation variables the choice is often made to mass-weight in post processing.

In this study, the method of retrieving mass-weighted quantities is necessitated by the use of free-ice categorisation schemes in which the entire ice hydrometeor field is collectively grouped. Mass weighting over a single free-ice category, such as in the P3 scheme, follows the method laid out in Appendix R.1. For the ISHMAEL scheme, which simulates two free-ice categories and three categories in total, the mass weighting can be performed across both free-ice categories (or including the third, aggregate category) using a multi-variable approach as shown in Appendix R.2. Where specified in the text, all mass-weighted quantities that are not output as standard have been produced in post-processing using the procedures outlined in Appendix R.

3.4.3 Isolated-Active-Deposition Cell Analysis

In Part III Chapter 11.3 it is necessary to understand how the deposition process alters ice properties throughout the cloud, rather than at the cloud top. To retrieve this information, a methodology is required that isolates changes in the ice-particle properties when deposition is present but that does not record these changes when non-depositional processes are influential. For example, a cell in which deposition and riming are taking place simultaneously will alter the ice qualities, such as shape, density and fall speed, through the combination of their respective tendencies, specifically through the average inherent ice growth ratio δ_*, which incorporates all in-cell ice tendencies at the end of the time step into one averaged value.

Consider the general form of the mass tendency equation for ice in a bulk microphysics scheme shown in Equation 3.2. The rate of change of ice mass is equal to the sum of all mass tendencies that are contributed by each microphysical process during the time step:

$$\frac{dm_I}{dt} = \Delta m_{\text{dep}} + \Delta m_{\text{rime}} + \Delta m_{\text{nuc}} \dots \tag{3.2}$$

The combined mass tendency is multiplied by the model time step Δt to approximate the total mass gained over the time step time period and at the end of all physical calculations, the new mass is added to the total mass thus conserved mass between model time steps. The new cell mass can be used to form the gamma distribution of particle size at the time step end.

Properties of the ice field, such as geometry, density and fall speed are prognosed secondarily from the mass tendency. For example, the ice particle density at the beginning of a time step ρ_t is used to compute the mass riming rate. Once the mass riming rate and the resulting rimed mass tendency Δm_{rime} is established, the total rimed mass can be redistributed across the particle and the density ρ_{t+1} recalculated:

$$\rho_{t+1} = \rho_t(\Delta m_{\text{rime}}) \tag{3.3}$$

This methodology is repeated for subsequent processes such that after each mass tendency is obtained, the density can be updated. This ensures that the calculations are sequential and that the mass (and therefore ice properties) are conserved:

$$\rho_{t_f} = \rho_{t_{i+1}}\left(\Delta m_{\text{melt}}(\rho_{t_i}(\Delta m_{\text{rime}}))\right), \tag{3.4}$$

where parentheses denote *functions of*,ρ_{t_i} is the initial density, $\rho_{t_{i+n}}$ is an intermediary density calculation between the microphysical processes that occur in a single time step described by $i, i+1 \dots i_f$, and ρ_f is the final density after all microphysical processes have been calculated. It is evident that the tendency of ice particle properties derives directly from the mass tendency components on the right hand side of the mass tendency Equation 3.2.

Hypothetically, suppose that in a single cell, only the deposition process was active, and all other microphysical processes were not activated or resulted in zero mass growth. Then all microphysical process mass tendencies except for deposition will go to zero, and the total combined mass tendency during the time step will be directly proportional to the deposition mass tendency only, as shown in Equation 3.6.

$$\frac{dm_I}{dt} = \left(\sum_{i=0}^{n} \Delta m_{i \neq \text{dep}}\right) + \Delta m_{i=\text{dep}} \tag{3.5}$$

$$= (0) + \Delta m_{\text{dep}} \tag{3.6}$$

Consequently in this cell, the mass gained by ice is a result of the deposition process alone. The *change* in ice properties will then also be a direct consequence of only the deposition process, because zero valued mass tendencies do not change the ice qualities:

$$\rho_{t_{i+n+1}}(\Delta m_{\text{rime}} = 0) = \rho_{t_{i+n}} \tag{3.7}$$

Then for a sequence of microphysical processes:

$$\begin{aligned}\rho_{t_f} &= \rho_{t_{i+2}}\left(\Delta m_{\text{dep}}\left(\rho_{t_{i+1}}\left(\Delta m_{\text{melt}}(\rho_{t_i}(\Delta m_{\text{rime}} = 0)) = 0\right)\right)\right)\\ &= \rho_{t_{i+2}}(m_{\text{dep}}(\rho_i))\end{aligned}$$

The density at the end of the time step is a function of only the mass deposition process. This example illustrates the direct relationship between mass tendency terms and ice particle properties, namely that ice particle evolution is generated by active microphysical processes in the cell. This information can be used to determine the ice particle evolution owed to a specific process in the case that all other processes in a cell have a zero net tendency.

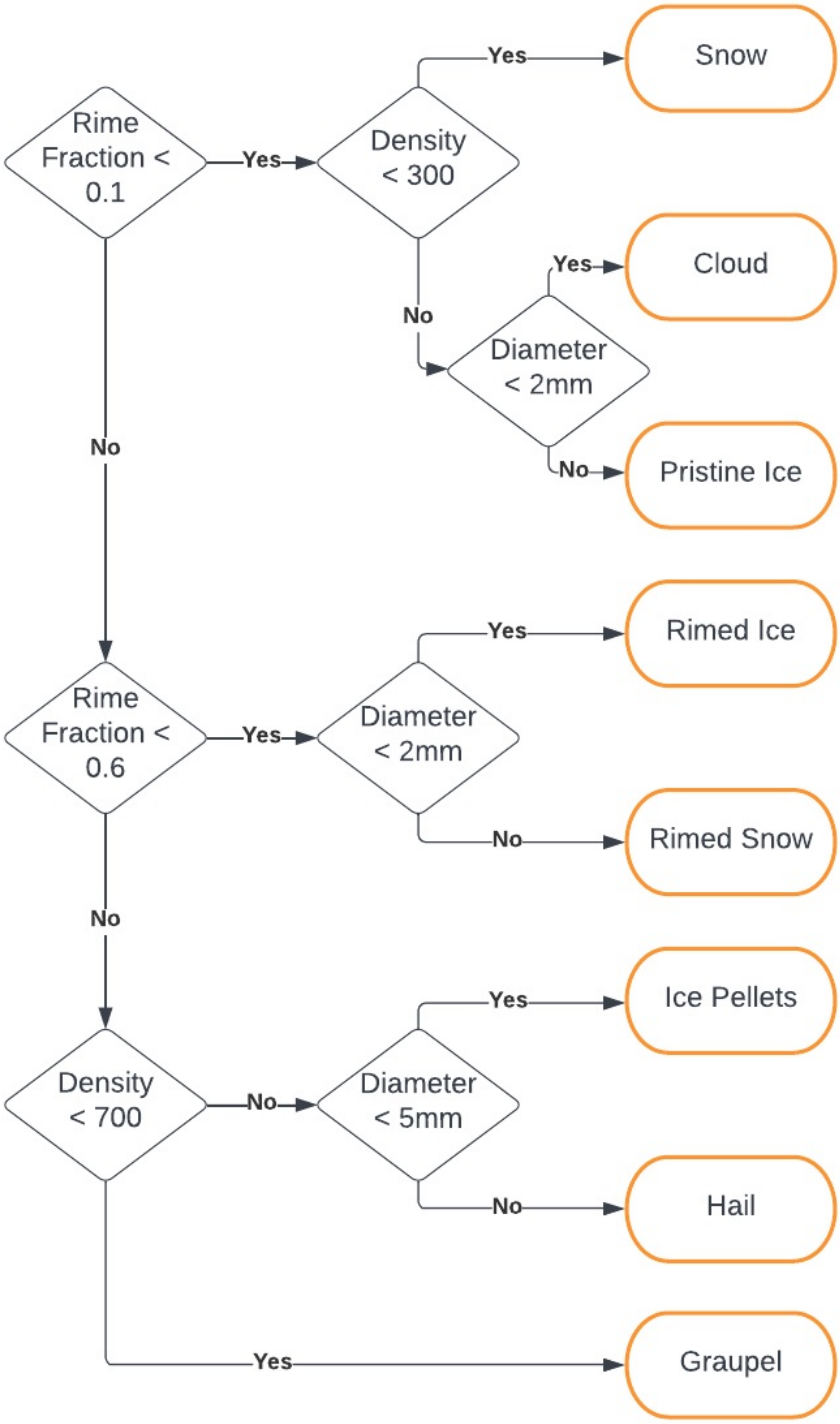
Rime Fraction < 0.1
Yes
Density < 300
Yes
Snow
No
Diameter < 2mm
Yes
Cloud
No
Pristine Ice
No
Rime Fraction < 0.6
Yes
Diameter < 2mm
Yes
Rimed Ice
No
Rimed Snow
No
Density < 700
No
Diameter < 5mm
Yes
Ice Pellets
No
Hail
Yes
Graupel

Figure 3.3. Partitioning flowchart for the retrieval of precipitation types (orange) from the P3 generalised-ice category. In this study, only one generalised ice category is simulated for the P3 scheme. Precipitation type is determined by partitioning ice-particle characteristic variables (diamonds); density $\bar{\rho}$, rime fraction F_r and diameter D. Flowchart format ensures that no ice remains uncharacterised. All precipitation types are mutually exclusive such that only one precipitation type can exist per cell

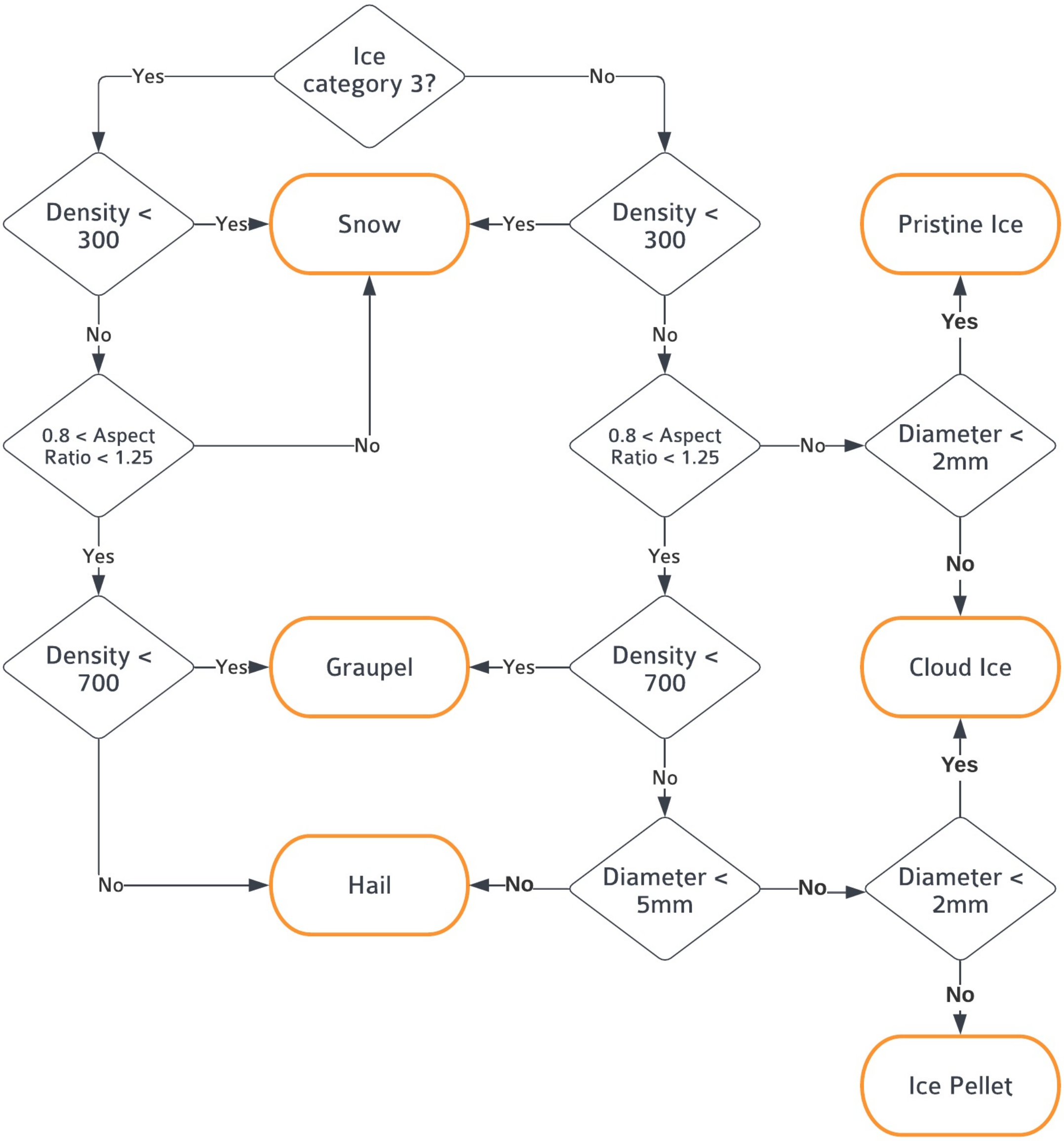
Ice category 3?
Yes
No
Density < 300
Yes
Snow
Yes
Density < 300
Pristine Ice
No
No
Yes
0.8 < Aspect Ratio < 1.25
No
0.8 < Aspect Ratio < 1.25
No
Diameter < 2mm
Yes
Yes
No
Density < 700
Yes
Graupel
Yes
Density < 700
Cloud Ice
No
Yes
No
Hail
No
Diameter < 5mm
No
Diameter < 2mm
No
Ice Pellet

Figure 3.4. Partitioning flowchart for the retrieval of precipitation types (orange) from the ISHMAEL generalised-ice categories. Precipitation type is determined by partitioning ice-particle characteristic variables (diamonds); density $\bar{\rho}$, aspect ratio ϕ and diameter D. Flowchart format ensures that no ice remains uncharacterised. Ice category 3 is an aggregate-only ice category, so is held separate to general ice categories 1 (planar-nucleated) and 2 (prolate-nucleated). All precipitation types are mutually exclusive such that only one precipitation type per ice category can exist per cell

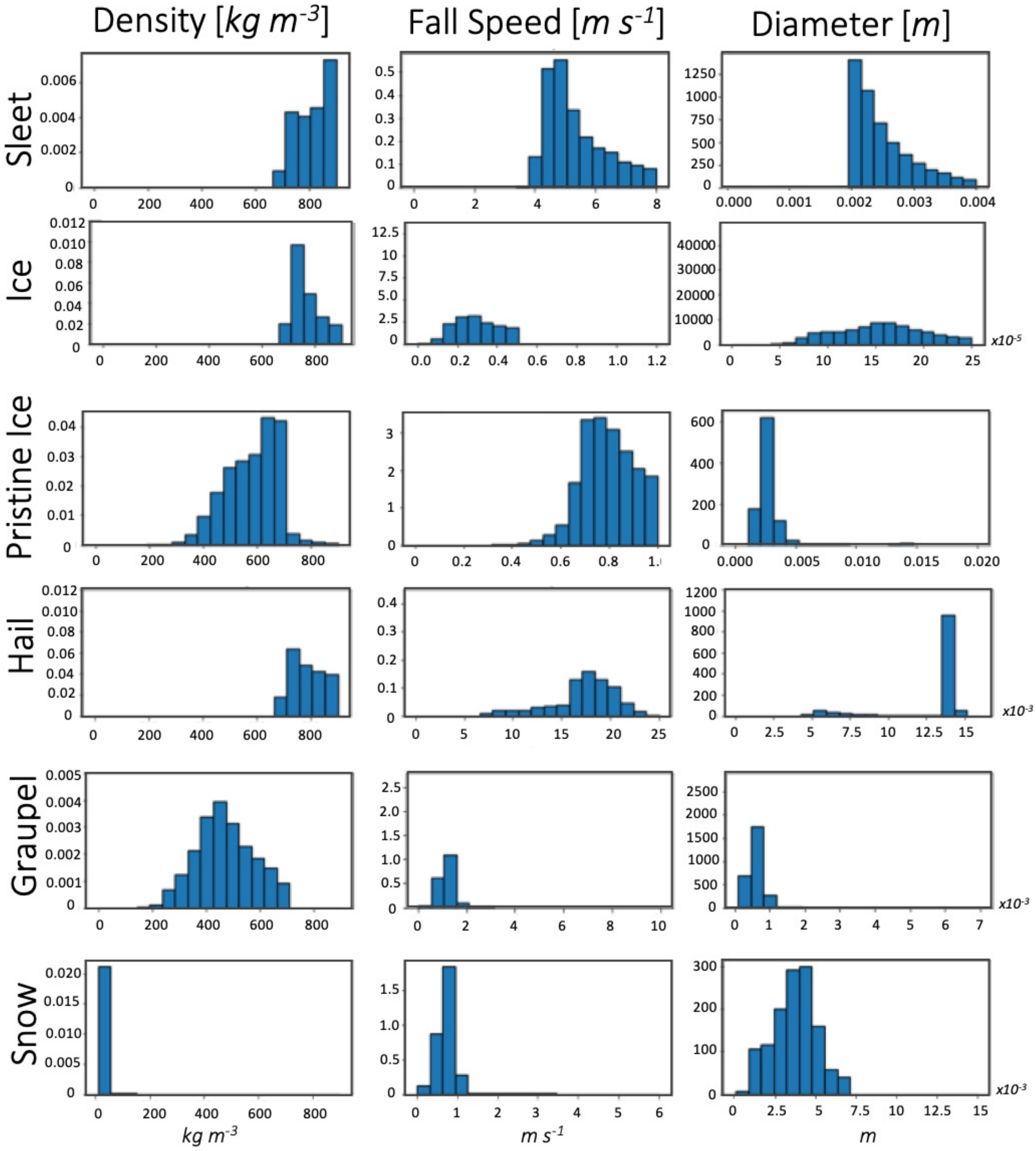

Figure 3.5. Normalised histograms of precipitation density (left), fall speed (middle), and diameter (right), for precipitation types; sleet (row 1), ice (row 2), pristine ice (row 3), hail (row 4), graupel (row 5), snow (row 6) in the ISHMAEL scheme. Precipitation types are extracted according to boundary conditions of the ice particle properties $\bar{\rho}$ (kg m^{-3}, ϕ and D (m) (see Figure 3.4).

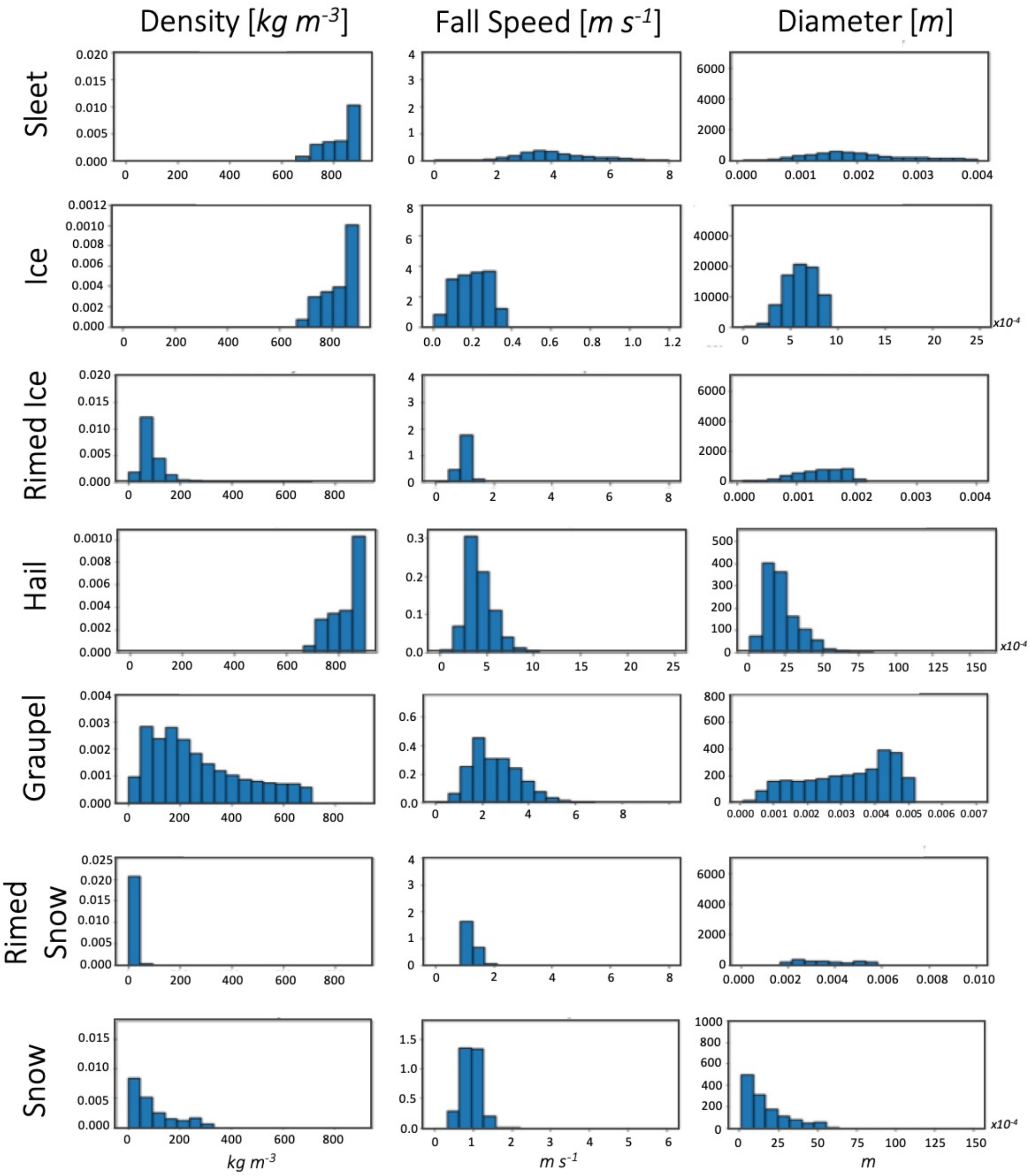

Figure 3.6. Normalised histograms of precipitation density (left), fall speed (middle), and diameter (right), for precipitation types; sleet (row 1), ice (row 2), rimed ice (row 3), hail (row 4), graupel (row 5), rimed snow (row 6), and unrimed snow (row 7) in the P3 scheme. Precipitation types are extracted according to boundary conditions of the ice particle properties $\bar{\rho}$, F_r and D (see Figure 3.3)

Part II

Riming, Snowfall and Reflectivity in a North-East US Winter Storm.

Chapter 4

Simulated Precipitation Fields

The precipitation observed during the 8–9 February storm displayed significant diversity and dependence on mixed-phase processes aloft. This chapter will investigate how successful each microphysics scheme is at reproducing the observed precipitation field, both in type and spatial distribution at the ground, before comparing the model output to observations of habit.The presence of riming and wet growth in particular are an especially interesting test case for the P3 and ISHMAEL schemes, which specifically aim to improve the parameterised of the riming process.

4.1 Simulated Precipitation Type and Spatial Distribution

In phase one, observations of precipitation indicated that south of Long Island was primarily rain and to the north precipitation was largely uniform snow, but between these regions, and positioned approximately parallel with the length of Long Island, lay a transitional zone that mirrored the approximate spatial location of the high reflectivity band shown in Figure 2.3 and was associated with complex mixtures of precipitation types at the ground. In phase two, this zone reoriented north-south and exhibited moderate to heavy degrees of riming, wet growth, melting and refreezing, which was identified in habit observations at the surface (see Figure 2.5). By phase three, the transitional zone had dissipated, and the precipitation field returned to aggregated snow with small amounts of rime.

The cumulative and combined precipitation fields produced at the surface of Long Island by each microphysics scheme are shown in Figures 4.1 and 4.2, respectively. The cumulative precipitation field shows the precipitation type (shaded) that accumulated the largest mass per surface level latitude-longitude grid cell per phase. The cumulative distribution is related to both the longevity and intensity of precipitation per phase, so represents the most dominant precipitation type produced by each microphysics scheme in each region of the domain.

Figure 4.1 indicates that the broad regions of rain to the south of Long Island and snow to the north were generally replicated by all microphysics schemes, but that considerable differences were apparent across Long Island where mixed-phase processes were most influential to the precipitation arriving at the surface. The Morrison scheme (Figure 4.1 row 1) produced the least diverse cumulative precipitation field of all schemes, with snow dominating northern and central Long Island, and even reaching south of the Long Island coastline for phases one and two (columns 1–2). In phase three, snow became the dominant precipitation type for all cells in the domain.

The ISHMAEL scheme (Figure 4.1 row 2), produced a larger rain-dominated region south of Long Island than Morrison for both of phases one and two. Unlike Morrison, the ISHMAEL scheme produced a considerable region of graupel that occupied only the northern tip of Long Island in phase one, but grew in size to intersect central Long Island and cover the U.S. mainland approximately over coastal Connecticut due east of New Haven, during phase two. Notably, graupel production continued and even increased in size during phase three. Quite unusually, throughout all phases, the northern sector of the domain was not dominated by snow but instead by small ice (blue shading). This is a remarkable divergence, because even though the spatial distribution suggests that ISHMAEL captured the northern snowfall field, the characteristics of this precipitation, such as size and importantly density, were extremely dissimilar to the expected and observed charateristics of snowfall.

The P3 scheme (Figure 4.1 row 3) produced the most diverse cumulative precipitation field of all schemes in a transitional band whose position and phase-to-phase reorientation closely resembled the transitional mixed-phase band associated with high-reflectivity in Ganetis and Colle (2015). Within this cumulative band was a mixture of graupel and sleet (ice pellets) during phase one, that appeared to transition from wet-grown hydrometeors (sleet) to the south positioned at the leading edge of the rain-region, to dry growth hydrometeors (graupel and partially rimed snow) in the north, positioned at the southern edge of the snow dominated-region. In phase two, the north-south oriented transitional band primarily contained rain, but produced graupel at its northern tip and was surrounded by a buffer zone of sleet before the snow-dominated northern region. These results show impressive recreations of mixed-phase precipitation in accordance with observations during these phases. Additionally, in phase three P3 underwent a significant decrease in the cumulative dominance of rain, graupel and sleet that mirrored the observed transition to intense snowfall during this time. interestingly, rimed snow continued to persist across the eastern half of the domain, coincident with the graupel-dominated area in the ISHMAEL scheme during this time.

Overall, the cumulative mass field is a broad examination of a much more complex precipitation field but it does highlight some important tendencies in each scheme. The P3 and ISHMAEL schemes produced an accumulated precipitation field that was dominated by mixed-phase precipitation in small regions. This is in complete contrast to the Morrison scheme, which was dominated by snow. Considering that the cumulative rain field was also the smallest in Morrison, these early results imply that the Morrison scheme is less sensitive mixed-phase processes, and that relative to the other precipitation types, this scheme produces considerably more snow overall. In comparison, the P3 and ISHMAEL schemes produced a greater proportion of the overall precipitation mass in mixed-phase hydrometeor categories, which implies that the adaptations used by these schemes may make them more sensitive to mixed-phase processes. However, the type of precipitation produced in the greatest overall amount by these schemes was dissimilar. ISHMAEL was more likely to simulate graupel, whilst P3 produced a mixture of graupel, sleet and partially rimed snow. This indicates that riming was likely to be more efficient in ISHMAEL, and this is corroborated for example by the similarity of the mixed-phase precipitation region in phase three, where ISHMAEL produced graupel but P3 produced only partially rimed snow. It is most interesting to note that the ISHMAEL scheme was not dominated by snow in any area of the domain, which is divergent from both the other microphysics schemes and the observations for each phase. The broad and consistent regions of small ice in the north of the domain indicate that snow production is unusually low in comparison to the growth of singular ice, perhaps implying that the aggregation routine is inefficient.

In contrast to the accumulated precipitation shown in Figure 4.1, which indicates the precipitation type with the greatest mass production, the total precipitation mixture plot shown in Figure 4.2 captures the variety of precipitation types exhibited by each microphysics scheme per phase. This is a useful resource because the distribution of precipitation types, such as mixed-phase precipitation, can be ascertained regardless of production rate.

It is evident that each microphysics scheme supported the production of a wide variety of precipitation types during this case. The ISHMAEL scheme (Figure 4.2 row 2) produced 7 unique precipitation types (dark red)) across much of the domain over all phases but most surprising is the existence of a yellow band that lacks riming. This band occupies a similar position to that of the mixed-phase transitional band observed in Ganetis and Colle (2015), which suggests that where mixed-phase activity was identified in observations, the ISHMAEL scheme does not exhibit riming, at least not via the precipitation that reaches the surface. Interestingly, the position of the graupel-free yellow band in ISHMAEL during phases one and two (Figure 4.2 row 2, left, middle) is similar to that of the P3 rain dominated band in the cumulative mass field (Figure 4.1, row 3, left, middle) and . This indicates that both P3 and ISHMAEL are sensitive to the melting layer aloft, which is likely to inhibit riming and increase rain mass in both schemes.

The P3 scheme exhibited an interesting relationship between mixed-phase zones that contained rimed ice and snow (red) and those that did not (aqua). For phase one, rimed snow and graupel were present in a transitional zone that showed close agreement with the observed high reflectivity band aloft. However, in phase two the expected mixed-phase region lacked snow and rimed snow entirely. This suggests that riming was highly effective in the transitional zone during phase two, and that mixed-phase hydrometeors developed quickly and comprehensively from the snow hydrometeors. This is a clear divergence from the conventional scheme, Morrison, in which snow is present in almost all grid cells for all phases. It is likely then, that the most obvious caveat of a free-ice category framework is to limit the simultaneous presence of ices; a task that is less challenging for separated category schemes.

4.2 Comparison to Habit Observations Taken at Stony Brook, NY

Having identified that the predicted precipitation field varies considerably with the choice of microphysics scheme, it is now useful to compare these predictions with more precise *in situ* observations of precipitation taken at Stony Brook University, New York (SBNY, Black Star in Figures 4.1–4.2. Figure 4.3 shows the observed ice habit (or precipitation type) as a percentage of the sample set, as well as the degree of rime observed on the crystal surface, at irregular time intervals spanning each phase of this storm. The make-up of precipitation during phase one (2000–2300 UTC) was primarily plate-like or dendritic ice with a low to moderate degree (1–2) of riming, but during phase two (2300–0200 UTC) a more diverse set of plates, columns, needles and sleet were apparent and the degree of riming became heavy (~ 4). By the onset of phase three (0200 UTC-onward), columnnar and plate like ice was common and riming low (~ 1) but at 0500 UTC the observed riming increased to moderate levels (~ 2) and the precipitation field became dominated by plate like or dendritic crystals.

The simulated precipitation field was retrieved within a 20 km by 20 km square area situated approximately over Stony Brook University, that was simulated within the high resolution (800 m grid space) domain situated over Long Island (see Figure 3.1). The mass-weighted average precipitation type and mass riming rate were determined across the entire area in order minimise the chance of an otherwise accurate precipitation field being missed due to a small deviation from the expected location. This was an acceptable compromise because here we are chiefly concerned with the accuracy of the predicted precipitation type rather than the predicted location. Figure 4.4 shows the tendency of precipitation type with time for the ISHMAEL, P3, and Morrison microphysics schemes, in rows 1–3, respectively. Precipitation is given as a percentage of the total precipitation mass per time period for consistency with Figure 4.3, and each precipitation type is shaded according to the subfigure legend. It is evident from the simulated precipitation fields shown in Figure 4.4 that the pre-

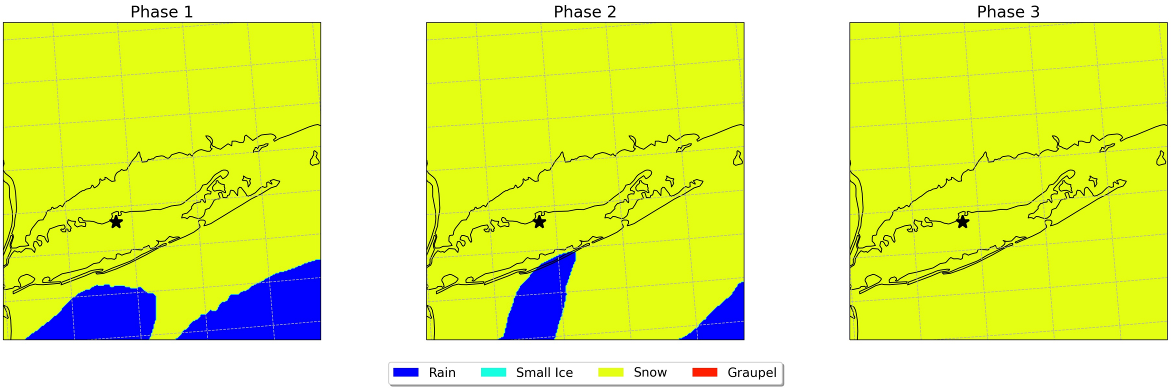
Phase 1
Phase 2
Phase 3
Rain
Small Ice
Snow
Graupel

(a) Morrison

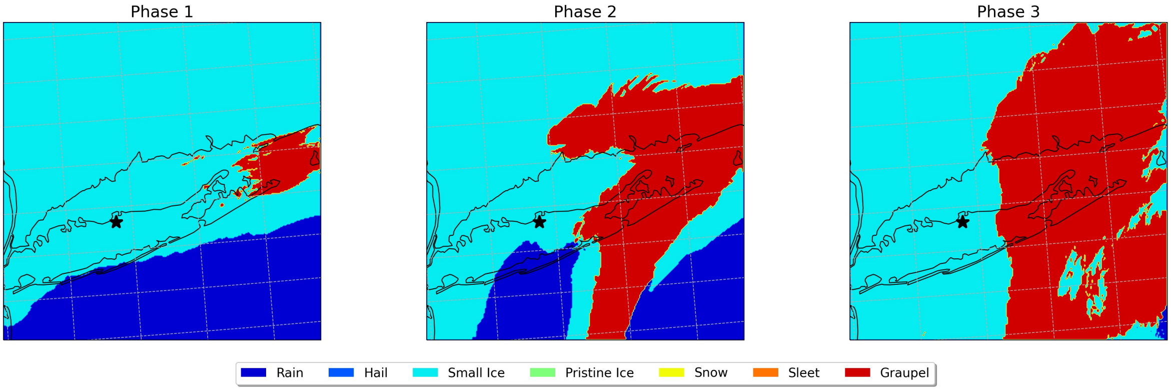
Phase 1
Phase 2
Phase 3
Rain
Hail
Small Ice
Pristine Ice
Snow
Sleet
Graupel

(b) ISHMAEL

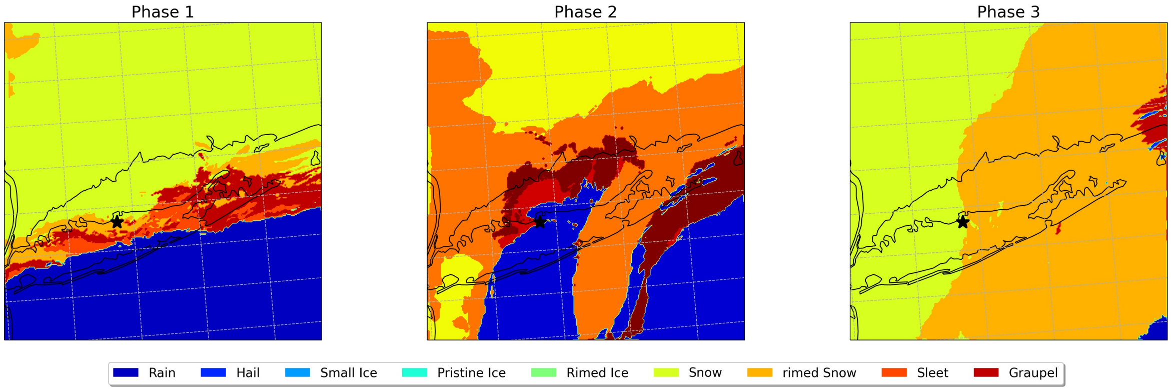
Phase 1
Phase 2
Phase 3
Rain
Hail
Small Ice
Pristine Ice
Rimed Ice
Snow
rimed Snow
Sleet
Graupel

(c) P3

Figure 4.1. Shaded contour plot of dominant precipitation-type per surface grid cell per phase: phase one (left), phase two (middle) and phase three (right) simulated by the Morrison (a), ISHMAEL (b), and P3 (c) microphysics schemes. Dominant precipitation type is determined by the largest overall accumulated mass over the course of the phase. Precipitation type is given in the panel legend for each scheme.

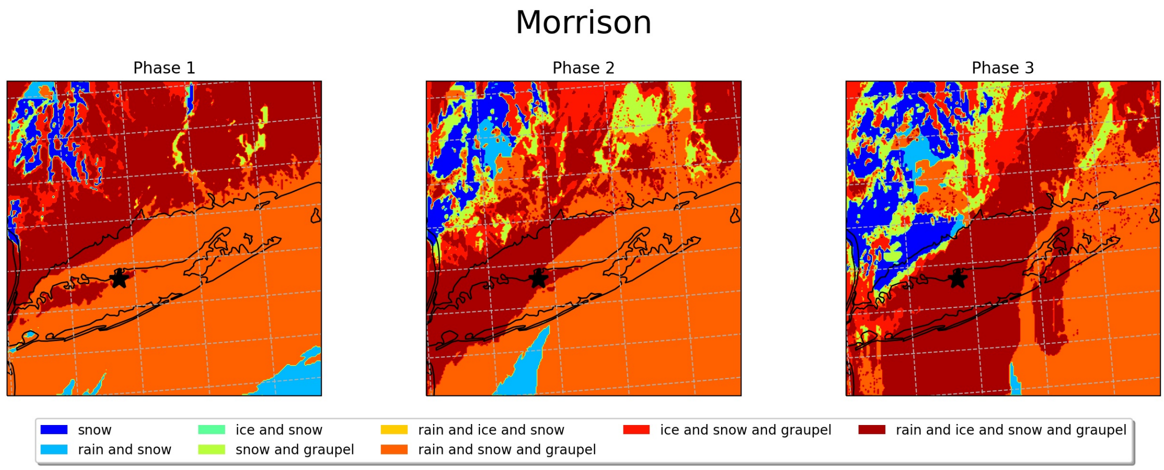
Morrison
Phase 1
Phase 2
Phase 3
snow
rain and snow
ice and snow
snow and graupel
rain and ice and snow
rain and snow and graupel
ice and snow and graupel
rain and ice and snow and graupel

(a) Morrison Microphysics

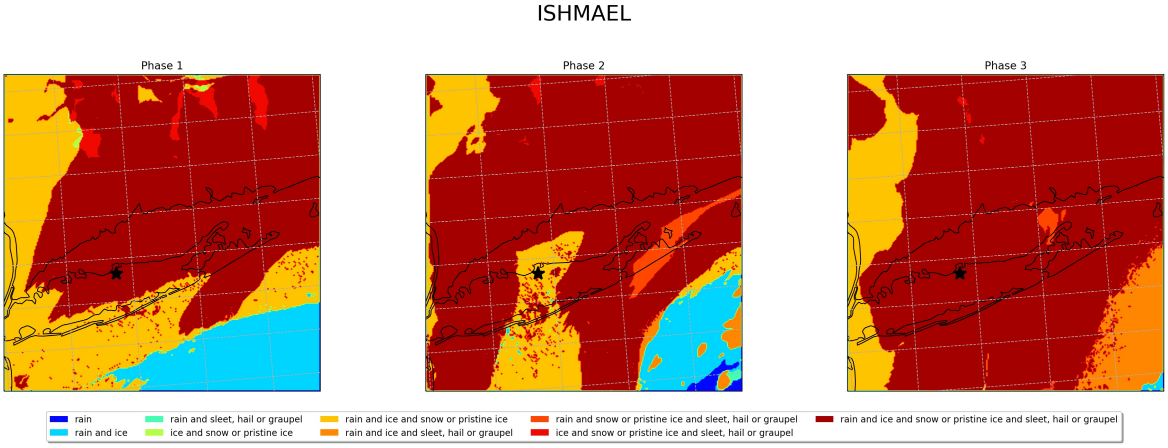
ISHMAEL
Phase 1
Phase 2
Phase 3
rain
rain and ice
rain and sleet, hail or graupel
ice and snow or pristine ice
rain and ice and snow or pristine ice
rain and ice and sleet, hail or graupel
rain and snow or pristine ice and sleet, hail or graupel
ice and snow or pristine ice and sleet, hail or graupel
rain and ice and snow or pristine ice and sleet, hail or graupel

(b) ISHMAEL Microphysics

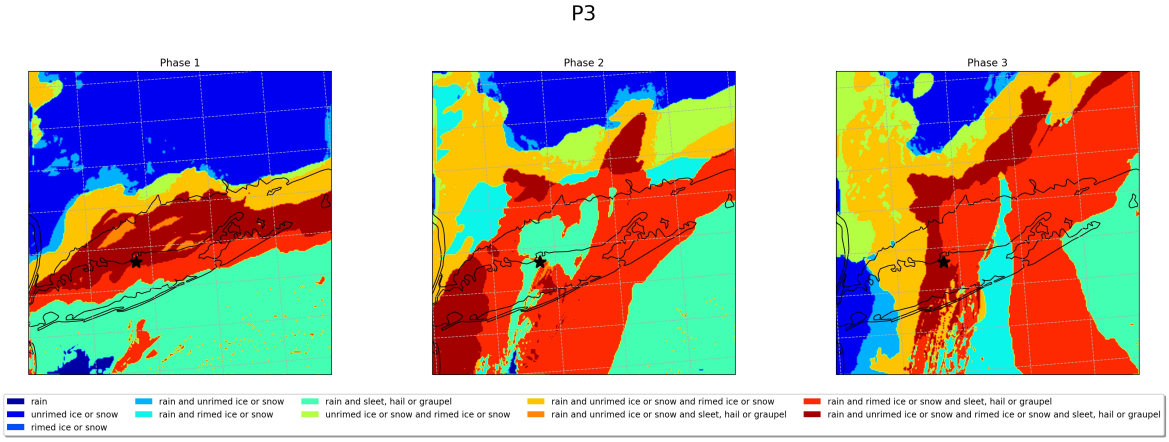
P3
Phase 1
Phase 2
Phase 3
rain
unrimed ice or snow
rimed ice or snow
rain and unrimed ice or snow
rain and rimed ice or snow
rain and sleet, hail or graupel
unrimed ice or snow and rimed ice or snow
rain and unrimed ice or snow and rimed ice or snow
rain and unrimed ice or snow and sleet, hail or graupel
rain and rimed ice or snow and sleet, hail or graupel
rain and unrimed ice or snow and rimed ice or snow and sleet, hail or graupel

(c) P3 Microphysics

Figure 4.2. Shaded contour plot of all predicted precipitation types per surface-level grid cell during phase one (left), phase two (middle) and phase three (right) simulated by the Morrison (a), ISHMAEL (b), and P3 (c) microphysics schemes. Precipitation types (given in the panel legend per scheme) are independent, that is they do not indicate co-location, but simply the presence of the precipitation in that grid cell at some time during the phase.

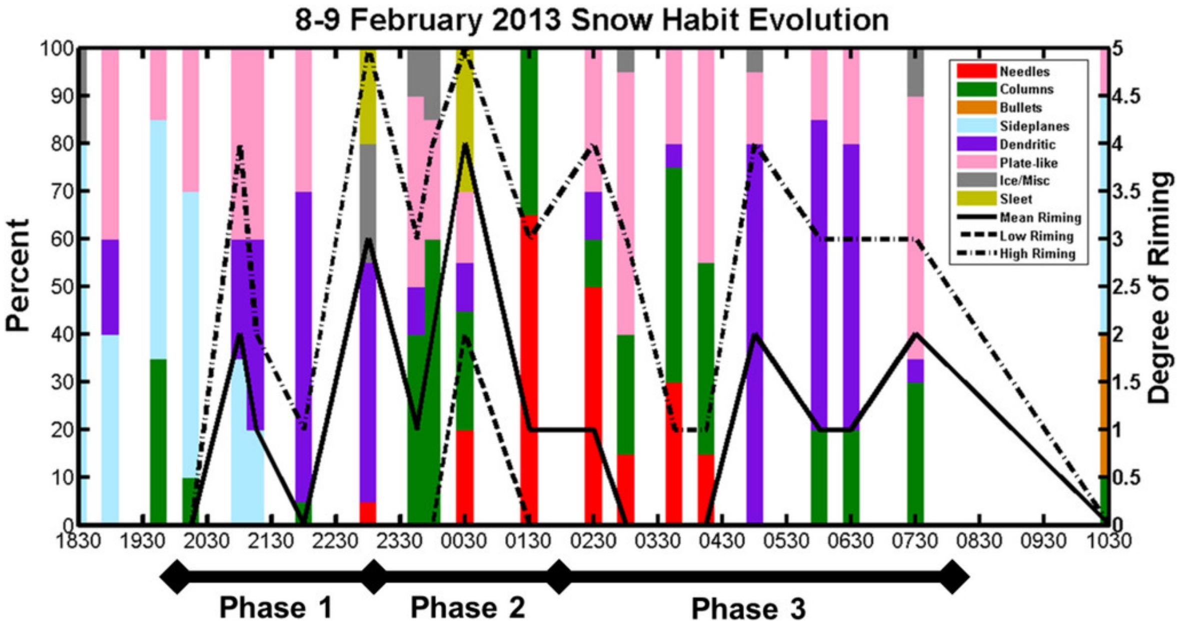

Figure 4.3. Observations of ice habit and degree of rime adapted from Ganetis and Colle (2015) for the period 1830–1030 UTC. Shaded vertical bars indicate the types and relative proportions of sampled precipitation given in the legend. Degree of riming is shown in black for the high (dotted-dashed), low (dashed), and mean (solid) riming.

dicted precipitation field at Stony Brook was extremely variable amongst these schemes.

The Morrison scheme (Figure 4.4 row 3) predicted the least variation in precipitation of all schemes across all three phases of the storm. As in Figure 4.1 panel (a), the precipitation field was dominated (80–100%) by snow for all time periods showing that snow production in Morrison was not only cumulatively large, but consistent throughout the storm, even during phase two when the observed precipitation at Stony Brook was dominated by mixed-phase hydrometeors. During this phase, Morrison did predict a small mixed-phase period but graupel accounted for only $\sim$ 10% of the total precipitation mass and rain accounted for only 5%.

Conversely, the ISHMAEL and P3 schemes showed much more sensitivity to the presence of mixed-phase precipitation. In ISHMAEL (Figure 4.4 row 1), the precipitation varies between graupel and rain production but primarily predicted the presence of small ice (red). The onset of the mixed-phase period during phase two (2300–0200 UTC) coincided with an increasingly large rain output resulting in approximately 80% of the total mass by 0100 UTC. Interestingly, graupel is present at Stony Brook, but only during phases one and three, at which time only moderate riming was observed. The tendency and timing of the transitions between graupel and rain may corroborate that ISHMAEL is sensitive to melting, which was most prominent during the observed mixed-phase period.

In P3, the precipitation at SBNY also appeared to be sensitive to melting. During phase two, when the melting layer was aloft of Stony Brook, the majority of the precipitation field

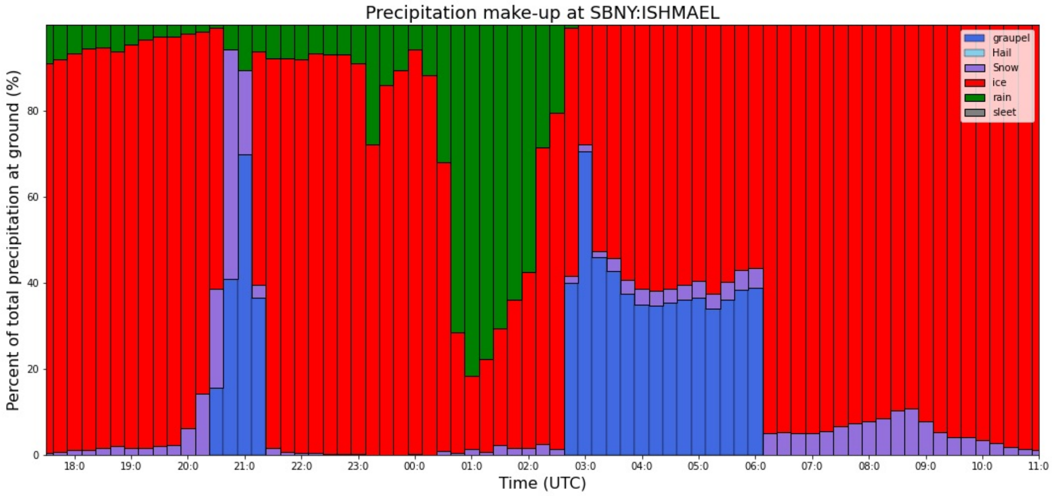

(a) ISHMAEL Microphysics

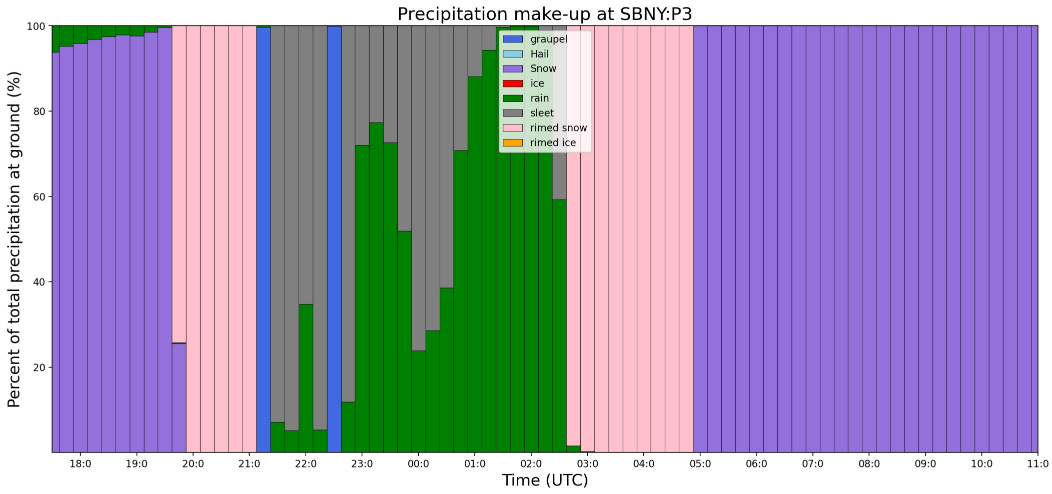

(b) P3 Microphysics

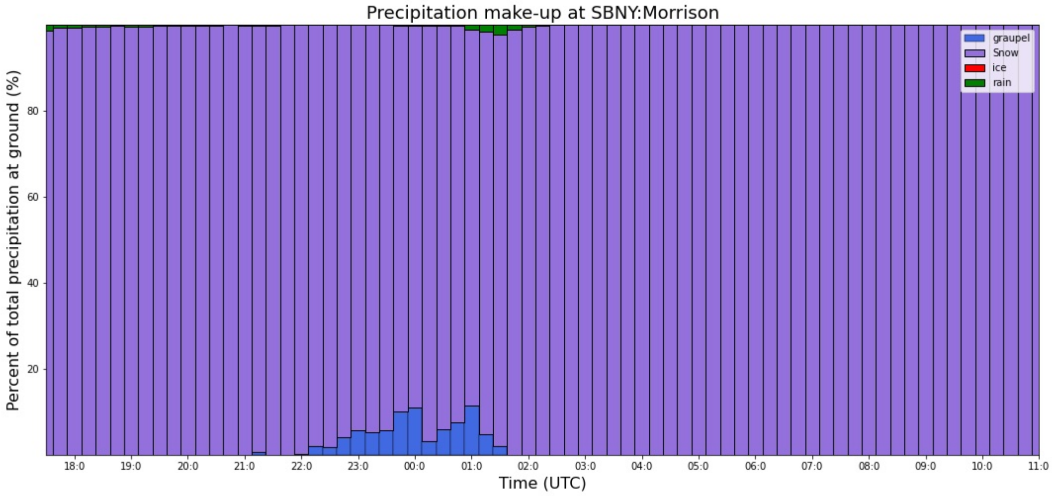

(c) Morrison Microphysics

Figure 4.4. Precipitation type at Stony Brook as a percentage of the total precipitation mass received at the surface (vertical shaded bars) predicted by the ISHMAEL (a), P3 (b), and Morrison (c) microphysics schemes between 1800–1100 UTC 8–9th February. Precipitation type is indicated by shading detailed in the subfigure legend. Data is a mass-weighted average over all surface level cells within a 20 km by 20 km area centred over Stony Brook.

was converted to rain and the only ice present was sleet (analogous to ice pellets or small ice particles). Graupel was generally not produced at SBNY by the P3 scheme, and indeed overall graupel was produced more frequently by Morrison. However, the P3 scheme produced partially rimed snow during phases one and three that broadly aligned with observations of moderate riming at this time.

Overall, it is apparent that no single microphysics scheme provided an ideal prediction of precipitation type or tendency at Stony Brook. The ISHMAEL scheme and P3 schemes showed similar precipitation type tendencies per phase and achieved a reasonable prediction of riming during the ramping-up/down period of phases one and three, when mixed-phase activity was moderate. However, both schemes were too sensitive to melting during phase two resulting in an overproduction of rain mass and loss of mixed-phase precipitation (presumably aloft). That's not to say there were no successes, as during phase two rain was accompanied by pellet-like ice in both schemes that was representative of the ice pellets experienced at the ground. Comparatively, the Morrison scheme showed far less sensitivity to the mixed-phase period, and consequently continued to produce snowfall at Stony Brook for the extent of the simulation. It is possible that the inability to perceive partial riming in Morrison likely played a role during phases one and three, when riming may have occurred but not in significant enough quantities to produce graupel. Therefore, during these phases, the precipitation was confined to only snowfall with no riming evident. During phase two, the appropriate timing of graupel production by Morrison was still a successful indication of mixed-phase activity. However, the amount of graupel produced was not enough to resemble observations of riming.

Unlike Morrison and P3, the ISHMAEL scheme parameterises ice aspect ratio which allows for the comparison of observed and predicted ice habit. This motivates a comparative study of ice habit prediction. For this analysis, the raw observational data of ice habit was reorganised into three aspect ratio categories; oblate, prolate, or spherical ice crystals. An overview of the ISHMAEL-predicted distribution of these categories is shown in Figure 4.5, where it is evident that oblate ice is the most widely predicted precipitation type, followed by near spherical, and then columnar. However, interestingly the amount of columnar crystals as a proportion of the entire precipitation field increases toward the surface. This provides some evidence that the ISHMAEL scheme may simulate enough columnar ice to recreate the observations. However, the ISHMAEL scheme did not simulate the appropriate ice habit at SBNY in Figure 4.4. To proceed with this analysis, it is assumed that the precipitation field may be displaced further north-east than observed, which is corroborated by the location of cumulative graupel mass further north-east than expected in Figure 4.1. The suitability of this assumption can be checked by examining the frequency of column-like crystals produced by the ISHMAEL scheme north-east of SBNY. Columnar crystals were observed in great frequency between 0030 UTC and 0430 UTC, and at this time Figure 4.7

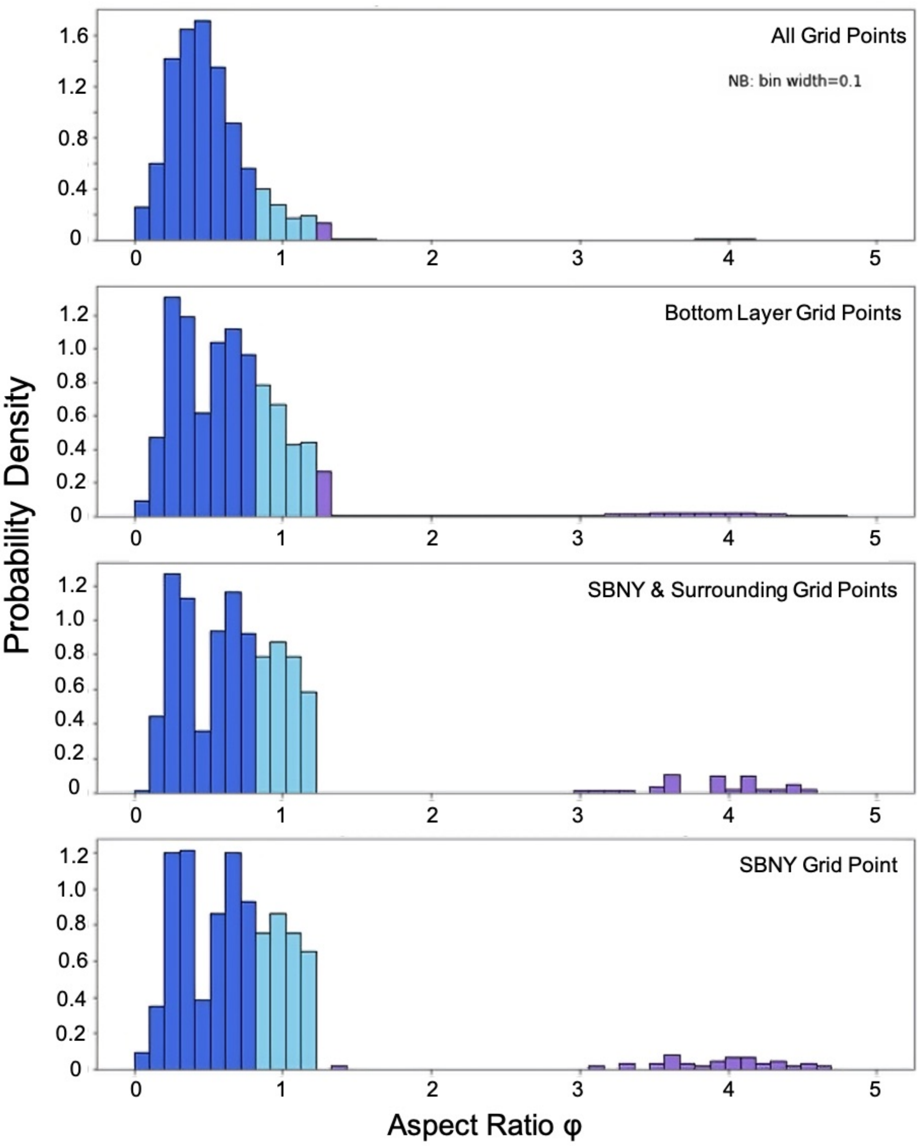

Figure 4.5. Histograms of ice-particle aspect ratios throughout domain 3 for all grid points (row 1), bottom layer (*surface*) points (row 2), grids including, and in close proximity to, SBNY (row 3), SBNY grid cell only. Bars are shaded according to the habit-type associated with each aspect ratio, oblate (ϕ < 0.8, dark blue), spherical ($0.8 < \phi < 1.2$, light blue), and prolate (ϕ > 1.2, purple)

shows that columns did occur to the east of SBNY. This motivates a comparison of the simulated aspect ratios at three eastern locations. These three points are shown in Figure 4.7 with black markers (see Figure legend).

Figure 4.6 compares the aspect ratio categories that were observed (row one) and ISHMAEL-simulated (rows 2–4) at three points on Long Island. Precipitation is given as a percentage of the total crystal sample size, and comparably the ISHMAEL data is given as a number-weighting. For comparison to the degree of rime (row one, overlaid black lines) the average tendency of riming is used as a proxy and overlaid in black for rows 2–4.

The simulated aspect ratio shown in Figure 4.6 indicates that, whilst the ISHMAEL scheme

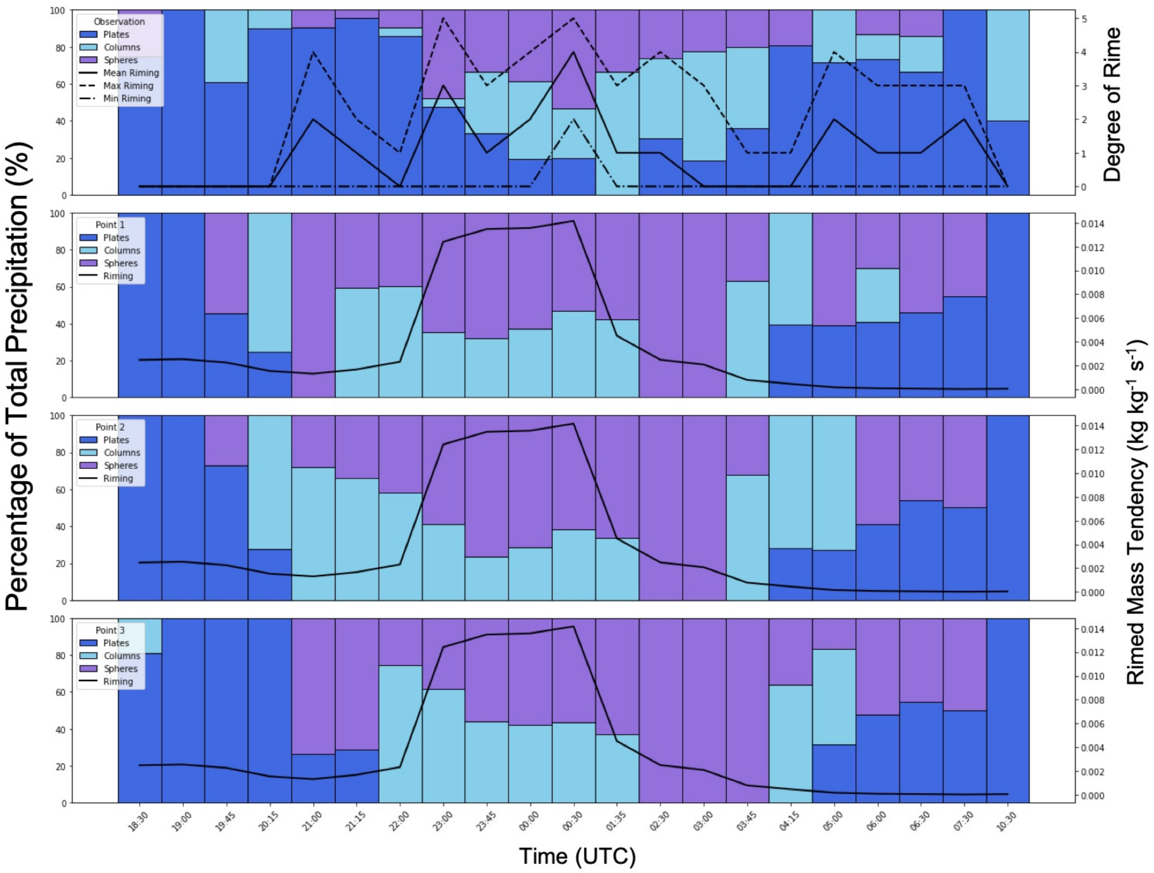

Figure 4.6. Aspect ratio of ice observed at SBNY (top) and simulated by the ISHMAEL scheme at three points in proximity to SBNY (shown in Figure 4.7). Observational data derives directly from a re-categorisation of precipitation type as shown in Figure 4.3. Aspect ratios are grouped into plates (dark blue), columns (light blue), and spherical (purple). The observed high, low and mean riming rate 4.3 is shown for observations (top). A proxy to the degree of riming, the rime mass tendency is shown for the ISHMAEL scheme in (black, solid)

did not produce an appropriate aspect ratio distribution exactly at SBNY, east of this region the aspect ratios were in moderate agreement with observations. For example, the observed aspect ratio tendency was from plates in phase one, to columns and spheres in phase two, and columns followed by plates in phase three. A similar tendency is observed in the ISHMAEL scheme where an initially plate-dominated field gives way to columns and spheres, and is then replaced by plates and columns. However, we note that the ISHMAEL scheme was too quick to produce spherical particles, and maintained their production than for longer than was observed. This is likely related to the increased sensitivity to riming and melting posed by ISHMAEL, which serves to tend the aspect ratio towards spherical. Importantly, the simulated riming mass tendency (black overlaid line) shows good agreement with the peak of the observed riming during phase two. These results are promising for habit parameterising schemes, and more work in this vein should be conducted to verify their development with observational data.

Throughout this chapter, it has been stated that precipitation predictions in the mixed-phase

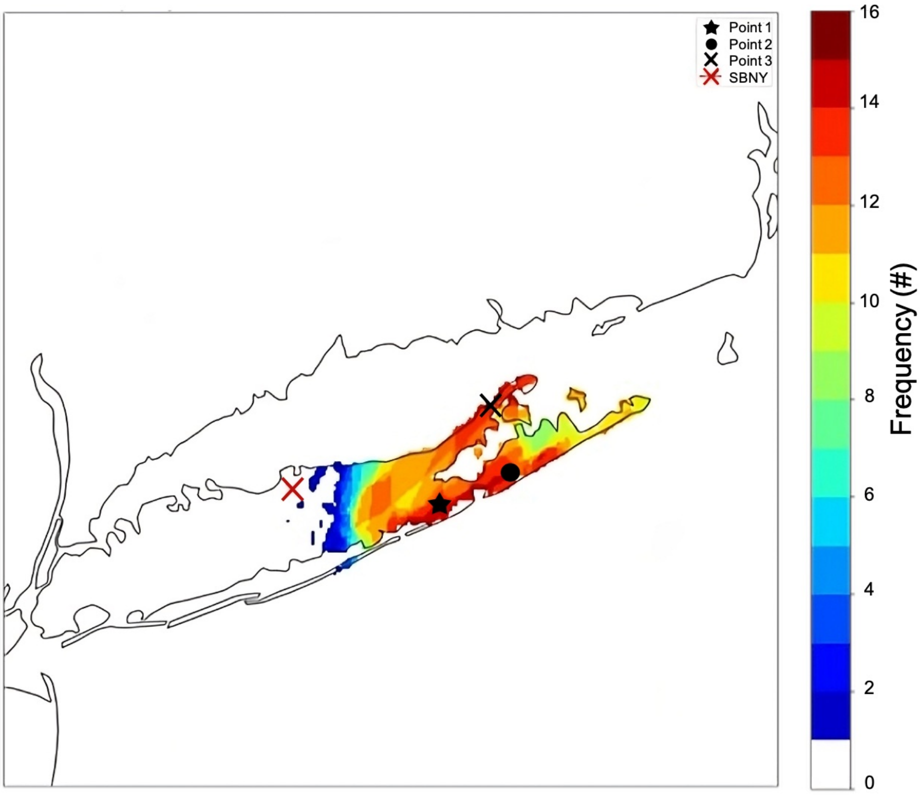

Figure 4.7. Grid-cell frequency of prolate crystals simulated at the surface by ISHMAEL between 2300–0430 UTC. Frequency is defined as number of times present per time step, and the domain 3 time step was 15 minutes (4 per hour). The location of Stony Brook is shown with a red cross. The location of three sample points for aspect ratio analysis (see Figure 4.6) are shown in black and given by the Figure legend.

have been influenced by each scheme's sensitivity to the melting layer. Examination of the ISHMAEL, P3 and Morrison precipitation fields imply that the generalised-ice framework appears more susceptible to the effects of melting, which materialises in a comparably more rain-filled precipitation field, mixed with small ices such as ice pellets. In this case, the melting layer was responsible for much of the observed mixed-phase precipitation throughout the transitional zone, so it is desirable to compare the melting layer extent and magnitude to determine if this was a factor to the simulated precipitation at the ground. Figure 4.8 shows the melting layer (determined by T > 0°C) aloft of Stony Brook per phase and per scheme. Column 1 shows a time series of the melting layer top (green) and melting layer bottom (blue) versus height, as well as the location of the maximum temperature within the melting layer (red). Column 2 shows the descent rate of the upper and lower melting layer boundaries. Column 3 shows the width of the melting layer, determined by the absolute difference of both top and bottom boundaries.

Figure 4.8 shows that there are large differences in the elevation and width of the melting layer during phase two that likely led to the very different precipitation fields and perceived melting sensitivities per scheme. For example, in phase one all schemes show a similar melting layer width and elevation above the surface (lower bound > 1 km). However, in phase two the melting layer in ISHMAEL descends rapidly to very near to the ground level. This effect is not found in the Morrison scheme, and occurs later in the P3 scheme. Consequently, the melting layer width in ISHMAEL is more than 500 m larger than in P3 on average during phase two, and more than double that of Morrison. The melting layer width is a important because particles falling into the melting layer must traverse a larger distance to ground than in other schemes and thus have more time to fully melt. This likely played a role in the increased rainfall and reduced mixed-phase precipitation predicted by ISHMAEL during phase two. For example, the peak in melt layer width from 2330–0100 UTC coincides with the onset of increased rainfall in Figure 4.4. It is also notable that the peak in melt layer width for the P3 scheme also coincides with considerable rainfall in Figure 4.4. However, the melt layer width in P3 is half that found in the ISHMAEL scheme, so it is likely then that of both free-ice categorisation schemes it is P3 that is the more sensitive to melting, and it is ISHMAEL that produces larger melt layers. The origin of this increased melting layer width in the ISHMAEL scheme is of particular interest, not only due to the effect of this upon the precipitation at the surface, but also due to many similarities with observations that were detailed by Griffin et al. 2014. Griffin noted that the melting layer descent was pivotal to the precipitation simulated at the ground, and hypothesised that this descent was due to either latent heating or the size and fall speed of large hydrometeors at the fastest descending point. In this instance, more research is needed to examine the relationship between the melting layer and its descent in the ISHMAEL scheme.

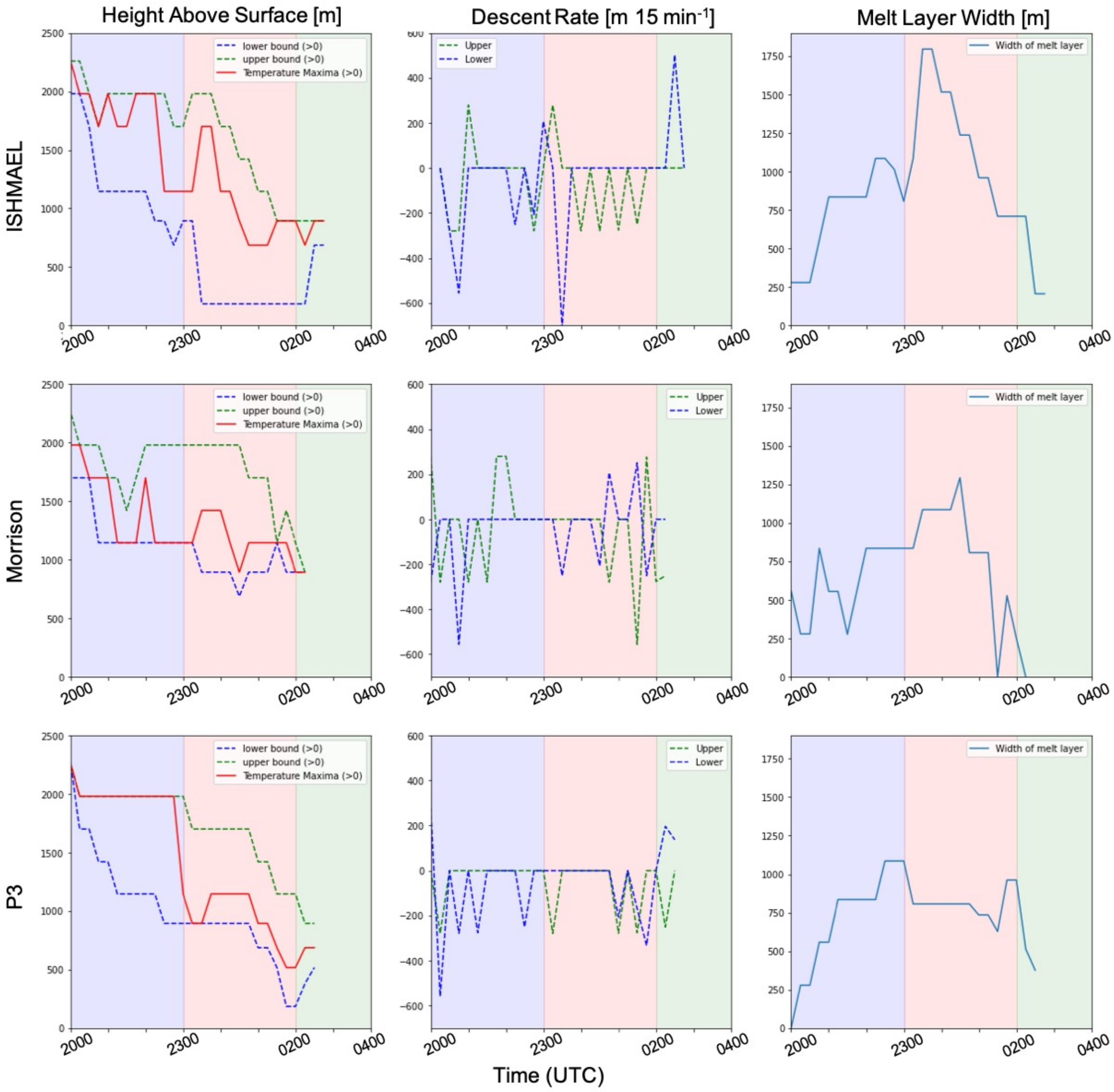

Figure 4.8. Vertical distribution and characteristics of the melting layer (T > 0°C) aloft of Stony Brook for phase one (blue shading), phase two (red shading), and phase three (green shading) simulated by the ISHMAEL (top), Morrison (middle), and P3 (bottom) microphysics schemes. Column 1; elevation of the melting layer top (green dotted), bottom (blue dotted), and maximum temperature (red, solid). Column 2; descent rate (m 15 min^{-1}) of the melting layer top (green, dotted) and bottom (blue, dotted). Column 3; melting layer width (top layer elevation minus bottom layer elevation).

Chapter 5

Riming

The process of riming played a significant role in the development of precipitation at the surface for the storm in this case. Modification of ice crystal habit was not only commonplace during phase two of the storm, but was well-captured by ground-based photography of ice crystal habits that showed copious surface riming. The resulting products of riming, such as graupel and miscellaneous ice pellets formed a substantial portion of the precipitation. It is important then to determine which microphysics scheme, if any, can adequately reproduce these observations.

This case provides an ideal-test bed for the ISHMAEL and P3 schemes, which each employ novel methods to improve the ice characteristics during riming, with the intention to improve the accuracy of ice particle growth during this process. This investigation is ideal too for the Morrison scheme, that simulates graupel in the conventional categorisation framework that has been the subject of scrutiny and debate.Therefore, the goal of this chapter is to investigate the differences in the extent of riming produced by these schemes, and associate these differences with process rates. ISHMAEL and P3 will be thoroughly examined within a realistic ice growth scenario, and the limitations and weaknesses of each framework will be evaluated and discussed.

5.1 Rimed Precipitation and Riming Rates

Given the differences in the location and frequency of rimed particles simulated at the surface by each microphysics scheme (see Figures 4.1–4.2), it is interesting to examine and compare the amount of rimed particles that were present throughout the entire domain. For this analysis the particles that meet the “rimed” criteria must first be established. In Morrison, rimed particles are represented by the graupel category only. Whereas in ISHMAEL, riming can occur for any frozen precipitation type by modification of the precipitation qualities such as density and aspect ratio, but the rime-specific components that modify the precipitation are not tracked. Partially rimed ices in ISHMAEL are, therefore, difficult to distinguish with high confidence, so for the sake of clarity only precipitation meeting the

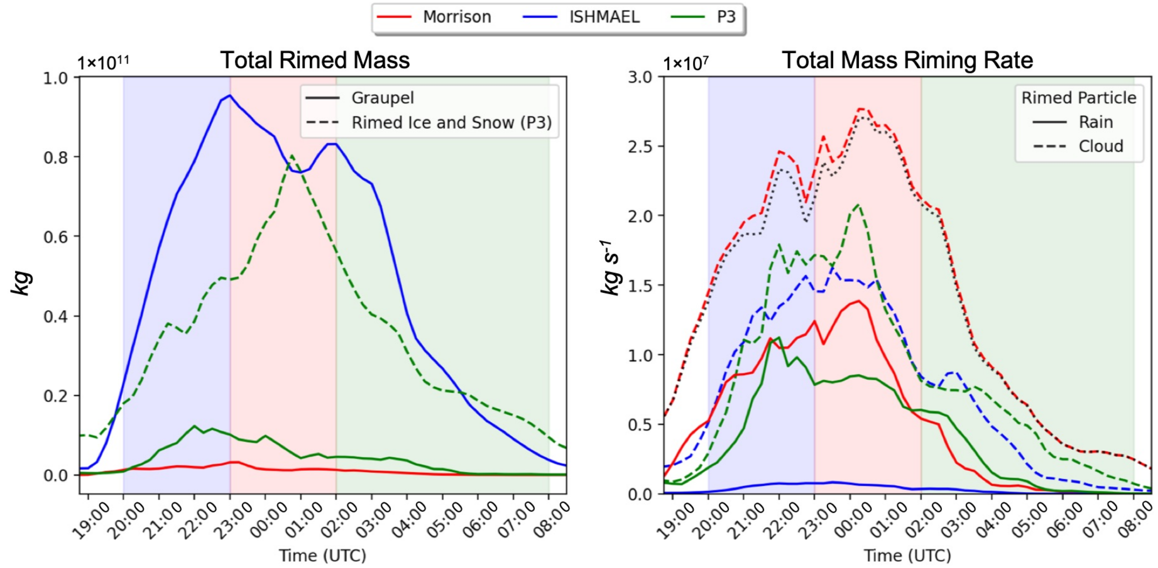

Figure 5.1. Time series of total rimed-particle mass (kg, left) and total riming rate (kg s^{-1}, right) per microphysics scheme in domain 3. Quantities associated with the ISHMAEL, Morrison and P3 microphysics schemes are shown in blue, red and green, respectively. Blue, orange and green backgrounds span phases one, two and three, respectively. Rimed-particles are graupel (solid) in the ISHMAEL, Morrison and P3 schemes, and also partially rimed ice (dashed) in the P3 scheme only.

criteria of graupel is considered as a rimed-particle in this microphysics scheme. For P3, a particle's historical rime mass and volume can be used to determine rime fraction enabling partially rimed precipitation to be identified in addition to graupel. Therefore, the rimed particle mass considered for summation is graupel for all microphysics schemes, and additionally, partially rimed ice for P3.

The total rimed particle mass was obtained by summation over all cells in the highest resolution domain (domain 3), situated over Long Island where riming was observed. The timeseries of total rimed mass per time step isshown in Figure 5.1 (left) for each scheme (see Figure legend). The time periods for phase 1 (2000–2300 UTC), phase 2 (2300–0200 UTC), and phase 3 (0200–0800 UTC) are indicated by blue, red, and green background shading, respectively.

Figure 5.1 (left) shows that prior to the onset of phase one ($\sim$ 1900 UTC) each microphysics scheme simulated a relatively small ($< 1 \times 10^{10}$ kg) amount of graupel but by the onset of phase one ($\sim$ 2000 UTC) ISHMAEL (blue) had already increased its graupel production considerably. This large rate of increase in graupel mass was sustained for the entirety of phase one. By 2130 UTC, the total graupel mass mixing ratio in ISHMAEL had increased to $< \ 7 \times 10^{10}$ kg and continued to increase until reaching a peak total graupel mass of $< 9.4 \times 10^{10}$ kg by the onset of phase two (2300 UTC), before declining gradually during phase three. By comparison, P3 (green, solid) produced considerably less graupel through all three phases, reaching a maximum graupel mass of $< \ 1 \times 10^{10}$ kg at 2200 UTC, its highest total of all three phases and almost ten times smaller than the maximum produced by ISHMAEL. Total graupel mass in P3 then reduced quickly over the course of phase two, and more gradually during phase three. Morrison (red) produced the least total graupel mass of all schemes, reaching a peak value of $< 2 \times 10^9$ kg at 2300 UTC, before decreasing gradually during phase three. For comparison, partially rimed snow and ice generated by the P3 microphysics scheme is also shown in Figure 5.1 (green, dashed). This precipitation has a similar tendency and peak magnitude to the graupel mass produced by ISHMAEL, rising and falling during phases one and three about a peak mass of $< 8 \times 10^{10}$ kg at 0100 UTC during phase two.

Three key conclusions may be taken from Figure 5.1 (left). First, that ISHMAEL consistently produced considerably more graupel mass than any other scheme both overall and within each phase. This very large difference (i.e. ISHMAEL peak graupel mass was a factor of ten times larger than P3, and nearly 50 times larger than Morrison) indicates that the ISHMAEL scheme may be more prone to the overproduction of graupel. Similarly, a second noteworthy point is that Morrison produced much less graupel than other schemes, which may indicate that this scheme underestimates riming or the production of graupel precipitation in general, a common criticism of conventional schemes. Finally, we note that whilst the P3 simulated total graupel mass was quite small, the total mass of partially rimed ice was comparable to graupel in ISHMAEL, which may indicate that riming is taking place in P3 at a similar rate to ISHMAEL, but that the resulting precipitation does not reach a fully rimed state, perhaps due to some limiting factor. These points require further investigation.

A key uncertainty discussed above is the relationship between the rimed mass that is produced and the riming rate that produces it. To understand this link, the total rimed mass time series per scheme in Figure 5.1 (left) can be compared to a time series of the total mass riming rate, shown in Figure 5.1 (right). The total mass riming rate (kg s^{-1}) is a component to the total mass tendency equation that is calculated according to the riming framework in each scheme and so is innately dissimilar between the microphysics schemes used in this case. The mass riming rate of a single cell describes the mass of a liquid (cloud or rain) droplet population that is transferred to the frozen precipitation mass each second due to riming. The total mass riming rate plotted in Figure 5.1 (right) is the summation of the single cell mass riming rate for all cells per time step and thus represents the instantaneous riming rate.

The total mass riming rate shown in Figure 5.1 (right) is separated for rimed mass stemming from accreted rain (solid) and accreted cloud droplets (dashed). Remarkably, Morrison cloud droplet riming was the largest riming rate of all schemes and liquid types, reaching a maximum of 2.7×10^7 kg s^{-1} at 0030 UTC (phase two), and was consistently larger than the riming rates of all other schemes by 5×10^6–1×10^7 kg s^{-1} per time step during phases one and two. Additionally, total riming mass rate due to rain was larger than in both ISHMAEL and P3. These results are surprising given that Morrison produced the smallest total graupel mass of all schemes, but may indicate that the underestimation of graupel is not due to a lack of riming in this scheme, rather, that considerable riming does occur but this mass is not transferred to the graupel hydrometeor category.

The opposite relationship is found for the ISHMAEL scheme (blue), which produced the lowest peak total mass riming rate from rain, and the lowest overall riming rate (from cloud droplets), yet was found to produce the most rimed mass overall. In this case, a similar conclusion is implied, that riming is infrequent, or that the riming process calculates that less rimed mass is produced in ISHMAEL, but that the incorporation of the rimed mass to graupel is comparably more efficient than in other schemes. By comparison, the P3 scheme had a similar cloud droplet riming rate, and a much larger rain riming rate than ISHMAEL, but only produced partially rimed ice. This difference in the degree of riming that is simulated by P3 and ISHMAEL implies that the growth path toward graupel is dissimilar in each framework

The combined evidence from Figure 5.1 indicates that the fundamental differences between the riming frameworks of each scheme can produce a wide variety of riming rates that have very different relationships to the production of rimed mass. For Morrison, relatively high riming rates do not translate to large masses of graupel, and in ISHMAEL, relatively modest riming rates produce considerable masses of rimed ice. P3, which bears many similarities to ISHMAEL (i.e. by evolving ice characteristics) simulated a precipitation field with less riming than was simulated by ISHMAEL, despite P3 having a much higher total riming rate.

The outstanding question is, where do the differences in the relationship between rime rate and rimed precipitation originate? All three microphysics schemes strictly conserve mass, therefore the should be no discrepancy between rimed mass and rimed precipitation. However, this directly contradicts the findings in Figure 5.1, namely that the relationship between riming rates and rimed particles is dissimilar between schemes. Indeed, whilst mass is conserved in these schemes, the mechanism of precipitation production in each provides ample opportunity for the rime mass tendency and the precipitation field to become seemingly disjointed. In the following sections, the relationships between riming and precipitation for each framework will be explored, namely the fixed hydrometeor-category system used Morrison, and the ice particle property evolution system used by ISHMAEL and P3.

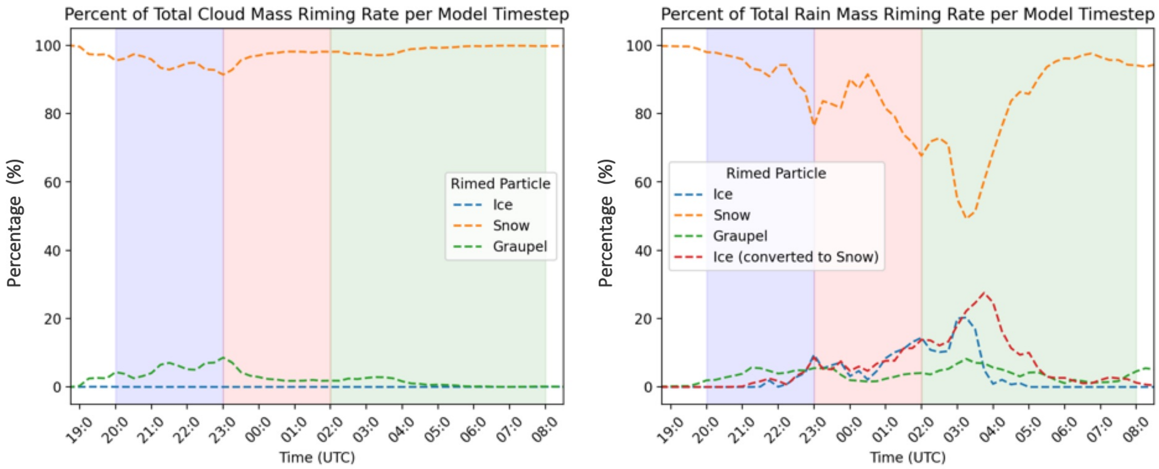

Figure 5.2. Time series of percentage rimed particle mass (%) applied to each hydrometeor category at the end of the model time step, simulated by Morrison microphysics in WRF domain 3. Left: cloud droplet riming. Right: raindrop riming. Three hydrometeor categories are considered; Graupel (green), Snow (orange), and Ice (blue). For rain droplet riming, rimed cloud ice mass that is subsequently added to snow mass (auto-converted) is also shown (red). Blue, orange and green backgrounds span phases one, two and three, respectively.

5.2 Riming-Rates and Graupel Production in the Morrison Scheme

First, we will investigate the relationship between riming and graupel production in Morrison. One of the most surprising results of Figure 5.1 was the relatively low total graupel mass produced in domain three, despite the total mass riming rate being relatively large. Given that mass is a strictly conserved quality in Morrison, we seek to determine the destination of rimed mass if not graupel.

In Morrison, the mass riming rate is calculated for each hydrometeor category, and added to the hydrometeor's total mass tendency at the end of each time step, which enables the destination of rime mass to be determined per precipitation type. In Figure 5.2, the total rimed mass applied to each precipitation category at the end of the time step is summed for all cells in domain three and combined into one value per time step. The resulting time series is shown as a percentage of the total rimed mass per time step per precipitation type. Figure 5.2 (left) shows the times series for rime mass that originates from cloud droplets, and Figure 5.2 (right) shows the equivalent quantity that originated from the riming of rain droplets.

The destination of cloud droplet rimed mass shown in Figure 5.2 (left) in the Morrison scheme was predominantly snow in this case. Cloud droplet accretion to snow consistently accounted for at least 90% of the total rimed mass destination per time step, and on average snow captured 96.5% of rimed cloud droplet mass through all three phases. By comparison, the second-highest recipient of rimed cloud droplet mass was graupel, which obtained only 3.5% of the rime mass in total.

The destination of rain droplet rimed mass shown in Figure 5.2 (right) was more varied than for rimed cloud droplets, but still dominated by the riming of snow. The snow category captured 85.7% of all rimed rain mass on average and exceeded 80% of the total for the majority of phases one and two. Whereas graupel rarely captured 5% of the total rimed rain mass. In fact, cloud ice captured and retained more rimed rain droplets than graupel in phase two, and had a larger peak of 20% of the total mass at 0300 UTC. An important factor in this case was the rimed rain captured by ice that was subsequently auto-converted to snow (red). This quantity peaked at almost 30% of the total rimed mass gained, and was the second largest destination on average for all rain-rimed precipitation types.

Overall, Figure 5.2 begins to consolidate the seemingly disjointed relationship between riming and graupel. The vast majority of rimed mass from both cloud droplet and rain riming was absorbed into the snow category by the end of the model time step, either directly, or via autoconversion of cloud ice. Importantly, on average the snow category gained more than 95% of the total cloud droplet mass, which was the largest contributor of rimed mass of any scheme or droplet type (Figure 5.1). For comparison, the proportion of rimed cloud droplet mass transferred to the snow category is shown in Figure. 5.1 (right, black, dotted). Not only does this bias negatively impact graupel production in the Morrison scheme, but it also contributes to the Morrison snow hydrometeor category, which was shown to have by far the largest total mass of all schemes and precipitation types.

Care must be taken to discern the results of Figure 5.2 in the context of the precipitation field. It is difficult to disentangle cause from effect, for example, the vast majority of rimed mass did contribute to the snow category and therefore, the snow category was a direct beneficiary of the riming process. However, snow mass was the most numerous and extensive precipitation type in the Morrison scheme, so it makes sense that in riming cells snow would incur a larger proportion of the total rime mass. Indeed, both scenarios are logical, but the outcome must be consolidated; the largest amount of riming should not lead to the smallest amount of graupel. This motivates an investigation of the conversion process from snow to graupel.

Morrison cannot represent partially rimed ice, so the autoconversion rate of snow to graupel is crucial in determining the production rate of graupel. To determine the autoconversion rate of rimed mass on snow to graupel in the Morrison scheme, cells that were found to rime upon snow were isolated, and the percentage of the resulting rime mass that was added to snow versus that added to graupel was retrieved. The rimed mass added directly to graupel is not considered here, as we are concerned only with the growth of the snow category by riming and the proportion of this mass that is subsequently transferred to the graupel category. Figure 5.3 shows the typical percentage of accreted mass that is transferred to the graupel category in several $\log_{10}$ scaled bins. The frequency of each bin count

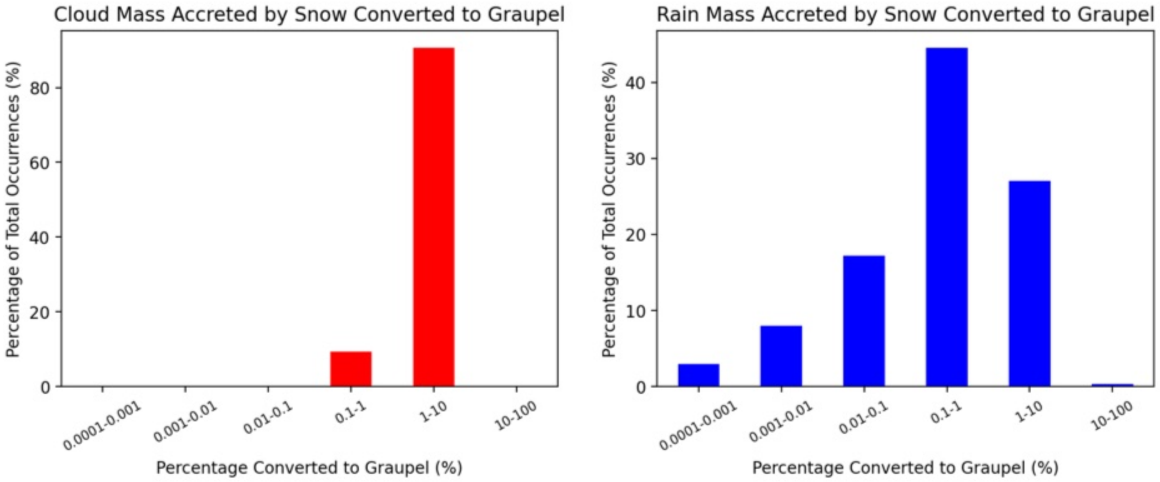

Figure 5.3. Percentage of mass accreted to snow that is transferred to the graupel category (x-axis) as a percentage of the total number of autoconversion cases (y-axis) in the Morrison scheme. Left: the proportion of converted mass owed to cloud droplet riming. Right: the proportion of converted mass owed to rain droplet riming.

was shown as a percentage of the total number of snow-riming cells. Figure 5.3 (left) shows the typical amount of cloud droplet rime mass that is converted to graupel from the snow category, whereas Figure 5.3 (right) shows the typical conversion amount for rimed rain drops.

Figure 5.3 shows that conversions of more than 10% rimed snow mass to graupel rarely occur, despite the high riming rates that were simulated in this case. For cloud droplet rime (Figure 5.3, left), a 10–100% conversion of rime mass to the graupel category occurred in only 0.001% of cases. The most common conversion rate was between 1–10% of rimed cloud droplet mass that accounted for more than 90% of all cases. The remaining proportion of cases were found to convert between 0.1 and 1% of the rimed cloud droplet mass to the graupel category, with the remaining > 99% of mass retained by the snow category. In comparison, the rain droplet rimed mass was found to be retained by the snow category more often, and in greater overall amount, than for cloud droplets. For example, the 1–10% conversion bin accounted for less than 30% of all conversions, with the vast majority of rain-rimed snow instances converting 1% or even less of the total rimed mass to graupel.

As previously stated, the absorption of a portion of the rimed mass into the snow category is a logical and necessary choice in the categorised-precipitation framework. However, the portion of rimed mass that is converted to the graupel category is shown by Figure 5.3 to be extremely small in comparison to the amount of rime added to snow. Not only does this artificially restrict the production of graupel, but it simultaneously and unexpectedly provides a mechanism for the enhancement of snowfall. It is arguable that the enhancement of the snow field is natural, as light riming increases the mass of snow without producing graupel. However, in the following paragraphs we argue by counter example that the partitioning of rime mass in Figure 5.3 is unrealistic and detrimental to the production of graupel in Morrison's current formulation.

Consider a cell in which snow is present with graupel, and where snow mass vastly outnumbers graupel mass. The partition of rimed mass must be balanced by two factors; the relative amount of each hydrometeor type to be rimed upon, and the degree of riming that constitutes graupel. For example, in this example cell, one might expect that the sum-total rime mass lost to the light riming of many snow particles, is larger than the sum-total rime mass spread across very few graupel particles. Consideration of the relative amount hydrometeor types can therefore allow the proportion of droplet mass retained by snow to vastly exceed that obtained by graupel. This scenario is in agreement with Figure 5.3.

However, we note that the scenario posed by Figure 5.3 can only occur when the riming of snow crystals is light, and more broadly, that the degree of riming is considered by the snow field. To illuminate this point, consider the same cell where snow mass vastly outnumbers graupel mass. Suppose that light riming occurs, such that the mass gained by graupel is small due to the large-scale riming of many snow crystals. After one instance of riming, the snow field rime fraction is $F_r > 0$, where $0 < F_r < 1$ denotes the proportion of the crystal that is rimed and $F_r = 1$ is graupel. Then by extension, After $1/F_r$ riming instances the snow field will reach the graupel criteria and a jump in the graupel field will be apparent as the very large snow mass is converted to graupel. This jump condition is essential for an accurate relationship between riming and graupel production. This simple example indicates that, conditions exist in which the majority of rimed mass can be applied to snow (i.e. Figure 5.3), and simultaneously, the majority of the precipitation that is produced is graupel. In fact, the conditions posed by Figure 5.3 are only possible if such a consideration of rime fraction as posed here is present.

Without consideration for rime fraction, the graupel jump condition is not realised and the snow field perpetually grows at the expense of the graupel field. Indeed, without consideration of rime fraction, the partition found in Figure 5.3 is potentially physically unrealistic; it shows that riming is dependent on the relative amounts of snow and graupel, whilst simultaneously growing snow mass at the expense of graupel mass. This cyclical relationship indicates that the severity of riming is intrinsically related to snow production more so than graupel production and goes some way toward explaining the relationship observed in Figure 5.1. Beyond an unusual relationship between riming and graupel production, this methodology poses several additional problems for the precipitation field, not least that partially rimed snow retains the density and fall speed characteristics of unrimed snow.

Two solutions are posed here to remedy the current Morrison framework (and by extension, the frameworks of other microphysics schemes that utilise categorised precipitation). First, the expansion of the snow category into several partially rimed subcategories, which would allow a transitional path toward the graupel jump condition and incorporation of modified density and fall speeds for rimed ice. This option is likely to increase the computational time required during time steps, and is rarely incorporated in bulk schemes, but is similar to the approach of binned-spectral schemes. A second, more simple solution would be the inclusion of an autoconversion term between snow and graupel that is related to the riming rate and the relative amounts of each hydrometeor type. An autoconversion term from snow to graupel does not exist in Morrison, which leaves the population distribution entirely down to the partitioning of rime mass. However, an additional autoconversion term would be a crude parameterisation of rime fraction.

A third option does exist, namely to explicitly track rime fraction as a prognosed quantity, but this is not compatible with the framework posed by Morrison. Rather, this is a motivating factor for the transition to a different framework that considers rime fraction explicitly, or incorporates riming gradually to the precipitation field, as in P3 and ISHMAEL.

5.3 Relating Rimed Particle Growth to Riming Rate in P3 and ISHMAEL

Analysis of the rimed particle population and the total mass riming rate in Figure 5.1 showed that the ISHMAEL and P3 schemes produced vastly different precipitation types and quantities despite similar riming rates. For example, the total cloud droplet mass riming rate in both schemes were similar in size at all time steps, and larger overall in P3 when both cloud and rain droplet riming was considered. However, the total mass of rimed particles was much larger in ISHMAEL than P3. ISHMAEL's large, fully rimed graupel mass outweighed the partially rimed ice and, much smaller graupel quantity, simulated by P3. Here we investigate the discrepancy between riming rate and rimed particle production for these schemes, with the intention of better understanding or improving the novel frameworks that these schemes are built upon.

To determine the application of riming rates to rimed particle formation in ISHMAEL and P3, we must examine the variables that define the precipitation field in each scheme. This is a logical approach, as the development of graupel, or any other rimed particle, is simply shorthand for the development of the defining variables towards the criteria for graupel. First consider the precipitation variables and their respective scales per microphysics scheme shown in Figure 5.4. The characteristic variables used to partition graupel and rimed snow in P3 (Figure 5.4, left) are rime mass fraction F_r (0–1) and density ρ (kg m^3). Whereas in ISHMAEL, the characteristic variables of importance are the ice aspect ratio ϕ and density ρ (kg m^3). Unlike Morrison, in which rime mass is calculated and redistributed amongst fixed hydrometeor categories, the riming process in the P3 and ISHMAEL schemes evolves the characteristic variables of the precipitation distribution and the precipitation type is left

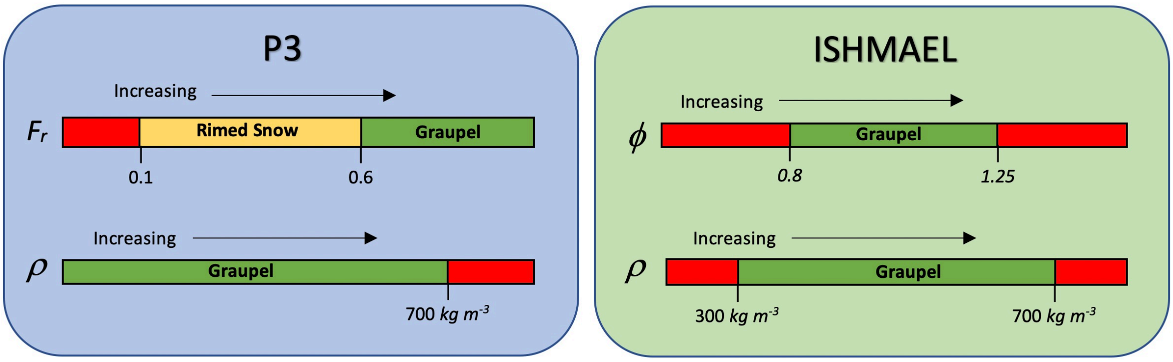

Figure 5.4. Visual aid for the development of rimed particles in the ISHMAEL and P3 schemes. The P3 scheme (left, blue) tracks the rime fraction F_r and density ρ (kg m^3) of the precipitation field. The ISHMAEL scheme (right) tracks the aspect ratio ϕ and density ρ (kg m^3) of the precipitation field. Precipitation type is indicated by the sub range of each variable; graupel (green) and rimed snow (yellow) are considered here. Note that graupel occurs when the criteria for both variables is met simultaneously

for the end user to diagnose in post-processing. The characteristic variables can therefore be visualised as moving on a sliding scale, which has sub ranges for each precipitation type. Figure 5.4 shows the respective sliding scales of each variable, and highlights the relevant sub range of a precipitation type with a colour. In both schemes, the graupel sub range of each variable is highlighted in green, and in P3 partially rimed ice is highlighted in yellow. sub ranges that are not relevant to the investigation of rimed ice are highlighted in red. Note that, for precipitation to be considered graupel, it must meet the graupel condition (green) across both characteristic variables.

We will conduct the following analysis on the basis of precipitation identification as in Figure 5.4 i.e. assuming that the production of graupel is related to the tendency of each characteristic variable along the sliding scale. The rate of progression along each scale is determined by the riming process of each scheme, and and so consideration of the sliding scale enables a direct comparison of the rimed particle production rate and the mass riming rate. Given the similarity of riming rates but dissimilarity of graupel production shown in Figure 5.1 for these schemes, it is likely that the rate of change of the characteristic variables in each scheme (i.e. their rate of progression along the sliding scale) is quite different.

It is useful to understand how each variable changes within a sub range of the scale (e.g. the graupel (green) sub range of the ϕ scale). For example, one can expect that crystals with a very prolate aspect ratio may have a different rime-rate, and therefore different aspect-ratio evolution, to very oblate crystals. Similar arguments can be made for sub ranges of other characteristic variables. Therefore, in this analysis the rate of change of characteristic variable is ordered according to its initial value and sub range. The variable evolution rates are shown in Figures 5.6 and 5.5.

To determine the evolution of the characteristic variables in each scheme during riming, the change in each variable before and after riming was calculated for all riming grid cells.

This indicates the typical progression of a variable along its scale as a consequence of riming. The typical change due to riming was then averaged throughout the domain and retrieved per time step in a time series. These are shown for the density variable in Figure 5.5 and the rime fraction and aspect ratio variables in Figure 5.6.

Figure 5.5 shows the rate of change $\Delta\rho$ of ice particle density ρ within riming cells for the P3 and ISHMAEL schemes. The rate of change produced in the ISHMAEL scheme is separated according to the ice category; ice-type 1 (planar-nucleated, blue), ice-type 2 (columnar-nucleated, red) and ice-type 3 (aggregated, black). Whereas P3, which has only one ice category, is shown in green. From Figure 5.4 we find that ISHMAEL density has three sub ranges; $\rho < 300$ kg m^3 indicating low density, snow-like crystals (Figure 5.5 column 1), $300 < \rho < 700$ kg m^3 indicating graupel-like density ranges or heavy riming (column 2), and $\rho > 700$ kg m^3 which indicates high density ice, such as cloud ice or hail (column 3). In the P3 scheme, low density ice is not required to be specified so there are two sub ranges of interest; $\rho < 700$ kg m^3 and $\rho > 700$ kg m^3, shown in columns 2 and 3, respectively.

Comparison of how quickly characteristic variables change during riming indicates how quickly the ISHMAEL and P3 models produce graupel by evolving particle qualities toward a graupel-like state. The density characteristic variable, shown in Figure 5.5, is useful to compare as it is evolved by both schemes and required to define graupel-like precipitation. For low density ice (column 1), the rate of change of density for ice undergoing riming is quite large. Ice-types 1 and 2 are found to increase by an average of 156 and 257 kg m^3 15 min^{-1} on average, indicating that riming increases the density more so in prolate crystals than oblate. Ice-type 3 (aggregated ice) has a much lower average change in density of 14.6 kg m^3 15 min^{-1} on average. The large difference in $\Delta\rho$ implies that aggregated ice is much more likely to retain its low density despite undergoing riming, an effect that likely originates from the larger typical size of aggregated ice that might requires comparatively more riming to impart density changes. Consequently, where riming does occur, it is likely to quickly densify smaller ices.

By comparison, high density ice (column 3) demonstrates a similarly large but negative typical rate of change of average 102 and 116 kg m^3 15 min^{-1} for ice-types 1 and 2 in ISHMAEL. In this case, aggregated ice experiences a much larger reduction in density due to riming, indicating that this ice-type naturally tends toward lower densities and is unlikely to be found at high densities if riming is present. Interestingly, the rate of change indicated by P3 is much larger than all three ISHMAEL ice-types, particularly during phase three, when the environment cooled, typical snow mass increased, and the density of rime mass was likely less than during the previous phases. On average the reduction in density applied to high density ice was -280 kg m^3 15 min^{-1}, the largest (absolute) rate of change observed in the density field for any sub range.

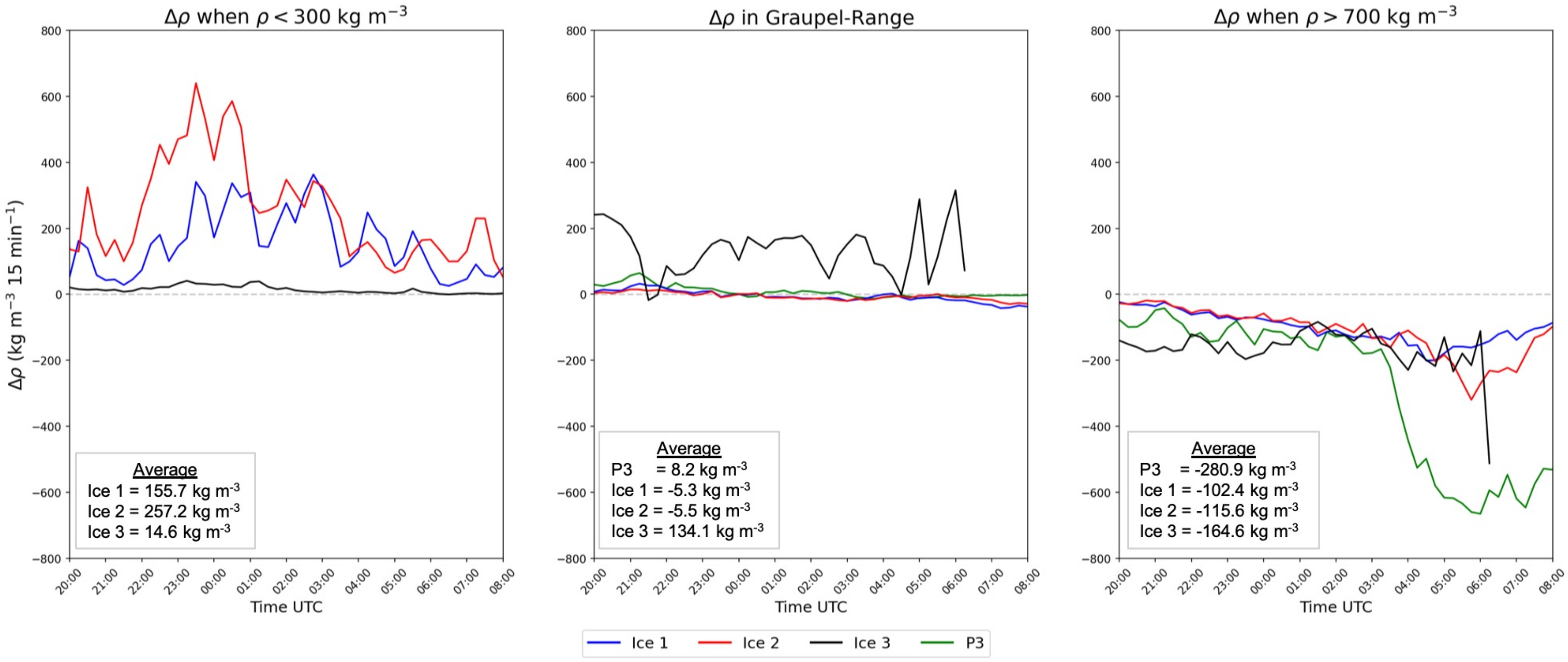

Figure 5.5. Time series of average change in characteristic density in the ISHMAEL and P3 microphysics schemes across all riming cells per time step. Average change is split between sub ranges of density (see Figure 5.4). Column 1: $\rho < 300$ kg m^3. Column 2: ρ in graupel range, Column 3: $\rho > 700$ kg m^3. Note that ISHMAEL ice-types are distinguished ice-type 1 (orange), ice-type 2 (green), ice-type 3 (red)

Examining the rate of change of density for precipitation that already meets the graupel criteria (column 2), we find that ISHMAEL ice-types 1 and 2, and P3 ice, show a very small (< 10 kg m^3 15 min^{-1}) average tendency. Given that the graupel density sub range can span up to 700 kg m^{-3}, the density range completion is approximately 1% per time step. This is not surprising, rather, it indicates that this density range is optimal for rimed ice, and therefore the effect of riming on graupel is simply to maintain a consistent density. However, the tendency of aggregated ice (ice 3) in ISHMAEL is large and positive, at 134 kg m^3 15 min^{-1}. This is a surprising result, as it appears that riming substantially increases the density of this ice-type beyond the expected graupel range.

The overall tendency of the density field is to decrease toward the graupel range, as expected, but Figure 5.5 indicates that there are substantial differences in the rate at which precipitation density decreases, both per precipitation type and microphysics scheme. In ISHMAEL rimed low density ice rapidly increases in density, but ice that is high density will undergo a comparatively slower reduction in density. So whilst riming does produce graupel, it is likely to remove the lowest density ices from the precipitation field first, effectively weighting the ice distribution toward more dense, and therefore faster falling precipitation. However, P3 has a typically greater reduction in density for its high density precipitation, that would lead to a comparatively lower density precipitation field than in ISHMAEL.

In the context of graupel production and riming rates, it is somewhat surprising that P3 should tend high density precipitation toward graupel more rapidly than ISHMAEL. This result implies that graupel production is more efficient in P3, but that was not apparent in Figure 5.1. However, the graupel criteria must be met by all characteristic variables simultaneously (i.e. both green graupel sub ranges in Figure 5.4. Now we turn our attention to the rate of change of the remaining variables, rime fraction F_r in P3 and aspect ratio ϕ in ISHMAEL.

Unlike the density characteristic variable, the rime mass fraction and aspect ratio are more difficult to compare as they are unique to their respective schemes, and have differing sub ranges. In ISHMAEL, graupel must have an approximately spherical aspect ratio between 0.8 and 1.2. This allows the graupel range to be approached from two directions that must both be considered. In P3, the graupel sub range of the rime fraction variable must exceed 0.6, so can only be approached from one direction, and must pass through two sub ranges to achieve a graupel-like state. Additionally, the range for each non-graupel sub range in P3 is definite, i.e. rime fraction spans 0 to 1 linearly, and cannot exceed either limit. Whereas, the ISHMAEL aspect ratio has a more ambiguous upper and lower limit that progresses logarithmically as crystals become very oblate or very prolate. The rate of change of each variable therefore must be considered in the context of these factors.

Figure 5.6 shows the rate of change of characteristic variables rime fraction F_r (green) and

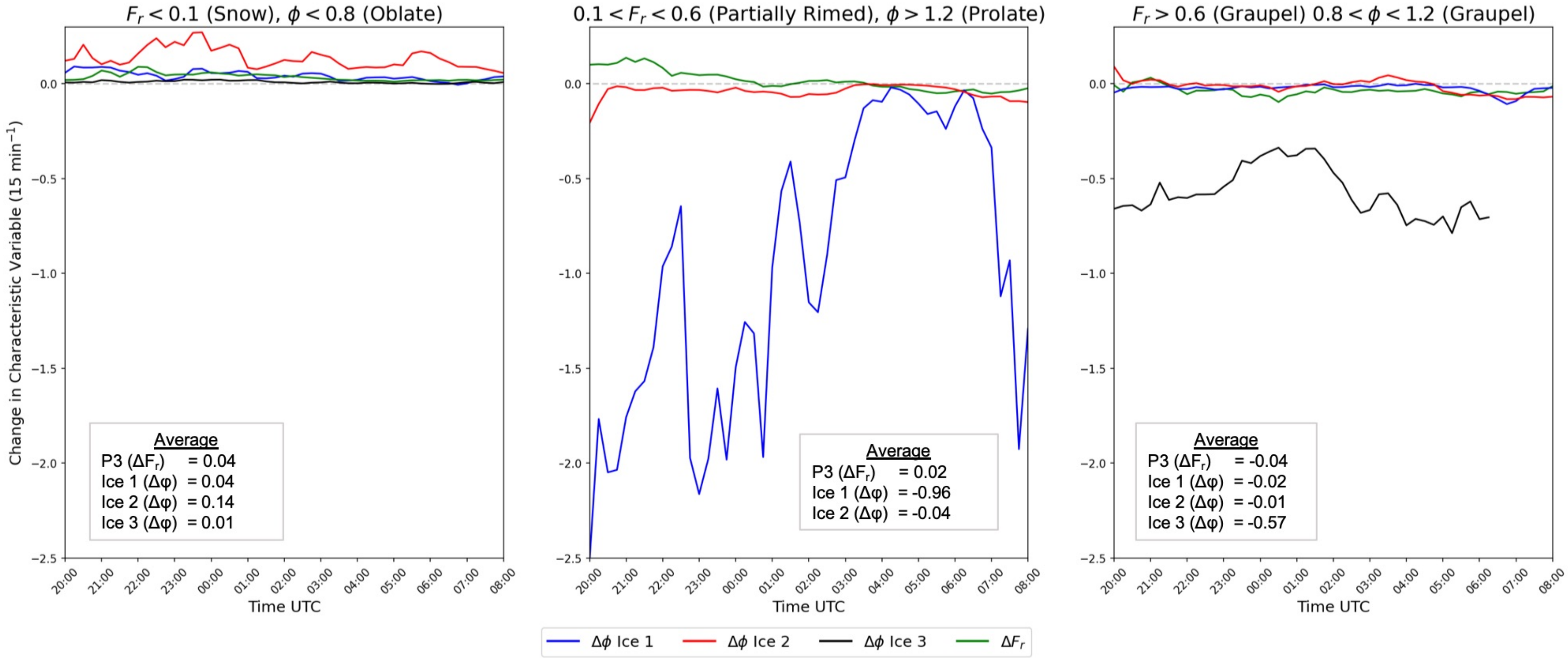

Figure 5.6. Time series of average change in characteristic variable: rime fraction F_r (P3, blue) and ϕ (ISHMAEL) within riming cells per time step. Average change is split between sub ranges of each characteristic variable (see Figure 5.4). Row 1: $F_r < 0.1$, $\phi > 1.2$. Row 2: $0.1 < F_r < 0.6$, $0.8 < \phi$. Row 3: $0.6 < F_r < 0.1$, $0.8 < \phi < 1.2$. Note that ISHMAEL ice-types are distinguished ice-type 1 (orange), ice-type 2 (green), ice-type 3 (red)

aspect ratio ϕ (multiple colours) in P3 and ISHMAEL, respectively. The rate of change of aspect ratio in ISHMAEL is distinguished between ice-types; ice 1 (planar-nucleated, blue), ice 2 (columnar-nucleated, red) and ice-type 3 (aggregated, black). The characteristic variables are plotted as a times series and separated according to their sub ranges (see Figure 5.4). Figure 5.6 column 1 shows ΔF_r when $F_r < 0.1$ (unrimed crystals) and $\Delta\phi$ when $\phi < 0.8$ (oblate crystals). Figure 5.6 column 2 shows ΔF_r when $0.1 < F_r < 0.6$ (partially rimed crystals) and $\Delta\phi$ when $\phi > 1.2$ (prolate crystals). Figure 5.6 column 3 shows ΔF_r and $\Delta\phi$ when each variable is in the graupel sub range, $F_r > 0.6$ (severe riming/graupel) and $0.8 < \phi < 1.2$ (prolate crystals).

Examination of Figure 5.6 shows that the graupel criteria is approached from below at a moderate rate of change that is similar in each scheme. In ISHMAEL, oblate crystals $\phi < 0.8$ (column 1) increase in aspect ratio by an average of 0.04 for ice-type 1 (blue) and 0.14 (red) for ice-type 2. This is comparable to the average rate of change of rime fraction for unrimed ice ($F_r < 0.1$) in P3 which is approximately 0.04. However, a considerably larger difference is found in the rate of change for particles within the remaining non-graupel sub category (column 2). In P3, the rime fraction of partially rimed ice grows half as fast as unrimed ice during riming, with an average rate of change of 0.02. Whereas, prolate crystals in the ISHMAEL scheme decrease their aspect ratio much more substantially, by an average of almost -1 per time step. This is almost 50 times larger than the average in P3, though care must be taken with direct comparison as the prolate aspect ratio range grows non-linearly.

Examination of the rate of change of these variables within the graupel sub range provides a very interesting result, that the rate of change in this region is typically negative, but that more importantly, in P3 the absolute value of the average tendency is larger for ice leaving the graupel sub range (-0.04) than it is entering this sub range (+0.02). This implies that the net tendency of rime fraction in riming cells is actually towards partially rimed snow, and not toward graupel. By comparison, the ISHMAEL tendency of ϕ is on average -0.02 and -0.01 for ice-types 1 and 2 respectively, which indicate a net tendency toward the graupel sub range.

To discuss these findings, the average rate of change is shown in the context of each variable sub range shown in Figure 5.7 for P3 (left) and ISHMAEL (right). For each characteristic variable F_r (P3), ϕ (ISHMAEL), ρ (Both), the appropriate precipitation sub range is indicated above the sliding scale with a short description and a black arrow, with the exception of the graupel sub range, which is indicated by a red arrow. The average rate of change of each variable is shown above the sub range with which it is associated. In addition, the average *residency time* T_R is calculated for each variable sub range. For example, consider the average rate of change of density for a sub range of length L is:

$$\frac{\Delta\rho}{\Delta t} = \frac{\rho_2 - \rho_1}{t}[\mathrm{kg\ m^{-3}t^{-1}}]$$

where t is the unit of the model history interval. Then a residency time can be determined from the rate of change of ρ and the total length of the sub range:

$$T_R = \frac{L}{\Delta\rho}\left[\frac{\mathrm{kg\ m^{-3}t}}{\mathrm{kg\ m^{-3}}}\right]$$

The residency time is therefore calculated from the average rate (15 min^{-1}) and is shown below the respective sub range in Figure 5.6. This quantity is analogous to the average time required for ice in the sub range to transit the complete length of the sub range. For example, unrimed ice that is being rimed will require 37.5 minutes to transition from a rime fraction of 0 to a rime fraction of 0.1 at an average rate of $\Delta F_r = 0.04$ 15 min^{-1}.

As the average rates of change of each variable were discussed in Figures 5.5 and 5.6, here we will discuss the nature of the average tendencies in the broader context of each schemes precipitation definitions. Figure 5.6 shows that, during riming, the evolution of both characteristic variables in ISHMAEL occurs more quickly than both variables in P3. This was, at first, not apparent for the density field, which progressed much more quickly in P3's high density ice, at a rate of -280 kg m^3 15 min^{-1}, almost three times more quickly than the density in ISHMAEL for the high density sub range of equivalent length. An additional, prohibitive factor in ISHMAEL was that a second density sub range for low density ice was present. This further restricted the span of the graupel sub range, and required the riming process to increase the density of low density ice in order for it to be classified as graupel. This low density sub range is not present in P3 as a high rime fraction supersedes the ice particle density during classification. Thus, precipitation in P3 is more likely to be found within the graupel sub range, both by virtue of the broader graupel sub range at low density, but also by the quicker rate of change in density that takes place for high density particles during riming in the P3 scheme.

The differing tendency of density in both schemes is notable for graupel and the wider precipitation field that encounters riming. However, recall that both variables must be simultaneously within the graupel sub range for precipitation to be defined as graupel. Therefore, the production of graupel is actually limited by the slowest-changing characteristic variable, which restricts the graupel sub range from being reached.

The net tendencies of the characteristic variables ϕ and F_r were much smaller in size (with respect to their proportion of their respective sub range length) than was observed with density. Therefore, it was actually the evolution of ϕ and F_r that determined graupel production in each scheme. For ISHMAEL the average residency time of prolate ices was only 28 minutes, based on an upper limit (observed in this simulation) of $\phi = 3$, and so prolate ices that encountered riming were very likely to enter the graupel sub range. Similarly, unrimed ice in P3 progressed relatively quickly into the rimed-ice sub range, with a residency time of only 37.5 minutes. Thus, these ice scenarios were not limiting factors to the graupel tendency. Instead, oblate crystals ($\phi < 0.8$) in ISHMAEL, and partially rimed ice ($0.1 < F_r < 0.6$) in P3 exhibited the smallest rate of change, and longest residency times per scheme so were therefore the most likely ice-type to resist the effect of riming and avoid the graupel sub range. The rate of change of $\phi < 0.8$ in ISHMAEL was double the rate of change of $01 < F_r < 0.6$ for a similar sub range length and therefore the residency time of ice in the partially rimed sub range was twice as large as the residency time of oblate crystals. In a constant riming environment, the evolution toward graupel would occur more quickly in ISHMAEL and therefore more graupel is produced at a given time. Note also, that net tendency of rimed ice in the ISHMAEL scheme is toward the graupel category, but for Morrison, the net tendency is actually towards the partially rimed mass sub range. This is an unusual feature, but it might possibly derive from the hard upper limit that rime fraction implements. Once rime fraction is equal to 1, then graupel may only lose its rime fraction, and this may contribute to a net negative tendency in the graupel sub range.

The faster development of graupel in the ISHMAEL scheme is likely to be exacerbated by the differing sub range criteria in each scheme. For example, all ice begins as unrimed in P3, and therefore ice must traverse the entire sub range of unrimed, and partially rimed ice, in order to become graupel. Whereas, in the ISHMAEL scheme, ice is nucleated at both prolate and oblate ratios that need not be at the extreme ends of the sub range.

Related to this is the integration of the characteristic variable to other process outside of the riming process. For example, the ISHMAEL aspect ratio is integrated to most microphysical processes, which enables it to potentially evolve toward more spherical aspect ratios before riming is even a factor. For example, consider a hail particle that has developed in a region of zero riming. In ISHMAEL, the hail particle is near spherical and need only reduce its density during riming (a relatively fast variable evolution) to be considered graupel. Whereas in P3, rime fraction is explicitly determined by the riming process, and cannot be aided by other processes before riming occurs. This may imply that P3 has an advantage when it comes to accurately predicting graupel that has explicitly derived from riming alone. However, in this case it is evident that the differing prognostic variables tracked during particle evolution have a significant impact on the amount of graupel produced throughout the domain.

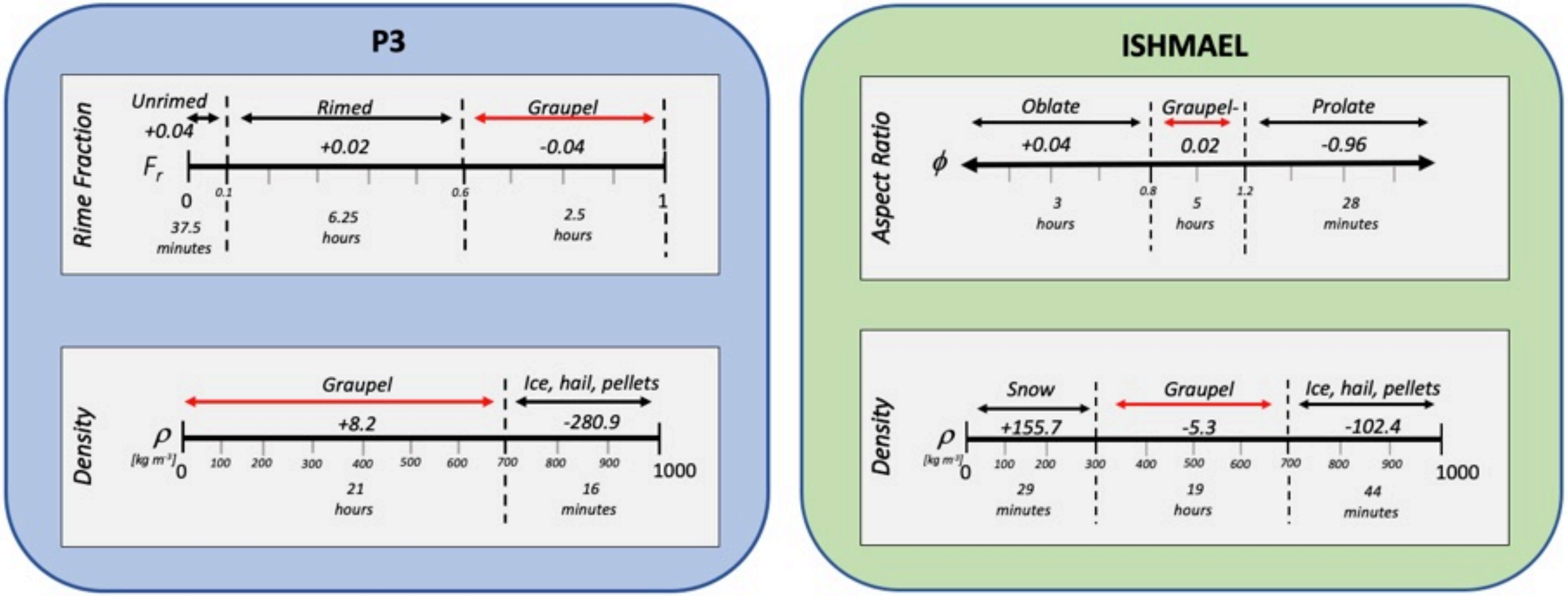
P3
Rime Fraction
Unrimed
+0.04
Rimed
+0.02
Graupel
-0.04
F_r
0
0.1
0.6
1
37.5 minutes
6.25 hours
2.5 hours
Density
Graupel
+8.2
Ice, hail, pellets
-280.9
ρ [kg m⁻³]
0
100
200
300
400
500
600
700
800
900
1000
21 hours
16 minutes
ISHMAEL
Aspect Ratio
Oblate
+0.04
Graupel-
0.02
Prolate
-0.96
ϕ
0.8
1.2
3 hours
5 hours
28 minutes
Density
Snow
+155.7
Graupel
-5.3
Ice, hail, pellets
-102.4
ρ [kg m⁻³]
0
100
200
300
400
500
600
700
800
900
1000
29 minutes
19 hours
44 minutes

Figure 5.7. Rate of change of characteristic variables F_r, ρ in the P3 scheme (left) and ϕ, ρ in the ISHMAEL scheme (right). Each characteristic variable is depicted as a scale of possible values (increasing from left to right), wherein sub ranges of each scale determine a precipitation type, denoted above the sub range and indicated by a double-headed arrow. The rate of change of each characteristic variable for particles within a sub range, is shown above the respective sub range. The residency time proportional to the inverse of the rate of change is given below the respective sub range.

Chapter 6

Reflectivity Simulated by Three Microphysics Schemes

6.1 Comparison of Simulated Reflectivity to Observations

The 8th–9th February storm was of particular interest to the meteorological community due to its unusually high reflectivity (horizontal reflectivity factor Z_H) that was embedded within the storm's associated snowband and associated with mixed-phase processes. Both ISHMAEL and P3 aim to improve mixed-phase processes but, as discussed in the Chapter 4, these schemes demonstrated considerable variability in the prediction of mixed-phase processes. It is of interest then to investigate the radar reflectivity predicted by these schemes in this case.

Here we seek to understand whether these microphysics schemes can emulate the spatial distribution and extreme maximum of reflectivity, and if so, with what precipitation are very large radar reflectivity values associated with? In the remainder of this chapter the parameterisation of reflectivity in each scheme will be examined and discussed in the context of mixed-phase precipitation. Note that the predicted radar reflectivity is a calculated variable in the ISHMAEL and P3 schemes but not in Morrison, for which the wrf-python `getvar` routine was utilised in post-processing (Ladwig 2017).

6.1.1 Observed and Simulated Spatial Distribution of Radar Reflectivity

Plan position indicators (PPI) of dual-polarisation radar reflectivity taken at NWS KOKX were analysed across Long Island by Ganetis and Colle (2015) and are shown in Figure 6.1 row 4, where columns 1–3 represent phases 1–3, respectively. To produce comparable plots for the scheme-predicted reflectivity, only a subset of the high-resolution domain data within a 1500 m near-surface layer was examined, which is in accordance with analysis by Ganetis and Colle (2015) and Griffin et al. (2014) who observed that the largest reflectivity factor was isolated within a shallow, 1.5 km deep layer. The resulting three-dimensional subset was condensed into a contour plot by computing the maximum reflectivity of each vertical column in the latitude-longitude grid. This method ensures that isolated pockets of high reflectivity are not lost to smoothing as can occur during interpolation. This predicted reflectivity is shown in Figure 6.1 rows 1–3 for the ISHMAEL, Morrison and P3 microphysics schemes, respectively. Columns 1–3 show snapshots of reflectivity at times 2130 UTC, 0030 UTC and 0345 UTC, respectively, which approximate the times of the radar observations pictured in row 4; 2129 UTC, 0042 UTC and 0340 UTC per column respectively.

In phase one (Figure 6.1 column 1, 2129 UTC), observations (row 4) show that elevated (> 30 dBZ) radar reflectivity was observed within multiple bands positioned approximately along the southern coast of Long Island and extending south into the Atlantic. High (> 40 dBZ) reflectivity was embedded centrally within the elevated reflectivity banded structure. The intensity of reflectivity was greatest over the approximate centre of Long Island's southern coast at this time where a maximum value of approximately 55 dBZ was observed. By 0029 UTC of phase two (Figure 6.1, column 2) the observed high reflectivity banded structure had tightened and reoriented into two sectors, the first was positioned north-south between the Atlantic and the northern coast of Long Island, covering the central third of Long Island and the second situated over Connecticut, with orientation close to parallel with the coast of the U.S. mainland. The band reflectivity exceeded 30 dBZ and was approximately 45 dBZ toward the interior, with some localised areas exceeding 55 dBZ. The onset of phase three was notable for the sudden reduction of reflectivity from more than 40 dBZ before 0200 UTC to 30 dBZ within an hour. Observations shown at 0340 UTC in (Figure 6.1, column 3 row 4) indicate that reflectivity returned to a uniform coverage of 20–30 dBZ across Long Island and the U.S. mainland. Whereas south of Long Island reflectivity dropped below 15 dBZ.

During phase one, the ISHMAEL scheme (Figure 6.1 column 1, row 1) simulated an elevated (> 30 dBZ) reflectivity band positioned south of Long Island, that was appropriately north-east oriented but that extended too far south-west. Similarly, the in-band maxima of 41 dBZ was also situated south of observations and underestimated the peak magnitude considerably. During phase two, the ISHMAEL simulated band (Figure 6.1, column 2 row 1) continued to underestimate the observed reflectivity over Long Island by 10–15 dBZ, and retained a distribution that was comparatively too narrow. The elevated reflectivity region had reoriented as in observations, but covered the smallest total area of all schemes, and failed to reach much of the Connecticut coastline. Indeed, comparison of the > 25 dBZ region shows a closer distribution to the observations. By phase three (Figure 6.1, column 3 row 1), the simulated reflectivity in ISHMAEL had returned to the sub 25 dBZ background level over the entirety of the domain, with small areas exceeding 25 dBZ but no greater

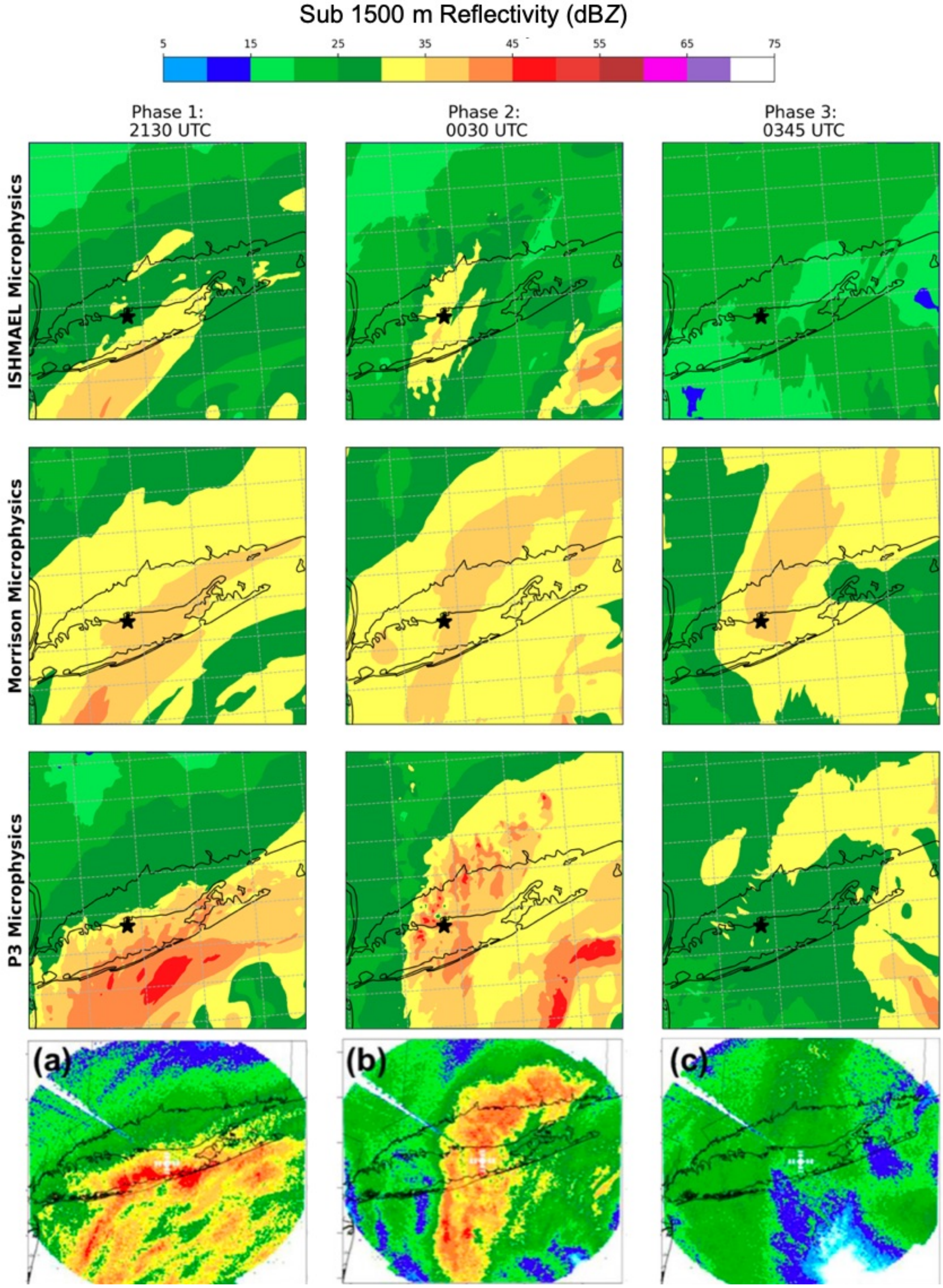
Sub 1500 m Reflectivity (dBZ)
5
15
25
35
45
55
65
75
Phase 1:
2130 UTC
Phase 2:
0030 UTC
Phase 3:
0345 UTC
ISHMAEL Microphysics
Morrison Microphysics
P3 Microphysics
(a)
(b)
(c)

Figure 6.1. Contours of simulated maximum reflectivity factor Z_H (dBZ) at times 2130 UTC (column 1), 0045 UTC (column 2), 0345 UTC (column 3), for microphysics schemes ISHMAEL (row 1), Morrison (row 2) and P3 (row 3) up to a maximum elevation of 1.5 km (replicating the observed shallow layer). Observations of KOKX radar reflectivity (dBZ) adapted from Ganetis and Colle (2015) (see their Figure 4) shown in row 4 for comparison at times: 2129 UTC (column 1), 0042 UTC (column 2), 0340 UTC (column 3). Contours shaded according to scale.

than 30 dBZ. This brought ISHMAEL closely in line with observations, but represented a phase-on-phase reduction of only 10–15 dBZ compared to the > 20 dBZ reduction that was observed.

The reflectivity simulated by Morrison (Figure 6.1 column 1, row 2) exhibited a similar range of values to ISHMAEL, but the spatial distribution was quite different. During phase one, Morrison simulated an elevated (> 30 dBZ) band that covered the largest total area of all schemes, extending from below Long Island's south coast to as far north as the U.S. mainland. This elevated region was similar in spatial extent to that of the large-scale snowband found in the observations that exceed 25 dBZ, possibly indicating that this elevated band was closely related to snow production in the Morrison scheme. More closely resembling ISHMAEL was an interior high (> 35 dBZ) reflectivity sub band that had similar area and orientation to the ISHMAEL > 30 dBZ band, but no banded substructure was apparent. The maximum reflectivity at this time was predicted south west of Long Island that did not exceed 50 dBZ nor adequately capture the observed location of very high reflectivity.

During phase two, Morrison (Figure 6.1 column 2, row 2) continued to predict the largest total area of elevated reflectivity of all schemes, closely resembling the broad scale snowband of the observations but overestimating its reflectivity by 5–10 dBZ. A centrally embedded, high (> 35 dBZ) band was accurately situated over central and southern Long Island, and exhibited the expected change in orientation north of Long Island but peak reflectivity reached only 40 dBZ, which was a reduction over the phase one maximum. In phase three, Morrison (Figure 6.1 column 3, row 2) was the least responsive of all schemes to the observed reduction in reflectivity. Morrison continued to simulate a north-south oriented band of reflectivity in excess of 35 dBZ, representing a negligible decrease on the maximum of the previous phase, demonstrating poor sensitivity to the underlying factors that caused high reflectivity in this case.

P3 (Figure 6.1 column 1, row 3) provided the most similar band to the observations, both in distribution and magnitude. An elevated (> 30 dBZ) band of reflectivity was produced over Long Island that extended further east than observed but was confined to a more realistic area south of the mainland than in Morrison, and was oriented more closely to Long Island south coast than either of the other two schemes. Very high (> 45 dBZ) reflectivity was found centrally in a sub band of high reflectivity close to the centre of Long Island's southern coast, slightly south of observations. Interestingly, P3 exhibited more local variation in the sub 1.5 km layer than either of the other schemes at this time, providing an imperfect but closest match to observations of all schemes tested.

In phase two (Figure 6.1 column 2, row 3) reproduced the most accurate distribution of the high (> 35 dBZ) reflectivity region, effectively capturing the correct position of the band over Long Island, and also over the U.S. coast. Values within the band exceeded 50 dBZ

in localised pockets as observed, but were generally less widespread than in observations. Interestingly, P3 also produced a very high reflectivity region southeast of Long Island as in ISHMAEL, indicating that both schemes recognise this area similarly to each other, and dissimilarly to Morrison.

By phase three (Figure 6.1 column 3, row 3), the P3 scheme which had produced the greatest reflectivity over central Long Island in the previous phase, reduced its reflectivity over Long Island to a sub 30 dBZ uniform field. This represented up to a 25 dBZ reduction that was in keeping with the observation of rapid drop in peak reflectivity between these phases. However, high reflectivity in excess of 40 dBZ continued to be simulated southeast of Long Island and a region of elevated reflectivity continued to persist east of Long Island at this time.

Overall, the P3 scheme provided the closest prediction of the observed reflectivity across all three phases. The spatial distribution, location and maxima were most representative, and the observed drop in reflectivity during phase three was appropriate in magnitude and spatial extent. ISHMAEL and Morrison were somewhat opposites, the former produced elevated reflectivity over small areas in the correct locations whilst the latter produced typically larger reflectivity maxima that were distributed far more broadly.

6.1.2 Observed and Simulated Vertical Distribution of Radar Reflectivity

It is important to note that the conclusions derived from Figure 6.1 are limited by the spatial extent that was examined. Though reasonably motivated, the top down contours of a 1.5 km surface layer provide only a snapshot of the vertical reflectivity structure. The vertical distribution of radar reflectivity products are important for forecasters and researchers, who depend on them to determine the precipitation type aloft and the microphysical mechanisms that occurred in their vicinity. In this case, the vertical distribution has revealed the location and descent of the melting layer, as well as the narrow height of the shallow layer that encapsulated the highest observed reflectivity (Griffin et al. 2014). To improve confidence in the use of these schemes for forecasters, it is important to briefly examine the distribution of the observed and simulated reflectivity in this case.

The vertical cross sections described in Ganetis and Colle (2015) (their Figure 5) occur at the same times (2129 UTC, 0042 UTC, 0340 UTC) as the top-down contours adapted in Figure 6.1 and so are a suitable source of comparison for the vertical cross section of reflectivity simulated by each scheme. The cross section of simulated reflectivity was chosen to match that of the observational data adapted from Ganetis and Colle (2015). The simulated data was extracted by latitudinal-longitudinal interpolation along the line shown in Figure 6.2 (right) which mirrors the cross sectional line of observations shown in Figure 6.2

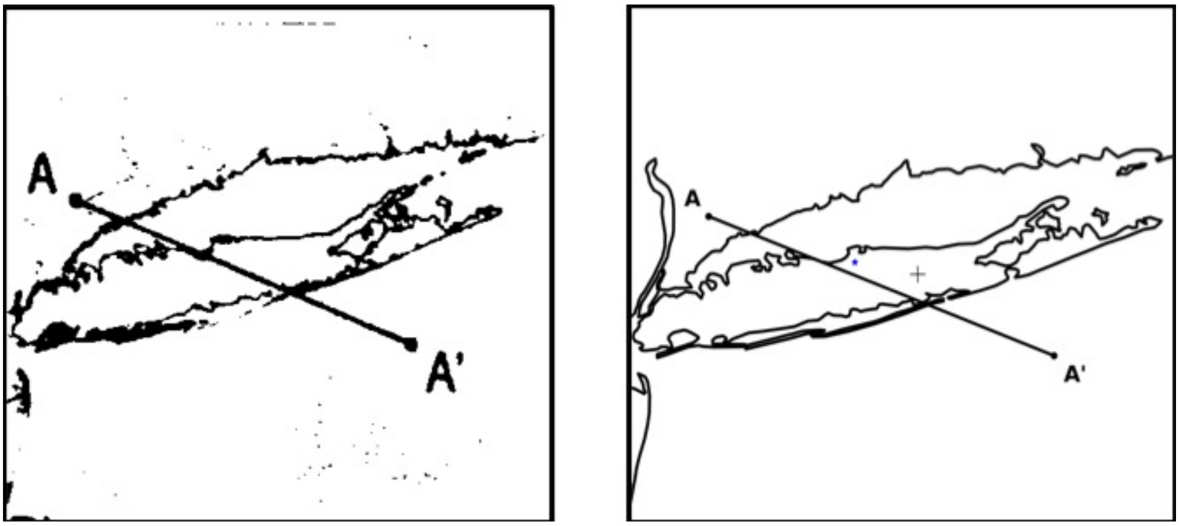

Figure 6.2. Latitudinal-Longitudinal position of vertical cross section chosen for horizontal interpolation. Left: position adapted from Ganetis and Colle (2015) (see their Figure 4 Panel i) for their vertical interpolation of observed radar reflectivity shown in Figure 6.3 (column 4). Right: position of horizontal interpolation used for simulated microphysics schemes shown in Figure 6.3 rows 1–3. Position of KOKX radar shown by black plus $+$ marker. Position of Stony Brook University shown by blue dot ·

(left). Vertical interpolation was not used so as to avoid data smoothing over localised cells of high reflectivity, instead the data retains the original vertical levels output by the WRF model. By the same logic, caution should be applied to the vertical cross section due to its horizontal interpolation; however, we are satisfied that this data is representative of the vertical structure, as will be shown in later analysis of the in-column maxima.

Figure 6.3 compares the vertical cross section of reflectivity for ISHMAEL (row 1), P3 (row 2) and Morrison (row 3) to the observed reflectivity (row 4) adapted from Ganetis and Colle (2015). At 2129 UTC, observations (Figure 6.3, column 1 row 4) show that north of Long Island, where primarily snow aggregates were observed, reflectivity reached a maximum ($\sim$30 dBZ) at the surface and decreased with increasing altitude in a step-wise fashion of approximately 5–10 dBZ per km. Aloft of Stony Brook (northern Long Island), the maximum reflectivity at the surface exceeded 30 dBZ, and just south of Long Island a surface level maximum of approximately 55 dBZ was apparent, in corroboration with the maximum observed along the Long Island southern coastline in Figure 6.1 (column 1, row 4). High (> 35 dBZ) reflectivity was confined to the vertical at or below 1.5 km south or Long Island, and the in-band maxima were confined vertically to the surface level (< 1 km).

The observed reflectivity in the vertical remained similarly distributed in phase two (Figure 6.3 column 2 row 4) but some key differences were apparent. For example, south and north of SBNY a 1 km deep depression of the reflectivity field was present whilst the surface directly over SBNY increased by $\sim$5 dBZ and between 1–2 km had increased by 10 dBZ. This is in keeping with the reorientation of the band over central Long Island by this time and coincides with reports of increased riming and graupel production at this location.

In the final phase, the change in reflectivity was a more drastic shift in magnitude than in the previous phases. Previously high (> 40 dBZ) dissipated, and elevated reflectivity (> 25 dBZ) was confined to a shallow (< 2 km) surface layer to the northwest of SBNY. Reflectivity was absent above 4 km in the northwest above 3.5 km, and this feature is present as low as 1.5 km in the southeastern portion of the cross section.

The simulated vertical distribution in Figure 6.3 rows 1–3 demonstrated considerable differences with the choice of microphysics scheme. Some features of the distribution were consistently captured amongst schemes, namely the reduction in the northern most and southern most reflectivity during phase two, which reflected the reorientation of the band at this time. All schemes also overestimated the vertical height, with elevated (> 15 dBZ) reflectivity extending several kilometres too high for all phases. However, the ISHMAEL and P3 schemes provided a more physically reasonable prediction of the spatial distribution overall.

In ISHMAEL, the phase one simulated reflectivity maximum was 10–15 dBZ less than observed, but this maximum was appropriately confined to the 1.5 km layer. However, by phase two the ISHMAEL elevated (> 30 dBZ) reflectivity region had reduced in horizontal and vertical extent, confined to a shallow 1 km deep surface layer. Reflectivity in excess of 25 dBZ was approximately 1.5 km lower than observed, and reflectivity in excess of 15 dBZ extended 2 km higher than expected. During phase two, ISHMAEL simulated the split in reflectivity aloft of SBNY and by phase three, a reduction of the order 5–15 dBZ was apparent throughout the vertical northwest of SBNY, which is similar to observations.

In comparison to ISHMAEL, both Morrison and P3 had a vertical distribution of elevated (> 30 dBZ) reflectivity that occurred far above the observed altitude, as high as 5 km greater than observed in both schemes for phase one. Despite this exaggerated reflectivity aloft, P3 did achieve the largest surface level reflectivity maximum of all schemes, exceeding 40 dBZ in a sub 1.5 km layer southwest of Stony Brook which indicates that, as in Figure 6.1, P3 was the most effective scheme at capturing the abnormally high reflectivity in this region. By phase two, P3 predicted a reduction in the extent of the surface level reflectivity, but crucially retained the surface level maximum in excess of 40 dBZ. Good agreement of the distribution at the surface is apparent, however, the distribution of elevated (> 30 dBZ) reflectivity is too high across the entirety of Long Island. By phase three, P3 had displayed a decrease in reflectivity of approximately 5–10 dBZ in the sub 3 km layer, which is similar to that observed and predicted in the ISHMAEL scheme.

Of all schemes, Morrison produced the least accurate spatial distribution. During phase one, a broad region of elevated reflectivity that spanned too far north-east and achieved a high (> 35 dBZ) maximum that was both significantly ($\sim$15 dBZ) less than observed at the surface and, extended significantly higher ($\sim$3 km) than was observed aloft of Long Island's south coast during phases one and two. In addition, to poor spatial coverage, the surface level reflectivity maximum at SBNY even decreased during phase two. The most clear evidence for a lack of sensitivity to the root cause of reflectivity was evidenced in phase three when Morrison produced the smallest reduction in reflectivity and therefore had the least agreement with the observed reflectivity factor of all schemes. In fact, over SBNY reflectivity remained above 35 dBZ in a sub 1 km shallow layer, which was more similar to observations during the mixed-phase period.

From the analysis of the vertical distribution of reflectivity shown in Figure 6.3 it is evident that the reflectivity field is overestimated at high elevations, but underestimated at the surface by all schemes. This characterisation is corroborated in the horizontal by Figure 6.1, which shows overestimation of the reflectivity factor across broad areas of the domain yet underestimation of the peak reflectivity factor in the location that it was observed. The simulated reflectivity fields do not produce the sharp gradients across very small, localised areas that were observed in reality. Instead, the predicted reflectivity field appears to lack an integral relationship with precipitation that is evident in reality.

Of these schemes, Morrison provides the most extreme example of broad-scale, elevated radar reflectivity. We shall seek to understand why Morrison is inclined to produce a more uniform field than other schemes, and why these consistent reflectivity values occur over such large swathes of the domain in this case. ISHMAEL and P3 demonstrated more localised variability than Morrison, for example producing small, embedded areas of elevated reflectivity within the 2 km shallow vertical layer. However, the difference in magnitude of simulated reflectivity between these schemes was stark. P3 reproduced the small centres of embedded reflectivity within 10 dBZ of those observed, whereas ISHMAEL was often 20 dBZ less than expected in these pockets. We shall explore where these differences have arisen in each scheme and why.

6.1.3 Simulated and Observed Reflectivity Maxima

A key shortcoming of each scheme was the failure to predict the observed reflectivity maxima of the embedded bands whilst overestimating the middling background reflectivity of the surrounding snow band. Here we might seek to understand which conditions are required to produce the expected reflectivity values in each scheme, and compare them to the simulated environment, but first we seek to overcome some limitations to our analysis so far.

One limitation of the comparison shown in Figure 6.1 was that the simulated data was confined to the lowest 1.5 km of the domain where observations indicated the greatest reflectivity values were present. However, analysis of vertical cross sections in Figure 6.3 indicate

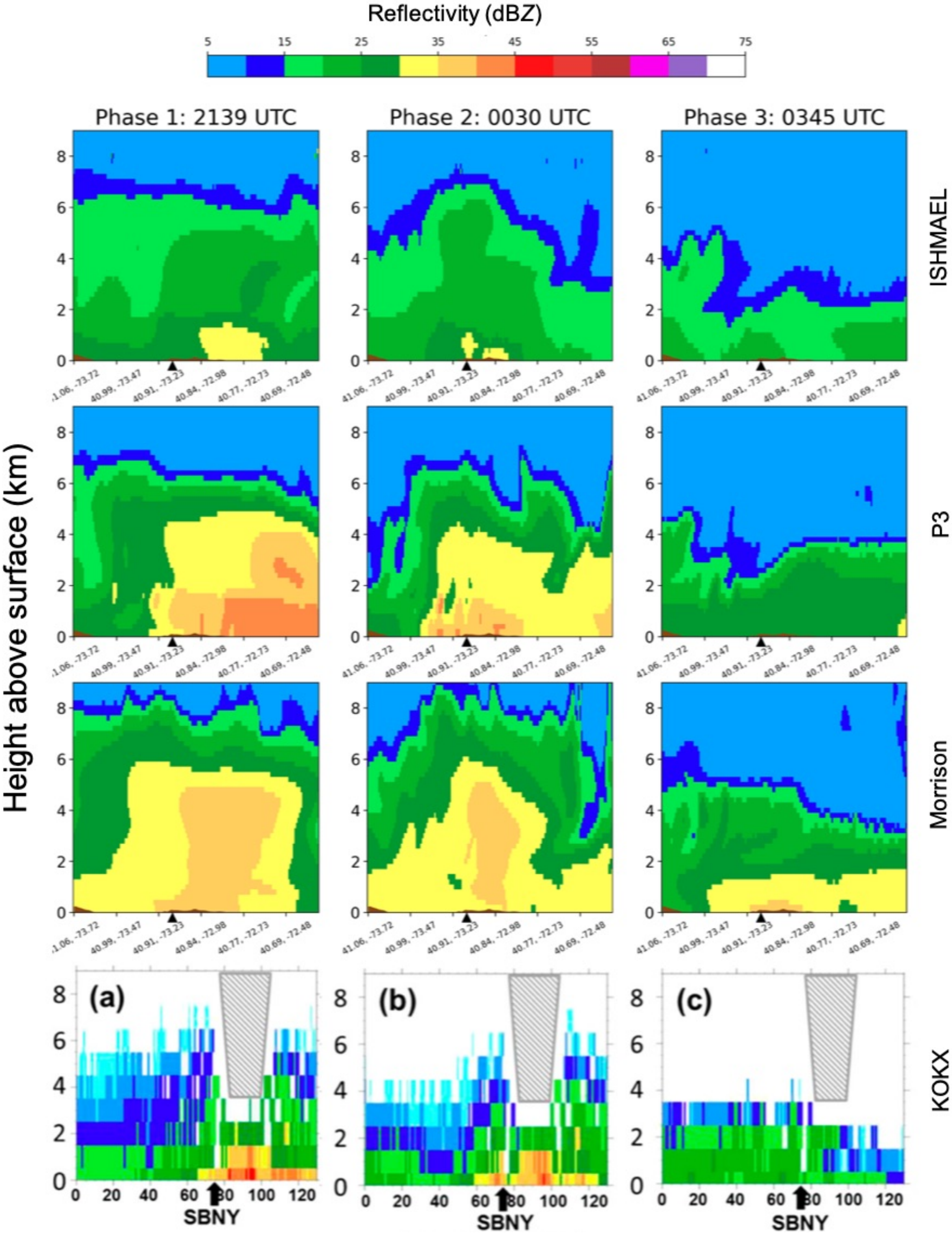

Figure 6.3. Contours of simulated reflectivity factor Z_H (dBZ) in vertical cross section along line A to A' (see Figure 6.2) at times 2130 UTC (column 1), 0045 UTC (column 2), 0345 UTC (column 3), for microphysics schemes ISHMAEL (row 1), P3 (row 2) and Morrison (row 3). Observations of KOKX radar reflectivity (dBZ) adapted from Ganetis and Colle (2015) (see their Figure 5) shown in row 4 for comparison at times: 2129 UTC (column 1), 0042 UTC (column 2), 0340 UTC (column 3). Contours shaded according to scale. Hatched area indicates radar cone of silence. Position of SBNY along the cross section is indicated by black arrow below the x-axis.

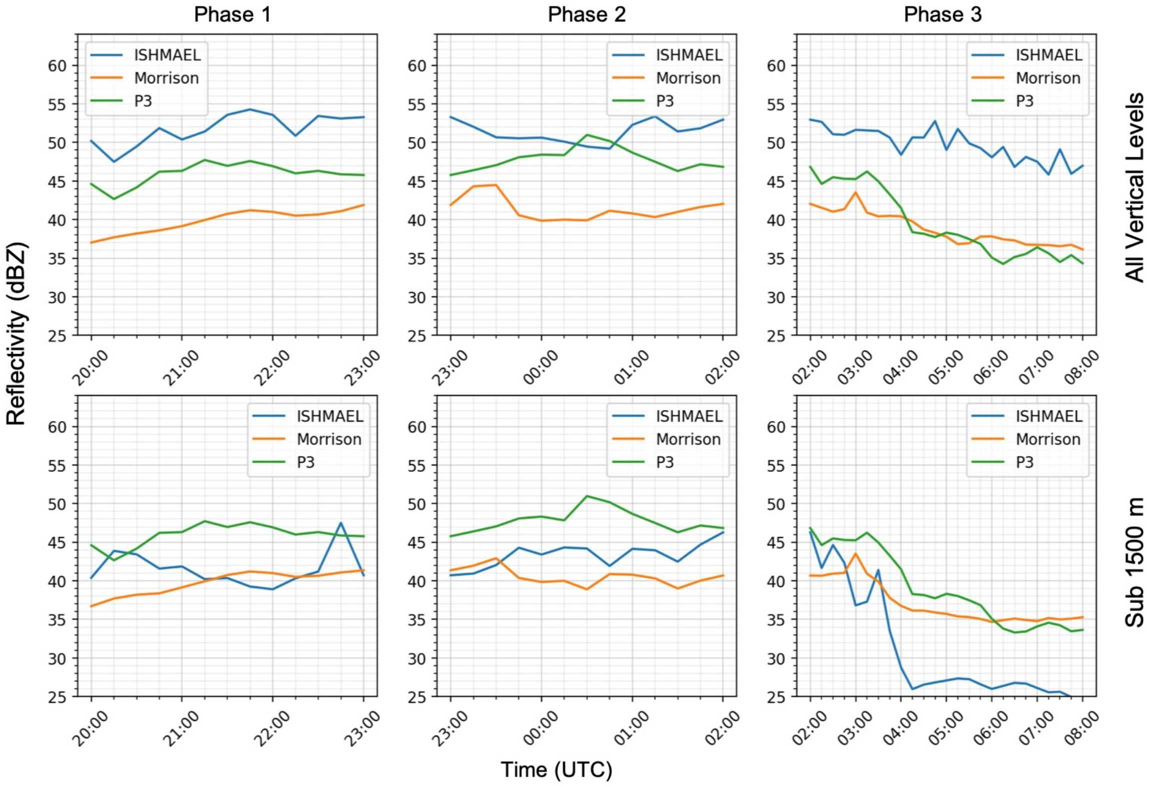

Figure 6.4. Time series of the maximum simulated reflectivity (dBZ) per microphysics scheme: ISHMAEL (blue), Morrison (orange), and P3 (green). Time series is separated into three columns for phases one, two, and three, respectively. Row 1: maximum reflectivity is determined throughout all vertical levels of domain 3. Row 2: maximum reflectivity determined from within a 1.5 km surface layer only.

that the microphysics schemes generally failed to simulate the low level reflectivity maxima but did overestimate the reflectivity aloft. A similar limitation is present in our analysis of the vertical cross section, which considers only a narrow line in latitudinal-longitudinal space at one point in time, when analysis of the top-down contoured reflectivity shows that the reflectivity maximum did not necessarily occur along this line. Thus, whilst we have evaluated the schemes in these narrow areas we now wish to seek a broader view of their reflectivity ranges throughout all phases and vertical levels of the domain.

Figure 6.4 provides a time series of the maximum reflectivity simulated per scheme (see Legend) across phases one, two and three (columns one, two and three, respectively). Reflectivity maxima were derived from domain three, which encompasses Long Island and the north-east U.S. coast as pictured in Figure 6.1. Row one shows reflectivity maxima as determined from the entire vertical extent of the domain, whereas row two shows reflectivity maxima for only the shallow, 1.5 km deep layer previously discussed.

Comparison of the maximum reflectivity above and below the shallow layer provides a new understanding of the reflectivity simulated in each scheme. The most notable feature being that ISHMAEL, which was shown to simulate the lowest magnitude reflectivity in general, consistently produced the highest reflectivity maxima of all schemes when the entire vertical and spatial extent is considered. Indeed, for all phases the maximum reflectivity exhibited throughout the domain is quite consistent per scheme, with ISHMAEL exhibiting a typical increase of 2–4 dBZ higher reflectivity than in P3, and P3 exhibiting a 2–10 dBZ increase over Morrison for phases one and two. Notably, at 0030 UTC, P3 reached its highest total reflectivity of all phases of 51 dBZ which coincides with observations of a peak observed reflectivity of 57.5 dBZ at 0042 UTC (Ganetis and Colle 2015).

Analysis of maximum reflectivity within the sub 1.5 km layer shows that, while P3 typically produced the greatest reflectivity across all three phases, the difference in magnitude between P3 and ISHMAEL was not as severe as implied by the earlier comparisons to observations, with P3 producing reflectivity typically 1–6 dBZ greater than ISHMAEL, far smaller than the 10–15 dBZ difference assumed in Figures 6.1 and 6.3. In fact, ISHMAEL simulates the greatest reflectivity of all schemes during the mixed-phase peak of 53 dBZ at 0030 UTC. P3 also reproduces a local spike in reflectivity at this time, reaching 51 dBZ. Whereas Morrison failed to exceed 40 dBZ at this time, not only within the shallow layer but throughout the entire domain.

An additional, notable feature is the tendency of the reflectivity maxima during phase three. While all schemes show a decline in reflectivity over the course of this phase, specifically the ISHMAEL scheme shows a sharp ($\sim$30 minute) and severe ($>$ 15 dBZ) reduction in reflectivity between 0300 UTC and 0400 UTC. This time period coincides with reports of a sharp decline in observed reflectivity that characterised this phase (Ganetis and Colle 2015; Picca et al. 2014). The decline in maximum reflectivity was considerably faster and more severe than other schemes, which reduced gradually by less than 10 dBZ total during this time. Finally, for the Morrison and P3 schemes, the time series of maximum reflectivity throughout the entire domain closely resembles that found in the shallow layer, yet this is not the case for ISHMAEL. This implies that the vertical distribution of the reflectivity maxima is not confined to the shallow layer in ISHMAEL.

These findings are consistent with those of the Figures 6.1 and 6.3 but do indicate that the simulated reflectivity is much more complicated than may have first been anticipated. For example, comparison of these results show that, while ISHMAEL provides the weakest simulated reflectivity within the shallow layer and vertical cross section, ISHMAEL consistently produces the greatest reflectivity maxima of all schemes throughout the domain. In fact, ISHMAEL reproduces the observed reflectivity maxima in both cases one and two when the whole domain is considered, and additionally, ISHMAEL is the only scheme to produce the observed sharp-drop in reflectivity during phase three, implying that the scheme does in fact closely follow observations.

From analysis of only height maxima, ISHMAEL can produce a typically greater reflectiv-

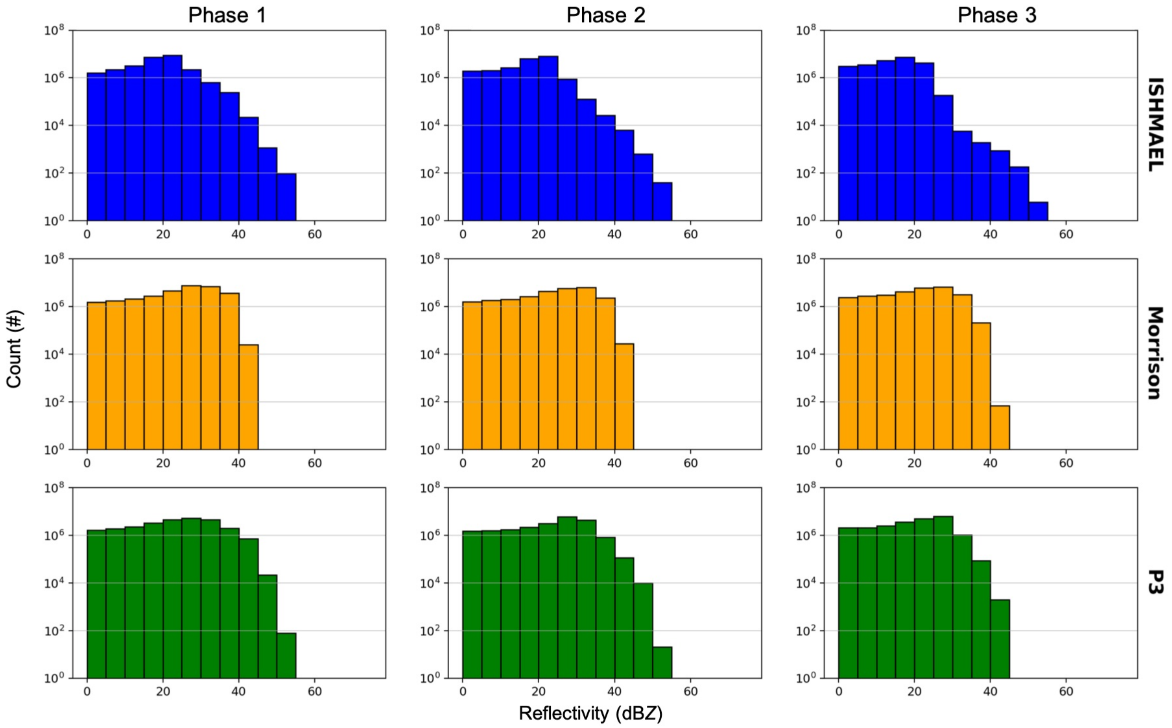

Figure 6.5. Histograms of simulated reflectivity factor frequency for microphysics schemes ISHMAEL (row 1), Morrison (row 2), and P3 (row 3) and phases 1–3 (columns 1–3, respectively) for all cells in domain 3.

ity maxima than other schemes, but it is not evident the extent to which these values occur. This motivates a brief examination of the frequency distribution of high reflectivity cells in each scheme. Figure 6.5 provides a histogram of all computed reflectivity for each phase of the storm and each microphysics scheme throughout domain three.

In phase one (Figure 6.5 row 1), the distribution modal reflectivity value simulated by ISHMAEL is centred at approximately 20 dBZ, whereas P3 and Morrison have a modal reflectivity much closer to 30 dBZ. However, throughout all phases, ISHMAEL maintains a wide distribution range that exceeds 50 dBZ in similar frequency to P3. In contrast, Morrison does not exceed 45 dBZ and therefore maintains a comparatively more narrow reflectivity range than P3 or ISHMAEL. Therefore, ISHMAEL provides peak reflectivity values amongst a weaker typical background reflectivity than other schemes. Furthermore, ISHMAEL maxima occur in comparable frequency to those in P3 and are therefore a significant feature in the ISHMAEL reflectivity field that is otherwise not apparent in Figures 6.1 and 6.3.

To consolidate our understanding of reflectivity in these schemes, we must determine where ISHMAEL's high reflectivity maxima occur in the domain. To achieve this, we examine the vertical and horizontal distribution of localised reflectivity maxima throughout the domain. Figure 6.6 shows the height at which each maximum simulated reflectivity value occurred per scheme. The height of the 1.5 km shallow layer is indicated with a red line.

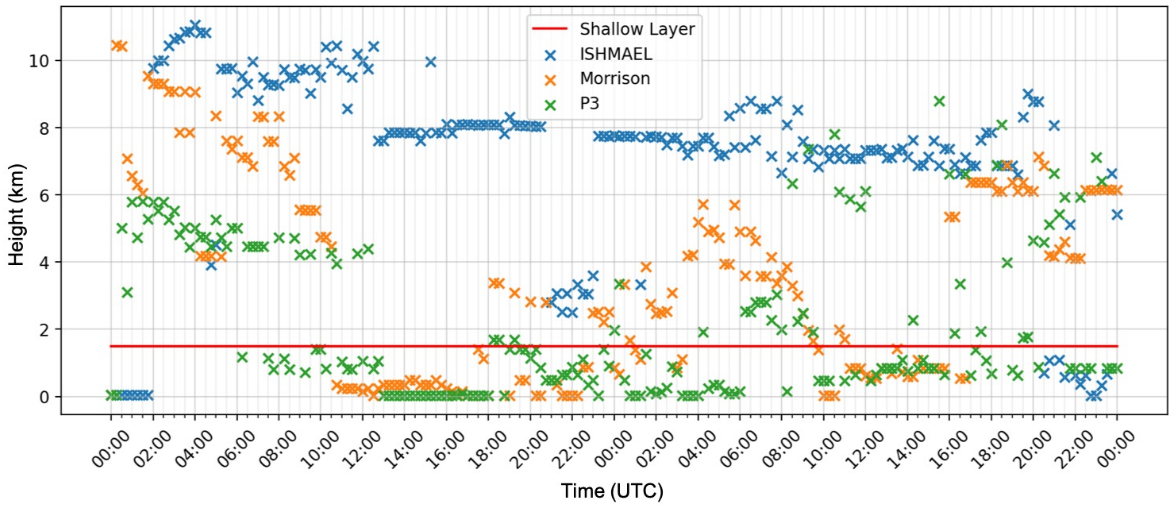

Figure 6.6. Scatter plot time series of the height (km) at which maximum reflectivity occurs in domain three for microphysics schemes: ISHMAEL (blue), Morrison (orange) and P3 (green). Height of the shallow 1.5 km layer is indicated with a red line.

The most notable feature of Figure 6.6 is that maximum reflectivity in ISHMAEL occurred most often at an altitude of 6–10 km, well above the shallow layer and the typical heights of both Morrison and P3. In comparison, Morrison and particularly P3 regularly exhibit maximum reflectivity close to the surface. Despite this, shortly after the onset of phase one at 2000 UTC ISHMAEL's maximum reflectivity fall to a height of between 2 and 4 km. High reflectivity can be found at this point as late as 0100 UTC in phase three, which implies a longevity of a high reflectivity region above the shallow layer but far below the typical 8–10 km height of high reflectivity in ISHMAEL. This explains why the shallow layer analysis of reflectivity indicates that ISHMAEL simulates the lowest overall reflectivity, whereas the time series indicates the opposite: high reflectivity in ISHMAEL is found exclusively outside of the shallow layer, whereas in Morrison and P3 high reflectivity occurs close to the surface.

Overall, evaluation of the maximum reflectivity factor at greater heights than the shallow layer, indicates that earlier comparisons of only the shallow reflectivity sub domain mischaracterised the ISHMAEL model as a scheme that severely underestimated the maximum reflectivity. Instead, ISHMAEL simulated a maximum reflectivity factor that was close to observations but occurred at greater elevation than was observed. The occurrence of high reflectivity cells at approximately 4 km or below in ISHMAEL and Morrison during phases one to three, motivate a re-examination of the distribution of maximum reflectivity at, and below, this altitude.

6.1.4 Re-examination of the Spatial Distribution Below 4 km

Figure 6.7 shows the re-examined reflectivity contours as in Figure 6.1 but to a comparatively greater vertical height of 4 km . The P3 scheme (Figure 6.7 column 3, row 1) produced minimal change at greater elevation in comparison to previous analysis within the shallow layer (Figure 6.1). For example, a more northerly distribution of high (> 45 dBZ) reflectivity is apparent in phase one, and the occurrence of small patches of reflectivity maxima in excess of 45 dBZ is increased in phase two. These results are not unexpected, as the majority of high reflectivity cells in P3 occur within the shallow layer (see Figure 6.6).

Of greater interest are the changes to ISHMAEL and Morrison, which both showed a high reflectivity region aloft of the shallow layer in Figure 6.6. In Morrison (Figure 6.7, row 2), the occurrence of high (> 45 dBZ) reflectivity is increased over large areas, and the distribution becomes less precise, but the maxima achieved remains the same. Therefore, the inclusion of higher vertical levels does not provide any new insights into the handling of reflectivity by Morrison.

In ISHMAEL (Figure 6.7, row 1) the distribution of the elevated reflectivity band remains largely identical to below the shallow layer, but a marked change in reflectivity maxima is found when greater elevations are considered. ISHMAEL produces small, localised pockets of very high reflectivity throughout the snowband. This feature is a remarkable departure from other schemes that lack fine-scale perturbations in the reflectivity field. From this Figure we begin to understand how ISHMAEL can achieve the largest reflectivity maxima, whilst providing a comparatively weak reflectivity field across the domain. Perhaps the greatest success of the ISHMAEL scheme is its production of fine scale, high reflectivity bands to the southeast of Long Island in phase one. These bands were a key source of intrigue in the observations at this time and were smoothed over by other microphysics schemes in this study.

In summary, analysis of the reflectivity in Figure 6.7 reveals a previously omitted feature of the ISHMAEL simulated reflectivity field; the production of very high magnitude reflectivity in small, isolated areas. ISHMAEL is the only scheme to produce the localised high reflectivity bands in phase one, potentially indicating that this feature is essential in order to resolve high reflectivity as observed in this case. ISHMAEL presents a notable departure from Morrison and P3 as it produces severe gradients in the reflectivity field. This is notable as throughout phase one when observations show that peak reflectivity (> 50 dBZ) was embedded within regions of reflectivity less than 25 dBZ. Such extremes in gradient are not found by P3 or Morrison, which produce much smoother gradients surrounding areas of peak reflectivity.

Of course, the ISHMAEL model is not perfect and the findings here are with caveats. The high reflectivity bands shown in phase one are too tight, exhibiting too steep a gradient to the surrounding field. Speckles of high reflectivity determined by ISHMAEL are also not found in this frequency in the observations, and the distribution of these areas is too far north. Perhaps most importantly we stress that this analysis takes place 1–2 km aloft of the shallow layer, whereas observations indicate that maximum reflectivity was within this shallow region and so the ISHMAEL scheme simulates high reflectivity in regions that are too high.

6.2 Precipitation Associated with High Reflectivity

Extensive analysis of dual-polarisation radar products supported by surface observations of precipitation type, have enabled the high reflectivity bands observed in this case to be associated with likely precipitation-types (Ganetis and Colle 2015; Griffin et al. 2014; Picca et al. 2014). For example, radar reflectivity signatures were used to diagnose precipitation type by Picca et al. (2014) who concluded that high reflectivity was not a result of pure snow, but a mixture of sleet, rain and snow during phase one. Similarly, Griffin et al. (2014) associated high reflectivity with wet snow and ice pellets that were verified by mPING reports at the ground during phase one ($\sim$2216 UTC). Picca et al. (2014) drew attention to the high density of precipitation types in high reflectivity regions during phases one and two; even associating sudden reduction in reflectivity during phase three with the cessation of melting and return to less-dense aggregates. In addition to precipitation, radar products can be used to infer the presence of microphysical processes. For example, Picca et al. (2014) used correlation coefficient CC and differential reflectivity Z_{DR} to determine the approximate location and orientation of an offshore melting-layer and subsequent refreezing layer. Picca et al. (2014) also noted that updraft signatures at the surface indicated efficient wet growth of hydrometeors in a weakly convective environment. Griffin et al. (2014) identified that the greatest reflectivity occurred below the “nose” of the melting layer, where a local depression in the layer indicated typically larger hydrometeors melting at greater depth due to their greater terminal velocity. Thus, the precipitation field and reflectivity are intricately related in reality and this relationship was particularly evident in the production of very high reflectivity in this case.

The question remains whether microphysics schemes can appropriately attribute reflectivity to specific precipitation types and combinations. The high reflectivity observed in this case was strongly associated with mixed-phase activity, the collocation of multiple precipitation types, and the size and density of hydrometeors of precipitation types aloft. Significantly, the precipitation and its resulting reflectivity were dependent on the successive interactions of several dynamically changing vertical layers, spanning depositional growth, melting, re-

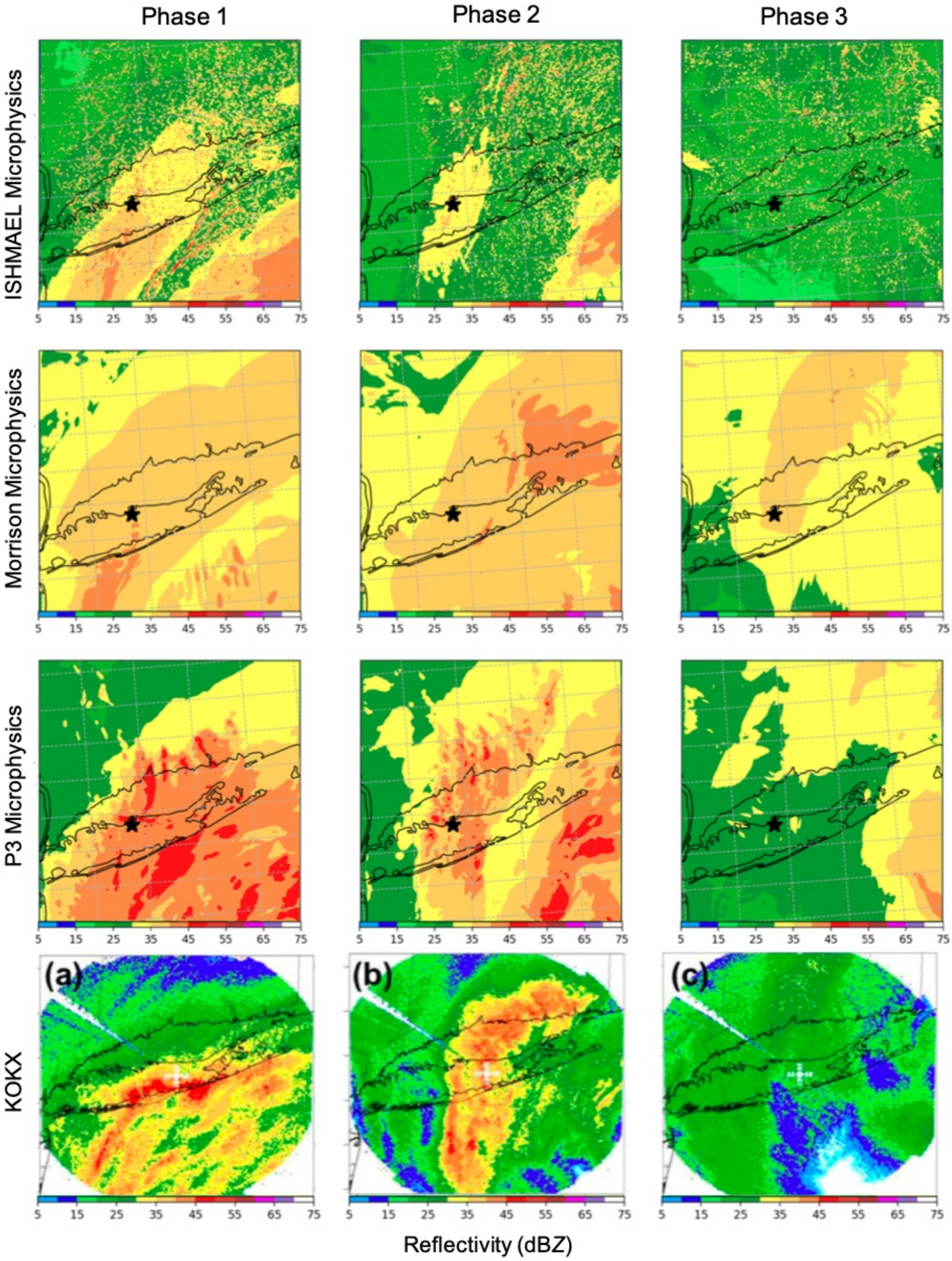
Phase 1
Phase 2
Phase 3
ISHMAEL Microphysics
Morrison Microphysics
P3 Microphysics
KOKX
(a)
(b)
(c)
5 15 25 35 45 55 65 75
Reflectivity (dBZ)

Figure 6.7. Contours of simulated maximum reflectivity factor Z_H (dBZ) at times 2130 UTC (column 1), 0045 UTC (column 2), 0345 UTC (column 3), for microphysics schemes ISHMAEL (row 1), Morrison (row 2) and P3 (row 3) as in Figure 6.1 but up to an altitude of 4 km. Observations of KOKX radar reflectivity (dBZ) adapted from Ganetis and Colle (2015) (see their Figure 4) shown in row 4 for comparison at times: 2129 UTC (column 1), 0042 UTC (column 2), 0340 UTC (column 3). Contours shaded according to scale.

freezing and riming. The accuracy of each scheme's predicted reflectivity field was therefore highly dependent on the correct prediction of precipitation type and microphysical process rates. In this section we will focus on the type(s) of precipitation simulated by each scheme at locations of high reflectivity.

The analysis in this section considers only high reflectivity cells that occupy the 99th percentile of reflectivity per scheme; i.e. in excess of 34 dBZ, 25 dBZ and 32 dBZ in Morrison, ISHMAEL and P3 respectively. Cells within the 99th percentile of reflectivity are referred to as high reflectivity cells hereafter. Variables that are the subject of analysis, such as precipitation type or density, originate from within high reflectivity cells unless otherwise stated.

6.2.1 Precipitation Coincident with High Reflectivity Cells

Figure 6.8 shows the percentage of per-phase high reflectivity cells that contain each hydrometeor type as simulated per microphysics scheme. Co-existing precipitation types from within the same cell are treated as if independent from each other, and percentages are calculated with respect to the specific phase of the storm only (shown per Figure column).

In ISHMAEL (row one) the most common precipitation types found in high reflectivity cells during phases one and two were rain and snow, which were present in more than 80% of cells across both phases. Whereas in phase three, snow and ice occupied this percentage range and rain dropped to below 60% of cells. This transition reflects the higher degree of mixed-phase activity and precipitation diversity that were present during phases one and two, compared to the subsequent cessation of mixed-phase activity as the environment cooled in phase three. The relationship between high reflectivity cells and the mixed-phase is made less clear by the consistently small proportion of these cells that contained graupel. However, ice was consistently present in more than 80% of cells, and given that in ISHMAEL ice can encapsulate small pellets or sleet, it is possible that these wet growth hydrometeors, in addition to rain, are driving the elevated mixed-phase reflectivity signature.

In Morrison, snow and rain featured in 80–100% of high reflectivity cells, with exception for phase three when rain fell to 60%. Graupel was also consistently associated with high reflectivity in more than 80% of high reflectivity cells across all three phases. This is markedly different to ISHMAEL, but all the more intriguing considering that in Morrison, graupel accounts for more than 80% of high reflectivity cells, but only $\sim$1% of the precipitated mass. Thus, while both ISHMAEL and Morrison show that mixed-phase hydrometeors can produce high reflectivity, this effect may be more pronounced in Morrison.

P3 is dissimilar to ISHMAEL and Morrison in that high reflectivity is dominated by the

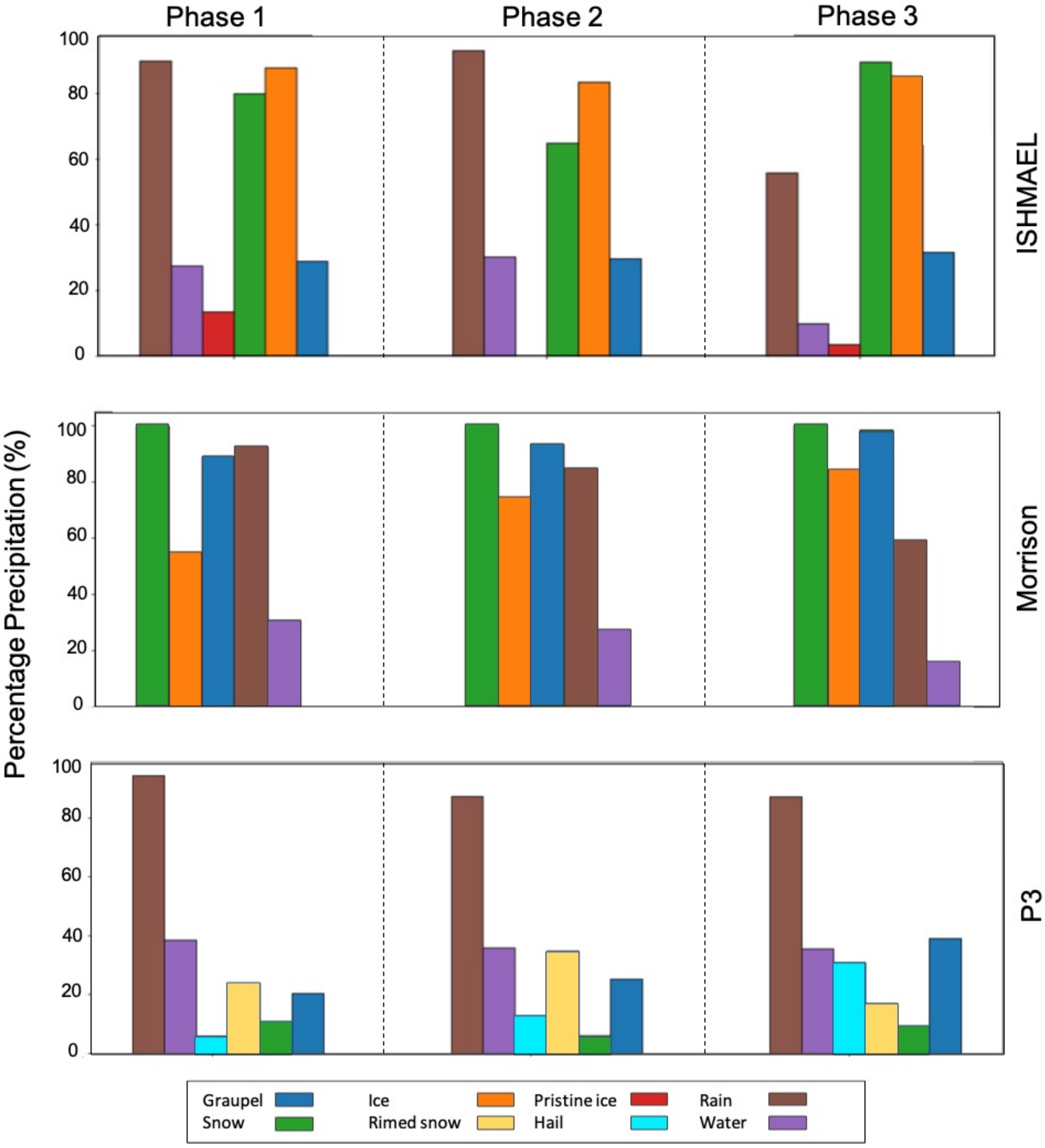

Figure 6.8. Percentage (%) of high reflectivity grid cells (99th percentile of reflectivity per scheme) containing precipitation type for microphysics schemes ISHMAEL (top), Morrison (middle), and P3 (bottom). Phases one to three are separate and percentages are calculated per phase only. Precipitation type indicated by Figure legend.

liquid phase rather than solid hydrometeors. Rain is apparent in 90% of high reflectivity cells and water droplets present in 40%, but solid precipitation does not exceed 40% of high reflectivity cells across any phase. Products of mixed-phase activity, such as rimed snow (25%) and graupel (20%) are the most common solid hydrometeor types in P3's high reflectivity cells during phases one and two. It seems then, that the relationship between mixed-phase precipitation and high reflectivity amongst these schemes is quite variable. However, the presence of liquid water is significant across schemes. This may have enabled the P3 scheme, which produced the most rain during the mixed-phase, to enhance its reflectivity signature due to its comparatively high sensitivity to melting.

6.2.2 Collocation of Multiple Precipitation Types within High Reflectivity Cells

As noted by Ganetis and Colle (2015), Griffin et al. (2014) and Picca et al. (2014), the highest values of reflectivity were found in areas that contained multiple precipitation types, and were the result of differing severities of melted snow, rain and ice, some of which was undergoing or had undergone refreezing. To examine the correlation between multiple precipitation-type combinations and high reflectivity, the co-located precipitants within the 99th percentile of high reflectivity cells were grouped into mixtures. The percentage of high reflectivity grid cells that were occupied by each precipitation mixture across all phases is shown in Figure 6.9 for each microphysics scheme.

As ISHMAEL has three ice categories, it can simultaneously support 3 distinct ice precipitation types in addition to rain and water droplets, totalling a maximum of 5 collocated precipitation types. In P3, only one ice category is used, providing for up to three mixed types, including rain and cloud droplets (referred to as *water*). In Morrison, each of the categorised precipitation types (ice, snow, graupel, rain, water) can coexist within a cell, numbering 5 types in total. The stacked bars in Figure 6.9 are shown in ascending order of the number of collocated precipitants in the mixture. Each mixture is mutually exclusive i.e. rain refers to grid cells in which only rain was present and does not contribute to further combinations containing rain.

In ISHMAEL, high reflectivity cells frequently consisted of multiple mixed precipitation types, with 98% of cells containing more than one precipitation type and $\sim 80\%$ containing three precipitants or greater. High reflectivity was also commonly associated with a mixture of solid and liquid water, single-phase cells account for only 8% of the total number indicating a high reliance on the mixed-phase environment to produce high reflectivity in this scheme. The most common number of mixed precipitation types was 3 which occupied more than 40% of the total high reflectivity cells, and of all possible mixtures the snow, ice and rain combination was the most dominant accounting for a quarter of all high reflectivity

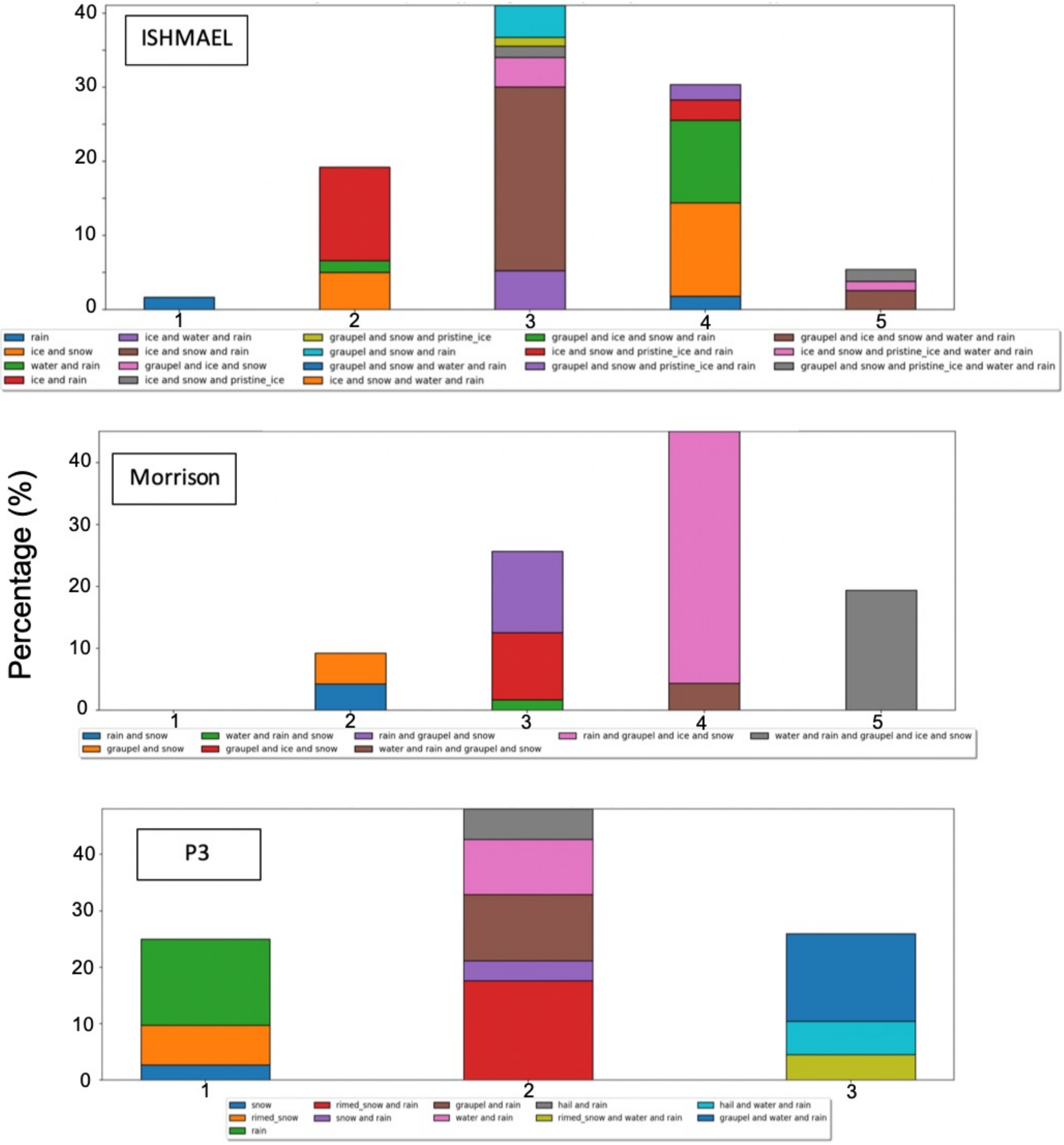

Figure 6.9. Percentage (%) of high reflectivity grid cells (99th percentile of reflectivity per scheme) containing specified collocated precipitation types for microphysics schemes ISHMAEL (top), Morrison (middle), and P3 (bottom). Percentage is calculated across all three phases. Bars are vertically stacked and ordered by number of precipitation types per mixture in increasing number from left to right. Precipitation type combination is indicated by Figure legend.

cells in total. This is in agreement with observations by Griffin et al. (2014) of wet snow in high reflectivity regions. Additionally, cells containing higher density hydrometeors such as ice and graupel resulting from mixed-phase processes were frequently associated with high reflectivity when found in combination, or when in the presence of rain.

In Morrison, mixing of hydrometeors was also essential to the production of high reflectivity as 100% of high reflectivity cells were found to contain more than one type of precipitation, and to contain at least one ice-type. Additionally, more than 85% of cells contained a mixture of liquid and solid water, indicating that this was an influential component for achieving peak reflectivity. The most dominant combination of precipitation for high reflectivity was rain, graupel, ice and snow, present in $\sim 40\%$ of cells and in good agreement with observations, especially as Morrison cannot produce sleet but this is accounted for by graupel. In fact, combinations of snow, rain and graupel accounted for 78% of all simulated high reflectivity cells. However, it is difficult to overlook that the presence of snow is such a dominant component to high reflectivity cells, and thus is likely the primary component when yielding the high reflectivity values simulated by this scheme.

P3 is unique in this case, as cells containing only one precipitation type made up a considerable component (25%) of the reflectivity field and more than half of this amount was owed to rain alone. Unlike in ISHMAEL and Morrison, the liquid-only water and rain combination is present in a third of high reflectivity cells and therefore it is expected that the liquid phase plays a key role in the determination of peak reflectivity in this scheme. However, the most common number of mixed precipitation types was 2, wherein the most dominant combination of precipitations was rimed snow and rain (∼19%), which is in keeping with the associated high reflectivity of wet snow observed. P3 does show a high dependence on mixed-phase products, for example mixtures including hail, graupel and rimed snow account for 62% of all high reflectivity cells, highlighting that though P3 may be more reliant on the liquid phase than other schemes, ultimately the combination of liquid and solid phases is required in the majority of cases.

6.2.3 Precipitation Coincident with the Melting Layer Aloft

As noted in previous sections, high reflectivity cells are often associated with liquid phase precipitation, which may be present in isolation or as a component of a precipitation mixture. An important source of liquid water in this case was melting, which occurred within a melting layer aloft of Stony Brook during the mixed-phase (high-reflectivity) periods of the storm. It is of interest then to determine if the melt layer was the driving force behind enhanced reflectivity in these schemes, especially in P3 that showed the most sensitivity to melting and the strongest correlation between the presence of liquid water and high re-

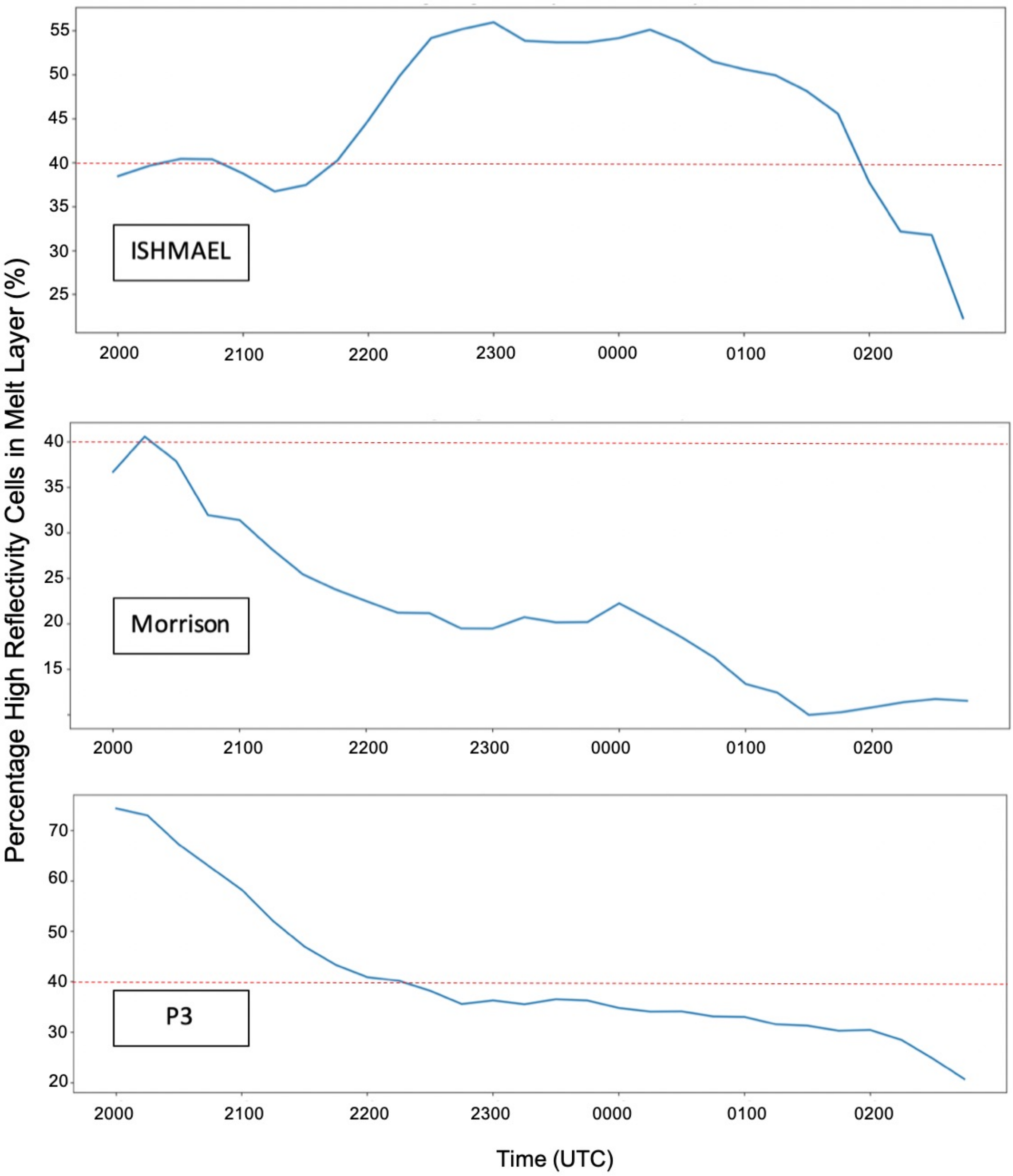

Figure 6.10. Time series of the percentage of high reflectivity grid cells (99th percentile of reflectivity per scheme) coincident with the melting layer (T ≥0°C) at time T. Time range spans phases 1–3 for the duration of the melting layer lifespan. Shown for schemes ISHMAEL (top), Morrison (Middle) and P3 (Bottom). Red dashed line indicates 40% for comparison.

flectivity. Figure 6.10 shows a time series of the percentage of high reflectivity grid cells that were situated within the simulated melting layer, defined as having (T $>$ 0°C). Note that the time series ends prior to the end of phase three due to complete dissipation of the melting layer.

In the ISHMAEL scheme (Figure 6.10, top), melting is collocated with high reflectivity for between 35–60% of all cells. This value tends to be lower during phase one, prior to 2100 UTC when the melting layer deepened (see Figure 4.8), and after 0130 UTC when the melting layer began to reduce in size. However, during phase two when the mixed-phase activity was observed to be at its maximum and when the melting layer was at its greatest depth, more than 50% of high reflectivity cells were found within the melting layer. This suggests that melting was an influential process for the production of high reflectivity in this scheme. Melting causes the break up of large particles including snow to generate small ice and rain, which each were present in $> 80\%$ of high reflectivity cells during phases one and two (i.e. Figure 6.8) but the presence of rain notably decreased in phase three at which time reflectivity also reduced. Analysis of collocated precipitation found that ice and rain were jointly present in $\sim$60% of high reflectivity cases (i.e. Figure 6.9), so it is likely that melting was a key generating process for these constituents, and for the high reflectivity with which they were associated. The importance of melting cannot be understated for the remaining 45% of cells outside the melting layer too, which may have contained partially melted or refrozen constituents which were found to be correlated with elevated reflectivity in this scheme. Therefore, it is important to recognise the direct and indirect contributions that melting may have had an on the high reflectivity signature..

In Morrison (Figure 6.10 middle), collocation of high reflectivity and melting was much less common than in ISHMAEL. At the onset of phase one, 40% of high reflectivity cells were located within the melting layer, but this proportion gradually decreased over the course of the phase, resulting in only 20% of high reflectivity cells being present within the melting layer. This is unusual because the Morrison scheme did exhibit an increase in reflectivity between phases one and two. It is possible that, given Morrison produced the most shallow melting layer (see Figure 4.8) melting was less influential on the reflectivity field than in ISHMAEL and P3. This is further corroborated by the widespread distribution of the Morrison reflectivity field that contrasts the much more narrow melt layer aloft. However, a local maximum at 0000 UTC may indicate that, though not a primary influence, melting may have played a role in the generation of high reflectivity during the most intense mixed-phase period.

In P3 (Figure 6.10 bottom), high reflectivity grid cells were initially strongly correlated with melting at the onset of phase one, and declined from 80% to 40% during this phase. The proportion of high reflectivity cells remained at approximately 35% during phase two, before declining in phase three. The most common constituents of high reflectivity cells in P3 were rain and water droplets, direct products of melting, so it is somewhat unusual to find that so few high reflectivity cells were located within the melting layer. However, as shown in Figure 6.7 the majority of high reflectivity cells in P3 occurred further south than in other schemes, which coincides with large swathes of rain production. Comparatively, the proportion of high reflectivity cells found in the relatively narrow melting layer appears significant. Additionally, the height of the reflectivity maxima typically occurred at the surface level (see Figure 6.6) where the products of the melting layer, including rain were more likely to be found.

It is apparent that the melting layer plays a direct role in the production of very high reflectivity cells, but that this effect is both direct and indirect. For example, the products of melting provide the necessary collocation of mixed-phase precipitation that was highly important for high reflectivity cells (see Figure 6.9) and such collocation of liquid and ice are key for generating graupel, which was found in $\sim$90% of all high reflectivity cells (Figure 6.8). This only serves to emphasise the importance of constraining emergent schemes to ensure that they are not overly sensitive to melting. Not only does overactive melting disturb the predicted precipitation field, but it is also likely to affect the accuracy of reflectivity forecasts, especially in extreme cases such as this winter storm.

6.2.4 Density of Precipitation Coincident with High Reflectivity Cells

A final factor that requires investigation is the density of frozen precipitation found within high reflectivity cells. High density ices reflect more energy back to the radar than equivalent low density particles, increasing the recieved reflectivity signal. This effect was mentioned by Picca et al. (2014) in relation to the high radar reflectivity identified during phase two, that was associated with relatively dense wet-growth hydrometeors, and the subsequent, rapid drop in reflectivity, associated with widespread transition to less-dense snow. To evaluate the relationship between ice density and high reflectivity, the mass-weighted density of ice within high-reflectivity cells was compared to the background density exhibited by cells outside of the 99th percentile of reflectivity. This analysis is described in Figure 6.11 per phase (column) and per scheme (row).

Each scheme demonstrated a unique relationship between the density of precipitation and the resulting grid cell reflectivity. In P3 (Figure 6.11 row 3), ice density was consistently larger in high reflectivity cells than background cells across all three phases of the storm. For example, in phases two and three high reflectivity cells had densities more than 30% that of background levels, and in phase one high reflectivity cells contained ices that were more than twice as dense. The large increase in density during phase one may be in part

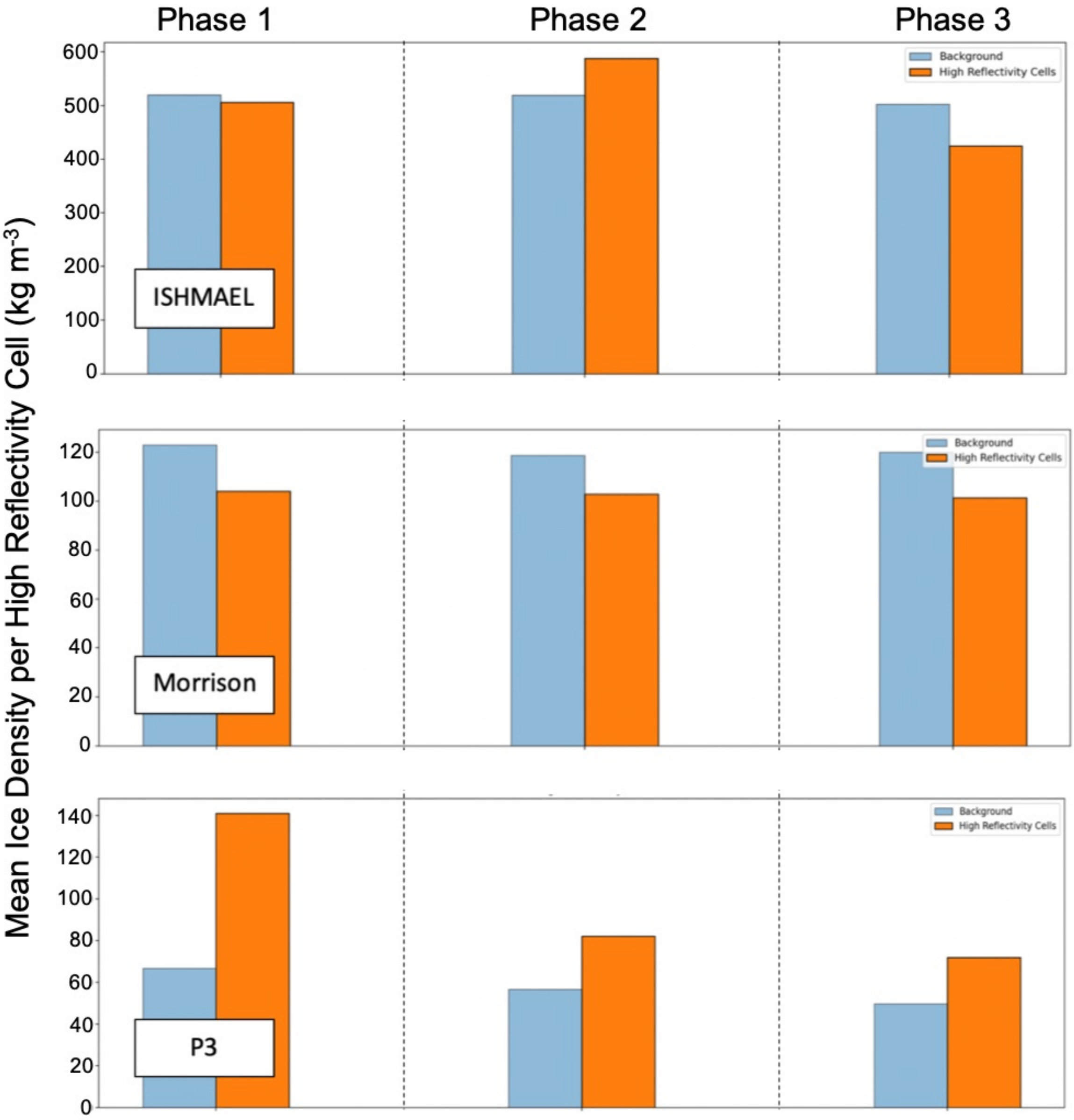

Figure 6.11. Comparison of average mass-weighted ice density present within 99th percentile high reflectivity grid cells (orange), to average mass-weighted ice density within background cells (blue). Average density is determined for all non-zero mass valued cells present in all domain three grid cells, per phase (columns 1–3) and per microphysics scheme: ISHMAEL (top), Morrison (Middle) and P3 (Bottom)

due to the high prevalence of reflectivity in the melting layer at this time (see Figure 6.10). Melting, increases the density of ice through surface layer *soak in*. Thus, P3's relation between density and reflectivity is in keeping with the hypothesis of Picca et al. (2014) that more dense ices are responsible for generally greater reflectivity.

In contrast, Morrison (Figure 6.11, row 2) showed the opposite effect. High reflectivity cells consistently contained less-dense ice than found in background levels, and were up to 20% less dense across all three phases. Though surprising, this is consistent with the lack of high reflectivity ice found in the melting layer in Morrison, where higher density ice is likely to exist. It is likely therefore, that snow, which is present in more than 90% of high reflectivity cells, is the main driving factor in the calculation of reflectivity maxima for this scheme. In this case, more so than with ISHMAEL and P3, the mass weighting of density within highly reflective grid cells (orange) is strongly biased by the significantly larger contribution of snow in Morrison than graupel.

The relationship between reflectivity and density implied by Figure 6.11 in ISHMAEL (row one) is far less obvious. Phase-to-phase fluctuations in reflectivity may indicate that the high reflectivity simulated by ISHMAEL is more dependent on the environmental conditions than other schemes, which show a consistent relationship regardless of phase. For example, in phase two, when high reflectivity grid cells were primarily found within the melting layer, reflectivity tended to be related to higher density hydrometeors that resulted from densification during melting. In comparison, during phase three, when melting ceased and high reflectivity cells tended to contain more snow and ice and less rain (i.e. Figure 6.8) high reflectivity cells were typically less dense than the background level. This indicates that, while high density hydrometeors that result from the mixed-phase can produce elevated reflectivity, the relationship between peak reflectivity and density in ISHMAEL is more complicated and dependent on multiple factors that may be more important in this case.

6.3 Analysis of Reflectivity Parameterisations

In previous sections of this chapter, the character of each scheme's predicted reflectivity field and the typical precipitation mixtures with which high reflectivity is associated were investigated. It was established that, independent of the accuracy of the forecast precipitation field, similar precipitation types produced very different radar reflectivity signatures, which is surprising as the relationship between radar reflectivity and precipitation type is a matter of fundamental physical law. This motivates an investigation of the underlying mathematical formulations of reflectivity in these schemes, to determine where divergences in the simulated reflectivity may occur.

6.3.1 Radar Reflectivity Parameterisations per Microphysics Scheme

The parameterisation of reflectivity is based upon Rayleigh scattering, which considers reflectivity as proportional to the sixth power of droplet diameter D. Therefore, the total radar reflectivity Z of a droplet distribution takes the form:

$$Z = \int_0^\infty N(D) D^6 \, \mathrm{d}D \tag{6.1}$$

Where $N(D)$ is number concentration of droplets per unit length. Integration of Equation 6.1 over the entire size distribution, such as within a simulated grid cell, yields the total distribution radar reflectivity value (full method shown in Appendix F). However, to obtain this quantity a particle size distribution and a mass-dimensional ($m - D$) relationship must be specified. The former is usually of the gamma (often Marshall-Palmer) or log-normal type and the latter may be taken as the constant density sphere. These choices yield a radar reflectivity of the form:

$$Z_r = \Gamma(7) N_0 \lambda^{-7} \tag{6.2}$$

Where λ is the distribution slope parameter and Γ is the Euler-Gamma function. Equation 6.2 can be generalised to the ice phase, assuming that ice hydrometeors also follow a gamma distribution and, most notably, can be represented as constant density spheres. Using the method of Stoelinga (2005) (see Appendix F) the radar reflectivity of hydrometeor type H is:

$$Z_H = \Gamma(7) N_0 \lambda^{-7} \left(\frac{\rho_H}{\rho_l} \right)^2 \alpha_\odot, \tag{6.3}$$

where $\alpha_\odot$ accounts for the reduced reflectivity of ice compared to liquid water. The reflectivity per hydrometer type is additive, so a combined reflectivity value can be obtained for all solid and liquid hydrometeors using Equations 6.2 and 6.3:

$$Z \, \textbf{[dBZ]} = 10 \log_{10} \left(10^{18} \left(Z_r + Z_s + Z_g \right) \right), \tag{6.4}$$

given in decibels of Z by convention.

The Morrison scheme is well suited to this additive parameterisation as its precipitation field is already partitioned into discrete hydrometeors that are represented as constant density spheres. Thus the reflectivity components of its hydrometeor categories can be calculated individually and summed as above. Unlike in ISHMAEL and P3, the Morrison scheme does not have a reflectivity routine, so instead the wrf-python `getvar` routine is used to produce this field in post processing (Ladwig 2017). This is a useful test case for a library that is sure to receive use amongst the WRF community, and represents a good test for the large number of microphysics schemes that do not calculate reflectivity.

The wrf-python `getvar` uses the conventional formulation as in Equation 6.4 but determines only the rain, snow, and graupel components to the equivalent reflectivity. These values are obtained using the mass-mixing ratios output by the microphysics scheme. To satisfy Equation 6.3, the routine uses fixed gamma distribution slope parameters of $\lambda_r = 8 \times 10^6$ m^{-1}, $\lambda_s = 2 \times 10^7$ m^{-1}, and $\lambda_g = 4 \times 10^6$ m^{-1} and fixed densities of $\rho_r = 1000$ kg m^{-3}, $\rho_s = 100$ kg m^{-3} and $\rho_g = 400$ kg m^{-3} for rain snow and graupel, respectively. A complete breakdown of the getvar derived reflectivity equation is given in Appendix G.

In the ISHMAEL microphysics scheme, the reflectivity parameterisation diverges from the conventional approach due to the presence of two free-ice categories and an aggregate category, which results in a different formulation of the total reflectivity equation:

$$Z_H = \max\{-35, 10\log_{10}(Z_{\text{rain}} + Z_{\text{i1}} + Z_{\text{i2}} + Z_{\text{i3}})\}, \tag{6.5}$$

Furthermore, the components of reflectivity for each hydrometeor are also different because a more complex particle size distribution $N(D)$ is used for liquid and ice particles, and a spheroidal m-D hypothesis with non-constant density is used for ice. After integration these factors produce the following rain component of reflectivity Z_{rain}:

$$Z_{\text{rain}} = 1 \times 10^{18} \left(\frac{\Gamma(7)\rho_a n_r}{\lambda_r^6} \right), \tag{6.6}$$

and the following generalised-ice reflectivity component Z_{ice}:

$$Z_{\text{ice}} = 1 \times 10^{18} \left[\frac{0.176}{0.93} \left(\frac{6}{\pi} \right)^2 \left(\frac{4\pi}{3} \frac{\bar{\rho}_i a_o^{1-\delta_*}}{2^{2+\delta_*}} \right)^2 \frac{\rho_a n_i}{900^2} (2a_{\text{ni}})^{2(2+\delta_*)} \frac{\Gamma(\nu + 2(2+\delta_*))}{\Gamma(\nu)} \right], \tag{6.7}$$

Full derivation of these equations can be found in appendix E.

A simple analysis can illuminate how predicted reflectivity may vary with precipitation in these parameterisations. For example, the solid-phase Morrison reflectivity components given in Equation 6.3 depend on the hydrometeor density, implying that some hydrometeor types will intrinsically posses greater reflectivity than others. However, the mass mixing ratio of the species is also a factor which places importance on the predicted precipitation field. The ratio of hydrometeor reflectivities are:

$$\frac{Z_s}{Z_r} = \frac{\alpha_{\odot}\lambda_r}{\lambda_s}\left(\frac{\rho_s}{\rho_w}\right)^{0.25}\left(\frac{q_s}{q_r}\right)^{1.75} \approx 0.05\left(\frac{q_s}{q_r}\right)^{1.75}$$

$$\frac{Z_s}{Z_g} = \frac{\alpha_{\odot}\lambda_r}{\lambda_g}\left(\frac{\rho_g}{\rho_w}\right)^{0.25}\left(\frac{q_g}{q_r}\right)^{1.75} \approx 0.36\left(\frac{q_g}{q_r}\right)^{1.75}$$

Assuming reflective parity (i.e $Z_s/Z_r = 1$), $q_s = 5.5\,q_r$ and $q_g = 1.8\,q_r$ thus, five times as much snow and almost twice as much graupel is required to achieve the same reflectivity factor of rain. Similarly, graupel is 3 times more reflective than snow in this framework. We note that these components aren't additive within the logarithm, but these differences indicate the tendency of the routine to output a greater reflectivity factor in cells that are biased toward rain and graupel, rather than those containing primarily snow.

The ISHMAEL reflectivity component of ice given in Equation 6.7 implies that radar reflectivity will be greater for higher density ice with a greater number concentration and greater characteristic radius (related to the average crystal size). By comparison, the reflectivity component for liquid (Equation 6.6) will be increased when the mass mixing ratio of droplets is large, and their number is few. Taking the ratio of q_r/n_r to be average droplet size, then the rain reflectivity component is maximised for large mass mixing ratios of relatively large droplets. From this information it is reasonable to estimate that regions of intense riming would theoretically provide the best opportunity for very high reflectivity prediction.

6.3.2 More Detailed Analysis of the ISHMAEL Reflectivity Equation

Surface level analysis, can only hint at the differences in reflectivity amongst a varied precipitation field, but it cannot precisely examine the relationship between the ice or raindrop characteristics and the simulated reflectivity factor. For example, δ_* is present in the numerator, denominator, Euler gamma function and parameter indices in Equation 6.7. It is difficult then to determine the precise role of such complex variables by observation alone. Instead, the reflectivity can be analysed as a function of two components, liquid and frozen water, whose relative magnitude dictates the value of simulated reflectivity.

We may rearrange Equation 6.5 as:

$$Z = 10\log_{10}(10^{18}) + \underbrace{10\log_{10}(Z_{\text{ice}})}_{\text{A (Ice)}} + \underbrace{10\log_{10}(\varepsilon + 1)}_{\text{B(Mixed-Phase)}} \tag{6.8}$$

Where $Z_{\text{ice}} > 0$ is the combined ice reflectivity component and $\varepsilon = \frac{Z_{\text{rain}}}{Z_{\text{ice}}}$.

Thus, Equation 6.8 re-frames the total reflectivity as a function of ice reflectivity (A) and the relative reflectivity factors of ice and water (B). Physically, B represents co-located phases of water and is analogous to the mixed-phase. Also note that, the leading factor $10\log_{10}(10^{18}) = 180$ implies that A and B will be negative, and that increasingly negative values of these terms will reduce the total reflectivity. In the following analysis we will seek to vary the A and B terms in order to understand the relative importance of both components.

Given the large number of interwoven parameters that make up A and B, it is necessary to constrain the parameters to reasonable scenarios for this case. To achieve this, three frozen hydrometeor-type *profiles* were chosen with qualities given in Table 6.1. These hydrometeor types were chosen as they are comparable to the hydrometeor category definitions in Morrison, and their profiles span the complete ranges of both δ_* and $\bar{\rho_i}$ allowing for comprehensive analysis of Equation 6.8. With these quantities fixed, ε varies only with its remaining parameters, which are functions of the number and mass mixing ratios of rain and hydrometeors only. By varying the mass and number mixing ratios an understanding of term A could be gained.

Type	Density $\bar{\rho_i}$ (kg m^3)	Inherent Growth Ratio (IGR) δ_*	Radius r (m)
Dendrites	100	0.6	8×10^{-3}
Graupel	400	1	1×10^{-3}
Prolates	100	1.3	1×10^{-4}

Table 6.1. Characteristic density (kg m^3), Inherent Growth Ratio (IGR) and radius (m) for three characteristic precipitation-type profiles in the ISHMAEL scheme.

Ice Component

Figure 6.12 plots the ice reflectivity factor Z_{ice} of the A component from Equation 6.8. This is varied with ice crystal number concentration n_{ice} in the interval 1×10^2–1×10^5 kg^{-1}, which was representative of ice crystal concentrations predicted by the ISHMAEL scheme in this case. Columns one, two, and three show the hydrometeor profiles from Table 6.1; dendrites, graupel and prolate crystals, respectively. The Z_{ice} parameter is plot with four values of particle radius a_{ni} that are representative of ice in this case but may not occur for each specific hydrometeor type at all values. Note that Z_{ice} in excess of approximately $1.26\times$

10^{-18} produces A on the order 10^1 i.e. $\geq$ 1 dBZ (non-negligible) so the $Z_{\text{ice}} = 1.26 \times 10^{-18}$ line is shown in grey (dotted).

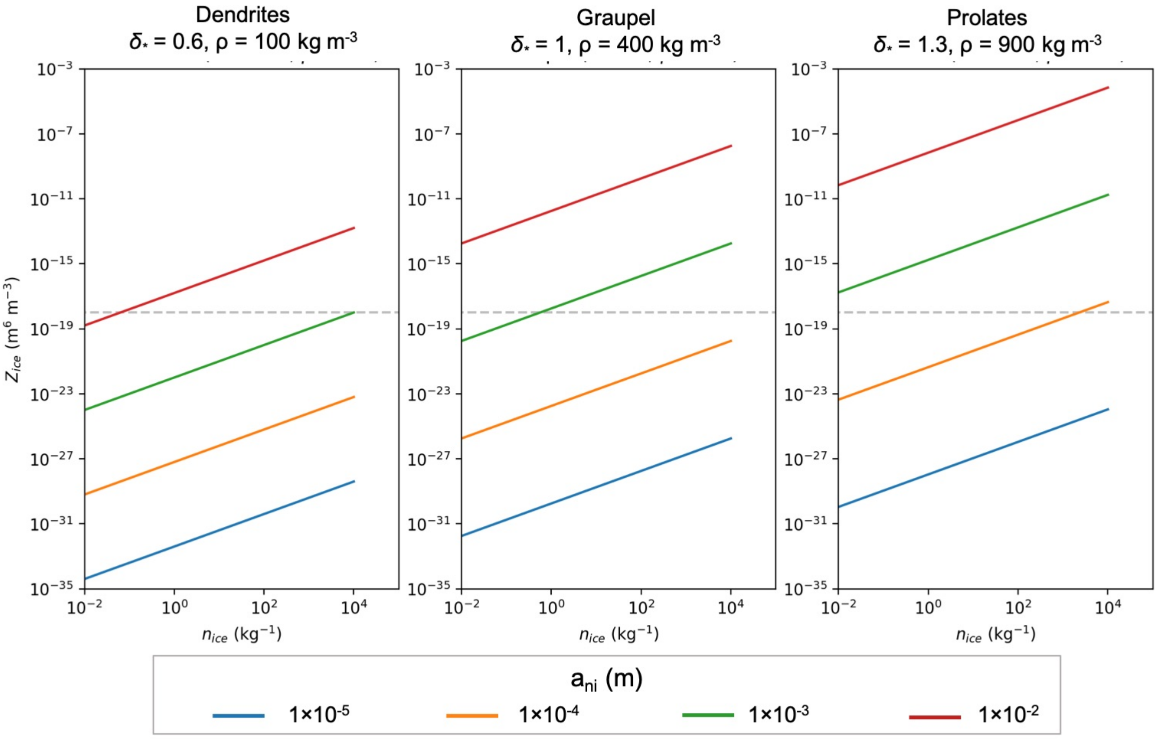

Figure 6.12. ISHMAEL ice-reflectivity component to the total reflectivity calculation (see Equation 6.8 versus ice number concentration n_{ice}. Three example precipitation types are considered; Dendrites (left), Graupel (middle), and Prolates (right). Four values of the ice characteristic radius a_{ni} are shown by coloured lines given in the Figure legend.

Figure 6.12 shows that Z_{ice} goes between 1×10^{-35}–1×10^{-3} for the precipitation profiles, number concentrations and radii considered here.

Z_{ice} is found to increase with the hydrometeor aspect ratio and density, as well as the characteristic particle diameter. This suggests that dense, prolate or large particles will achieve an enhancement in predicted reflectivity component, and that when these characteristics are found in combination, their influence on the reflectivity field is even greater. For example, this implies that the presence of hailstones or dendrites may inflate the reflectivity field over less dense or smaller counterparts. In addition, the reflectivity increases even more when number concentrations are large, which suggests that particularly intense bouts of these precipitation types will achieve exceptionally high reflectivity.

Comparison of the Z_{ice} growth between these factors can indicate which is more influential to the reflectivity field. For example, the ice radius induces Z_{ice} growth by several orders of magnitude when radius increases by only one order of magnitude. However, it is notable that the size of this growth is dependent on the crystal aspect ratio, for example, between values of a_{ni}, the dendrite reflectivity component increases by approximately five orders of magnitude, whereas for prolates this difference is 6 orders of magnitude. Therefore, prolate hydrometeors benefit from a larger relative increase in reflectivity than oblates. This is significant because prolates have a typically small radius, but the aspect ratio enables even very small crystals ($a_{\text{ni}} = 1 \times 10^{-4}$) to produce non-negligible reflectivity (exceeds grey line). In a similar sense, the aspect ratio dependence serves to limit the reflectivity contribution from dendrites field unless very high number concentrations are achieved.

Considering these features, we might conclude that high reflectivity is unlikely to be obtained by dendrites, which require very high number concentrations, and unlikely to be obtained by prolates, which do not usually possess a large radius. Therefore, the middle ground hydrometeor, graupel, is likely to be ideally situated to produce the largest reflectivity signatures in ISHMAEL, due to its ability to produce non-negligible reflectivity at only moderate radial size and number concentration.

Mixed-Phase Component

To complete the analysis of Equation 6.8 we can perform a similar investigation of the remaining term; $\varepsilon = Z_{\text{rain}}/Z_{\text{ice}}$ which measures the relative dominance of the rain reflectivity component to the ice reflectivity component. Derivation of the ε equation in Appendix H produces the following form:

$$\varepsilon(\delta_*, \bar{\rho}_i, a_{\text{ni}}, \gamma_n, m_r) \approx [2.47 \times 10^{15}][\gamma_n m_r^2] \left[\frac{a_0^{2\delta_*}}{(\bar{\rho}_i a_{\text{ni}}^{2+\delta *})^2 \Gamma(8 + 2\delta_*)} \right], \tag{6.9}$$

Where $\gamma_n = n_r/n_i$ is the ratio of raindrop number mixing ratio to ice number mixing ratio, and $m_r = q_r/n_r$ is the ratio of raindrop mass to raindrop number mixing ratio, which is analogous to the average raindrop mass.

It is notable that once the hydrometeor distribution is defined, ε varies only with the third bracket in Equation 6.9. We may denote this bracket as F/ρ_i^2 where:

$$F(a_{\text{ni}}, \delta_*) = \frac{a_0^{2\delta_*}}{(a_{\text{ni}}^{2+\delta *})^2 \Gamma(8 + 2\delta_*)} \tag{6.10}$$

Which depends only on the geometry of ice. Therefore, the component of reflectivity in ISHMAEL that is associated with the co-location of ice and liquid will be enhanced depending on the geometric qualities of the ice.

Figure 6.13 shows plots of F versus a_{ni} for the same precipitation type profiles as were examined in Figure 6.12 (see Table 6.1). The value of F was varied for radii in the range 10^{-5}–10^{-2}

showing an extremely broad (1×10^{-14}–1×10^{10}) array of possible values. The value of F decreases as both the radius and aspect ratio increase, but the magnitude change in F with radius is far greater. For example, the change in F between the minimum $\delta_* = 0.6$ and maximum possible $\delta_* = 1.3$ is 5 orders of magnitude for small a_{ni} and 9 orders of magnitude for high a_{ni}. Whereas, variation in a_{ni} between 4×10^{-2} and 4×10^{-4} produces a 14–18 order of magnitude difference in F that is larger (smaller) for larger (smaller) δ_*. These findings indicate that the mixed-phase ε component of ISHMAEL predicted reflectivity is likely to be enhanced when ice has a small size, such as during rime splintering.

Given that the value of ε in Equation 6.9 varies with the factor F/ρ_i^2, it is important to consider how the density might alter our understanding of ice geometries contribution to reflectivity in mixed-phase environments. Overlaid on Figure 6.13 are the exact values of F (black dot) and $1/\bar{\rho}_i{}^2$ (blue cross, right y-axis) for the assumed a_{ni} and δ_* given in Table 6.1. For these hydrometeor profiles, the inverse relationship between F and a_{ni} causes the predicted F to occupy similar magnitudes between 1×10^{-2}–1×10^{2}. Substitution of $F/\bar{\rho}_i^2$ back into Equation 6.9 per hydrometeor produces:

$$\begin{aligned} \varepsilon_{\text{graupel}} &\approx 10^{8}\gamma_n m_r^2 \\ \varepsilon_{\text{dendrites}} &\approx 10^{9}\gamma_n m_r^2 \\ \varepsilon_{\text{prolates}} &\approx 10^{11}\gamma_n m_r^2 \end{aligned} \tag{6.11}$$

In the context of Equation 6.9, larger leading factors will offset the $\gamma_n m_r^2$ term, which is expected to be extremely small because typical rain drop masses are of the order $<\sim 10^{-5}$ kg and this factor is squared. By offsetting this factor, the negative mixed-phase term B in Equation 6.8 will have a smaller absolute value, allowing more of the leading factor to be retained and thus produce a greater reflectivity factor. As shown above, the constant factor is largest in prolates, followed by dendrites and then graupel, which implies that the mixed-phase contribution of reflectivity in the ISHMAEL scheme will be greatest when small, columnar ice particles are in the vicinity of liquid water.

In addition to the frozen hydrometeor qualities, ε depends on the average mass of rain droplets m_r and the relative ratio of droplet number to crystal number γ_n (i.e. bracket two of Equation 6.9). Histograms of these qualities in the ISHMAEL scheme (domain 1) are shown in Figure 6.14 for cells containing each hydrometeor type. The typical range of γ_n in this case was 1×10^{-6}–1×10^{4} for all hydrometeors. The range for m_r was 2×10^{-11}– 1×10^{-7} for all hydrometeors. However, graupel was coincident with rain more often than other hydrometeor types, and large raindrops ($m_r > 1 \times 10^{-9}$) represented a larger proportion of the droplet field collocated with graupel than other precipitation types. Comparison of these

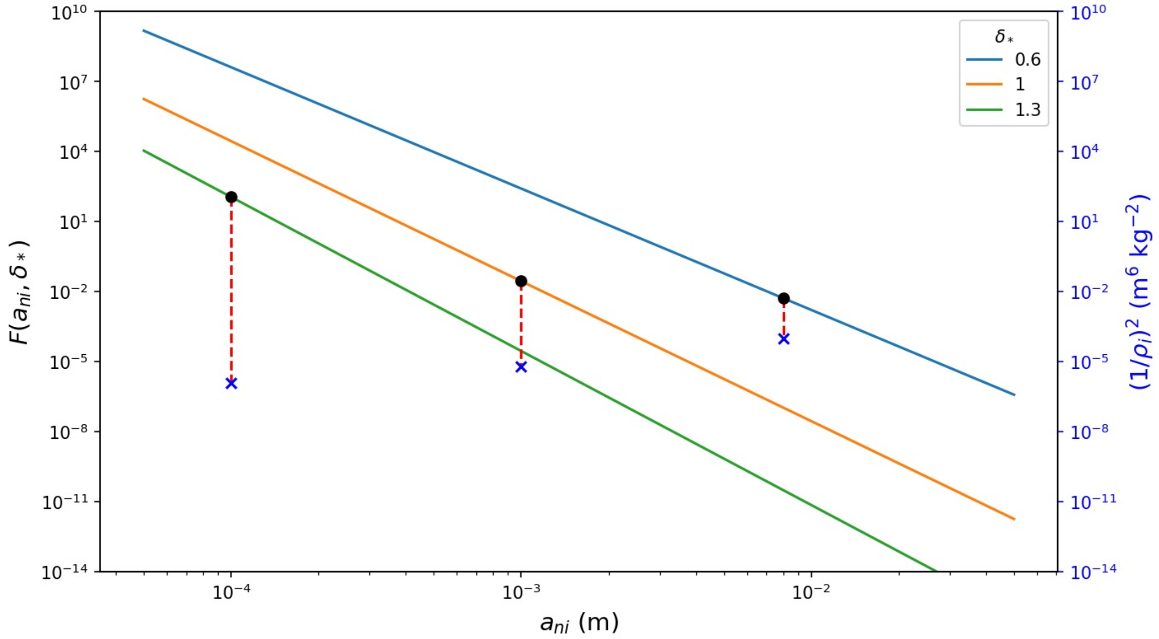

Figure 6.13. Plot of factor F (see Equation 6.9) versus characteristic ice radius for three values of the inherent growth ratio δ_* that are indicative of oblate (blue), spherical (orange), and prolate (green) ice crystals. Black dots indicate the characteristic radius of each example precipitation type; dendrites, graupel, prolate ice. Blue crosses adjoined by red dashes correspond to the inverse square density associated with each precipitation type (blue axis, right).

ranges produce the maximum and minimum hypothetical extent of $\gamma_n m_r^2$ term:

$$4 \times 10^{-28} < \gamma_n m_r^2 < 1 \times 10^{-10}$$

This range is termed *hypothetical* because the extremes of γ_n, m_r^2 are not confirmed to coincide during this simulation. Substituting into the identities found in Equation 6.11:

$$5 \times 10^{-19} < \varepsilon_{\text{dendrites}} < 1 \times 10^{-1} \tag{6.12}$$

$$1.7 \times 10^{-19} < \varepsilon_{\text{graupel}} < 4 \times 10^{-2} \tag{6.13}$$

$$1 \times 10^{-16} < \varepsilon_{\text{prolates}} < 3 \times 10^{1} \tag{6.14}$$

Thus, the mixed-phase factor is most likely to play a considerable role when $\gamma_n m_r^2$ is large, such as in intense regions of large-raindrops, and will be enhanced by the presence of small columnar ice. Having examined ε we now seek to determine its role in the overall reflectivity calculation, recall Equation 6.8:

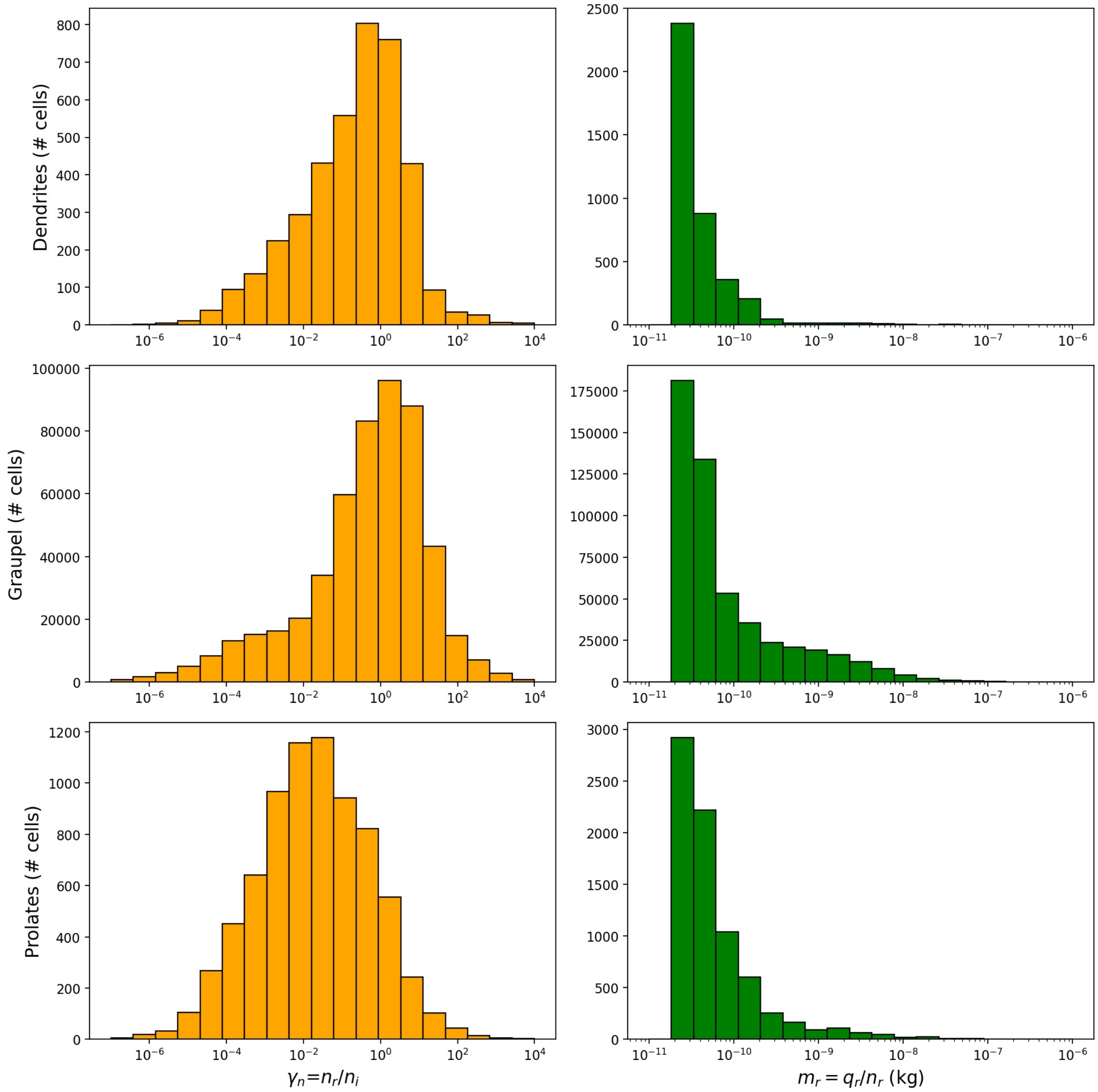

Figure 6.14. Distributions of γ_n, the ratio of rain to ice number concentration (orange, left) and average crystal mass m_i (green, right) simulated by ISHMAEL during case one for precipitation classed as dendrites (row 1), graupel (row 2), and prolates (row 3).

$$Z = \underbrace{10\log_{10}(10^{18}Z_{\text{ice}})}_{\text{A}} + \underbrace{10\log_{10}(\varepsilon+1)}_{\text{B}}$$

When $\varepsilon \rightarrow 0$, $B \rightarrow 0$ and reflectivity is entirely due to ice. Non negligible mixed-phase contributions i.e. B > 1 dBZ are not expected until $\varepsilon \gtrsim 0.26$, which is at the very highest end of the ranges shown in Equations 6.14. Therefore, the contribution of the mixed-phase will only be non-negligible until raindrops are suitably large, ice particles are small and dense, and the number of droplets is much greater than the number of crystals. As such, any net contributions to the reflectivity field from mixed-phase cells, and by extension the ice geometry,can occur in only a small subset of all possible scenarios.

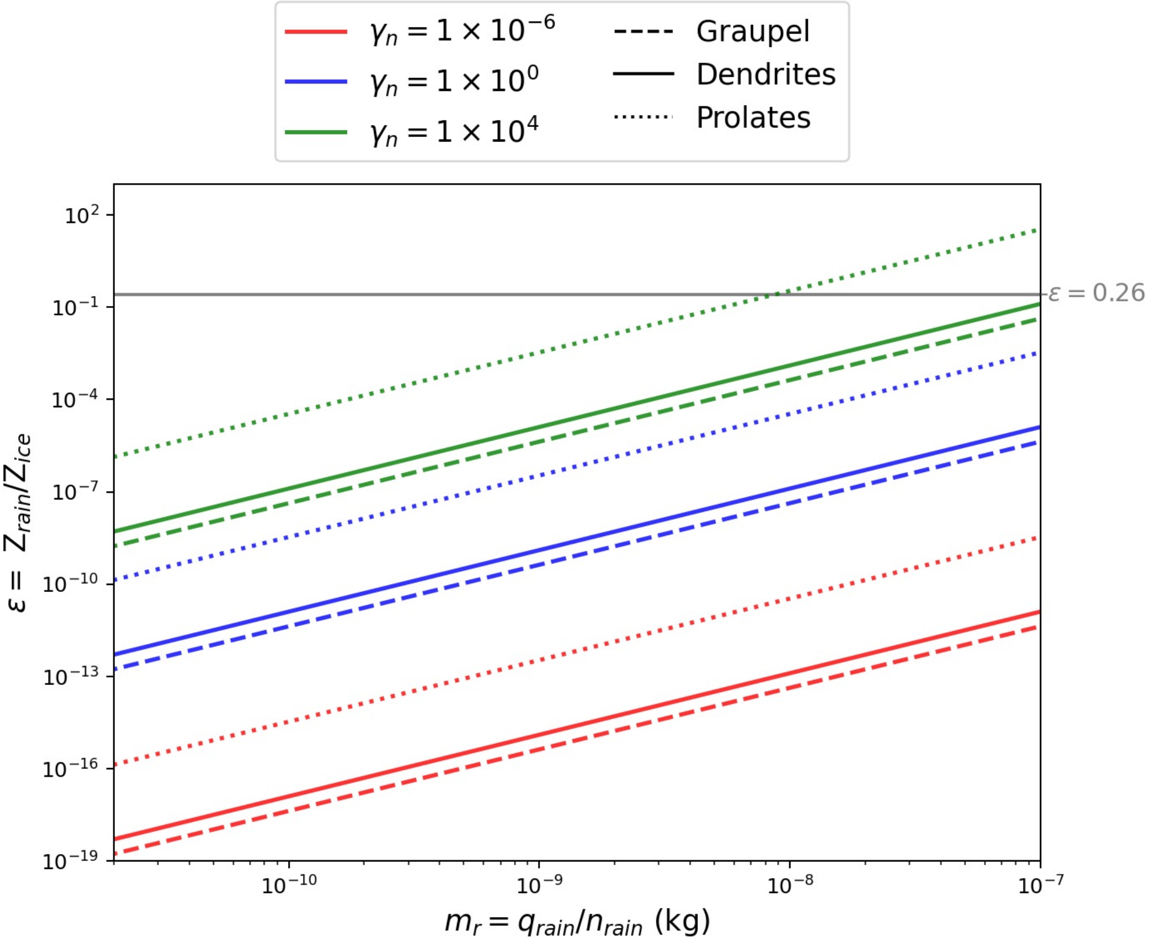

Figure 6.15. Plot of the ratio of reflectivity components in ISHMAEL $\varepsilon = Z_{\text{rain}}/Z_{\text{ice}}$. The log (base 10) of the summation of components $Z_{\text{rain}} + Z_{\text{ice}}$ is equal to the reflectivity on the dBZ scale. ε is plotted versus the ratio of raindrop number to ice crystal number, across three scenarios: Dendrites ($\delta_* = 0.6$, $\bar{\rho} = 100$), Graupel ($\delta_* = 1$, $\bar{\rho} = 400$) and needles ($\delta_* = 1.3$, $\bar{\rho} = 900$) in columns 1–3, respectively. In each case, the ratio ε is plotted for several values of its parameters rain mass mixing ratio q_r (kg kg^{-1}) and ice characteristic radius a_{ni} (m) specified in the Figure legend. Inflection points of the y and x-axis ratios are shown with grey lines.

The range of possible scenarios in which the mixed-phase component of reflectivity is significant are examined in Figure 6.15. The ε function is shown for the aforementioned ranges of average rain droplet mass m_r (x-axis) and for several values of γ_n (shaded). Dendrites, graupel, and prolates (solid, dashed and dotted lines, respectively) are plotted to understand the enhancement of the mixed-phase due to particle geometry. The boundary of $\varepsilon = 0.26$ (at which point $10\log_{10}(\varepsilon + 1) > 1$ dBZ) is shown in grey for reference.

In these specific hydrometeor cases, ε does not exceed 0.26 with the exception of prolate ice that is collocated with large ($m_r > 1 \times 10^{-8}$ kg) raindrops that outnumber ice crystals by a factor of $\gamma_n = 1 \times 10^4$. The contribution of term B (see Equation 6.8) is therefore negligible for dendrites and graupel, even when γ_n and m_r are large. ε decreases with reducing rain drop size, and droplet number relative to ice, and for any given γ_n graupel exhibits the lowest ε.

Though Figure 6.15 indicates that ε will produce negligible reflectivity for the majority of the hydrometeors and mixing ratios explored here, this result is not necessarily representative of the entire simulated precipitation field in this case, nor the possible fields in other cases. For example, larger m_r and γ_n are possible, and would each increase ε. Similarly, higher density and smaller ices are possible than the hydrometeor types explored here, each of which would also increase ε considerably. For example, Figure 6.13 shows that large gains in magnitude of the factor F are achieved with only a small decrease in characteristic ice radius. Likewise, increasing the density of large ices, such as graupel or snow via melting and wet growth, would provide an increase in ε.

Overall Characterisation of Reflectivity

Here we complete the analysis by investigating ε amongst the broader context of the total reflectivity field Z for the case of prolate crystals, which were most associated with high reflectivity in the mixed-phase. Similar analysis has been conducted for both dendrites and graupel and is available in Appendix M. To obtain Z_{ice}, the ice number concentration n_i must be specified (see Equation H.3). To maintain consistency with m_r and n_i, γ_n is calculated like so:

$$\gamma_n = \frac{n_r}{n_i} = \frac{q_r}{n_i m_r}$$

which requires that q_r is supplied. This is more convenient as $Z \sim Z(q_r, n_i, m_r)$ depends on the mass of droplets, number of crystals, and average rain drop mass per cell which are more simple to interpret physically than γ_n. These variables are also readily retrieved from the simulation output to appropriately constrain Z to realistic values.

Figure 6.16 plots the total reflectivity function $Z(\delta_*, \bar{\rho}_i, a_{\text{ni}}, m_r, q_r, n_i)$ and its components, A (dashed) and B (dotted) for the prolates hydrometeor profile ($\delta_* = 1.3$, $\bar{\rho}_i = 900$). Columns 1–3 span three ice number concentrations n_i (kg^{-1}); 1×10^5, 1×10^2, 1×10^-1, respectively, and rows 1–3 span three values of the rain mass mixing ratio q_r (kg kg^{-1}): 1×10^{-8}, 1×10^{-4}, 1×10^{-2}. The values of n_i and q_r were determined from the range of each quantity produced during the simulation. The total reflectivity is plotted for two values of characteristic radius a_{ni} (m): 1×10^{-4} (blue) and 1×10^{-5} (red).

Figure 6.16 shows that total reflectivity was close to or less than zero for almost all combinations of rain mass and ice number. However, the largest reflectivity signature was apparent in panel 1 (row 1, column 1) where rain mass was lowest and ice number was greatest. The general tendency of increasing rain mass mixing ratios was to elevate the mixed-phase component of reflectivity ε and to reduce the required rain mass threshold to achieve non-negligible reflectivity. In comparison, as the ice number concentration increased the rain mass threshold increased considerably. This result reiterates the importance of ice for the determination of reflectivity in the ISHMAEL scheme. When ice number is large, the total reflectivity is approximately equal to the component of Z_{ice} only, and the contribution of the mixed-phase is negligible, even when rain drop mass mixing ratio is very high.

The mixed-phase component (dotted) began to influence the total reflectivity when ice number was reduced and the mass mixing ratio of droplets became high. The onset of the increased $B(\varepsilon)$ is related to the typical mass of rain droplets, such that when q_r is smaller, the average rain drop mass must be larger, and when q_r is larger, the average rain drop mass can be less to produce a non-negligible mixed-phase reflectivity component. Consequently, the mixed-phase component affects the total reflectivity (translucent) in environments with few crystals, and more so with larger raindrops, and larger total raindrop mass. However, comparison of the total reflectivity (translucent) shows that even though the mixed-phase contribution increases with decreasing crystal number, the additive effect of the mixed-phase $B(\varepsilon)$ is outweighed by the negative effect of the decreasing $A(Z_{\text{ice}})$ component and so, in total, reflectivity reduces at low crystal number overall.

Comparison of Figure 6.16 and other precipitation types (Appendix M) shows that large dendrites that occur in large number concentrations will produce the greatest possible reflectivity, regardless of the presence of rain. Whereas the smallest reflectivity is produced by low concentrations of small, high density crystals with minimal rain. The $A(Z_{\text{ice}})$ component of reflectivity is largest for dendrites, then graupel and smallest for prolates and the onset of the non-negligible mixed-phase (dotted) contribution is apparent at lower average droplet mass (m_r) per q_r. In combination, this indicates that smaller and more dense crystals exhibit less influence over the reflectivity field, and so the mixed-phase contribution is relatively more influential to these crystal types.

It is important to remember that the highest reflectivity is linked not only to the values of the aforementioned variables, but to the likelihood of their occurrence. For example, it is unlikely that very large number concentrations of very large dendrites will exist, and rather, more numerous, small dendrites or fewer large dendrites are two more likely scenarios. Examination of these cases in Figure M.1 shows that they would produce a small reflectivity signature. Similarly, cloud ice crystals are likely to occur in greater number concentrations, but are limited by their small size, producing relatively small ($\sim$ 20 dBZ) reflectivity even at high n_i. Therefore, the high reflectivity scenario of interest is actually graupel, which is capable of reaching large radial sizes and number concentrations simultaneously.

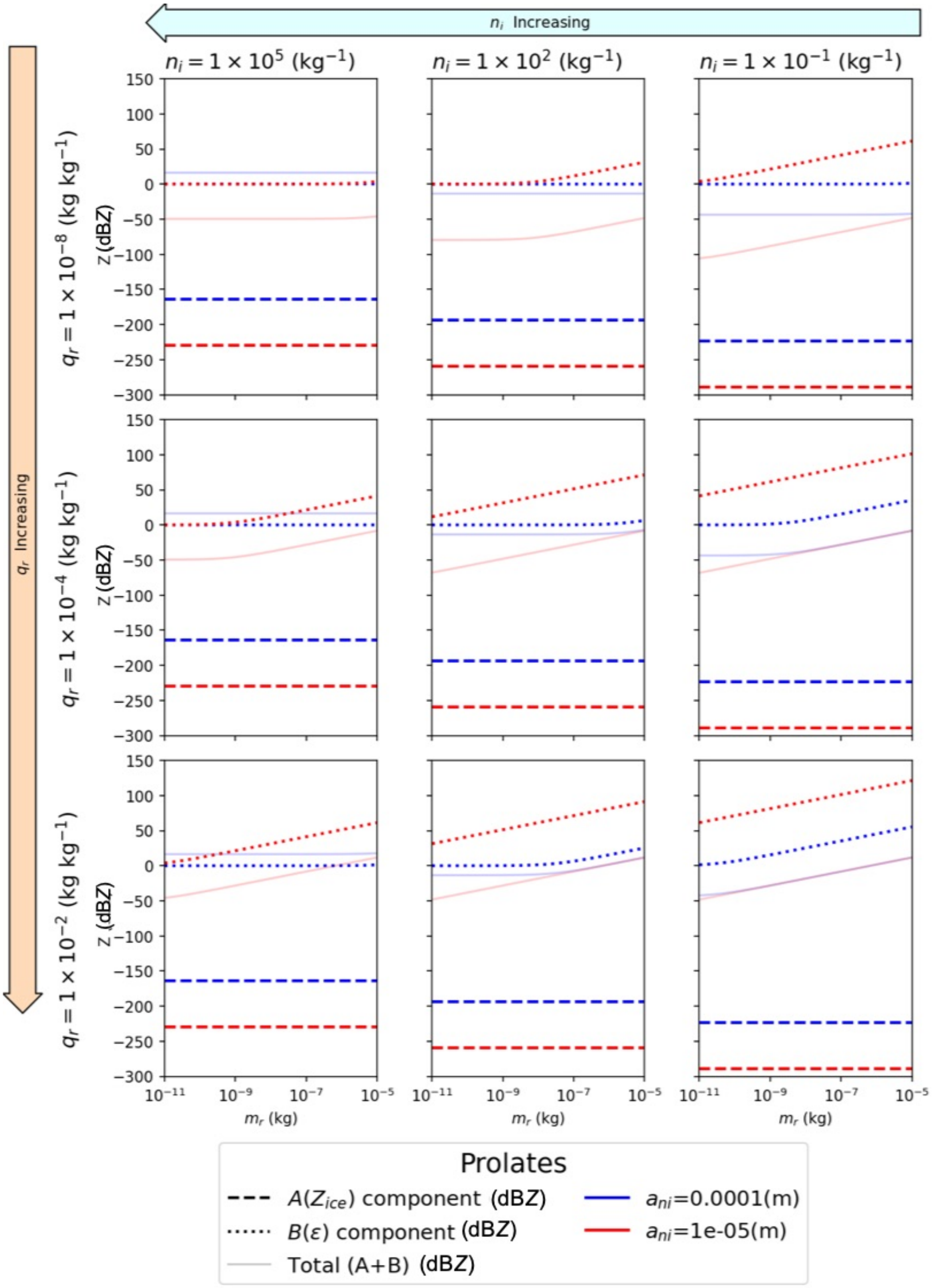

Figure 6.16. Reflectivity components A and B (see Equation 6.8) and their summation (multiplied by 10) the total reflectivity Z_{total} (dBZ) versus the average rain droplet mass m_r (kg) for prolates ($\delta_* = 1.3$, $\bar{\rho} = 900$. Terms A, B and the total are shown by dashed, dotted, and translucent lines. Components are plotted for three values of the ice number concentration n_i (kg^{-1}): 1×10^5, 1×10^2, 1×10^{-1} in columns 1–3, respectively, and three values of ice mass mixing ratio q_r (kg kg^{-1}): 1×10^{-8}, 1×10^{-4}, 1×10^{-2} in rows 1–3, respectively.

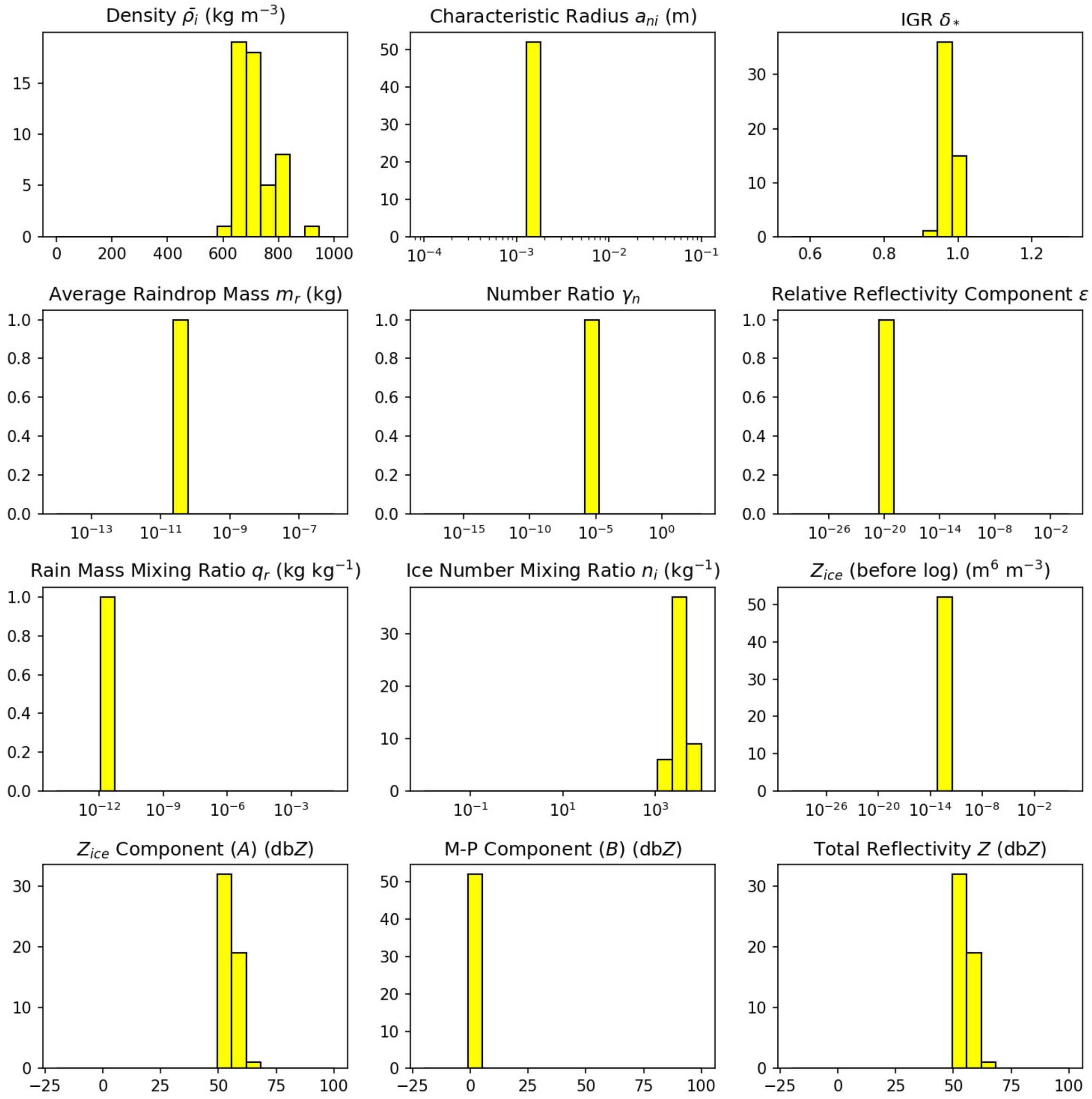

Figure 6.17. Histograms of reflectivity dependencies in the ISHMAEL scheme. Each dependency type is titled per panel

To conclude, we examine the types of precipitation found in the very high reflectivity spots in Figure 6.7 to see if they corroborate the findings of this functional analysis. Figure 6.17 shows a collection of histograms for precipitation qualities taken from the cells that exhibited > 50 dBZ reflectivity in localised areas. Row 1 (columns 1–3, respectively) shows the frozen hydrometeor characteristics of these cells; density $\bar{\rho}_i$, characteristic radius a_{ni}, and the inherent growth ratio δ_*. Row 2 shows the additional variables required to specify the contribution of the mixed-phase reflectivity component ε; the average rain drop mass m_r, and ratio of rain number to ice number γ_n (columns 1–2); ε is shown in column 3. Row 3 shows the additional variables required to specify the contribution of the ice reflectivity component Z_{ice}; raindrop mass mixing ratio q_r and ice number mixing ratio n_r (columns 1–2); Z_{ice} is shown in column 3. Row 4 shows the components of the total reflectivity due to ice $A(Z_{\text{ice}})$, and due to the mixed-phase $B(\varepsilon)$ (columns 1–2); the total reflectivity is shown in column 3.

Figure 6.17 row 1 columns 1–3 shows that, within the very small, high-reflectivity hot spots seen in Figure 6.7, precipitation has moderate to high density, a relatively large ($\sim$ mm) radius, and an aspect ratio that is near-spherical. These qualities are consistent with graupel or possibly hail. Rows 2–3 columns 1–2 show that these cells contained small (low mass) raindrops with low total combined mass, whereas the ice number was very high ($\sim\ 10^3$ kg^{-1}). The number ratio of rain droplets to ice crystals was therefore very low, which resulted in a similarly low mixed-phase reflectivity ratio ε but a large Z_{ice} component to the reflectivity. This is evidenced in row 4, where the total reflectivity is very large and the mixed-phase component negligible, thus the total reflectivity was entirely due to the contribution of the ice. It is deduced then, that small reflectivity patches in Figure 6.7 are locations of intense riming or melting of crystal populations that are high in number concentration. Both of these processes produce the ice characteristics observed in Figure 6.17 row 1, though the very low rain mass implies that riming is present, which reduces the rain mass mixing ratio rather than melting, which increases the rain mass mixing ratio.

P3 Reflectivity Formulation

In the P3 scheme, the reflectivity is derived from the sixth moment of the distribution (see Appendix I) to produce an identical formulation of reflectivity as in ISHMAEL:

$$Z = 10\log_{10}\left(1\times10^{18}\right) + \underbrace{10\log_{10}\left(Z_{\text{ice}}\right)}_{\text{A (ice)}} + \underbrace{10\log_{10}\left(\varepsilon+1\right)}_{\text{B (Mixed-Phase)}} \tag{6.15}$$

Where $Z_{\text{ice}} > 0$ is the combined ice reflectivity component and $\varepsilon = \frac{Z_{\text{rain}}}{Z_{\text{ice}}}$ is the enhancement due to the mixed-phase as in Equation 6.8. As in our previous analysis, $Z_{\text{ice}}(r, n_i, q_i, F_r, \rho_i)$ and $\varepsilon(r, n_i, q_i, F_r, \rho_i, n_r, q_r)$ may be simplified by specifying the average ice mass $m_i = q_i/n_i$ and average rain mass $m_r = q_r/n_r$ and continuing our analysis across hydrometeor profiles with fixed rime fraction F_r and density ρ_i as given in Table 6.2.

Type	Density $\bar{\rho}_i$ (kg m^3)	Rime Fraction F_r
Unrimed Snow	100	0
Rimed Snow	400	0.667
Graupel	600	1

Table 6.2. Characteristic density (kg m^3) and rime fraction F_r for three characteristic precipitation-type profiles in the P3 scheme.

Figure 6.18 plots the mixed-phase term ε versus ice particle radius for three hydrometeor types: unrimed snow, rimed snow, and graupel (see Table 6.2), in rows 1–3, respectively. The value of ε is varied across three values of the average ice particle mass m_r (columns 1–3) and four values of raindrop mass m_r (shaded). Finally, three ice and rain mass mixing ratio scenarios are considered (solid, dotted and dashed). The total reflectivity in Equation 6.15) has non-negligible mixed-phase component when $\varepsilon > 10^1$ (shown in grey).

For all three hydrometeor types considered in Figure 6.18, the reflectivity enhancement by the mixed-phase is non-negligible (above grey line) when ice particle radius is small, when rain droplets and ice particles are heavy, and when the ice and rain mass mixing ratio is large. It is evident that the negative relationship between ε and ice radius begins to break down for very large (r 10^{-2}) particles that are heavily rimed (i.e. graupel). This becomes significant at large average ice mass, enabling large graupel particles to contribute to the reflectivity when unrimed snow of the same mass would not. Thus, rimed fraction is a key factor in the enhancement of reflectivity in P3.The mixed-phase may contribute a comparable or larger component of the total reflectivity for cells where large populations of heavy rain drops occur (i.e. in intense rain or melting). From these findings, it is likely that regions with riming or melting processes are highly reflective in the P3 scheme, particularly when they are seeded by intense (high number concentration) and large (mass) rain and ice particles.

To determine the consequences of the mixed-phase and ice component of reflectivity in combination, these components and the total reflectivity are shown in Figure 6.19. Here we consider only graupel, the most likely hydrometeor to be present in heavy riming environments, which were shown to enhance the reflectivity (see Figure 6.18). The total reflectivity was varied across; three average ice mass m_i values 1×10^{-10}, 1×10^{-8}, 1×10^{-6} kg in columns 1–3, respectively, and three average rain mass m_r values: 1×10^{-10}, 1×10^{-6}, 1×10^{-4} kg in rows 1–3, respectively. Three rain and ice mass mixing ratios were considered (solid, dashed, dotted) as in Figure 6.18. The ice component (A), mixed-phase component (B) and the total reflectivity were shown in blue, red and black, respectively. Note that total reflectivity analysis for dendrites and rimed snow are also available in Appendix N.

The highest total reflectivity (black) was generated for graupel particles with small average mass (column 1) but high mass mixing ratios which implies large number concentrations. Furthermore, ice radius was large which, in combination with low particle mass, indicates that ice density was very low. Larger ice mass mixing ratios (i.e. solid or dashed) provided a slight enhancement when ice radius was large, but as average ice crystal size reduced the average rain mass (row) and mass mixing ratio became the most influential factors for reflectivity. Large rain droplets produced very high reflectivity values independent of the ice field qualities.

It is interesting to compare the reflectivity components originating from the ice (blue) and

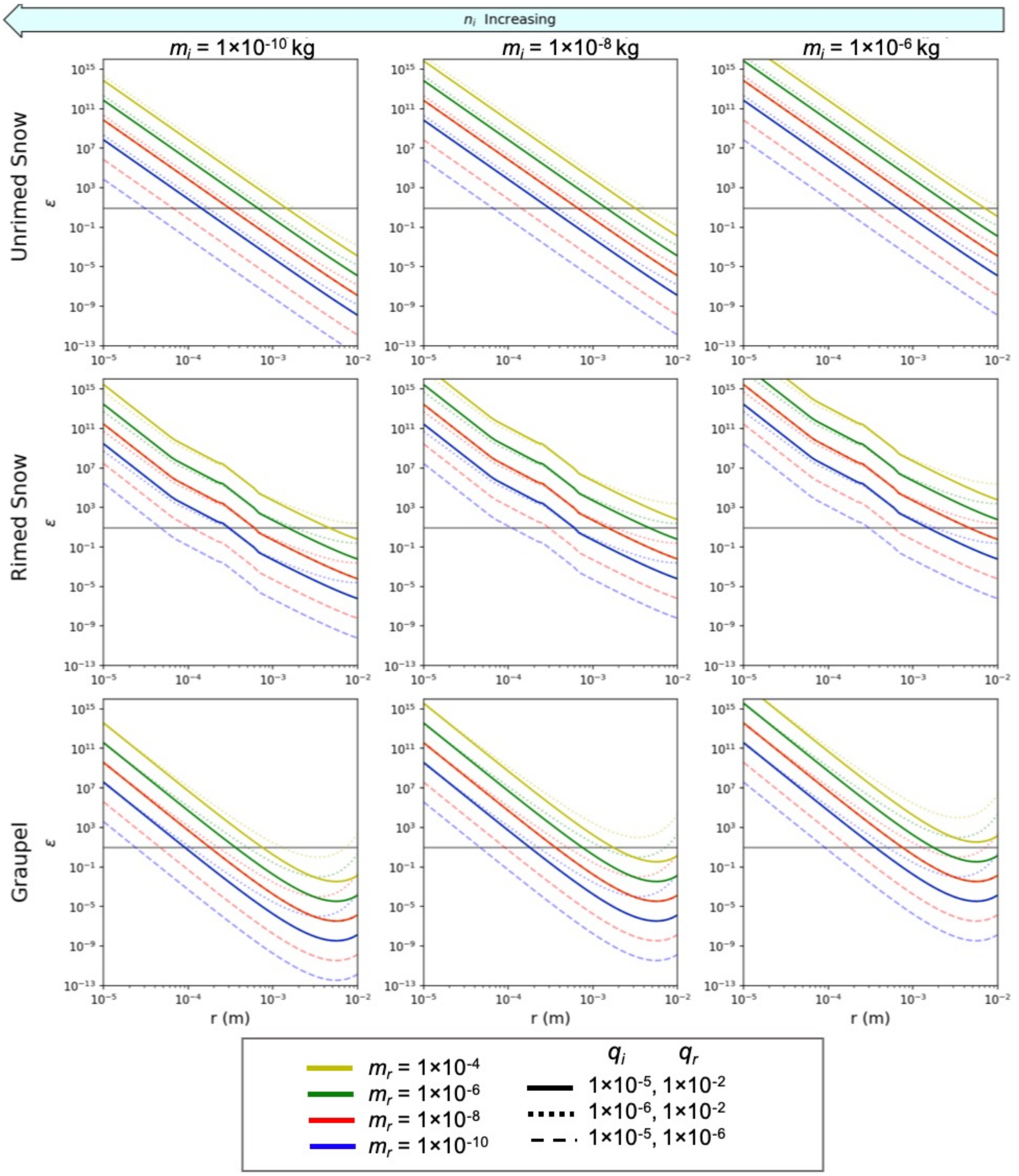

Figure 6.18. Plots of the P3 ε function versus ice particle radius r for three hydrometeor types: unrimed snow ($F_r = 0$, $\rho = 100$), rimed snow ($F_r = 0.667$, $\rho = 400$), and graupel ($F_r = 1$, $\rho = 600$) (rows 1–3) and three ice mass m_i values 1×10^{-10}, 1×10^{-8}, 1×10^{-6} (columns 1–3). ε is shown for four average rain mass (m_r) values; 1×10^{-4} (yellow), 1×10^{-6} (green), 1×10^{-8} (red), 1×10^{-10} (blue). Three fixed values of ice mass and rain mass are considered; base state $q_i = 1 \times 10^{-5}, q_r = 1 \times 10^{-2}$, decreased ice $q_i = 1 \times 10^{-6}, q_r = 1 \times 10^{-2}$ and decreased rain $q_i = 1 \times 10^{-5}, q_r = 1 \times 10^{-6}$ shown by solid, dotted, and dashed lines, respectively.

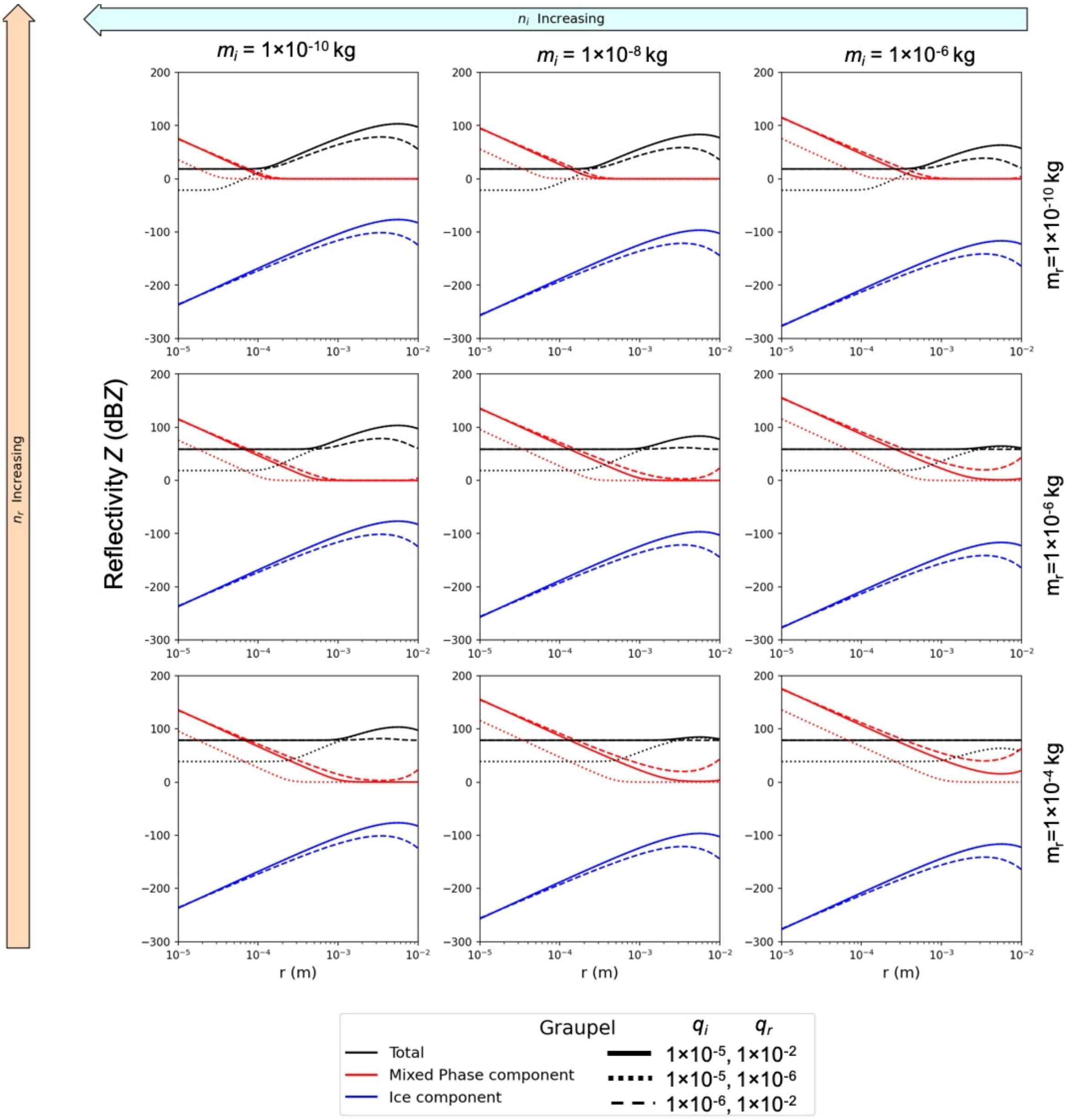

Figure 6.19. Total reflectivity Z (dBZ, black), ice reflectivity component A (dBZ, blue), and mixed-phase reflectivity component B (dBZ, red) as shown in Equation 6.15 versus average ice particle radius r (m) for graupel (see Table 6.2). Average crystal mass $m_i = 1 \times 10^{-10}$, 1×10^{-8}, 1×10^{-6} kg in columns 1–3, respectively. Average raindrop mass $m_r = 1 \times 10^{-10}$, 1×10^{-6}, 1×10^{-4} kg in rows 1–3, respectively. Three sets of fixed ice mass mixing ratio q_i (kg kg^{-1}) and rain mass mixing ratio q_r (kg kg^{-1}) are shown with differing line styles; base state $q_i = 1 \times 10^{-5}$, $q_r = 1 \times 10^{-2}$, decreased ice $q_i = 1 \times 10^{-6}$, $q_r = 1 \times 10^{-2}$ and decreased rain $q_i = 1 \times 10^{-5}$, $q_r = 1 \times 10^{-6}$ shown by solid, dashed, and dotted lines, respectively.

the mixed-phase (red) components, as these were often in direct opposition. The ice phase component was consistently negative (subtraction from the leading constant in Equation 6.15), so reflectivity increased most when the absolute value became small. In contrast, the mixed-phase component was positive, so contributed an enhancement of the reflectivity field. Interestingly, there was an inverse relationship between ice and mixed-phase components, so the peak total reflectivity was obtained when the absolute value of both components became very small. The only role of the mixed-phase component was to obtain any reflectivity at all when ice radius was small, but overall the mixed-phase was not a direct, influential factor when obtaining peak reflectivity in the P3 scheme. Overall, the greatest reflectivity was obtained when large raindrops or high concentrations of large graupel were found, but the overlap of both simultaneously was not an important factor.

Overall, there are two mutually exclusive environments that P3 predicts will be most reflective. The first will contain high concentrations of large graupel particles with low average mass. Thus, a reasonable scenario is one in which high ice crystal concentrations are subject to low density riming, producing a graupel population with a high reflectivity signature. The second, more-flexible environment has numerous large raindrops, which is indicative of intense rainfall originating from prolonged efficient coalescence, such as in convective updrafts. In the context of the reflectivity distribution seen in Figure 6.1, these two scenarios may explain the very high-reflectivity bright band over Long Island. For example, the transitional band was situated where elevated and intense riming were present, which might enhance the radar reflectivity signature. Furthermore, the unobserved high reflectivity region that was predicted south of Long Island coincided with a region of heavy rainfall, which the P3 scheme perceives as high reflectivity even in the absence of ice.

6.3.3 Application of a Liquid-Skin Parameterisation to the Morrison Simulated Reflectivity Field

The production of high reflectivity bands during phases one and two, was highly dependent on the presence of liquid coated precipitation. Here we examine the use of a non-default option in the wrf-python `getvar` routine that accounts for liquid coated hydrometeors. Note that P3 has no liquid skin, so the effects of wet ice on reflectivity are not included in the model. Therefore, it is not able to produce the distinct bright band just below the freezing level (4 km) seen in the observations (Morrison et al. 2015).

The reflectivity component per hydrometeor is calculated by the `getvar` routine as shown in Equation G.1, in which the frozen components (graupel and snow) are multiplied by a leading constant $\alpha_{\odot} = 0.224$ that arises in frozen precipitation only. To account for a liquid surface, when liquid skin is turned on alpha is removed from the frozen hydrometeor formulation. This brings it in line with the reflectivity component of liquid water, with some additional density factors. Discrimination between normal and liquid-coated frozen precipitation is achieved by selectively removing α for cells that have a warm (T > 0°C) ambient temperature.

We may determine the effect of this modification analytically by comparing the predicted reflectivity with (Z_2) and without a liquid skin parameterisation (Z_1) across three possible precipitation scenarios: only liquid precipitation, only frozen precipitation, or a combination of both. It is trivial to show that, in scenario 1, cells devoid of frozen precipitation will experience no change in reflectivity (ΔZ = 0) as a consequence of the liquid skin parameterisation.

Scenario 2 considers only frozen hydrometeors so the rain mass mixing ratio and therefore reflectivity component $z_r = 0$:

$$\begin{aligned} Z_1 &= 10\log_{10}(z_s + z_g) \\ Z_2 &= 10\log_{10}\left(\frac{z_s + z_g}{\alpha_\odot}\right), \end{aligned}$$

where z_i is the component of reflectivity for precipitation type i. The mass-mixing ratios of each frozen hydrometeor species, and therefore their reflectivity components, are constant and identical in the liquid skin Z_2 and non liquid skin Z_1 determined reflectivity. Using log rules i.e log$(x/y) =$ log$(x) -$ log(y) Z_2 can be expressed in terms of Z_1:

$$\begin{aligned} Z_2 &= 10\left(\log_{10}\left(z_s + z_g\right) - \log_{10}(\alpha)\right) \\ &= Z_1 - 10\log_{10}(\alpha_\odot) \\ \Delta Z &\approx 6.5 \end{aligned} \tag{6.16}$$

Warm (T > 0°C) cells that contain frozen precipitation but no rain will exhibit a change in reflectivity factor due to the inclusion of liquid skin (ΔZ) of approximately 6.5 dBZ.

Scenario 3 considers precipitation mixtures of mixed-phase. Cells that contain rain in addition to frozen mass will experience a less obvious change (ΔZ) due to the inseparability of added quantities in logarithms. To examine ΔZ in this scenario, Z_1 and Z_2 are considered like-for-like in identical cells, that span a range of in-cell combinations of hydrometeor mass-mixing ratios. Consider the non-liquid skin formulation of reflectivity in Equation

G.1. The difference in computed reflectivity ΔZ between the liquid skin and default parameterisation, can be determined by deducting Z_1 from Z_2 as derived in Appendix J:

$$\Delta Z = 10\Bigg[\log_{10}\left(C_r(\omega(1+\delta))^{1.75} + \left(\frac{C_s}{\alpha_\odot} + \frac{C_g}{\alpha_\odot}\delta^{1.75}\right)\right) - \log_{10}\left(C_r(\omega(1+\delta))^{1.75} + \left(C_s + C_g\delta^{1.75}\right)\right)\Bigg], \tag{6.17}$$

where ω is the ratio of liquid to solid precipitation mass. Thus, the mass mixing ratios of any one hydrometeor are not direct factors when determining the additional reflectivity gained by utilising the liquid skin method. Rather, the mass mixing ratios indirectly influence ΔZ through their ratios δ and ω. The limits of Equation 6.17 are evaluated in appendix D, and are shown in Equation D.5:

$$\begin{aligned}
\lim_{\delta\to 0,\omega\to 0} \Delta Z &= 10\log_{10}(n) \approx 6.5\\
\lim_{\delta\to 0,\omega\to \infty} \Delta Z &= 10\log_{10}(1) = 0\\
\lim_{\delta\to \infty,\omega\to 0} \Delta Z &= 10\log_{10}(n) \approx 6.5\\
\lim_{\delta\to \infty,\omega\to \infty} \Delta Z &= 10\log_{10}(1) = 0
\end{aligned} \tag{6.18}$$

The maximum possible gain in reflectivity via the liquid skin method is 6.5 dBZ. This value is typically used for the difference in reflectivity factor between rain and frozen particles of equivalent size. It is apparent that, in this case, the liquid skin method will provide an increase in reflectivity that is insufficient compared to the 15 dBZ increase required to reach the very high reflectivity observed in this case.

In reality, a 15 dBZ increase within a bright band is not uncommon, and is usually associated with dry snow entering a melting layer. When this happens, snow develops a liquid skin that increases the surface density and therefore invokes the $\sim$ 7 dBZ increase that brings it inline with reflectivity of equivalent sized raindrops as described above. However, an additional effect is present that further increase reflectivity, increased aggregation efficiency of liquid-coated snowflakes. Aggregation increases average particle dimension of the wet snow field over the dry snow field, causing a corresponding growth in liquid equivalent size that further enhances the reflectivity by up to 15 dBZ. However, this effect is not seen with `getvar` simulated reflectivity in Morrison.

The formulation of `getvar` simulated reflectivity is limited because it lacks an appreciation of average crystal size within the melting layer. Instead, only the mass mixing ratios are considered, and ΔZ is dependent only on the ratio of precipitation masses (see Equation 6.17). Hence, the maximum increase in ΔZ is capped at 6.5 dBZ, i.e. considering a dimensionless increase due to the change in phase only.

An improvement to the liquid skin parameterisation could be made if average crystal size was considered, but this depends on the microphysics scheme to appropriately increase the size of crystals during aggregation. In Morrison, aggregation is computed using the size-dependent formulation as in Passarelli (1978):

$$n_{\text{agg}} = -\frac{277\rho_a}{\Gamma(7)} E_{\text{II}} A_{\text{sn}} \pi^{\frac{1-B_S}{3}} n_s^{\frac{4-B_s}{3}} \left(\frac{q_s}{\rho_s}\right)^{\frac{2+B_s}{3}} \tag{6.19}$$

Where $E_{\text{II}} = 0.1$ is the collection efficiency of ice-ice collisions, $A_s = 11.72$ $B_s = 0.42$ are constants in the fall-speed-diameter relation for snow. Notably, the collection efficiency, and indeed the entire aggregation tendency, is not temperature dependent and so simulated snow crystal size will not increase in the melting layer (in comparison to background aggregation rates). This is a limitation, not only to the accuracy of the simulated precipitation field, but to derived products that depend on aggregation, such as reflectivity. For example, if the `getvar` computed reflectivity were to consider average crystal size, it would not have been able to fully realise the maximum observed reflectivity because Morrison did not simulate an increase in snow crystal dimension within the melting layer. Therefore, achieving the extreme reflectivity values, such as those observed in this case, will require improvements to the formulation of both aggregation and reflectivity, and will be aided by close integration between the two frameworks.

6.3.4 Comparison to Observations

Despite the inability of the liquid-skin parameterisation to simulate large gains in reflectivity that might be expected, it is still useful to inspect the size and distribution of ΔZ when the liquid skin option is turned on.

Figure 6.20 plots ΔZ versus the ratio of liquid to solid mass ω. An ω range of $0.01 \geq \omega \leq 100$ was selected to best display the variation in ΔZ; a greater range than this is possible during simulations but with near negligible variation in ΔZ. For comparison, the solution for ΔZ when $\delta \to 0$ and $\delta \to \infty$ are shown with dashed and dotted lines, respectively (see Equation D.4). The derivation of these functions is shown in appendix D.

The most important factor to obtain the largest possible ΔZ was ω. Values of ω that were approximately 4×10^{-2} or less produce ΔZ in excess of 6 dBZ regardless of the value of δ, and similarly, values of ω greater than or equal to 4 produced $\Delta Z \approx 0$ for all δ. Therefore, cells that are dominated by frozen precipitation will yield the largest gains as a result of liquid skin consideration. This is not unexpected, cells with a higher proportion of frozen hydrometeors have the most reflectivity to gain by considering frozen precipitation as equivalent sized liquid drops. In contrast, cells that are already dominated by liquid will see the least gain in reflectivity when a small minority of frozen precipitation is treated as a liquid.

Cells that are within the interior region $4 \times 10^{-2} < \omega < 4$ will exhibit a change in reflectivity that is more dependent on δ. Between these values, Figure 6.20 indicates that an envelope of possible ΔZ exist that increase (decrease) with increasing (decreasing) δ, which is in line with observations of very high reflectivity in strong localised updrafts often sustaining wet growth of particles such as hail or graupel. The largest increases to be gained in ΔZ exist at $\omega \approx 0.5$, where the difference in reflectivity can be as high as 2.5 dBZ between the limits of largest and smallest δ. Though not as significant in the determination of ΔZ as ω, this indicates that the liquid skin parameterisation is sensitive to the partitioning of graupel and snow. Cells that are dominated by graupel mass can increase their reflectivity so long as ω is within the appropriate range, and indeed an ideal graupel-driven maximisation exists at $\omega = 0.5$, i.e. a cell that is a mixture of only graupel and rain in which graupel mass is approximately twice the mass of rain.

Overall, the largest gains in reflectivity from the use of the liquid skin parameterisation will occur in cells that are dominated by frozen precipitation and lack rainfall, regardless of the amount of graupel mass. Environments that have little frozen mass will also yield minimal increase in reflectivity, and between these criteria, where the partitioning of liquid and frozen mass is similar in magnitude, the proportion of mass that is graupel will become more important. Given these findings, the simulated reflectivity with and without liquid skin option can be interpreted for the Morrison scheme.

Figure 6.21 plots filled contours of the simulated reflectivity field for Morrison in the lowest 1.5 km layer of domain 3 (as in Figure 6.1) with and without the liquid skin parameterisation turned on. The two-dimensional contours are obtained by retrieving the reflectivity maximum per grid cell within a shallow layer within 1.5 km of the surface. Previous comparisons of simulated reflectivity that included higher vertical levels (see Figure 6.7) generated worse agreement with observations versus the simulated reflectivity in the shallow layer, so the distribution is plotted using simulated reflectivity retrieved from the shallow layer depth only. Columns 1–3 show snapshots of phases 1–3; 2129 UTC, 0030 UTC and 0340 UTC, respectively. These times are equivalent to the times at which observations of reflectivity were taken in Figure 6.1 adapted from Ganetis and Colle (2015).

Figure 6.21 row 1 shows the wrf-python derived reflectivity for the Morrison simulated precipitation field, with liquid-skin option for wet surface particles turned on. Whereas row

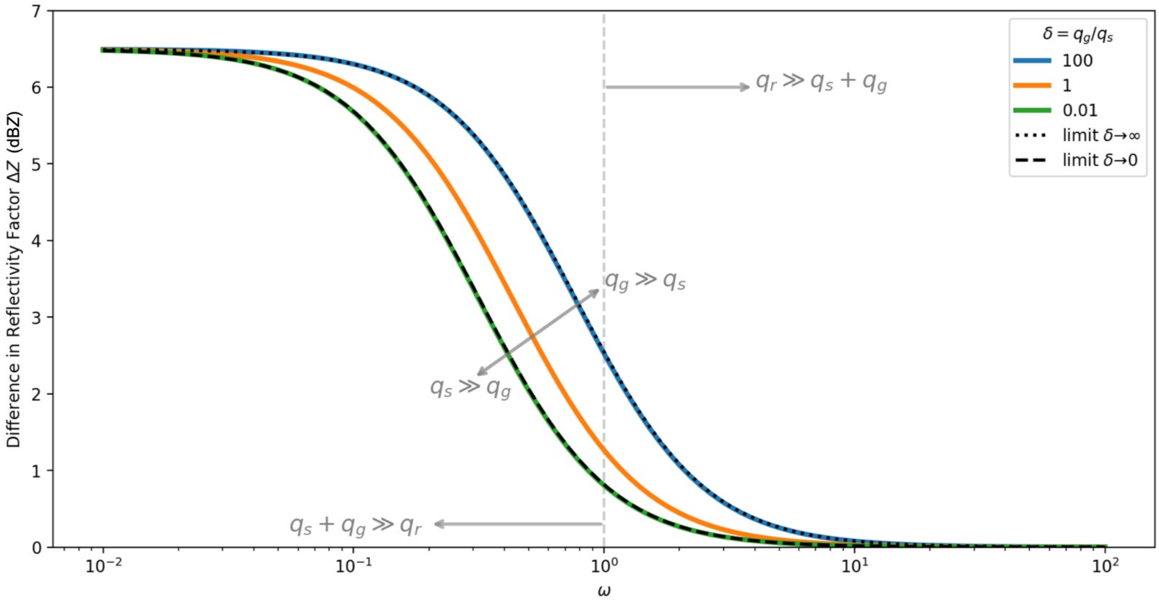

Figure 6.20. Net gain in simulated radar reflectivity factor by inclusion of liquid skin parameterisation over default parameterisation ΔZ. ω is the ratio of rain mass mixing ratio to frozen mass mixing ratio (combined snow and graupel). Plotted for multiple ratios of graupel mass mixing ratio to snow mass mixing ratio δ. i.e. $\delta > 1$ indicates an environment with more graupel mass than snow, $\omega > 1$ indicates an environment with more liquid (rain) mass than frozen mass.

2 shows the reflectivity with liquid skin turned off (default). Without consideration for a liquid skin, the high reflectivity band in phase one was positioned slightly too far south, and oriented north-east as opposed to observations that indicated a more west-east oriented band approximately across Long Island's southern coastline. The peak of simulated reflectivity was also 15 dBZ below the observed maximum at this time. The liquid skin parameterisation provided a small improvement in the orientation of the simulated high-reflectivity band, which occurred further north and was oriented more so from west to east. Peak reflectivity increased in size by approximately 2 dBZ, but more noticeably, moderate reflectivity values of between 30–40 dBZ increased by up to 6.5 dBZ across a large area that encompassed the southern coast.

The changes identified in phase one were also present in phase two. The liquid-skin parameterisation increased the maximum simulated reflectivity factor by 6.5 dBZ, resulting in > 40 dBZ reflectivity factors. The emergence of a very high reflectivity band also signalled a change in the distribution of peak reflectivity during this phase. The high reflectivity band was present in a narrow line to the north of Long Island, and was approximately isolated to the shoreline of the north-eastern U.S. as was observed. Segmentation and fracturing of the high reflectivity band north of Long Island was also apparent, and the difference in orientation of these two sectors of the band became more distinct.

However, despite these improvements, the liquid skin parameterisation did little to improve upon the incorrect characteristics of the overall distribution that had been present in the default case. The non-liquid skin reflectivity field lacked specificity and local variability, particularly in the high reflectivity band where sub structures of high (> 30 dBZ) and very high (> 50 dBZ) reflectivity were observed in close proximity to lower background (< 25 dBZ) reflectivity levels. The inclusion of liquid skin did little to change these characteristics or improve upon them. Rather, the liquid skin parameterisation increased the reflectivity across areas that already overestimated the reflectivity factor, exacerbating the overprediction across much of the U.S. mainland in phases one and two, and particularly south of Long Island in phase two. Elevated (> 30 dBZ) reflectivity covered a much larger area than reflectivity without a liquid skin, which was already larger than observations. This point is most pertinent during phase three, when the observed reflectivity maximum had dropped by 30 dBZ to less than 25 dBZ in observations. Calculated reflectivity failed to capture this drop and overestimated reflectivity across central Long Island but the liquid skin parameterisation only increased both the peak value of reflectivity, and the spatial coverage of elevated reflectivity.

The absolute difference in reflectivity factor ΔZ between the liquid-skin and non-liquid-skin methods is shown in row 3. This quantity was determined by deduction of the full 3-dimensional reflectivity fields and condensed into a two-dimensional filled contour plot using the in-column maximum per grid cell within a shallow, 1.5 km vertical layer as in rows 1–2.

There is minimal variation in the size of ΔZ across the majority of the domain for all three phases. Where a difference in reflectivity was present, the size of the increase was almost always 6.5 dBZ, the maximum possible increase allowed by the liquid skin framework (i.e. Equation 6.16), indicating a strong bias ($\omega \leq 0.04$) in the mass mixing ratio towards frozen hydrometeors in these grid cells (see Figure 6.20). During phase one, the uniform, 6.5 dBZ increase occurred across and north of Long Island, much farther north than the observed bright band at the southern coastline, and similarly in phase two, the 6.5 dBZ uniform increase was across a large area south of Long Island, when observations show the bright band was positioned over central Long Island in a north-south orientation. Therefore, the liquid skin parameterisation enhanced reflectivity outside the expected areas. Interestingly, where enhancement of the reflectivity field was expected based on the approximate position of the observed bright band in phases 1–2, the liquid skin parameterisation actually showed a smaller increase in reflectivity than the surrounding area. These departures from the uniform 6.5 dBZ ΔZ field spanned values of 1–6 dBZ, signalling a more even partition of liquid and frozen precipitation (moderate ω) and implying that graupel may play a role in enhancement of the reflectivity field at these areas.

Row 4 shows the ratio of liquid to solid precipitation ω. Figure 6.20 indicated that ω is the primary determinant for the change in reflectivity that is produced when using the liquid

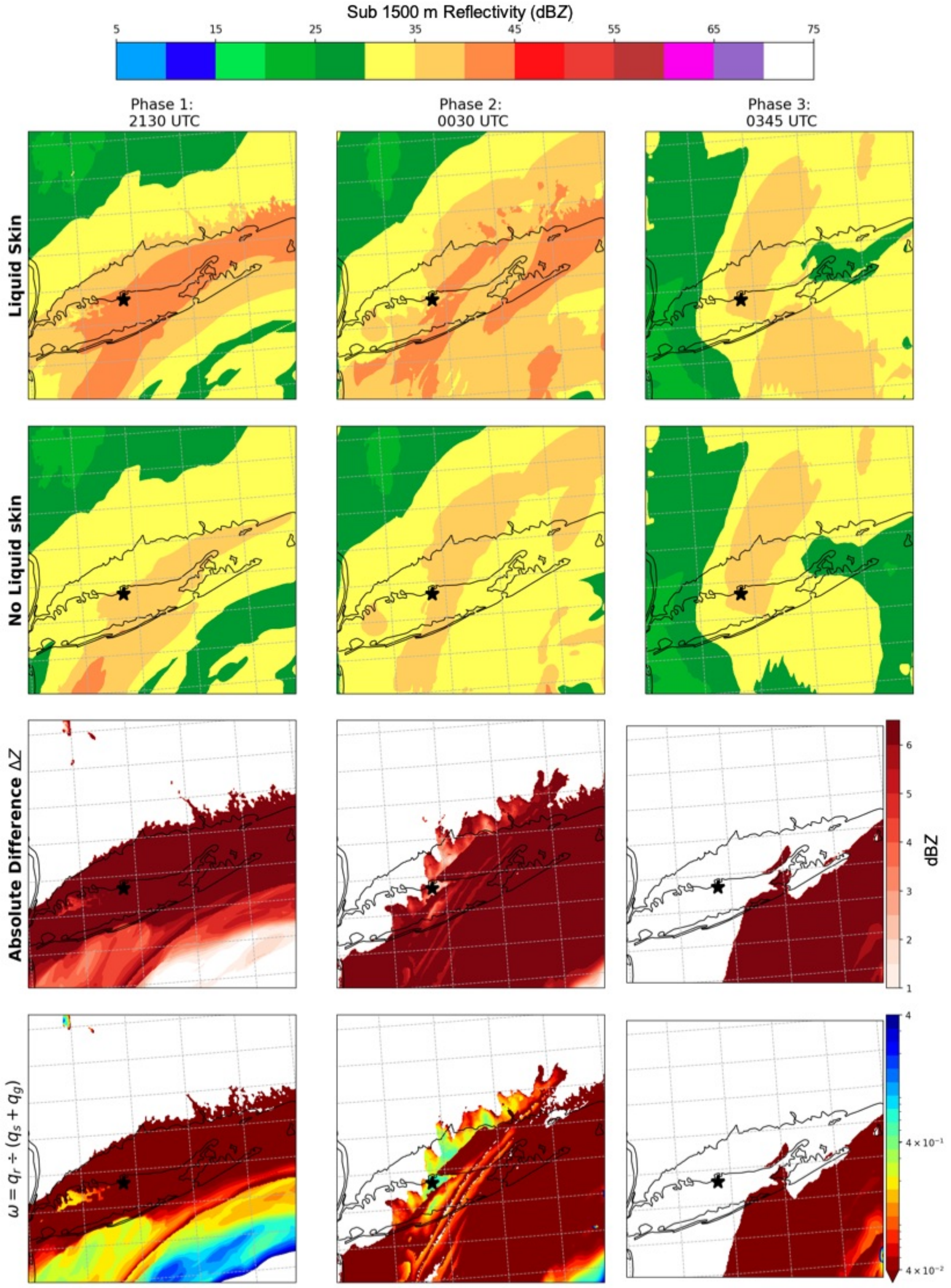
Sub 1500 m Reflectivity (dBZ)
5
15
25
35
45
55
65
75
Phase 1:
2130 UTC
Phase 2:
0030 UTC
Phase 3:
0345 UTC
Liquid Skin
No Liquid skin
Absolute Difference ΔZ
$\omega = q_r \div (q_s + q_g)$
6
5
4
3
2
1
dBZ
4
4 × 10⁻¹
4 × 10⁻²

Figure 6.21. Contours of maximum radar reflectivity factor Z_H (dBZ) at times 2130 UTC (column 1), 0045 UTC (column 2), 0345 UTC (column 3), derived from Morrison simulated precipitation using the wrf-python `getvar` routine (Ladwig 2017). Row 1: Liquid skin calculation turned on. Row 2: Liquid skin calculation turned off (as in Figure 6.1). Row 3: Absolute difference in reflectivity factor between liquid skin options. Contours shaded in rows 1–2 according to top scale. Contours shaded in row 3 according to bottom scale.

skin option. The contour plot of ω shown in row 4 was retrieved from the same cells as the maximum difference ΔZ shown in row 3. The range of contour values spans 4×10^{-2}–4, which are the boundaries of the envelope in which the size of δ becomes influential to ΔZ (see Figure 6.20).

Examination of ω indicates that broad, uniform regions of $\Delta Z = 6.5$ in row 3 are associated with very low ($\leq 4 \times 10^{-2}$) values of ω as expected. For this value of ω, the proportion of frozen mass that is graupel or snow is irrelevant to the final value of ΔZ. The increase in reflectivity identified across broad areas in row 1 therefore derives from copious snowfall and minimal rain in these locations. Regions of comparably smaller ΔZ are shown to occur when ω is equal to, or exceeds 1×10^{-1}, indicating that cells contained a mixture of solid and liquid precipitation types. At this value of ω, the ratio of graupel to snow mass may be significant for the computed reflectivity,. However, analysis of the graupel distribution indicated that $\delta \leq 0.01$ for all phases and therefore provided no increase to the simulated reflectivity in the liquid skin parameterisation.

Overall, Figure 6.21 indicates that the only advantage of the liquid skin parameterisation was to increase the maximum simulated reflectivity, a value that had already been underpredicted compared to observations. However, this increase was applied without precision, affecting large swathes of an already overpredicted reflectivity field. Near uniform increases of 6.5 dBZ resulted from snow dominated grid cells, whereas smaller increases took place in areas of mixed-phase precipitation, including the areas where a high reflectivity band was observed in phases one and two.

The liquid skin parameterisation provides a poor improvement due to the type of precipitation that was associated with the high reflectivity band in this case. Observations showed that the bright band was associated with, but not found within, a melting layer. In actuality, the bright band occurred north-west of both the melting layer reflectivity signature and the subsequent (lower elevation) refreezing signature south of Long Island (Picca et al. 2014). It was evident that peak radar reflectivity likely resulted from a mixture of partially melted and refrozen ices, as well as rain, below a melting layer. Thus, the liquid skin parameterisation, which maximises ΔZ for uniform snow, rather than mixed precipitation, is unable to identify the bright band in the horizontal distribution.

Analysis by Griffin et al. (2014) indicated that very high (> 50 dBZ) reflectivity at the surface was produced by wet (liquid coated) hydrometeors that persisted below the melting layer. Of these hydrometeors, wet snow was present, and there was evidence for the presence of wet-growth hydrometeors. For example, Ganetis et al. (2013) attributed high Z_H to sleet-like hydrometeors that had grown in a convective environment stemming from the presence of the warm layer aloft. Griffin et al. (2014) corroborated this with the identification of a low Z_{DR} region aloft of the bright band that indicated riming and subsequently lead to the depression or descent of the melting layer in this area. If these features are replicated in Morrison, the inclusion of liquid skin might provide a localised bright band at the surface that is enhanced by the presence of graupel (δ). To investigate this the vertical cross section of simulated reflectivity was re-examined with and without the liquid skin option.

Figure 6.22 shows the cross section of `getvar` computed reflectivity along the line A–A' (see Figure 6.2 for each phase of the storm based on the simulated precipitation field by Morrison. Rows 1 and 2 show the simulated reflectivity with and without the liquid skin parameterisation, respectively. As opposed to the horizontal cross section, the reflectivity distribution in the vertical shows some important improvements that bring it more in line with observations when liquid coated particles are considered.

Observations (see Figure 6.3, row 4) indicated that reflectivity was at a maximum very near to the surface (< 1 km) south-east of SBNY at the times shown for phases one and two but these local maxima were not identified in the simulated reflectivity field of the Morrison scheme without liquid skin particles. By including a liquid surface option, an appropriately positioned local maximum is achieved at the surface in phase one, and in phase two, a local maximum is also present at the surface, albeit smaller and further south than was observed.

Examination of the ratio of liquid to mass partition ω (row 4) and the absolute difference ΔZ (row 3) shows that, during phase one, increased peak reflectivity at the surface of approximately 6.5 dBZ originated from low $(\sim\ 1 \times 10^{-2})$ ω within a surface level melting layer. Therefore, cells in this location contained primarily frozen precipitation with minimal rain. Further south-east of Long Island, ω increased with the presence of more rain and or less solid precipitation, resulting in comparatively smaller increases in reflectivity of 3.5 dBZ and above.

Contours of the ratio of graupel to snow mass δ (coloured contour lines- navy (0.1), light blue (0.2), yellow (0.3)) indicated that graupel mass was non-negligible in a narrow region south-east of SBNY between 0 and 4 km from the surface. These contours intersected the surface level ω but did not result in a substantial increase in reflectivity due to the small δ fraction, and low ω, which itself reduced the influence of δ to nil.

A surprising result was the formation of a second bright band aloft ($\sim$2 km) during phase one in the liquid skin calculated reflectivity field. This was not produced when liquid skin was turned off, and similarly was not observed in reality. The band exhibited an increase of $\Delta Z = 6.5$ aloft of SBNY, but smaller ΔZ were present throughout much of the band. The ω field indicated that the south-east section of the bright band exhibited $\omega \approx 0.4$, which coincided with an elevated δ region of > 0.3. In this area, a small region received a moderate (2 dBZ) increase in reflectivity due to the direct effect of δ.

During phase two, the surface level reflectivity to the immediate south-east of SBNY remained elevated but across a smaller area than in phase one, whilst the melting layer aloft had descended and connected to the surface. The location of this descent is in the same region as large δ during phase one, implying that the descent of the melting layer was related to faster falling rimed particles descending through it. In this case, the inclusion of the liquid skin parameterisation is shown to be advantageous for the determination of reflectivity at the surface as well as the identification of a melting layer depression.

6.3.5 Discussion

Analysis of the liquid skin derived reflectivity implies that a consideration of liquid skin is required to achieve the very high peaks in reflectivity that are found in this case, but that the implementation of this parameterisation may require some modification if it is to achieve the observed maximum in the correct position.

Some small benefits were apparent, such as an increase to the predicted maximum reflectivity, which was sorely underpredicted without liquid skin. However, the distribution of these maxima had mixed success, in the vertical a surface level increase in line with observations was achieved, but an additional simulated bright band aloft was not apparent in observations. Similarly, top-down filled contours of reflectivity across domain 3 showed small increases in reflectivity in the location of the observed bright band, but showed much larger increases outside of the observed bright band across broad areas. The liquid skin parameterisation generally exacerbated the wide-scale overprediction of the background reflectivity field in areas of high snow mass, and underpredicted gains in mixed-phase areas.

The internal framework of the liquid skin option could be improved on several fronts. For example, the framework lacks an appreciation of particle size, which is likely to be an important factor to obtaining the very highest reflectivity in melting layers due to the enhanced aggregation of liquid skin particles. Additionally, the framework is applied only within the melting layer, and so lacks an appreciation of liquid skin particles in cooler sub layers. Not only does this fail to capture potential high reflectivity zones, but it also produces a sudden sub melting layer drop in the simulated reflectivity field that is unrealistic in this case.

As a post-processing tool, the `getvar` routine is limited by the accuracy, and output fields, of the microphysics scheme. In this case, it was shown that an appreciation of hydrometeor size would not have improved the liquid-skin simulated reflectivity, as the Morrison scheme did not incorporate a temperature dependent aggregation coefficient. This motivates the closer integration of reflectivity to microphysics schemes, where a liquid-skin parameterisation can be made consistent with the microphysical processes that are being calculated. This would also allow for constants, such as hydrometeor densities, to match those of the microphysics scheme.

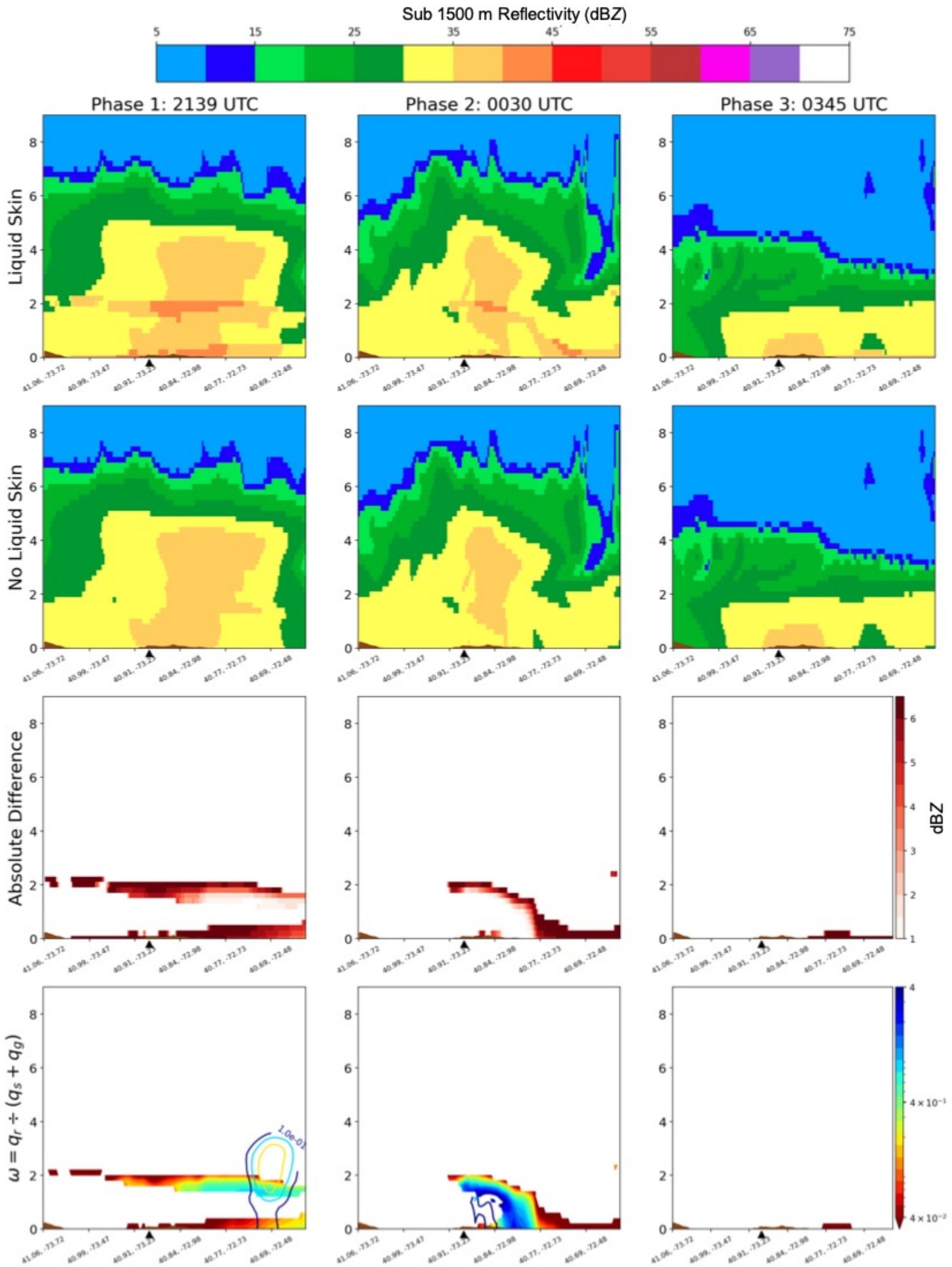

Figure 6.22. Contours of simulated reflectivity factor Z_H (dBZ) in vertical cross section along line A to A' (see Figure 6.2) at times 2130 UTC (column 1), 0045 UTC (column 2), 0345 UTC (column 3), derived from Morrison simulated precipitation using the wrf-python `getvar` routine (Ladwig 2017). Row 1: Liquid skin calculation turned on. Row 2: Liquid skin calculation turned off (as in Figure 6.1). Row 3: Absolute difference in reflectivity factor between liquid skin options. Contours shaded in rows 1–2 according to top scale. Contours shaded in row 3 according to bottom scale. Position of SBNY along the cross section is indicated by black arrow below the x-axis.

More broadly, the `getvar` routine must accommodate a range of potential microphysics schemes beyond Morrison, each with stark differences in output fields and process parameterisation. Clearly, the relatively simple parameterisation of liquid skin is chosen to remain as flexible as possible across multiple schemes. However, here we argue that such broad flexibility is not only poorly integrated but may also be misleading and dangerous. The post-processing routine will output a simulated reflectivity field regardless of inconsistencies, and its admirable flexibility raises few warnings to end users despite incompatibility, which may lead to users incorrectly interpreting the output as representative. For example, `getvar` will happily retrieve reflectivity for P3 and ISHMAEL, despite both schemes having an integrated reflectivity routine. Schemes such as P3 and ISHMAEL that depart from the categorised hydrometeor framework are entirely incompatible with `getvar`, but without careful consideration of the routine's internals, the end user would be none the wiser. Therefore, users should be vigilant of flexible post processing routines, and developers of microphysics schemes should be motivated to include reflectivity as part of the microphysics scheme's calculations.

6.4 Conclusions on the Simulated Reflectivity

In this chapter, the spatial distribution and magnitude of dual-polarisation radar measurements were compared to the predicted reflectivity field for the ISHMAEL, Morrison, and P3 microphysics schemes. The accuracy of the features of the simulated reflectivity field was mixed, and occasionally quite disappointing. Of all schemes, P3 produced the most reasonable comparison of spatial distribution, and peak reflectivity came within 10 dBZ of observations. Whereas the Morrison scheme produced broad swathes of elevated reflectivity that lacked spatial complexity or specificity, and produced peak reflectivity values more than 15 dBZ below the maximum observed. ISHMAEL reflectivity was reasonably well distributed, but severely underestimated the magnitude of the radar reflectivity. Overall, it was apparent that all schemes lacked key, fine scale features of the observed reflectivity distribution and failed to achieve the very large values of reflectivity that distinguished this storm.

However, a more complex understanding of the reflectivity arose when considering larger portions of the domain. Analysis of the maximum reflectivity produced by each scheme contradicted the notion that ISHMAEL consistently under predicted maximum reflectivity, and instead this scheme in fact produced the largest total reflectivity maxima of all schemes but at the wrong elevation. A review of the vertical distribution of these maxima indicated that they occurred aloft of the observed shallow region that had been used in earlier comparisons. Thus, ISHMAEL did not underestimate reflectivity, rather, it had failed to correctly place the high reflectivity band at a low enough altitude. A review of the horizontal distribution using an elevated maximum vertical level revealed an interesting display of small, high-reflectivity pockets aloft that were not present in other schemes.

An analysis of the precipitation types associated with high reflectivity helped to explain some features of the simulated distribution by each scheme. Morrison produced high reflectivity in cells that contained snow, and were often not associated with the melting layer, perhaps explaining the widespread distribution of reflectivity and lack of local variation in this scheme. However, most highly reflective cells were associated with a collocated mixture of graupel, snow and rain, implying an indirect relation to the process of melting and riming. Having produced a comparatively small amount of graupel to snow, the reflectivity in Morrison was not found to be density dependent, and in fact leaned toward lower density ice on average.

P3 was the least reliant on precipitation collocation to produce high reflectivity regions, and in fact showed the greatest reliance upon rain and water droplets of all schemes. Given the near surface-level height of the reflectivity maxima, the prevalence of the liquid phase and reducing dependence on the melting layer with time, it is likely that P3 high reflectivity cells were highly dependent on melted mass and therefore were tied to the development of the melting layer aloft. High reflectivity found in this scheme at the surface is therefore due not only to the formulation of reflectivity, but the exaggerated melt rate and rapid densification of ice during descent.

ISHMAEL proved highly dependent on the co-location of snow, ice and rain and the greatest reflectivity was found within the melting layer in phase two, when sleet like ice and pellets were produced. However, this is likely a consequence of the relatively large melting layer produced by this scheme which likely resulted in an underestimation of surface level reflectivity, due to the absence of essential frozen hydrometeors that had otherwise melted.

In summary, the origins of high reflectivity in each scheme stem from different factors owed to their unique formulations, no one scheme seems to represent the exact reality of reflectivity that we might expect, demonstrating that there is still much work to be done to constrain reflectivity calculations in models for the purpose of model validation. Reflectivity is often used to infer precipitation or storm features by forecasters who may not be aware of the model (or scheme) internals that produce this variable, and which provide considerable variation before the simulation even begins. It is surprising then that model-derived reflectivity has not been paid more attention, given the prevalence of radar reflectivity in the literature for both model verification and observational analysis,

Chapter 7

Snow Depth, SLR and Density

The storm simulated in this case was notable for its very large accumulated snow depth that exceeded 24 in. (61 cm) across central Long Island and 36 in. (91 cm) at New Haven, CT Krekeler (2013). Snow depth may be viewed as an extension of particularly intense snowfall, but this is an oversimplification of the mechanisms that contribute to large snowfall accumulations, which are dependent on several variables including ground temperature, compaction, ice crystal habit and precipitation density. These are important features of the snowpack that should be considered by microphysics schemes if the total snow accumulation is to be correctly predicted.

Accumulated snow depth is arguably one of the most important variables for end users, from forecasters to the general public. It is amongst the few parameterised variables that directly impact regional infrastructure, energy supply, travel and commerce. Large accumulated snow depths can pose a life threatening situation for the public, and can be financially devastating to local areas, particularly due to overwhelmed irrigation networks, flooding and damage to property. However, these effects can be mitigated with preparatory measures by individuals, businesses and regional governance if they are given enough lead time by weather models. Mitigating actions, whilst essential, are financially costly for governance to implement and may adversely affect local economies in which they are applied, so must be taken only when absolutely necessary. Poor snowfall predictions by numerical models can result in the unnecessary implementation of mitigating actions, or the absence of mitigating actions when they are required. Both scenarios fuel mistrust between the public or regional governance and forecasters which may lead to poor disaster management, wasted finances, or loss of life or livelihood in future events. It is therefore crucial to accurately predict the severity of accumulated snowfall in winter storms.

In this chapter, the forecast accumulated snow height produced by three microphysics schemes is examined for the February 8th north-east U.S. winter storm. The results produced by each scheme are analysed from the reference point of the end user, by considering the mechanisms used to output this variable from the WRF model, and any caveats they may hold. The three microphysics schemes used in this study; ISHMAEL, Morrison and P3, are interesting choices for this study. Morrison is a well established microphysics scheme that uses a conventional categorised framework of the type most likely to be used by operational forecast models. Whereas, P3 and ISHMAEL are based on an emerging particle-properties framework that aims to explicitly simulate precipitation density, which is an important dependency of snowfall depth. In theory, the introduction of variable precipitation density may enable these schemes to better predict snowfall depth overall. However, they operate in a wider framework of land surface schemes that have been built and optimised for the conventional categorised formulations of precipitation. The discussion here will determine both the efficacy of the density predicting schemes in producing snowfall, and the compatibility of these schemes with current model formulations going forwards.

7.1 Preliminary Results

The accumulated snow depth in this case was well documented at the ground. A band of high (> 24 in.) accumulated snowfall was recorded close to the eastern U.S. coastline between Long Island and southwestern Maine and southeastern New Hampshire, spanning Maine's southernmost tip, southern and eastern Massachusetts and the entirety of Connecticut. The depth of snow decreased in concentric bands that decreased in height radially. A large band of > 12 in. snowfall depth was present from northern New Jersey to northern Maine, and shallower bands (> 4 in.) were present further inland. The high snowfall band was associated with the offshore low pressure centre that travelled north-east, and its associated snowbands that extended from the low across the coastal U.S. states. Two regions of exceptionally high (> 36 in.) snow depth were identified in Connecticut, between New Haven and Hartford, and Portland, Maine. Note that, a second area of elevated (> 12 in.) snowfall occurred at Watertown, NY east of lake Ontario that was associated with the eastern path of the northern low.

The sole accumulated snow depth parameter `SNOWH` was retrieved from the WRF model for each microphysics simulated case and contours of the accumulated depth were plotted for the period 0000–0000 UTC 8–9th February. This period is in keeping with the observations of snow depth documented by the National Weather Service (NWS) and frequently cited in the literature (Ganetis and Colle 2015; Griffin et al. 2014; Krekeler 2013; Picca et al. 2014). The observations adapted from Ganetis and Colle (2015) are compared to the simulated snow depth with identical contour levels in Figure 7.1.

Snow depths shown in Figure 7.1 indicate that the predicted snowfall accumulation varied considerably with the choice of microphysics scheme. The simulated distribution of the > 12 in. snow depth band (dark blue) was similar in all schemes, extending no further south than northern New Jersey, in agreement with observations, but further north the simulated

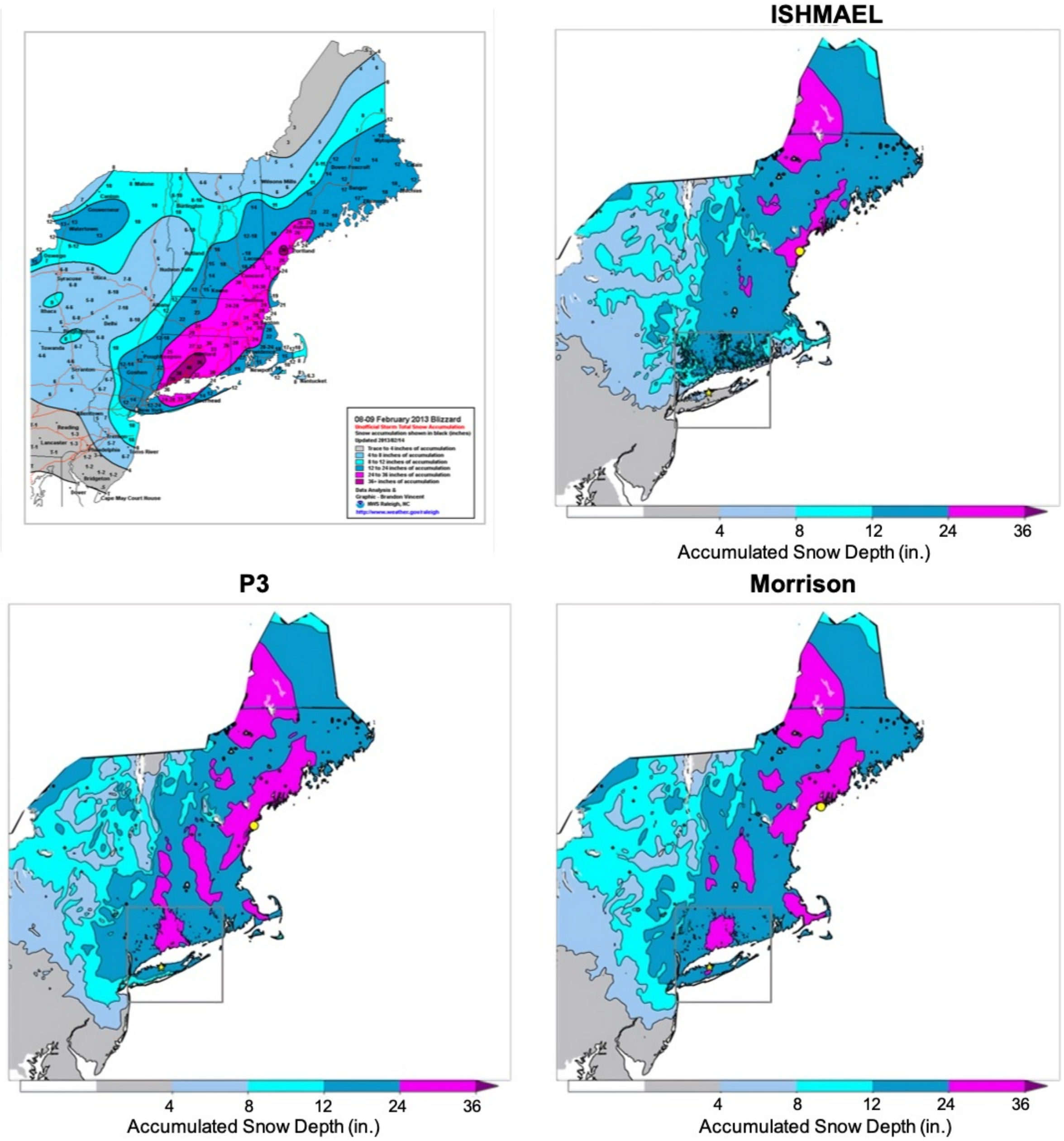
08-09 February 2013 Blizzard
Unofficial Storm Total Snow Accumulation
Snow accumulation shown in black (inches)
Updated 2013/02/14
Trace to 4 inches of accumulation
4 to 8 inches of accumulation
8 to 12 inches of accumulation
12 to 24 inches of accumulation
24 to 36 inches of accumulation
36+ inches of accumulation
Data Analysis &
Graphic - Brandon Vincent
NWS Raleigh, NC
http://www.weather.gov/raleigh
ISHMAEL
4
8
12
24
36
Accumulated Snow Depth (in.)
P3
4
8
12
24
36
Accumulated Snow Depth (in.)
Morrison
4
8
12
24
36
Accumulated Snow Depth (in.)

Figure 7.1. Accumulated snow depth (in.) between 0000–0000 UTC 8–9th February. Observed depth adapted from Ganetis and Colle (2015) (row 1, column 1), ISHMAEL simulated depth (row 1, column 2), P3 simulated depth (row 2, column 1) and Morrison simulated depth (row 2, column 2). Contour levels are equivalent in all sub figures. Location of Stony Brook University (SBNY) indicated by yellow star. Location of the maximum simulated snow depth per microphysics scheme indicated by yellow circle.

band extended further west than was observed, producing an overestimation of snow depth in north-eastern Maine and northwest Vermont. All schemes also overestimated the extent of elevated (> 8 in.) snowfall depth across central Pennsylvania and New York State, where snowfall depth was typically between 4–8 inches in total.

The most notable distinction between the simulated snow depth of all microphysics schemes was the distribution of the > 24 in. (pink) snowfall band that was north-east orientated along the U.S. coast. Morrison and P3 produced a similar patchy distribution of snow depths in excess of 24 inches embedded within the > 12 in. (dark blue) band. These patches included New Haven, CT and a coastal strip over Portland, Maine which were both locations of the highest observed snowfall depths. However, whilst peak reflectivity in all schemes was located near Portland, Maine, the peak simulated accumulated snowfall depth was 31.2, 39.6, 35.3 inches in the ISHMAEL, P3 and Morrison microphysics schemes, respectively, so no scheme was able to replicate the extremely high snow depths observed. In fact, quite unusually, the largest area of high (> 24 in.) snow depth occurred on the border of Maine and Canada, in a location where sub 4 in. snow depths were observed.

ISHMAEL was unique in that it simulated the fewest high-depth (> 24 in.) patches, replicating only the small band at Portland, but in a more narrow distribution than was produced by the Morrison and P3 schemes. The snow depth simulated by ISHMAEL over Long Island diverged considerably from observations, underestimating the snow depth by up to 32 inches, which was most severe underestimation of all schemes. Observations show that Long Island was the base of a transitional mixed-phase precipitation one for several hours of the simulation period, and the considerable difference in this simulated snow depth at this location implies that the scheme's snowfall production was highly sensitive to mixed-phase activity in this case.

The lack of snow over Long Island that was predicted by the ISHMAEL scheme is a significant departure from other schemes. It may be assumed that this difference derived from the microphysics scheme underestimating precipitated mass in this region. To examine the mass falling at the ground, the total liquid equivalent frozen precipitation was retrieved from each scheme and compared. Liquid equivalent is a common metric used to diagnose snow total and can be retrieved using the product of the precipitated mass and the fall speed in the lowest cell:

$$j = q_f \rho_a v_f \text{ (kg m}^{-2}\text{s}^{-1}\text{)}, \tag{7.1}$$

where v_f (m s^{-1}) is the mass weighted fall speed of frozen precipitation, q_f (kg kg^{-1}) is the mass mixing ratio of frozen hydrometeors and the product $q_f \rho_a = Q$ (kg m^{-3}) is the total mass of precipitation per unit volume. Therefore, j (kg m^{-2}s^{-1}) is the total mass flux of precipitation that reaches the surface per second. The total flux (accumulation) over a time period T can be written:

$$J = \int_0^T j \,\mathrm{d}t \tag{7.2}$$

However, we note that for the purpose of examining model output data, we write this as a summation:

$$J = \sum_{i=t}^{T} j(t) \times \Delta t_h \tag{7.3}$$

where Δt_h is the time period between output data points (the WRF *history interval*) in seconds.

The liquid equivalent height of frozen precipitation is the depth of fluid achieved by frozen precipitation if it were melted. Supposing that liquid water disperses evenly, that the surface is flat, and that the cell is rectangular then a mass of water will disperse according to its density:

$$\begin{aligned}
\rho_w &= \frac{m}{V} \\
&= \frac{m}{A \times z} \\
z &= \frac{m}{A\rho_w} \\
&= J\frac{1}{\rho_w} \qquad (7.4)
\end{aligned}$$

Where we have used that mass is conserved between frozen and liquid states. Note that liquid equivalent depth z is often given in units of mm. Taking $\rho_w \approx 1000$ kg m^{-3} this factor is cancelled during conversion, and z (mm) $= J$ (kg m).

The accumulated liquid equivalent precipitation at the surface was retrieved using the method above over the period 0000–0000 UTC 8–10th February for each microphysics scheme, shown in Figure 7.2.

The distribution of liquid equivalent in each scheme was dissimilar to the distribution of the total snowfall depth variable `SNOWH`, but very similar amongst all schemes and was in closer agreement with the distribution of observed snow depth shown in Figure 7.1. For example, all schemes simulated high (> 48 mm) liquid equivalent across Long Island that followed the coastline to the north. The location of very high snowfall depth that was observed

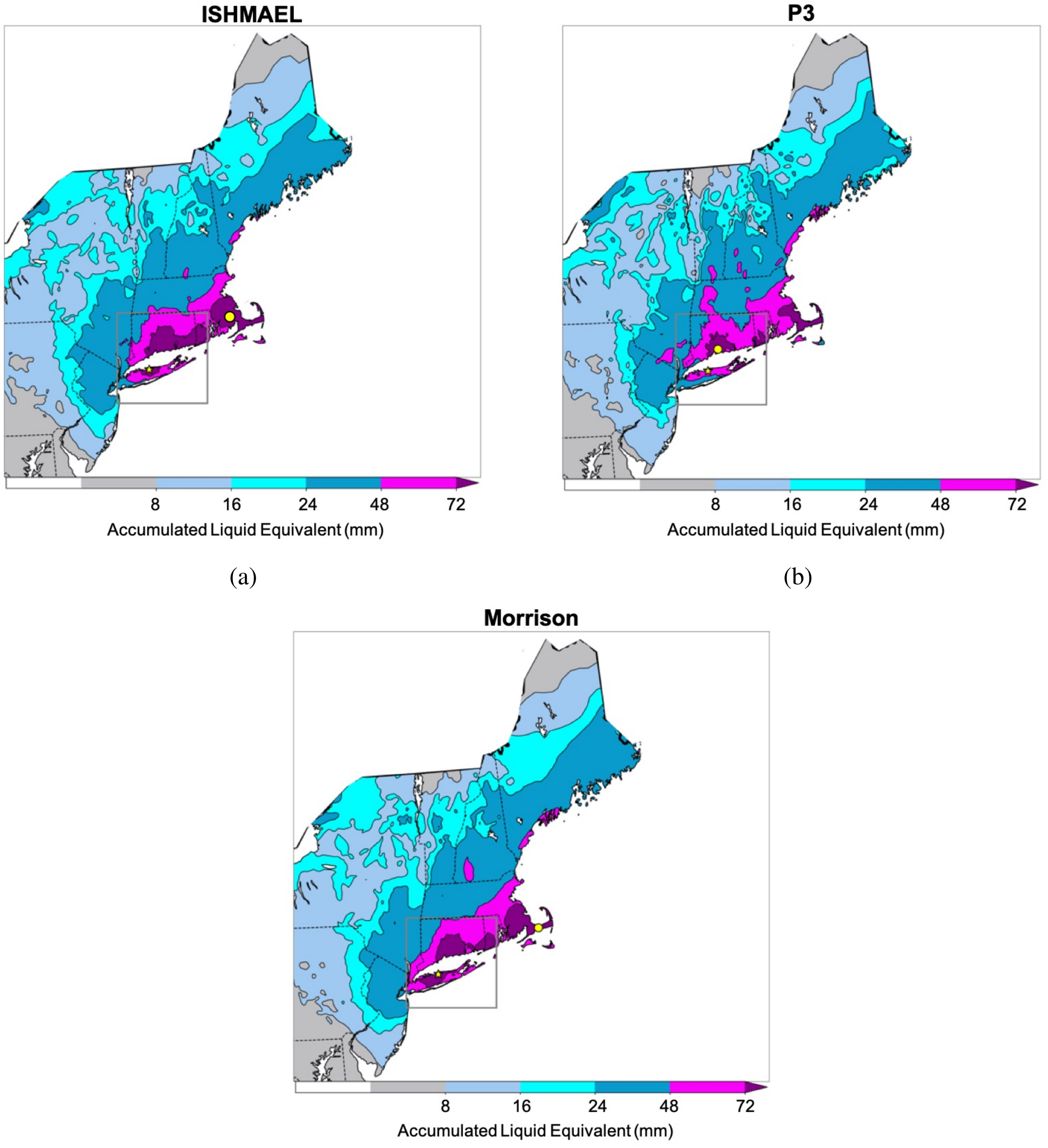
ISHMAEL
8
16
24
48
72
Accumulated Liquid Equivalent (mm)
P3
8
16
24
48
72
Accumulated Liquid Equivalent (mm)
Morrison
8
16
24
48
72
Accumulated Liquid Equivalent (mm)

(a)

(b)

(c)

Figure 7.2. Contours of accumulated liquid equivalent frozen precipitation (mm) between 0000–0000 UTC 8–10th February simulated by ISHMAEL (top left), P3 (top right) and Morrison (bottom) microphysics schemes. Location of Stony Brook University (SBNY) indicated by yellow star. Location of the maximum simulated liquid equivalent per microphysics scheme indicated by yellow circle.

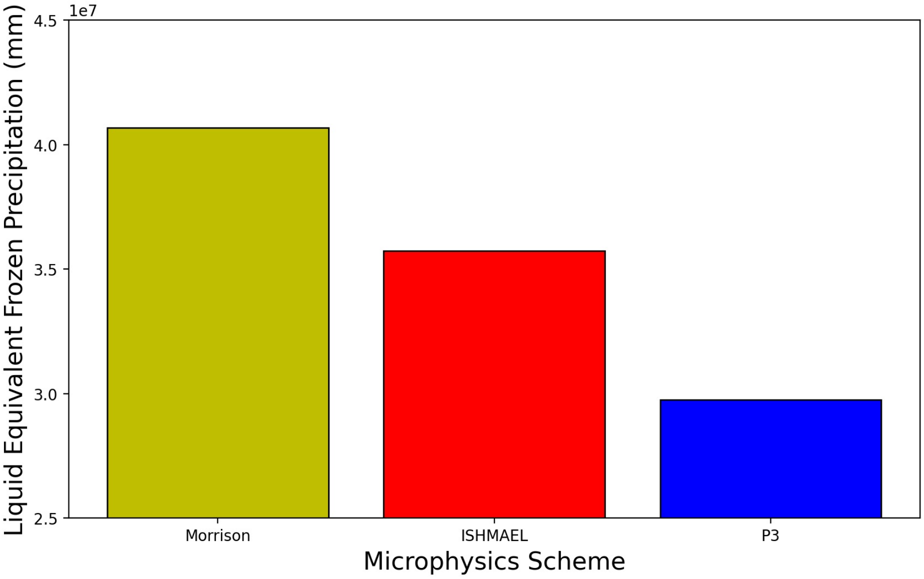

Figure 7.3. Total accumulated liquid equivalent frozen precipitation (mm) on Long Island between 0000–0000 UTC 8–9th February simulated by ISHMAEL (left), P3 (middle) and Morrison microphysics schemes (right).

at New Haven was also shown by very high (> 72 mm) liquid equivalent in all schemes, whereas this area was not captured well (in size or distribution) by the simulated snow depth in Figure 7.1, particularly by the ISHMAEL scheme. Further agreement with the observed snow depth is visible across central New York state and Pennsylvania, where snow depth was typically higher than observed in the west, but the liquid equivalent mirrored the observed distribution of more narrow, concentric bands. Additionally, the large overestimation of snow depth on the western border of Maine with Canada was not present in the liquid equivalent distribution, instead this region showed that small amounts of precipitation were found here, in increasingly small amounts west of the coast.

The apparent similarity of liquid equivalent to the observed snow depth distributions raises more suspicions surrounding the computation of snow depth. For example, the ISHMAEL-simulated snow depth over Long Island was considerably lower than in other schemes (Figure 7.1) but the liquid equivalent distribution showed that Long Island received some of the largest total precipitation output (Figure 7.2). Figure 7.3 shows the simulated accumulated liquid equivalent precipitation over Long Island only for each microphysics scheme. ISHMAEL simulated more total frozen precipitation (3.5×10^7 mm) than P3 (3×10^7 mm) at the surface of Long Island, but snow height was between 3 and 24 times larger in P3. This implies that the snow-to-liquid ratio (SLR) was the main factor in the determination of snow height in this location, and the discrepancy between liquid equivalent and snow height distributions indicate that precipitation density was an important factor across the domains.

Figure 7.4 plots contours of the average SLR derived from the ratio of the accumulated

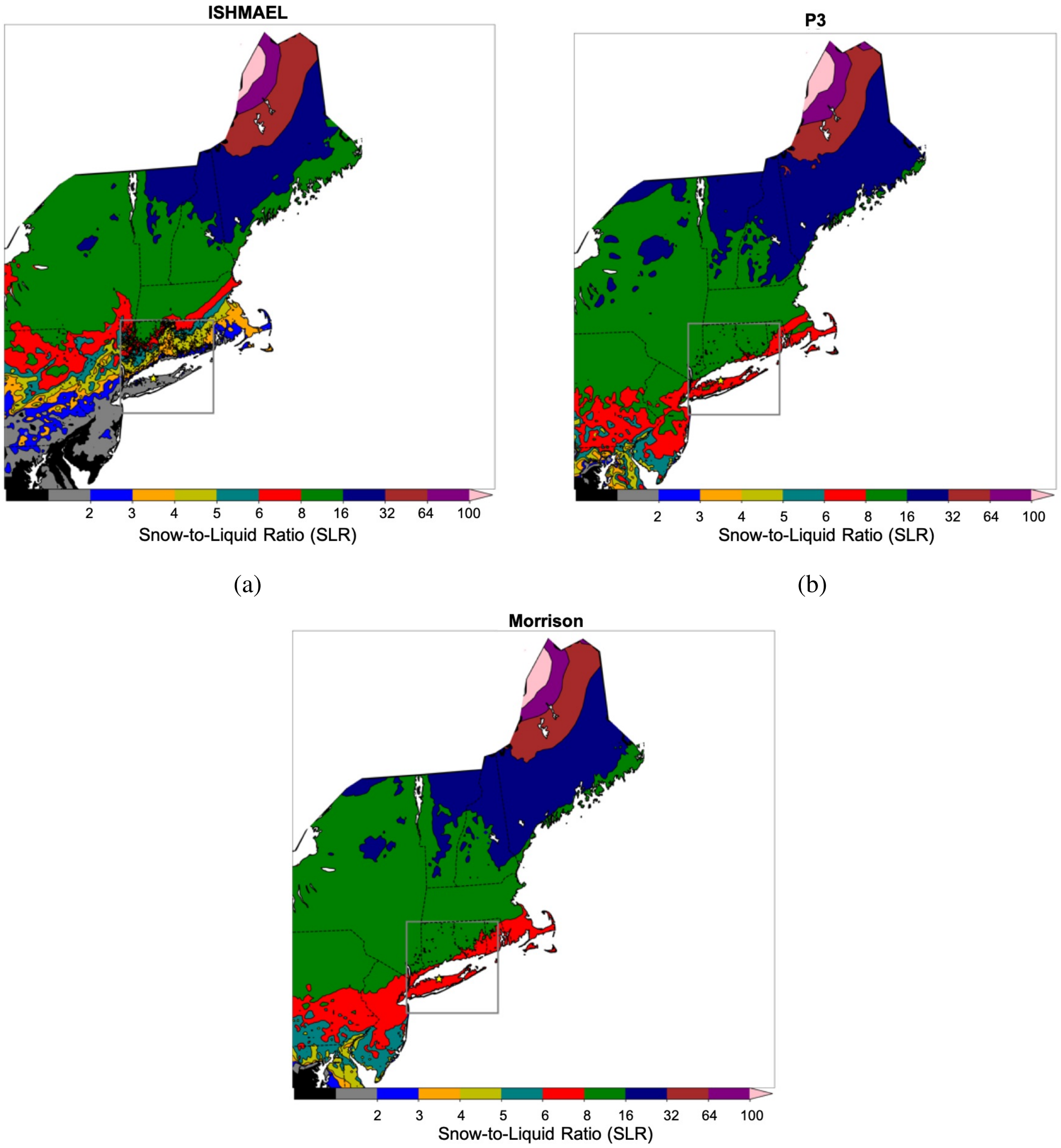
ISHMAEL
2
3
4
5
6
8
16
32
64
100
Snow-to-Liquid Ratio (SLR)
P3
2
3
4
5
6
8
16
32
64
100
Snow-to-Liquid Ratio (SLR)
Morrison
2
3
4
5
6
8
16
32
64
100
Snow-to-Liquid Ratio (SLR)

(a)

(b)

(c)

Figure 7.4. Average SLR (`SNOWH` [m] ÷ liquid equivalent [m]) deriving from total snow height and liquid equivalent depth between 0000–0000 UTC 8–10th February simulated by ISHMAEL (top left), P3 (top right) and Morrison microphysics schemes (bottom).

snow depth calculated by the `SNOWH` variable, and the accumulated liquid equivalent precipitation, in the period 0000–0000 UTC 8–9th February.

Figure 7.4 highlights the broad range of SLR that were produced using this methodology. Each scheme spans a total SLR range from 1:1 to more than 100:1, which is analogous to precipitation spanning solid ice to extremely light, powder-like snow. The distribution of SLR north of Massachusetts was near identical amongst schemes, and spanned an SLR of 8–32 south of Maine, which is in keeping with observations of typical heavy snowfall in this region. However, in Maine, particularly in the north, the SLR became extremely large.

Simulated SLR at the Maine-Canada border was in excess of 100:1, in an area of liquid equivalent of around 8–16 mm, and snow depth within 24–36 inches, despite observations showing that this area had accumulated snowfall depths no larger than 4 inches. Comparison of the distributions of liquid equivalent and SLR indicate that the SLR is most likely to blame for the overestimation in the snow depth.

South of Massachusetts, the SLR decreases through a west-east oriented band of low (< 8:1) SLR that reduced in value further south. This band occurs across Long Island in P3 and Morrison but was found much further north in ISHMAEL, causing the lowest SLR values at the rear (south) of the band to coincide with Long Island. Additionally, the low SLR band in ISHMAEL reached lower values than in other schemes, and reduced in size over a much sharper gradient and smaller area, causing ice-like SLR values of 2:1 or less to coincide with Long Island. Whereas, in P3 and Morrison, the SLR was above 6:1 across the entirety of Long Island, and even south of this area into New Jersey. The very low SLR (high density) ice present across Long Island was an overwhelming factor in the computation of snow height across Long Island for the ISHMAEL scheme. It is likely that the excessive production of high density ice in ISHMAEL is therefore to blame for the poor snow depth produced by this scheme.

Whilst SLR can be viewed as a direct and consequential feature of the precipitation field for the determination of snow depth, there are several reasons that caution should be taken with these results. The SLR shown in Figure 7.4 is a strong determinant of the poor snow depth over Long Island in the ISHMAEL scheme, but is also a factor in the poor prediction of elevated snow depth in the north of Maine. Peak snow depth observed at New Haven and Portland also received moderate SLR (8:1–32:1) in P3 and Morrison, and large liquid equivalent precipitation in all schemes, but failed to simulate the peak accumulated snow depth values observed. So, whilst very low SLR is a factor in poor snow height predictions over Long Island in ISHMAEL, comparatively greater SLR in P3 and Morrison did not resolve the issues of the snow depth distribution in these schemes, especially in the north of Maine where SLR was excessively high in all schemes.

The method of analysis conducted here also brings into doubt the importance and reliability of the SLR shown in Figure 7.4. This SLR is derived from the snow depth variable `SNOWH`. Whereas the liquid equivalent derives from the output of the microphysics schemes directly. Any issue with the snow depth is therefore more likely to be associated with the SLR, which is derived directly from the snow depth variable, than with liquid equivalent.

Finally, there is reason to believe that the `SNOWH` variable is not only inaccurate in this case, but also poorly implemented and therefore unreliable. For example, consider the high snow depth region on the Maine-Canada border where simulated snow depths are more than six times larger than observed. The liquid equivalent distribution appeared to be appropriately declining west of the Maine coast (see Figure 7.2) whilst SLR increased to extremely large (> 100:1) values. SLR of this size are not impossible in reality, although the likelihood of an SLR of this magnitude occurring in a winter storm is certainly unusual. However, more concerning is that this SLR was apparent in the Morrison scheme, where snow density is fixed at 100 kg m^{-3}, or an SLR of 10:1. Indeed, it is not apparent how variation in the SLR field can exist in the Morrison scheme as is shown in Figure 7.2. This inconsistency motivates a more thorough examination of the snow depth parameterisation.

7.2 Overview of Snow Depth Parameterisation

The snow depth variable `SNOWH` is a product of the land surface scheme that uses variables predicted by the microphysics scheme in its calculations. In this case, all simulations varied only with microphysics scheme, and so the land surface scheme used in this case, Noah-MP (Niu et al. 2011), was common amongst all simulated cases. The general form of the snow depth calculated per time step by the scheme is:

$$\Delta D = \frac{L_{\text{total}} \times F_{\text{ice}}}{\rho}, \qquad \texttt{SNOWH} = \sum_{t=0}^{T} \Delta D(t) \tag{7.5}$$

Where L_{total} is the combined liquid equivalent (liquid and solid) precipitation gained over the time step, F_{ice} is the fraction of the total precipitation that is frozen, and ρ is the mass weighted density of the precipitation arriving at the surface. Therefore, the snow depth variable can be analysed component-wise to understand how each variable is retrieved or computed.

7.2.1 Frozen Fraction of Precipitation

According to the Noah-MP Land Surface Model (LSM) User Guide (Niu and Yang 2011), the frozen fraction can be determined from four different parameterisation options specified with parameter `OPT_SNF`:

1. Jordan (Jordan 1991) [default]
2. Biosphere-Atmosphere Transfer Scheme (BATS) (Yang and Dickinson 1996)
3. Surface Temperature
4. Microphysics

All options (except for the microphysics) are functions of only surface temperature, assumed to be the temperature of the lowest grid cell, and the freezing temperature $T_{\text{fz}} = 273.16$ K. The analytical form of function options 1–3 are shown in Figure 7.5. Option 4 is not shown as it is dependent on the output variables of the microphysics scheme.

Option 3 is the most technically simple. In this case, if the surface temperature is less than the freezing temperature T_{fz} then the entire precipitation field is assumed to be frozen. If the surface temperature is warmer than the freezing temperature, then the entire precipitation field is assumed to be liquid:

$$F_{\text{ice}} = f(T_s) = \begin{cases} 0, & T_s \leq 273.16\text{ K} \\ 1, & T_s > 273.16\text{ K} \end{cases} \tag{7.6}$$

This parameterisation is naturally quite limited, but can be a computationally efficient mechanism when used appropriately. The frozen fractions given here are the expected frozen fractions in the limit that $T_s \rightarrow 0$ and $T_s \rightarrow \infty$, and so will be moderately accurate for very cold or very warm environments (though in the latter its use is negligible). This parameterisation is likely to falter when the surface temperature is close to the freezing temperature. Frozen precipitation can persist even when ground temperatures are several degrees above freezing due to the evaporative cooling effect of melting snow. Therefore, frozen precipitation can still arrive and accumulate at the surface. In this case, the parameterisation used by the Biosphere-Atmosphere Transfer Scheme (BATS) model may be more appropriate (Yang and Dickinson 1996):

$$F_{\text{ice}} = f(T_s) = \begin{cases} 0, & T_s \leq 275.16\text{ K} \\ 1, & T_s > 275.16\text{ K} \end{cases} \tag{7.7}$$

Thus, the BATS methodology may provide an improved snowfall depth calculation for snowfall events in which the ground temperature is near-freezing. The difference between the simple surface temperature and BATS methods is highlighted in Figure 7.5 as green and red lines (row 2 column 2). BATS considers frozen precipitation for a larger portion of the temperature range and will therefore increase the total amount of precipitation considered in the snow depth calculation.

The most obvious limitation to this method is that it cannot incorporate partially frozen precipitation accumulations such as those including rain and snow. This is a necessary consideration in warm, near-freezing environments where melting crystals generate an associated rain-droplet field. It is important to capture variable fractions of frozen precipitation to properly account for the depth of different constituents that exhibit different densities. For this, the Jordan (1991) parameterisation was developed:

$$F_{\text{ice}} = f(T_s) = \begin{cases} 1, & T_s \leq 273.66\ \text{K} \\ 1 - \left(\frac{T_s}{5} - 54.632\right), & 273.66\ \text{K} < T_s \leq 275.16\ \text{K} \\ 0.6, & 275.16\ \text{K} < T_s \leq 275.66\ \text{K} \\ 0, & T_s > 275.66\ \text{K} \end{cases} \tag{7.8}$$

In this method shown in Figure 7.5 (row 1 column 1), environments that are below freezing (< 273.16 K) completely freeze all precipitation arriving at the surface, and environments warmer than 275.66 K completely melt the entire precipitation field. Between these values, a temperature dependent function determines the precipitation fraction. For the interval 273.66 K $< T <$ 275.16 K the frozen fraction varies between 1 and 0.6, whereas for the interval 275.16 K $< T <$ 275.66 K the frozen fraction is fixed at 0.6. This enables a portion of the precipitation that is liquid to be subtracted from the final snow depth. Like the BATS method, the Jordan (1991) method is more likely to classify precipitation in a warm cell as frozen precipitation over the simple surface temperature method. However, unlike in BATS, only a portion of that precipitation is considered to be frozen. This causes the Jordan (1991) method to estimate frozen precipitation between both previous methods and integrates temperature sensitivity to the amount of precipitation considered in the snow depth.

The final option for calculation of frozen fraction is to refer directly to the precipitation mass mixing ratios output by the microphysics scheme. In this case, the ratio of the liquid equivalent frozen precipitation to the combined liquid equivalent of the entire precipitation population provides the mass fraction that is frozen:

$$L_{\text{Total}} = L_{\text{Frozen}} + L_{\text{Rain}}$$
$$L_{\text{Frozen}} = L_{\text{Snow}} + L_{\text{Graupel}} + L_{\text{Hail}}$$

$$F = \frac{L_{\text{Frozen}}}{L_{\text{Total}}}$$

This option is arguably the most appropriate method for categorising mass fraction. Directly referencing the precipitation output by the microphysics scheme ensures cohesion between the precipitation field aloft and the precipitation arriving at the surface. The microphysics scheme is also more likely to consider the effect of dependencies that are beyond the scope of the land surface scheme. For example, the liquid equivalent precipitation per

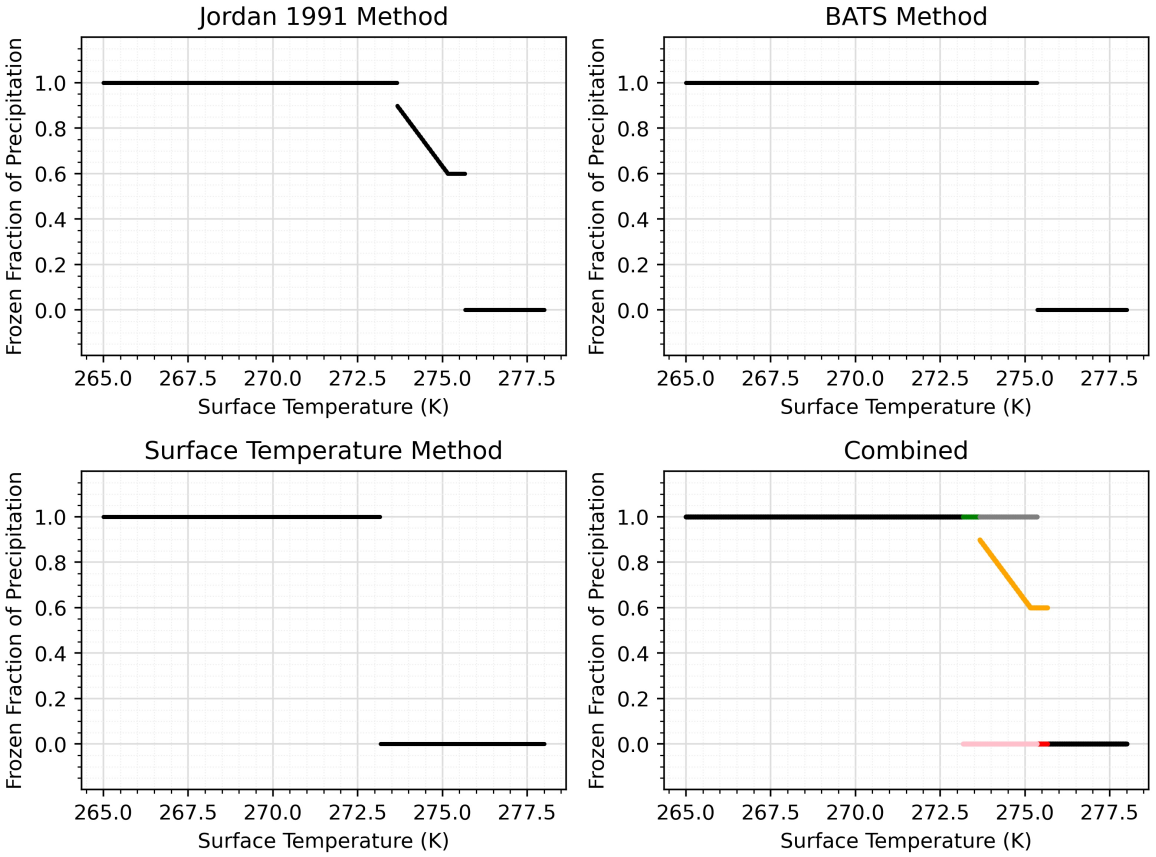

Figure 7.5. Noah-MP LSM parameterised functions for the determination of the fraction of total precipitated mass arriving at the surface that is frozen. By default the Jordan (1991) parameterisation is used during snow depth calculations (row 1 column 1). The surface temperature method (row 2 column 1) and surface temperature method with BATS adjustment (row 1 column 2) are non-default options.

hydrometeor produced by the microphysics scheme accounts for the mass mixing ratio of precipitation, the air density, and the mass weighted fall speed of particles (i.e. Equation 7.4). Each of these components plays an important role in the determination of how much precipitation arrives at the ground.

However, it is not surprising that the microphysics derived mass fraction is not used by default. The land surface scheme cannot guarantee or control the presence of these variables being output by microphysics schemes. For example, in Morrison hail and graupel are interchangeable simulation options that cannot be simultaneously tracked, and so the liquid equivalent component of either hydrometeor will not be available to the land surface scheme. A more extreme example is provided by ISHMAEL and P3, which do not categorise precipitation at all. therefore, liquid equivalent contributions of individual hydrometeors is not an output component of these schemes. Even amongst only three microphysics schemes, there are a handful of possible hurdles that can occur. Therefore, for the sake of compatibility, the potentially less accurate, but more flexible approach used by Jordan (1991) is preferred.

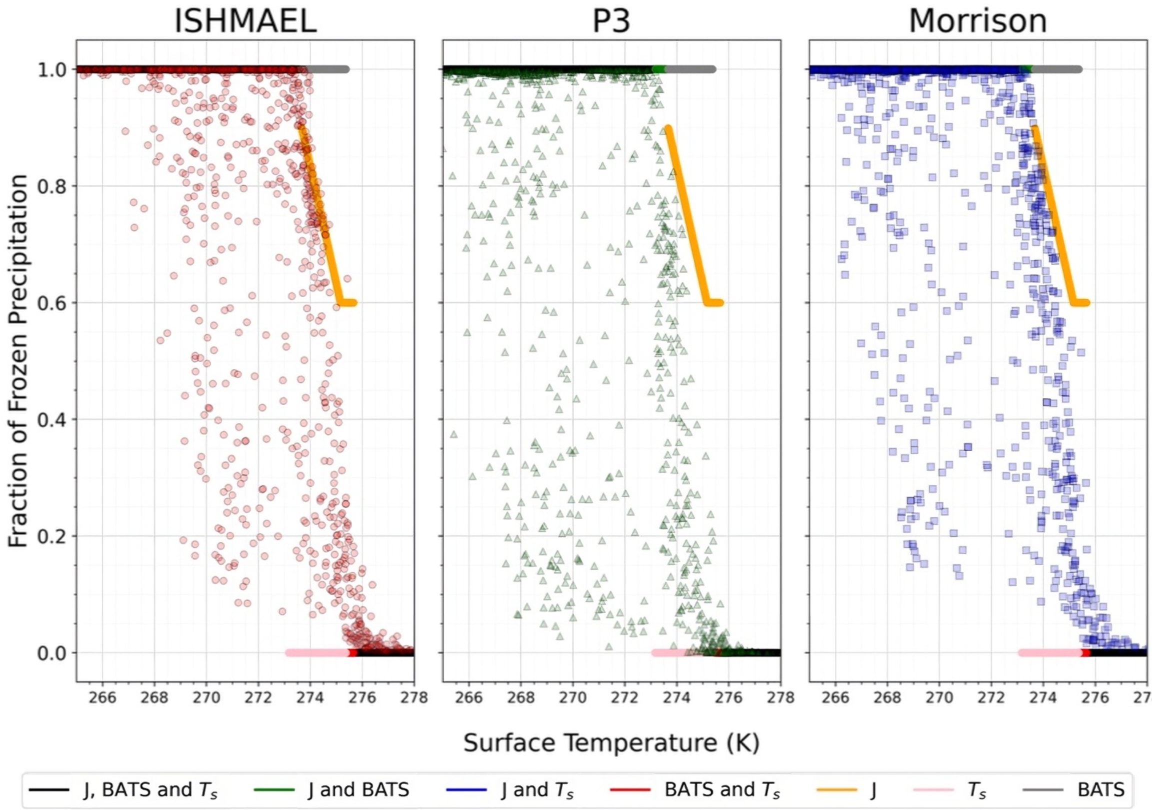

Figure 7.6. Scatter diagram of simulated frozen fraction at the surface in ISHMAEL (left, red), P3 (middle, green), and Morrison (right, blue) versus surface temperature. Scattered points are a randomly sampled subset ($\sim$ 1000) of the frozen fraction data set. Parameterised frozen fraction is overlaid for comparison, and the parameterisation type is indicated in the Figure legend (see Figure 7.5 "Combined")

To determine the efficacy and limitations of the parameterisation options for frozen mass fraction, the functions from options 1–3 were plotted in Figure 7.6 and compared to the actual frozen mass fraction produced by each microphysics scheme (in accordance with the methodology of option 4). A random sub sample of 1000 points is shown per microphysics scheme. The overlaid functional forms of options 1–3 are identical to the combined functions shown in Figure 7.5 (row 2 column 2).

The distribution of frozen fraction with surface temperature was similar in each scheme, and followed the approximate functional form of all parameterisation options at high and low temperatures. For example, all microphysics schemes shown in Figure 7.6 exhibited an accumulation of frozen fractions at 1 and 0 for cold ($T_s < 274$ K) and warm temperatures ($T_s > 276$ K), respectively. Indeed, the density of randomly sampled points at each value and in each scheme, shows that the vast majority of mass fractions in all schemes are in approximate agreement with these two values, and only a minority of points occurred between 1 and 0.

However, for the points between these values, there was a considerable spread in mass fraction and the temperature at which each mass fraction occurred. In the ISHMAEL scheme

(Figure 7.6, column 1) frozen mass fraction between the limits of 1 and 0 is confined to a relatively narrow region of surface temperatures between 270–276 K. Whereas, in Morrison (column 3), a broad array of frozen fractions between 0.1 and 1 occurred as low as 268 K, and below this temperature mass fractions continued to vary between the upper limit and 0.6. In P3, the frozen mass fraction spanned an even larger temperature range. Frozen mass fractions between 0.3 and 1 were identified as low as 266 K. The broad distribution of frozen mass fractions with temperature amongst these three microphysics schemes is certainly an argument against the use of the Jordan (1991) method (Figure 7.6 orange), which is an appropriate representation of the microphysics schemes only over its relatively narrow variable temperature range (273–276 K). Certainly, the results provided by the microphysics schemes show that large portions (80%) of the precipitation field can remain in a liquid state as low as 269 K. The consequence of this is that the Jordan (1991) parameterisation is likely to consider this precipitation as entirely frozen, therefore artificially increasing the frozen mass supplied to the snow depth routine.

7.2.2 Density of Precipitation

The Noah-MP LSM provides two methods of calculating the bulk density ρ of freshly added frozen precipitation.

1. Hedstrom and Pomeroy Method (Hedstrom and Pomeroy 1998)
2. Microphysics

In either case the Hedstrom and Pomeroy (1998) method (hereafter Hedstrom) is used, either to calculate the final density or to initialise the density routine for method 2. The Hedstrom method uses a simple temperature dependent parameterisation to predict the precipitation density of freshly fallen snow:

$$\rho_s(T_s) = \min\left\{120\ ,\ 67.92 + 51.25 \times \exp\left(T_s - T_{\text{fz}}/2.59\right)\right\} \tag{7.9}$$

where T_s is the temperature at the surface and $T_{\text{fz}} = 273.16$ K is the freezing temperature. The limits are:

$$\lim_{T_s \to 0} \rho_s(T_s) = 67.92$$
$$\lim_{T_s \to \infty} \rho_s(T_s) = 120$$
$$\lim_{T_s \to T_{\text{fz}}} \rho_s(T_s) = 119.17$$

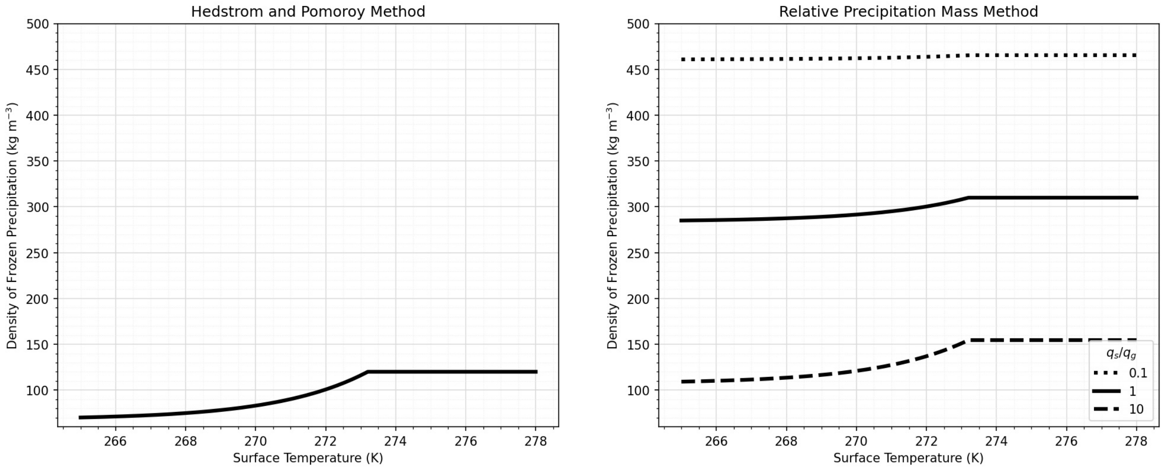

Figure 7.7. Parameterisation of density versus surface temperature in the Noah-MP land surface scheme given by the Hedstrom and Pomeroy method (left) and the weighted-precipitation method (right). For the weighted method, three example weightings are shown; snow dominated (dashed), graupel dominated (dotted), and equivalent (solid).

Therefore precipitation density is confined between 67–120 kg m^{-3}, and density becomes increasingly large for increasingly warm temperatures. The functional form of this method is plotted in Figure 7.7 (left), demonstrating the smooth exponential increase in density that occurs below the freezing level, before abruptly flattening to the fixed upper limit of 120 kg m^{-3} when warm temperatures occur.

The Hedstrom parameterisation is very likely to oversimplify the snow density that arrives at the surface due to its narrow total range and lack of appreciation for precipitation formation that can only be determined aloft of the surface layer. The narrow density range produced by this parameterisation likely stems from the limited data set on which it is based (Schmidt and Gluns 1991), and the context of the original study, which examined the retention likelihood of snowfall by forest canopies. Dense, spherical particles are less likely to be retained by foliage and therefore do not contribute to the fresh snow density measurements on which this parameterisation is based. By comparison, snowfall that reaches the surface in urban environments will contain a combination of all precipitation types that have reached the surface. The narrow range predicted by Hedstrom is in contradiction with numerous studies of fresh snow density that observe a much wider variety of possible densities from 10 kg m^{-3} to as high as 500 kg m^{-3} (Helfricht et al. 2018; Judson and Doesken 2000; Sexstone and Fassnacht 2014). This method also fails to consider the broad variety of densities offered by a mixture of precipitation types, including graupel and hail, observed during this storm. Therefore, it is likely that this parameterisation may be inappropriate for the type of precipitation observed in this case.

Method 2 uses the relative amount of each hydrometeor species produced by the microphysics scheme to effectively mass-weight the total density:

$$\rho_s = \rho_s \frac{L_s}{L_{\text{total}}} + \rho_g \times \frac{L_g}{L_{\text{total}}} + \rho_h \times \frac{L_h}{L_{\text{total}}} \tag{7.10}$$

Where L_s, L_g, and L_h are the liquid equivalent snow, graupel, and hail respectively. ρ_g and ρ_h are the constant, assumed densities of graupel and hail equal to 500 kg m^{-3} and 917 kg m^{-3}, respectively. The snow density ρ_s is calculated using the Hedstrom and Pomeroy (1998) method.

Several examples of the prediction made by method 2 are shown in Figure 7.7 (right) by neglecting the hail term, and by fixing the ratio of snow mass to graupel mass. It can be seen that as the mass of graupel becomes small, the density approaches that predicted in the Hedstrom method, and as the mass of snow becomes small, the density approaches that of graupel. Combinations of the graupel and snow mass between these two extremes serve to move the density between both limits.

As with the parameterisation of frozen fraction, the default density used by the Noah-MP LSM is chosen to be the most flexible option, possibly at the expense of accuracy. Method 2 described here encounters many of the same problems as microphysics option 4 for the frozen fraction parameterisation. There is no guarantee that the liquid equivalent component for a species, such as hail, will be present. As in the P3 and ISHMAEL schemes, hydrometeor categories do not exist in the conventional sense, which makes mass weighting the density impossible in the current framework. Thus, to avoid compatibility issues the output of the microphysics scheme is not considered.

The components of constant density are also a source of possible inaccuracy. Fixed density hydrometeor categories, such as those used in Morrison, fail to realise the wide range of possible densities that exist in reality, and the same argument can be made for the use of fixed weighting densities in method 2. However, an additional compatibility issue arises with the use of constant densities defined within the land surface scheme; they may not be consistent with the microphysics scheme that produces the precipitation in the first place. This point is illustrated by comparing the Noah-MP LSM fixed density of graupel, which is equal to 500 kg m^{-3}, and the Morrison scheme fixed density of graupel, which is fixed at 400 kg m^{-3}. This may be only a small difference, but over several time steps this difference may materialise in a comparably more dense snow field than was intended by the Morrison scheme.

The density parameterisation was evaluated against the predicted density simulated at the surface by each microphysics scheme. For this analysis, the density at the surface was assumed to be identical to the mass-weighted density of the precipitation in the lowest grid cell per latitude-longitude column. This is a reasonable assumption as, for example, the liquid equivalent mass at the surface is a direct function of the mass mixing ratio and mass-weighted fall speed of the lowest cell, and so no adjustment is required or assumed when differentiating between the qualities of the lowest cell and those qualities that reach the surface.

Figure 7.8 shows a subset of 1000 randomly sampled surface-level ice-density (kg m^{-3}) data points versus the surface temperature (K) in which they were found. Density simulated by the ISHMAEL, Morrison, and P3 microphysics schemes are shown in columns 1–3, respectively. ISHMAEL simulates ice across three separate free-ice categories, so data points shown in Figure 7.8 were retrieved from a combined, mass-weighted density array. Similarly, a combined, mass-weighted density array was formed for the three frozen hydrometeor categories simulated by Morrison using the fixed densities defined in-code. P3 used only one free-ice hydrometeor category and so no modifications were applied to retrieve mass weighted density. In addition to the simulated precipitation density, the functional form of the Hedstrom parameterisation is overlaid in red for each subfigure. Three additional functions were overlaid for the prediction of parameterisation method 2 (yellow) using fixed snow to graupel ratios of 0.1 (dotted), 1 (solid), and 10 (dashed). Note that hail was neglected for these functions.

Unlike the previous comparison of frozen mass fraction versus temperature in Figure 7.6, the relationship between surface temperature and precipitation density in Figure 7.8 is unique to each scheme. In the ISHMAEL scheme (Figure 7.8, left), when temperatures were at or below the freezing point ($\sim$ 273 K), precipitation density spanned 300–700 kg m^{-3}, and within this range, showed no dependence on surface temperature. This density range coincided with the graupel dominated parameterisation (yellow, dotted) but there was no obvious correlation between this function and the predicted density. The simulated precipitation density was between 3 and 6 times larger than predicted by the Hedstrom parameterisation (red), indicating that this method would likely be poorly suited to predicting the snow depth in ISHMAEL.

The Morrison surface level density had a more narrow distribution than ISHMAEL. Typical precipitation densities were approximately 100 kg m^{-3} for temperatures up to 277 K. This is consistent with bulk density of snow in the Morrison scheme, and shows that the mass of snow produced by Morrison was large enough to bias the density of the precipitation field toward this hydrometeor type. The density of precipitation is in loose agreement with Hedstrom parameterisation (red), though below 272 K the Hedstrom parameterisation falls below the bulk density of snow, which is a lower limit for the Morrison scheme.

In P3, the simulated density is much lower than the density of other schemes, most often having a value of less than 50 kg m^{-3} which occurred for temperatures below 274 K. This

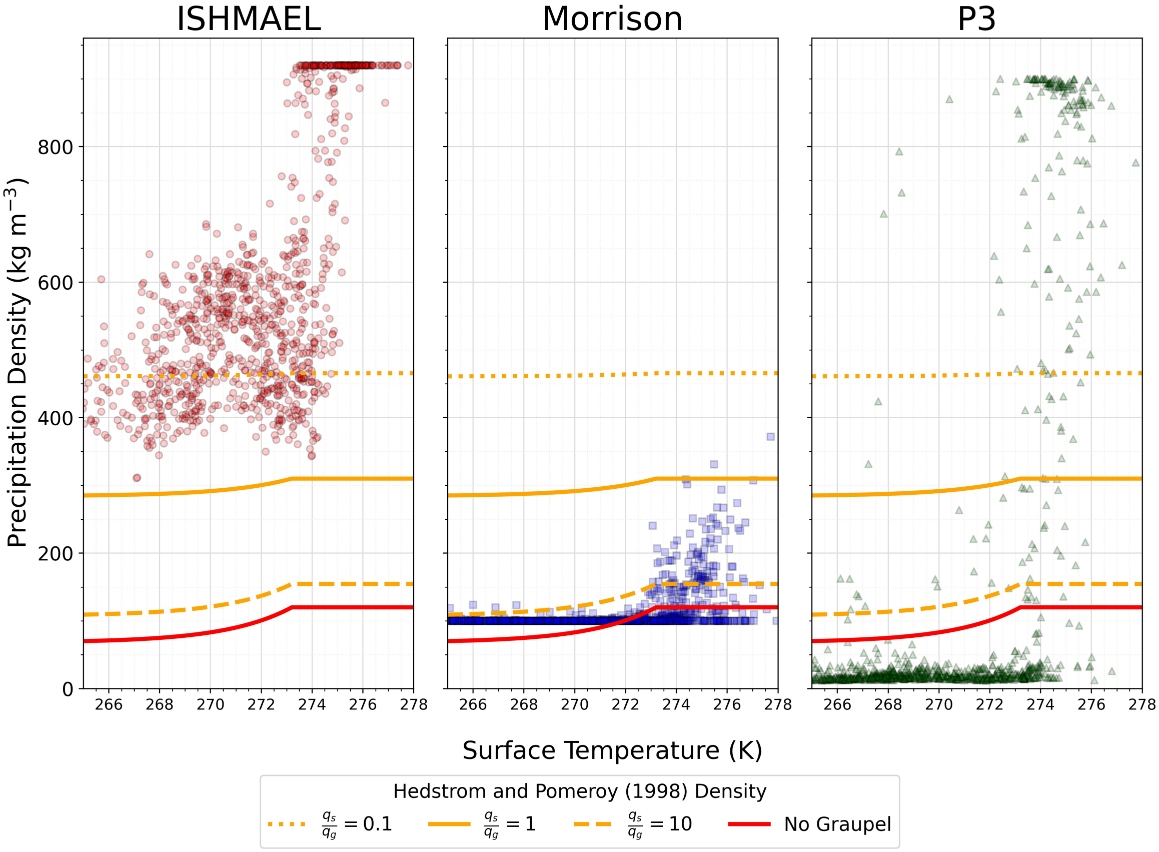

Figure 7.8. Scatter diagram of simulated precipitation density at the surface in ISHMAEL (left, red), Morrison (middle, blue), and P3 (right, green), versus surface temperature. Scattered points are a randomly sampled subset ($\sim$ 1000) of the entire simulated density data set. Parameterised density is overlaid for comparison; the weighted precipitation method (orange) is given for several values of snow to graupel mass ratio (see Figure legend). As graupel mass approaches zero, the weighted method approaches the original Hedstrom and Pomeroy (1998) method (red).

was far below the Hedstrom parameterisation, which indicates that snow density is likely overpredicted in the formation of snow depth. An interesting feature in the P3 scheme is the occurrence of ice densities between 100 and 900 kg m^{-3} across a range of low surface temperatures. In ISHMAEL, this indicates that, not only is the Hedstrom parameterisation a poor fit, but that density parameterisation by the LSM cannot be achieved on the basis of surface temperature alone.

One common feature amongst the simulated density was the occurrence of high densities above the freezing temperature. This is directly parameterised by Hedstrom, though a cap at 120 kg m^{-3} is implemented that is too low in comparison to the predicted density amongst these schemes. Only the Morrison predicted density typically remains below 300 kg m^{-3} above the freezing level. Both ISHMAEL and P3 produce the highest possible density of ice above this range, which not only hints at the rapid densification of ice in these schemes, but also highlights the inadequacy of the Hedstrom parameterisation to fully represent the density of precipitation found in this case, as well as the likelihood of significant underestimation of snow density leading to exaggerated snow depth predictions.

7.3 Toward an Improved Snow Depth Parameterisation

In the previous section, several inaccuracies incurred by the snow depth parameterisation were detailed and investigated to determine their likely effect on the snowfall distribution in each scheme. It was found that several variables that are explicitly calculated by the microphysics scheme are subsequently recalculated by the (Noah-MP) land surface model using flexible but simplistic parameterisations. When used in the calculation of snow depth, the parameterised snow qualities introduce unnecessary errors. For example, snow density was underpredicted in ISHMAEL and overpredicted in P3, which results in an overestimation and underestimation of snow depth, respectively. Similarly, the fraction of frozen precipitation parameterised by the Noah-MP scheme overestimated the proportion of precipitation that was frozen at low temperatures, likely resulting in an overestimation of snow depth when surface temperatures were close to the freezing temperature.

The parameterisation and recalculation of microphysical variables is made necessary by the absence of standardisation amongst microphysics schemes. Unlike physical parameterisations of microphysical processes, the components of the snow depth parameterisation are required only due to computational necessity i.e. for flexibility, compatibility, and computational efficiency. The snow depth could therefore be improved with better integration to the microphysics scheme. We note that, better integration would improve consistency with the output of the microphysics scheme, but an improvement to the forecast accuracy remains to be seen. Certainly in the case of ISHMAEL and P3, where the framework of the microphysics scheme is wholly inconsistent with the snow depth calculation, increased integration should improve the reliability of results. However, ultimately the accuracy of the snow depth field is constrained by the accuracy of the simulated precipitation that a microphysics scheme produces. The microphysics scheme, which has the capacity to consider a great many variables aloft, is better suited to produce key snow depth dependencies, than the land surface scheme alone.

In this section, we develop a simple snow depth framework that derives directly from each microphysics scheme used in this case, so that the result may be tested and compared to the snow depth determined by the land surface model.

The accumulated snow depth is defined as:

$$D_T = \sum_{t=0}^{T} \bar{D}(t)\Delta t \tag{7.11}$$

Where $\bar{D}(t)$ is the snow depth generated by precipitation over a time period t, Δt is the time interval between subsequent $\bar{D}(t)$, and T is the total time period for which the depth is accumulated. For the purposes of post processing, we assume that the Δt is equal to the history interval of the WRF output, given in seconds. Then $\bar{D}(t)$ has units [m s^{-1}].

The depth gain in the snow field at the surface per unit time is equal to the liquid equivalent precipitation at the surface per unit time $\bar{L}(t)$ multiplied by the average snow-to-liquid ratio (SLR):

$$\bar{D}(t) = \bar{L}(t) \times \text{SLR} \tag{7.12}$$

Liquid equivalent precipitation can be determined using the mass flux j of precipitation at the surface per unit time as in Equation 7.4:

$$\bar{L}(t) = j\frac{1}{\rho_w} \tag{7.13}$$

and the mass flux is defined in Equation 7.1:

$$j = q_H \rho_a v_H \tag{7.14}$$

where q_H is the mass mixing ratio of hydrometeor species H (i.e. snow, graupel etc.) and v_H is the mass weighted fall speed of hydrometeor species H. The depth generated by each hydrometeor species $H_1, H_2 ... H_n$ is assumed to be an additive quantity. Therefore, the total depth is:

$$D_T = \sum_{H=0}^{n} \sum_{t=0}^{T} q_H \rho_a v_H \text{SLR}_H \Delta t \tag{7.15}$$

where the factor $1/\rho_w$ has been cancelled by a factor of 1000 during conversion of the depth from metres to millimetres. At the surface it is reasonable to assume $\rho_a \approx 1.225$ kg m^{-3} in this case.

The only component that is required in Equation 7.15 but not output by the microphysics scheme is the SLR. This can be derived by considering that the mass of frozen hydrometeor

H across an area A is equal to the mass of water over the same area:

$$\rho_H V_H = \rho_w V_w$$
$$\rho_H A z_H = \rho_w A z_w$$

$$\frac{z_H}{z_w} = \frac{\rho_w}{\rho_H} = \text{SLR}$$

The SLR of a hydrometeor species H can therefore be derived from the mass weighted density of the hydrometeor, which is a predicted property in P3 and ISHMAEL, and a fixed property in Morrison.

$$D_T = \sum_{H=0}^{n} \sum_{t=0}^{T} \frac{\rho_w \rho_a}{\rho_H} q_H v_H \Delta t \tag{7.16}$$

Thus, the snow depth $D_T(q_H, v_H, \rho_H, \Delta t)$ is a function of variables obtained directly from the microphysics scheme.

Computing snow depth with this method (the microphysics-derived snow depth or, MP snow depth, hereafter) improves upon the snow depth formulation in the Noah-MP land surface model by sourcing key snow depth dependencies directly from the qualities of the simulated precipitation field. This alleviates the need for re-parameterisation of pre-existing variables, and united the precipitation field aloft with the precipitation reaching the ground.

This method is a particularly interesting use-case for the P3 and ISHMAEL schemes, which compute variable precipitation density over time. This novel feature is intended to improve upon fixed-density schemes by introducing a broader spectrum of densities in response to microphysical processes, which in turn also affect the mass weighted fall speed of precipitation. Both fall speed and density are used in the MP snow depth parameterisation, and play a role in determining the amount, and density, of fresh snow arriving at the surface, respectively. Importantly, these variables are sensitive to mixed-phase processes, which were observed in this storm, and therefore the MP methodology should allow for improved snow depth deriving from mixed-phase precipitation. Examination of the snow depth via this method, will also allow for a comparison of the simulated precipitation density to observations. This ice property is particularly difficult to measure *in situ*, but comparison of the precipitation density arriving at the surface and the density of the snowpack is a useful verification method for an otherwise hard to constrain variable.

The MP accumulated snow depth was retrieved for each microphysics scheme between 0000–0000 UTC 8-10th February, across domains 2 and 3, which encompassed the area of snow depth observations. Figure 7.9 compares the MP accumulated snow depth (in.) (row 2) against the observed accumulated snow depth (in.) adapted from Ganetis and Colle (2015) (row 1), and the Noah-MP land surface scheme derived accumulated snow depth `SNOWH` (row 3) over the same time period. Where possible, identical contour shading has been used to match contour levels amongst different plots. The Morrison, P3, and ISHMAEL derived results are shown in columns 1–3, respectively.

The MP derived snow depth shown in Figure 7.9 row 1 has a very different magnitude to that predicted by the Noah-MP LSM per scheme, but a similar distribution amongst all schemes that shows a moderate improvement to the distribution of snow depth.

In Morrison, Figure 7.9 (row 1 column 1), the distribution of the moderate (> 12 in.) and high (> 24 in.) snow depth bands, showed reasonable agreement with the observed locations of these bands, indicated by overlaid dashed and dotted ovals, respectively, and were a marked improvement over the SNOWH simulated distribution (row 3 column 1). Elevated snow depth was positioned and orientated appropriately along the coastline in the MP derived formulation, and the distribution and magnitude of snow depth over Maine was extremely similar to observations. This was a large improvement over the Noah-MP simulated depth that had produced an erroneous area of high snow depth along the Maine-Canada border. However, whilst the high snow depth MP simulated band (pink, dotted) was a tighter, and more appropriately positioned distribution than had been previously achieved by the land surface scheme, it failed to reach the south of Maine, where there had been particularly high snowfall observed at Portland. Nonetheless, peak expected snowfall increased from 35 inches to 40 inches, which is more representative of the largest snowfall accumulations observed at the ground. Overall, the MP derived depth improved the distribution of snow depth, especially in the south and across Long Island, and removed erroneously high patches of snow depth that were apparent in the Noah-MP derived depth but not observations. However, the simulated high depth bands did not extend far enough north, which caused an area of peak snowfall depth near Portland to be poorly predicted with the new method.

Compared to the MP snow depth produced with the Morrison scheme, which had a modest change in simulated depth and primarily showed a re-distribution of the existing depth range, the MP snow depth in the P3 and ISHMAEL schemes produced stark changes to the magnitude of simulated snow depth.

In the P3 scheme, MP predicted snow depths were in excess of 150 in. near New Haven, and exceeded 72 in. for vast swathes of Connecticut and Massachusetts. This represented a 3 fold increase on both the observed snow depth and Noah-MP simulated depth within the observed moderate (> 12 in.) depth band shown with dashed contours. However,the overall distribution showed signs of improvement when the MP snow depth was used. For

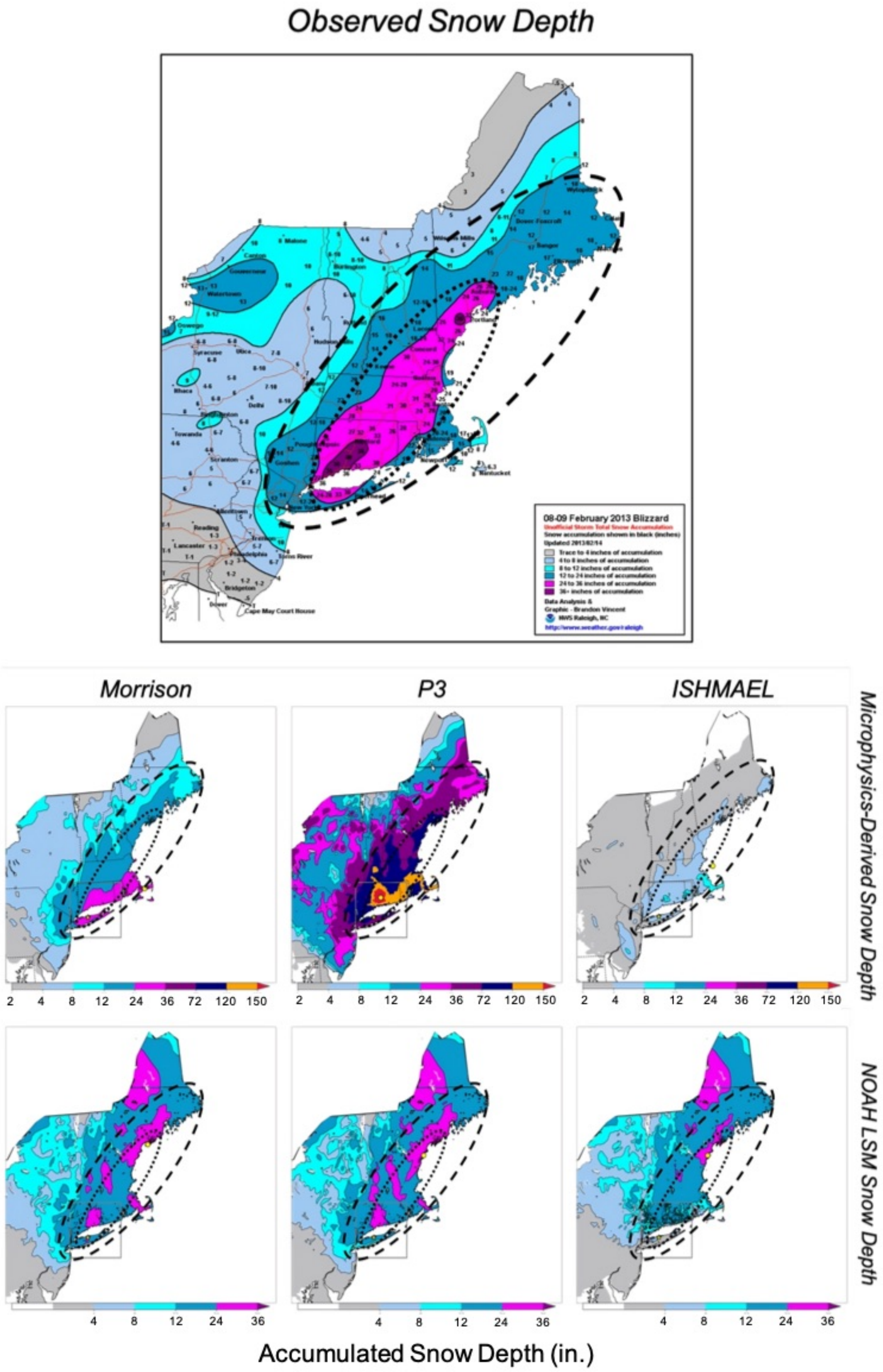
Observed Snow Depth
08-09 February 2013 Blizzard
Morrison
P3
ISHMAEL
Microphysics-Derived Snow Depth
2 4 8 12 24 36 72 120 150
NOAH LSM Snow Depth
4 8 12 24 36
Accumulated Snow Depth (in.)

Figure 7.9. Comparison of the accumulated snow depth (in.) between 0000–0000 UTC 8–9th February. Top: observations of accumulated snow depth adapted from Ganetis and Colle (2015). Row 2: accumulated snow depth derived directly from microphysics scheme output variables. Row 3: accumulated snow depth parameterised by the Noah-MP land-surface model i.e. variable `SNOWH`. Columns 1–3: Morrison, P3 and ISHMAEL microphysics schemes, respectively. Contours of the observed > 12 inch snow depth (dark blue), and > 24 inch snow depth (light pink) are approximately modelled by dashed and dotted ovals respectively. The ovals are overlaid on simulated snow depths for comparison.

example, > 36 inch MP depths were approximately confined to the dashed contour, and > 72 inch depths were approximately confined to the dotted contour. This is in contrast with the Noah-MP simulated depth, which produced patches of high (> 24 in.) depth in a distribution that lacked cohesion or similarity to observations. Additionally, the erroneous high depth area on the Maine-Canada border is absent when MP depth is applied, and instead an appropriate, declining depth gradient occurs from east-to west between the coast of Maine and the Canadian border. Therefore, whilst the MP depth severely overestimates the magnitude of snowfall when applied to the P3 microphysics output, the distribution shows quite considerable improvement.

The ISHMAEL MP depth is similarly distributed to the MP depth used in conjunction with the Morrison and P3 schemes. Improvements to the distribution include the absence of the northern erroneous high depth zone and the comparatively more narrow high-depth band positioned appropriately (within the dotted contour) along the coast, as discussed in the previous two schemes. However, the distribution shows a more significant improvement over Long Island, where the Noah-MP snow depth parameterisation had drastically underpredicted snowfall. When the MP snow depth is applied to the ISHMAEL precipitation field, the Long Island snow depth increases, which is even more stark given the broad overall decrease and underestimation of snowfall when the MP method is used with this scheme. Across the domain, predicted snowfall from the MP method reduced the ISHMAEL predicted depth by a factor of 2 to 10 over the Noah-MP LSM method. Consequently, peak snow depth is underestimated by a factor of 4 in comparison to the Noah-MP predicted maximum depth, which was already a large underestimation of the observed maximum depth.

The success of the MP derived snow depth is mixed, and varies quite significantly between choice of microphysics scheme. Analysis of the Noah-MP LSM snow depth variable `SNOWH` shows that it is poorly integrated to the simulated precipitation field and so is forced to recalculate snow depth parameters using simple methods that do not accurately represent the findings of the microphysics schemes. In the best case, the Noah-MP LSM snow depth is sufficiently constrained to produce reasonable estimations of snow depth, and is flexible enough to operate in conjunction with any choice of microphysics scheme, which makes for a hassle-free affair for the end user. However, we argue that that such flexibility is not only inaccurate, but potentially misleading. As shown with the ISHMAEL scheme, the Noah-MP snow depth is output even when the input data is inappropriate, and no error or warning is evident to the user. Unfortunately, the convenience of flexible parameterisations can lead to unintentionally misleading meteorological products, that are hard to identify without thorough examination of their underlying formulations.

Whilst caveats to the Noah-MP snow depth are present, there are certainly advantages to a simple parameterisation trained on real world data. For example, the mass fraction F_r and the bulk density of snow ρ_s are both constrained to realistic values, 0–1 and 67–120 kg m^{-3}, respectively. This helps to artificially limit the possible depth, and confine the possible error to the only remaining parameter of snow depth, the liquid equivalent precipitation. As shown by the analysis of liquid equivalent mass in Figure 7.2, liquid equivalent precipitation does not vary considerably between schemes, so is likely to be reasonable in magnitude. This enables the Noah-MP predicted snow depth to make a fair estimation of the likely snow depth observed in reality (so long as the liquid equivalent input is in the expected form). As discussed in comparisons of this method to the more complex microphysics derived variables, the range of snow depths estimated by the Noah-MP scheme are broadly realistic. Whereas, relying on the microphysics exposes the depth parameterisation to much greater possible variability, as the precipitation extracted from the surface level is not fundamentally constrained to best represent snow depths.

The Noah-MP snow depth parameterisation is certainly a *safe* option, and for this reason it should remain within the WRF arsenal. However, accurate and precise snowfall predictions, particularly in storms with a mixed-phase precipitation component, are unlikely to be made with the Noah-MP methodology, and so additional methods, such as that posed here, should be explored. Results for the MP (microphysics-derived) snow depth in Figure 7.9 showed that this method provided an improved distribution of snow depth that more closely matched the observations, and this improvement was found amongst all microphysics schemes tested. This motivates an increased integration of the snow depth parameter with microphysics schemes, either by directly including the snow depth calculation in the microphysics, or by standardising the microphysics output variables so that they are available for the land surface scheme to make more detailed calculations. The latter option is preferable, as it would allow the land surface scheme to apply additional modifications to the final snow depth, such as compression, melting and sublimation, which are beyond the scope of microphysics schemes.

Whilst the availability of snow depth dependencies calculated in detail by microphysics schemes is an attractive prospect, caution must be taken to ensure that these variables are appropriately calculated. The snow depth can only be as accurate as its dependencies, and poorly constrained dependencies may severely hamper snow depth prediction. This was evident in Figure 7.9 where improved snow depth distribution can at the expense of highly varied total snow depth magnitudes. For example, Morrison simulated an appropriate peak snow depth and a general depth field that was similar to observations, whereas the P3 and ISHMAEL schemes overestimated and underestimated the magnitude of the snow field by a factor of 3, respectively. Given that the liquid equivalent distribution was similar to the distribution of MP snow depth in all schemes, it is likely that the source of inaccurate depth magnitudes in the ISHMAEL and P3 schemes was likely the SLR (ice density) or fall speeds or both. These variables are key prognostic variables that each scheme aimed to improve and, indeed, motivated the development of each scheme. So it is particularly interesting to find that the explicit computation of these variables may be poorly constrained or inaccurate in this case, as evidenced by comparison of the simulated snow depths to observations. In this instance, the ISHMAEL and P3 schemes make a good case for the continuing presence of simple, but well constrained parameterisations such as the Noah-MP snow depth that may be used comparatively whilst density predicting schemes are developed.

Chapter 8

Predicted Density and Snow-to-Liquid Ratio

In the previous chapter, the snowfall depth that was produced by each microphysics scheme during simulation of the 8–9th February storm was examined. The snow depth in this case was observed to reach exceptionally high (record breaking) depths, that were physically and financially damaging to infrastructure in the affected regions, and posed a threat to life for citizens caught in the blizzard. The accuracy of forecast snow depth magnitude and distributions were therefore of paramount importance. The snow depth output by the WRF model for all schemes was shown (Figure 7.1) to underestimate the peak snowfall depth, and produced a poor distribution of snow depth in comparison to observations.

The snow depth routine was examined and found to originate not with the microphysics schemes, but with the land surface scheme, which in all simulated cases was the Noah-MP Land surface model (LSM). The snow depth variable `SNOWH` depends on several qualities of the precipitation field that are often-times the result of multiple, complex, physical calculations over several time steps. However, poor integration between the land surface scheme and microphysics schemes, led these variables to be re-parameterised in a simplistic manner that did not represent the diversity of values simulated by the microphysics schemes (Figures. 7.8, 7.6), and therefore was not consistent with the simulated precipitation field.

A new method of snow depth calculation was proposed (Equation 7.16) that directly implements the variables that are determined from microphysics schemes. This method is based on a simple, first-principles approach that is consistent with the Noah-MP LSM snow depth equation as well as the precipitation qualities determined by the microphysics. Results showed a significant improvement in the predicted distribution of snow-depth compared to observations, but the magnitude of snow depth was poorly constrained by the ISHMAEL and P3 schemes. The relative similarity of the liquid equivalent fields, indicates that the inaccuracy stemmed from density and fall speed components of the snow depth equation. This is corroborated by the fact that the fixed density scheme (Morrison) produced an accurate range of snow depths. Whereas, the density predicting schemes (ISHMAEL and P3) produced significant over and underestimations of the snowfall depth range.

The apparent difference between simulated densities amongst schemes and the consequences of this on the simulated snow depth motivate a closer examination of the simulated precipitation density at the surface. In this case, measurements of liquid equivalent precipitation, SLR, and snow depth were taken at Stony Brook University (SBNY) for each phase of the storm, which allow for the simulated snow depth qualities to be directly verified. In this chapter, we consider the role of simulated density to the precipitation field and examine its accuracy for concurrent use in the snow depth parameterisation.

8.1 Simulated Snow Depth Qualities at Stony Brook

Measured values of the phase-averaged SLR, liquid equivalent and snow depth at Stony Brook are shown in Figure 8.1 per phase (highlighted orange). These products are a direct observation of the accumulated snow pack, and so do not consider the individual contributions of specific precipitation types. However, the type of precipitation can be inferred from the average SLR. For example, in phase one the observed SLR was 10:1, which is the typical value of SLR attributed to snow. In phase two, the SLR reduced to 6.8, implying that the average density of precipitation had increased. This is in line with observations of dense, wet-grown particles at this time by Picca et al. (2014) and the presence of the mixed-phase transition line (i.e. Ganetis and Colle (2015)) aloft of central Long Island. Finally, in phase three, SLR returned to 9.4:1 which indicates that the precipitation field had largely transitioned to snow as in phase one. Observations during phase three record an increase in cold formed crystals (such as stellars) aloft of Stony Brook, and dual reflectivity radar observations showed a sudden decrease in the reflectivity field, likely hinting that the mixed-phase interactions aloft of Stony Brook had ceased.

Comparing the observed values of SLR directly to the average observed snow depths in Figure 8.1 column 2 (orange), it is clear that SLR alone is not a reliable indicator of snow depth. Whilst a less-than-snow SLR during phase two reduced the overall snow depth at this time, the average SLR in phase three was less than observed during phase one, yet the snow depth had doubled. This highlights the importance of liquid equivalent precipitation in determining the snow depth., However, note that the liquid equivalent was also not a perfect indicator of observed depth during phase two. Instead, the product of both variables, the SLR and liquid equivalent, is the most accurate determinant for the average snow depth. This product accounted for 99%, 96% and 100% of the snow depth for phases 1–3, respectively. Therefore, both variables must be accurately simulated by microphysics schemes if they are to accurately predict the snow depth.

The product of SLR and liquid equivalent precipitation is used to derive the simulated snow depth in the microphysics-derived snow depth method (MP snow depth) detailed in the last chapter. Recall that the depth contributed by hydrometeor species H over a time period T is calculated in this method as:

$$D_H = \sum_{t=0}^{T} \text{SLR} \cdot L_H \Delta t, \tag{8.1}$$

where the snow-to-liquid-ratio (SLR) is a function of the simulated mass-weighted hydrometeor density:

$$\text{SLR} = \frac{\rho_w}{\rho_H},$$

and the liquid equivalent precipitation arriving at the surface (mm s^{-1}) is the product of the surface level cell mass mixing ratio of hydrometeor species H (kg kg^{-1}), the density of air (kg m^{-3}), and the fall speed (m s^{-1}) of the hydrometeor species:

$$1 \times 10^3 \left(q_H \rho_a v_H\right)$$

In this framework, the depths of individual hydrometeors are assumed to be additive and the total snowfall depth is therefore the sum of each individual snow depth total per hydrometeor type:

$$D_T = \sum_{H=0}^{n} \sum_{H=0}^{n} D_H \tag{8.2}$$

The contributions of SLR and liquid equivalent derived from different hydrometeor components can therefore be compared across schemes. Additionally, the values can be combined across hydrometeor species and used to determine a combined total value. The snow depth and liquid equivalent variables are assumed to be additive, so the total combined value of these variables is simply the summation of the individual value per hydrometeor species. In contrast, the SLR is not an additive property. A natural choice is to mass weight this property according to the total mass mixing ratio of each hydrometeor species in the cell. The combination of these variables across all precipitation types provides a combined variable that can be temporally averaged across each phase of the storm and compared to observations.

Figure 8.1 shows the average values of snow depth (column 3), liquid equivalent (column 4), and SLR (column 5), at Stony Brook for each phase of the storm (large rows 2–3, respectively). The observed values are shown in the first sub row of each phase-row and highlighted in orange. Additional sub rows show the variable value as determined by the ISHMAEL, P3 and Morrison microphysics schemes using the MP snow depth framework. The combined (overall snowpack) value of each variable is shown in bold typeface. For simulated variables, the portion of each variable attributed to a hydrometeor species is known, and two contributions are determined: the snow contribution (shown in parentheses) and other (denoted *ice*, shown in square brackets). Other refers to frozen precipitation that is not considered to be snow. In the Morrison scheme, this is the graupel and cloud ice categories. Whereas in the P3 and ISHMAEL schemes, other refers to ice that does not meet the snow partition criteria, including graupel, sleet, partially rimed ice, hail and cloud ice.

Examination of the snow depth qualities amongst schemes in Figure 8.1 shows that the average SLR (column 5) simulated by the density-predicting schemes (ISHMAEL and P3) did not match observations, although the phase-to-phase tendency was in keeping with the tendency observed between phases. For example, the observed and simulated SLR decreased from phase one to phase two, and increased from phase two to phase three and this was reproduced by all microphysics schemes. This tendency was important to capture, as it effectively quantified the change in characteristic precipitation density that was observed during phase two. The tendency of the simulated SLR therefore shows that each scheme was sensitive to the changing density with time, and by extension the mixed-phase processes (or their absence) that drove density changes during each phase.

	Microphysics Scheme	**Combined Snow Depth (cm)** (Snow) [Ice]	**Total Liquid Equivalent Snow and Ice (cm)** (Snow) [Ice]	**SLR** (Snow) [Ice]
Phase 1	Observed	**20.3**	**2.0**	**10**
	ISHMAEL	**2.5** (0.3) [2.2]	**1.9** (0.2) [1.7]	**1.3** (1.7) [1.3]
	P3	**25.2** (22.9) [2.3]	**1.8** (0.4) [1.4]	**13.9** (51.8) [1.7]
	Morrison	**16.5** (16.3) [0.2]	**1.7** (1.6) [0.1]	**9.6** (10.0) [2.5]
Phase 2	Observed	**10.2**	**1.5**	**6.8**
	ISHMAEL	**2.7** (0.0) [2.7]	**2.4** (0.0) [2.4]	**1.1** (1.2) [1.1]
	P3	**0.9** (0.0) [0.9]	**0.8** (0.0) [0.8]	**1.1** (57.4) [1.1]
	Morrison	**17.1** (15.2) [1.8]	**2.3** (1.5) [0.7]	**7.5** (10.0) [2.5]
Phase 3	Observed	**40.6**	**4.3**	**9.4**
	ISHMAEL	**1.9** (0.3) [1.6]	**0.9** (0.0) [0.9]	**2.2** (15.6) [1.9]
	P3	**43.0** (42.9) [0.2]	**0.7** (0.7) [0.0]	**63.1** (64.5) [10.6]
	Morrison	**9.4** (9.4) [0.0]	**0.9** (0.9) [0.0]	**10.0** (10.0)[2.5]

Table 8.1. Observed and simulated snow depth parameters in the ISHMAEL and Morrison schemes. Parentheses indicate values owed to snow only. Square brackets indicate values owed to ice components only.

Whilst the general tendency of the SLR was appropriate, the magnitude of the SLR (column 5, bold) that was predicted diverged considerably from what was observed. For example, phases one and three were predominantly characterised by heavy snowfall at Stony Brook, with observations citing moderate to minimal riming and the presence of aggregates, and hence the SLR was relatively high at approximately 10:1 for both phases. Morrison made the best prediction of SLR during these phases, but its success is somewhat overshadowed by the fact that its fixed snowfall density ensures a 10:1 SLR that conveniently coincides with the observed total. In the P3 and ISHMAEL schemes, which explicitly predict density, the SLR varied considerably for these snowy phases. ISHMAEL under predicted the SLR in both phases one and three by a factor of 8 and 4, respectively. This indicated that ISHMAEL was simulating dense ice dissimilar to snow and more similar to graupel or hail at these times. P3 produced a small overestimation of SLR during phase one, but a considerable over-estimation in phase three that was almost 7 times larger than observed and is indicative of extremely light and fluffy snow. Both density predicting schemes were therefore shown to poorly predict SLR during snowy phases but in opposite ways, ISHMAEL produced ice that was far too dense, and P3 ice that was not dense enough.

The SLR in phase two was observed to be lower than in phases one and two, highlighting the increase in average precipitation density observed at this time. Observations of precipitation at Stony Brook recorded rimed and partially melted crystals with ice pellets and some rain which would increase the density of the fresh snowfall layer considerably. However, the SLR is still quite high. A back of the envelope calculation can show that the average density associated with this SLR is less than 150 kg m^{-3}. It is important then not to overstate the density or dominance or mixed-phase precipitation at this time. The Morrison scheme produced the most similar SLR to observations during phase two, furthering its case as the most accurate predictor of SLR amongst these three schemes. As Morrison is a fixed-density scheme, the reduction in average density came from the increased production of graupel, which reduced the SLR through the mass weighting of hydrometeors only. By comparison, the density predicting schemes, ISHMAEL and P3, both underestimated the SLR and, in fact, produced the lowest possible SLR i.e. both schemes reached the maximum density limit of bulk ice $\sim$ 920 kg m^{-3}. This indicates that both schemes were extremely sensitive to the presence of mixed-phase processes at this time, resulting in a mass densification of the precipitation field at Stony Brook.

As opposed to the SLR, whose effect on the precipitation field is felt through significant changes to the observed hydrometeors, the liquid equivalent precipitation is more subtle and harder to identify physically. Observations of liquid equivalent show that the smallest liquid equivalent was identified during phase two, possibly due to the loss of some frozen precipitation to liquid. Whereas, the largest average liquid equivalent occurred in phase three. Across all three phases, the relative inaccuracy of liquid equivalent (as a factor of the observed total) was typically smaller than was found for the simulated SLR. For example, all three schemes produced a liquid equivalent that was within 85% of the observed total for phase one. In phase two, the simulated liquid equivalent was over estimated by ISHMAEL and Morrison, but underestimated by P3, possibly indicating that during the mixed-phase period, precipitation in P3 was more susceptible to complete melting. However, all schemes produced a remarkably similar underestimation ($\approx$ 4 times smaller) of liquid equivalent in phase three. The consistency of the simulated value suggests that the inaccuracy in this instance is not due to he method of microphysical parameterisation but likely stems from a common factor amongst these schemes or even amongst schemes more generally. For example, simulations of this storm performed by Ganetis and Colle (2015) using the Thompson microphysics scheme also found that the total liquid equivalent mass of snow was poorly predicted, especially in phase three when the model simulated 2.8 times less than the observed total.

From the results found in Figure 8.1 it is evident that snow depth calculated using microphysics output (i.e. MP snow depth) will be significantly affected by the inaccuracies of simulated SLR and liquid equivalent. The fixed density framework used by Morrison in this case provides an advantage, because the density is always appropriately constrained and therefore, inaccuracies to the snow depth were largely isolated to the liquid equivalent parameter in this case. This is evident when comparing the observed snow depth to the Morrison snow depth (Figure 8.1 column 2) in phase one, when liquid equivalent was accurately predicted and SLR was well suited to the fixed density of snow in the Morrison scheme. However, when the liquid equivalent was poorly predicted such as in phase three, the error was carried into the snow depth variable, which was underpredicted by a near identical factor. Somewhat surprisingly, the Morrison scheme simulated the best SLR prediction of all schemes in phase two. In this case, it appears that mass weighting of fixed density categories is an appropriate method of SLR prediction during mixed-phase events.

These results do not lend as much support to density predicting schemes as was expected. Indeed, a motivating factor for the development of density-predicting schemes was an improved ability to represent mixed-phase processes and the resulting modifications to precipitation density. In theory, ISHMAEL and P3 should have a natural advantage over Morrison during the mixed-phase (phase 2), when these schemes were more appropriately positioned to calculate the change in SLR than Morrison. However, both P3 and ISHMAEL drastically overestimated particle density, resulting in a considerable underestimation of snow depth for this phase. Additionally, the incorporation of variable density in these schemes only reduced the accuracy of simulated precipitation during phases one and three, where a fixed, conventional SLR of 10:1 would have provided a more accurate SLR prediction, as was the case in Morrison. It is evident then, that whilst inaccuracies exist in the liquid equivalent prediction of all schemes in this case, the ability to predict density did not improve the prediction of SLR at Stony Brook during the mixed-phase, and instead reduced the accuracy of the predicted SLR during snow-dominated periods. This resulted in a snow depth field that was drastically under predicted by ISHMAEL. For P3, the snow depth was coincidentally more accurate than ISHMAEL, but only due to an large and opposing inaccuracies in the SLR and liquid equivalent fields simultaneously.

8.1.1 Sources of Change in Density Predicting Schemes

A comparison of the variables required for snow depth in the previous section found that the predicted SLR was a primary cause of the poor snow depth prediction in ISHMAEL and P3. The simulated SLR in these schemes is of particular interest as it is derived from the predicted density, arguably a flagship variable that had motivated the creation of the particle-properties framework. In this section, we investigate the origin of the erroneous density values simulated at Stony Brook by considering the microphysical processes aloft of Stony Brook, and the formulations of density in each scheme.

A vertical column with 20 km^2 base centred over Stony Brook was isolated and at each vertical level. This column base size was chosen to appropriately characterise the local meteorological environment at Stony Brook whilst minimising the effect of incoming and outgoing hydrometeors as a result of wind shear. Within the column, the mass tendency rate of several important microphysical processes for the prediction of density were determined. For comparison, the average, mass-weighted precipitation density was also determined for the same vertical column. The aim of this analysis is to relate changes in the magnitude of microphysical processes to corresponding changes in the simulated density field particle during descent. A vertical distribution was chosen to capture a range of processes that occur in isolation at different heights, and to determine if changes to the precipitation density at high elevation persist to low elevations.

The distribution of process mass-tendency terms and precipitation density were averaged per vertical layer per phase in Figures 8.1–8.2 showing the vertical distribution of ISHMAEL and P3-simulated processes, respectively. Data for each vertical layer corresponds is retrieved directly from the vertical level determined by the WRF vertical grid structure, which is non constant and has smaller vertical lengths close to the surface. No modification was made to the vertical length scale in order to avoid interpolation and smoothing. Per phase averaging (i.e. columns 1–3) was chosen as each phase exhibited a unique thermodynamic and microphysical environment aloft that modified the precipitation at the surface. Per-phase averages also allow for the process rates and density changes to be directly compared to the per-phase average SLR obtained at the surface in Figure 8.1. Note that in Figures 8.1–8.2 the average mass tendency per vertical layer is represented as a fraction of the total (summed) mass tendency. This choice was made as the density tendency (white solid line) showed much better correlation with the presence of a microphysical process, rather than the specific value of the mass tendency.

Both ISHMAEL (Figure 8.1) and P3 (Figure 8.2) show similar overall tendencies in density per phase but the value of density (and therefore SLR) at the surface typically results from the presence (or absence) of specific microphysical processes in the lowest 2 km of the atmosphere.

First, considering the effect of deposition on the ice density distribution, we find that the net tendency of deposition was to reduce average density in both schemes. In P3 (Figure8.2) ice density aloft of the cloud top (indicated approximately by the highest depositional layer) exhibited a high (> 800 kg m^{-3}) density originating from the initial nucleation density of ice that is fixed at the bulk density of ice $\sim$ 920 kg m^{-3}. Within approximately 5 km of the cloud top during phases one and two (columns 1 and 2), deposition was the dominant process, reducing the density of ice to its lowest possible value permitted by the P3 scheme. Continued deposition below this vertical height continued to suppress density in P3 as low as 2 km, when other microphysical processes began to modify the density field. In phase three (Figure8.2 column 3), deposition was less consistent at the cloud top, and instead, interspersed regions of sublimation were present. However, sublimation had minimal effect on the overall density, as shown in the 5.5–6 km layer, and its presence served only to temporarily prevent the deposition from reducing density in this height range.

The deposition process in ISHMAEL (Figure 8.1) played a similar role as in P3, but produced less severe reductions in density. For example, during phases one and two (columns 1 and 2), the entire 5 km vertical layer below the cloud top was entirely dominated by deposition, as in P3, but the density reduced to no less than 400 kg m^{-3} in this region. Indeed, in the highest 2 km of the cloud, average particle density actually increased slightly, likely indicating that nucleation of high density cloud ice in this region was sufficient to balance out any reduction due to deposition. It was not until much deeper in the atmosphere that the nucleation rate waned, and deposition gradually reduced the precipitation density at a much slower rate than P3. During phase three (column 3), the deposition layer became interspersed with sublimation, as in P3. In this instance, sublimation layers had a much more significant impact on particle density in ISHMAEL than in P3, with sublimation effectively increasing particle density. Consequently, precipitation in ISHMAEL retained a high density similar to that of bulk ice as low as 5 km above the surface, and the density of precipitation entering the mixed-phase layer (lowest 2 km) was 8 times larger in ISHMAEL (400 kg m^{-3}) than in the P3 scheme (50 kg m^{-3}).

Within the lowest 2 km of the atmosphere, the mass tendency field became dominated by mixed-phase processes in both schemes, which ultimately determined the drastic differences in density achieved at the surface. In the P3 scheme (Figure8.2) the processes found in the sub 2 km layer were extremely similar, spanning melting, wet growth, and riming, but their relative dominance as a fraction of the entire mass tendency was unique in each phase. For example, in phase one (column 1), melting (red) was dominant in a narrow layer between 1.8 and 2.3 km, and in phase 2 this decreased in elevation slightly to 1.5 km. Whereas in phase three, melting was present only in a small layer around 1.5 km and contributed less than 0.2% of the overall mass tendency. Comparisons of the melting layer to the density tendency (white) indicate that density was not directly influenced by melting in P3. For example, during phase two when the melting layer was deepest and vertical layers were not shared by other processes, density did not substantively increase from the minimum density that had been achieved by the deposition process. We note that increases in density within the melting layer during phase one were therefore likely due to other processes. It is likely that, if the effect of melting was not directly incorporated to precipitation density, then a corresponding density change would be invoked by wet growth (purple). However, an examination of density changes during wet growth generally indicate that this process also had little influence on average density. For example, during phase three wet growth had a negligible effect on the density of precipitation. The most severe increases in density occurred in the presence of wet growth, but were not directly associated with wet growth. Instead, large increases in density were attributed to the riming process (yellow) during phases one and two. During phase one, when riming formed less than 20% of the mass tendency and wet growth contributed more than 80% of the mass tendency, density was stagnant at approximately 300–400 kg m^{-3}, and the largest increase in density came in a narrow layer (2 km) where riming was present in an environment of relatively low (< 30%) wet growth, indicating that riming was a source of the increasing density. This is corroborated during phase two (column 2), where riming takes an increasing portion of the mass tendency (45%), which increases the density from 50 kg m^{-3} to more than 800 kg m^{-3}). This analysis therefore shows that the density in P3, and by extension the SLR, at the surface were dependent on the two microphysical processes: the deposition process, which produced very low densities of ice, and the riming process which produced large densities of ice.

Now consider the mixed-phase processes that occurred within the lowest 2 km of the atmosphere in the ISHMAEL scheme (Figure8.1). It is apparent that the largest density increases were associated directly with melting (red). For example, in phase one (column 1), melting between 1.5 km and 2.3 km produced a 200 kg m^{-3} increase in density, and a subsequent surface level melting layer induced a second 200 kg m^{-3} increase in density. During phase two (column 2), melting became dominant throughout the lowest 2 km of the domain, and consequently density increased by approximately 500 kg m^{-3} until the maximum allowed density was obtained. In phase three, melting took a smaller portion (40–60%) of the mass

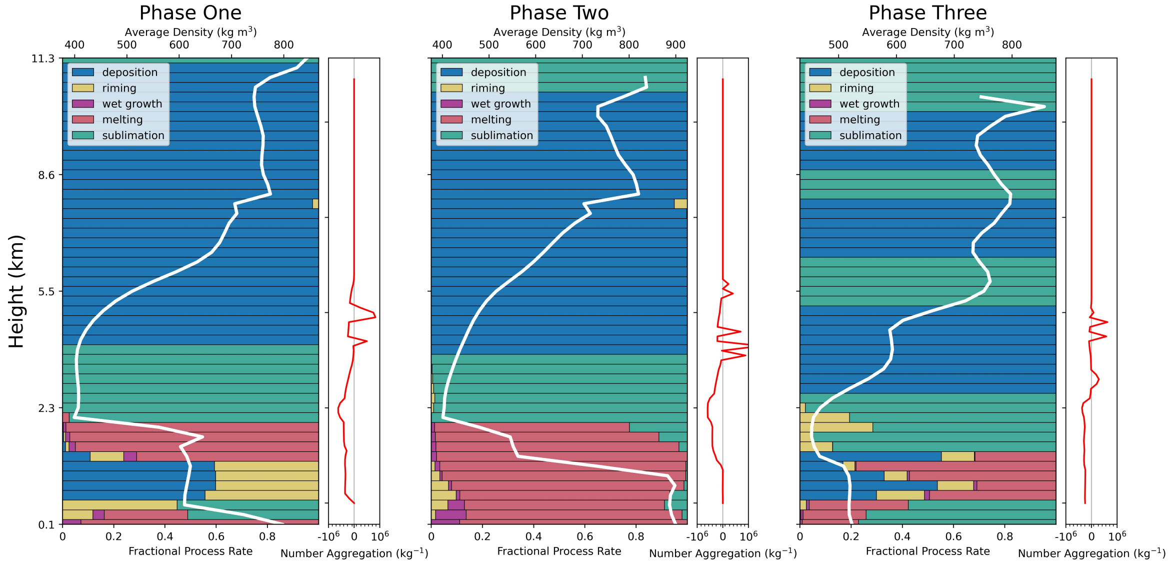

Figure 8.1. Phase-averaged density and microphysical process rate with elevation at SBNY for the ISHMAEL microphysics scheme. Values averaged per vertical layer in a column with 20 km^2 base centred on SBNY. Average density in each vertical layer (White line). Average microphysical process mass tendency rate as a fraction of the total microphysical process mass tendency rates per vertical layer (see legend). Phase averaged number aggregation rate per vertical layer given in side plot per phase with symmetric logarithmic scale.

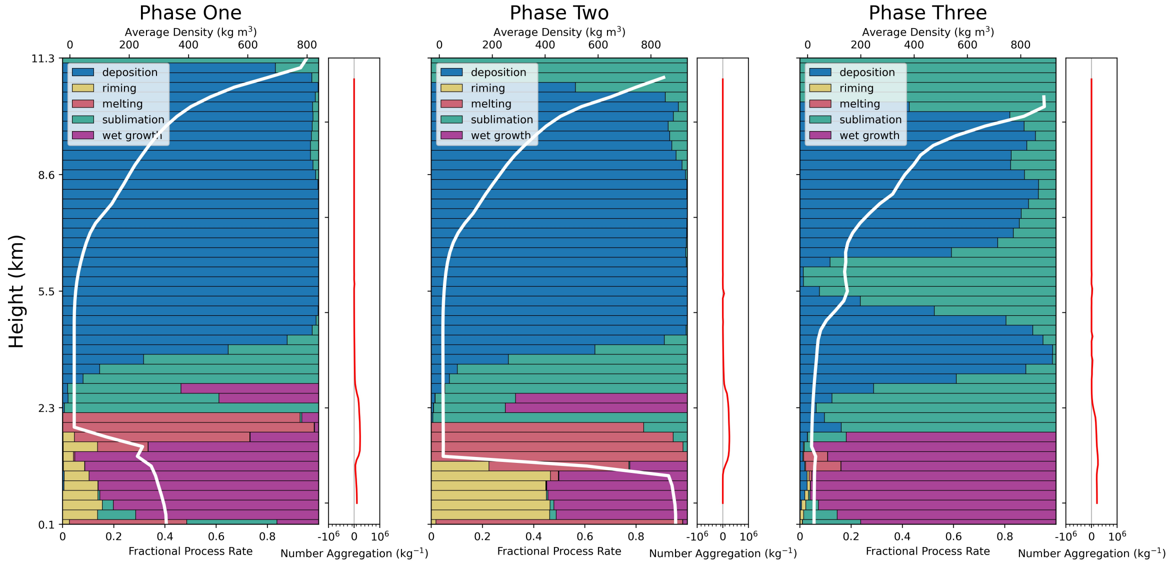

Figure 8.2. As in Figure 8.1 but for the P3 microphysics scheme.

tendency, and so the density increased only marginally. This effect was likely mitigated by the simultaneous presence of deposition and riming. From this analysis, it is difficult to interpret the role of riming on the precipitation density. In phases one and three, riming was coincident with stagnation of the density value, and whilst this may be interpreted as having a negligible effect on the precipitation density, we instead argue that riming tends the density toward a moderate value (500–600 kg m^{-3}) and so the effect of riming appears inconsequential.

The analysis shown in Figures 8.1–8.2 help to illuminate the processes responsible for the largely inaccurate SLR found at the surface in Figure 8.1. For example, ISHMAEL continuously underestimated the SLR (column 5) during all phases due to the production of densities that were between 6 and 8 times too large. It is evident that this poor prediction originated with the melting process, which dominated the mass tendency of the lowest layers during phases one and two, and was also responsible for the most severe increases in density. However, it is notable that the aloft of the mixed-phase layer, deposition and aggregation failed to reduce the precipitation density to below 400 kg m^{-3} and so the precipitation field that descended into the melting layer already had a high density. This was most evident in phase three, when high average SLR (2.2) remained relatively unchanged from the deposition layer at 2.5 km. The importance of deposition for the SLR can therefore not be understated, even during phases one and two, where a substantially reduced density aloft of the melting layer would likely have mitigated the densification experienced in the melting layer below.

The P3 scheme SLR was shown to be almost entirely dependent on riming. For example, the density of the precipitation field was uniform across phases as low as 2 km, but it was within this shallow layer that the final value of density was determined. Analysis of the vertical distribution of microphysical mass tendencies in Figure 8.2 showed that the amount of riming within the shallow layer was responsible for the density prediction at the ground. For example, during phase two the SLR was 6 times smaller than observed when riming increased the density of precipitation to near the bulk value of ice, and in phase three, riming was not typically present, the density remained low and the surface level SLR was high. It is notable though, that the density predicted in phases one and three is only an indicator of the surface SLR shown in Figure 8.1 column 5. In fact, the SLR in P3 especially is biased by the partitioning of ice mass amongst snow and ice. The liquid equivalent snow mass was much larger in phases one and three, which biased the mass toward the density of snow. Whereas in ISHMAEL, the snow mass was the smallest portion of the precipitation field. It is important then, that the snow depth is considered not only as a density and mass product, but in terms of the individual contributions of hydrometeor types.

8.2 Analysis of Density Formulations

From Figure 8.1 direct comparison of the density field to observations was conducted, and through Figures 8.1–8.2 the microphysical processes that induced the simulated surface level densities were determined. In P3, the most substantial process was identified to be riming, whereas in ISHMAEL, melting and deposition were more important. Additionally, it was found that the relative mass was an important factor when mass weighting the final

SLR. Thus, the aggregation routine of each scheme is called into question. Here we will analyse the mathematical relationship between density and these microphysical processes for each scheme.

8.2.1 Density Formulation per Scheme

In ISHMAEL, the mass-weighted density of precipitation is modified by microphysical processes via their effect on the precipitation mass tendency. From Jensen et al. (2017) (their Equation 14), the average particle density after a microphysical process has occurred is:

$$\rho_I(t+\delta t) = (1-w_x)\rho_I(t) + w_x\rho_x, \tag{8.3}$$

where w_x is a weighting function that ensures that the final particle density is related to the change in mass that originates with process x:

$$w_x = \frac{(dq_I/dt)_x}{q_I(t)}\Delta t \tag{8.4}$$

In the ISHMAEL code this applied per process as:

$$\bar{\rho}_{t+1} = \bar{\rho}_t\left(1-\frac{q_{\text{mlt}}\Delta t}{q_i}\right) + \rho_l\left(\frac{q_{\text{mlt}}\Delta t}{q_i}\right) \tag{8.5}$$

$$\bar{\rho}_{t+1} = \bar{\rho}_t\left(\frac{q_i}{q_i+q_{\text{dep}}\Delta t}\right) + \rho_{\text{dep}}\left(1-\frac{q_i}{q_i+q_{\text{dep}}\Delta t}\right) \tag{8.6}$$

$$\bar{\rho}_{t+1} = \bar{\rho}_t\left(\frac{q_i}{q_i+q_{\text{rime}}\Delta t}\right) + \rho_{\text{rime}}\left(1-\frac{q_i}{q_i+q_{\text{rime}}\Delta t}\right) \tag{8.7}$$

$$\bar{\rho}_{t+1} = \bar{\rho}_t\left(\frac{q_i}{q_i+q_{\text{wet growth}}\Delta t}\right) + \rho_l\left(1-\frac{q_i}{q_i+q_{\text{wet growth}}\Delta t}\right) \tag{8.8}$$

$$\bar{\rho}_{t+1} = \bar{\rho}_t\left(1-\frac{q_{\text{nuc}}}{q_i}\right) + \rho_I\left(\frac{q_{\text{nuc}}}{q_i}\right) \tag{8.9}$$

Equations 8.5–8.9 indicate density changes for melting, deposition, riming, wet growth, and nucleation respectively. Net tendencies are positive.

Note that the formulation for melting differs from other microphysical processes. This change enables the density to be calculated based on a loss of initial mass i.e. $q_{\text{mlt}}\Delta t/q_i \leq 1$. Whereas the formulation for other microphysical processes determine density when external mass is added, i.e. $q_i/(q_i + q_{\text{x}\Delta t}) < 1$.

Considering these formulations it is evident that the change in density per process depends only on the size of the mass tendency relative to the ice mass mixing ratio, and the size of the density associated with the microphysical process.

A simple analysis can be done by considering the ratio of mass tendency rates. For example, we might consider the mass tendency for wet growth and melting, as both processes occurred in close proximity. We may write the equation for density change due to melting as a ratio of the initial and final densities indicating growth or contraction of the density variable:

$$M_{\delta t} = \frac{\bar{\rho}_{t+1}}{\bar{\rho}_t} = (1-m) + \frac{\rho_l}{\bar{\rho}_t}m, \qquad m = \frac{q_{\text{mlt}}\Delta t}{q_i}$$

and the wet growth density as:

$$W_{\delta t} = \frac{\bar{\rho}_{t+1}}{\bar{\rho}_t} = w + \frac{\rho_l}{\bar{\rho}_t}(1-w), \qquad w = \frac{q_i}{q_i + q_{\text{wet growth}}\Delta t}$$

The ratio of these density tendencies $M_{\delta t}/W_{\delta t}$ describes the relative change in density that occurs amongst both processes. This information can be compared:

$$\frac{M_{\delta t}}{W_{\delta t}} = \frac{(1-m)\bar{\rho}_t + \rho_l m}{(1-w)\rho_l + w\bar{\rho}_t} \tag{8.10}$$

Examine the limits as the mass tendency becomes very small:

$$\lim_{q_{\text{mlt}}\Delta t \to 0} m = 0, \qquad \lim_{q_{\text{wet growth}}\Delta t \to 0} w = 1, \qquad \therefore \lim_{q_{\text{i}}\Delta t \to 0} \frac{M_{\delta t}}{W_{\delta t}} = 1$$

so when the mass tendency of wet growth and melting is very small, then the density change due to both processes is equivalent.

Now examine the limits as the mass tendency approaches q_i, i.e. the mass tendency is close to the mass of the entire precipitation field.

$$\lim_{q_{\text{mlt}}\Delta t \to q_i} m = 1, \qquad \lim_{q_{\text{wet growth}}\Delta t \to q_i} w = 1/2, \qquad \therefore \lim_{q_{\text{i}}\Delta t \to q_i} \frac{M_{\delta t}}{W_{\delta t}} = \frac{2\rho_l}{\rho_l + \bar{\rho}},$$

which is maximised for small $\bar{\rho}$. It is evident that as the average ice density approaches zero this ratio will approach 2. However, assuming the lower limit of ice density is approximately 50 kg m^{-3} then the ratio is slightly less:

$$\frac{M_{\delta t}}{W_{\delta t}} = \frac{2000}{1050} \approx 1.9, \tag{8.11}$$

i.e:

$$\begin{aligned} M_{\delta t} &\approx 1.9 W_{\delta t} \\ \bar{\rho}_{M,t+1} &\approx 1.9 \bar{\rho}_{W,t+1} \end{aligned}$$

So assuming identical initial masses of ice, and identical mass tendencies of wet growth and melting, the density due to melting can be almost double the density due to wet growth after one time step if the initial density is low enough.

A similar calculation can be made for general process X with associated process density ρ_x:

$$\frac{M_{\delta t}}{X_{\delta t}} = \frac{(1-m)\bar{\rho}_t + \rho_l m}{(1-x)\rho_x + x\bar{\rho}_t}, \qquad x = \frac{q_i}{q_i + q_x}$$

which has slightly different limit as the mass tendency approaches the ice mass mixing ratio.

$$\begin{aligned} \lim_{q_{\text{i}}\Delta t \to q_i} \frac{M_{\delta t}}{X_{\delta t}} &= \frac{2\rho_l}{\rho_x + \bar{\rho}} \\ &= \frac{2\rho_l}{\rho_x + 50}, \end{aligned}$$

which is maximised when the denominator is minimised. Therefore, assuming that the average density of ice particles is very low ($\sim$ 50 kg m^{-3}), the density factor difference will be dependent on the density of the added mass ρ_x. Considering the processes given in Equations 8.5–8.9 the two lowest densities of external mass will be ρ_{rime} and ρ_{dep}, which each have lower limits of 50 kg m^{-3}. Thus the theoretical maximum limit allowed by the ISHMAEL code is:

$$\lim_{q_i \Delta t \to q_i} \frac{M_{\delta t}}{X_{\delta t}} = \frac{2\rho_l}{50+50} = 20$$

$$\bar{\rho}_{M,t+1} = 20\bar{\rho}_{X,t+1}$$

Therefore, for identical initial masses of ice, the density due to melting is 20 times larger than the density due to deposition after one time step if the initial density of ice is small, and if the density of accreted rime or deposited vapour are also small. Of course, the tendencies of each process are opposite, the melting process increases density, whilst the deposition process tends to decrease density. Ice that exhibits a low initial density will experience little change if it accretes mass with a low density. However, this analysis indicates that the form of the density tendency equation for the melting process generally invokes much larger changes in density than other, competing processes. This is best illustrated for wet growth, which uses liquid density and occurs in the same temperature regime as melting.

The main limitation to this analysis is understanding the range of values that occurred for each process in the simulation. For example, the substantial differences in density examined theoretically here might not occur during the simulation. An ideal situation to investigate this effect is the density change during phases one and two within the melting layer. It was evident in Figure 8.1 that the greatest density change was found within the melting layer in ISHMAEL during phases one and two, and that melting was coincident with wet growth and sometimes riming. Therefore, the average values of mass mixing ratio, density of ice, and mass tendencies of each process could be collected, and the effect of the equation formulation could be examined.

Figures 8.3 and 8.5 show the average ice qualities per vertical level aloft of Stony Brook during phases one and two, respectively. In phase one, the melting layer, indicated when the average temperature (red, solid) exceeded 273.15 K (grey, dashed), was present between approximately 1.6–2.6 km in elevation. In the melting layer, ice mass mixing ratio (blue, solid) decreased and melting (black, dashed) and riming (black, dotted) became active processes, with melting typically 2–3 orders of magnitude greater than riming. The corresponding density field (Figure 8.3, right), showed a large average increase in density within the melting layer, rising from 600 to 800 kg m^{-3}.

The value of $M_{\delta_t}/W_{\delta t}$ was determined at approximately 2.5 km elevation, which aligned with a zone of melting and riming. In this region the ice mass was found to decrease on average, and the density increased. The corresponding average values for phase one were:

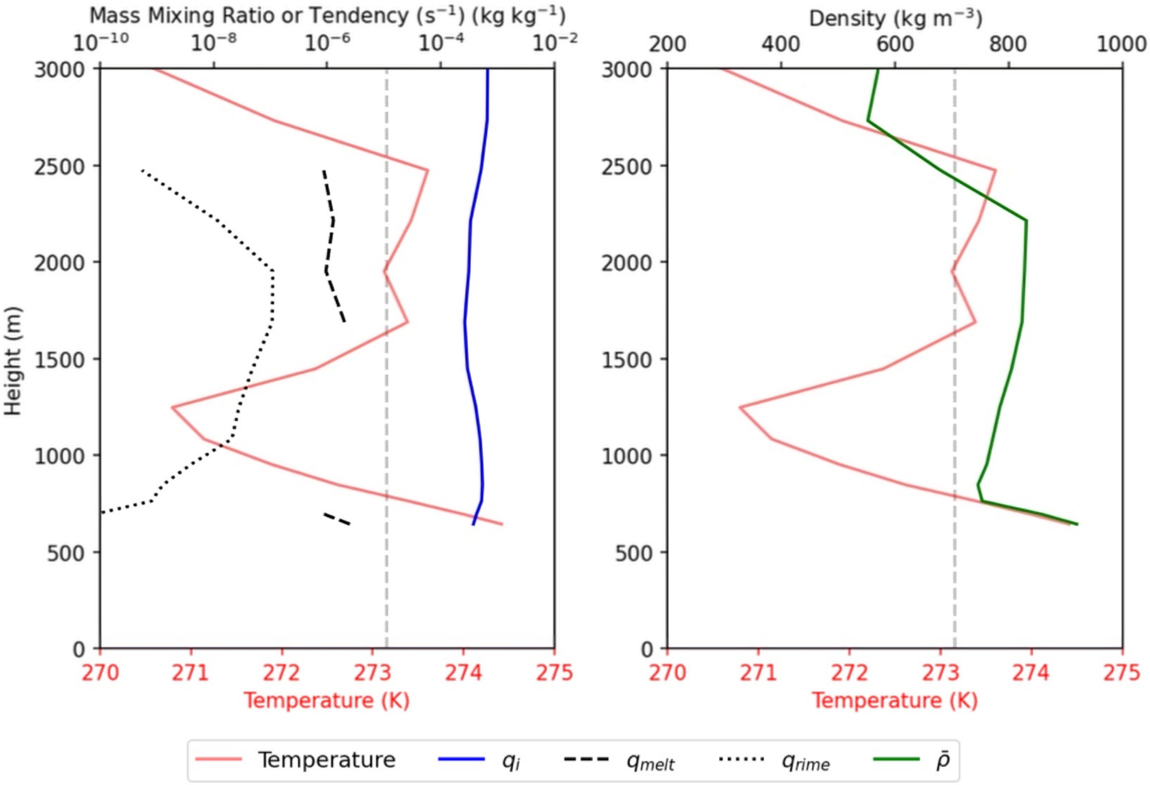

Figure 8.3. Change in microphysical process rate and density with height aloft of Stony Brook for phase one. Left: change [kg kg s^{-1}] in cloud droplet mass mixing ratio (blue), riming mass tendency (black, dotted) and melting mass tendency (black, dashed). Right: average density (green) [kg m^{-3}]. Temperature (K) overlaid for both panels in red.

$q_i = 5.1 \times 10^{-4}$ kg kg^{-1}, $q_{\text{melt}}\Delta t = 8.71 \times 10^{-7}$ kg kg^{-1}, $q_{\text{wet growth}}\Delta t = 5.47 \times 10^{-10}$ kg kg^{-1}, $\bar{\rho} = 680$ kg m^{-3}.

The resulting density evolution was obtained by direct substitution into Equations 8.5 and 8.8. The resulting density evolution for the values associated with the melting layer in phase one is shown in Figure 8.4. Density growth due to melting (red, solid) is considerably larger than the density growth found with the wet growth variable set (blue, solid). For example, after 15 minutes of simulation time, in which the mass tendency rates and ice mass mixing ratio are held constant, melting causes the density to increase by 100 kg m^{-3}. Whereas a negligible density change was found after 15 minutes for the wet growth equation.

An increased density due to melting was expected due to the high melt rate (8.71×10^{-7}) compared to the wet growth rate (5.47×10^{-10}). To test the difference in density arising from each framework specifically, the mass rates of wet growth and melting were swapped and the density evolution was recalculated. The result is shown in Figure 8.4 where dashed lines corresponding to each process i.e. density due to a low melt rate of 5.47×10^{-10} (red, dashed) and density due to a high wet growth rate 8.71×10^{-7} (blue, dashed). It is important to note that these mass tendencies were not associated with the simulation data and are

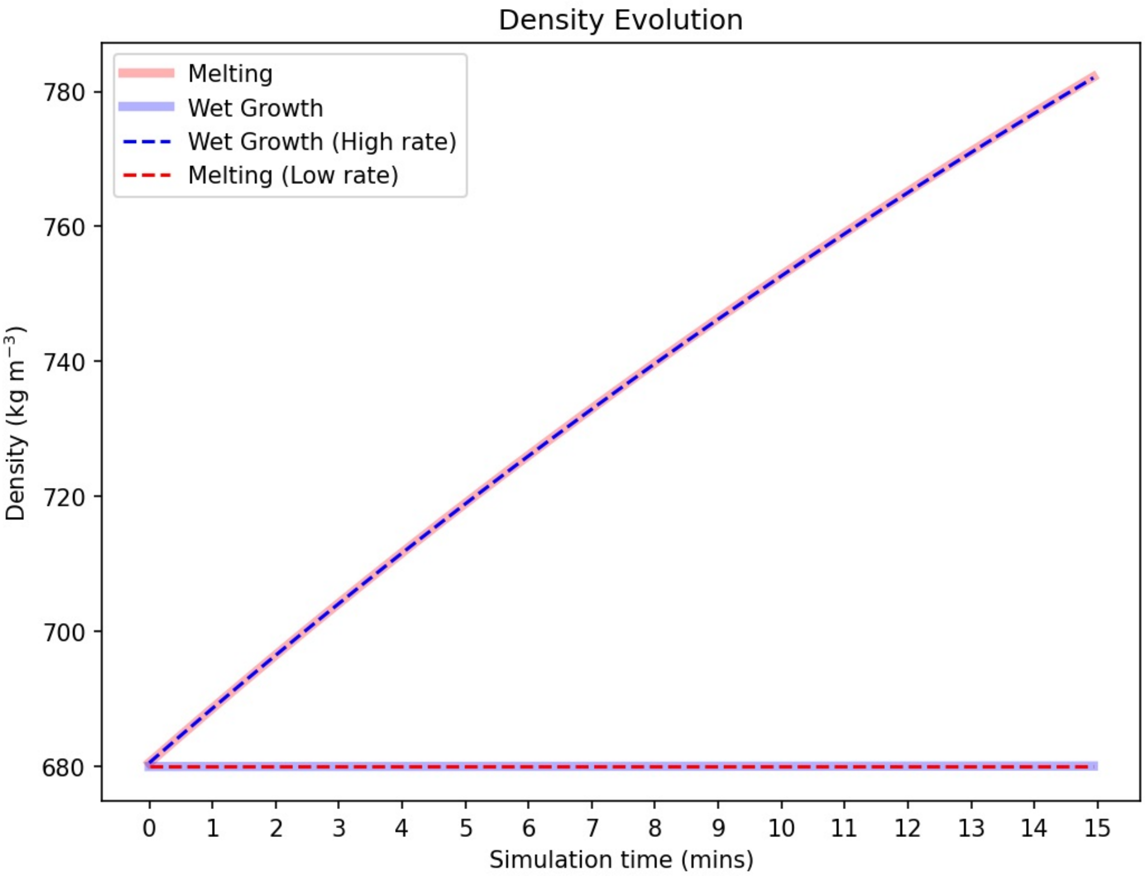

Figure 8.4. Density evolution during melting and wet growth for switched mass tendency rates.

shown here only for comparison of each density function.

The density evolution predicted by the melting equation and the wet growth equation swap when the value of the mass tendencies were swapped. A small difference was found in the net increase in density that indicated that the melting routine for either rate produced a slightly larger density than the wet growth routine for the same rate, but the difference was less than 1 kg m^{-3} in this case. The melting framework, whilst possibly influential, was therefore unlikely to be the source of the rapid densification that was observed in the ISHMAEL scheme.

Now we examine the variables that each density parameterisation is dependent upon. In the case of melting, the only variable is the mass tendency of melting and q_i. Therefore, here we consider possible sources for an erroneously large tendency, before cross examining the functions for wet growth. The mass tendency for melting largely follows from Lamb and Verlinde (2011) (p 374, Equation 8.85):

$$q_{\text{mlt}} = \frac{2\pi n_i \nu \max(a_{\text{ni}}, c_{\text{ni}})}{l_f} \left(k_T f_h (273.15 - T) + \rho_a l_v D_v f_v (q_{\text{sat0}} - q_v) \right) -$$

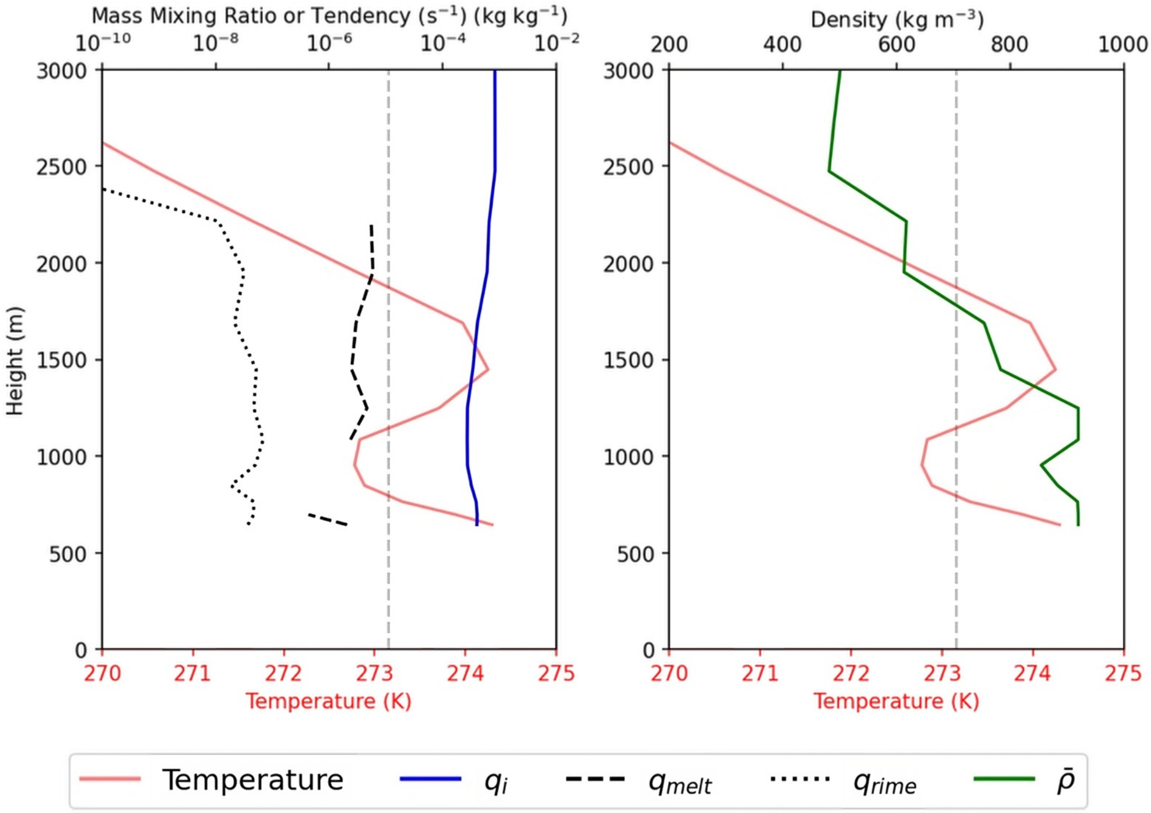

Figure 8.5. As in Figure 8.3 for phase 2.

$$\underbrace{\left(\frac{C_{\mathrm{pw}}}{l_f}(T-273.15)\frac{q_{\mathrm{rime}}}{\rho_a+q_{\mathrm{mlt,r,i}}}\right)}_{\text{Collision Enhancement Term}},$$

where k_T is the thermal conductivity, f_h and f_v are the particle-size dependent ventilation coefficients, l_v and l_f are the enthalpy of vaporisation and fusion, respectively, D_v is the diffusion coefficient, and C_{pw} is the heat capacity of water. The variables n_i, q_v, and q_{sat} are the number mixing ratio of ice crystals, the vapour mixing ratio, and the saturation vapour mixing ratio at 0°C, respectively. The largest of the particle characteristic radii a_{ni} and c_{ni} is also used. Finally, the variables q_{rime} and $q_{\mathrm{mlt,r,i}}$ are the mass tendency of riming and the mass tendency of melting due to contact of rain with ice in a warm environment.

In P3, the formulation is very similar:

$$q_{\mathrm{mlt}} = \frac{2\pi n_i}{l_f}\left(F_5 + F_{14}Sc^{1/3}\left(\frac{\chi_\rho \rho_a}{\mu}\right)^{0.5}\right)\left(\kappa(273.15-T) + \rho_a l_v D_v (q_{\mathrm{sat0}} - q_v)\right) \quad (8.12)$$

where $\kappa = 1.414 \times 10^3 \mu$, χ_ρ is a fall speed density correction term. F_5 and F_{14} are fall speed related variables derived from the particle size distribution. Notably, P3 does not incorporate enhancement of the melting term by collisions of ice and rain as in ISHMAEL.

The similarity of the melting formulation in each scheme allows for the parameters to the melting mass tendency to be directly compared. We note that there are four factors that could potentially drive differences in the mass tendency due to melting between P3 and ISHMAEL; the number concentration of ice n_i, the temperature above zero $273.15 - T$, the saturation mixing ratio difference $q_{\text{sat0}} - q_v$ and the collision enhancement term, which only plays a role in the ISHMAEL scheme. These terms were output and averaged in a shallow vertical column over Stony Brook in Figure 8.6.

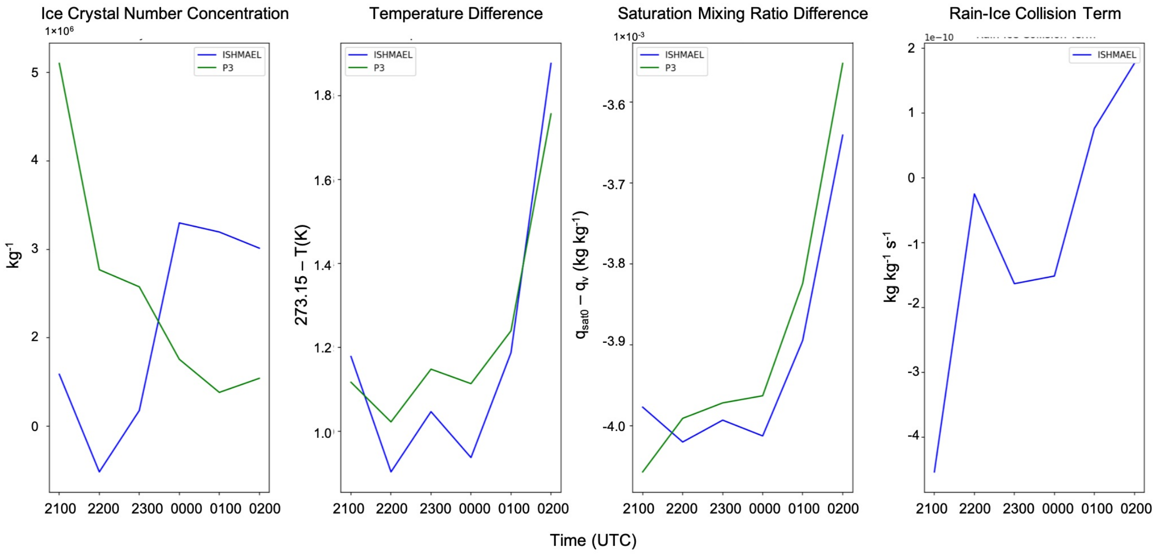

Figure 8.6. Time series of dependencies for the mass-melting process in a shallow layer aloft of Stony Brook during phases one and two; ice crystal number concentration (kg^{-1}) (left), temperature (K) (column 2), vapour mixing ratio (kg kg^{-1}) (column 3), and rain ice collision term (kg kg^{-1} s^{-1}) (column 4).

Comparison of the melting dependencies across the P3 and ISHMAEL schemes did not indicate that a substantial difference was present, and therefore did not explain the larger apparent effect of melting upon density in the ISHMAEL scheme. Figure 8.6 columns 2–3 show the temperature difference and saturation mixing ratio difference, respectively for the ISHMAEL (blue) and P3 (green) schemes. Both of these variables were similar in magnitude, and maintained very similar magnitudes and tendencies throughout phases one and two implying that the thermodynamic environment was consistent.

The most obvious candidate for a difference in mass tendency was the rain-ice collision term in ISHMAEL. This microphysical process ensures that rain colliding with ice in a warm environment melts the entire crystal, and thus, in the melting layer, where mixed-phase interactions are likely it might be assumed that this term could provide a substantial additional melting effect. However, analysis of this term in the ISHMAEL scheme (Figure 8.6 column 4) showed that the magnitude of this component did not generally exceed 10^{-10} kg kg^{-1} s^{-1}. Therefore, this component provided minimal adjustment to the melting tend-

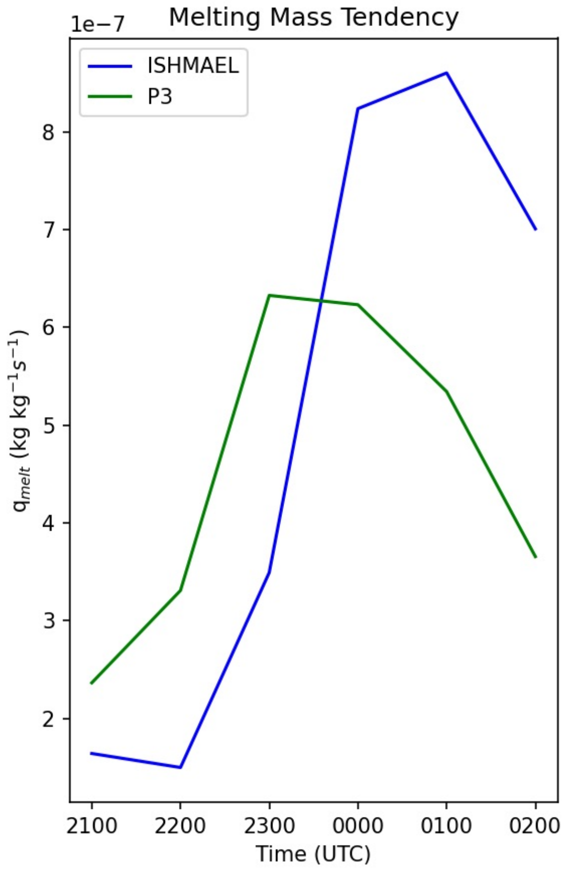

Figure 8.7. Tendency of melting for the ISHMAEL and P3 schemes during phases one and two in a shallow vertical layer aloft of Stony Brook.

ency and was not substantial enough to drastically alter the density profile of melting ice.

The number concentration (Figure 8.6 column 1) shows the largest deviation between microphysics schemes of all melting dependencies considered here. During phase one, ISHMAEL produced up to 6 times fewer crystals than P3 in the melting layer aloft of Stony Brook, but during phase two ISHMAEL simulated twice as many crystals as P3. It is possible that the relative difference in ice number concentration was a factor in the different density sensitivities for this schemes during melting. For example, Figure 8.1 shows that density increased more so in phase two when the melting layer was larger and when number concentration in ISHMAEL exceeded that of P3. However, even in the more narrow melting region during phase one, the increase in density was substantial (> 200 kg m^{-3}), especially compared to P3, which would contradict the influence of number concentration.

Similarities of the melting dependencies in both schemes do not generally indicate that a large difference in the mass tendency was present from these terms. The average melting mass tendency of ice in the melting layer was therefore retrieved for both schemes in the shallow layer aloft of Stony Brook and compared in Figure 8.7.

The most notable feature of Figure 8.7 is that the mass tendency exhibited by ISHMAEL is in good agreement with the shape of the number concentration curve in Figure 8.6 (column 1). For example, local inflections in the number concentration at 2200 UTC and again at 0000 UTC are mirrored by inflections in the melted-mass tendency at the same times. Additionally, at approximately 2330 UTC the ice crystal number concentration in ISHMAEL intersects the number concentration in P3, and exceeds it for the remainder of phase two. An identical relationship is found in the melted-mass tendency, positing that the number concentration is a significant factor in the melted mass parameterisation of both schemes, and the relative difference in number concentration may be a key factor for the loss and densification of ice. However, Figure 8.7 shows that this relationship is not apparent in P3, which continually reduces its number concentration during phase one whilst simultaneously increasing the melted mass tendency. This highlights an important consideration for this analysis, namely that, whilst number concentration is a dependency of the melting mass tendency, the number concentration is also dependent upon the ability of the melting process to remove ice crystals by conversion to rain. The apparent difference in relationship between number concentration and melted mass tendency posited by comparison of Figures 8.6 and 8.7 may indicate that the causal relationship in these two schemes differs. In P3, the relationship indicates that melting tends to reduce the crystal concentration, and therefore the rate of crystal reduction by melting is likely larger than the flux of crystals entering the melting layer. Whereas in ISHMAEL, the opposite relationship indicates that the melting process is directly driven by the number of ice crystals. It is possible therefore, that ISHMAEL has a larger net flux of crystal number to the melting layer, which sustains and enhances the melting process.

Overall, the SLR simulated at Stony Brook and determined in the previous chapter was found to originate with the melting process in ISHMAEL, and with the riming process in P3. The mass tendency profiles of these processes aloft of Stony Brook were analysed, and it was found that the melting mass tendency did not differ significantly between each scheme. The difference in simulated density tendency within the melting layer is therefore likely to originate with differences between the frameworks of the microphysics schemes, such as the mass distribution hypothesis.

Part III

Deposition and Riming in Two North-East US Winter Storms Captured by IMPACTS

Chapter 9

Introduction

In Part II, the development of precipitation by three microphysical schemes was detailed for a simulated north-east U.S winter storm. The character of the precipitation field at the surface was found to be unique to each scheme. The precipitation type and distribution predicted at the surface varied considerably from observations, and mixed success was achieved by each scheme in specific areas. For example, the Morrison scheme, which uses a conventional categorised-hydrometeor framework, was found to produce heavy snow over the entire domain for the entirety of the simulation. Whereas the ISHMAEL scheme, which is built on a generalised-ice framework that advects ice particle properties including ice particle shape, produced considerably more rimed particles, proving especially sensitive to mixed-phase processes. The P3 scheme, which is also built on a generalised-ice framework but explicitly tracks rime density, produced a more balanced precipitation field of some snow and some mixed-phase precipitation, but also tended to be extremely sensitive to melting aloft.

The large discrepancies identified in the simulated precipitation field for this case are a cause for concern. Such extreme differences in predicted precipitation with only the choice of scheme implies that even the act of choosing a microphysics scheme prior to the simulation start may be a considerable source of error. Indeed, the highly variable precipitation field that was found in this case, both at the surface and aloft, shows that the introduction of new prognostic variables and considerably more complex ice particle frameworks are not guaranteed to improve forecasts.

The divergence of forecasts from observations, and from each other, that was exhibited by these schemes requires further investigation if the source of these divergences are to be established and remedied. The most interesting case was the ISHMAEL scheme, which aims to incorporate crystal habit. This is an interesting development, because ice crystal geometry plays a role in many microphysical processes and therefore provides numerous opportunity to improve upon their existing parameterisations. However, the inclusion of habit was found to increase sensitivity to mixed-phase processes, whilst reducing aggregation efficiency, causing a severe underestimation of snow depth. Examining the qualities of ISH-

MAEL simulated ice crystals in the vertical, it was found that their qualities often originated with the deposition process, which produced a considerably larger deposition mass tendency in this scheme than in either Morrison or P3. As a result, the cloud ice field was very large in total mass, and travelled to low elevations relatively unaffected by other processes. Therefore, deposition was likely highly influential to the final precipitation type that reached the surface. It is therefore of interest to consider the habit parameterisations role during deposition, and its ultimate influence on subsequent microphysical processes.

9.1 Motivation from a Previous Study

Given the commonality of single-dimensioned capacitance formulations amongst bulk microphysics schemes, it is of interest to determine if the inclusion of a three-dimensional capacitance formulation to the ISHMAEL scheme may provide improvements to the particle size distribution of cloud ice that results from the deposition process. This is similar in nature to the questions previously posed for ISHMAEL in Part 1, that namely discussed how the inclusion of parameterised habit affected the rate of microphysical processes, and ultimately the precipitation simulated at the model surface. Indeed, the inclusion of habit is a complex update to a bulk scheme because the effects span all microphysical processes, and all types of ice. In ISHMAEL, the habit depends on the microphysical process rates provided by the inherent growth ratio of ice δ_* and additionally, the opposite is true such that the microphysical process rates are also dependent on the ice crystal geometry. Therefore the ramifications of geometry are far reaching in their extent, not only because this adaptation is novel, but because the ice habit affects almost every component of the microphysics scheme, from riming to capacitance.

In Part 1, the ISHMAEL scheme was compared to the P3 and Morrison schemes during a mid-latitude winter storm event that featured periods of heavy riming, a precipitation type each scheme had hoped to improve the forecasting of upon its release. Only ISHMAEL parameterised habit, whereas P3 captured rime density and Morrison used a discrete graupel category. The microphysical process mass-tendencies simulated by each scheme were compared, as well as the type and distribution of precipitation on the ground.

The results of Part 1 led to several important conclusions, but here we focus on the extent of ice production in the ISHMAEL scheme. During the simulation of three phases of the storm, ISHMAEL produced more graupel and small, high density ice crystal mass than other schemes, which resulted in an unusually high average density of the precipitation received at the surface and an unexpectedly small snow depth. The precipitation field was strongly influenced by sensitivity to melting, but poor aggregation and increased vapour deposition were also considerable aggravating factors. The consistent presence of high-density ice at all stages of the simulation was found to originate at high elevations indicating that early crystal growth at high altitude was an influential factor to the simulated precipitation density at the ground. Figure 9.1 showed that the total and average number concentrations and masses of cloud ice were much larger in ISHMAEL and Figure 9.2 indicated that the vapour deposition to graupel-like ice was considerably larger in magnitude and occurred high up in the cloud. It was hypothesised that vapour deposition produced high density and spherical ice at high elevation, and that these ice qualities caused resistance to aggregation during descent. Additionally, high masses of ice aloft of the melting layer at Stony Brook were likely to have increased the mass melting and rain production, with refreezing enabling the rapid descent of the melting layer base.

Given the increased total mass of cloud ice and density of cloud ice in the ISHMAEL scheme compared to other bulk schemes in Part 1, it is likely that the inclusion of habit has enabled a much larger deposition mass tendencies to ice particles than found in other schemes. When assessing the relationship between ice particle geometry and deposition, the natural course of investigation was to pursue the predicted ice crystal capacitance, which relates the ice geometry to the deposition mass tendency. It is hypothesised that the increased vapour deposition rates and comparably heavier and geometrically larger ices found in ISHMAEL were a direct consequence of the ice-habit parameterisation and that the source of the mass tendency difference is likely to be the capacitance term.

9.2 Investigation

In this part, the capacitance term is investigated to determine if it is likely to be artificially enhanced in the ISHMAEL scheme in comparison to other bulk schemes, and by extension, an influential component to the accurate simulation of the precipitation field in the ISHMAEL scheme. The capacitance forms a constant in the mass tendency equation:

$$\frac{\mathrm{d}q_i}{\mathrm{d}t}_{\text{dep}} = \frac{1}{\rho_a}\int_0^\infty 4\pi C_i G_i s_i n(a_i) da_i = \frac{N_i}{\rho_a} 4\pi C_I G_i \tag{9.1}$$

Therefore, if the capacitance term is increased a proportional increase in mass tendency is expected. This results in more efficient mass growth to crystals and ultimately a larger total mass of cloud ice.

In addition to investigating if the capacitance is a factor for deposition and cloud ice growth efficiency, it is also desirable to quantify the effects of this enhanced precipitation type for subsequent processes such as riming. For example, ices crystals that grow to large dimen-

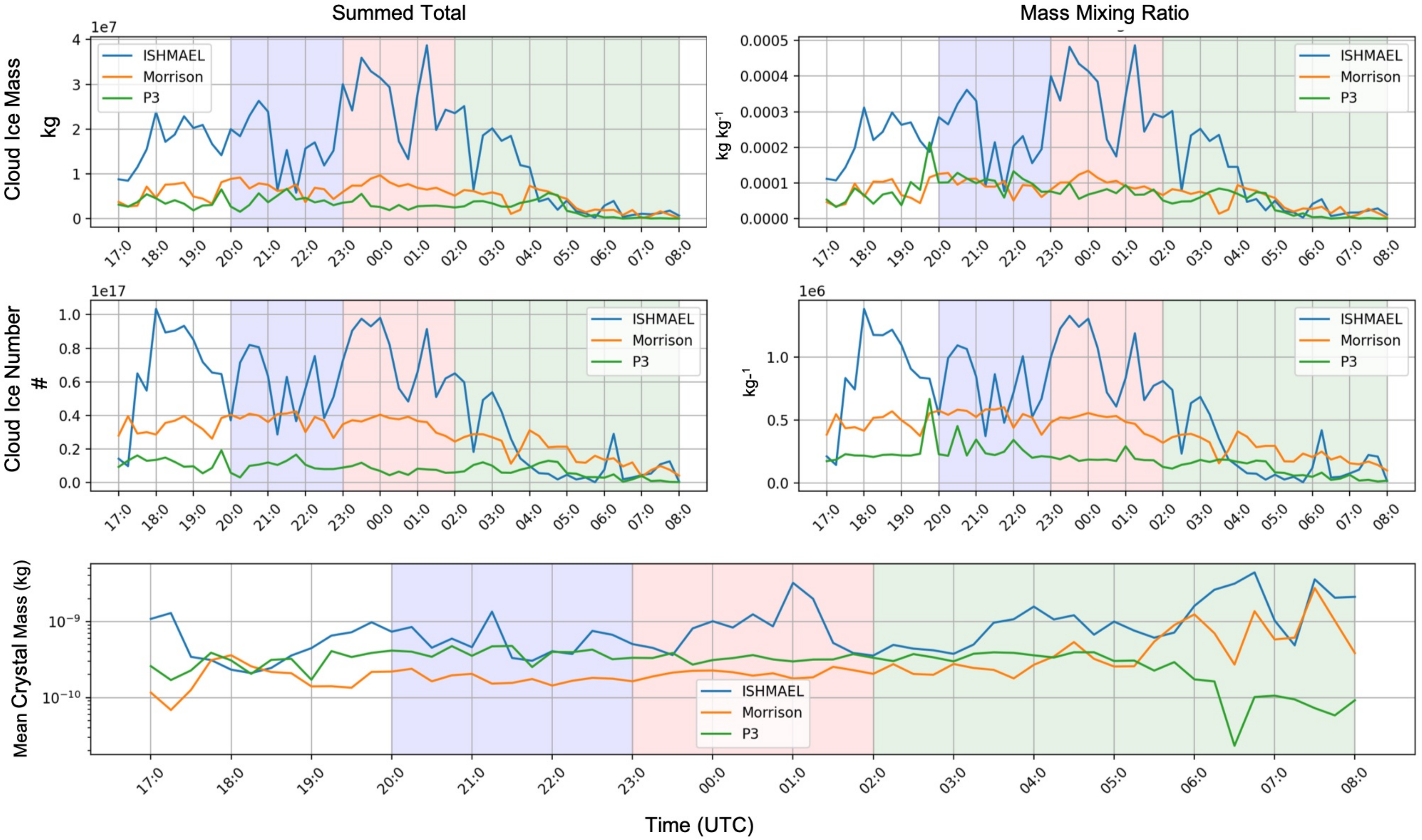

Figure 9.1. Cloud ice qualities as determined in a previous simulation of a north-east winter storm using WRF. Left column: Total summed mass and number concentration timeseries. Right column: variables as in left but averaged amongst non-zero valued cells. Bottom: mass divided by number indicating the average crystal mass. Background shading indicates phases of precipitation: Blue: mixed-phase and snow. Orange: mixed-phase and graupel. Green: Snow.

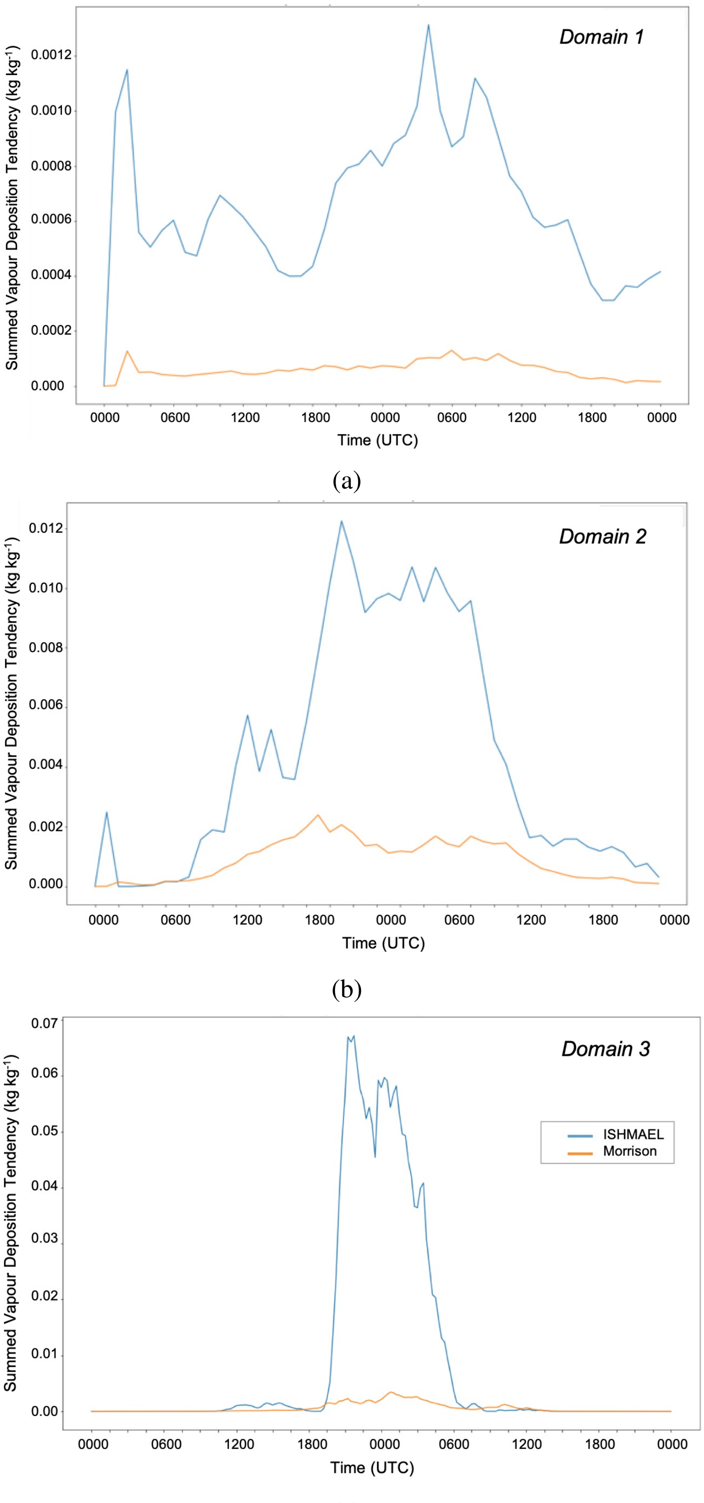

(a)

(b)

(c)

Figure 9.2. Time series of total vapour deposition mass tendency to graupel as determined in a previous simulation of a north-east winter storm using WRF for domains 1–3.

sions have greater fall speeds and surface areas than smaller crystals of similar density, and these variables are key dependencies to the riming process. As was shown in the previous study, riming, and especially wet growth, produce densification of the ice and tend its geometry towards spherical, features that typically resist aggregation and snow production. Therefore, the production of cloud ice crystals that are larger, may lead to the comparatively more dense ice precipitation field, and limited snow depth. In addition, spherical geometries stubbornly resist geometric change and fall with typically greater speed. Thus, the habit parameterisation may inhibit aggregation by not only creating spherical particles, but producing a faster falling precipitation field that reaches the surface quickly, and so reduces the total time frame available for aggregation to occur.

This study aims to investigate several questions pertaining to the capacitance, vapour deposition and riming across the two IMPACTS cases detailed earlier. This analysis is conducted using two microphysics schemes, the Morrison and ISHMAEL schemes, which provide a conventional one-dimensional, and novel three dimensional parameterisation of capacitance, respectively. The aims of this study are to determine the relative difference in ice qualities directly or secondarily resulting from the vapour deposition process. For example, the magnitude of the vapour-deposition mass-tendency to cloud ice, the relative difference in cloud ice mass and number concentration between schemes, and the consequences of elevated mass and number upon key riming or aggregation dependencies, such as fall speed, average crystal mass and density.

These questions are analysed using simulations of two north-east U.S. winter storms: the first on 18 January 2020 and the second on 25 February 2020 (hereafter Case 1 and Case 2, respectively). These storms were chosen for several reasons; first, that the cases resemble similar environments, meteorological events and locations as the storm simulated in Part 1. All, for example, are north-east U.S. winter storms that underwent a period of mixed-phase precipitation production amongst a more broad, snow-laden precipitation field at the surface. Also important was the availability of data, which was on the whole very thorough throughout the IMPACTS campaign, but was found to be most comprehensive for these two cases (see Figure 2.9). Observational data was recorded by the IMPACTS (The Investigation of Microphysics and Precipitation for Atlantic Coast-Threatening Snowstorms) study, a multi U.S. state, coordinated measurement run that combined simultaneous *in situ* and remote-sensing observations for a given storm. The data sets available include ice-particle size-distributions, crystal number concentrations, habit data, and precipitation code, which form useful verification data for the simulated ice particle size distributions, and in ISHMAEL, the approximate ice habit. Additionally, dual-polarisation radar data and multiple thermodynamic soundings are available for both cases to ensure a similar thermodynamic environment.

Simulation of these cases is conducted by the WRF model using ISHMAEL and Morrison microphysics schemes for otherwise identical model namelist settings. Three nested domains were centred over Long Island, and the central to eastern mainland United States, extending from the Gulf of Mexico to central Canada. The locations of these domains are are shown in Figure 2.9. The parent domain had 20 km grid spacing, and a grid-space ratio of 5:1 per nested domain was used for nested domains resulting in a domain 3 grid spacing of 800 m. The parent domain in each case was chosen to ensure that it encompassed any significant mesoscale features of the respective storm. Domain 3 was placed over the flight path of the P-3 to compare *in situ* measurement data at the highest possible resolution. The comparison of ISHMAEL shape parameterisation and *in situ* ice particle measurement is perhaps the first ever verification of three dimensional, scheme-derived capacitance in a mesoscale model.

To conduct the study, one must determine the spatial range and the precipitation to be included in the analysis. The following sections briefly describe the motivation for analysis over the given spatial subsection, the results obtained, and the shortcomings of this spatial analysis.

Chapter 10

Preliminary Results

To begin an investigation into the deposition process, it was important to first establish the cloud ice characteristics of both simulated IMPACTS cases. The cases were simulated using the ISHMAEL and Morrison microphysics schemes with otherwise identical namelist settings. The cloud ice precipitation-type was of interest as it is assumed to primarily grow via the vapour deposition process at high elevations within the cloud structure and so consequently acts as a seeding precipitation type for subsequent mixed-phase processes during descent.

10.1 Broad-scale Analysis of Cloud Ice

To understand the general character of each scheme's cloud ice production, the broadest possible comparison of cloud ice mass and number were made. Figure 10.1 shows the total cloud ice mass (top row) and number (bottom row) per time step over the parent domain for the ISHMAEL and Morrison (black) microphysics schemes. The Morrison scheme outputs the cloud ice category directly, whilst the ISHMAEL cloud ice is filtered using the partition method to obtain only cloud ice-like particles. In ISHMAEL, the cloud ice can derive from both of the simulated ice-type categories 1 and 2, which are based on aspect ratio at point of nucleation, so mass and number originating from both types are shown in blue and yellow, respectively. Note that the ice-type 3 category (aggregated ice) is omitted as cloud ice is not assumed to undergo aggregation (at which point it is classified as snow). The total ice mass (kg) and number (dimensionless) are calculated from the product of each respective mixing ratio with the air density ρ_a and the cell volume V. For these simulated cases, ρ_a was output by the WRF model directly and V was calculated in post-processing using the WRF staggered grid based at the cell edge, and the dynamic vertical grid height spacing determined by the WRF model during initialisation. The total mass or number is then retrieved by summation over each value throughout the entirety of the domain per time step, and the result is shown as an unstacked bar chart.

The results for the simulated total mass and number shown in Figure 10.1 indicate that ISH-

MAEL ice-type 1 produces a consistently larger total mass (Figure 10.1, top) than the Morrison scheme for both simulated cases (left, right), but that total ice number (bottom) remains remarkably similar. During case 1, the total cloud ice mass simulated by the ISHMAEL scheme for both ice-types was on average 4.9 times larger than that simulated by the Morrison, and 4.7 times larger on average during case 2. Perhaps most remarkable was the consistency of the total mass field simulated by each scheme. For example, the relative difference in ice mass between ISHMAEL ice-type 1 (blue) and Morrison (black) was broadly consistent for all time steps and for both cases, which indicates that the almost 5 fold factor difference in ice mass is likely to be a characteristic quality of the microphysics scheme rather than a consequence of the simulated meteorological environment. Notably, the total mass simulated within ISHMAEL's ice-type 2 category was considerably less (note the logarithmic y-axis scale) than ice-type 1. This is perhaps expected, as the ice category determines only the initial, nucleated ice aspect ratio, and the majority of cloud ice crystals are oblate at very cold (nucleation) temperatures. This finding is consistent with that of the previous simulation in Part 1, where the ISHMAEL ice-type 2 category was also found to typically contain far less mass than category 1.

In contrast with the simulated mass field, the total number of cloud ice particles (Figure 10.1 bottom) in the ISHMAEL ice-type 1 category was much more similar to that found in Morrison. On average, the ISHMAEL scheme had approximately 1.7 times as many ice particles in categories 1 and 2 as the Morrison scheme, and the difference between ice-type 1 and Morrison cloud ice was even less, reiterating the similarity between these categories. As with the total mass field, the number concentration retained a remarkable consistency in magnitude per scheme and per case, and the relative difference between ISHMAEL cloud ice number and Morrison cloud ice number remained very small at all times. For example, during case two (right) a period of declining number concentration was closely replicated by both schemes simultaneously. This consistency implies the same conclusion as with the total cloud ice mass, that the typical magnitude of the ice crystal number is likely to be characteristic of the microphysics scheme it pertains to, whilst the overall tendency depends on the meteorological event that is simulated. In the case of number concentration, these characteristic total numbers show very good agreement.

Given that the primary difference in cloud ice between the ISHMAEL and Morrison schemes was the production of cloud ice mass, it is advantageous to examine the deposition mass tendency in both schemes, which ultimately determines the mass growth of crystals by conventional means (i.e. ignoring computational amendments to the mass field such as autoconversion). The total deposition mass tendency is shown in Figure 10.1 per case as a subfigure in the top right of the total mass plot, respectively. The total deposition mass tendency is computed in a similar manner to the total mass and number, by multiplication of ρ_a and V, and summation over the entire domain per time step. Note that the per-second tendency unit is not modified. This choice was made because the domain 1 data was output with a *history interval* period of 1 hour between data points and it is therefore likely that the per-second deposition tendency integrated over an hour long period would be potentially inaccurate. However, the general magnitude and tendency of the mass deposition can be deemed to be broadly representative of each scheme over time. The mass tendency was filtered to account for only cells that were characterised as containing cloud ice. Physically, the total deposition tendency shown in each subfigure is indicates the amount of mass that was being redistributed from the vapour field to the cloud ice mass field per second across the entire domain.

The overall character of the total deposition mass tendency is similar amongst both of the simulated cases (Figure 10.1). The deposition was mainly applied to ice-type 1 (blue) in ISHMAEL, which is expected given that this ice category had a much greater total crystal mass and number than ice-type 2. The Morrison (black) scheme mass tendency was considerably smaller than was found in ISHMAEL, by almost one order of magnitude across both cases. Interestingly, the magnitude of the deposition tendency in Morrison is quite similar to that of the ISHMAEL ice-type 2 (yellow) category, which is surprising given that a large mass and number difference existed between these ice-types. Comparison of the total ice deposition tendency in Figure 10.1 (subfigures) to the total mass field (top) per simulated case, indicates that the large difference in mass tendency is likely a causal factor in the development of much larger total mass in the ISHMAEL scheme. Indeed the relative difference between ISHMAEL ice-type 1 and Morrison mass is reflected in the shape of the deposition tendency and shows good agreement over time. For example, reductions in the ISHMAEL ice-type 1 mass tendency rate at time step 40 in case one, and time steps 28 and 42 in cases one and two, respectively, are strongly correlated with corresponding reductions in the total mass field at identical times. Thus, it is a reasonable conclusion that not only is cloud ice mass typically larger in the ISHMAEL scheme than the Morrison scheme, as indicated across both simulated cases here and the simulated case in Part 1, but that this difference is a direct consequence of much greater mass deposition rates in the ISHMAEL scheme, and by extension the parameterisation of habit.

It is notable that the amount of ice considered at all stages in the simulation and at all elevations reduces the reliability of this analysis and, therefore, the reliability of the resulting conclusions. For example, we note that by considering the cloud ice qualities across the entire domain for all vertical levels, this analysis fails to consider variations of the cloud ice with height. This is an important feature to capture to ensure that the cloud ice mass originates from the expected location, i.e. at high elevations in the cloud consisting of mainly small, recently nucleated ice that grows primarily via deposition. Ice at high vertical levels is less likely to undergo simultaneous mass growth mechanisms via riming or wet growth and so is reliant directly on the deposition tendency. It is advantageous therefore, to corrob-

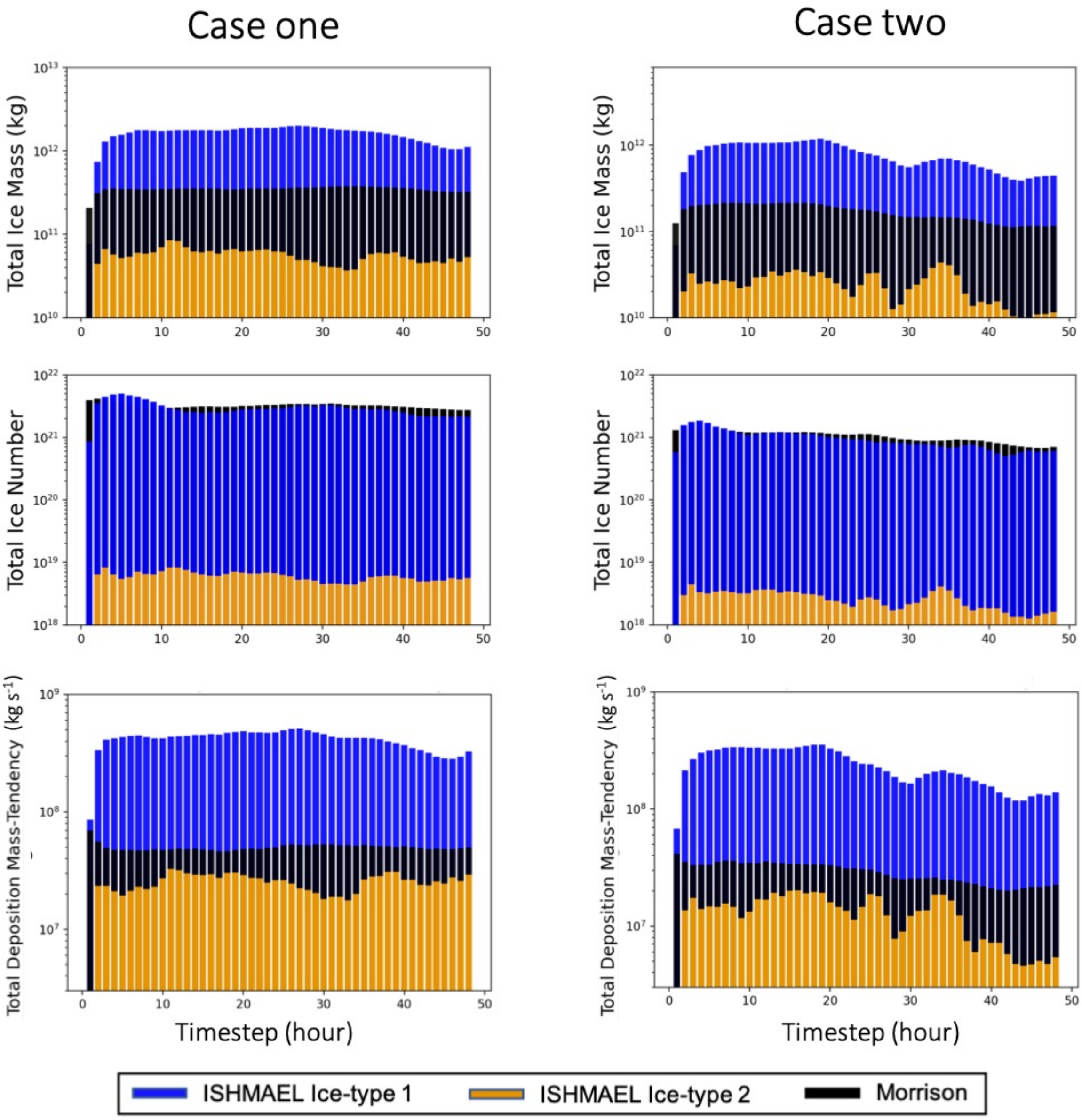

Figure 10.1. Time series of total cloud ice mass (kg) (row 1), total crystal number (dimensionless) (row 2), and total deposition mass tendency (kg s^{-1}) (row 3) simulated by ISHMAEL (blue, yellow) and Morrison (Black) during cases one (left) and two (right). ISHMAEL ice-type 1 (oblate-nucleated) and ice-type 2 (prolate-nucleated) are blue and orange, respectively. The x-axis is given in time steps, which are hourly from midnight.

orate the previous findings with a vertical analysis.

Figure 10.2 shows the total deposition mass tendency, total mass, and number (columns 1–3, respectively) per time step for cloud ice particles only in Case 1. Each quantity is given as a sum-total for the duration of the simulation time per vertical height layer between the surface and a maximum elevation of 15 km, which was determined to be the maximum elevation of the cloud top. The vertical distribution of the total quantities is given for the cloud ice filtered ice-types 1 (top, blue) and 2 (middle, yellow) in the ISHMAEL microphysics scheme, and the cloud ice hydrometeor category (black, bottom) in the Morrison scheme. Note that the simulated case 2 is not shown, but was found to be almost identical in distribution.

The vertical distributions in Figure 10.2 illuminate some key differences in the typical elevation of residency for cloud ice mass amongst both the ISHMAEL and Morrison schemes. The total mass field (column 2) shows the greatest overall difference in distribution with scheme. For example, in the Morrison scheme (black), cloud ice mass is top-heavy within the cloud, with peak simulated mass ($\sim 10^{12}$ kg) typically present between 7–11 km in elevation, and reduces gradually below this region by a factor of 10 at the surface. In stark contrast, the vertical distribution of the ISHMAEL (blue) ice-type 1 cloud ice mass is bottom-heavy, with peak simulated mass 7–10 times greater than in Morrison, and situated between 2–5 km elevation. A small reduction in cloud ice mass is apparent between this peak and the surface, such that cloud ice reaching the ground is on the order 10^{12} kg, approximately 30 times greater than was predicted by Morrison. The difference in overall vertical distribution is shown in Figure 10.3 where black shading indicates Morrison, light blue shading indicates ISHMAEL and dark blue indicates co-location of both schemes. It is evident that the mass distribution actually follows a very similar relationship amongst both schemes aloft of 9 km, which highlights that the total mass difference derives from persistent, lower level ice in the ISHMAEL scheme. A possible explanation for the difference in mass distribution at low elevations is that cloud ice in Morrison reaches the threshold for snow autoconversion, and therefore large quantities of the cloud ice mass are removed and added to the snow hydrometeor class. This results in an apparent decline in cloud ice mass and number simultaneously below 7 km. Whereas the ISHMAEL scheme does not autoconvert cloud ice mass and number, but rather, the ice can be transferred to an aggregated class if the aggregation criteria are met. As identified in Part 1, aggregation is far less efficient in ISHMAEL than Morrison, so cloud ice is likely to persist to low elevations and continue to gain mass by deposition. A second explanation is that the mass deposition process in ISHMAEL is larger than in Morrison, which increases crystal mass non-linearly with time. This would result in exponentially larger crystal mass, with crystals resident for the longest time having the greatest mass, and therefore descending deeper through the cloud.

In addition to the very large mass at the surface contributed by the ISHMAEL ice-type 1, the ice-type 2 category (yellow) also produces bottom-heavy vertical distribution that occurs somewhat lower in the atmosphere and results in a sizeable mass at the surface that is similar in magnitude to the Morrison scheme. The initialisation of the ice-type 2 category at approximately 10–11 km is interesting because it indicates that the onset of nucleation for prolate crystals is somehow tied to the elevation in a different manner to oblate crystals, although no such discrepancy exists in the nucleation formulation. Indeed, both ice categories are nucleated at the same rate. Therefore, the relative difference in elevation is theorised to originate with a greater depositional growth rate for oblate crystals that enhances the mass of oblate nucleated ice rapidly at the cloud top. In contrast, a slower depositional rate for prolate-nucleated ice results in less overall mass in this category, which materialises in Figure 10.2 as lower elevation onset nucleation. Importantly, this conclusion corroborates that the ISHMAEL cloud ice deposition rate is sensitive to the ice particle dimensions, and it is reasonable therefore to conclude that ice habit is a primary factor in the difference of deposition rates found in Figure 10.1, both between the ice-types in ISHMAEL, but also between the ISHMAEL and Morrison schemes overall.

In column 3 of Figure 10.2, the vertical distribution of cloud ice number is far more similar between the ISHMAEL (ice-type 1) and Morrison schemes. This is significant because it reveals that the similarities in total number throughout the domain (i.e. Figure 10.1, bottom) are also realised in the vertical. The peak simulated number concentration and surface level ice crystal number were broadly similar, which provides further evidence that the ice crystal number production rate is consistent amongst both schemes and therefore was not significantly affected by the inclusion of ice habit.

The vertical distribution of deposition in both schemes is shown in column 1 of Figure 10.2, and the approximate location of its maximum is highlighted with a translucent horizontal bar that spans all three columns for the purposes of comparison. It is evident that peak deposition occurs lower in ISHMAEL ($\sim$ 4–8 km) than Morrison ($\sim$ 8–11 km) and that these peaks closely correlate to the mass distribution. For example, in each scheme (and ice-type) the peak deposition region aligns closely to the peak, or just aloft of the peak ice mass layer. However, no such relationship is found with ice number. The correlation between deposition mass and ice mass are not surprising, but do provide additional evidence that the broad cloud ice qualities considered in Figures 10.1–10.2 are strongly tied to the deposition process, rather than other competing processes in the mass tendency equation, which not only increases confidence in the conclusions stated here but also corroborates that the deposition process is very influential to the precipitation field in the ISHMAEL scheme. The large difference in total cloud ice mass found in ISHMAEL at all elevations (but more so low elevations) is closely tied to the mass deposition rate, and therefore, the qualities of ice arriving at low elevations such as density, aspect ratio and fall speed will be largely determ-

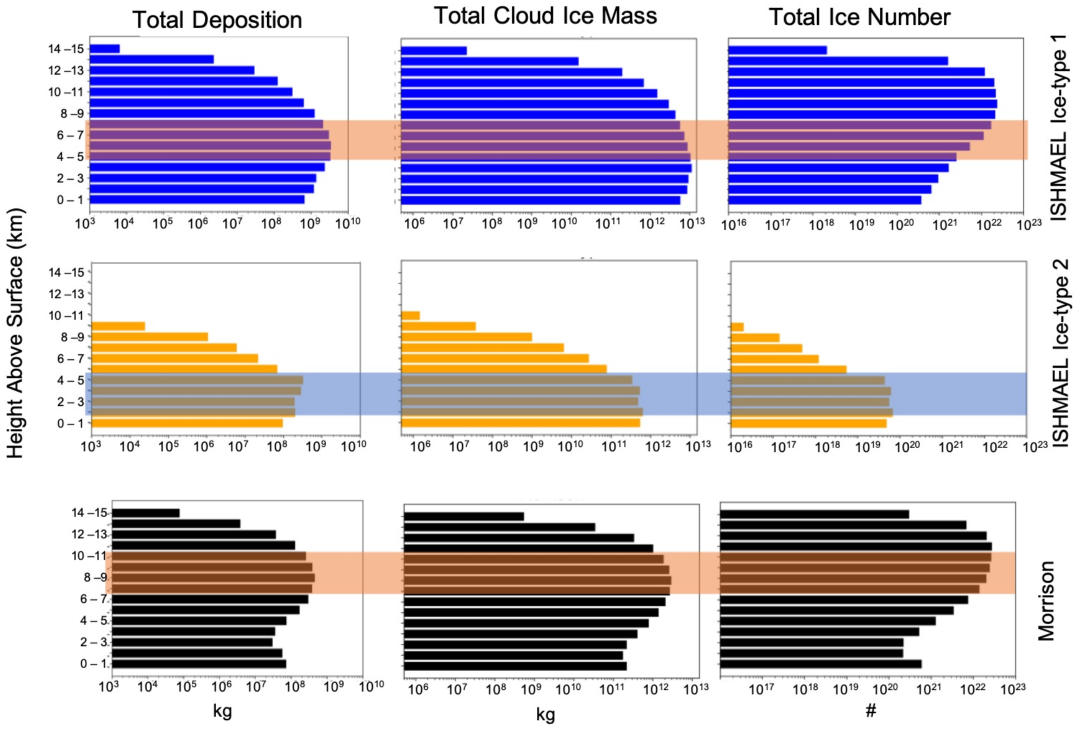

Figure 10.2. Average vertical distribution of total vapour depositional mass (kg)(left), cloud ice mass (kg) (middle), and crystal number (right) over the duration of the simulation for Case 1. ISHMAEL ice-types one (blue) and two (orange) are shown in rows 1–2, respectively. Morrison is shown in row 3 (black). Area of maximum deposition per scheme and ice-type is highlighted with coloured rectangle per row.

ined by the deposition process. These qualities are dependencies for the riming process and therefore, it is a reasonable assumption that riming and graupel production will depend on the efficiency and extent of the deposition process in the ISHMAEL scheme.

Having established that ice grown by deposition is likely to be larger in ISHMAEL than in Morrison, the next examination is on the origins of elevated cloud ice. We remain interested in ice grown by deposition, so it's important to determine of the whole ice cloud population, how much of it is grown under other microphysical methods? Figure 10.4 shows the mass growth tendency of several processes for the cloud ice category.

Now we seek to understand which microphysical process is driving the additional growth in ISHMAEL. The crystal capacitance used in ISHMAEL's vapour deposition parameterisation is expected to increase the mass growth rates proportionally, and hence may be a factor for exaggerated mass growth. Interestingly, the ice mass factor difference is within the expected error of the capacitance indicated by Bailey and Hallett (2006) but this presumes that Morrison presents an accurate benchmark of reality. Later, we will compare the simulation to IMPACTS data to determine the actual number concentration of ice found in each case.

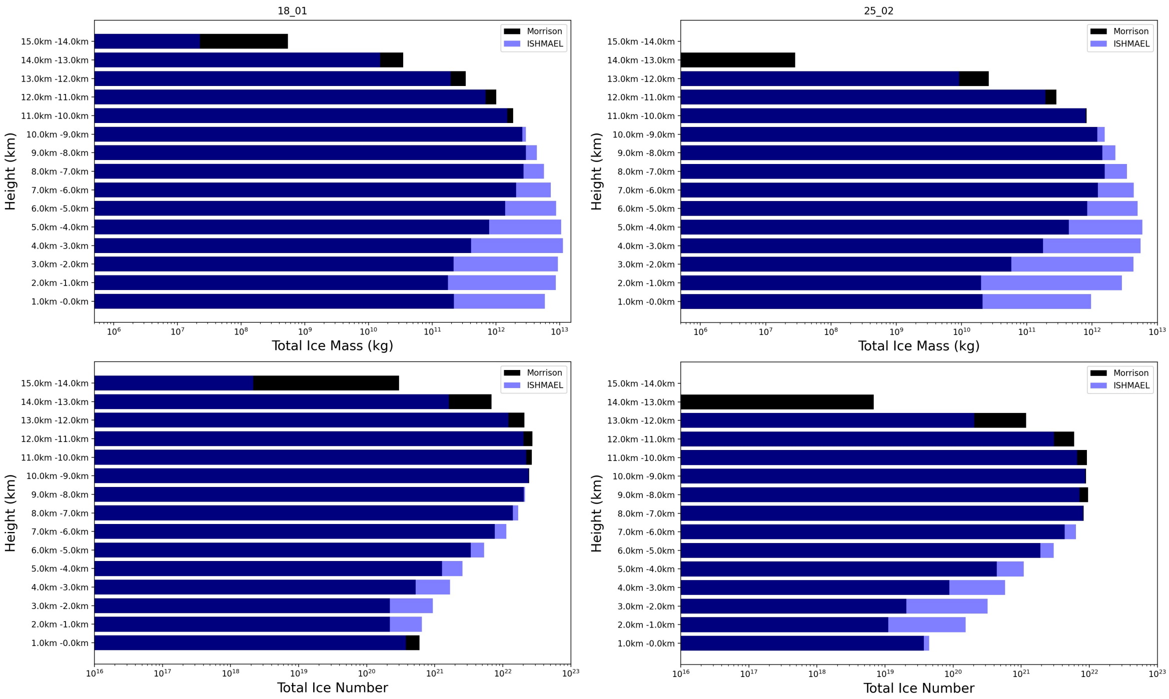

(a) Case 1

(b) Case 2

Figure 10.3. Vertical Distribution of total cloud ice mass (kg) and total cloud ice number (dimensionless) in the ISHMAEL (light blue) and Morrison (black) schemes (as in Figure 10.2 but overlaid). Overlapping ice mass is shown in dark blue.

10.2 Vapour Deposition to Cloud Ice

Given the consistently larger average cloud ice mass in ISHMAEL than Morrison, it is important to quantify which processes were responsible for this difference. To achieve this, the components of the cloud ice mass tendency equation can be examined. These components contribute directly to the mass growth of cloud ice and are therefore intrinsically linked to the cloud ice mass field. In the Morrison scheme, the mass tendency for cloud ice is a distinct equation that can be directly retrieved. For the ISHMAEL scheme, cloud ice forms only a subset of the overall generalised ice categories, and therefore the mass tendencies for cloud ice were extracted using a filtering method (see *Methods* section).

Figure 10.4 shows the total mass tendency components of differing microphysical processes that are applied to cloud ice with time for simulated cases 1 (left) and 2 (right). The mass tendency is obtained by summing over the entire domain (domain 3) per time step, and therefore indicates the total mass gained by the cloud ice category across the entire domain in a single time step. Note that the unit of per second (s^{-1}) is maintained.

In ISHMAEL, four processes that are important to the ice mass tendency are shown: the vapour deposition rate (blue), riming rate (yellow), wet growth rate (green), and rain-contact-freezing rate (red), the latter referring to ice mass added by ice-rain collisions that freeze raindrops. In Morrison, wet growth and contact freezing are not components of the mass tendency of cloud ice, so only deposition and riming are shown. Processes that were components of the mass tendency but that tend to reduce average mass, such as nucleation, secondary ice production and melting, are not shown, as this investigation aims to understand the sources of elevated cloud ice mass only.

Figure 10.4 shows that vapour deposition rates were the single largest contributor of total ice mass in both microphysics schemes for all time periods and across both cases. In ISHMAEL (Figure 10.4, left middle), deposition produced by far the most ice mass of all microphysics processes, consistently achieving summed total mass tendency rates of the order 10^{-1} for ice-type 1. By comparison, the next largest contributor of mass was riming, which produced mass on the order 10^{-1} kg kg^{-1} s^{-1}. In the Morrison scheme (Figure 10.4, right), the deposition process was approximately one order of magnitude smaller than in ISHMAEL on average, and interestingly, the summed riming mass tendency in the Morrison scheme was approximately two orders of magnitude smaller than in the ISHMAEL scheme.

Analysis of the average total mass per time step contributed by each process over the duration of the simulation showed that, in ISHMAEL, vapour deposition accounted for 94% and 95% of total ice mass growth on average for cases one and two, respectively. In Morrison the influence of vapour deposition was even more prevalent, with total mass from vapour deposition two accounting for more than 99% of total growth on average per time step in both cases. Thus, the cloud ice mass overall is practically determined by the vapour deposition process alone, with other process having minimal overall effect. Interestingly, the mass contributed by deposition was considerably less ($\sim$75%) for ISHMAEL ice-type 2 than for ice-type 1 ($\sim$95%) in both cases. This difference might indicate that deposition is less effective for column-like crystals.

Given the stark difference in deposition mass tendency between Morrison and ISHMAEL ice-type 1, and the weaker deposition tendency exhibited by ice-type 2, it is of interest to determine where cloud ice crystals typically receive the mass tendency of each process in the vertical. Figure 10.5 plots the average mass-weighted height of the occurrence of each mass tendency component to the cloud ice precipitation type as a timeseries. The average height of deposition is shown with dashed lines, and the average height of riming is shown with dotted lines. Additionally, the mass weighted height of cloud ice crystals is also shown for Morrison (black triangles), and ISHMAEL ice-types 1 (red circles) and 2 (green circles) for comparison.

Figure 10.5 indicates that Morrison cloud ice and ISHMAEL ice-type 1 cloud ice are located on average at approximately 6 km, and are co-located with the average height of the deposition mass tendency (dashed). This implies that cloud ice mass and the cloud ice de-

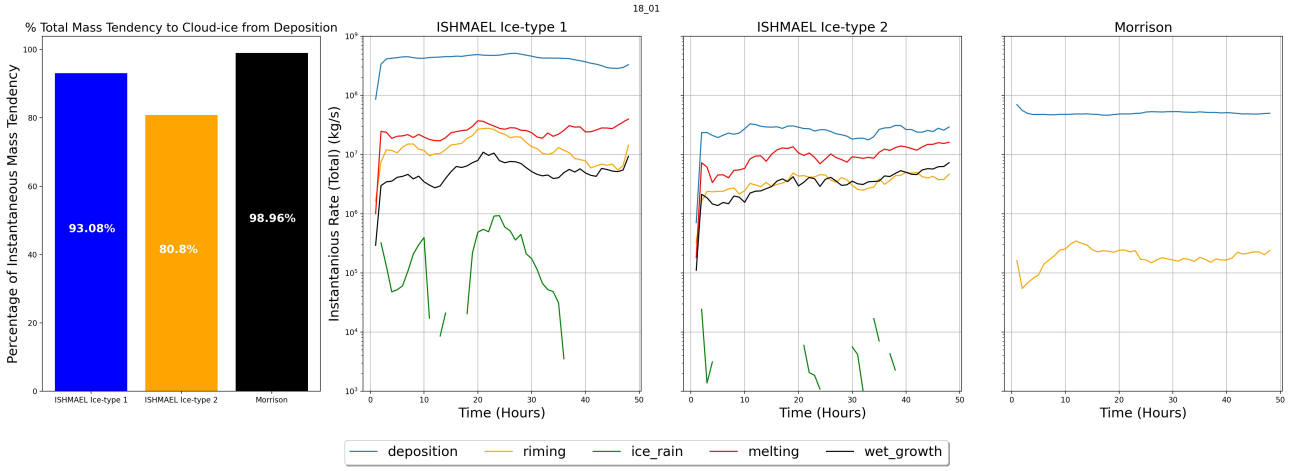

(a) Case 1

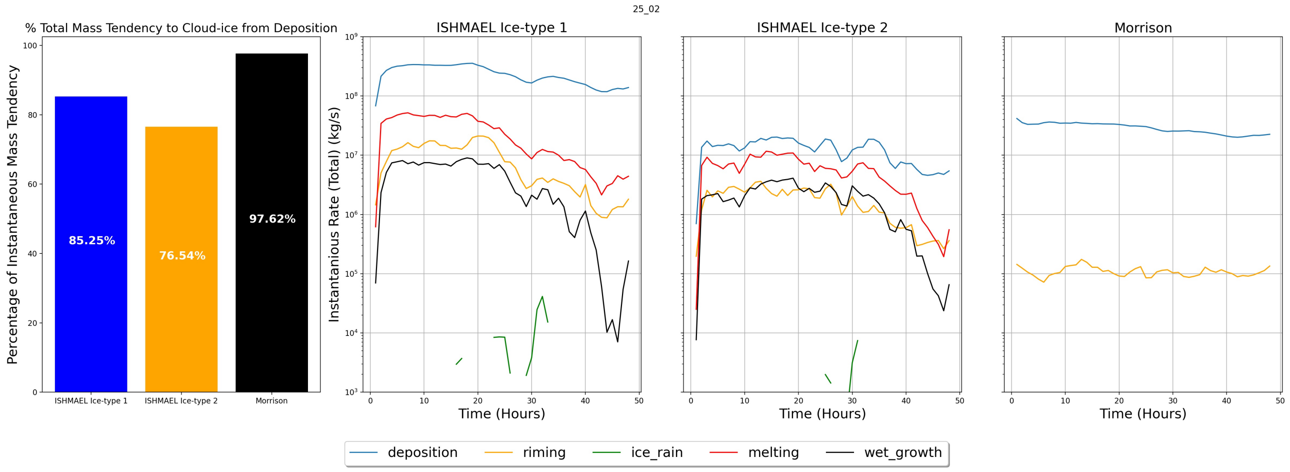

(b) Case 2

Figure 10.4. Mass tendency components for microphysical processes in cases one (a) and two (b). Left; the percentage of the total mass tendency to cloud ice that derives from the deposition process for ISHMAEL ice-type 1 (blue), ice-type 2 (orange), and Morrison (black). Right; timeseries of total mass tendency to cloud ice for microphysics processes (see Figure legend) for ISHMAEL ice-type 1 (column 2), ISHMAEL ice-type 2 (column 3), and Morrison (column 4).

position tendency are likely to be causally linked. In comparison, the typical riming level was between 3–4 km elevation for both cases, and for all ice-types. Interestingly, ice-type 2 forms much lower than cloud ice-type 1 or cloud ice in Morrison and is therefore likely to be present in an environment with more constituents for mixed-phase activity. The average height of cloud ice-type 2 is co-located with the average vertical level for both riming and deposition, which implies that the lower relative proportion of mass growth by deposition for this ice-type (see Figure 10.4) is a result of increased riming rather than reduced deposition. The location of the deposition layer for ice-type 2 so low in the domain also indicates that this ice-type may be nucleated at a lower region of the cloud.

To account for the difference in ice number for ice-type 2 shown in Figure 10.1, the average deposition rate was determined per ice-type and is shown in Figure 10.6. Here it becomes apparent ISHMAEL ice-type 2 does not undergo deposition less efficiently than ice one, rather both ISHMAEL ice-types 1 (red dashed) and 2 (green dashed) exhibit similar average deposition rates over both simulated cases. It is likely then given the findings of Figure 10.4, that ice-type 2 simply occurs at lower elevation in environments with considerably more riming and wet growth, and so these processes provide a higher proportion of the total mass growth overall, but the average deposition rate between ice-types 1 and 2 in the ISHMAEL scheme remain very similar in magnitude. In comparison, the average mass tendency exhibited by the Morrison scheme 10.6 (black solid), is almost two magnitudes smaller than the ISHMAEL scheme, highlighting the large difference in deposition rate exhibited between these schemes.

In terms of the broader picture, and the overarching aim to establish the origin of overall cloud ice mass differences, the large bias of mass in ISHMAEL towards the ice-type 1 category makes the location of columnar-nucleated ices less important to the cloud ice field overall. Ice-type 1, which accounts for the vast majority of all cloud ice, is almost entirely driven by deposition. Thus, it is likely that vapour deposition is the process responsible for the overall difference in cloud ice mass between the ISHMAEL and Morrison schemes.

The comparison of the total cloud ice deposition rates and the typical cloud ice particle mass in each scheme indicates that an inflated mass deposition tendency in the ISHMAEL scheme is likely responsible for the elevated growth over Morrison. Recall that, the typical ice crystal mass in ISHMAEL was 4.9 times larger than Morrison in case one, and 4.7 times larger in case two. This correlates well with the difference in total mass growth by deposition in each scheme, whereby ISHMAEL depositional growth produced approximately 4 times more mass than Morrison in case one and case two. The difference in ice mass between the schemes can therefore be partially attributed to the different mass growth rates provided by each vapour deposition formulation. That the deposition process is responsible for more than 94% of mass growth in each scheme and case only emphasises that this process is chiefly

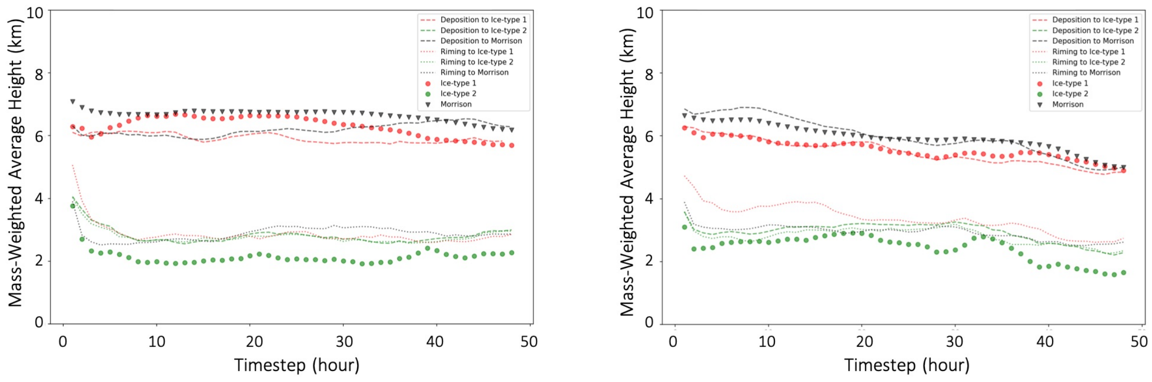

(a) Case 1

(b) Case 2

Figure 10.5. Time series of the mass-weighted average vertical elevation (km) of cloud ice, deposition to cloud ice, and riming of cloud ice in cases one (a) and two (b). ISHMAEL ice-type 1 (red), ice-type 2 (green), and Morrison (black) are shown with circles and triangles for each respective scheme. Deposition (dashed) and riming (dotted) are coloured with respect to each ice-type.

responsible.

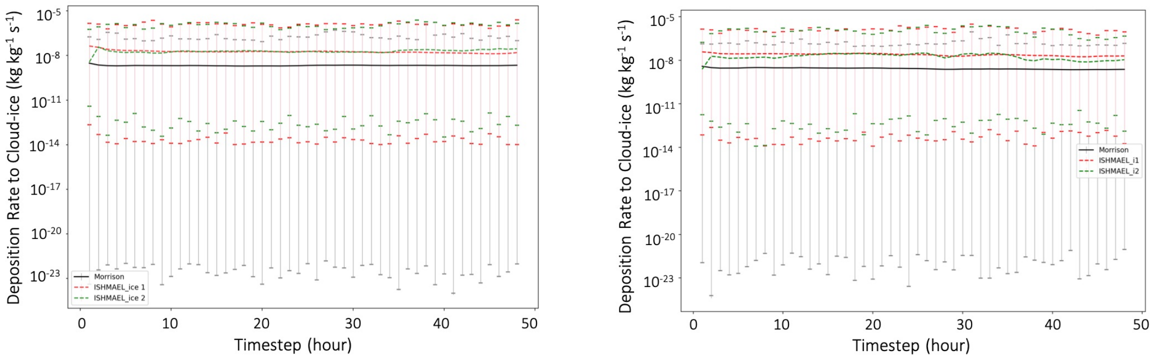

(a) Case 1

(b) Case 2

Figure 10.6. Time series of average, per-grid cell vapour deposition rate kg kg^{-1} s^{-1} for domain 1 in cases one (a) and two (b) simulated by Morrison (black) and ISHMAEL ice-types 1 (red) and 2 (green). Vertical bars (coloured according to scheme) indicate the (non-zero) minimum and maximum deposition rate simulated by the respective scheme in the time step.

10.2.1 Consequences of Elevated Vapour Deposition for Riming

Elevated ice mass-mixing-ratios and average ice-crystal mass resulting from deposition are significant qualities for latter microphysical processes. Here, the implications of these factors for the subsequent riming process are examined, namely any changes to the amount of riming per crystal (the riming rate) or the total amount of graupel produced by each scheme. The amount of riming that can take place is broadly dependent on two factors; the number of ice crystals with the potential to rime and the efficiency of those crystals to collect rime. Increases in either factor can be expected to result in a corresponding increase to the graupel field.

One key dependency for the riming process is the fall speed of cloud ice crystals. Fall speed is directly related to the ice crystal density and the flux of crystals is related to the distribution mass mixing ratio. Given that the average crystal mass in ISHMAEL is larger than found in Morrison due to increased deposition, the average ice fall speed in ISHMAEL is expected to be enhanced. Figure 10.7 shows a brief comparison of average cloud ice fall speeds for cases one (left) and two (right) averaged throughout the domain at all vertical levels.

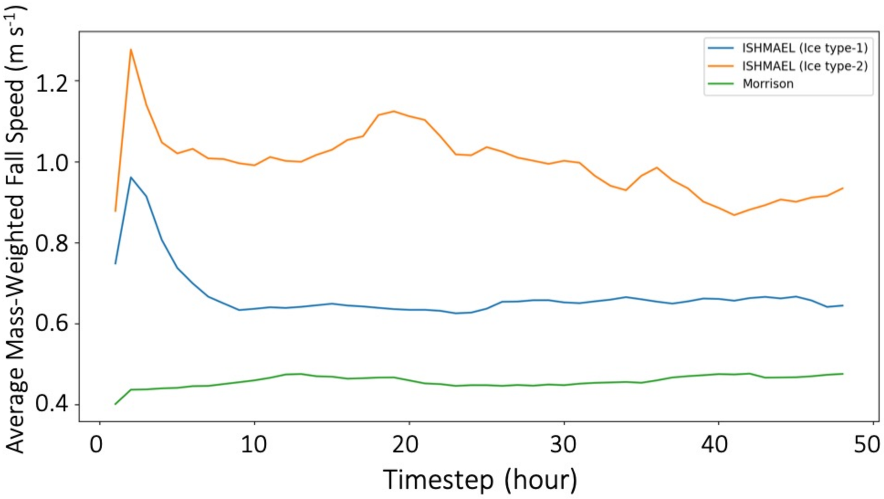

(a) Case 1

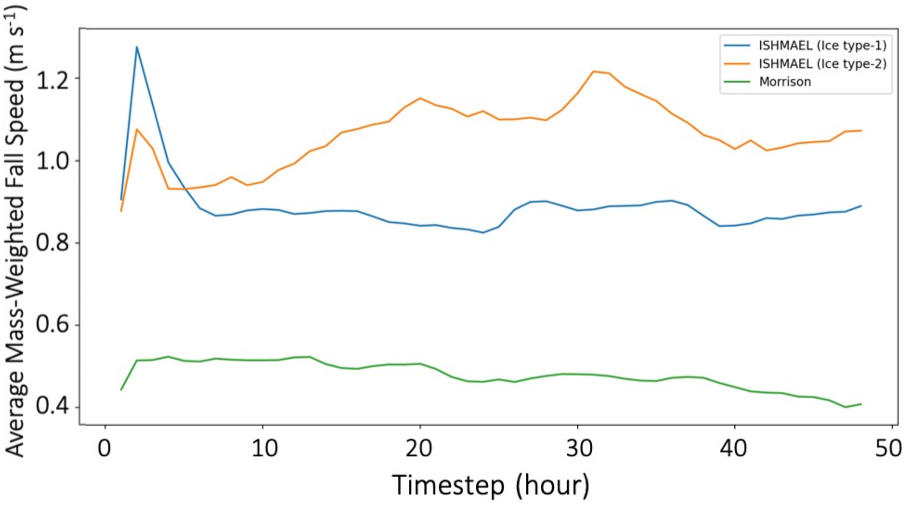

(b) Case 2

Figure 10.7. Time series of average, mass-weighted fall speed (m s^{-1}) of cloud ice particles simulated by Morrison (green) and ISHMAEL ice-types 1 (blue) and 2 (orange), for cases one (a) and two (b).

Figure 10.7 shows that on average, the ISHMAEL ice crystal fall speed was consistently greater than found in Morrison. Both of ISHMAEL simulated ice categories, ice-type 1 (blue) and 2 (orange) exceed the Morrison ice fall speed by a factor of 1.3 and 2, respectively, and this was found throughout the entire simulation. Notably, ISHMAEL ice-type 2 (prolate-nucleated) had a higher average fall speed than ice-type 1. It is likely that this difference derives from the different average altitudes of growth identified in Figure 10.5, where ice-type 2 was found to occur much lower in elevation near the typical height of riming, and so is likely to accrete mass increasing its fall speed. In contrast, ice-type 1 was found much higher in the cloud, and therefore likely exhibited lower fall speeds that reduce the overall average.

Figure 10.7 is a very coarse overview of the fall speeds that are actually applied by the riming parameterisation in each simulation. To increase confidence in a causal relationship between elevated ice mass and fall speed, the distribution of these two variables can be represented explicitly by extracting both values per cell and plotting the resulting value-pair in a scatter diagram. This method is is shown for each simulated ice-type and each case in Figure 10.8. As the number of data points is very large, a density component was applied via colour-mapping of the data points in accordance with their local density on the plot, which helps to identify where each ice-type's fall speed falls most frequently. In Figure 10.8, density colour-mapping is carried out in accordance with the pixel density of the graph, which is a reasonable indicator of the fall-speed ice-mass relationship. The average crystal mass is plotted rather than the ice mass mixing ratio, to reduce the likelihood of artefacts from number-weighting, and because this variable is a physically realistic dependency for fall speed.

The relationship between fall speed and average crystal mass shown in Figure 10.8 for cases one (top) and two (bottom) are remarkably similar, highlighting that these distributions are likely to capture a fall speed relationship that is characteristic to the scheme. The average crystal mass range of both ISHMAEL and Morrison ices is approximately 6 orders of magnitude, but the ISHMAEL range (10^{-12}–10^{-6}) is one order of magnitude larger than that of Morrison (1×10^{-13}– 10^{-7}) which is in keeping with the difference in average ice-crystal mass-mixing ratio. The majority of this ice, signified in yellow, follows a near exponential path (in log space) which eludes to linear proportionality between ice mass and fall speed. In the range 10^{-11} and 10^{-9} ice fall speeds follow a very similar path for ISHMAEL ice-type 1 (Figure 10.8, left) and Morrison ice (right), but ices with mass larger than this range have a slightly greater fall speed in ISHMAEL. Indeed, the most notable feature is the significantly larger spread in fall speeds in ISHMAEL, with ice reaching and exceeding 5 m s^{-1} whereas Morrison ice does not exceed 1.5 m s^{-1}. This latter fall speed limit is exceeded by ISHMAEL ice at values as low as 10^{-9} kg, enabling faster fall speeds for comparable ice crystal mass.

Overall, both schemes show that crystals with the largest masses are correlated with the highest fall speeds, and both schemes follow a similar relationship between these two vari-

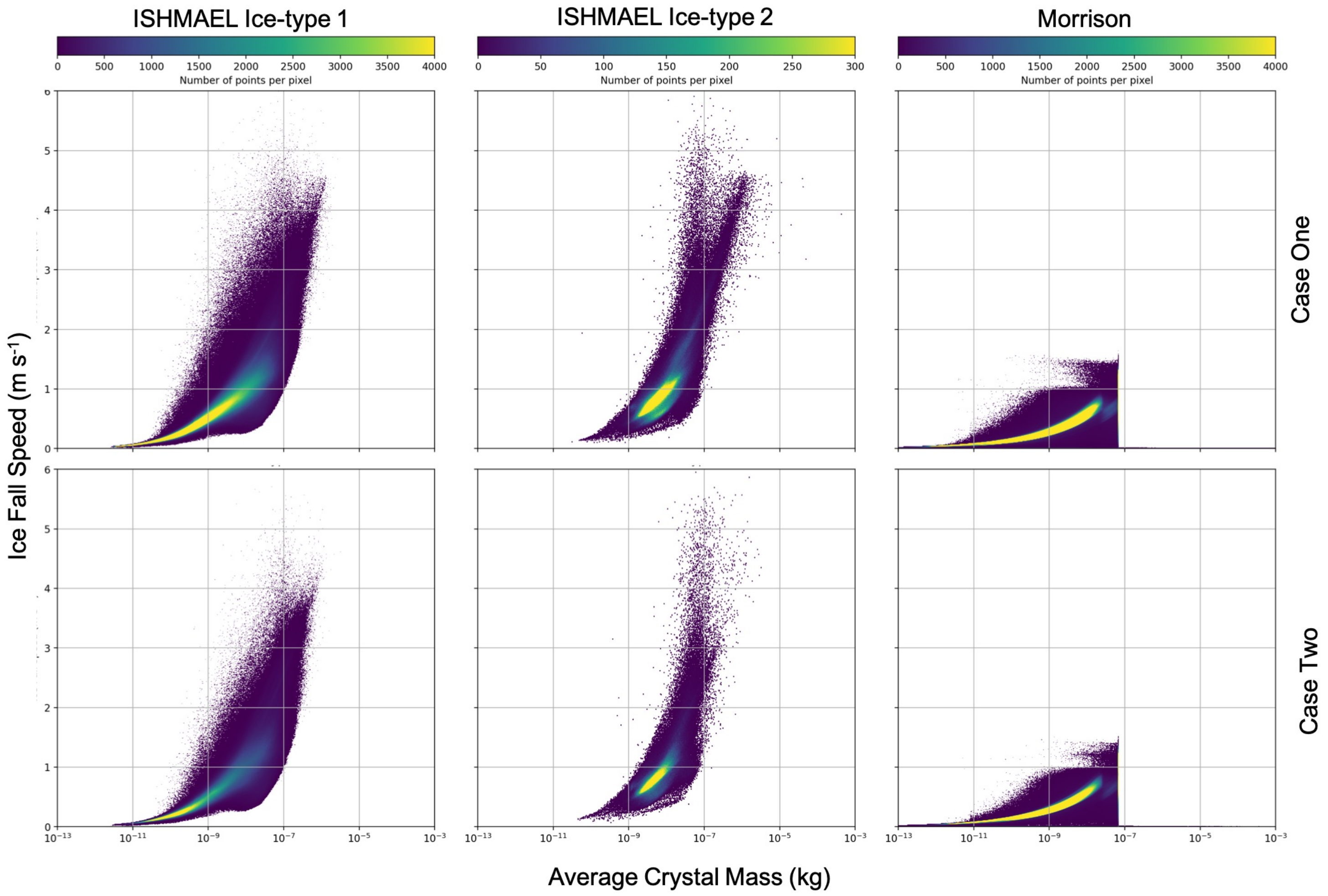

Figure 10.8. Scatter-density plot of ice fall speed (m s^{-1}) versus average crystal mass (kg) per cell in domain 1 for ISHMAEL ice-type 1 (left) and ice-type 2 (middle), and the Morrison scheme (right) during cases one (top) and two (bottom). Density colour mapping is per graph-pixel.

ables. However, the ISHMAEL scheme exhibits a much larger spread in possible fall speeds per mass than was found in Morrison. For example, ice crystals with an average mass of 10^{-8} kg might obtain a fall speed of 1.5 m s^{-1} but a similar crystal in ISHMAEL readily attains twice this fall speed value. Comparison between this relationship, and the typically greater average crystal mass in ISHMAEL draws a direct relationship between the deposition mass tendency and the average fall speed of ice that will likely be consequential for riming.

In ISHMAEL, the riming procedure states that collection of rime occurs only when ice crystal fall speeds exceed those of co-located rain droplets, so ice that exceeds the rain droplet fall speed can therefore be considered to have riming potential. Given that we have established a link between increased deposition mass tendency and increased fall speeds, it might be expected that elevated deposition in the ISHMAEL scheme will enable a greater proportion of the ice crystal field to exhibit a fall speed in excess of the rain drop fall speed. Under the assumption that rain droplet fall speeds remain unchanged, a heavier and faster falling cloud ice population would lead to a correspondingly higher proportion of ice meeting the criterion for riming, thus increasing the constituents available to be rimed upon. Given that this criteria defines the upper limit of the total number of graupel particles that can be produced, overactive deposition in ISHMAEL helps to maximise the potential for riming by increasing the particles that may be rimed.

Beyond this, further consideration must be given to the collection efficiency which, too, depends on fall speed, or rather the relative fall speed of droplets and ice. Faster falling ices tend to rime more, as aerodynamic deflection becomes less likely, and thus it is expected that faster falling ice will collect rime more quickly. Additionally, the process of accretion increases the average crystal mass and therefore the fall speeds, the ice growth is likely non-linear. Increased ice fall speeds are likely to compound this non-linear growth by increasing the initial value of fall speed, which will resulting increase at a far faster rate.

To determine the relationship between the riming mass tendency and fall speed, both qualities were retrieved for the ISHMAEL scheme, and are shown in Figure 10.9. An identical method to Figure 10.8 was used in which the value of the riming mass tendency and the falls speed are determined from each cell and shown in a scatter density plot, where colour-mapping is in accordance with the local pixel density.

Figure 10.9 shows that both ISHMAEL ice-types have a similar distribution that primarily follows a broadly exponential (log-space linear) relationship in which the riming mass tendency increases with average crystal mass mixing ratio. However, the spread in riming mass tendency is large in the mass mixing ratio interval 10^{-3}–10^{-7}indicating that there are considerable variations in the degree of riming with ice mass, likely due to further riming dependencies such as ice shape or droplet distribution. Nonetheless, a generally casual re-

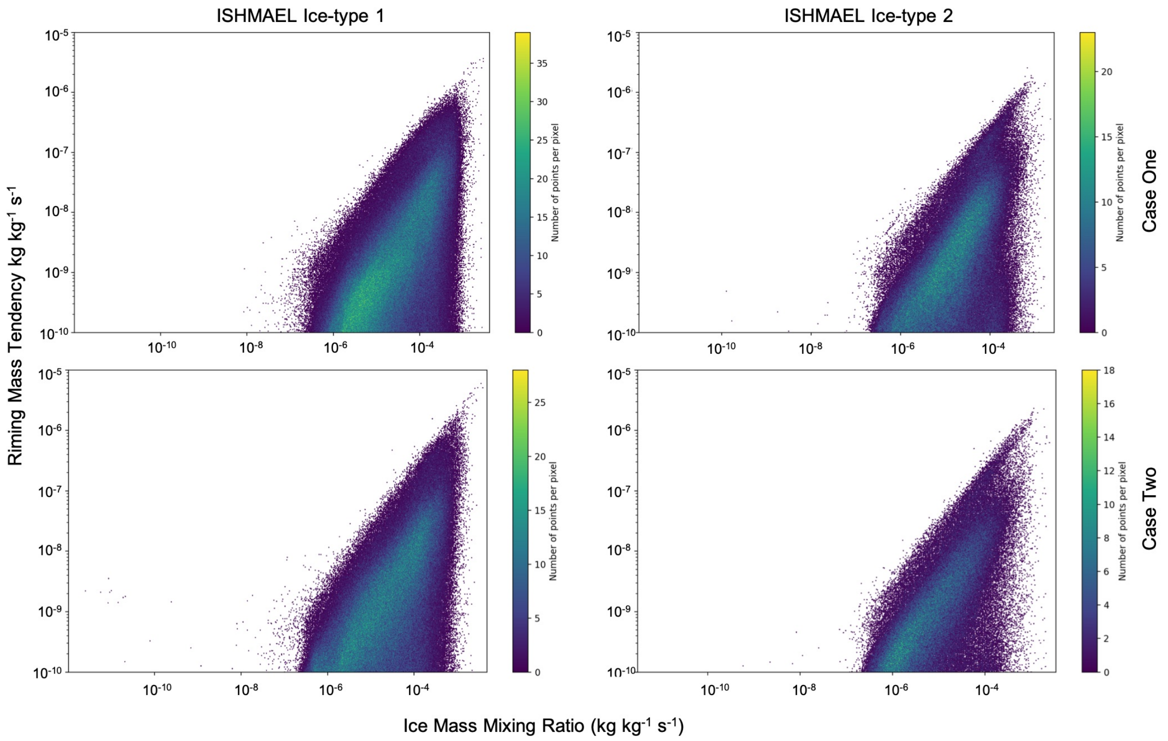

Figure 10.9. Scatter-density plot of ice riming mass tendency (kg kg^{-1} s^{-1}) versus ice mass mixing ratio (kg kg^{-1}) per cell in domain 1 for ISHMAEL ice-type 1 (left) and ice-type 2 (right) during cases one (top) and two (bottom). Density colour mapping is per graph-pixel.

lationship is identifiable, in which larger ice fall speeds will incur larger riming mass tendencies. Therefore, the argument built so far, that increased ice mass resulting from the deposition process also produces an increased ice fall speed, can be extended to the riming process, namely that these increased fall speeds will increase the rime-mass tendency, and therefore produce more graupel over time.

For collection efficiency, riming has several dependencies including fall speed, droplet size distribution and the ice geometry. An increase in the typical ice crystal mass will produce proportionally greater ice fall speeds, which in turn, will affect droplet collection efficiency in the manner described above. Greater ice crystal mass must also affect the geometry of ice as the additional mass not only increases typical crystal volume, but is also distributed along the crystal axes. Of these two further considerations, increased volume will generally increase the potential for riming due to a proportional increase in surface area available for sweep-out. However, the impact of shape or habit of ice on the riming efficiency is less obvious. Some geometries rime more effectively than others, so not only is the volume gain important to assess, but also the mass distribution hypothesis during the deposition process.

Chapter 11

Cloud Overview

There are some limitations to the analysis discussed in Figure 10.2 that it would be advantageous to contextualise and mitigate. One feature of the ice mass field shown in Figure 10.2 is that cloud ice in ISHMAEL persists at lower depths than in Morrison. This complicates the results, namely because at these low elevations more so than at the cloud top, other microphysical processes are likely to modify the ice qualities and thus we have reduced confidence that the difference in ice mass, fall speed or geometry (i.e. riming dependencies) originates exclusively from the vapour deposition process. Recall that the investigation of vapour deposition mass tendency in relation to the inflated cloud ice mass field is a proxy for the larger investigation that seeks to determine the influence of parameterised ice habit on deposition and mass growth. The focus so far has been on the magnitude of the deposition mass tendency, which is a function of the ice particle axes in ISHMAEL through the capacitance term. In order to make direct comparisons between the ice habit parameterisation and the cloud ice field during deposition, it is important to isolate the cloud ice field to only ice growing via the deposition process. For example, ice that grows primarily through non-depositional microphysical processes will have a different relationship to ice particle axes that is unrelated to the capacitance analogy and may therefore invalidate any conclusions.

To increase confidence in the relationship between deposition and cloud ice throughout the domain, a methodology was developed to compare the magnitude of the mass tendency to the resulting changes in the cloud ice qualities without external interference of these qualities by other processes. Such a task is usually reserved for idealised simulations, but in this case we wish to examine the effect in the wider context of the simulated storm. Consequently, we shall make some assumptions and allow ourselves a degree of lenience in order to achieve a semi-idealised or quasi-idealised level of analysis.

A key part of this investigation will be to determine the rate of change of ice qualities (i.e. riming dependencies) in the ISHMAEL scheme as a consequence of the deposition mass tendency. For example, how the density or shape of ice evolves during deposition. It is important to note that the change in these ice qualities is a non-linear process, as the deposition rate and ice particle qualities are mutually co-dependent. Therefore, we expect to see corresponding non-linear changes in the qualities of ices. The previous analysis has been coarse in the sense that conclusions were drawn based on bulk properties of the ice field over many cells simultaneously, such as summed-total mass. A more natural choice is to isolate the ice to vertical layers (where mass and deposition are likely to be more uniform), and then determine the change with height. This is a good analogue for the evolution of the hydrometeor field with time, perhaps more so than the averaged timeseries of a vertical layer, as ice particles are constantly descending and changing in height with time. In summary, the following analysis attempts to analyse ice that is as independent as possible from non-depositional processes, and relate the mass tendency to a corresponding change in ice particle variable.

11.1 Cloud Top

The most simple choice of spatial analysis to isolate deposition is to narrow the scope of the investigated cloud ice to the cloud top. This choice is motivated by the reduced likelihood of non-depositional processes near the cloud top. For example, near the top of the cloud, temperatures are low enough to initiate homogeneous freezing of droplets, which fully glaciates the environment and immediately removes the presence of mixed-phase growth processes, whilst also eliminating the possibility of melting. Additionally, cloud ice at the very top of the cloud is likely to be smaller, both due to the likelihood of recent nucleation, and its associated low fall speed. Small ice crystals are less likely to interact as they occupy are relatively smaller volume of the grid cell, which limits the extent of ice-phase multiplication processes, and inhibits aggregation. In short, examining only ice at the cloud top is a reasonable method of limiting the likelihood of non-depositional processes without comprehensive analysis of all possible processes and all cells. The primary growth methods in this region are likely to be dominated by nucleation and vapour deposition.

The *cloud* environment was defined as a cell that contained non-zero cloud ice mass mixing ratio and the *cloud-top* was defined as the highest elevation cloud-cell per column per time step. Columns that exhibited no cloud ice were omitted from the analysis in a given time step, and cloud tops that occurred at temperatures warmer than the homogeneous freezing limit were also excluded. The cloud-top spatial region that was analysed was defined as being within two grid-cells of the cloud-top cell, in which ice mass mixing ratio was greater than zero.

Figure 11.1 shows the averaged, summed cloud ice mass-mixing ratio (top) and number mixing ratio (bottom) at the cloud top in domain 1 for case one and case two, shown in panels (a) and (b), respectively. In ISHMAEL, the ice-type 1 and ice-type 2 categories are combined. Unlike in the previous analysis, the mixing ratios of each quantity were not converted to total quantities (i.e. by multiplication of $\rho_a V$) as the grid cell size and air density in the cloud top environment were assumed to vary less significantly than the previous analysis (see Figures 10.1–10.2), which encompassed all vertical levels of the domain. The average was formed per time step by summing the total mixing ratio of each quantity in the top 3 grid cells of each vertical column containing cloud, and dividing by the total number of non-zero mass columns or cloud-top events.

Examination of the typical, summed ice mass at the cloud top in Figure 11.1 (panels a, b, top) shows that the summed mass mixing ratio per time step in ISHMAEL (red) was 7.5 and 4.7 times larger than in Morrison (black) for cases 1 and 2, respectively. The relative difference in mass between the ISHMAEL and Morrison schemes were also remarkably consistent, which corroborates the conclusion stated previously for consistent relative factors; that this indicates the character of the microphysics scheme rather than specific effects associated with the simulated meteorological event. Despite a consistent difference in the total ice mass field, there were large differences between the magnitude of the typical cloud ice mass mixing ratio associated with each scheme. To indicate this, the minimum and maximum summed mass mixing ratio per column cloud top was extracted per time step and plotted using vertical bars on Figure 11.1 for the ISHMAEL (red bars) and Morrison (black bars) microphysics schemes. From this additional information it is evident that the ISHMAEL scheme produced typically much larger quantities of ice mass than the Morrison scheme. The minima in ISHMAEL varied from $\sim$ 10^{-1}–10^{3} kg kg^{-1} per column cloud top and was typically $\sim 10^{2}$ kg kg^{-1} per cloud top region sampled, whilst the maxima consistently exceeded 10^{7} kg kg^{-1}. In contrast, the Morrison simulated cloud top frequently exhibited minimum mass mixing ratios of 10^{-2} kg kg^{-1}, typically smaller than the ISHMAEL minimum, and maximum $\sim$ 10^{6} kg kg^{-1}, which was also smaller than the ISHMAEL maximum. These findings, which occurred across both simulated cases, indicate that at the cloud top the ISHMAEL scheme simulated a larger average mass of ice than Morrison, and the summed mass mixing ratio occupied a range of possible mass values that were more narrow and higher in mass content than in Morrison.

In contrast to the ice mass, the average ice number mixing ratio at the cloud top was much closer between these schemes, at 1.9 and 1.7 times larger in the ISHMAEL scheme for cases one and two, respectively. As with mass, the relative ice crystal number is consistent throughout all time steps. The spread of minimum and maximum total number concentrations per cloud-top column per time step show that the schemes simulated more similar number concentration ranges than with mass but some differences were still present. The maximum of the average cloud ice number in a single summed cloud top column were consistent, which indicates that it is likely the scheme has imposed a maximum ice number constraint on the cells. We note that the ISHMAEL maximum is larger than that found in Morrison, which is in keeping with the maximum in-code number concentrations limit per cell of $3 \times 10^5/\rho_a$ and $3 \times 10^6/\rho_a$ kg^{-1} for Morrison and ISHMAEL, respectively. The minima of ice crystal number in Morrison were $\sim 10^6$ kg^{-1} but the ISHMAEL scheme showed that it typically had a larger minimum cloud top ice total concentration of $10^6 - 10^{10}$ kg^{-1}. This showed that the ISHMAEL scheme typically had a larger number of ice crystals at the cloud top, but the relative range in the number concentration was much more similar to Morrison than was found in the mass field.

Overall, Figure 11.1 showed that at the cloud top, the ISHMAEL scheme simulated typically larger ice mass mixing ratios and to a lesser extent slightly increased number concentrations in comparison to the Morrison scheme, and using the logic of the assumptions laid out for this analysis we may conclude that this difference derives primarily from the deposition process alone. To evaluate this conclusion, the average crystal mass (i.e. average total mass mixing ratio $\div$ average total number concentration), the average in-cell deposition per time step, and the total deposition in the domain per time step were output in Figure 11.2 columns 1–3, respectively.

The average crystal mass is a useful method of combining the differences in total mass and number mixing ratio identified in Figure 11.1 and is indicative of the efficiency of the deposition process at the cloud top. For example, it is evident that whilst the ISHMAEL scheme generally exhibited a larger mass mixing ratio and number concentration than Morrison for both simulated cases, the average crystal mass in case (Figure 11.2, left) shows that at approximately midnight during the simulation, the average crystal mass at the cloud top was actually larger in Morrison. Despite this it is evident that the cloud top average crystal mass is between 2 and 3 times larger on average in ISHMAEL for both simulated cases. This difference likely originated from the deposition process (Figure 11.2, middle) which was 4 and 3 times larger on average per ISHMAEL cell than in Morrison for cases 1 and 2, and approximately 9 times larger when the summed cloud top deposition across the entire domain is considered in (Figure 11.2, right). The large difference in summed cloud top deposition mass tendency highlights that not only was the deposition greater per cell (i.e. Figure 11.2, middle) but that the total number of cells at the cloud top were greater in ISHMAEL, which limits the average per cell deposition to only a factor 3 when the overall summed total mass tendency was in fact much larger.

11.2 On The Effects of Nucleation

Analysis of the cloud ice field isolated to the cloud-top region is a useful way to examine a portion of the cloud ice that is likely growing by only deposition. From this analysis, it is evident that vapour deposition is an influential property for the growth of cloud ice, and its

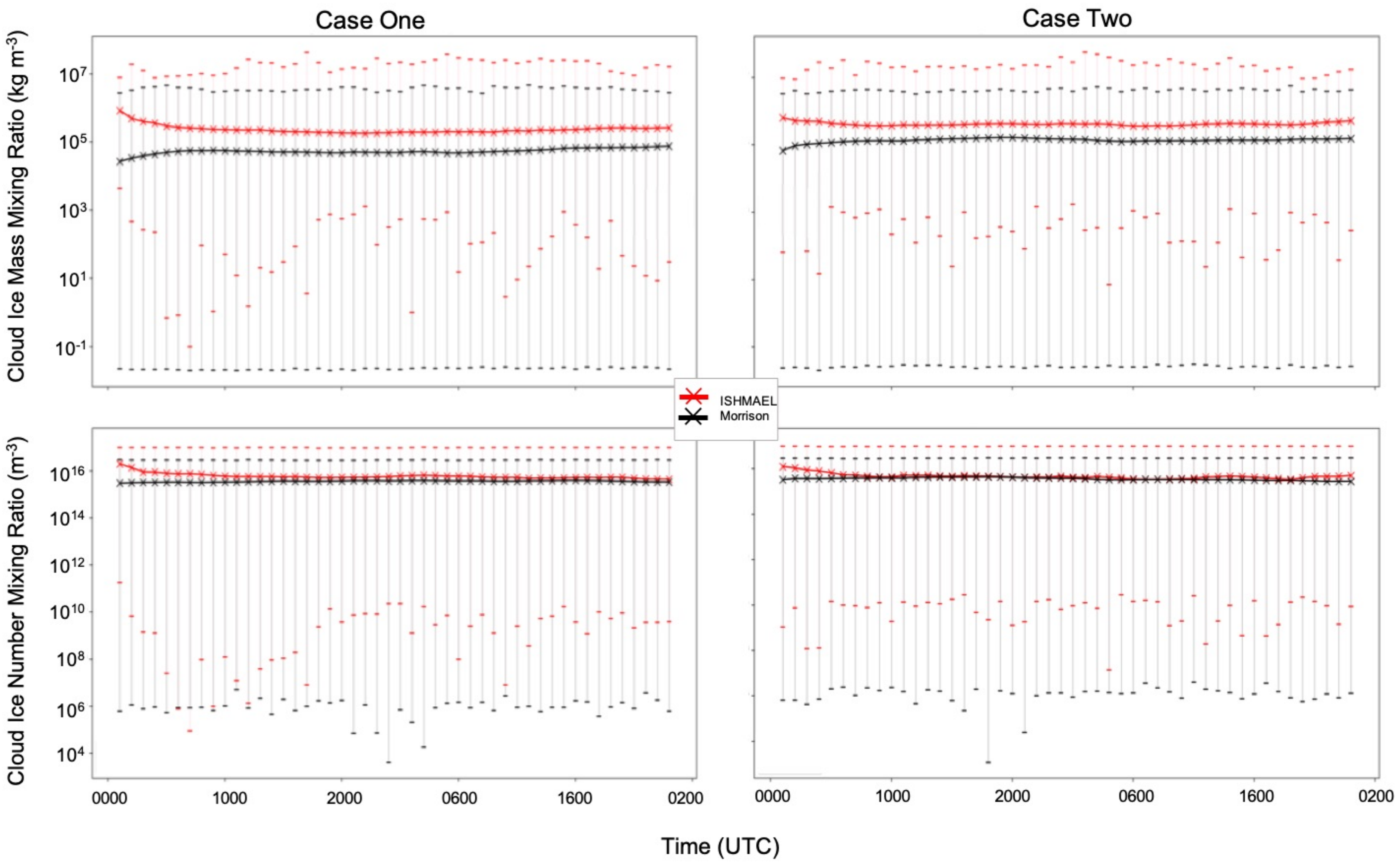

Figure 11.1. Time series of sum-total cloud ice mass concentration (kg m^{-3}, top) and number concentration (m^{-3}, bottom) per time step for Case one (left) and Case two (right) as simulated by ISHMAEL (red) and Morrison (black) at the cloud top.. Vertical bars indicate the maximum and minimum value of mass or number concentration produced at the cloud top by each scheme (colour) during the time step

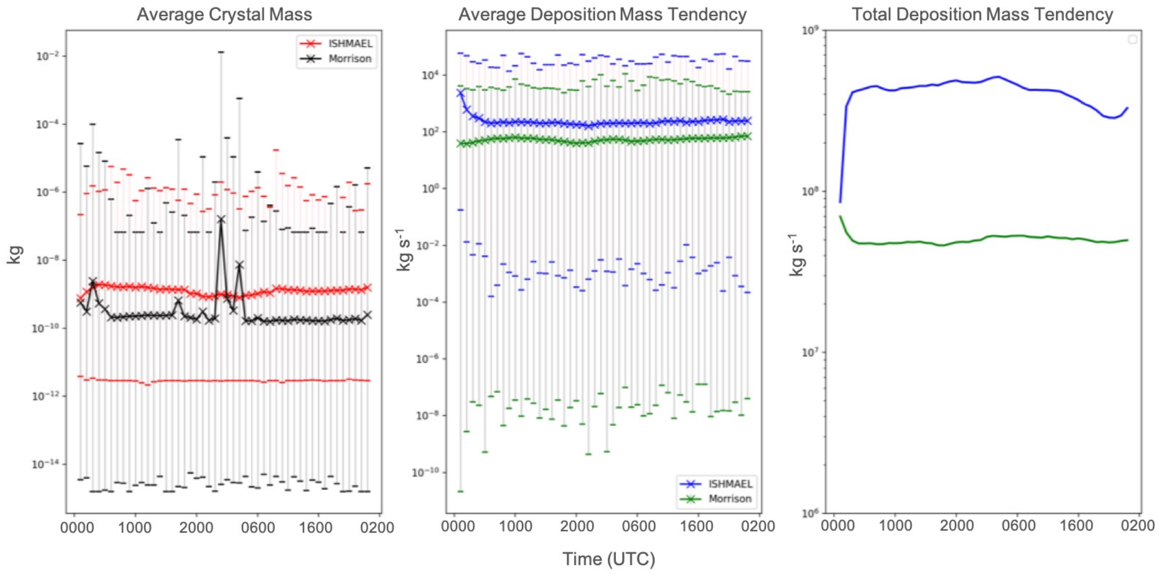

(a) Case 1

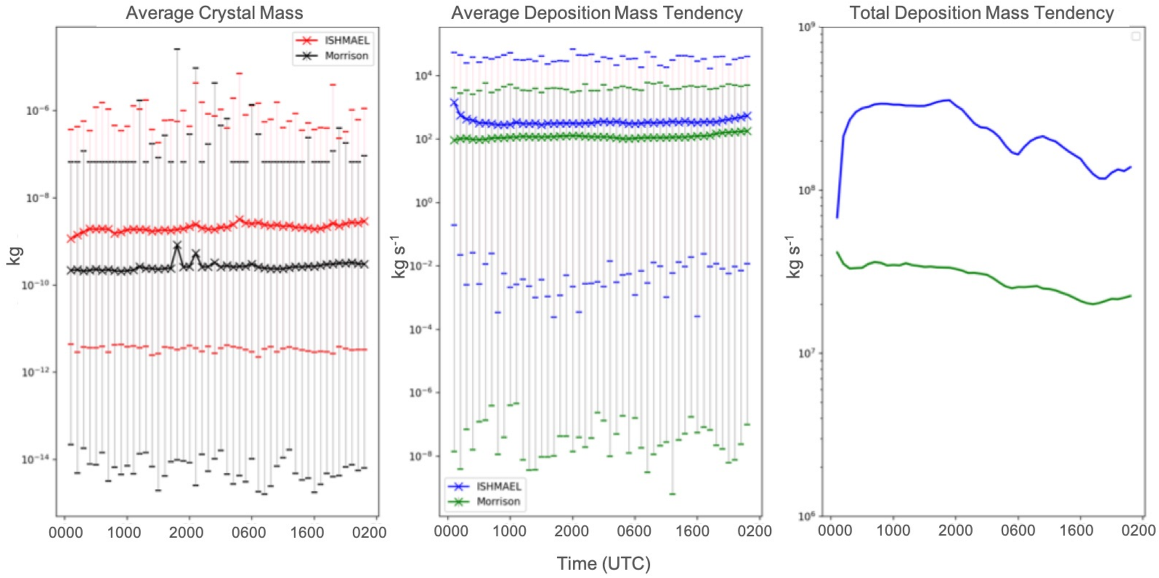

(b) Case 2

Figure 11.2. Time series of average crystal mass (kg) (left), average deposition mass tendency per cell (kg s^{-1}) (centre), and total deposition mass tendency (kg s^{-1}) (right) in domain 1 per time step during case one (a) and case two (b). Vertical bars indicate the maximum and (non-zero) minimum value of each variable produced during the time step (coloured with respect to scheme).

relatively high mass tendency in the ISHMAEL scheme is responsible for a comparatively greater overall cloud ice mass than in the Morrison scheme. Therefore, ice deposition will be a key determinant the of ice qualities at the onset of subsequent mixed-phase microphysical processes.

It is important to note that the effects of nucleation cannot be easily discerned from deposition in the cloud top region. Nucleation increases the ice mass and number concentrations simultaneously, so we might expect find that both qualities increase proportionally in the previous cloud top analysis if nucleation is a contributing factor. However, as shown in Figure 11.1 the relative mass difference between schemes is considerably larger than the ice crystal number difference. Comparison of the ISHMAEL mass field to elevated deposition rates indicate that there is good evidence that these qualities are causally linked but for the sake of contradiction, we examine the possibility that the cloud ice field is artificially increased in ISHMAEL by the nucleation process. This could arise if the initial nucleated ice mass in ISHMAEL is larger than in Morrison, then for every nucleated crystal the ISHMAEL scheme might expect to gain slightly more mass than Morrison, and over the entire distribution this could produce a larger overall cloud ice field. If this process were occurring, then the total ice mass difference would be proportional to the difference in nucleated mass for an equivalent number of particles. Examining the initial crystal mass in both schemes, we find that each follows the same mass distribution hypothesis:

$$m_{i0} = \frac{4\pi}{3}\rho_i r_{i0}^3, \tag{11.1}$$

where r_{i0} is the initial radius of a nucleated ice particle equal to 1×10^{-5} in both schemes and ρ_i is the density of ice. In Morrison the ice density is fixed at 500 kg m^{-3}, but in ISHMAEL it is 920 kg m^{-3}. Therefore, the typical nucleated crystal in ISHMAEL is 1.84 times heavier than the equivalent in Morrison. Multiplying this value by the average ratio of number concentrations; 1.9 and 1.7 in cases 1 and 2, indicates the typical expected mass difference at the cloud top i.e. a mass difference of 3.5 and 3.1 times for cases 1 and 2, respectively. These factors are less than the factors of 7.5 and 4.7 found in Figure 11.1 and so it is reasonable to assume that the mass difference in simulated cloud ice between these schemes is not solely due to nucleation, whilst accepting that the different nucleation densities may be a contributing factor to the severity of the inflated total cloud ice mass in the ISHMAEL scheme. A brief overview of nucleation mechanisms in each scheme is given in Appendix K.

11.3 Analysis of Deposition in Isolation

The effect of differing combinations and magnitudes of microphysical process rates upon ice properties is beyond the scope of this study. However, we have shown that in ISHMAEL the deposition process is strongly related to cloud ice mass growth for much of the clouds vertical extent, and therefore the tendencies exhibited by the deposition process upon ice properties are likely to be maintained as low 2 km in the domain. It is hypothesised that the ice particle properties evolved by deposition will affect riming, as the properties are key dependencies in the mass riming rate. Additionally, it is expected that the origins of elevated deposition lie in the novel incorporation of habit in the ISHMAEL scheme. It is important therefore to clarify the evolution of ice properties during deposition to link habit parameterisation indirectly to the riming process.

To this point, the summed total mass and number of the whole domain, including all microphysical processes, has been considered and the cloud top region, where deposition and nucleation are the only processes present, has been reviewed. The evidence suggests that the mass deposition tendency of cloud ice differs by a large factor between non-habit parameterising and habit parameterising schemes; Morrison and ISHMAEL, respectively, resulting in an inflated cloud ice field. Additionally, the location of the deposition maximum occurs at lower elevation in ISHMAEL and is closely tied to the vertical distribution of cloud ice mass, indicating that the deposition process is influential to the precipitation field far below the cloud top. We now wish to isolate deposition and determine how it alters cloud ice qualities with depth, so that these effects may examined in the context of riming dependencies and the formation of graupel. This may be achieved by applying the method of process isolation shown in Methods section 3.4.3. This methodology enables a single process of influence to be isolated and its resulting affect on particle qualities can thus be directly associated to that process. Whilst it is unlikely that grid cells exist in which only deposition is the active process, we can assume that if the deposition mass tendency is reasonably large and the combined net mass tendency of other processes is very small, then the mass tendency owed to none depositional processes can be assumed negligible and the mass tendency is approximately a function of only deposition. Additionally, this assumption is extended to the change in prognostic variable, i.e. it is assumed that when a mass tendency is small enough to be considered negligible, it invokes a similarly small, and therefore negligible evolution tendency for the prognostic variables.

Using these assumptions, cells containing cloud ice in which the mass tendency is almost or totally dominated by deposition can be isolated and their effect on prognostic variable evolution examined. This will give an average indication of the typical prognostic variable evolution associated with deposition in both simulated cases.

To implement this method computationally, the assumptions outlined above are formed into a set of conditional statements that can determine which cells are permissible for further investigation. The criteria for cells is as follows:

1. More than 95% of the total cell mass tendency must originate from deposition (i.e. *deposition dominated* cell)
2. the cell must maintain 95% of the total mass tendency originating from deposition for at least two consecutive time steps
3. Cell must exist in a columnar grouping that is not divided by other microphysical processes.
4. Cell should be within 4 kilometres of the cloud top

Justification for Criterion 1 has been explained above. Criterion 2 ensures that the dominant depositional mass-tendency is not anomalous and remains consistent for at least a short period of time. Criterion 3 ensures that changes to particle properties originate from the mass tendency of the deposition process only, rather than an intersecting process. For example, the presence of a microphysical process might alter a prognostic variable in a different manner to deposition and bias the overall tendency. Criterion 4 was chosen to aid comparisons between the Morrison and ISHMAEL schemes. Cloud ice in Morrison tended to reduce quickly at low elevations, during artificial extraction and conversion to snow (autoconversion), to omit any bias from autoconversion the analysis could be constrained to near the cloud top where autoconversion was less likely. Similarly, aggregation in ISHMAEL is generally inefficient so cloud ice persists for longer than it is likely to in reality. The decision was made based on these findings (see Figure 10.2) that cloud ice moderately close to the cloud top was most likely to be growing in a comparable way between schemes.

An example of how these criterion might be imagined is shown in Figure 11.3. Here, a latitudinal-longitudinal slice along a vertical column simulated by the ISHMAEL microphysics scheme is considered. On the left of Figure 11.3, the hypothetical contents of column are examined qualitatively in accordance with the criterion outlined above. Cell shading is in accordance with microphysical processes, such that blue cells indicate deposition, orange cells indicate non-depositional processes, and green shaded cells indicate the cloud top. By default, only cells that contain non-zero deposition mass tendencies (blue) are considered for further analysis. For each deposition cell, contextual information is given and the font colour indicates if the cell meets the criteria (green) or breaks them (red). On the right of Figure 11.3, the corresponding binary-filter for the column array is shown (see §*Methods*). The areas in green would be considered for further analysis.

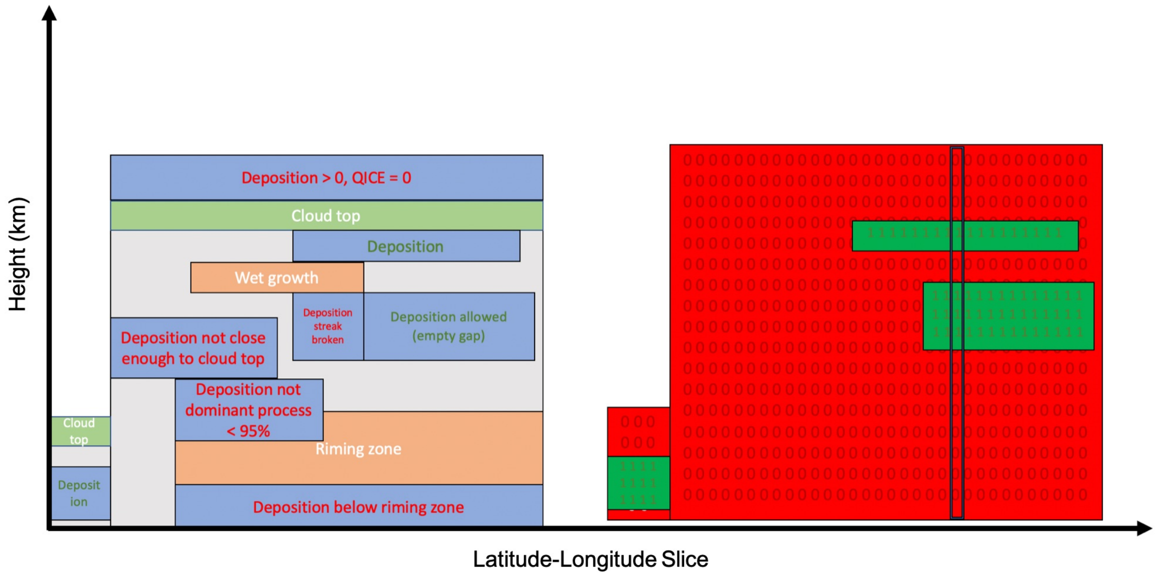
Height (km)
Deposition > 0, QICE = 0
Cloud top
Deposition
Wet growth
Deposition streak broken
Deposition allowed (empty gap)
Deposition not close enough to cloud top
Deposition not dominant process < 95%
Riming zone
Deposition below riming zone
Cloud top
Deposit ion
Latitude-Longitude Slice

Figure 11.3. Example of the deposition “zone” criteria (left) for a latitude-longitude slice of the domain and the corresponding binary mask associated with these criteria being fulfilled (right). Blue boxes indicate deposition is non zero. Orange boxes indicate that a non-depositional process is non-zero. Green boxes highlight the cloud top as defined in the cloud top analysis. Grey box highlights where cloud ice mass > 0 but no process is taking place.

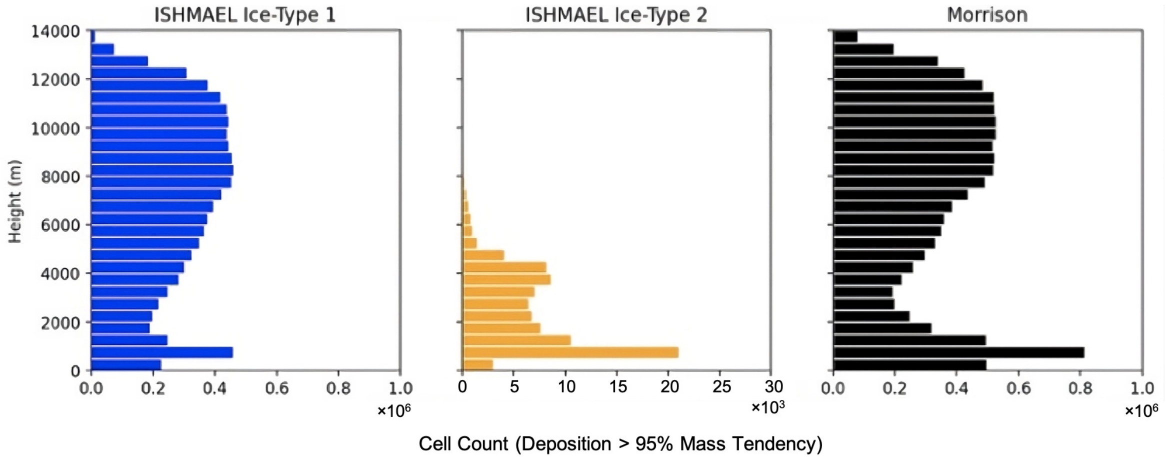

Figure 11.4. Simulation-averaged vertical distribution (m) of deposition layer height for ISHMAEL ice-type 1 (blue, left) and ice-type 2 (yellow, middle), and Morrison (black).

Using the methodology outline here, the average vertical distribution of deposition layers was determined. Figure 11.4 shows that the typical depositional height for Morrison and ISHMAEL (ice-type 1) was between 6–14 km, and the overall distribution was very similar amongst schemes. This indicates that the qualities assessed in the deposition layer are most often at high elevations, close to the cloud top and in similar locations across schemes ensuring that the results obtained from the deposition layer are broadly comparable per scheme. ISHMAEL ice-type 2 occurs at lower elevations and therefore its deposition also takes place closer to the surface.

The methodology outlined here was used to examine the change in selected variables with depth. In the first instance, the method was used to retrieve the evolution of cloud ice mass mixing ratio and cloud ice number mixing ratio with time for deposition-dominated cells. Figure 11.5 shows plots of ice mass mixing ratio timeseries (top), and ice number concentration timeseries (bottom) for these deposition dominated cells, and for the discrete vertical levels in which they were calculated and subsequently averaged. Each individual panel therefore shows the general tendency of the ice variable during deposition at a set height, and reading the panels from left to right indicates how the property changes with height.

In Figure 11.5 (top) the timeseries of mass mixing ratio per vertical height level is shown. In the ISHMAEL scheme (blue), cloud ice mass mixing ratio is shown to be greater than in the Morrison scheme (orange) for all vertical levels and at all times. Comparing the average mass mixing ratio of each timeseries, it is evident that as the panels decrease in elevation, the average mass exhibited by the Morrison scheme is quite consistent, whilst the average mass in the ISHMAEL scheme tends to increase. These tendencies with height are indicated by blue and orange arrows for the ISHMAEL and Morrison microphysics schemes, respectively. As this analysis is strictly confined to depositional cells, the mass tendency with vertical level indicates growth that is a direct consequence of the deposition process. Therefore, deposition in ISHMAEL is directly related to an increasing crystal mass at lower elevation, and is also the main driver of an increasing rate of change of mass with height (i.e. the arrow gradient) which much greater in ISHMAEL than in Morrison. In combination, these results indicate that the deposition process in ISHMAEL grows the average ice mass more effectively than Morrison during descent.

The conclusions established for ice mass can be compared to the ice crystal number in Figure 11.5 (bottom). It is immediately apparent that the number of ice crystals with height experiences a far less severe change with height than was found for the mass mixing ratio. The average tendency of the ice number is slightly negative with height, indicating that the ice crystal number is consistent and slightly decreasing within depositional cells between 7–11 km elevation. This slight decrease is attributed to removal of the ice crystal number by aggregation, which is not considered explicitly in the nil-mass tendency condition. Overall, deposition appears to have little effect on ice crystal number, which is as expected.

The layers shown by separate panels in Figure 11.5 can be used to determine the rate of change of a variable with height by plotting the timeseries average against depth. This mathematically approximates the tendency of a variable as was done in discussion of Figure 11.5 using blue and orange tendency-arrows. Figure 11.6 provides the rate of change of cloud ice mass (left) and number mixing ratio (middle) with vertical elevation for the deposition-dominated cells, and additionally, the ratio of mass to ice crystal number forming the average ice crystal mass is also shown (right).

The mass and number mixing ratio evolution in Figure 11.6 (left, middle) shows that the ISHMAEL (blue) cloud ice depositional growth persists to deeper levels than in Morrison (yellow), likely because of efficient autoconversion of cloud ice to the snow category in the Morrison and relatively weak aggregation in ISHMAEL. Conversely, Morrison's ice number is on average much greater than ISHMAEL's for an equivalent height, until low altitudes when the schemes converge. In combination (Figure 11.6 right), these factors combine to produce an average cloud ice mass that is similar amongst schemes at high elevation but grows significantly larger in ISHMAEL at lower elevations than in Morrison. The non-linear growth of average cloud ice mass in ISHMAEL indicates that continuously greater depositional growth from cloud top to base enables the relative difference in ice mass to grow exponentially, resulting in a much larger cloud ice mass in ISHMAEL overall.

The results briefly outlined here are a sample of results already obtained for both cases. As stated in the introduction, the aim of this study is to understand two key aspects of the capacitance parameterisation: to determine if this parameterisation causes enlarged ice mass, and then, to determine the consequences of this for the riming parameterisation and ultimately the amount of graupel precipitation produced.

Further work should be undertaken to determine the effect of vapour deposition on ice properties such as fall speed, shape and and density as alluded to previously. Additionally, comparison to hundreds of measurements and observations across the domain have been retrieved and will be used to verify each scheme and determine the accuracy of the ice PSD as well as the precipitation type produced.

11.4 Impacts for the Cloud Droplet Field

One important riming dependency that is not related to the ice particle specifically but is still very influential for the riming rate is the cloud droplet field, in particular the total amount of droplets collocated with ice and their size distribution. The rime efficiency is dependent on droplet size because smaller droplets are more likely to be deflected by near-surface aerodynamic effects and larger droplets are more likely to splinter on impact. Thus the riming process exhibits a preferential droplet radius for maximum efficiency and so the development (or inhibition) of ice droplets inside or outside of this preferential range is significant to the riming process.

The overall riming rate is also highly dependent on the concentration of droplets collocated with ice crystals. For example, as the liquid droplet field tends toward very high number concentrations, the statistical likelihood of collision with an ice particle increases, and correspondingly, as the water droplet field tends toward negligible concentrations, the likeli-

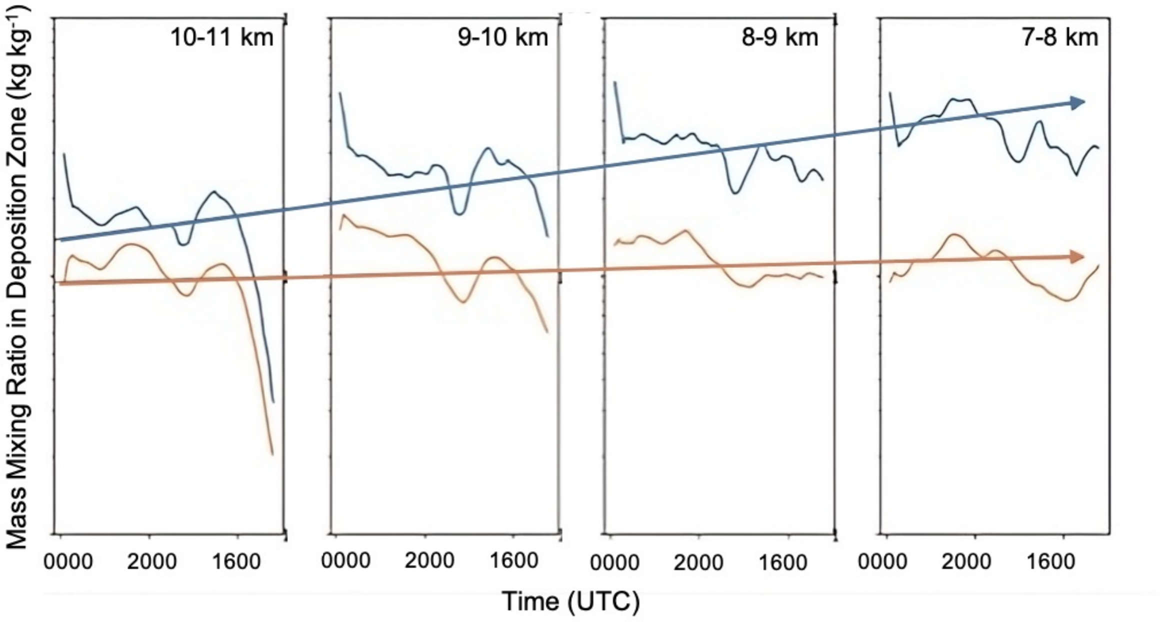

(a) Mass mixing ratio (kg kg^{-1})

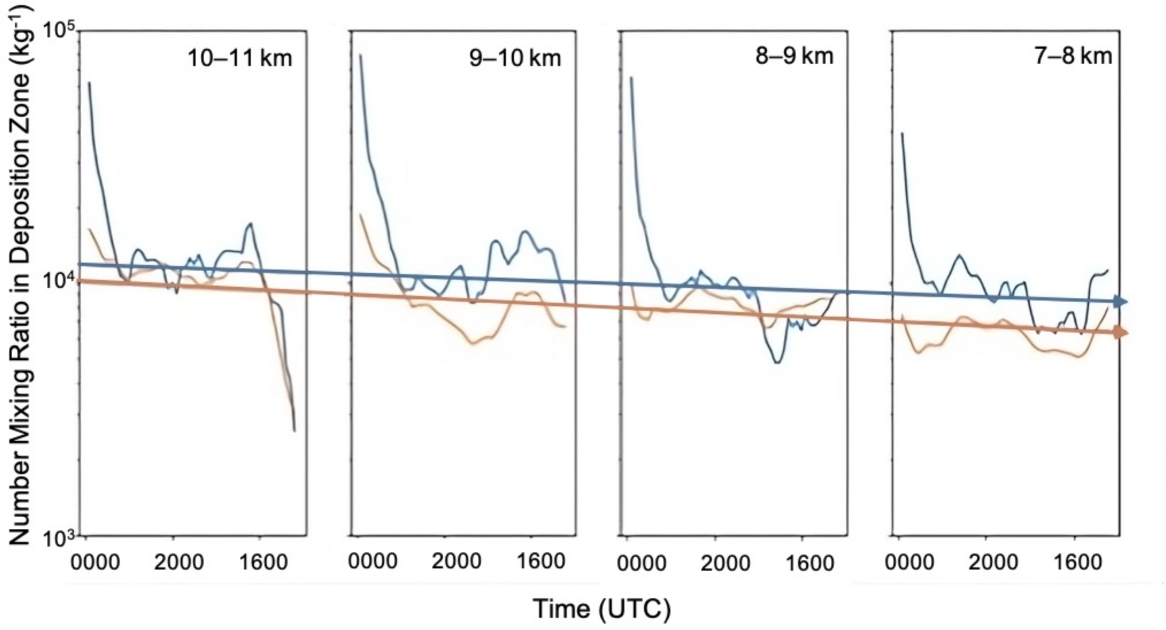

(b) Number mixing ratio (kg^{-1})

Figure 11.5. Example time series of mass mixing ratio (kg kg^{-1}) and number mixing ratio (kg^{-1}) of cloud ice obtained per vertical level when considering ice that is within the depositional zone. ISHMAEL shown in blue, Morrison in orange. Each subfigure represents a vertical height indicated by respective axis title. The tendency of increase or decrease with cloud depth is shown by large arrows (coloured according to scheme). Arrow gradient indicates the rate of change of each variable with height due to deposition only.

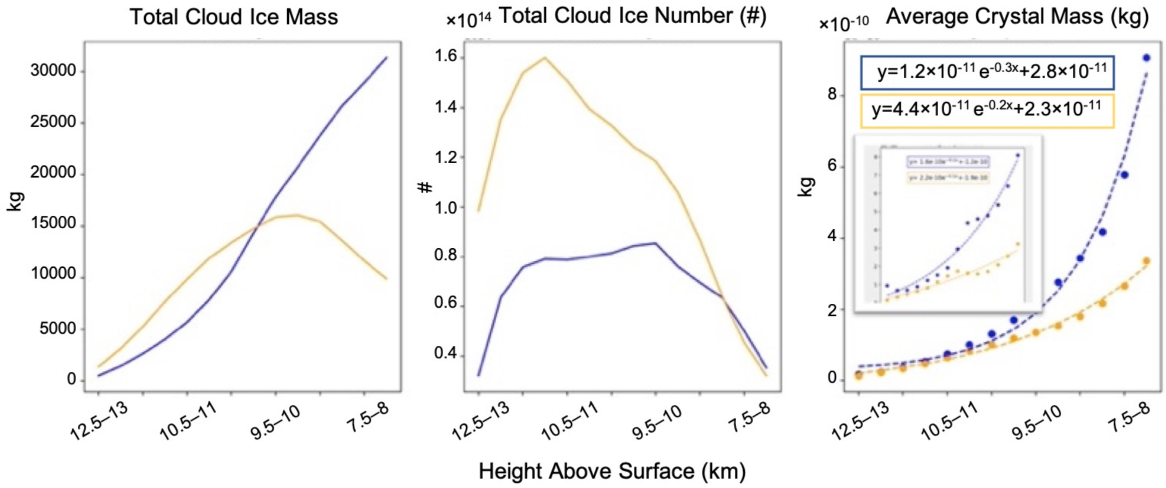

Figure 11.6. Average, in-deposition layer mass mixing ratio (kg kg^{-1}) (left), ice number (kg^{-1}) (centre) and average crystal mass (kg) (right) with cloud depth for cloud ice meeting the deposition zone criteria in ISHMAEL (ice-type 1, blue) and Morrison (yellow). Results are for Case 1 only but Case 2 average crystal mass is shown in subfigure of panel 3. For average crystal mass an exponential fit has been produced for each case with good agreement.

hood of ice particle and droplet collision is greatly reduced. Between these limits, the interaction rate of ice particles is a function of the relative ice crystal and droplet particle concentrations.

The vapour deposition process is likely to play a role in both the size and number concentration of droplet field qualities via the Bergeron process, in which ice crystals scavenge vapour at the expense of droplets. For example, if the deposition process has a net positive tendency (addition of mass) to ice then the ambient environment is supersaturated with respect to ice. For suitably cold environments where supercooled droplets exist, it is likely that the environment with respect to liquid water remains saturated. The deposition process will remove water vapour, rendering the environment subsaturated with respect to liquid water and encourage evaporation of droplets to supply the deposition rate. Therefore, the deposition mass tendency rate can be viewed not only as a conversion process for vapour mass and ice mass, but as an intermediary process that connects growth in the ice crystal mass to reduction of the liquid droplet mass.

Given the connection between liquid droplets and deposition, it might be expected that the increased deposition rate observed in ISHMAEL will cause a corresponding reduction in the droplet field. So it is possible that ISHMAEL will exhibit a reduced droplet population, with secondary effects for the mass riming rate. However, the scavenging of liquid drops is not homogeneous amongst the droplet PSD. Larger droplets with greater surface areas will reduce in size more rapidly than smaller droplets, so increased deposition might cause a more rapid homogenisation of the cloud droplet size. This is important for the formation of precipitation generally, because homogeneous droplet size spectra inhibit the coalescence process, but is also significant to the riming process, which is sensitive to liquid droplet radius.

To determine the relationship between the deposition process and the vapour and cloud droplet mass, the mass variables of each were extracted across all grid cells in domain 1 for the ISHMAEL and Morrison microphysics schemes and are shown in Figures 11.7 and 11.8 for cases one and two, respectively. Histograms of the distribution of mass per-grid-cell are shown in column one and timeseries of the sum-total mass are shown in column 2. Plots are provided for the vapour mass and cloud droplet mass in rows one and two of each subplot respectively. Subplot (a) considers these qualities throughout the entire domain, whereas subplot (b) considers them only within a deposition zone which will be discussed later. Note that Figures 11.7 and 11.8 for cases one and two show remarkably similar results, so a discussion of only case one is conducted for brevity but the concluding arguments are applicable to, and derive from, both cases. The results of case two are shown for comparison by the reader.

First, examining the vapour mass field for the ISHMAEL (blue) and Morrison (orange bars) microphysics schemes in all grid cells (Figure 11.7 subfigure (a) row 1) it is evident that the vapour mass simulated by either microphysics scheme is extremely similar. The histogram of vapour mass shows minimal variation in the distribution of the mass or the frequency in which each mass is found in the model. The variation of the vapour mass with time (right) corroborates this finding throughout the entire simulation time, where the absolute difference between schemes is at most 2 orders of magnitude smaller than the total vapour mass. Comparing this to the droplet mass (Figure 11.7 subfigure (a) row 2) provides a more notable difference. The ISHMAEL droplet mass is larger by an average factor of 1.4 quite consistently throughout the simulation. This is reflected in the distribution of cloud droplet mass, which gather towards much higher in-cell masses for the ISHMAEL scheme than in the Morrison scheme. This results in a slightly larger frequency of cells with total droplet mass of 10^7 kg or above in the ISHMAEL scheme. However, the Morrison scheme more frequently simulates cells that contain lower total droplet masses. This broad distribution *tail* reaches as low as $\sim 10^0$ kg, approximately 4 orders of magnitude less than the droplet mass in the ISHMAEL scheme.

These results show that, whilst the vapour mass available in both schemes is remarkably consistent, the droplet fields are quite dissimilar. There are many possible reasons for the droplet mass difference that may be generalised into a difference between the positive and negative cloud-droplet mass-tendency components per scheme. More informative than the overall mass difference with time is the distribution of cloud droplet mass. The top-heavy distribution in ISHMAEL might indicate an increased condensation rate in this scheme which enables small droplet masses to grow quickly and therefore limits the extent of smal-

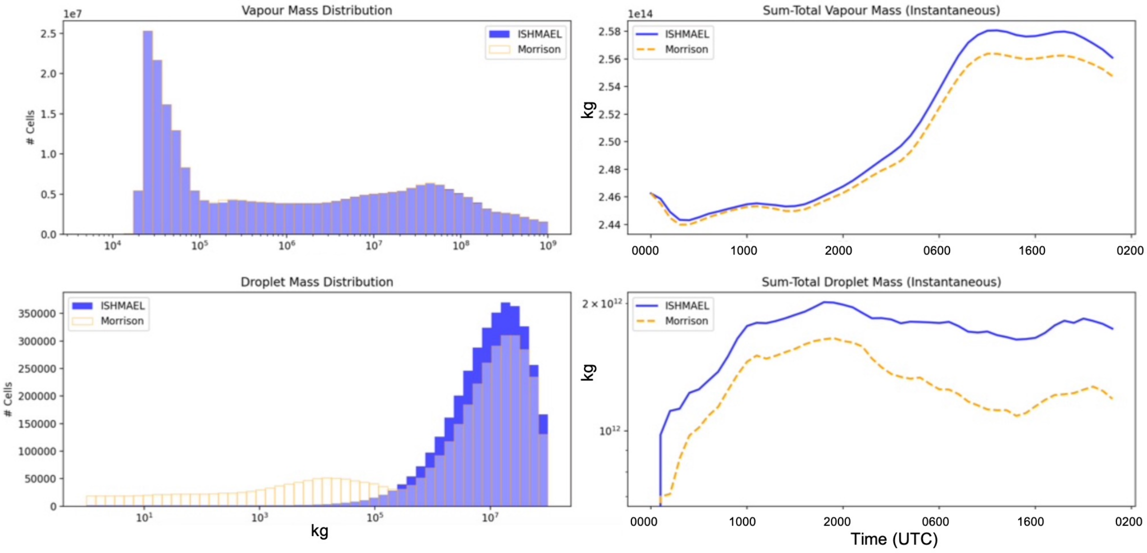

(a) Overall domain

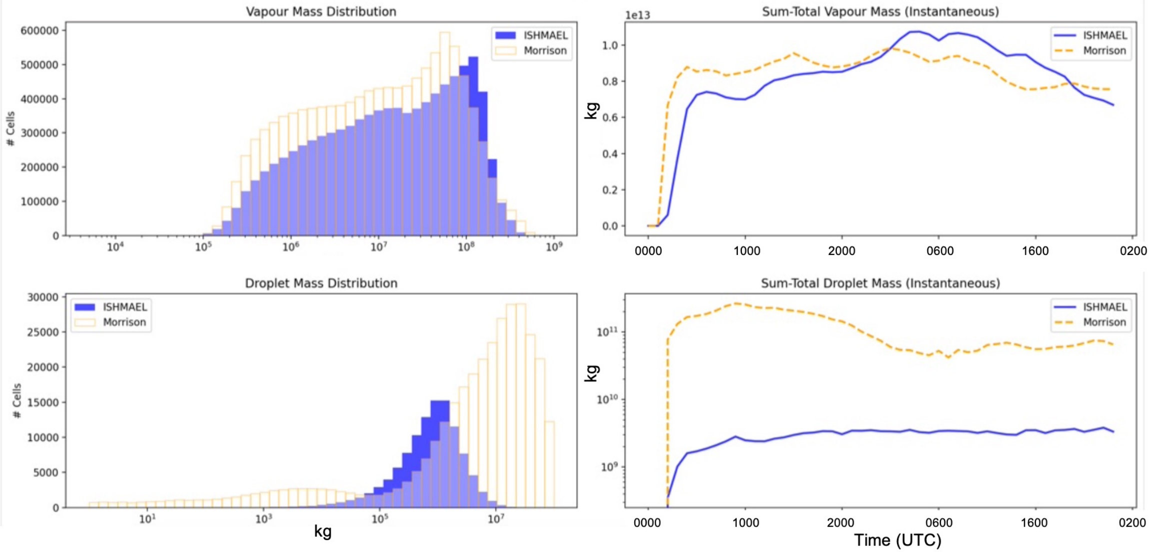

(b) Deposition zone only

Figure 11.7. Vapour and cloud droplet total mass (kg) for the whole of domain 1 (a) and inside the deposition zone (b) for case 1. Left; histograms of mass distribution for vapour (top) and cloud droplet (bottom) mass for entire simulation in the ISHMAEL (dark blue) and Morrison (clear, orange border) schemes. Overlap indicated by purple shading. Right; timeseries of sum-total vapour mass (kg) (top) and droplet mass (kg) (bottom) for domain 1 in ISHMAEL (blue) and Morrison (yellow, dashed)

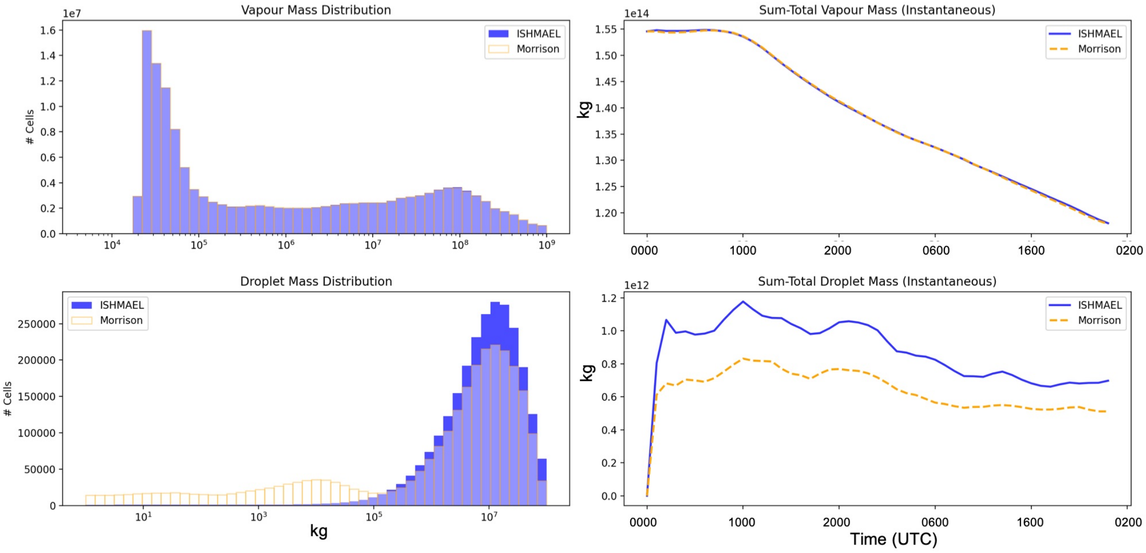

(a) Overall domain

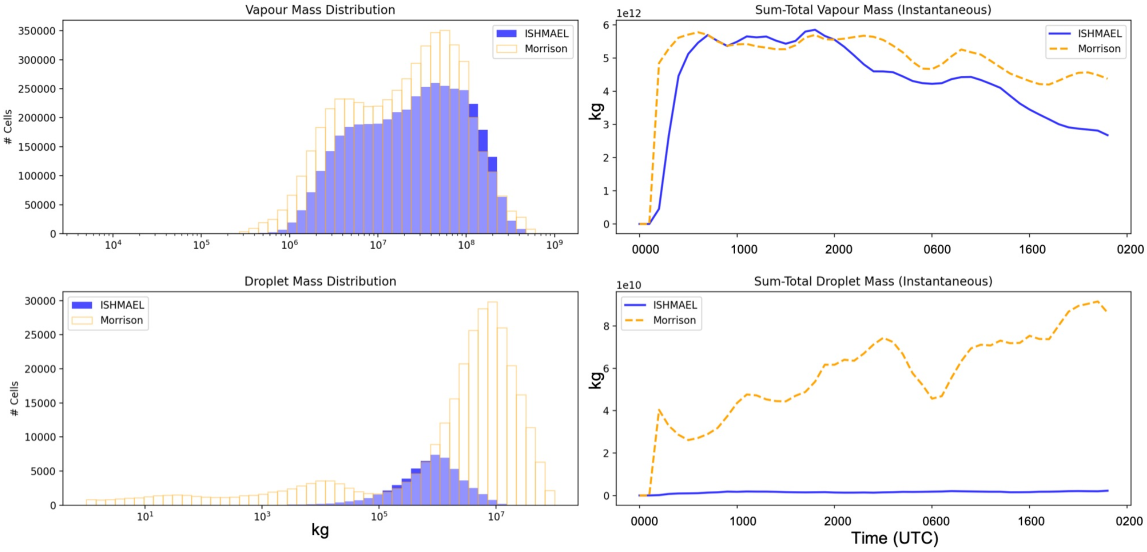

(b) Deposition zone only

Figure 11.8. As in Figure 11.7 for case two.

ler mass concentrations.

It is not possible to link the deposition rate in ISHMAEL to the cloud droplet mass explicitly in Figure 11.7 subfigure (a) because consideration of the entire domain in this example includes the effect of multiple microphysics processes that might each alter the droplet distribution. In order to more closely link the cloud droplet mass to the deposition process, it is important to examine only cells in which the deposition is the primary microphysical process. To do this, the deposition layer analysis method was used to examine only the cells that are deposition-dominated,. The qualities of the cloud droplet field examined in these cells are therefore related to the deposition process.

Examining the vapour mass field for the ISHMAEL (blue) and Morrison (orange bars) microphysics schemes in the deposition zone (Figure 11.7 subfigure (b) row 1) it is apparent that depositional cells tend to contain a larger average mass of vapour that is spans a smaller range of values in both schemes. The distribution of the vapour mass and comparisons of the sum-total vapour mass in the deposition zone are still very similar amongst the schemes, indicating a relatively similar vapour field that was consistent with time, which is somewhat surprising given the elevated mass tendency rate in ISHMAEL. Indeed, the existence of high depositional mass tendency and consistent vapour levels are corroborated by considerable losses in the cloud droplet mass (subfigure (b) row 2) . The ISHMAEL scheme produced a more narrow droplet mass distribution than Morrison, implying that cloud droplets within the deposition layer were much smaller in total mass. For example, the ISHMAEL droplet mass distribution tended toward 10^6 kg, which was an order of magnitude less than typical in-cell droplet mass across the entire domain. Examination of the total cloud droplet mass with time in the deposition zone (subfigure (b) row 2, right) shows that the ISHMAEL scheme total droplet mass is up to two orders of magnitude smaller than in Morrison throughout the simulation. Comparing this with the mass distribution, it is likely that the cloud droplet mass lost in the ISHMAEL scheme was primarily across cells that contained the largest amounts of cloud droplet mass. This is significant because the efficiency of the Bergeron process is dependent on the relative amount of droplets to crystals and cells with large total droplet masses might be expected to grow ice more efficiently. Therefore, it is likely that the consistent total vapour mass throughout the deposition zone in spite of high mass deposition rates, was sustained by a comparatively larger reduction in cloud droplet mass.

The relationship between vapour deposition and droplet evaporation can be examined in the vertical to determine where in the cloud this typically occurs. The vertical distribution of vapour mass is shown in Figure 11.9 where the summed total mass per vertical layer is retrieved for the entire simulation run. An interesting feature in the vertical distribution of vapour mass is shown between 2–7 km (green shading) when the ISHMAEL vapour mass grows consistently, but the Morrison vapour mass is smaller and occasionally reducing. In this region, the parameterisation of vapour deviates for an unknown region, but given the altitude this is likely to be related to deposition or condensation. Analysis of the cloud ice mass and deposition fields (i.e. Figures 10.2 and 10.3) showed that this region is positioned at the peak of the deposition mass tendency in ISHMAEL and below the peak in Morrison. This elevation therefore marked the onset of a reducing cloud ice mass in Morrison but an increasing cloud ice mass in ISHMAEL and so is highly likely to be related to the mass deposition process. Conclusions from Figure 11.7 illustrate that consistently high vapour mass in spite of high deposition rates causes severe scavenging of the largest cloud droplet mass populations. Therefore, it is reasonable to assume that between 2–7 km in Figure 11.9 the ISHMAEL scheme may indirectly reduce the cloud droplet population.

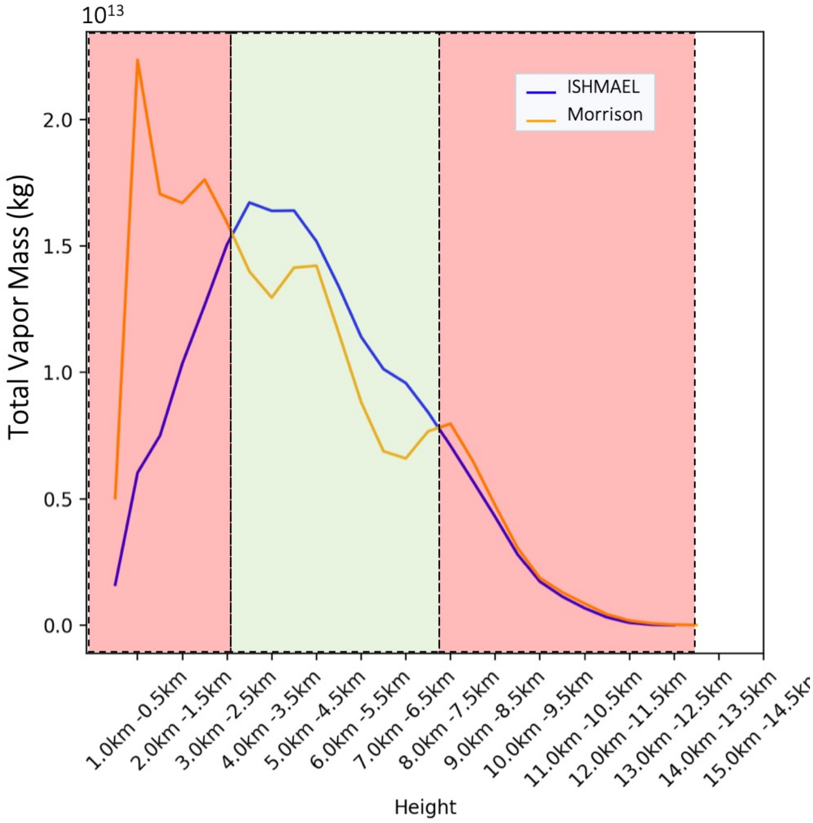

Figure 11.9. Total vapour mass (kg) distribution versus vertical elevation (km) for ISHMAEL (blue) and Morrison (yellow) schemes in case one. Green shaded region indicates deviation of the deposition mass tendency between schemes.

To evaluate this conclusion, the cloud droplet mass was compared to the vapour mass in the vertical for each case. Figure 11.10 shows the summed total vapour mass (solid) and droplet mass (dashed) per vertical layer for the ISHMAEL (blue) and Morrison (orange) schemes in case one. The vertical 2–7 km layer in which the ISHMAEL vapour mass becomes larger than the ISHMAEL vapour mass is shaded.

The region of increased vapour deposition in the ISHMAEL scheme shown in Figure 11.10 is correlated with a vertical layer of stagnation in the cloud droplet mass distribution, but in the Morrison scheme, where the vapour deposition is reduced the cloud droplet field increases consistently by approximately one order of magnitude. Quite remarkably, the onset of reduced deposition at in Morrison at 7 km elevation is almost identically aligned with intersection of the ISHMAEL and Morrison cloud droplet masses, and similarly, at 3 km when Morrison vapour content is equal to that in ISHMAEL, both cloud droplet fields undergo a similar increase in mass. This pattern is found in the second simulated case shown in Figure 11.10 (bottom), indicating that this is a characteristic property of the microphysics schemes, or the two simulated cases.

Given the previous conclusions regarding the relationship of enhanced deposition and cloud

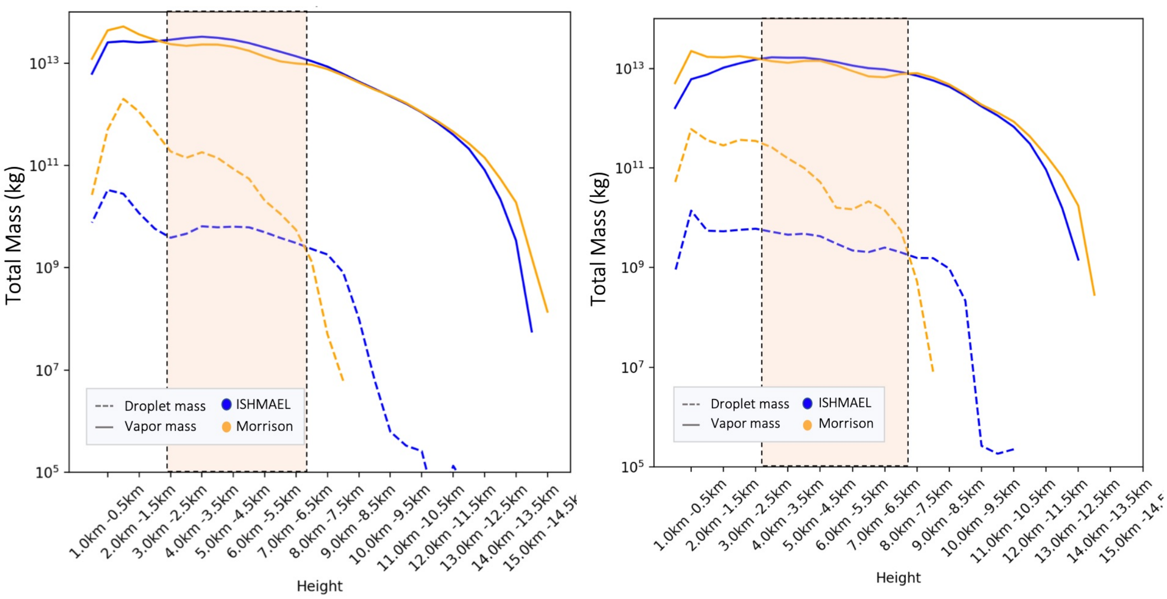

(a) Case 1

(b) Case 2

Figure 11.10. Total vapour mass (kg) (solid) and cloud droplet mass (kg) (dashed) distribution versus vertical elevation (km) for ISHMAEL (blue) and Morrison (yellow) schemes in cases one (a) and two (b). Shaded region indicates deviation of the deposition mass tendency between schemes per respective case.

droplets in the ISHMAEL scheme, the results shown in Figure 11.10 corroborate that high mass deposition rates in ISHMAEL are fed and sustained by the cloud droplet field, resulting in relatively fewer cloud droplets, and more ice crystal mass in the ISHMAEL scheme than in Morrison. The similarity of the simulated vapour fields is likely owed to the governing thermodynamics that are not controlled by the microphysics scheme, and the similarities of the vapour computation routines used by both schemes, which differ primarily in the ice phase. This similarity allows the differences in mass tendencies of other hydrometeors to be all the more visible. For example, the precise coordination of the 7 km intersection of vapour and droplet mass in Figure 11.10 was likely due to near-identical vapour and droplet fields until deposition reduced in Morrison causing a simultaneous divergence in vapour and droplet content. Thus whilst the elevated fall speeds stemming from enhanced vapour deposition of ice may increase riming, there is a corresponding alteration of the cloud droplet field that may also reduce riming overall.

Chapter 12

Capacitance Investigation

In the previous chapters it was found that the ISHMAEL microphysics scheme tended to simulate a larger total cloud ice mass than the Morrison scheme across two simulations (cases) of north-east U.S. winter storms, corroborating the findings of a further winter storm case simulated in Part II. The source of this difference has been related to the deposition mass-tendency that is consistently larger in the ISHMAEL scheme, and results in a much larger cloud ice mass at low elevations owed to non-linear cloud ice crystal growth. Several consequences of the heightened cloud ice mass are apparent, including greater average fall speeds of cloud ice in ISHMAEL, and a reduction in the ambient cloud droplet mass field. These factors are significant for the riming process, because the cloud ice qualities that are determined and sustained by the mass deposition tendency until very low elevations are key dependencies to the riming mass tendency. Additionally, scavenging of the cloud droplet field causes a reduced total droplet number and smaller droplets, which fall more slowly. These factors are also influential to riming, and are likely to play a role in the increased graupel and ice-pellet mass simulated at the surface by the ISHMAEL scheme (see Part II).

The previous chapters have focused on the relationship between cloud ice mass and the deposition mass tendency in the ISHMAEL scheme, but this has been a foundational argument for the broader examination of how ISHMAEL's ice habit parameterisation affects the simulated precipitation field. To relate habit to the observed effects detailed in previous chapters, the incorporation of ice habit must be related to the highly influential mass deposition tendency. In the introduction, it was identified that the incorporation of ice geometry to the mass deposition rate was via a capacitance term that originates from the electrostatic analogy of cloud ice. Therefore, in this chapter the relationship between the capacitance term and the vapour deposition mass tendency is evaluated explicitly. To begin, a review of the spheroid approximation of ice crystal habit is carried out. Then, an examination of the fundamental particle distribution hypotheses is conducted for the ISHMAEL scheme, and a comparative, non-geometric bulk scheme (Morrison). Finally, an idealised box-model is built for explicit testing of the capacitance function during deposition.

12.1 Overview of Spheroid Approximations

The ISHMAEL scheme approximates ice habit with spheroids. This choice is motivated by the broad continuum of aspect ratios and volumes a deformed spheroid can represent, making it a suitable candidate for the approximation of crystal habits. Spheroids are ideally suited to the parameterisation of crystal habit in bulk microphysics schemes, as their geometry is mathematically simple to define and to deform analytically, which allows for changes in the size and shape of the spheroid to be determined quickly and at minimal computational cost.

Consider the ellipse in Figure 12.1 whose geometry is defined by two mutually perpendicular lengths that maximise and minimise the ellipse diameter. The largest length is the major diameter and the smallest length the minor diameter but these are usually referred to in their radial form, the semi-major and semi-minor axes. Importantly, these axes are independent of a coordinate system, such that swapping the lengths of the ellipse axes is equivalent to a rotation. Note that this is not the case for the conventionally described spheroid, which is defined in accordance with a frame of reference i.e. a fixed Cartesian coordinate system.

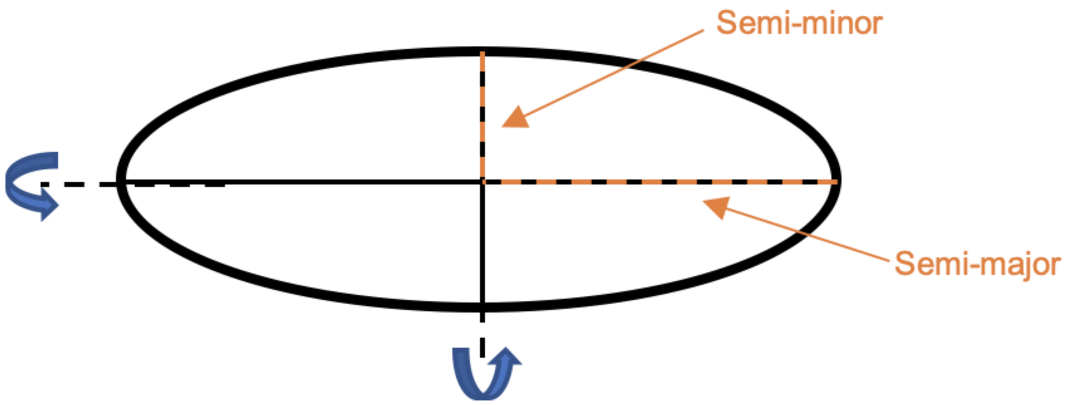

Figure 12.1. A standard ellipse. The semi-minor and semi-major radii are shown in orange. The axes of rotation are the minor and major axes which extend beyond the ellipse.

A spheroid (here used interchangeably with ellipsoid) is formed by rotating an ellipse (thereafter the *governing ellipse*) through 2π about one of its radial axes. Figure 12.2 shows two spheroids, oblate and prolate, used to represent planar and columnar ice crystals, respectively. Each spheroid has an identical governing ellipse but is formed with a different axis of rotation; the prolate has been rotated about the major axis and the oblate about the minor axis. Note that the spheroid is symmetric about its axis of rotation, which provides a useful mathematical and dimensional simplification for ice crystal geometries. Under the assumption that these geometries are broadly symmetric, then a three dimensional spheroid can be defined using only the two-dimensional ellipse axes a and c. The assumption of ice crystal symmetry has a basis in reality because ice crystals form with hexagonal basal faces, so retain (in theory) symmetry along the crystal axis normal to the hexagonal basal face.

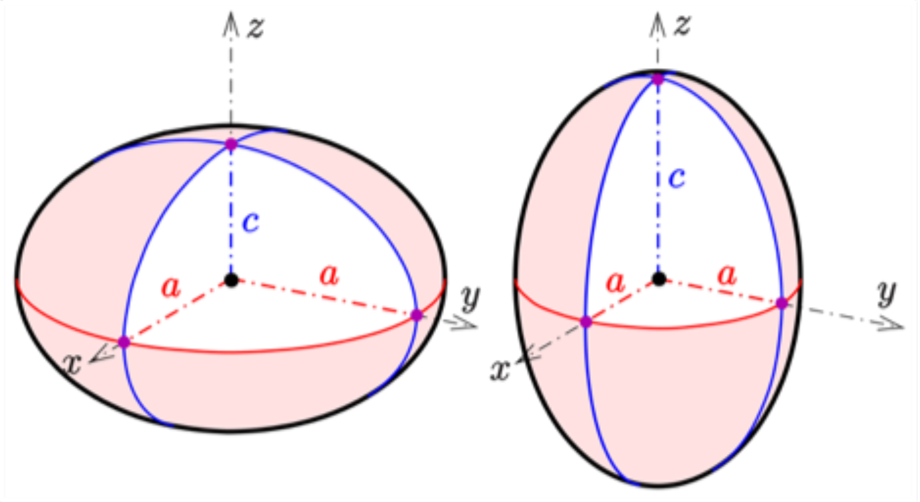

Figure 12.2. Oblate (left) and Prolate (right) spheroids adapted from Wikimedia Commons (2015). The spheroid a and c axes are related to the Cartesian coordinate system. The spheroid is formed by rotating a two-dimensional ellipse by π.

Figure 12.3 provides four examples of typical cloud ice crystals and their hexagonal structures. The crystals in column 1 and two show plates and columns, which tend exhibit a high degree of symmetry, whilst columns 3–4 show more elaborate, branched crystals indicative of dendrites or stellars. At the crystal length scale, even elaborate ice crystals tend to retain six-fold hexagonal symmetry and may therefore be reasonably parameterised by a spheroid. It is important to note however, that these crystals are highly idealised, and at finer length scales the symmetrical nature of ice crystals tends to break down as defects and chaotic, non-linear growth features become apparent.

Although the aspect ratios and particle boundaries of ice crystals can be represented by spheroids with reasonable accuracy, the surface area and volume of the crystal are likely to differ more considerably due to crystal porosity or filling-factor. For example, ice crystal 4 in Figure 12.3 exhibits narrow branching, which extends the maximum particle dimension at a greater rate than the total volume. Branching leaves gaps in the equivalent spheroid area that cannot be well represented in the spheroid parameterisation method. This is unfortunate because porosity and filling-factor of a crystal are important factors for airflow and vapour flux to the crystal surface. Overall, spheroids are most well suited to highly symmetric and simplistic ice habits such as plates, discs, columns and bullets and less well suited to more complex and porous types. As less porous and more geometrically simple crystals are formed at typically greater elevation (cooler temperatures and small supersaturation over ice see Figure 1.8), it is likely that the spheroid approximation is best suited to early (recent nucleation) crystal growth environments, but less suited to precipitation development in warmer environments closer to the ground. Subsequent analysis of spheroid geometry will be in comparison to non-porous ice crystal habits only.

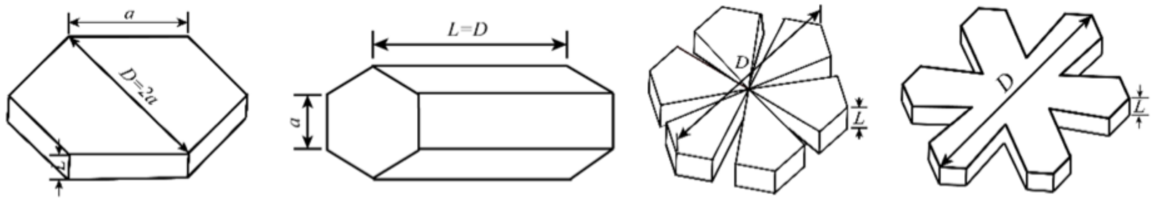

Figure 12.3. Ice particle geometries adapted from Ding and Liu (2020). Plate (left), Column (left-centre), sector-like plate (right centre), branched stellar (right). Maximum crystal dimension D and side length a indicated.

Spheroid Type	a	c	Axis of Rotation
Prolate	semi-minor	semi-major	major axis
Oblate	semi-major	semi-minor	minor-axis

Table 12.1. Relationship between spheroid axes a and c and the axes of a governing ellipse

To apply the spheroid approximation to a column or plate, one must define the *equivalent* spheroid that best matches the crystal geometry. This may be done by seeking like-axes, for example by equating the basal axis length with the major or minor axis of the governing ellipse. Caution must be taken when translating the axes between the governing ellipse, the spheroid, and the crystal. For example, compare Figures 12.2 and 12.1. The conventional spheroid in Figure 12.2 is imposed onto a fixed Cartesian coordinate system with the a and c spheroid radial lengths parallel to the $\hat{x}$, $\hat{y}$, and $\hat{z}$-axes such that prolate spheroids extend along the $\hat{z}$-axis, and oblate crystals extend along the $\hat{x}$ and $\hat{y}$ axes. In contrast, the governing ellipse in Figure 12.1 is independent of a coordinate system, but rather the semi-major and semi-minor radii are self-defined by their lengths. Consequently, the a and c lengths in Figure 12.2 do not correspond to the semi-major and semi-minor radii of the same governing ellipse in Figure 12.1. Table 12.1 indicates how the governing ellipse axes swap between a an c dependent on the type of spheroid.

Now consider the plates and columns in Figure 12.3. Measured crystals in the literature may be referred to using their maximum dimension D or the lengths of the principal and basal axes of the hexagonal crystal. In the latter case, the basal and principal radial lengths are equivalent to the a and c spheroid axes in Figure 12.2 and the governing ellipse can be referred to as in Table 12.1. Maximum dimension D (sometimes called the longest length L) is more difficult to approximate. If D lies in a two-dimensional coordinate plane then the crystal can be described by the spheroid radii. Whereas a maximum dimension described in three dimensions (such as aggregates) requires a more complex relation to the spheroid axes. Importantly, D is independent of the Cartesian coordinate system but is instead equivalent to the semi-major axis of the governing ellipse (see Figure 12.1). Characterisation by

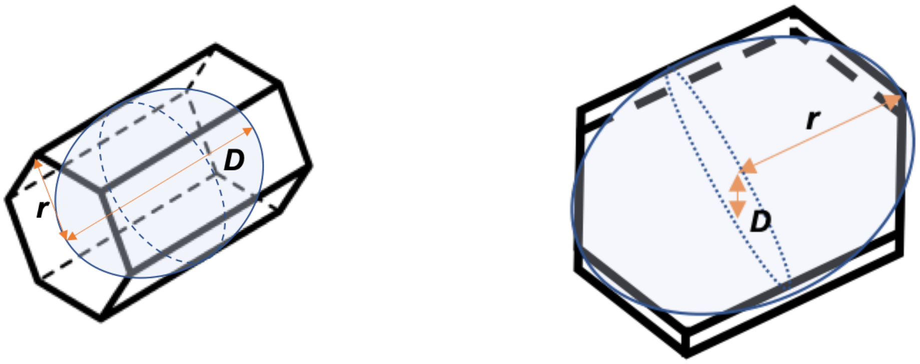

(a) Columnar hexagonal crystal and prolate spheroid approximation

(b) Plate-like hexagonal crystal and oblate spheroid approximation

Figure 12.4. Schematic of prolate (a) and oblate (b) spheroids (light blue) encapsulated within a crystal with equivalent radial lengths.

D, or the semi-major axis, can be useful as it gives an indication of *oblate-ness* or *prolate-ness*.

12.1.1 Differences in Volume and Surface Area

Consider a crystal defined by the basal face radius r and principal axis length D_c as in Figure 12.4. We wish to determine the difference in both surface area and volume between a crystal and its equivalent spheroid approximation. A simple approximation can be made by choosing a spheroid whose governing ellipse has semi-minor axis length r and semi-major axis length $\frac{D_c}{2}$ (direct axis comparison method). The volume of a spheroid is:

$$V_{\text{sph}} = \frac{4}{3}\pi a^2 c,$$

where a and c are as defined in Figure 12.2. We can compare the radii between spheroid and crystal directly i.e. $a \equiv r$ and $c \equiv \frac{D_c}{2}$:

$$V_{\text{sph}} = \frac{2}{3}\pi r^2 D_c, \tag{12.1}$$

The volume of a regular hexagonal prism is given by:

$$V_{\text{hp}} = \frac{3\sqrt{3}}{2}\pi s^2 h,$$

where s is the side length, and h the height. Given the symmetry of the spheroid in the $\hat{x}-\hat{y}$ (basal) plane, the hexagonal prism base will form a regular hexagon and the side length s is equal to the circumcircular radius. Thus, $s \equiv r$ and $h \equiv D_c$, hence:

$$V_{\text{hp}} = \frac{3\sqrt{3}}{2}\pi r^2 D_c \tag{12.2}$$

By comparison:

$$\begin{aligned} V_{\text{hp}} &= \frac{9\sqrt{3}}{4} V_{\text{sph}} \\ &\approx 3.90 V_{\text{sph}} \end{aligned}$$

Thus the volume of a spheroid can be considerably less than the crystal it aims to represent. This is a consequence of the choice of axial relation, whereby the maximum diameter of the spheroid is bound within that of a hexagonal prism. Consequently, the curvature from this maximum along a crystal plane causes an increasing reduction in volume. The deviation from the crystal volume may seem significant geometrically, but this is more likely to be a problem for the correct parameterisation of crystal density.

In the case of vapour deposition, the most important feature of a crystal is its surface geometry and principally its surface area. Here we will compare the surface area of a crystal and its equivalent spheroid using the radial relation in the previous section i.e. for a hexagonal prism $s \equiv r$ and $h \equiv D_c$ and for a spheroid $a \equiv r$ and $c \equiv D_c/2$. The surface of area of a hexagonal prism is defined by:

$$\begin{aligned} A_{\text{hp}} &= 6sh + 3\sqrt{3}s^2 \\ &= 6rD_c + 3\sqrt{3}r^2 \end{aligned}$$

The surface area of a prolate spheroid is defined as:

$$\begin{aligned} A_{\text{pr}} &= 2\pi a^2 \left(1 + \frac{c}{ae_p} \arcsin(e_p)\right) \qquad (12.3) \\ &= 2\pi r^2 \left(1 + \frac{D_c}{2re_p} \arcsin(e_p)\right), \qquad (12.4) \end{aligned}$$

where the prolate eccentricity $e_p = \sqrt{1 - \frac{a^2}{c^2}} \equiv \sqrt{1 - \frac{(2r)^2}{D_c^2}}$

The surface area of an oblate spheroid is:

$$A_{\text{ob}} = 2\pi a^2 + \pi\frac{c^2}{e_o}\log\left(\frac{1+e_o}{1-e_o}\right) \tag{12.5}$$

$$= 2\pi r^2 + \pi\frac{D_c^2}{4e_o}\log\left(\frac{1+e_o}{1-e_o}\right), \tag{12.6}$$

where the eccentricity $e_o = \sqrt{1-\frac{c^2}{a^2}} \equiv \sqrt{1-\frac{D_c^2}{(2r)^2}}$.

The surface area can be plot against aspect ratio for each case by substituting $\phi = \frac{c}{a} = \frac{D_c}{2r}$, then for oblates the surface area becomes:

$$A_{\text{ob}} = 2\pi\left(\frac{D_c}{2\phi}\right)^2 + \pi\frac{D_c^2}{4e_o}\log\left(\frac{1+e_o}{1-e_o}\right), \tag{12.7}$$

and correspondingly, for prolates:

$$A_{\text{pr}} = 2\pi r^2\left(1+\frac{\phi}{e_p}\text{arcsin}(e_p)\right), \tag{12.8}$$

where the eccentricity of each spheroid type is related to the aspect ratio as:

$$e_o = \sqrt{1-\phi^2} \tag{12.9}$$

$$e_p = \sqrt{1-\frac{1}{\phi^2}} \tag{12.10}$$

Thus, the surface area is defined by ϕ, D and r for both A_{ob} and A_{pr}, which allows the surface area to be plotted for a continuous range of aspect ratios wherein the major axis of the governing ellipse is elongated and the minor is fixed. This is equivalent to elongating each spheroid type to achieve more extreme aspect ratios. Consequently, the minor axis has to be fixed. We find that the surface area is independent of the value of each fixed parameter so long as $D = 2r$, this result can be derived by setting $A_{\text{pr}} = A_{\text{ob}}$ when $\phi = 1$.

To achieve a good comparison with each case, the hexagonal prism can be split into two subcategories:

$$\begin{aligned} A_{\text{hp}_{\text{prolate}}} &= 6rD_c + 3\sqrt{3}r^2 \\ &= r^2\left(12\phi + 3\sqrt{3}\right) \end{aligned}$$

$$\begin{aligned} A_{\text{hp}_{\text{oblate}}} &= 6rD_c + 3\sqrt{3}r^2 \\ &= 3\left(\frac{D_c^2}{\phi}\right)\phi + 3\sqrt{3}\left(\frac{D_c^2}{4\phi^2}\right) \end{aligned}$$

The surface area of each sub type can be plot to determine how it changes with aspect ratio. Figure 12.5 panel (a) shows the surface area for spheroids and hexagonal crystals versus aspect ratio, where the surface area has been made non-dimensional by a division of r^2. Panel (b) shows the ratio of hexagonal crystal surface area to the spheroid. Both figures indicate that the spheroid provides a reasonably close approximation to the surface area of hexagonal crystals, with the accuracy closest for the most severe aspect ratios and least accurate as the crystal approaches an aspect ratio of one. Close to one, oblates and prolates provide approximately 73% of the surface area of an equivalent crystal, but with increasing aspect ratio prolates can attain around 80% of the surface area of hexagonal prisms, and oblates tend towards 100%. This would indicate that flat, plate like ices such as plates, dendrites, and stellars can expect to be the most closely represented by spheroids and may have a slight advantage when it comes to the accurate prediction of vapour deposition. Prolates, such as columns or bullets will be reasonably well represented, with their thinner counterparts such as needles having an increasingly close surface area value to the spheroid. Of course, the least well represented will be rounder particles, such as graupel, aggregates, and capped columns. For these crystal types, the spheroid is likely to more severely underestimate the surface area.

12.2 Two Cases of Capacitance in the Literature

In the previous section the spheroid approximation was compared to the geometry of crystals in general. In this section, the capacitance of spheroids and crystals is examined and compared. Two example cases from the literature are used for this comparison, the theoretical capacitance of generalised spheroids by McDonald (1963), and the computed capacitance of ice crystal geometries by Westbrook et al. (2008).

12.2.1 Theoretical Capacitance of Spheroids

In their paper on the determination of capacitance using metal crystals, McDonald (1963) noted that the electrostatic capacitance of spheroids was already known for simple deformations. They list four theoretical capacitances shown in Table 1: Spheres, oblates, prolates and a thin disc.

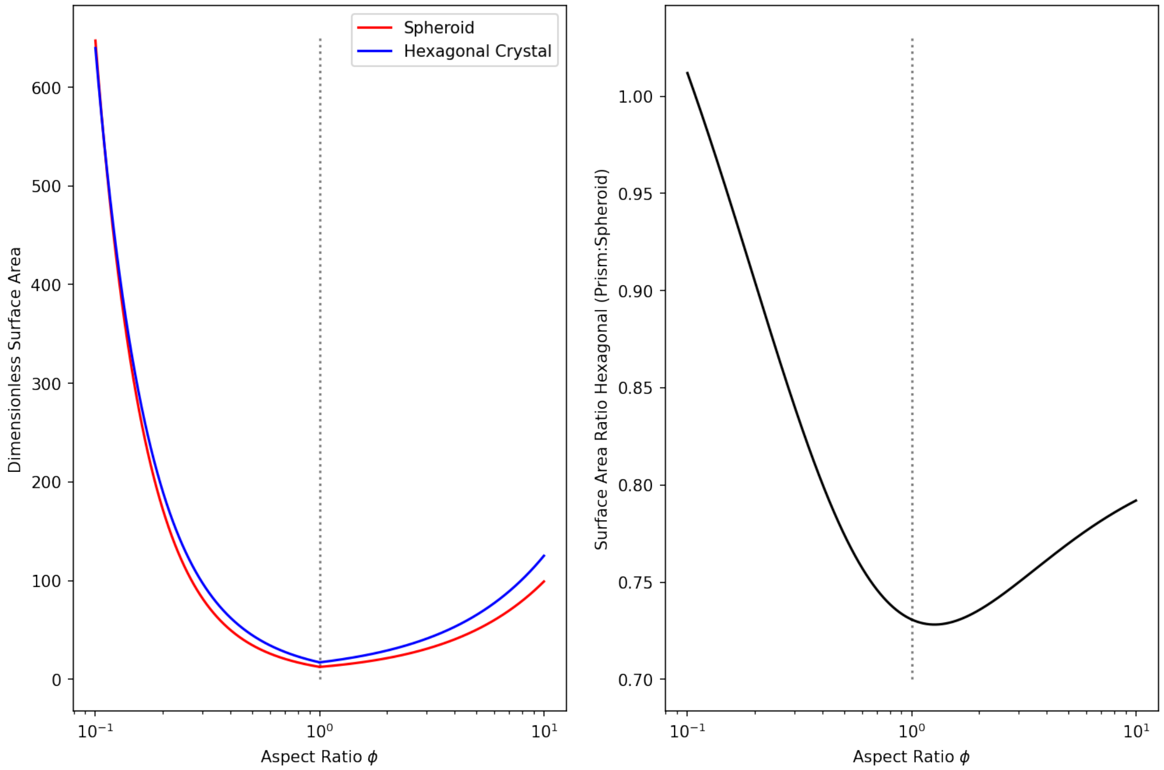

Figure 12.5. The ratio of volume and surface area of spheroids to their equivalent hexagonal prisms.

Shape	Capacitance
Sphere, radius r	$C = r$
Thin disk, radius r	$C = 2r/\pi$
Prolate Spheroid: major, minor semi-axes a,b	$C = A/\ln[(a+A)/b]$, where $A = \sqrt{a^2 - b^2}$
Oblate Spheroid: major, minor semi-axes a,c	$C = ae/\sin^{-1} e$, where $e = \sqrt{1 - c^2/a^2}$

Table 12.2. Theoretical Capacitance of spheroids adapted from McDonald (1963)

The capacitance for each spheroid sub type can be determined using the relations in Table 12.2 by providing a radius r and the major and minor semi-axes of the governing ellipse. Given that a wide range of aspect ratios can occur for any given maximum crystal dimension, it is useful to instead compare the capacitance for changing oblate-*ness* or prolate-*ness* i.e. by varying the ellipse major axis. We assume the disc can be represented as an oblate spheroid and therefore r is equivalent to the semi-major axis.

The variation of capacitance with semi-major axis (a oblates, c prolates) is given in Figure 12.6 (left). In this analysis, the semi-minor axis is fixed at 1×10^{-5} m, a typical nucleation length scale for microphysics schemes (Jensen et al. 2017; Morrison and Grabowski 2008). Additionally, the equations in Table 12.2 can be re-parameterised in terms of aspect ratio ϕ by fixing the semi-minor axis and varying the semi-major axis. A plot of the analytical capacitance varying with ϕ is shown in Figure 12.6 (right).

In Figure 12.6 (left), as the semi-major axis approaches the fixed semi-minor axis all spher-

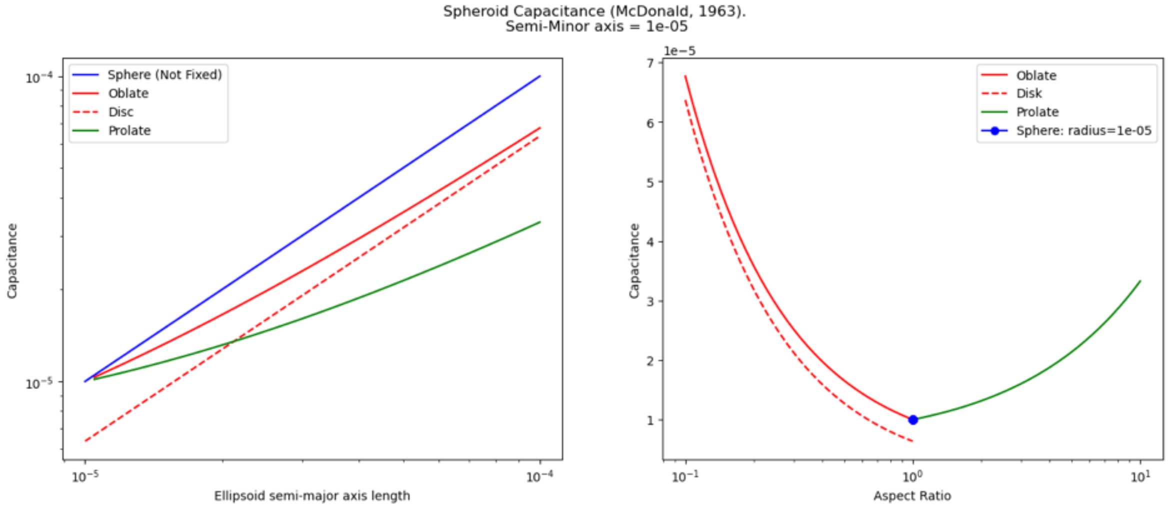

Figure 12.6. Capacitance of spheroid types with fixed semi-minor axis versus semi-major axis. The semi-major axis is an indication of the extremity of prolate or oblate crystals. Right: as in left but re-parameterised for aspect ratio.

oids capacitances converge to the sphere value. For oblates, large semi-major axis lengths tend towards the disc approximation. It is notable that prolate spheroids have a smaller analytical capacitance than oblate spheroids for the same governing ellipse, and this difference becomes more drastic with increasing semi-major axis length. This indicates that ices represented by very oblate spheroids, such as stellars and dendrites have a significant geometric advantage over those represented by very prolate spheroids, such as needles and bullets. The variation of capacitance with aspect ratio in Figure 12.6 (right), highlights the more rapid growth of capacitance in oblates compares to prolates, and indicates the adjoining sphere approximation for the fixed semi-minor axis length.

12.2.2 Computed Capacitance of Ice Crystal Geometries

In their paper on the determination of capacitance using computational methods, Westbrook et al. (2008) derived best fit functions for the capacitance of several ice habits. These functions are shown in Table 12.3.

To draw comparisons with the analytical spheroid capacitance by McDonald (1963), the axis lengths in each function are made equivalent to that of a spheroid in the McDonald scheme. The difference in capacitance provided by each framework can therefore be compared without significant bias.

In the Westbrook et al. (2008) formulation, the crystal basal face has length $2a$, so for columns a_W is the prolate semi-minor axis length b_M and for plate-like crystals a_W is the oblate semi-major axis length a_M. The 4-bullet rosette used in this case is of planar type, so the maximum dimension, D_{max} is approximately equal to twice the semi-major axis of an oblate

Crystal	Capacitance
Hexagonal plates and columns	$C = 0.58(1 + 0.95\mathcal{A}^{0.75})a$
4-Bullet Rosette	$C = 0.35\mathcal{A}^{-0.27}D_{\text{max}}$
6-Bullet Rosette	$C = 0.40\mathcal{A}^{-0.25}D_{\text{max}}$
Stellar	$C = 0.596(1 - 0.38e^{-4.7\mathcal{A}})a$
Dendrite	$C = 0.596(1 - 0.30e^{-5.8\mathcal{A}})a$

Table 12.3. Functions for the capacitance of ice crystals as determined by Westbrook et al. (2008). The capacitance is a function of the maximum crystal dimension D, the length of the basal face a, and the aspect ratio $\mathcal{A}$.

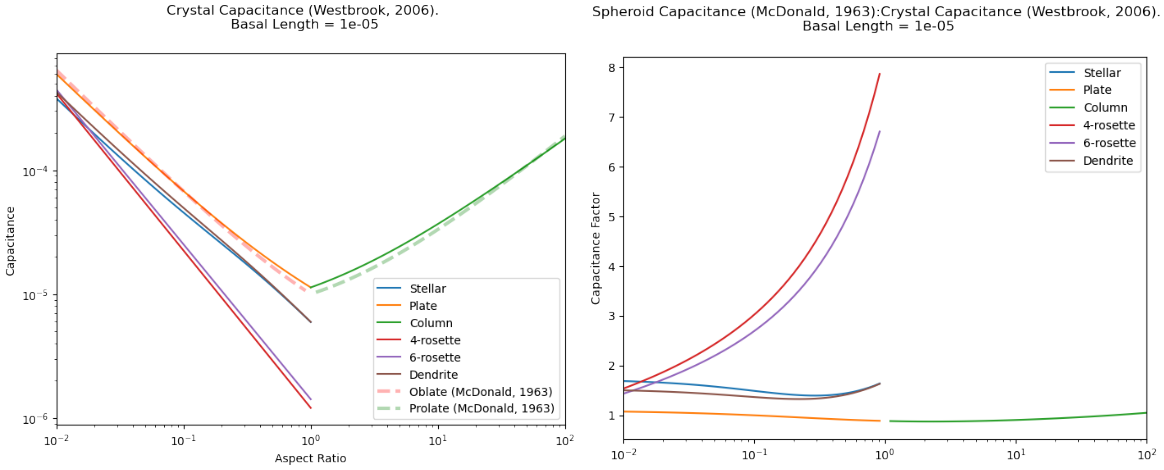

(a) A

(b) B

Figure 12.7. Functions for the capacitance of ice crystals as determined by Westbrook et al. (2008) and McDonald (1963) (left) and the ratio of capacitance derived in the McDonald (1963) equation set to that derived by Westbrook et al. (2008) (right) .

A_M. The 6-bullet rosette is more complicated, having a near-spheroidal geometry. The author has determined that the oblate case is most appropriate for the model used, so D_{max} is approximately equal to twice the semi-major axis of an oblate A_M.

The capacitance functions in Table 12.3 were calculated and are shown in Figure 12.7 (left). The relative difference in capacitance between the Westbrook et al. (2008) and McDonald (1963) methods are shown in Figure 12.7 (right).

In Figure 12.7 it is evident that the typical ice crystal habits in Westbrook et al. (2008) have capacitance below the spheroid approximation, and the overestimation of the spheroid approximation grows with more extreme aspect ratios. The more porous and complex the habit, the greater the overestimation of spheroids . Simple habits such as plates and bullets have the closest resemblance, with spheroids overestimating plates and column capacitance only at extreme aspect ratios. Whereas, stellars and dendrites show the next greatest difference, and then the greatest overestimation. Rosettes have the smallest total capacitance, reaching approximately one third that of oblate spheroids. Dendrites and stellars are comparatively closer in capacitance to spheroids, but still are overestimated by the spheroid approximation with increasing amounts at more extreme aspect ratios.

12.3 Box-Model Setup

Having established the equations that govern vapour deposition in the previous section, a box model can be built to examine the difference in ice growth over time for like conditions, with the intention to monitor and compare this process for the purposes of evaluating the role of capacitance. The box model will update the cloud ice distribution using the formulation of particle size distributions in each microphysics scheme formulation, which are the ISHMAEL and Morrison schemes.

12.3.1 Particle Distributions

First the number distribution of ice crystals is examined. Each scheme assumes that the ice number N is a randomly distributed variable that follows a gamma distribution $N \sim \text{Gam}(\alpha, \beta)$ and that N is related to, and therefore a function of, the particle dimension x. The gamma distribution probability density function $f(x)$ has the general form:

$$f(x) = N_0 x^{\alpha-1} e^{-\beta x} \, \{\alpha > 0, \beta > 0\}, \tag{12.11}$$

where α and β are the shape parameter and the rate parameter of the distribution, sometimes named the spectral index and slope, respectively. The intercept is denoted N_0. Consequently, the particle size distribution of any hydrometeor class can be defined at an instant by calculating the parameters. In this section we determine values of the parameters for each scheme. The first moment of the distribution is the number concentration N, which is found by integrating over the entire distribution:

$$N = \int_0^\infty f(x) \, \mathrm{d}x, \tag{12.12}$$

and has the general solution:

$$N = N_0 \frac{\Gamma(\alpha)}{\beta^\alpha}, \tag{12.13}$$

where $\Gamma(\alpha)$ is the Euler gamma function. Proof can be found in appendix B.1.

The second moment of the distribution is the mass mixing ratio Q, found by integrating the product of the particle mass q and number distribution:

$$Q = \int_0^\infty q(x) \cdot f(x)\ \mathrm{d}x \tag{12.14}$$

12.3.2 Morrison Solution

To complete the integral each scheme must specify a mass distribution hypothesis that allows $q(x)$ to be defined as a function of x only. In Morrison the m-D relationship follows a power law of the form:

$$m = c_m D^{d_m}, \tag{12.15}$$

where D is particle diameter, and c_m, d_m are constants. The Morrison scheme sets $c_m = \frac{\pi\rho}{6}$, $d_m = 3$:

$$m = \frac{4\pi}{3}\rho r^3$$

Hence cloud ice crystals are modelled as constant density spheres. Using this relation in Equation 12.14, Q has the general solution:

$$Q = N_0 c_m \frac{\Gamma(\alpha + d_m)}{\beta^{\alpha + d_m}} \tag{12.16}$$

Proof of this relation can be found in appendix B.2. For Morrison, we can obtain a definition for N_0 based on Equation 12.13:

$$N_0 = N\frac{\beta^\alpha}{\Gamma(\alpha)} \tag{12.17}$$

Substitution of this identity into Equation 12.16 yields:

$$Q = N c_m \frac{1}{\beta^{d_m}} \frac{\Gamma(\alpha + d_m)}{\Gamma(\alpha)}$$

$$\beta = \left(\frac{N c_m}{Q} \frac{\Gamma(\alpha + d_m)}{\Gamma(\alpha)} \right)^{\frac{1}{d_m}} \tag{12.18}$$

Therefore, both β and N_0 are diagnosed based on the ice number concentration and mass concentration. The distribution can be updated by forming new values of N and Q after microphysical process calculations and subsequently updating the distribution parameter definitions.

12.3.3 ISHMAEL Solution

For ISHMAEL, the mass distribution hypothesis follows a similar format but uses the volume of a spheroid instead of that of a sphere:

$$m = \frac{4\pi\bar{\rho}}{3}a^2c, \tag{12.19}$$

where a and c are the spheroid axes. This identity can be used in a substitution of $q(x)$ in Equation 12.14 if we let $x \equiv a$. However, to close the integral, c must be related to the a-axis length. To do this, ISHMAEL relies on the mass distribution hypothesis for spheroids first proposed by J.-P. Chen and Lamb (1994) that enables relation of the axes as in Jensen et al. (2017):

$$c_i = a_0^{1-\delta_*}a_i^{\delta_*}, \tag{12.20}$$

where a_0 is the initial particle size at the time step start, and δ_* represents the mean inherent growth ratio of ice across all ice growth processes. At $\delta_* = 1$ the c-axis $c_i = a_i$ and the ice is isometric (spherical); in the current version of ISHMAEL (WRF v.4.3) all ices are nucleated as isometric but evolve toward oblate ($\delta_* < 1$) or prolate ($\delta_* > 1$).

The relationship between δ_* and spheroid aspect ratio is not immediately apparent, but can be shown by rearranging Equation 12.20. Let $\varphi = c_i/a_i$ be the aspect ratio, and let R be the ratio of the initial to the current particle a-axis a_i/a_0 indicating growth or contraction. Substituting $a_i = a_0R$:

$$\varphi = R^{\delta_*-1}$$

A plot of ϕ versus δ_* for values of R is given in Figure 12.8. Note that δ_* is limited between 0.55 and 1.33. As R increases (the a-axis relative to its nucleation length), increasing (decreasing) values of δ_* make increasingly prolate (oblate) ices.

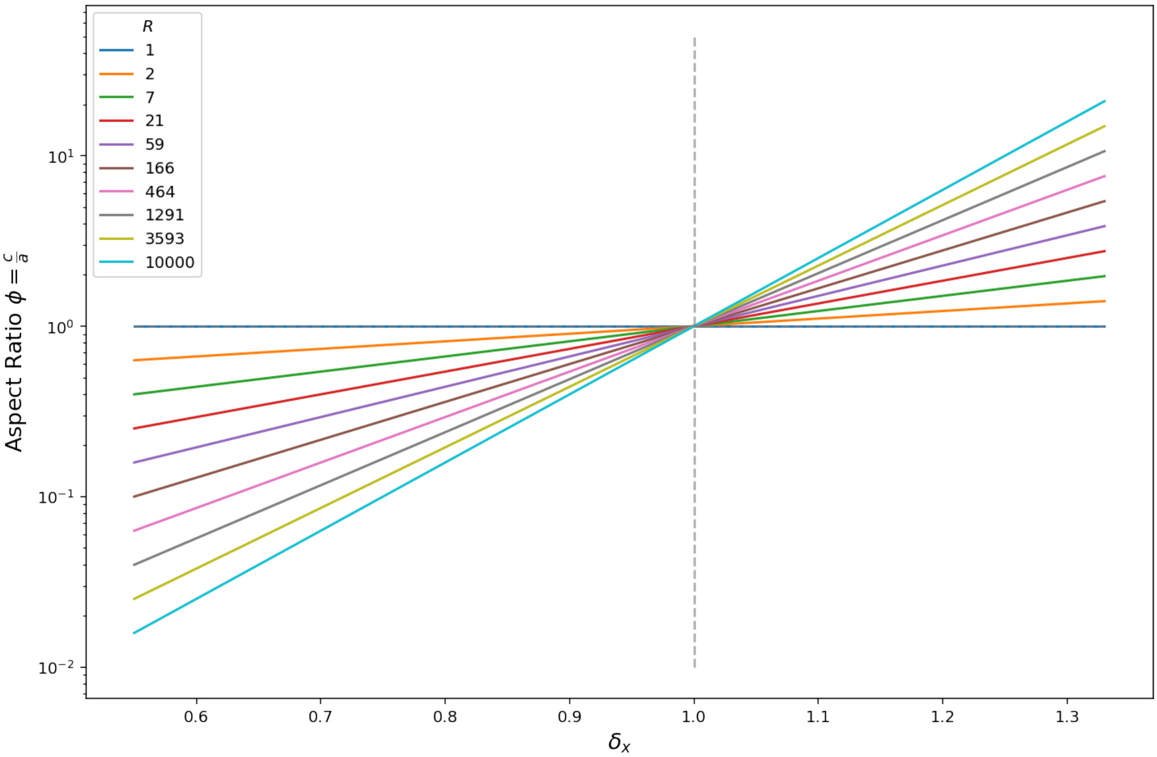

Figure 12.8. Relationship between the ice particle aspect ratio ϕ and the inherent growth ratio δ_* for differing values of the spheroid a-axis relative growth factor R

To determine δ_* we take the natural logarithm of Equation 12.20 and rearrange:

$$\delta_* = \log(c_i) - \log(a_0)/(\log(a_i) - \log(a_0))$$

The inherent growth ratio δ_* is implemented in this manner throughout the ISHMAEL code. Substituting 12.20 into the equation for spheroid mass and subsequently substituting for $q(x)$ in Equation 12.14 we retrieve the following:

$$Q = \frac{4\pi\bar{\rho}}{3} \int_0^\infty a_0^{1-\delta_*} a_i^{2+\delta_*} \cdot f(a_i)\, \mathrm{d}a_i \tag{12.21}$$

$$= \left[N_0 \frac{4\pi\bar{\rho}}{3} a_0^{1-\delta_*} \right] \frac{\Gamma(\alpha + \delta_* + 2)}{\beta^{\alpha+\delta_*+2}} \tag{12.22}$$

A derivation of this result is found in appendix B.3. This identity can be fully specified by substituting Equation 12.13 into 12.22:

$$Q = \left[N \frac{4\pi\bar{\rho}}{3} a_0^{1-\delta_*} \right] \frac{\Gamma(\alpha + \delta_* + 2)}{\Gamma(\alpha)} \frac{1}{\beta^{\delta_*+2}} \tag{12.23}$$

Additionally, recall that $\beta = 1/a_n$ where a_n is named the characteristic axis length. Making this substitution we derive Equation 9 of Jensen et al. (2017):

$$Q = \frac{4\pi\bar{\rho}}{3}\frac{N\Gamma(\delta_* + \alpha + 2)}{\Gamma(\alpha)}{a_0}^{1-\delta_*}a_n^{2+\delta_*} \tag{12.24}$$

To completely specify the distribution the value of β may be updated by microphysical process rates in terms of N and Q. This is evident by rearranging Equation 12.23 for $1/\beta$:

$$\frac{1}{\beta} = a_n = \left(\frac{Q}{N}\frac{3}{4\pi\bar{\rho}a_0^{1-\delta_*}}\frac{\Gamma(\alpha)}{\Gamma(\alpha + \delta_* + 2)}\right)^{\frac{1}{\delta_*+2}} \tag{12.25}$$

12.3.4 Comparison to the Literature

We may compare the derived functions to the literature for each scheme. Recall the general form of the gamma probability density function:

$$f(x) = N_0 x^{\alpha-1}e^{-\beta x}\,\{\alpha > 0, \beta > 0\}, \tag{12.26}$$

the parameters are given like so:

Morrison	ISHMAEL
$x = D$	$x = a_i$
$\alpha = 1 + p_c = 1$	$\alpha = \nu = 4$
$\beta = \lambda$	$\beta = 1/a_n$

Then Morrison has the distribution:

$$f(D) = N_0 D^{p_c}e^{-\lambda D}$$

and making the same parameter changes to the derived values of N_0, β in Equations: 12.17 and 12.18, respectively:

$$N_0 = \frac{N\lambda^{p_c+1}}{\Gamma(p_c + 1)}$$

$$\beta = \left[\frac{c_m N\Gamma(p_c + d_m + 1)}{Q_I\Gamma(p_c + 1)}\right]^{\frac{1}{d_m}} \equiv \lambda$$

Which collectively form $A1 - A3$ in Morrison et al. (2005). Setting $\alpha = 1$ and $p_c = 0$, creates a simple exponential distribution.

ISHMAEL has the distribution:

$$f(a_i) = \frac{N}{\Gamma(\nu)}\left(\frac{a_i}{a_n}\right)^{\nu-1}\frac{1}{a_n}e^{-\frac{a_i}{a_n}}$$

Where we have used the relation $N_0 = N\frac{\beta^\alpha}{\Gamma(\alpha)}$. This forms Equation 7 in Jensen et al. (2017).

12.3.5 Mean Particle Size

The particle size in each scheme is defined as the integral over the size distribution, which we have defined already for the number mixing ratio, in ISHMAEL this is:

$$\bar{a} = \int_0^\infty \frac{a}{\Gamma(\nu)}\left(\frac{a_i}{a_n}\right)^{\nu-1}\frac{1}{a_n}e^{-\frac{a_i}{a_n}} \tag{12.27}$$

Completing this using the definition for the Euler gamma function and the substitution method as in the appendix, we find that:

$$\bar{a} = \frac{\Gamma(\nu+1)}{\Gamma(\nu)}a_n = 4a_n \tag{12.28}$$

In Morrison we find that similarly:

$$\begin{aligned} a &= \int_0^\infty D\cdot f(D) = \int_0^\infty \frac{N_0}{N}D\cdot D^{p_c}e^{-\lambda D} \\ &= \frac{\beta^\alpha}{\Gamma(\alpha)}\int_0^\infty D^\alpha e^{-\lambda D} \\ &= \frac{\beta^\alpha}{\Gamma(\alpha)}\frac{\Gamma(\alpha+1)}{\beta^{\alpha+1}} \\ &= \frac{\alpha}{\beta^\alpha} \end{aligned}$$

In Morrison $\alpha = 1, \beta = \lambda$ so:

$$\bar{D} = \frac{1}{\lambda}$$

Thus in Morrison the average radius of a hydrometeor category is 1/2λ. However, care must be taken when converting between radius and diameter during comparisons to the ISHMAEL scheme and in general.

The ratio of average radius in ISHMAEL to Morrison for a given mass and number mixing ratio by taking the definitions of λ from Equation 12.18 and a_n from Equation 12.25:

$$\frac{\bar{D}}{2} = \bar{r} = \frac{1}{2}\left(\frac{N\pi\rho}{6Q}\frac{\Gamma(4)}{\Gamma(1)}\right)^{-\frac{1}{3}}$$

$$\bar{a} = 4\left(\frac{Q}{N}\frac{3}{4\pi\bar{\rho}}\frac{\Gamma(4)}{\Gamma(7)}\right)^{\frac{1}{3}},$$

where $\bar{r} = \bar{D}/2$ and $\delta_* = 1$ in order to obtain spherical particles that are comparable for both schemes. In accordance with each scheme setup $\alpha = 1$, $d = 3$ in Morrison, $\alpha = 4$ in ISHMAEL. When number and mass concentration are identical the following relationship is obtained between average radii in each framework:

$$\frac{\bar{r}}{\bar{a}} = \frac{1}{8}\left(\frac{160\rho}{\bar{\rho}}\right)^{\frac{1}{3}}$$

For like densities, $\frac{\bar{r}}{\bar{a}} \approx 0.6786$, or rather ISHMAEL's average radius is approximately 1.47 times larger than Morrison for spherical particles.

The relationship for differing δ_* (i.e. non spherical) is more complex and so is shown in Figure 12.9. Here the radius is plotted for the (artificially limited) δ_* range 0.55, 1.3 and for equal density amongst schemes. Several curves are shown for various ratios of mass to number concentration $K = q_i/n_i$.

The magnitude of the ratio of average particle size in ISHMAEL increases with increasing oblateness ($\delta_* < 1$), whereas for prolate crystals the opposite is true, increasingly prolate crystals drive the average radius of both schemes closer together until the point that both scheme's radii reach parity ($\bar{a} = \bar{r}$). Further increases in δ_* then yield increasingly smaller radii in ISHMAEL compared to Morrison.

This relationship is exacerbated with increasing crystal mass ratio K, such that with higher K the most severely oblate (prolate) crystals have larger (smaller) ratios and the inflection point $\bar{a} = \bar{r}$ occurs at less prolate geometries. This is consequential, as the point at which the average radius is larger in ISHMAEL than in Morrison is dynamic, and moves with average crystal mass accordingly. Therefore, one can imagine that in environments of very many small crystals on the most severely prolate crystals will enable Morrison to have a comparable average crystal radius. Conversely, for environments of few large crystals the inflection point is much closer to spherical, and so the average particle radius might be more comparable between schemes. Of course, the most striking feature is found for very oblate crystals when the mass is high, such as in snow. Here, the average particle radius becomes much larger in ISHMAEL than in Morrison. These features are notable as they can produce striking differences in the character of the cloud hydrometeor population despite having identical mass and number mixing ratios. The average radius is a factor in the determination of fall speeds and the calculation of several microphysical processes, not least deposition and riming.

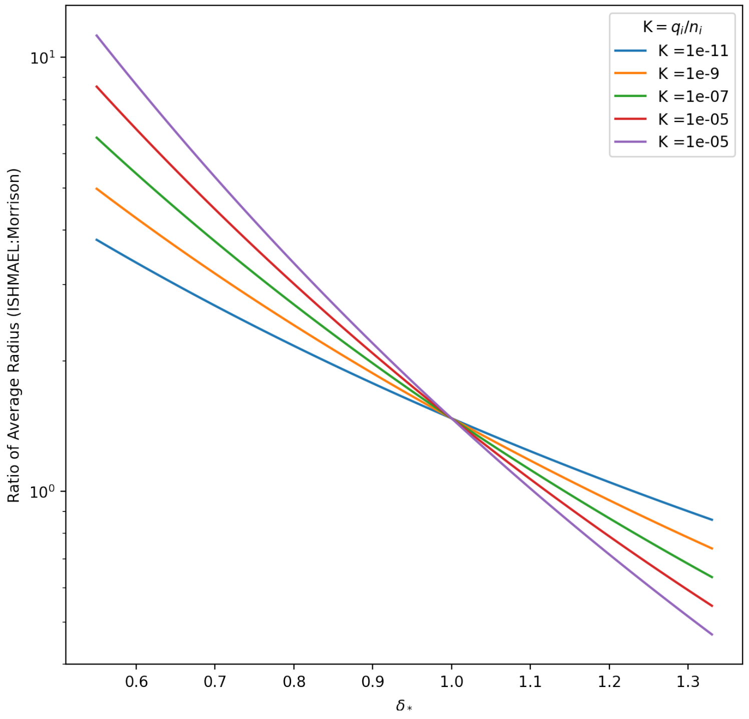

Figure 12.9. Ratio of the distribution average radius between the ISHMAEL and Morrison microphysics schemes versus the inherent growth ratio δ_*. When $\delta_* = 1$ both distributions simulate spherical particles. The ratio is plot for several values of the average ice-mass K shown in the Figure legend.

12.4 Deposition Frameworks per Scheme

As found in the previous section, the parameters β and N_0 of the gamma distribution are based on the mass and number of particles, not withstanding α which is determined from measurement spectra and defined *a priori*. Thus, to determine changes in the distribution due to deposition, each scheme must compute the change in N, Q with each time step.

In this section we will focus on the formulation of the deposition process in each scheme and, more specifically, how deposition changes the ice crystal mass and number mixing ratios.

12.4.1 Morrison Deposition Framework

For large scale models encompassing tens of thousands of grid cells simultaneously, it is reasonable to assume that a relatively large time step will be employed. Consequently supersaturation, which exists as a short term perturbation from equilibrium, is overlooked and the tendency of the model is to produce stable saturation levels at the end of each time step. A consistent saturation level is a reasonable assumption for liquid water hydrometeors which have short relaxation time scales and thus saturation is obtained relatively quickly, but the relaxation time of frozen hydrometeors is much larger (> 30 minutes) so supersaturation is maintained for large periods spanning multiple model time steps. To overcome the issue of resolving supersaturation, two separate methods are used for liquid water and ice in the Morrison framework, cloud water uses the saturation adjustment method, and ice hydrometeors use the vapour diffusion method. This section will focus on the parameterisation of the vapour diffusion method to ice crystals.

The deposition or condensation to ice by diffusion of vapour is given by Morrison et al. (2005) (their Equation 12 for rain evaporation):

$$\mathtt{PRD} = \frac{\delta_0}{Q_2 \tau}(q_{\mathrm{sw}} - q_{\mathrm{si}}), \tag{12.29}$$

where δ_0 is the supersaturation at the beginning of the time step (i.e. `QVI - QVS`), q_{sw} is the water vapour mixing ratio at saturation q_{si} is the saturation mixing ratio over ice and Q_2 is related to diffusional heating:

$$Q_2 = 1 + (dq_{\mathrm{si}}/dT)(L_s/c_p),$$

and L_s is the latent heat of sublimation. This can be compared directly to the in-code deposition to cloud ice given by variable `PRD`:

```
PRD(K) = EPSI*(QV3D(K)-QVI(K))/ABI(K)*DUM
```

Where each component corresponds to the following:

$$\begin{aligned}
\text{DUM} &= 1 - e^{-\lambda_i D_{\text{cs}}}(1 + \lambda_i D_{\text{cs}}) \\
\text{ABI} &= 1 + \frac{dq_{\text{si}}}{dT}\frac{\text{XXLS}}{c_p} \\
\text{XXLS} &= 3.15 \times 10^6 - 2370\text{T} + 3.337 \times 10^5 \\
\text{EPSI} &= 2\pi N_{0I}\rho_a \frac{1}{\lambda_I^2} D_v
\end{aligned}$$

Where `EPSI` is the phase relaxation time for ice, i.e $\epsilon = \tau_i^{-1}$ and ABI $\equiv Q_2$ is a heating term. Therefore:

$$\begin{aligned}
\text{PRD} &= 2\pi\rho D_v \times \frac{N\lambda^{p_c+1}}{\Gamma(P_c+1)} \times \frac{1}{\lambda_i^2} \times \frac{(q_v - q_{\text{si}})}{Q_2} \times 1 - e^{-\lambda_i D_{\text{cs}}}(1 + \lambda_i D_{\text{cs}}) \\
&= \frac{(q_v - q_{\text{si}})}{Q_2 \tau} \times 1 - e^{-\lambda_i D_{\text{cs}}}(1 + \lambda_i D_{\text{cs}}) \qquad (12.30)
\end{aligned}$$

This is identical to Equation 12.29 if $\delta_0 = 1$, which makes sense as the water vapour mixing ratio will be at saturation as condensation precedes ice deposition (due to difference in time scales). `DUM` is a factor that determines the proportion of the population whose diameter is smaller than a maximum dimensional limit $D_{\text{cs}} = 125 \times 10^{-6}$. If snow is present, the "tail end" or minority of the distribution that exists only for the largest particles (larger than `DCS`) is added to the snow category, whereas if no snow is present then this deposition is added to the ice. Figure 12.10 demonstrates how `DCS` partitions the population.

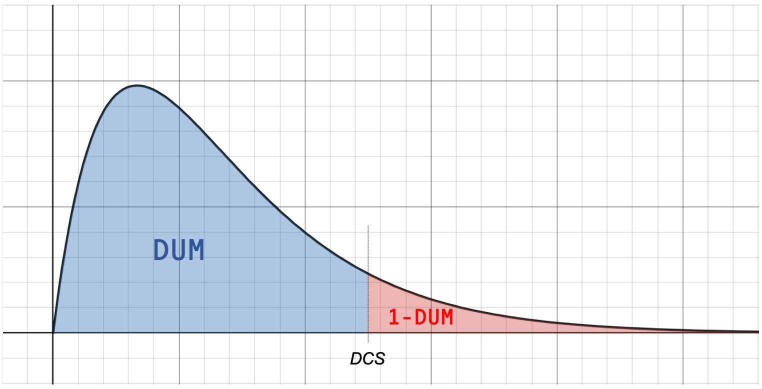

Figure 12.10. Visual schematic of how the ice maximum dimension `DCS` parameter partitions the particle distribution such that large ice particles enter into the snow category.

In either case, deposition to ice below this DCS is always added to the ice category. Therefore, Equation 12.30 can be used to determine the change in ice mass mixing ratio at the end of the time step. To understand how capacitance influences the deposition rate we must examine the complete form of the hydrometeor relaxation timescale τ_x given by Equation 4 of Morrison et al. (2005) and references therein:

$$\tau_x = \left\{ 2\pi\rho_a D_\nu C_0 N_0 \Gamma(p_c+2) \left[\frac{f_1}{\lambda^{P_c+2}} + f_2 \left(\frac{a_f \rho}{\mu_a}\right)^{\frac{1}{2}} S_c^{\frac{1}{3}} \Gamma\left(\frac{b_f+2p_c+5}{2}\right) \lambda^{-(b_f+2p_c+5)/2} \right] \right\}^{-1}, \tag{12.31}$$

where f_1 and f_2 are particle ventilation coefficients. a_f and b_f are parameters in the fall-speed dimensional relation, which takes the form of a power law. D_ν is the diffusivity of water vapour in air, ρ_a is the air density, μ_a is the dynamic viscosity, S_c is the Schmidt number. The parameter C_0 is the constant of proportionality in the capacitance-maximum-dimension relation $C = C_0 D$ known as the dimensionless capacitance. The remaining parameters Γ, N_0, P_c and λ are parameters of the gamma distribution provided in the previous section.

Direct comparison of the general form of the phase relaxation time scale can be made to that computed in the Morrison code. The snow relaxation time scale `EPSS` (denoting ϵ_s where $\epsilon_x = \tau_x^{-1}$) is:

$$\tau_s^{-1} = 2\pi\rho D_\nu N_{0s} \left[\frac{f_{1s}}{\lambda_s^2} + f_{2s} \left(a_f \frac{\rho}{\mu}\right)^{\frac{1}{2}} S_c^{\frac{1}{3}} \Gamma\left(\frac{b_f+5}{2}\right) \times \lambda_s^{-(b_f+5)/2} \right], \tag{12.32}$$

This follows the general form of Equation 12.31 with $p_c = 0$ (as specified in the previous section) and $C_0 = 1$. The phase relaxation time scales for graupel τ_g^{-1} and rain droplets τ_r^{-1} follow the same form. However, for cloud ice the effects of ventilation are neglected:

$$\tau_i^{-1} = 2\pi\rho D_\nu N_{0i} \frac{1}{\lambda_i^2} \tag{12.33}$$

This is equivalent to taking $p_c, f_2 = 0$, $C_0, f_1 = 1$ in Equation 12.31. It is clear from comparison of the in-code equations to the general form of τ_x that, in all cases, $C_0 = 1$, despite intentions to modify this at the time of publication- “Future versions of the scheme will take into account non-spherical ice particle habits” (Morrison et al. 2005). Therefore all hydrometeors have the capacitance of a sphere. To perform experiments with alternative values of the capacitance we may reintroduce the parameter C_0 as a factor of the relaxation timescale and modify it accordingly.

12.4.2 ISHMAEL Deposition Framework

The mass tendency equation for the deposition process in ISHMAEL can be found in Jensen et al. (2017) their Equation 22:

$$\frac{dq_I}{dt}_{\text{dep}} = \frac{1}{\rho_a} \int_0^{\infty} 4\pi C_i G_i s_i n(a_i)\, \mathrm{d}a_i = \frac{N_I}{\rho_a} 4\pi C_I G_i s_i \tag{12.34}$$

Where G_i is an effective diffusion coefficient (see Lamb and Verlinde (2011) their Equation (8.41), p. 343), s_i is the supersaturation over ice and C_I is the distribution averaged capacitance from Harrington et al. (2013) (their Equation B14).

Since both the a and c axes are changing, deriving a solution to the vapour diffusion is difficult. To overcome this, Equation 12.34 can be switched for the distribution of equivalent volume spheres following the method of Harrington et al. (2013) Equations B22–B25. This is done by the capacitance relation:

$$\bar{f}_s(r_n) = [C_I(a_n)/r_n]$$

Then Equation 12.34 becomes:

$$\frac{dq_I}{dt}_{\text{dep}} = \frac{N_I}{\rho_a} 4\pi \bar{f}_s(r_n) r_n G_i s_i \tag{12.35}$$

We cannot directly solve this for q_I as the time dependence is unclear. However we can form an expression of q_I by integrating the total particle mass distribution over r as shown in Harrington et al. (2013) Equation B5. Note that the volume:

$$V = \frac{4\pi}{3} N_i \frac{\Gamma(\alpha + \delta_* + 2)}{\Gamma(\alpha)} r_n^3 \tag{12.36}$$

Therefore:

$$q_i = \frac{4\pi}{3} r_n^3 \bar{\rho}_i N_i \frac{\Gamma(\alpha + \delta_* + 2)}{\Gamma(\alpha)} = \rho_i V_t \tag{12.37}$$

Consequently, the rate of change of mass during deposition can be re-framed as a change in particle volume and density as a consequence of deposition:

$$\frac{dq_I}{dt}_{\text{dep}} = \bar{\rho}_i(t + \Delta t) V_t(t + \Delta t) - \bar{\rho}_i(t) V_t(t)$$

We may assign the change in density as that obtained by the depositional density $\rho_{\text{dep}} = \bar{\rho}_i(t+\Delta t) - \bar{\rho}_i(t)$. Then the rate of change of ice mass becomes:

$$\frac{dq_I}{dt}_{\text{dep}} = \rho_{\text{dep}}[V_t(t+\Delta t) - V_t(t)]$$

To compute the right hand side of this equation, consider the identity evolution for time $t+\Delta t$:

$$\bar{\rho}_i(t+\Delta t)V_t(t+\Delta t) - \bar{\rho}_i(t)V_t(t) = \rho_{\text{dep}}[V_t(t+\Delta t) - V_t(t)]$$

This can be rearranged:

$$\bar{\rho}_i(t+\Delta t) = \rho_{\text{dep}}[1 - V_t(t)/V_t(t+\Delta t)] + \bar{\rho}_i(t)V_t(t)/V_t(t+\Delta t)]$$

Let the change in volume $V_t(t)/V_t(t+\Delta t) = w$ then:

$$\bar{\rho}_i(t+\Delta t) = \rho_{\text{dep}}[1-w] + \bar{\rho}_i(t)w]$$

With an expression for ρ_i defined, all that is required to complete the equation set is an expression of how volume changes with time during deposition. To obtain this, differentiate Equation 12.37 with respect to t:

$$\frac{dq_i}{dt} = 4\pi\rho_{\text{dep}}N_i\frac{\Gamma(\alpha+\delta_*+2)}{\Gamma(\alpha)}r_n^2\frac{dr_n}{dt}$$

This can be set equal to the derivation of mass mixing ratio time change in Equation 12.35 and integrated, keeping temperature, pressure, equivalent spherical shape factor $f_s(r_n)$, and ice supersaturation constant over a time step:

$$\frac{N_I}{\rho_a}4\pi\bar{f}_s(r_n)r_nG_is_i = 4\pi\rho_{\text{dep}}N_i\frac{\Gamma(\alpha+\delta_*+2)}{\Gamma(\alpha)}r_n^2\frac{\mathrm{d}r_n}{\mathrm{d}t}$$

Thus:

$$\begin{gathered}\frac{\bar{f}_s(r_n)G_is_i}{\rho_{\text{dep}}\rho_a}\frac{\Gamma(\alpha)}{\Gamma(\alpha+\delta_*+2)}\int_t^{t+\Delta t}\mathrm{d}t = \int_t^{t+\Delta t}r_n\,\mathrm{d}r_n\\ \frac{2\bar{f}_s(r_n)G_is_i}{\rho_{\text{dep}}\rho_a}\frac{\Gamma(\alpha)}{\Gamma(\alpha+\delta_*+2)}[t]_t^{t+\Delta t} = [r_n^2]_t^{t+\Delta t}\end{gathered}$$

$$\frac{2\bar{f}_s(r_n)G_i s_i}{\rho_{\text{dep}}\rho_a}\frac{\Gamma(\alpha)}{\Gamma(\alpha+\delta_*+2)}[t+\Delta t-t] = [r_n(t+\Delta t)^2 - r_n(t)^2]$$

and rearranging:

$$r_n(t+\Delta t) = \left[\frac{2\bar{f}_s(r_n)G_i s_i}{\rho_{\text{dep}}\rho_a}\frac{\Gamma(\alpha)}{\Gamma(\alpha+\delta_*+2)}\Delta t + r_n(t)^2\right]^{\frac{1}{2}} \tag{12.38}$$

So the progression of r_{nf} after deposition is known relative to the initial radius r_{ni}. We can now determine the change in ice mass due to deposition by finite difference approximation of the differential equation in q:

$$\frac{dq}{dt} \approx \frac{\Delta q}{\Delta t} \approx \frac{q(t_2)-q(t_1)}{t_2-t_1} \tag{12.39}$$

Solving Equation 12.37 for q at times t and Δt and subtracting the difference:

$$\begin{aligned} q(t) &= \rho_i(t)V(t) \\ &= n_i\rho_a\frac{4\pi}{3}\frac{\Gamma(\alpha+\delta_*+2)}{\Gamma(\alpha)}\rho_i r_{\text{ni}}^3 \end{aligned}$$

$$\begin{aligned} q(t+\Delta t) &= \rho_i(t+\Delta t)V(t+\Delta t) \\ &= \left(\rho_{\text{dep}}[1-w] + \bar{\rho}_i(t)w]\right)\frac{4\pi}{3}N_i\frac{\Gamma(\alpha+\delta_*+2)}{\Gamma(\alpha)}r_{\text{nf}}^3 \\ &= n_i\rho_a\frac{4\pi}{3}\frac{\Gamma(\alpha+\delta_*+2)}{\Gamma(\alpha)}\left[\rho_{\text{dep}}[1-\frac{r_{\text{ni}}}{r_{\text{nf}}}] + \bar{\rho}_i\frac{r_{\text{ni}}}{r_{\text{nf}}}]\right]r_{\text{nf}}^3 \end{aligned}$$

where we have used $n_i\rho_a = N_i$ and recognised that $w = V_t(t)/V_t(t+\Delta t) \equiv r_{\text{ni}}/r_{\text{nf}}$.

In the ISHMAEL code, the deposition is proportional to the difference between `iwci` and `iwcf`, which correspond directly to $q(t)$ and $q(t+\Delta t)$, respectively. Their difference is given by:

$$\texttt{prd} = \frac{\texttt{iwcf} - \texttt{iwci}}{\rho_a\Delta t}$$

12.5 Capacitance Function

As shown in the previous section, deposition in ISHMAEL materialises in a change to the equivalent spherical radius r defined in Equation 12.38. Importantly, r is a function of several variables, including the diffusion G, supersaturation s_i and the density of deposition ρ_{dep}, In ISHMAEL G and s_i are combined in `afn`. An examination of these variables finds a similar if not identical role as in Morrison, so the main difference in deposition tendency lies with the formulation of distribution averaged capacitance.

Since the a and c axes are related by Equation 12.20 the capacitance can be written in terms of one axis only, a_i, assuming $C \propto a$:

$$C(a, \varphi) = a_0^{1-\delta_*} a_i^{\delta_*} f_s(\varphi), \tag{12.40}$$

Where $f_s(\varphi)$ is the shape factor, a dimensionless quality that relates the axis length to the capacitance as a function of the aspect ratio. This is somewhat similar to the capacitance-diameter relation in Morrison, except that the shape factor incorporates the aspect ratio, enabling the capacitance to vary for otherwise identical a_i-axis lengths.

The shape factor function f_s must be defined for various aspect ratios of a spheroid. The analytical form of the shape factor for spheroids is not integrable but can be simplified using a power law as in Harrington et al. (2013):

$$f_s(\varphi) = a_1 \varphi^{b_1} + a_2 \varphi^{b_2} \tag{12.41}$$

Where:

	a_1	a_2	b_1	b_2
Oblate	0.6369427	0.363057	0	0.95
Prolate	0.5714285	0.428571	-1	-0.18

Table 12.4. Power law parameters for oblate and prolate crystals adapted from Harrington et al. (2013).

The form matches closely the shape factor, found as the ratio of surface areas for equivalent volume spheres. Substituting the definition of aspect ratio $\varphi(a) = \alpha_* a^{\delta_* - 1}$ the capacitance factor is derived for differing axial lengths and aspect ratios:

$$C(a) = c_1 a^{d_1} + c_2 a^{d_2}, \tag{12.42}$$

with coefficients:

$$\begin{aligned} c_1 &= a_1 \alpha_{\text{cap}} \alpha_*^{b_1} & \qquad c_2 &= a_2 \alpha_{\text{cap}} \alpha_*^{b_2} \\ d_1 &= b_1(\delta_* - 1) + \delta_{\text{cap}} & \qquad d_2 &= b_2(\delta_* - 1) + \delta_{\text{cap}} \end{aligned}$$

In this equation set $\alpha_* = a_0^{1-\delta_*}$. Oblates have $\alpha_{\text{cap}} = 1$ and $\delta_{\text{cap}} = 1$. Whereas prolates have $\alpha_{\text{cap}} = \alpha_*$ and $\delta_{cap} = \delta_*$ for prolates. The capacitance is formed using the above equation, and a distribution averaged $\bar{f}_s(a)$ is derived by division of $C(a)$ by r. Examining the relationship between `PRD` and capacitance:

$$\begin{aligned} \texttt{PRD} &\propto [\texttt{IWCF - IWCI}] \\ &\propto \left[\texttt{IWCF}\left(\left(r_{\text{nf}}\left(f_s^{\frac{1}{2}}\right)\right)^3\right) - \texttt{IWCI}\right] \end{aligned}$$

Thus the total deposition in ISHMAEL `PRD` is a function of $\bar{f}_s(a)^{3/2}$. This can be compared directly to the Morrison formulation:

$$\begin{aligned} \texttt{PRD} &\propto [\tau^{-1}] \\ &\propto [C_0] \end{aligned}$$

We note that deposition mass in Morrison is directly proportional to the shape factor, whereas in ISHMAEL the deposition mass is a more complex function of the shape factor to a comparatively higher power.

With the particle size distribution, its evolution during deposition, and the implementation of capacitance known, an investigation can be conducted to understand the influence of the capacitance upon the deposition rate over time within a box model.

12.6 Capacitance Testing

To begin, the capacitance function can be compared over a range of possible size distributions. As the size distributions are a function of n and q the range of these values must be chosen for testing. Given the capacitance is a function of the characteristic radius we shall also calculate this based on n and q. Finally we shall plot over a range of δ_*.

To limit the plotting options, it is convenient to choose ratios of n and q which allow the result to be combined as in Figure 12.9. We can consider the average crystal mass $\bar{m}$ to be

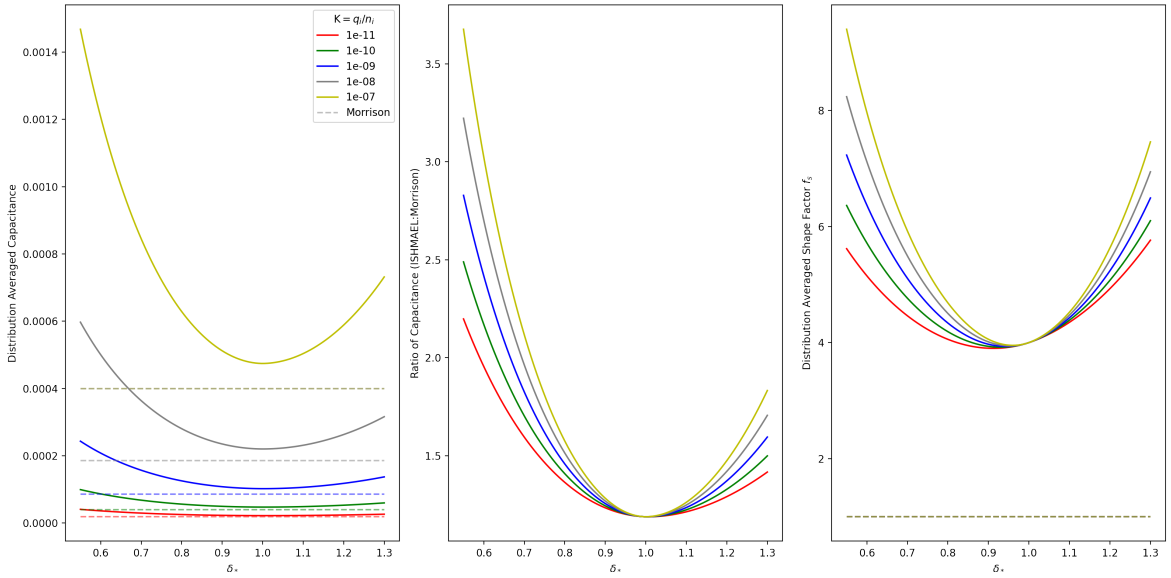

Figure 12.11. Distribution averaged capacitance (left), ratio of capacitance between ISHMAEL and Morrison (middle) and value of the distribution averaged shape factor (right) versus inherent growth ratio δ_* for varying average crystal mass K (kg) (see Figure legend)

the ratio $\frac{q_i}{n_i}$ to gain a physical understanding of this ratio. Consider also that the minimum limit for the mass mixing ratio `QSMALL` in ISHMAEL is 1×10^{-12} kg kg^{-1} and in Morrison is 1×10^{-14} kg kg^{-1}.

Given that the average crystal radius already differs between schemes for otherwise identical mass and particle number we shall fix the characteristic radius a_n which is an argument to the capacitance. Instead, a_n is recalculated based on the ratio of n and q via Equation 12.25. Note that the average density of crystals will be different in ISHMAEL than Morrison but that this can not be readily avoided, and is to be expected when comparing fixed and non-fixed density schemes. Additionally, the density plays no role in the capacitance calculation, which is purely geometric.

Finally, note that in Morrison the ratios depicted may not be applicable to solely ice crystals, as the autoconversion threshold `DCS` may be breached causing deposition to be added to the snow category rather than cloud ice. However, this is of no consequence as the dimensionless capacitance factor for all hydrometeors is set to unity and thus the capacitance can be compared regardless of hydrometeor.

Figure 12.11 compares the distribution averaged capacitance in both schemes. Panel (a) plots the capacitance equation (Equation 12.42) across a range of δ_* values between 0.55 and 1.3, which form the artificial limits in the ISHMAEL code and are a function of aspect ratio. Additionally, the capacitance is shown for multiple ratios of q_i to n_i, which indicates average crystal mass. The ratios of crystal mass and number shown here are representative of typical cloud ice mass and number ratios. For example, typical cloud masses of 0.1 mg kg^{-1} and 0.001 mg kg^{-1} and 0.1 to 1 per litre give an upper ratio range of $1 \times 10^{-7}/100 = 1 \times 10^{-5}$ kg and lower range of $1 \times 10^{-9}/1000 = 1 \times 10^{-12}$ kg. Also plotted in Panel (a) for comparison is the Morrison equivalent capacitance that is calculated using the relation $C = C_0 D$ where C_0 is the dimensionless capacitance equal to one and D is the distribution averaged diameter $1/\lambda_I$ which is derived for the same mass and number concentration but as outlined in section 12.3.5 may vary from the average diameter produced by ISHMAEL. It is also notable that ice density is non-constant in ISHMAEL and has been adjusted in line with the code-routines to ensure consistency. Panel (b) indicates the ratio of the ISHMAEL capacitance to that found in Morrison.

Panel (c) plots the distribution averaged shape factor f_s that relates the capacitance value to the ice crystal geometry. In Morrison $f_s = 1$, but in ISHMAEL $f_s = C/r$ where r is the spherical equivalent radius, which is calculated per mass and number ratio. Recall that in ISHMAEL `PRD` is a function of $\bar{f}_s(a)^{3/2}$ and in Morrison `PRD` is directly proportional to C_0, so f_s is a direct factor in the calculation of mass transferred to the crystal via deposition and is the primary difference between the formulations of deposition in each scheme.

From panel (a) we note that, for a given average crystal mass, the capacitance provided by ISHMAEL is consistently greater than that in Morrison, with the absolute difference becoming greater for the most severe aspect ratios (i.e. $\delta_* << 1$ or $\delta_* >> 1$), and amongst those severe aspect ratios, the greatest difference is provided by oblates. For increasingly larger average crystal mass (i.e. larger K) the magnitude of this difference increases disproportionately towards severe aspect ratios. This implies that environments with higher mass crystals will have greater deposition tendency by virtue of their increased capacitance and that if such environments were to contain crystals with severe aspect ratios, an even starker gulf in capacitance would occur between schemes. This difference is illustrated in panel (b) which shows the ratio of the ISHMAEL capacitance to that calculated in Morrison for several K. For all examples of K, the capacitance in ISHMAEL for moderate aspect ratios $0.8 < \delta_* < 1.2$ is at or below 1.5 times that produced in Morrison, but for the largest K the capacitance of prolate ice can reach double that of Morrison. The most oblate ices show an even greater factor of discrepancy, with the lowest K having capacitance exceeding twice that of Morrison, all the way up to the highest K which exceeds 3.5 times the Morrison calculated value.

Panel (c) is most pertinent to the discussion of deposition as it shows the shape factor which is a direct term in the calculation of deposition mass tendency. The shape factor in Morrison is fixed at one and thus plays no role in the calculation of deposition for Morrison. However, in ISHMAEL the shape factor provides an increase to the deposition mass tendency `PRD`. It is clear that when $\delta_* = 1$ the shape factor must equal four as the capacitance relation becomes:

$$C(a) = a_1 a_n \frac{\Gamma(5)}{\Gamma(4)} + a_2 a_n \frac{\Gamma(5)}{\Gamma(4)} \qquad\qquad = 4a_n(a_1 + a_2) = 4a_n = \bar{a}$$

and the spherical equivalent radius $r_n = a_n$, thus $f_s = C(a)/r_n = 4$. Thus the minimum shape factor in ISHMAEL is four and hence deposition will have a four fold equivalent increase in comparison to Morrison for equivalent mass and number mixing ratio. However, the shape factor can increase for more prolate crystals and even more so for the most oblate crystals. This factor is, as with the capacitance, increasingly severe for greater average crystal mass K, reaching almost a factor of 10 over Morrison for the most oblate and heavy crystals.

These results indicate that deposition growth in ISHMAEL is likely to be greater than in Morrison for an equivalent mass and number of crystals. Larger and larger shape factors are likely to be exacerbated by the deposition process, which tends to produce less spherical ices and more extreme aspect ratios, and thus there is a high likelihood of rapid depositional growth from a cycle of deposition which causes greater oblateness which increases deposition.

It is important to stress the non-linearity of the capacitance function. During deposition the crystal shape evolves and so the shape factor will change too. Therefore to understand crystal growth in this non-linear regime a box model is employed that will examine depositional growth and change in shape factor simultaneously.

12.7 Box-Model Testing

In this section the scheme formulations outlined previously are used to determine the mass deposition tendency and other features of the deposition during idealised scenarios. This will allow for the role played by the changing capacitance and shape-factor to be understood in a growth environment. For this we employ a simple box model that isolates the deposition process.

12.7.1 Initialisation of Environmental Variables

The initial state of the box model is set up to represent an initial cloud scenario that is derived from the model simulations. The box model thermodynamic inputs are temperature T and Pressure, P, and the microphysics inputs are ice-mass mixing ratio q_i, ice number mixing ratio n_i and vapour mixing ratio q_v. The crystal population is controlled by the selection of mass and number mixing ratio. By using mixing ratios the results of the box model can be extrapolated to larger masses of air without loss of generality and as such the box may be thought of as encapsulating a kilogram of air, containing n_i crystals weighing q_i kg. For simplification and consistency with each deposition formulation, the ratio K of the mass mixing ratio to number mixing ratio is used. Increasing K is indicative of increasingly large average crystal mass. These variables were sampled across simulations of cases 1 and 2 to determine their respective ranges and the relationships between these variables to produce representative ranges over which to compute the box model.

Figure 12.12 shows the frequency of the ratio $K = q_i/n_i$ for both microphysics schemes and both simulated cases. As we are concerned with the deposition process to cloud ice only, the mass and number mixing ratios of each scheme were masked to only cells in which the ice was characteristic of cloud ice and where deposition was non-zero.

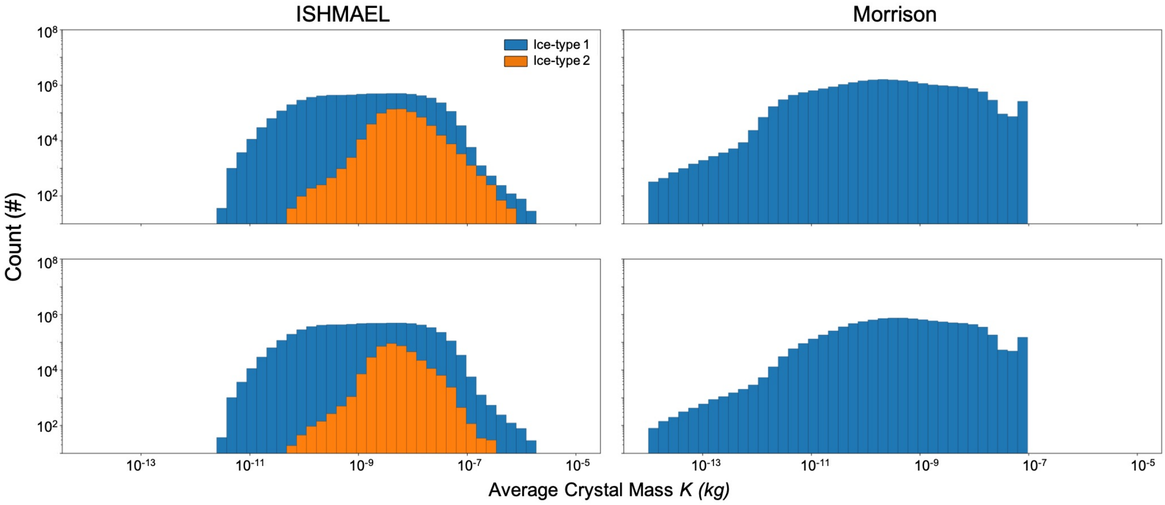

Figure 12.12. Simulated distribution of average crystal mass K in the ISHMAEL (left) and Morrison (right) microphysics schemes across cases one (top) and two (bottom)

The distributions of the ratio K are distinct between schemes, Morrison produces a larger spread of K that spans 1×10^{-14} and 1×10^{-7} kg whereas ISHMAEL ices are typically larger in mass, spanning between 1×10^{-12} and 1×10^{-6} kg for ice-type 1 (planar nucleated) and 1×10^{-10} and 1×10^{-6} kg for ice-type 2 (columnar nucleated). However the vast majority of crystals in both schemes occupy a range somewhat between 1×10^{-11} and 1×10^{-8} kg. One can assume that crystals at the larger end of the spectrum have already grown considerably by deposition, and thus it makes sense to focus more so on the smaller crystals for the initialisation. However, the smallest crystals in Morrison do not typically exist in ISHMAEL, and thus it makes sense to exclude this very small range for the purposes of comparison. An appropriate and comparable range in K is therefore 1×10^{-11} and 1×10^{-8}.

Next the likely temperature that crystals experience within each K range is required. Figure 12.13 is a scatter density plot of the ratio K versus temperature, where the local pixel density of data points has been highlighted.

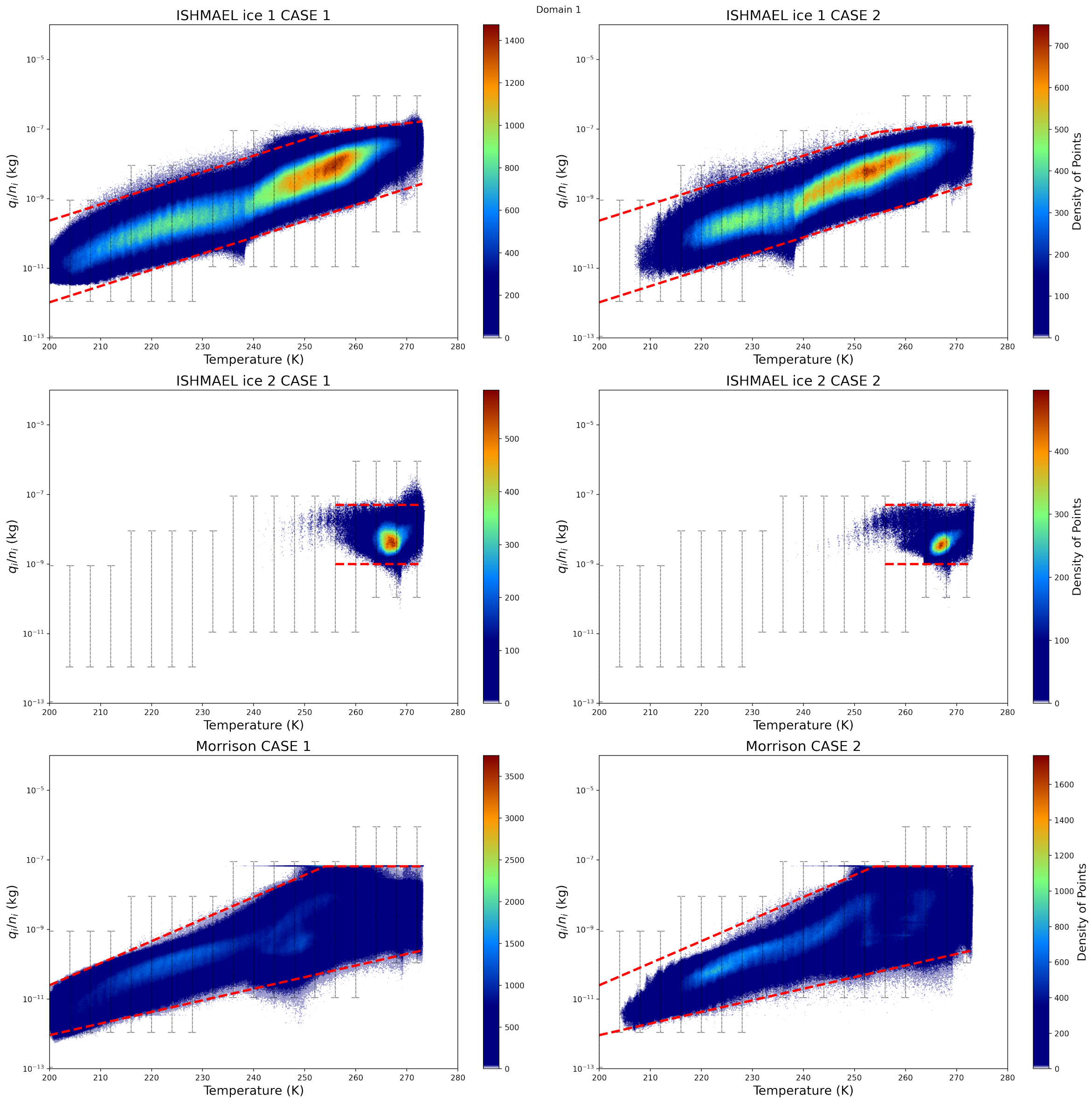

Figure 12.13. Scatter density plot of average crystal mass value K versus the ambient temperature in the ISHMAEL (top, middle) and Morrison (bottom) microphysics schemes. Density of points is indicated by color mapping, and is determined by the local pixel density.

ISHMAEL ice-type 1 (planar nucleated) and Morrison cloud ice show a similar, approximately linear relationship between the ratio K and ambient temperature. Colour grading indicates that the vast majority of data points occur at $K = 1 \times 10^{-9}$ kg and in the temperature range 250–260 K for ISHMAEL ice-type 1, though by comparison Morrison cloud ice has a more evenly spread distribution of cloud ice mass. Lines of best fit are plotted for the upper and lower K ranges of each scheme and are shown in red. The equations of these lines are:

ISHMAEL ice-type 1:

$$9e - 12 \times 10^{(2.8/60\times(T-220))} < K < 2e - 9 \times 10^{(2.8/60*(T-220))}$$

and for Morrison:

$$2 \times 10^{\frac{2}{60}(T-240)-11} < K < 2 \times 10^{\frac{3.8}{60}(T-230)-9}$$

Rearranging these to obtain temperature for a given K we have upper and lower bounds for ISHMAEL:

$$\frac{60}{2.8}\left(\log_{10}\left(\frac{K}{2}\right)+9\right)+220 < T < \frac{60}{2.8}\left(\log_{10}\left(\frac{K}{9}\right)+12\right)+220 \tag{12.43}$$

and for Morrison:

$$30\left(\log_{10}\left(\frac{K}{2}\right)+11\right)+240 < T < \frac{60}{3.8}\left(\log_{10}\left(\frac{K}{2}\right)+9\right)+230 \tag{12.44}$$

We may substitute values in the K range of interest (1×10^{-11}–1×10^{-8} kg) to these equations to determine the likely temperature bounds.

Finally, the likely pressure and vapour content for a given K and T is required. Figure 12.14 plots the pressure-temperature relation for K in the range of interest. The distribution is coloured in accordance with the vapour mass mixing ratio q_v.

As expected, the pressure-temperature relation is approximately exponential and consistent amongst both schemes for all variations in K. However, the simulated spread is considerable enough to require simplification. At present the dimensionality of the box model spans K and T so to avoid adding further dimensionality to the box model parameters we seek a simple relationship that approximately relates T and P. Using least squares curve-fitting we obtain:

$$P \approx 51.43e^{0.028147\mathrm{T}}, \tag{12.45}$$

which is accurate enough for the purpose of setting the environment. Finally, it is apparent that vapour content is strongly related to temperature only, therefore we can approximate the vapour content easily:

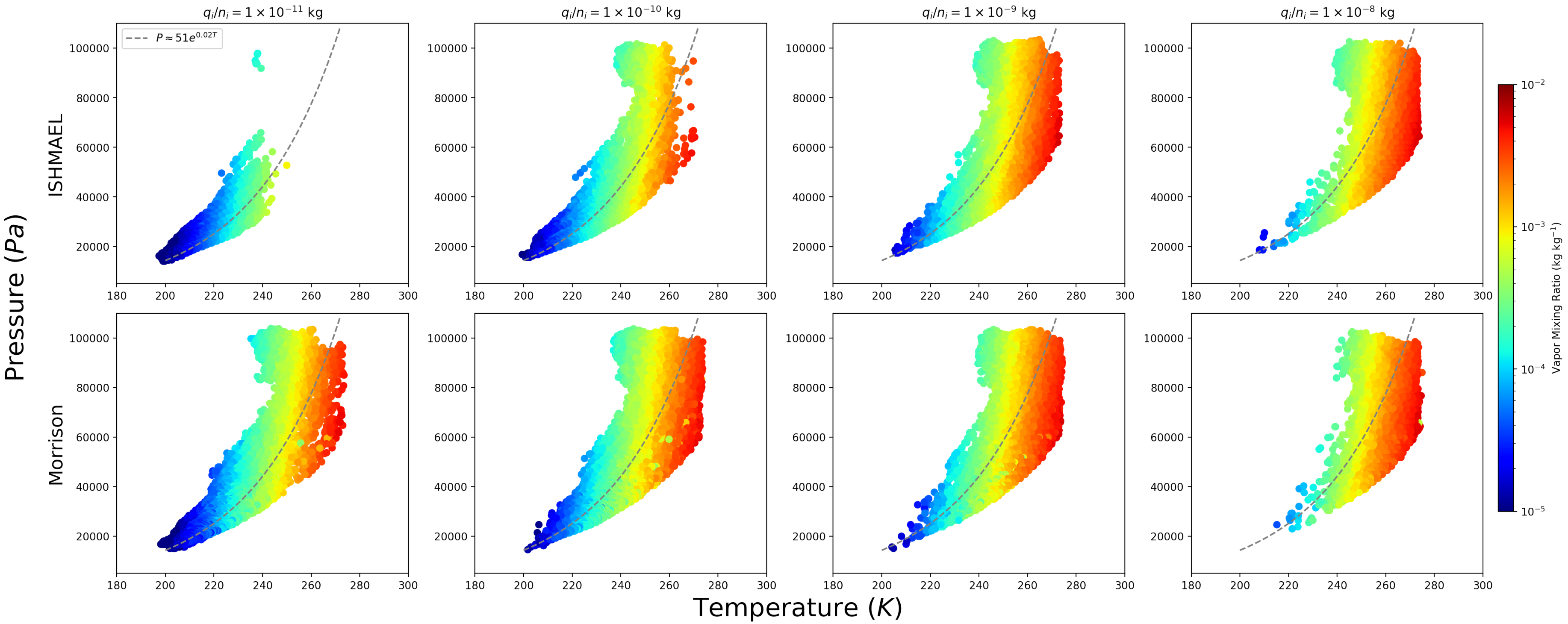

Figure 12.14. Scatter plot of pressure versus temperature in the ISHMAEL (top) and Morrison (bottom) microphysics schemes. Each panel (left to right) indicates a new average crystal mass (titled). Data point colouring is in accordance with the vapour mass mixing ratio.

$$Q_v = \begin{cases} 1 \times 10^{-5}\text{–}1 \times 10^{-4}\ \text{kg kg}^{-1}, & \text{if } T \leq 220\ \text{K} \\ 1 \times 10^{-4}\text{–}1 \times 10^{-3}\ \text{kg kg}^{-1}, & \text{if } 220 \geq T \leq 250\ \text{K} \\ 1 \times 10^{-3}\text{–}1 \times 10^{-2}\ \text{kg kg}^{-1}, & \text{if } T \geq 250\ \text{K} \end{cases}$$

We can assume that the relationship increases linearly in log-spaced q_v i.e. $\log_{10}(q_v) = mx + c$. An equation that satisfies the above conditions is:

$$q_v = 10^{\frac{T}{30} - 11.\dot{3}},$$

which provides a useful incorporation of vapour content to the box model.

In total we have specified the input variables $q_i/n_i, q_v, T$ and P for examination. Each K, and therein each T will be simulated in the box model with vapour mass and pressure specified as a function of T. We can be confident that the scenarios are representative of environments produced by each scheme for both cases.

$K = q_i/n_i$ (kg)	T (K)	P (Pa)	q_v (kg kg^{-1})
1×10^{-11}	200–230	$P \approx 51.43e^{0.028147T}$	$q_v = 10^{\frac{T}{30} - 11\dot{3}}$
1×10^{-10}	205–265		
1×10^{-9}	215–273		
1×10^{-8}	240–273		

Table 12.5. Variable values and ranges for a capacitance-testing box-model. Average crystal mass K (kg), Ambient Temperature T (K), Ambient pressure P (Pa), and vapour mass mixing ratio q_v (kg kg^{-1}).

12.7.2 Initialisation of Ice Variables

To simulate the growth of ice by deposition for the specified K ratios and temperatures without any additional complication from external processes, all microphysical processes besides deposition are excluded from the simulation including negative growth processes such as melting and sublimation. This is a suitable choice as we are concerned with the growth of ice as a consequence of its capacitance in a saturated environment only and any further compounding processes will only serve to complicate the role of capacitance. However, we note that this environment is not representative of reality or indeed that of the schemes described and so the results must be treated in isolation.

The box model is initialised with a ratio of K and an appropriate ambient temperature from Table 12.5 with which the initial pressure and vapour content can be calculated by approximation using the aforementioned equations. This set of initial conditions is a reasonable example scenario taken directly from the simulated cases and whilst it does not cater to all possible combinations, the set is assumed to be representative of each scheme. The K ratio is calculated from initial values of q_i and n_i in both schemes. The distributions of mass and number concentration for each scheme are shown in Figure12.15. Morrison has a considerably larger spread in possible values than ISHMAEL, but for a fair comparison we focus on the overlapping area of the distribution in the range q_i between 1×10^{-7}–1×10^{-4} (kg kg^{-1}) and n_i between 1×10^{2}–1×10^{6} (kg^{-1}). The K ratios of interest can be constructed from these ranges by choosing central points in the distribution, and are shown with coloured markers. This choice enables q_i, n_i and their ratio K to be representative of each simulation.

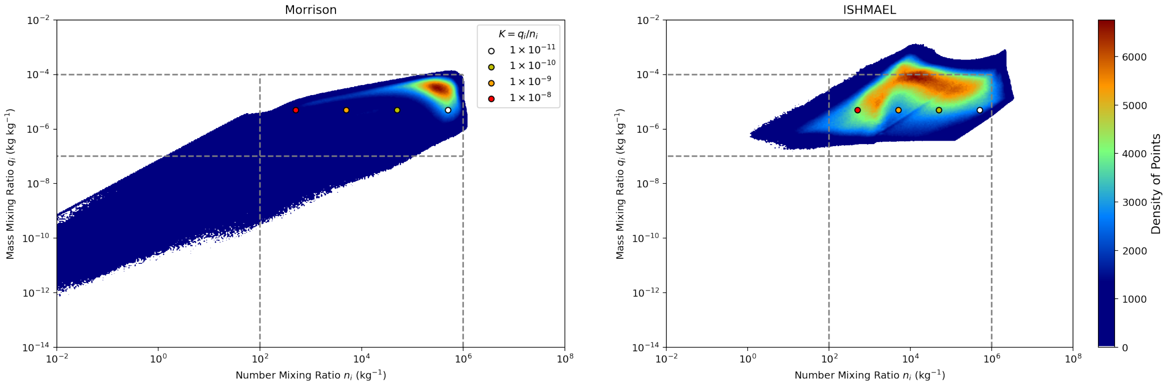

Figure 12.15. Scatter density plot of mass mixing ratio (kg kg^{-1}) for ice in Morrison (left) and ISHMAEL (right). Points chosen as Representative of the microphysics scheme are shown in coloured dots (see Figure legend)

Finally, in addition to the number and mass mixing ratios, the PSD in ISHMAEL also depends on the characteristic particle radius a_n. This radius can be calculated directly from q_i and n_i but requires the user to choose an initial δ_*. In accordance with the initialisation of the ISHMAEL scheme, and to produce parity with the Morrison scheme, δ_* is initialised with value 1, indicating spherical particles.

12.7.3 Progression of Variables per Time Step

The simplest thermodynamic choice is to employ a fixed thermodynamic environment such that pressure, air density and temperature remain constant for the duration of the simulation. This is akin to a non-closed box, whose thermodynamic qualities are governed by the surrounding air mass. Besides reducing complexity, this is also a useful choice as it removes the effect of thermodynamic changes upon the deposition process and allows the ice to grow as a consequence of only saturation, (and by proxy the capacitance). In this scenario, the values of P and T remain at their initial values during the simulation, whereas hydrometeor and vapour ratios are allowed to evolve via the tendency relations of each scheme. Latent heating from deposition is consequently negated and latent heating from secondary mechanisms such as riming are also set to zero. Comparative testing with latent heating turned on shows that the temperature corrections as a consequence of latent heating are near negligible, and certainly ineffectual upon deposition rate. In this scenario, we employ a 15 minute simulation time, which is sufficient to demonstrate the differences in deposition tendency between each scheme. Longer periods are found to converge as each scheme tends towards saturation equilibrium.

Microphysical variables are free to evolve in the box in accordance with the deposition formulation of their respective scheme. For example, the parameter q_i and, in ISHMAEL, a_n will change as particle mass increases during deposition and consequently so will the size distribution parameters. For the ISHMAEL scheme, the source code `varcheck` routine, which checks distribution parameters for consistency, is adapted and employed. The number mixing ratio n_i is fixed during deposition, as the deposition process does not affect particle number, and as sublimation is turned off. However, in Morrison n_i can evolve via the autoconversion process of cloud ice to snow.

Morrison's autoconversion process takes place when the cloud ice distribution begins to exceed a designated dimensional cut-off limit, this occurs routinely in Morrison as the deposition process increases the average crystal dimension. Consequently, the snow hydrometeor category which is initialised with $q_s = 0$, $n_s = 0$ can increase by conversion of the ice mass, and in accordance, the ice mass and number may decrease to accommodate this change. This feature should not affect the comparison to ISHMAEL whose single category can include snow, but does require the simultaneous inclusion of two deposition frameworks in Morrison for ice and snow respectively.

This framework can be used to determine the influence of capacitance on a growing cloud ice distribution. The variables output by the box model for the ISHMAEL and Morrison microphysics schemes are shown in Table 12.6 and Table 12.7, respectively.

12.8 Box-Model Results

The idealised box model was used to conduct a complete simulation run with total simulation time of 60 minutes and a 2 second time step of integration. The ice precipitation field was initialised in a distribution of fixed mass mixing ratio q_i (kg kg^{-1}) and number mixing ratio n_i (kg^{-1}). The ambient environment was initialised with a temperature value T (K) that could be used to feed parameterisations of the pressure P (Pa) and vapour mixing ratio q_v (kg kg^{-1}) calculated earlier and shown in Table 12.5. The box model is capable of simulating three idealised thermodynamic environments. Option one, a fixed T, P, and q_v run in which all initialisation conditions are held constant. Option two, a fixed T, P environment

Quantity	Unit and Notes
Ice mass mixing ratio	kg kg^{-1}
Ice number mixing ratio	kg^{-1}
Pressure	hPa
Temperature	K
Vapour mixing ratio	kg kg^{-1}
Deposition mass tendency	kg kg^{-1} s^{-1}
Air density	kg m^{-3}
Inherent Growth Ratio δ_*	
Characteristic a-axis size a_{ni}	m
Characteristic c-axis size c_{ni}	m
Characteristic radial size r_{ni}	m
ice density ρ	kg m^{-3}
Ice a^2c mixing ratio a_{i}	m^3 kg^{-1}
Ice $c^a c$ mixing ratio c_{i}	m^3 kg^{-1}
Distribution-weighted capacitance	m
Shape factor f_s	see Equation 12.40
Mean ice particle radius r_{av}	m
Ice aspect ratio ϕ	
Saturation pressure over ice	hPa
Deposition density ρ_{dep}	kg m^{-3}

Table 12.6. List of simulated qualities output by the idealised box model for the ISHMAEL microphysics scheme.

Quantity	Description
Ice mass mixing ratio	kg kg^{-1}
Ice number mixing ratio	kg^{-1}
Snow mass mixing ratio	kg kg^{-1}
Snow number mixing ratio	kg^{-1}
Graupel mass mixing ratio	kg kg^{-1}
Graupel number mixing ratio	kg^{-1}
Vapour mass mixing ratio	kg kg^{-1}
Pressure	hPa
Temperature	K
Deposition mass tendency to ice	kg kg^{-1} s^{-1}
Deposition mass tendency to snow	kg kg^{-1} s^{-1}
Deposition mass tendency to graupel	kg kg^{-1} s^{-1}
Air density	kg m^{-3}
Mean Ice Particle Radius	m
Mean Snow Particle Radius	m
Mean Graupel Particle Radius	m
Distribution Weighted Capacitance	Equivalent to mean diameter (m)
Saturation pressure over ice	hPa
Inverse phase relaxation time for snow ϵ_s	
Inverse phase relaxation time for ice ϵ_i	
Correction to deposition due to latent heating ABI	

Table 12.7. List of simulated qualities output by the idealised box model for the Morrison microphysics scheme.

with variable q_v, which allows deposition to be affected by vapour concentrations. Option three, an environment in which T, P, and q_v can all evolve in accordance with latent heating and vapour uptake by ice. In this case, we examine the effect of capacitance using option two. The initialisation conditions for this model run are given in Table 12.8.

Average ice mass q_i [kg]	Ice Number Mixing Ratio [kg^{-1}]	Ice Mass Mixing Ratio [kg kg^{-1}]	Temperatures [k]
1×10^{-11}	1×10^{6}	1×10^{-5}	[205, 215, 225, 235]
1×10^{-10}	1×10^{5}	1×10^{-5}	[215, 225, 235, 245 255, 265]
1×10^{-9}	1×10^{4}	1×10^{-5}	[225, 235, 245, 255, 265, 270]
1×10^{-8}	1×10^{3}	1×10^{-5}	[245, 255, 265, 270]

Table 12.8. Initial conditions for the box model as tested in this chapter.

Here we will not discuss all variables output by the model (see Tables 12.6 and 12.7) but we will examine a subset that is relevant to the argument of capacitance and the broader instigation, which seeks to determine the origin of elevated cloud ice mass mixing ratios in the ISHMAEL model. Figure 12.16 shows the progression of four (columns) simulated physical variables throughout the 60 minute model run. Each variable is plotted for a different value of initial temperature (shown in Figure legend), and the average ice mass is held constant at 1×10^{-9} kg (see Table 12.8). Columns one and two show the constant temperature and pressure fields that are used in this simulation (i.e. option two above). Columns three and four show the vapour mass mixing ratio (kg kg^{-1}) and frozen mass mixing ratio (kg kg^{-1}), where *frozen* refers to all ice in the ISHMAEL scheme's single free-ice category, and refers to the combined snow and ice categories in the Morrison scheme. Option two allows the vapour mass to vary during deposition, and it is evident that this results in a direct transfer of mass to the frozen precipitation. Note that the initial amount of vapour mass is dependent on the temperature and pressure. It is apparent that the Morrison scheme has a comparatively greater rate of mass deposition that is particularly severe at warmer temperatures. However, at cooler temperatures the deposition rate appears very similar between both schemes.

Further analysis of the mass mixing ratio across multiple initial average ice masses significantly complicates the relationship between mean ice mass and cloud-ice growth. Figure 12.17 compares the ratio of mass mixing ratio predicted by ISHMAEL to the mass mixing ratio predicted by Morrison over four values of the initial average ice mass (columns 1–4). Therefore, values of this ratio that are greater than zero (shown by dashed grey line) imply ISHMAEL has a larger ice mass mixing ratio and vice-versa. This relationship is shown for several values of temperature (shaded, see Figure legend).

Unlike Figure 12.16 the mass mixing ratios in Figure 12.17 show very large fluctuations in the relative ice mass field with time and it is difficult to determine a consistent relationship. For example, when average ice mass is small (columns 1–2) then at most temperatures the Morrison scheme accumulates much more ice mass than ISHMAEL within the first 10–20 minutes. However, this process appears short lived as the relative mass mixing ratios return

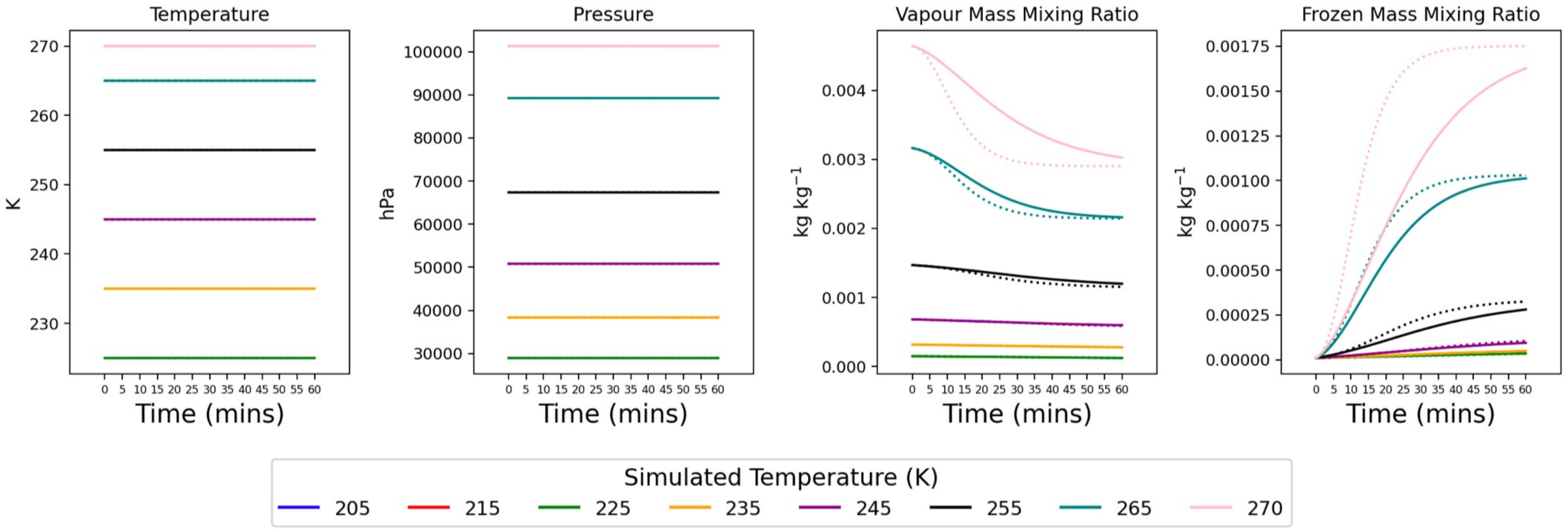

Figure 12.16. Time series of Temperature (K), Pressure (hPa), Vapour mass mixing ratio (kg kg^{-1} and frozen mass mixing ratio in an idealised deposition box model (columns 1–4, respectively). Results are obtained for multiple initial temperatures (shaded, see Figure legend). In this analysis, box model thermodynamic option two was chosen (pressure and temperature held constant). Average ice mass was fixed at 1×10^{-9} kg.

to parity by approximately 20–30 minutes, so it is not evident that on long time scales this rapid initial mass transfer by Morrison would be significant. In comparison, when the initial average ice mass is large (columns 3–4), the difference in mass uptake between scheme remains for much longer. In most warm temperature cases, the Morrison scheme takes up more mass than ISHMAEL, yet in colder environments it is ISHMAEL that becomes dominant. These features imply that in warm environments Morrison will have more efficient deposition, in cool environment ISHMAEL will become more efficient, and when average crystal mass is small the difference between schemes is likely negligible. We note that average crystal masses in the range shown are likely to occur in much cooler temperatures at high elevation, so it is likely that the ISHMAEL scheme may benefit from increased mass uptake.

It is prudent to examine the influence of capacitance in the production of these varied relationships. The idealised box model was run using the ISHMAEL deposition framework for two cases; variable (predicted) capacitance, and a fixed capacitance formulation. The fixed capacitance followed that employed by Morrison, in which the dimensionless capacitance is equal to one and the capacitance function is proportional to the particle radius only. Figure 12.18 shows the ratio of the ice mass mixing ratio when predicted capacitance is turned on versus when it is held constant. Thus, when the ratio exceeds one (shown in grey dashed line) the ice mass mixing ratio has increased due to the capacitance prediction, and when the ratio is below one, the constant the ice mass mixing ratio has increased under the constant capacitance framework.

Figure 12.18 indicates that across average crystal sizes and temperatures, the absolute difference was almost always negative and therefore the predicted capacitance actually reduced the ice mass growth rate in ISHMAEL compared to the constant capacitance relation. As in Figure 12.17, this effect appeared to be more significant when initial ice masses were larger, whereas for smaller ices, the difference reduced to nil in 20–40 minutes. The constant capacitance relation was found to enhance the mass uptake during deposition more effectively at warmer temperatures. However, an interesting and opposing case was apparent when the temperature was 265 K ($\sim -8^{\circ}$C). At this temperature, the parameterisation of capacitance enabled a substantial increase in ice deposition. Examination of the inherent growth ratio (IGR) in Figure 12.19 shows that this effect likely originated from the large peak in IGR at 265 K that tends the ice aspect ratio towards needles. It is notable, for example, that the complete IGR used in the ISHMAEL code (Figure 12.19 solid) is only a partial representation of the full function (dashed) which would provide similar positive changes in the aspect ratio and likely increase the deposition rate. The reason for the absence of the full function is not known at the time of writing. Whilst it is possible that elevated cloud ice mass in this case originated from crystals in the $\sim$ 265 K temperature range, evaluation of the overall ice aspect ratios in the ISHMAEL scheme show that plate-like ice

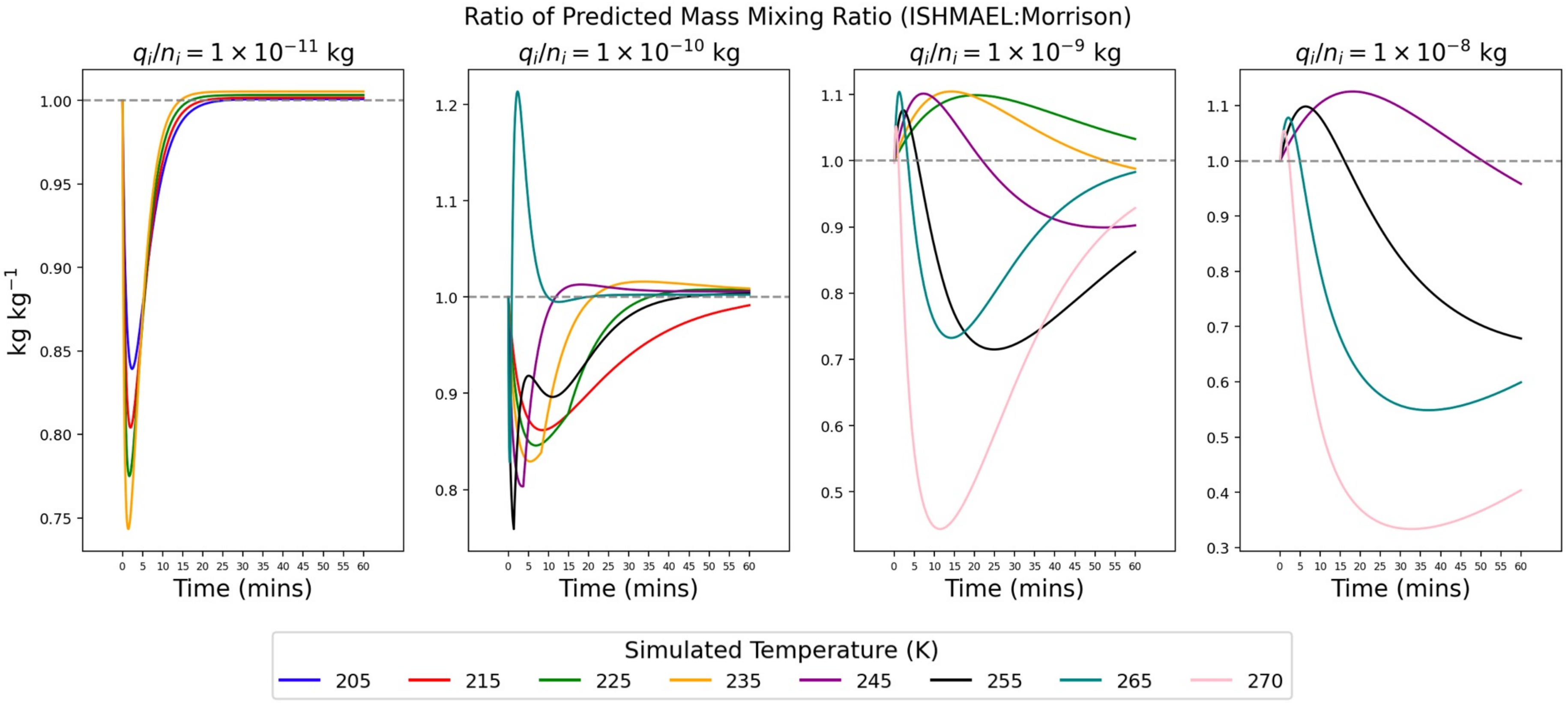

Figure 12.17. Ratio of ice mass mixing ratio produced by the ISHMAEL scheme and Morrison scheme (ISHMAEL:Morrison) for a 60 minute simulation using an idealised box model. Columns 1–4 vary with initial average ice mass. Each time series is shown for several initialisation temperatures (shaded), which remain constant. The parity value of 1 is indicated with a grey dashed line.

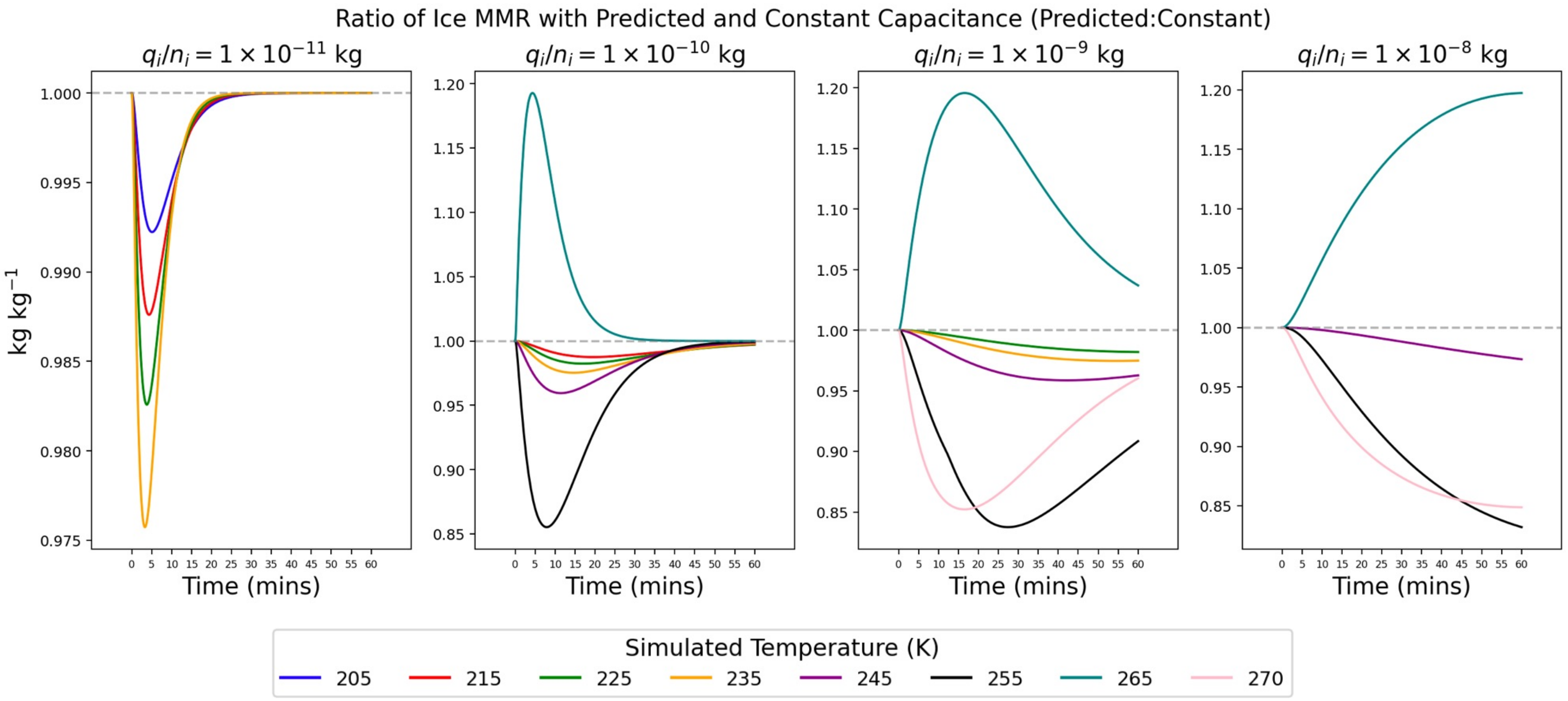

Figure 12.18. Ratio of the ice mass mixing ratio produced by the ISHMAEL scheme when capacitance is predicted, to the ice mass mixing ratio produced by ISHMAEL when capacitance is constant. Columns 1–4 vary with initial average ice mass. Each time series is shown for several initialisation temperatures (shaded), which remain constant. The parity value of 1 is indicated with a grey dashed line.

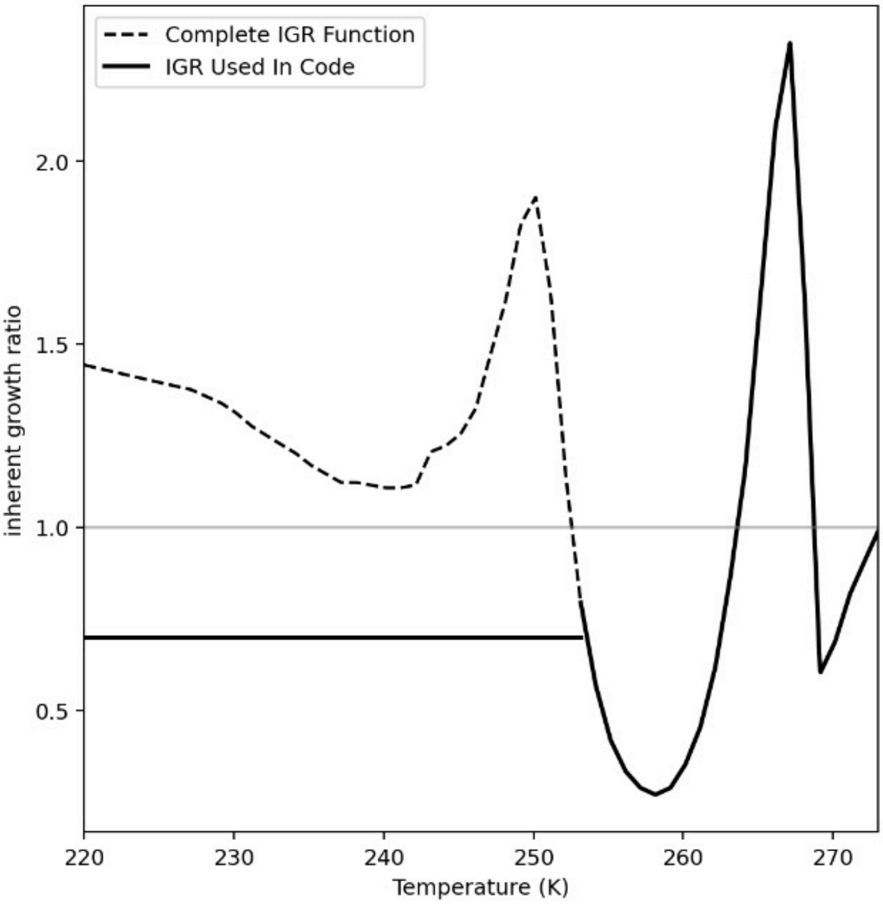

Figure 12.19. Graph of the inherent growth ratio (IGR) used in the ISHMAEL scheme, versus temperature (K). The form of the IGR function used for simulations in this study is shown in black (solid). The extended form that was not used is shown in black (dashed).

was present in much larger amounts, so this route is unlikely to affect the entire ice distribution.

Having identified that capacitance is unlikely to be the main driver of ice mass growth, we may turn to other deposition variables that are also simulated by the idealised box model in order to understand where the variability in Figure 12.17 originates. Consider that the deposition in ISHMAEL is a redistribution of the particle mass after deposition. The deposition rate is therefore proportional to the term:

$$\bar{\rho} = \rho_i \left(\frac{v_i}{v_f} \right) + \rho_{\text{dep}} \left(1 - \frac{v_i}{v_f} \right) \tag{12.46}$$

where the effect of deposition can be attributed to a change in radius and the application of deposition mass density. These terms are output by the box model and shown in Figure 12.18. Panel one (left) shows the difference in particle radius due to deposition, panel two (middle) shows the density of mass added by deposition, and panel three shows the combination of these terms which is proportional to the deposition rate. The ice mass mixing ratio is fixed at 1×10^{-9} kg, which showed interesting fluctuations for temperatures 245, 255, and 270 K in Figure 12.17

It is notable that the average radius change due to deposition tends to decrease with time, perhaps due to reducing vapour concentrations. At approximately fifteen minutes, both density and average ice particle radius reduce quickly, which coincides with the inversion of the 255 K curve in Figure 12.17. However, combination of these terms in panel three show that the combined effect does not imply an inversion would take place. It is likely then, that the inversions that took place around this time for the temperatures shown may have coincided with similar fluctuations in Morrison. These effects will not be considered here, as we are primarily interested in the role of capacitance and ice mass mixing ratios in ISHMAEL. However, this does motivate further investigation to further constrain these differences in deposition for identically initialised schemes.

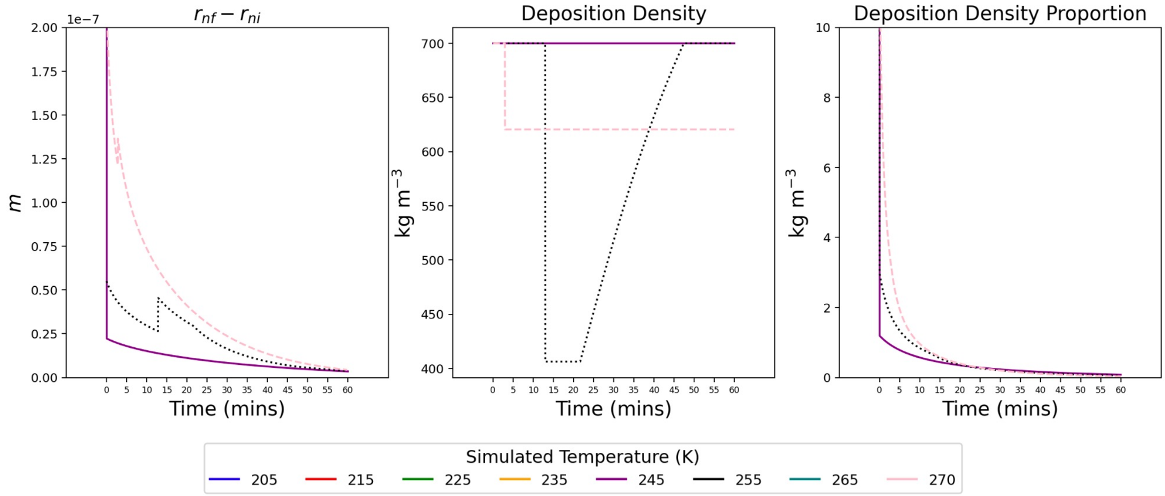

Figure 12.20. Time series of influential terms for the calculation of deposition rate in the ISHMAEL scheme. Left: the difference between initial and final ice particle radius (m) during deposition. Middle; the deposition density (kg m^{-3}). Right the combination of these terms as calculated in the deposition rate equation. Each variable is shown for a 60 minute simulation using an idealised box model with fixed average ice mass of 1×10^{-9} kg. Each time series is shown for several initialisation temperatures (shaded), which remain constant.

We propose that this platform is used for further studies of ice mass growth during deposition so that the capacitance factor for spheroids can be constrained, and its role in the development of ice more precisely measured. For example, this may be of particular interest for the re-integration of the full inherent growth ratio function. The box model and all figures are available on Github at the time of writing (Carter 2023).

Part IV

Discussion and Conclusions

Chapter 13

Summary and Conclusions

Several key differences exist in the ISHMAEL and P3 schemes that not only fail to accurately predict typical precipitation density at the ground, but fail to consolidate the effect of microphysical processes.

A key failure by ISHMAEL is the production of snow mass. Where snow is expected, ISHMAEL instead produces small ice that has similar features to cloud ice. While both precipitation types are very closely related, aggregation of these ices should produce significantly less dense hydrometeors but this process is hampered by several factors.

The inclusion of a separate mass category for aggregates poses an initial constraint on the partitioned mass category when compared to P3. In ISHMAEL, aggregates are explicitly defined, which poses little assistance to precipitation partitioning for the end user. After all, aggregated precipitation can still undergo melting, wet and dry growth that are ultimately more decisive when determining the final precipitation type. In P3, aggregation cannot be determined to have taken place, but rimed mass fraction is a much more useful indicator of precipitation type, clearly dividing snow and graupel. When considering snow as a low-density, aggregated particle only ISHMAEL may have less opportunity to produce snow, as this category is completely reliant upon aggregation rates. Whereas in P3, aggregation is simply a density reducing process, and low-density ice can be generated through several means. By not tracking aggregation, P3 may have more opportunity to produce snow. One example is that in P3, the largest and most sudden decrease in density occurs very high up (7–11 km) and is caused in part by high rates of deposition. In this region, ice is classified as snow despite aggregation rates remaining low. By comparison, low aggregation rates in ISHMAEL restrict the snow category, despite deposition rates decreasing typical density in this region. This is echoed by ISHMAEL simulating less snow mass than P3, despite having consistently higher average aggregation rates.

The partitioning of snow density beyond simply aggregates is reliant on low density, but ISHMAEL has more potential for densifying processes. ISHMAEL incorporates particle “soak in” that enables wet growth to increase mass by soaking into porous ice, a feature not found in P3, and this is only compounded in ISHMAEL as melting is also highly abundant. Whereas density reducing processes, such as aggregation, riming and deposition, have a much smaller effect on density despite similar mass tendency rates. This densification also leads to more spherical particles, in ISHMAEL which collect less efficiently than more extreme aspect ratios. ISHMAEL tends to produce predominantly spherical particles, thus limiting the aggregation potential.

To resolve the differences in these schemes, consolidation of density change and mass-process rates for each microphysical process must be undertaken. The magnitude of density reducing or increasing processes must be appropriate, and sensible bounds should be placed on the density to reduce the occurrence of extreme values.

13.1 Conclusions

The examinations undertaken in this thesis were intended to evaluate the inclusion of parameterised ice habit to a bulk microphysics model during simulations of north-east U.S. winter storms that exhibited mixed-phase activity aloft and mixed-phase precipitation at the surface.

The complexities associated with mixed-phase microphysics processes were detailed. It was evident that the conventional hydrometeor-categorisation framework was not best suited to capture mixed-phase activity such as riming, because the particle properties of ice categories are innately fixed, whereas microphysical processes tend to evolve ice particle properties along a continuum of possible values. For example, the Morrison bulk microphysics scheme has a fixed density value per simulated hydrometeor class. Therefore, the density of ice and snow cannot evolve to resemble the partially rimed states observed in reality. Fixing particle properties in this way requires that ice particles be converted between categories that more closely resemble the initial and end states of ice. However, this *autoconversion* of particle mass can cause unusual jumps in fall speed, which is a dependency for microphysics processes. Indeed, microphysical process rates are often dependent on the particle properties and *vice versa*, so failing to capture the transitional states of ice along a continuum of particle properties is a source of sensitivity in conventional bulk schemes. This sensitivity may materialise in poor precipitation forecasts.

Given the importance of representing ice particle properties along a continuum during growth, several bulk microphysics schemes have been built to capture this process computationally. These particle-property schemes employ a new framework that simulates generalised-ice categories rather than discrete hydrometeor categories, which removes the requirement for autoconversion. Within the generalised ice-category, particle properties are evolved explicitly via the effect of microphysical processes. However, due to computational restraints that bulk schemes aim to satisfy, only a limited number of ice prognostic variables are tracked. In the P3 scheme, the choice is made to prognose rime mass and rime volume, and in the ISHMAEL scheme the choice is made to prognose ice particle axis lengths.

The development of multiple particle-property bulk microphysics schemes in recent years motivated an investigation of these schemes during mesoscale events that exhibited a substantial mixed-phase precipitation component. The choice was made to test the P3 scheme, because it explicitly tracks the transitional rimed qualities of ice, which were proposed to improve the parameterisation of the riming process. The ISHMAEL scheme was also tested, as geometry is also an important riming dependency, and would provide a good point of comparison to the P3 scheme during this process. Finally, the Morrison scheme was also chosen for testing, as a representative of conventional bulk microphysics schemes.

A north-east U.S. winter storm that produced heavy snowfall and underwent a period of mixed-phase precipitation was chosen for this case study. This storm exhibited extremely high radar reflectivity factors aloft of Long Island, and at the surface of Stony Brook measurements of precipitation type were available to evaluate scheme performance.

The simulated precipitation type by each microphysics scheme was examined and compared to observations. Each scheme produced snow to the north of Long Island and rain to the south, as expected, but the central mixed-phase transitional zone simulated by each scheme varied in precipitation type and distribution. In general, Morrison exhibited the least sensitivity to mixed-phase activity aloft and therefore failed to capture the extent of graupel and sleet formation at Stony Brook. In comparison, the particle predicting schemes were very sensitive to the mixed-phase period. P3 produced ice pellets and rain, and ISHMAEL produced ice pellets and graupel in the correct time period. However, P3 produced more rain than expected and ISHMAEL was found to predict small ice in the north of the domain where snow was observed. It was found that the P3 scheme was particularly sensitive to melting, which was likely to increase rain mass unexpectedly at the surface. Whilst ISHMAEL exhibited a weak aggregation efficiency and poor prediction of snow overall.

The simulated radar reflectivity factor was examined for each scheme to determine if the very high reflectivity levels that were observed could be effectively captured by each scheme. Overall, P3 was the only scheme to simulate a reflectivity maximum close in magnitude to that observed. Instead, Morrison, and particularly ISHMAEL, simulated comparatively weak bands. However, the distribution of the band was found to be better captured by ISHMAEL and P3 than the Morrison scheme, which simulated a relatively broad reflectivity region. In the vertical, ISHMAEL-simulated reflectivity factors were found to be similar to observations but occurred far higher than expected. Reanalysis of the reflectivity at all vertical levels showed an improved reflectivity maximum, however contours of this maximum indicated that these maxima occurred in small isolated groups that did not resemble observations. Examination of the precipitation associated with high reflectivity in each scheme showed that high density was vital to reproduce the extremely high reflectivity observed, and that the attainment of high density was associated with mixed-phase activity in P3 and ISHMAEL.

To examine the underlying cause of these differences, the reflectivity parameterisations for each scheme were reviewed. It was determined that the reflectivity routines were not consistent amongst these schemes, and that similar environments could produce different reflectivity factors based on the choice of parameterisation. In-built reflectivity routines in ISHMAEL and P3 enabled mixed-phase activity to be closely associated with high reflectivity, as was found in observations of reflectivity in this case. The manual activation of a non-default liquid-skin parameter for the Morrison scheme could improve the reflectivity maxima, but provided no improvement to the distribution of reflectivity in this case.

The extent of riming was analysed in all schemes and it was found that each scheme had a different relationship between the riming mass tendency and the total mass of rimed particles it produced. In the Morrison scheme, the rimed-mass tendency was very large but failed to produce as much graupel as was observed. Further analysis found that a considerable portion of the accreted mass was absorbed by the snow hydrometeor category, and that Morrison's inability to represent partially rimed states of snow caused rimed mass to be effectively lost. In the ISHMAEL and P3 schemes, a larger riming-mass tendency in P3 resulted in less rimed particle mass than ISHMAEL. An investigation was conducted with respect to the evolution of particle properties during riming. It was found that similar riming rates evolve the tracked prognostic variables in different ways. Therefore, ice in ISHMAEL evolved more quickly toward the graupel category than in P3. It was determined that the generalised-ice framework, in addition to the non-standardised, user-defined precipitation partitions, were likely to be a significant source of sensitivity for the predicted precipitation field in these schemes.

The snow depth was very large for the winter storm used in this case, but the snow depth simulated by each microphysics scheme underestimated the severity of snowfall depth, and failed to reproduce the observed depth distribution. The snow depth variable, output by the Noah-MP land surface scheme was examined, and it was found that the snow depth variable was poorly integrated to the simulated qualities of the precipitation field in each microphysics scheme. To alleviate these limitations, a new framework was developed that was physically and computationally consistent. Under this new framework, the simulated distribution of snow depth was significantly improved across all schemes, but the magnitude of the snow depth varied extraordinarily for particle-property predicting schemes.

The snow depth field was found to be limited by the accuracy of the simulated liquid equivalent depth and the density of precipitation arriving at the ground. Comparison of these variables to observation showed that the density of ice was very poorly predicted by P3 and ISHMAEL, resulting in poorly constrained predictions of SLR. Analysis of the density formulations and comparison to the melting layer aloft of Stony Brook showed that melting increased the density of precipitation close to the ground, resulting in very dense precipitation during the mixed-phase period. The melting tendency was generally larger in ISHMAEL due to a greater number of ice crystals entering the melting layer from above compared to P3. This enhanced melting for phase one may have been responsible for the rapid descent of the melting layer depth identified in ISHMAEL, which increased the density of ice during phase one. In comparison, the P3 scheme had a more narrow melting layer during phase one, so snow-like density was retained. The origins of very low density in P3 were theorised to belong to low density rimed mass, but conclusive evidence could not be determined.

The simulated storm in Part II highlighted the large array of differences that exists between each microphysics scheme formulation, and that collectively resulted in significant variations to the predicted precipitation field. An interesting feature of the ISHMAEL scheme was the presence of a larger total cloud ice mass that persisted to very low elevations and was a feeder-mechanism for mixed-phase processes. Increased cloud ice mass was hypothesised to originate from the deposition process, and by extension was expected to be related to the parameterisation of ice geometry in the ISHMAEL scheme. Indeed in ISHMAEL, crystal geometry is integrated to many microphysical processes, which sets it apart from the riming-focused prognostic variables in P3 and is likely to introduce variability in all aspects of precipitation development.

Ice crystal geometry is related to the deposition mass tendency via the ice crystal capacitance. The capacitance derives from the *electrostatic analogy* that approximates the deposition process, but use of the capacitance is debated in the literature. It was posed that theoretical capacitances derived from spheroids might overestimate the capacitance of ice crystals, resulting in a larger than expected mass deposition rate. This is most relevant to the ISHMAEL scheme, which parameterises habit using a spheroid approximation.

The importance and extent of the cloud ice mass in the ISHMAEL scheme, as well as the hypothesised link between increased mass and ice habit parameterisation, motivated two further case studies. The objectives of these case studies were to determine if the elevated cloud ice mass field in ISHMAEL was reproduced, to determine how a larger cloud ice mass might affect mixed-phase process rates, and to establish if the capacitance is a source of error in the deposition framework.

The cloud ice fields of each simulation was examined and it was found that the tendency of ISHMAEL to exaggerate the total cloud ice mass field was repeated for both simulations.

This finding was in accordance with the total deposition-mass tendency, which was similarly inflated when compared to the Morrison scheme. An examination of the mass distribution in the vertical showed that ISHMAEL cloud ice persisted to lower depths than the Morrison scheme, partially due to reduced aggregation efficiency, but likely a result of increased average crystal mass that grew non-linearly during descent. Comparisons of the total mass tendency term showed that more than 90% of the mass transferred to cloud ice was owed to the deposition process. Per grid cell, the deposition process was larger than Morrison on average and occupied a comparatively more narrow total spread of deposition rates that were biased towards larger average values than the Morrison scheme.

Given an elevated cloud ice mass that primarily resulted from the deposition process and persisted to low elevations in the ISHMAEL scheme, the possible effect of this hydrometeor field for mixed-phase processes such as riming were evaluated. It was found that, on average, cloud ice in ISHMAEL had a larger fall speed than in the Morrison scheme. Additionally, for a given crystal mass, the ISHMAEL scheme attained larger average fall speeds than in the Morrison scheme. It was determined that increased cloud ice deposition in the ISHMAEL scheme was likely to produce faster falling ices, that rimed with greater efficiency. However, the co-location of numerous microphysical processes made it difficult to draw direct links between deposition and cloud ice qualities.

A subsequent set of analyses focused on isolating the cloud ice mass to regions dominated by deposition to increase confidence in the results. Analysis at the cloud top, where deposition was expected to be a dominant process for mass gain, showed that the mass-tendency was characteristically higher in the ISHMAEL scheme than in the Morrison scheme. However, these results could not be extended to lower elevations. A set of criteria were developed to isolate the cloud ice field qualities in relation to deposition at lower elevations. This methodology ensured that the mass tendency of ice resulted from only and therefore particle properties evolved as a direct consequence of the deposition process. It was found that the mass of cloud ice within the deposition layer in ISHMAEL grew at a larger rate than the Morrison scheme with decreasing elevation. Determination of the average crystal mass in this region showed an approximately exponential average-crystal growth in the ISHMAEL scheme, which implied that the effect of elevated mass tendency was non-linear during descent and growth of the cloud ice mass.

It was hypothesised that elevated mass deposition in ISHMAEL could correspondingly reduce the droplet field mass via the Bergeron process, so further analysis was carried out using the deposition layer methodology to examine the change in droplet mass over time. It was determined that elevated deposition in the ISHMAEL scheme was associated with a scavenging of cloud droplet mass that not only reduced the total cloud droplet mass and number concentration, but that preferentially reduced the prevalence of large raindrops.

The effects of a modified cloud droplet field may artificially increase the mass riming rate. For example, the reduced presence of large droplets is likely to reduce the overall cloud-droplet mass-weighted fall speed and increase the relative fall speed of cloud ice particles compared to cloud droplets, a key factor in the riming rate efficiency. Larger crystal dimension as a result of greater average crystal mass is also likely to increase the riming rate.

However, these factors should be balanced with possible reductions to the riming rate. Fewer droplets imply a smaller statistical probability of accretion, reducing the likelihood of riming events. The observed preferential reduction in large droplets may also reduce riming efficiency due to the presence of a riming-sweet spot at a specific droplet size interval. It is not known however, whether the reduction in average droplet size moves the droplet distribution closer to or further from the ideal riming interval.

Whilst the previous analysis indicated a causal link between elevated deposition, total cloud ice mass, average crystal mass and the riming rate. Relating these processes to the parameterised geometry explicitly requires an appreciation of the ice particle capacitance. To isolate the effect of capacitance on ice crystal growth during deposition, an idealised box model was built to study the effect of capacitance in the ISHMAEL and Morrison bulk frameworks. The box model was initialised using environmental and ice-particle variables that were valued from simulation output data to ensure that they were representative of the values produced during each simulation run. The box model was allowed to run for varying average ice crystal mass, and a key variables related to the deposition mass tendency were retrieved. Initial results indicate that the capacitance of ice is a factor in depositional growth, which only becomes more important with time. Deposition rapidly reduces the aspect ratio of crystals towards oblate, which enables them to obtain a larger capacitance and therefore increase their deposition potential. We argue that this factor is likely a key component in ice mass growth at the point of nucleation, and allows small ices to grow much more quickly than Morrison early in the lifetime. However, further research is required with this platform to determine the explicit effects for the qualities of ice that descend into regions of riming and other mixed-phase processes.

The results posed in this research can be used to inform several further research questions pertaining to the parameterisation of ice habit, and more broadly, the utility of generalised-ice categories in bulk microphysics schemes. More research is required to establish the role of capacitance during deposition, and it is expected that this question will only become more important as ice shape is increasingly studied and incorporated to bulk microphysics schemes. Generalised ice schemes are likely to improve the representation of mixed-phase processes in coming years, but at this stage considerable research is required to ensure that the evolution of particle properties is appropriately constrained during particle growth. At this current stage in the development of this novel framework, we pose that the parameterisations of ice microphysical processes are likely to be poorly constrained as they are adapted from well established conventional frameworks. However, the particle-properties framework has shown itself to be a promising avenue for the capture of transitional or continuous effects at the intersection of the solid, liquid and gaseous phases of water. We are hopeful that further development and integration of parameterisations to these schemes may enable improved precipitation forecasting in future.

References

Abdelmonem, A., E. Järvinen, D. Duft, E. Hirst, S. Vogt, T. Leisner and M. Schnaiter (2016a). 'PHIPS–HALO: the airborne Particle Habit Imaging and Polar Scattering probe – Part 1: Design and operation'. In: *Atmospheric Measurement Techniques* 9.7, pp. 3131–3144. DOI: `10.5194/amt-9-3131-2016`.

– (2016b). 'PHIPS–HALO: the airborne Particle Habit Imaging and Polar Scattering probe – Part 1: Design and operation'. In: *Atmospheric Measurement Techniques* 9.7, pp. 3131–3144. DOI: `10.5194/amt-9-3131-2016`.

Adirosi, E., L. Baldini, F. Lombardo, F. Russo, F. Napolitano, E. Volpi and A. Tokay (2015). 'Comparison of Different Fittings of Drop Spectra for Rainfall Retrievals'. In: *Advances in Water Resources* 83, pp. 55–67. ISSN: 0309-1708. DOI: `https://doi.org/10.1016/j.advwatres.2015.05.009`.

AMS (2020). *Glossary of Meteorology*. Portland, OR, Amer. Meteor. Soc., P16.5. American Meteorological Society. URL: `http://glossary.ametsoc.org/wiki/` (visited on 20/12/2022).

Andrić, Jelena, Matthew R. Kumjian, Dušan S. Zrnić, Jerry M. Straka and Valery M. Melnikov (2013). 'Polarimetric Signatures above the Melting Layer in Winter Storms: An Observational and Modeling Study'. In: *Journal of Applied Meteorology and Climatology* 52.3, pp. 682–700. DOI: `10.1175/JAMC-D-12-028.1`.

Árnason, Geirmundur and Philip S. Brown (1971). 'Growth of Cloud Droplets by Condensation: A Problem in Computational Stability'. In: *Journal of Atmospheric Sciences* 28.1, pp. 72–77. DOI: `10.1175/1520-0469(1971)028<0072:GOCDBC>2.0.CO;2`.

Ávila, E. E., N. E. Castellano, C. P. R. Saunders, R. E. Bürgesser and G. G. Aguirre Varela (2009). 'Initial stages of the riming process on ice crystals'. In: *Geophysical Research Letters* 36.9. DOI: `10.1029/2009GL037723`.

Bailey, Matthew P. and John Hallett (2004). 'Growth Rates and Habits of Ice Crystals between -20° and -70°C'. in: *Journal of the Atmospheric Sciences* 61.5, pp. 514–544. DOI: `10.1175/1520-0469(2004)061<0514:GRAHOI>2.0.CO;2`.

Bailey, Matthew P. and John Hallett (2006). ‘Measured Ice Crystal Capacitances: the Failure of the Electrostatic Analogy’. In: Desert Research Institute, Reno, Nevada.

– (2009). ‘A Comprehensive Habit Diagram for Atmospheric Ice Crystals: Confirmation from the Laboratory, AIRS II, and Other Field Studies’. In: *Journal of the Atmospheric Sciences* 66.9, pp. 2888–2899. DOI: `10.1175/2009JAS2883.1`.

Bansemer, Aaron, David Delene, Andrew Heymsfield, Joseph O’Brien, Michael R. Poellot, Kendra Sand, Jennifer Moore Sova Greg and Christian Nairy (2019). *Investigation of Microphysics and Precipitation for Atlantic Coast-Threatening Snowstorms (IMPACTS) Collection*. Data available online from the NASA EOSDIS Global Hydrology Resource Center Distributed Active Archive Center, Huntsville, Alabama, U.S.A URL: *http://ghrc.nsstc.nasa.gov/*. DOI: `http://dx.doi.org/10.5067/IMPACTS/DATA101`.

Beheng, K.D. (1994). ‘A parameterization of warm cloud microphysical conversion processes’. In: *Atmospheric Research* 33.1. 11th International Conference on Clouds and Precipitation, Part II, pp. 193–206. ISSN: 0169-8095. DOI: `https://doi.org/10.1016/0169-8095(94)90020-5`.

Bigg, E. K. (Aug. 1953). ‘The Supercooling of Water’. In: *Proceedings of the Physical Society. Section B* 66.8, pp. 688–694.

Bjerknes, Vilhelm (Dec. 1904). ‘Das Problem der Wettervorhersage, betrachtet vom Standpunkte der Mechanik und der Physik (The Problem of Weather Prediction, Considered from the Viewpoints of Mechanics and Physics).’ In: *Meteorologische Zeitschrift* 18.6. (translated and edited by Volken E. and S. Brönnimann. – Meteorol. Z. 18 (2009), 663–667), pp. 663–667. DOI: `10.1127/0941-2948/2009/416`.

Borys, Randolph D., Douglas H. Lowenthal and David L. Mitchell (2000). ‘The relationships among cloud microphysics, chemistry, and precipitation rate in cold mountain clouds’. In: *Atmospheric Environment* 34.16, pp. 2593–2602. ISSN: 1352-2310. DOI: `https://doi.org/10.1016/S1352-2310(99)00492-6`.

Braham, Roscoe R. (1963). ‘Some Measurements of Snow Pellet Bulk-Densities’. In: *Journal of Applied Meteorology and Climatology* 2.4, pp. 498–500. DOI: `https://doi.org/10.1175/1520-0450(1963)002<0498:SMOSPB>2.0.CO;2`.

Carter, Joshua (2023). *An Idealised Box Model for the Evaluation of Capacitance Parameterisations*. URL: *https://github.com/jcarter2024/Capacitance*. Last visited 2023-08-20.

Chagnon, Charles W. and Christian E. Junge (1961). ‘The Vertical Distribution of Sub-Micron Particles in the Stratosphere’. In: *Journal of Atmospheric Sciences* 18.6, pp. 746–752. doi: `https://doi.org/10.1175/1520-0469(1961)018<0746:TVDOSM>2.0.CO;2`.

Chen, Baojun and Hui Xiao (2010). ‘Silver iodide seeding impact on the microphysics and dynamics of convective clouds in the high plains’. In: *Atmospheric Research* 96.2. 15th International Conference on Clouds and Precipitation, pp. 186–207. issn: 0169-8095. doi: `https://doi.org/10.1016/j.atmosres.2009.04.001`.

Chen, Jen-Ping and Dennis Lamb (May 1994). ‘The Theoretical Basis for the Parameterization of Ice Crystal Habits: Growth by Vapor Deposition’. In: *Journal of the Atmospheric Sciences* 51.9, pp. 1206–1222.

Cheng, Anning and Kuan-Man Xu (2009). ‘A PDF-Based Microphysics Parameterization for Simulation of Drizzling Boundary Layer Clouds’. In: *Journal of the Atmospheric Sciences* 66.8, pp. 2317–2334. doi: `10.1175/2009JAS2944.1`.

Clark, Terry L. (1973). ‘Numerical Modeling of the Dynamics and Microphysics of Warm Cumulus Convection’. In: *Journal of Atmospheric Sciences* 30.5, pp. 857–878. doi: `10.1175/1520-0469(1973)030<0857:NMOTDA>2.0.CO;2`.

Colle, Brian A., Matthew F. Garvert, Justin B. Wolfe, Clifford F. Mass and Christopher P. Woods (2005). ‘The 13–14 December 2001 IMPROVE-2 Event. Part III: Simulated Microphysical Budgets and Sensitivity Studies’. In: *Journal of the Atmospheric Sciences* 62.10, pp. 3535–3558. doi: `10.1175/JAS3552.1`.

Colle, Brian A. and Yanguang Zeng (2004). ‘Bulk Microphysical Sensitivities within the MM5 for Orographic Precipitation. Part I: The Sierra 1986 Event’. In: *Monthly Weather Review* 132.12, pp. 2780–2801. doi: `10.1175/MWR2821.1`.

Cooper, William A. (1986). *Ice Initiation in Natural Clouds*. Boston, MA: American Meteorological Society, pp. 29–32. isbn: 978-1-935704-17-1. doi: `10.1007/978-1-935704-17-1-`

Crawford, I., K. N. Bower, T. W. Choularton, C. Dearden, J. Crosier, C. Westbrook, G. Capes, H. Coe, P. J. Connolly, J. R. Dorsey, M. W. Gallagher, P. Williams, J. Trembath, Z. Cui and A. Blyth (2012). ‘Ice formation and development in aged, wintertime cumulus over the UK: observations and modelling’. In: *Atmospheric Chemistry and Physics* 12.11, pp. 4963–4985. doi: `10.5194/acp-12-4963-2012`.

DeMott, P. J., A. J. Prenni, X. Liu, S. M. Kreidenweis, M. D. Petters, C. H. Twohy, M. S. Richardson, T. Eidhammer and D. C. Rogers (2010). 'Predicting global atmospheric ice nuclei distributions and their impacts on climate'. In: *Proceedings of the National Academy of Sciences* 107.25, pp. 11217–11222. DOI: `10.1073/pnas.0910818107`.

Desmos Studio, PBC (2023). *Desmos Graphing Calculator*. Progam URL: *https://www.desmos.com/calculator*. Documentation available at: *https://desmos.s3.amazonaws.com/Desmos_User_Guide.pdf*. Last visited 2023-06-12.

Ding, Han and Liping Liu (2020). 'Establishment and Preliminary Application of the Forward Modeling Method for Doppler Spectral Density of Ice Particles'. In: *Remote Sensing* 12.20. ISSN: 2072-4292. DOI: `10.3390/rs12203378`.

Donner, Leo J., Bruce L. Wyman, Richard S. Hemler, Larry W. Horowitz, Yi Ming, Ming Zhao, Jean-Christophe Golaz, Paul Ginoux, S.-J. Lin, M. Daniel Schwarzkopf, John Austin, Ghassan Alaka, William F. Cooke, Thomas L. Delworth, Stuart M. Freidenreich, C. T. Gordon, Stephen M. Griffies, Isaac M. Held, William J. Hurlin, Stephen A. Klein, Thomas R. Knutson, Amy R. Langenhorst, Hyun-Chul Lee, Yanluan Lin, Brian I. Magi, Sergey L. Malyshev, P. C. D. Milly, Vaishali Naik, Mary J. Nath, Robert Pincus, Jeffrey J. Ploshay, V. Ramaswamy, Charles J. Seman, Elena Shevliakova, Joseph J. Sirutis, William F. Stern, Ronald J. Stouffer, R. John Wilson, Michael Winton, Andrew T. Wittenberg and Fanrong Zeng (2011). 'The Dynamical Core, Physical Parameterizations, and Basic Simulation Characteristics of the Atmospheric Component AM3 of the GFDL Global Coupled Model CM3'. In: *Journal of Climate* 24.13, pp. 3484–3519. DOI: `https://doi.org/10.1175/2011JCLI3955.1`.

Dowling, David R. and Lawrence F. Radke (1990). 'A Summary of the Physical Properties of Cirrus Clouds'. In: *Journal of Applied Meteorology and Climatology* 29.9, pp. 970–978. DOI: `https://doi.org/10.1175/1520-0450(1990)029<0970:ASOTPP>2.0.CO;2`.

Dunnavan, Edwin L. and Zhiyuan Jiang (2019). 'A General Method for Estimating Bulk 2D Projections of Ice Particle Shape: Theory and Applications'. In: *Journal of the Atmospheric Sciences* 76.1, pp. 305–332. DOI: `10.1175/JAS-D-18-0177.1`.

Elmore, Kimberly L., Z. L. Flamig, V. Lakshmanan, B. T. Kaney, V. Farmer, Heather D. Reeves and Lans P. Rothfusz (2014). 'MPING: Crowd-Sourcing Weather Reports for Research'. In: *Bulletin of the American Meteorological Society* 95.9, pp. 1335–1342. DOI: `https://doi.org/10.1175/BAMS-D-13-00014.1`.

Erfani, Ehsan and David L. Mitchell (2017). 'Growth of ice particle mass and projected area during riming'. In: *Atmospheric Chemistry and Physics* 17.2, pp. 1241–1257. DOI: `10.5194/acp-17-1241-2017`.

Fan, Jiwen, Yuan Wang, Daniel Rosenfeld and Xiaohong Liu (Nov. 2016). 'Review of Aerosol–Cloud Interactions: Mechanisms, Significance, and Challenges'. In: *Journal of the Atmospheric Sciences* 73.11, pp. 4221–4252. ISSN: 1520-0469. DOI: `10.1175/jas-d-16-0037.1`.

FEMA, (The Federal Emergency Management Agency) (2022). *Connecticut Severe Winter Storm and Snowstorm Disaster Declaration*. URL: `https://www.fema.gov/disaster/4106-0` (visited on 20/12/2022).

Field, Paul R., Andrew Heymsfield, Aaron Bansemer and Cynthia H. Twohy (2008). 'Determination of the Combined Ventilation Factor and Capacitance for Ice Crystal Aggregates from Airborne Observations in a Tropical Anvil Cloud'. In: *Journal of the Atmospheric Sciences* 65.2, pp. 376–391. DOI: `10.1175/2007JAS2391.1`.

Fukuta, Norihiko and Tsuneya Takahashi (1999). 'The Growth of Atmospheric Ice Crystals: A Summary of Findings in Vertical Supercooled Cloud Tunnel Studies'. In: *Journal of the Atmospheric Sciences* 56.12, pp. 1963–1979. DOI: `10.1175/1520-0469(1999)056<1963:TGOAIC>2.0.CO;2`.

Furtado, Kalli and Paul R. Field (May 2017). 'The Role of Ice Microphysics Parametrizations in Determining the Prevalence of Supercooled Liquid Water in High-Resolution Simulations of a Southern Ocean Midlatitude Cyclone'. In: *Journal of the Atmospheric Sciences* 74.6, pp. 2001–2021. ISSN: 0022-4928. DOI: `10.1175/JAS-D-16-0165.1`.

Ganetis, Sara and Brian A. Colle (2015). 'The Thermodynamic and Microphysical Evolution of an Intense Snowband during the Northeast U.S. Blizzard of 8–9 February 2013'. In: *Monthly Weather Review* 143.10, pp. 4104–4125. DOI: `10.1175/MWR-D-14-00407.1`.

Ganetis, Sara, Brian A. Colle, Matthew J. Sienkiewicz, David M. Schultz, P. L. Heinselman and David R. Novak (2013). *Evolution of an intense mesoscale snowband during the 8–9 February 2013 Northeast U.S. blizzard.* Portland, OR, Amer. Meteor. Soc., P16.5. 15th Conf. on Mesoscale Processes. URL: `https://%20ams.confex.com/ams/15MESO/webprogram/Paper228054.html` (visited on 20/12/2022).

Garrett, Timothy J., Sandra E. Yuter, Cale Fallgatter, Konstantin Shkurko, Spencer R. Rhodes and Jason L. Endries (2015). 'Orientations and aspect ratios of falling snow'. In: *Geophysical Research Letters* 42.11, pp. 4617–4622. DOI: `https://doi.org/10.1002/2015GL064040`.

Gibson, Steven R., Ronald E. Stewart and William Henson (2009). 'On the variation of ice pellet characteristics'. In: *Journal of Geophysical Research: Atmospheres* 114.D9. DOI: `https://doi.org/10.1029/2008JD011260`.

Grabowski, Wojciech W., Hugh Morrison, Shin-ichiro Shima, Gustavo C. Abade, Piotr Dziekan and Hanna Pawlowska (Nov. 2018). 'Modeling of cloud microphysics: Can we do better?' In: *Bulletin of the American Meteorological Society*. ISSN: 1520-0477. DOI: `10.1175/bams-d-18-0005.1`.

Griffin, Erica M., Terry J. Schuur, Alexander V. Ryzhkov, Heather D. Reeves and Joseph C. Picca (2014). 'A Polarimetric and Microphysical Investigation of the Northeast Blizzard of 8–9 February 2013'. In: *Weather and Forecasting* 29.6, pp. 1271–1294. DOI: `10.1175/WAF-D-14-00056.1`.

Hall, William D. (1980). 'A Detailed Microphysical Model Within a Two-Dimensional Dynamic Framework: Model Description and Preliminary Results'. In: *Journal of Atmospheric Sciences* 37.11, pp. 2486–2507. DOI: `10.1175/1520-0469(1980)037<2486:ADMMWA>2.0.CO;2`.

Hallett, John and S Mossop (Apr. 1974). 'Production of secondary ice particles in the riming process'. In: *Nature* 249, pp. 26–28. DOI: `10.1038/249026a0`.

Harimaya, Toshio (1975). 'The Riming Properties of Snow Crystals'. In: *Journal of the Meteorological Society of Japan. Ser. II* 53.6, pp. 384–392. DOI: `10.2151/jmsj1965.53.6_384`.

Harrington, Jerry Y., Kara Sulia and Hugh Morrison (Feb. 2013). 'A Method for Adaptive Habit Prediction in Bulk Microphysical Models. Part I: Theoretical Development'. In: *Journal of the Atmospheric Sciences* 70.2, pp. 349–364.

Hedstrom, N. R. and J. W. Pomeroy (1998). 'Measurements and modelling of snow interception in the boreal forest'. In: *Hydrological Processes* 12.10-11, pp. 1611–1625. DOI: `https://doi.org/10.1002/(SICI)1099-1085(199808/09)12:10/11<1611::AID-HYP684>3.0.CO;2-4`.

Helfricht, K., L. Hartl, R. Koch, C. Marty and M. Olefs (2018). 'Obtaining sub-daily new snow density from automated measurements in high mountain regions'. In: *Hydrology and Earth System Sciences* 22.5, pp. 2655–2668. DOI: `10.5194/hess-22-2655-2018`.

Hersbach, Hans, Bill Bell, Paul Berrisford, Shoji Hirahara, András Horányi, Joaquín Muñoz-Sabater, Julien Nicolas, Carole Peubey, Raluca Radu, Dinand Schepers, Adrian Simmons, Cornel Soci, Saleh Abdalla, Xavier Abellan, Gianpaolo Balsamo, Peter Bechtold, Gionata Biavati, Jean Bidlot, Massimo Bonavita, Giovanna De Chiara, Per Dahlgren, Dick Dee, Michail Diamantakis, Rossana Dragani, Johannes Flemming, Richard Forbes, Manuel Fuentes, Alan Geer, Leo Haimberger, Sean Healy, Robin J. Hogan, Elías Hólm, Marta Janisková, Sarah Keeley, Patrick Laloyaux, Philippe Lopez, Cristina Lupu, Gabor Radnoti, Patricia de Rosnay, Iryna Rozum, Freja Vamborg, Sebastien Villaume and Jean-Noël Thépaut (2020). 'The ERA5 global reanalysis'. In: *Quarterly Journal of the Royal Meteorological Society* 146.730, pp. 1999–2049. DOI: `https://doi.org/10.1002/qj.3803`.

Heymsfield, Andrew (1982). 'A Comparative Study of the Rates of Development of Potential Graupel and Hail Embryos in High Plains Storms'. In: *Journal of the Atmospheric Sciences* 39.12, pp. 2867–2897. DOI: `10.1175/1520-0469(1982)039<2867:ACSOTR>2.0.CO;2`.

Heymsfield, Andrew, Aaron Bansemer, Paul R. Field, Stephen L. Durden, Jeffrey L. Stith, James E. Dye, William Hall and Cedric A. Grainger (Dec. 2002). 'Observations and Parameterizations of Particle Size Distributions in Deep Tropical Cirrus and Stratiform Precipitating Clouds: Results from In Situ Observations in TRMM Field Campaigns'. In: *Journal of the Atmospheric Sciences* 59.24, pp. 3457–3491.

Heymsfield, Andrew and Masahiro Kajikawa (1987). 'An Improved Approach to Calculating Terminal Velocities of Plate-like Crystals and Graupel'. In: *Journal of Atmospheric Sciences* 44.7, pp. 1088–1099. DOI: `https://doi.org/10.1175/1520-0469(1987)044<1088:AIATCT>2.0.CO;2`.

Heymsfield, Andrew, Miklós Szakáll, Alexander Jost, Ian Giammanco and Robert Wright (2018). 'A Comprehensive Observational Study of Graupel and Hail Terminal Velocity, Mass Flux, and Kinetic Energy'. In: *Journal of the Atmospheric Sciences* 75.11, pp. 3861–3885. DOI: `https://doi.org/10.1175/JAS-D-18-0035.1`.

Heymsfield, Andrew and C. Westbrook (2010). 'Advances in the Estimation of Ice Particle Fall Speeds Using Laboratory and Field Measurements'. In: *Journal of the Atmospheric Sciences* 67.8, pp. 2469–2482. DOI: `10.1175/2010JAS3379.1`.

Hong, Song-You, Jimy Dudhia and Shu-Hua Chen (2004). 'A Revised Approach to Ice Microphysical Processes for the Bulk Parameterization of Clouds and Precipitation'. In: *Monthly Weather Review* 132.1, pp. 103–120. DOI: `10.1175/1520-0493(2004)132<0103:ARATIM>2.0.CO;2`.

Hong, Song-You and Jeong-Ock Jade Lim (2006). 'The WRF single-moment 6-class microphysics scheme (WSM6)'. In: *Asia-Pacific Journal of Atmospheric Sciences* 42.2, pp. 129–151.

Hong, Song-You, Yign Noh and Jimy Dudhia (2006). 'A New Vertical Diffusion Package with an Explicit Treatment of Entrainment Processes'. In: *Monthly Weather Review* 134.9, pp. 2318–2341. DOI: `https://doi.org/10.1175/MWR3199.1`.

Hong, Song-You and Jeong-Ock Jade Lim (2006). 'The WRF Single-Moment 6-Class Microphysics Scheme (WSM6)'. In: *Asia-pacific Journal of Atmospheric Sciences* 42, pp. 129–151.

Ikawa, M. and Kazuo Saito (Dec. 1991). 'Description of a Non-hydrostatic Model Developed at the Forecast Research Department of the MRI'. in: *Technical Reports of the Meteorological Research Institute* 28, 238pp.

IPCC (2013). *Climate Change 2013: The Physical Science Basis. Contribution of Working Group I to the Fifth Assessment Report of the Intergovernmental Panel on Climate Change*. Cambridge, United Kingdom and New York, NY, USA: Cambridge University Press, p. 1535. ISBN: ISBN 978-1-107-66182-0. DOI: `10.1017/CBO9781107415324`.

Ishizaka, Masaaki (1993). 'An accurate measurement of densities of snowflakes using 3-D microphotographs'. In: *Annals of Glaciology* 18, pp. 92–96. DOI: `10.3189/S0260305500011319`.

Jensen, Anders A. and Jerry Y. Harrington (2015a). 'Modeling Ice Crystal Aspect Ratio Evolution during Riming: A Single-Particle Growth Model'. In: *Journal of the Atmospheric Sciences* 72.7, pp. 2569–2590. DOI: `10.1175/JAS-D-14-0297.1`.

– (July 2015b). 'Modeling Ice Crystal Aspect Ratio Evolution during Riming: A Single-Particle Growth Model'. In: *Journal of the Atmospheric Sciences* 72.7, pp. 2569–2590.

Jensen, Anders A., Jerry Y. Harrington and Hugh Morrison (Sept. 2018). 'Impacts of Ice Particle Shape and Density Evolution on the Distribution of Orographic Precipitation'. In: *Journal of the Atmospheric Sciences* 75.9, pp. 3095–3114. ISSN: 1520-0469. DOI: `10.1175/jas-d-17-0400.1`.

Jensen, Anders A., Jerry Y. Harrington, Hugh Morrison and Jason A. Milbrandt (2017). 'Predicting Ice Shape Evolution in a Bulk Microphysics Model'. In: *Journal of the Atmospheric Sciences* 74.6, pp. 2081–2104. DOI: `10.1175/JAS-D-16-0350.1`.

Jiang, Zhiyuan, Mariko Oue, Johannes Verlinde, Eugene E. Clothiaux, Kultegin Aydin, Giovanni Botta and Yinghui Lu (2017). 'What Can We Conclude about the Real Aspect Ratios of Ice Particle Aggregates from Two-Dimensional Images?' In: *Journal of Applied Meteorology and Climatology* 56.3, pp. 725–734. DOI: `https://doi.org/10.1175/JAMC-D-16-0248.1`.

Jordan, Rachael (1991). *A One-dimensional Temperature Model for a Snow Cover : Technical Documentation for SNTHERM.89*. Tech. rep. U.S. Army Corps of Engineers Cold Regions Research and Engineering Laboratory.

Judson, Arthur and Nolan Doesken (2000). 'Density of Freshly Fallen Snow in the Central Rocky Mountains'. In: *Bulletin of the American Meteorological Society* 81.7, pp. 1577–1588. DOI: `10.1175/1520-0477(2000)081<1577:DOFFSI>2.3.CO;2`.

Justice, Erin (2022). *Fast Cloud Droplet Probe (FCDP)*. National Aeronautics and Space Administration (NASA) URL: *https://airbornescience.nasa.gov/instrument/FCDP*. Last visited 2023-08-02.

Khvorostyanov, Vitaly I. and Judith A. Curry (1999). 'A simple analytical model of aerosol properties with account for hygroscopic growth: 1. Equilibrium size spectra and cloud condensation nuclei activity spectra'. In: *Journal of Geophysical Research: Atmospheres* 104.D2, pp. 2175–2184. DOI: `https://doi.org/10.1029/98JD02673`.

Kikuchi, Katsuhiro, Takao Kameda, Keiji Higuchi and Akira Yamashita (2013). 'A global classification of snow crystals, ice crystals, and solid precipitation based on observations from middle latitudes to polar regions'. In: *Atmospheric Research* 132-133, pp. 460–472. ISSN: 0169-8095. DOI: `https://doi.org/10.1016/j.atmosres.2013.06.006`.

Kneifel, Stefan and Dmitri Moisseev (2020). 'Long-Term Statistics of Riming in Nonconvective Clouds Derived from Ground-Based Doppler Cloud Radar Observations'. In: *Journal of the Atmospheric Sciences* 77.10, pp. 3495–3508. DOI: `https://doi.org/10.1175/JAS-D-20-0007.1`.

Knight, Nancy C. (1986). ‘Hailstone Shape Factor and Its Relation to Radar Interpretation of Hail’. In: *Journal of Applied Meteorology and Climatology* 25.12, pp. 1956–1958. DOI: `https://doi.org/10.1175/1520-0450(1986)025<1956:HSFAIR>2.0.CO;2`.

Knight, Nancy C. and Andrew Heymsfield (1983). ‘Measurement and Interpretation of Hailstone Density and Terminal Velocity’. In: *Journal of Atmospheric Sciences* 40.6, pp. 1510–1516. DOI: `https://doi.org/10.1175/1520-0469(1983)040<1510:MAIOHD>2.0.CO;2`.

Kong, Fanyou and M.K. Yau (1997). ‘An explicit approach to microphysics in MC2’. In: *Atmosphere-Ocean* 35.3, pp. 257–291.

Korolev, Alexei and George Isaac (2003). ‘Roundness and Aspect Ratio of Particles in Ice Clouds’. In: *Journal of the Atmospheric Sciences* 60.15, pp. 1795–1808. DOI: `https://doi.org/10.1175/1520-0469(2003)060<1795:RAAROP>2.0.CO;2`.

Krekeler, J. (2013). ‘Great Lakes to Northeast major winter storm’. In: *NOAA NCEP WPC event review* 143.10, p. 2. URL: `http://www.wpc.ncep.noaa.gov/winter_storm_summaries/event_reviews/2013/Great_Lakes_Northeast_Winter_%20Storm_Feb2013.pdf`.

Kruger, Anton and Witold F. Krajewski (2002). ‘Two-Dimensional Video Disdrometer: A Description’. In: *Journal of Atmospheric and Oceanic Technology* 19.5, pp. 602–617. DOI: `https://doi.org/10.1175/1520-0426(2002)019<0602:TDVDAD>2.0.CO;2`.

Ladwig, W. (2017). *wrf-python*. Version 1.3.4.1. Boulder, Colorado: UCAR/NCAR. DOI: `10.5065/D6W094P1`.

Lamb, Dennis and Johannes Verlinde (2011). *Physics and Chemistry of Clouds*. Cambridge University Press. DOI: `10.1017/CBO9780511976377`.

Lau, K. M. and H. T. Wu (2003). ‘Warm rain processes over tropical oceans and climate implications’. In: *Geophysical Research Letters* 30.24. DOI: `https://doi.org/10.1029/2003GL018567`.

Lawson, R. Paul, Brad A. Baker, Carl G. Schmitt and T. L. Jensen (2001). ‘An overview of microphysical properties of Arctic clouds observed in May and July 1998 during FIRE ACE’. in: *Journal of Geophysical Research: Atmospheres* 106.D14, pp. 14989–15014. DOI: `https://doi.org/10.1029/2000JD900789`.

Lee, Hyunho and Jong-Jin Baik (May 2017). ‘A Physically Based Autoconversion Parameterization’. In: *Journal of the Atmospheric Sciences* 74.5, pp. 1599–1616. ISSN: 1520-0469. DOI: `10.1175/jas-d-16-0207.1`.

Libbrecht, Kenneth G. (2001). 'Morphogenesis on Ice: The Physics of Snow Crystals'. In: *Engineering and Science* 64.1, pp. 10–19.

Lin, Yanluan and Brian A. Colle (2011). 'A New Bulk Microphysical Scheme That Includes Riming Intensity and Temperature-Dependent Ice Characteristics'. In: *Monthly Weather Review* 139.3, pp. 1013–1035. DOI: `10.1175/2010MWR3293.1`.

Lin, Yanluan, Leo J. Donner and Brian A. Colle (2011). 'Parameterization of Riming Intensity and Its Impact on Ice Fall Speed Using ARM Data'. In: *Monthly Weather Review* 139.3, pp. 1036–1047. DOI: `10.1175/2010MWR3299.1`.

Lin, Yuh-Lang, Richard D. Farley and Harold D. Orville (June 1983). 'Bulk Parameterization of the Snow Field in a Cloud Model'. In: *Journal of Climate and Applied Meteorology* 22.6, pp. 1065–1092.

List, Roland and Robert S. Schemenauer (1971). 'Free-Fall Behavior of Planar Snow Crystals, Conical Graupel and Small Hail'. In: *Journal of the Atmospheric Sciences* 28.1, pp. 110–115. DOI: `10.1175/1520-0469(1971)028<0110:FFBOPS>2.0.CO;2`.

Locatelli, John D. and Peter V. Hobbs (1974). 'Fall speeds and masses of solid precipitation particles'. In: *Journal of Geophysical Research (1896-1977)* 79.15, pp. 2185–2197. DOI: `https://doi.org/10.1029/JC079i015p02185`.

Loftus, A.M., W.R. Cotton and G.G. Carrió (2014). 'A Triple-moment Hail Bulk Microphysics Scheme. Part I: Description and Initial Evaluation'. In: *Atmospheric Research* 149, pp. 35–57. ISSN: 0169-8095. DOI: `https://doi.org/10.1016/j.atmosres.2014.05.013`.

Lohmann, U., J. Zhang and J. Pi (June 2003). 'Sensitivity studies of the effect of increased aerosol concentrations and snow crystal shape on the snowfall rate in the Arctic'. In: *Journal of Geophysical Research: Atmospheres (1984–2012)* 108.D11. ISSN: 2156-2202. DOI: `10.1029/2003JD003377`.

Lorenz, Edward N. (1963). 'Deterministic Nonperiodic Flow'. In: *Journal of Atmospheric Sciences* 20.2, pp. 130–141. DOI: `https://doi.org/10.1175/1520-0469(1963)020<0130:DNF>2.0.CO;2`.

Ludlam, F. H. (1951). 'The Heat Economy of a Rimed Cylinder'. In: *Quarterly Journal of the Royal Meteorological Society* 77, pp. 663–666. DOI: `10.1002/QJ.49707733410`.

Macklin, W. C. (1962). 'The density and structure of ice formed by accretion'. In: *Quarterly Journal of the Royal Meteorological Society* 88.375, pp. 30–50.

Magono, Choji (1962). 'Meteorological Classification of Snow Crystals'. In: *Journal of the Japanese Society of Snow and Ice* 24.2, pp. 33–37. DOI: `10.5331/seppyo.24.33`.

Manchester Research IT, University of (2023). *Computational Shared Facility version 3 (CSF3)*. The authors would like to acknowledge the assistance given by Research IT and the use of the Computational Shared Facility at The University of Manchester. URL: *https://ri.itservices.manchester.ac.uk/csf3*. Last visited 2023-08-20.

Marshall, J. S. and K. L. S. Gunn (1952). 'Measurement of Snow Parameters by Radar'. In: *Journal of Atmospheric Sciences* 9.5, pp. 322–327. DOI: `https://doi.org/10.1175/1520-0469(1952)009<0322:MOSPBR>2.0.CO;2`.

Marshall, J. S. and W. Mc K. Palmer (1948). 'The Distribution of Raindrops with Size'. In: *Journal of Atmospheric Sciences* 5.4, pp. 165–166. DOI: `https://doi.org/10.1175/1520-0469(1948)005<0165:TDORWS>2.0.CO;2`.

Martin, G, N Bellouin, W Collins, I Culverwell, P Halloran, S Hardiman, T Hinton, C Jones, R McDonald, A McLaren, F O'Connor, M Roberts, J Rodriguez, S Woodward, M Best, M Brooks, A Brown, N Butchart, C Dearden, S Derbyshire, I Dharssi, M Doutriaux-Boucher, J Edwards, P Falloon and N Gedney (2011). 'The HadGEM2 family of Met Office Unified Model climate configurations'. In: *Geoscientific Model Development* 4.3, pp. 723–757.

Martin, G, D. W. Johnson and A Spice (1994). 'The Measurement and Parameterization of Effective Radius of Droplets in Warm Stratocumulus Clouds'. In: *Journal of Atmospheric Sciences* 51.13, pp. 1823–1842.

McDonald, James E. (Sept. 1963). 'Use of the Electrostatic Analogy in Studies of Ice Crystal Growth'. In: *Z. Angew. Math. Phys.* 14.5, pp. 610–620. ISSN: 0044-2275. DOI: `10.1007/BF01601268`.

McMurdie, Lynn, Brian Colle, Sandra Yuter, Tim Lang, Matthew Miller, Joseph Finlon, Kendra Sand and Greg Sova (2020). *Snowbands in the pre-warm front, NE sector of a mature cyclone affecting upstate New York*. `http://catalog.eol.ucar.edu/impacts_2020/reports?utf8=%E2%9C%93&date=2020-01-18`. [Online; Last visited 05-18-2023].

McMurdie, Lynn, Gerald M. Heymsfield, John E. Yorks, Scott A. Braun, Gail Skofronick-Jackson, Robert M. Rauber, Sandra Yuter, Brian Colle, Greg M. McFarquhar, Michael Poellot, David R. Novak, Timothy J. Lang, Rachael Kroodsma, Matthew McLinden, Mariko Oue, Pavlos Kollias, Matthew R. Kumjian, Steven J. Greybush, Andrew J. Heymsfield, Joseph A. Finlon, Victoria L. McDonald and Stephen Nicholls (2022). 'Chasing Snowstorms: The Investigation of Microphysics and Precipitation for Atlantic Coast-Threatening Snowstorms (IMPACTS) Campaign'. In: *Bulletin of the American Meteorological Society* 103.5, E1243–E1269. DOI: `https://doi.org/10.1175/BAMS-D-20-0246.1`.

Meyers, Michael P., Paul J. DeMott and William R. Cotton (1992). 'New Primary Ice-Nucleation Parameterizations in an Explicit Cloud Model'. In: *Journal of Applied Meteorology and Climatology* 31.7, pp. 708–721. DOI: `10.1175/1520-0450(1992)031<0708:NPINPI>2.0.CO;2`.

Michibata, Takuro and Toshihiko Takemura (2015). 'Evaluation of autoconversion schemes in a single model framework with satellite observations'. In: *Journal of Geophysical Research: Atmospheres* 120.18, pp. 9570–9590. DOI: `10.1002/2015JD023818`.

Milbrandt, Jason A. and Hugh Morrison (2013). 'Prediction of Graupel Density in a Bulk Microphysics Scheme'. In: *Journal of the Atmospheric Sciences* 70.2, pp. 410–429. DOI: `10.1175/JAS-D-12-0204.1`.

Milbrandt, Jason A., Hugh Morrison, Daniel T. Dawson II and Marco Paukert (2021). 'A Triple-Moment Representation of Ice in the Predicted Particle Properties (P3) Microphysics Scheme'. In: *Journal of the Atmospheric Sciences* 78.2, pp. 439–458. DOI: `https://doi.org/10.1175/JAS-D-20-0084.1`.

Miller, James E. (June 1946). 'Cyclogenesis in the Atlantic Coastal Region of the United States'. In: *Journal of Meteorology* 3.2, pp. 31–44. ISSN: 0095-9634. DOI: `10.1175/1520-0469(1946)003<0031:CITACR>2.0.CO;2`.

Mitchell, David L. (June 1996). 'Use of Mass- and Area-Dimensional Power Laws for Determining Precipitation Particle Terminal Velocities'. In: *Journal of the Atmospheric Sciences* 53.12, pp. 1710–1723.

Mohammadlou, Mohammad, Abdolreza Bahremand, Daniel Princz, Nicholas Kinar, Amin Haghnegahdar and Saman Razavi (2022). 'Objective evaluation of the Global Environmental Multiscale Model (GEM) with precipitation and temperature for Iran'. In: *Natural Resource Modeling* 35.3, e12343. DOI: `https://doi.org/10.1111/nrm.12343`.

Molthan, Andrew L. (2011). *Evaluating the Performance of Single and Double Moment Microphysics Schemes During a Synoptic-Scale Snowfall Event.* 24th /20th AMS Conferences on Weather and Forecasting / Numerical Weather Prediction, Seattle, WA [Available online at *https://ntrs.nasa.gov/api/citations/20110008792/downloads/20110008792.pdf*]. Last visited 2023-07-18.

Morrison, Hugh, J. A. Curry and V. I. Khvorostyanov (June 2005). 'A New Double-Moment Microphysics Parameterization for Application in Cloud and Climate Models. Part I: Description'. In: *Journal of the Atmospheric Sciences* 62.6, pp. 1665–1677.

Morrison, Hugh and Wojciech W. Grabowski (2008). 'A Novel Approach for Representing Ice Microphysics in Models: Description and Tests Using a Kinematic Framework'. In: *Journal of the Atmospheric Sciences* 65.5, pp. 1528–1548. DOI: `10.1175/2007JAS2491.1`.

Morrison, Hugh and Jason A. Milbrandt (2015). 'Parameterization of Cloud Microphysics Based on the Prediction of Bulk Ice Particle Properties. Part I: Scheme Description and Idealized Tests'. In: *Journal of the Atmospheric Sciences* 72.1, pp. 287–311. DOI: `10.1175/JAS-D-14-0065.1`.

Morrison, Hugh, Jason A. Milbrandt, George H. Bryan, Kyoko Ikeda, Sarah A. Tessendorf and Gregory Thompson (Jan. 2015). 'Parameterization of Cloud Microphysics Based on the Prediction of Bulk Ice Particle Properties. Part II: Case Study Comparisons with Observations and Other Schemes'. In: *Journal of the Atmospheric Sciences* 72.1, pp. 312–339. ISSN: 1520-0469. DOI: `10.1175/jas-d-14-0066.1`.

Morrison, Hugh and J. O. Pinto (Oct. 2005). 'Mesoscale Modeling of Springtime Arctic Mixed-Phase Stratiform Clouds Using a New Two-Moment Bulk Microphysics Scheme'. In: *Journal of the Atmospheric Sciences* 62.10, pp. 3683–3704.

Morrison, Hugh, Marcus van Lier-Walqui, Ann M. Fridlind, Wojciech W. Grabowski, Jerry Y. Harrington, Corinna Hoose, Alexei Korolev, Matthew R. Kumjian, Jason A. Milbrandt, Hanna Pawlowska, Derek J. Posselt, Olivier P. Prat, Karly J. Reimel, Shin-Ichiro Shima, Bastiaan van Diedenhoven and Lulin Xue (2020). 'Confronting the Challenge of Modeling Cloud and Precipitation Microphysics'. In: *Journal of Advances in Modeling Earth Systems* 12.8. DOI: `https://doi.org/10.1029/2019MS001689`.

Mosimann, Lukas, Ernest Weingartner and Albert Waldvogel (1994). ‘An Analysis of Accreted Drop Sizes and Mass on Rimed Snow Crystals’. In: *Journal of Atmospheric Sciences* 51.11, pp. 1548–1558. DOI: `https://doi.org/10.1175/1520-0469(1994)051<1548:AAOADS>2.0.CO;2`.

Murakami, Masataka (1990). ‘Numerical Modeling of Dynamical and Microphysical Evolution of an Isolated Convective Cloud’. In: *Journal of the Meteorological Society of Japan. Ser. II* 68.2, pp. 107–128. DOI: `10.2151/jmsj1965.68.2_107`.

Nagumo, Nobuhiro and Yasushi Fujiyoshi (2015). ‘Microphysical Properties of Slow-Falling and Fast-Falling Ice Pellets Formed by Freezing Associated with Evaporative Cooling’. In: *Monthly Weather Review* 143.11, pp. 4376–4392. DOI: `https://doi.org/10.1175/MWR-D-15-0054.1`.

Nakaya, U. (1954). *Snow crystals: natural and artificial.* Harvard University Press.

Niu, Guo-Yue and Zong-Liang Yang (2011). *The Community Noah Land-Surface Model (LSM) with Multi-Physics Options: User’s Guide*. University of Texas at Austin Tech. Rep., 21 pp. [Available online at *https://www.jsg.utexas.edu/noah-mp/users-guide/*]. Last visited 2023-03-26.

Niu, Guo-Yue, Zong-Liang Yang, Kenneth E. Mitchell, Fei Chen, Michael B. Ek, Michael Barlage, Anil Kumar, Kevin Manning, Dev Niyogi, Enrique Rosero, Mukul Tewari and Youlong Xia (2011). ‘The community Noah land surface model with multiparameterization options (Noah-MP): 1. Model description and evaluation with local-scale measurements’. In: *Journal of Geophysical Research: Atmospheres* 116.D12. DOI: `https://doi.org/10.1029/2010JD015139`.

Ono, A. (1969). ‘The Shape and Riming Properties of Ice Crystals in Natural Clouds’. In: *Journal of the Atmospheric Sciences* 26.1, pp. 138–147. DOI: `10.1175/1520-0469(1969)026<0138:TSARPO>2.0.CO;2`.

Organization, World Meteorological (1975). *International Cloud Atlas*. International Cloud Atlas v. 2. Secretariat of the World Meteorological Organization. ISBN: 9789263124074.

Passarelli, Richard E. (1978). ‘An Approximate Analytical Model of the Vapor Deposition and Aggregation Growth of Snowflakes’. In: *Journal of Atmospheric Sciences* 35.1, pp. 118–124. DOI: `https://doi.org/10.1175/1520-0469(1978)035<0118:AAAMOT>2.0.CO;2`.

Phillips, Vaughan T. J., Alexander Khain, Nir Benmoshe and Eyal Ilotoviz (2014). 'Theory of Time-Dependent Freezing. Part I: Description of Scheme for Wet Growth of Hail'. In: *Journal of the Atmospheric Sciences* 71.12, pp. 4527–4557. DOI: `https://doi.org/10.1175/JAS-D-13-0375.1`.

Picca, Joseph C., David M. Schultz, Brian A. Colle, Sara Ganetis, David R. Novak and Matthew J. Sienkiewicz (2014). 'The Value of Dual-Polarization Radar in Diagnosing the Complex Microphysical Evolution of an Intense Snowband'. In: *Bulletin of the American Meteorological Society* 95.12, pp. 1825–1834. DOI: `10.1175/BAMS-D-13-00258.1`.

Pitter, R. L. and H. R. Pruppacher (1974). 'A Numerical Investigation of Collision Efficiencies of Simple Ice Plates Colliding With Supercooled Water Drops'. In: *Journal of Atmospheric Sciences* 31.2, pp. 551–559. DOI: `https://doi.org/10.1175/1520-0469(1974)031<0551:ANIOCE>2.0.CO;2`.

Praz, C., Y.-A. Roulet and A. Berne (2017). 'Solid hydrometeor classification and riming degree estimation from pictures collected with a Multi-Angle Snowflake Camera'. In: *Atmospheric Measurement Techniques* 10.4, pp. 1335–1357. DOI: `10.5194/amt-10-1335-2017`.

Prodi, Franco (1970). 'Measurements of Local Density in Artificial and Natural Hailstones'. In: *Journal of Applied Meteorology and Climatology* 9.6, pp. 903–910. DOI: `https://doi.org/10.1175/1520-0450(1970)009<0903:MOLDIA>2.0.CO;2`.

Pruppacher, H. R. and J. D. Klett (2010). *Microphysics of Clouds and Precipitation*. Atmospheric and Oceanographic Sciences Library. Springer Netherlands. ISBN: 9780306481000.

Rasmussen, Roy M., István Geresdi, Greg Thompson, Kevin Manning and Eli Karplus (2002). 'Freezing Drizzle Formation in Stably Stratified Layer Clouds: The Role of Radiative Cooling of Cloud Droplets, Cloud Condensation Nuclei, and Ice Initiation'. In: *Journal of the Atmospheric Sciences* 59.4, pp. 837–860. DOI: `10.1175/1520-0469(2002)059<0837:FDFISS>2.0.CO;2`.

Reisner, J., R. M. Rasmussen and R. T. Bruintjes (1998). 'Explicit Forecasting of Supercooled Liquid Water in Winter Storms using the MM5 Mesoscale Model'. In: *Quarterly Journal of the Royal Meteorological Society* 124.548, pp. 1071–1107.

Richardson, Lewis Fry (1922). *Weather Prediction by Numerical Process*. Cambridge Mathematical Library. 2nd ed. 2007, with Foreword by Peter Lynch. Cambridge University Press. DOI: `10.1017/CBO9780511618291`.

Roebber, Paul J., Sara L. Bruening, David M. Schultz and John V. Cortinas (2003). ‘Improving Snowfall Forecasting by Diagnosing Snow Density’. In: *Weather and Forecasting* 18.2, pp. 264–287.

Russell, John (2018). *New Deep Learning Algorithm Solves Rubik’s Cube*. URL: *https://www.hpcwire.com/2018/07/25/new-deep-learning-algorithm-solves-rubiks-cube*.

Rutledge, Steven A. and Peter V. Hobbs (Oct. 1984). ‘The Mesoscale and Microscale Structure and Organization of Clouds and Precipitation in Midlatitude Cyclones. XII: A Diagnostic Modeling Study of Precipitation Development in Narrow Cold-Frontal Rainbands’. In: *Journal of the Atmospheric Sciences* 41.20, pp. 2949–2972.

Sanders, Frederick and John R. Gyakum (1980). ‘Synoptic-Dynamic Climatology of the “Bomb”’. In: *Monthly Weather Review* 108.10, pp. 1589–1606. DOI: 10.1175/1520-0493(1980)108<1589:SDCOT>2.0.CO;2.

Satoh, Masaki, Toshiro Inoue and Hiroaki Miura (2010). ‘Evaluations of cloud properties of global and local cloud system resolving models using CALIPSO and CloudSat simulators’. In: *Journal of Geophysical Research: Atmospheres* 115.D4. DOI: 10.1029/2009JD012247.

Satoh, Masaki, Akira T. Noda, Tatsuya Seiki, Ying-Wen Chen, Chihiro Kodama, Yohei Yamada, Naomi Kuba and Yousuke Sato (2018). ‘Toward Reduction of the Uncertainties in Climate Sensitivity due to Cloud Processes Using a Global Non-Hydrostatic Atmospheric Model’. In: *Prog Earth Planet Sci* 5, p. 67. DOI: https://doi.org/10.1186/s40645-018-0226-1.

Schmidt, R. A. and David R. Gluns (1991). ‘Snowfall interception on branches of three conifer species’. In: *Canadian Journal of Forest Research* 21.8, pp. 1262–1269. DOI: 10.1139/x91-176.

Schnaiter, M., E. Järvinen, A. Abdelmonem and T. Leisner (2018). ‘PHIPS-HALO: the airborne particle habit imaging and polar scattering probe – Part 2: Characterization and first results’. In: *Atmospheric Measurement Techniques* 11.1, pp. 341–357. DOI: 10.5194/amt-11-341-2018.

Schneider, Tapio, João Teixeira, Christopher S. Bretherton, Florent Brient, Kyle G. Pressel, Christoph Schär and A. Pier Siebesma (Jan. 2017). ‘Climate Goals and Computing the Future of Clouds’. In: *Nature Climate Change* 7.1, pp. 3–5. DOI: 10.1038/nclimate3190.

Schön, Roland, Martin Schnaiter, Zbigniew Ulanowski, Carl Schmitt, Stefan Benz, Ottmar Möhler, Steffen Vogt, Robert Wagner and Ulrich Schurath (2011). 'Particle Habit Imaging Using Incoherent Light: A First Step toward a Novel Instrument for Cloud Microphysics'. In: *Journal of Atmospheric and Oceanic Technology* 28.4, pp. 493–512. DOI: `https://doi.org/10.1175/2011JTECHA1445.1`.

Schultz, David M. and Peter Lynch (2022). '100 Years of L. F. Richardson's Weather Prediction by Numerical Process'. In: *Monthly Weather Review* 150, pp. 693–695. DOI: `https://doi.org/10.1175/MWR-D-22-0068.1.`.

Sexstone, G. A. and S. R. Fassnacht (2014). 'What drives basin scale spatial variability of snowpack properties in northern Colorado?' In: *The Cryosphere* 8.2, pp. 329–344. DOI: `10.5194/tc-8-329-2014`.

Shan, Yunpeng, Eric M. Wilcox, Lan Gao, Lin Lin, David L. Mitchell, Yan Yin, Tianliang Zhao, Lei Zhang, Hongrong Shi and Meng Gao (2020). 'Evaluating Errors in Gamma-Function Representations of the Raindrop Size Distribution: A Method for Determining the Optimal Parameter Set for Use in Bulk Microphysics Schemes'. In: *Journal of the Atmospheric Sciences* 77.2, pp. 513–529. DOI: `https://doi.org/10.1175/JAS-D-18-0259.1`.

Skamarock, W. C., J. B. Klemp, J. Dudhia, D. O. Gill, Z. Liu, J. Berner, W. Wang, J. G. Powers, M. G. Duda, D. M. Barker and X.-Y. Huang. (2019). 'A Description of the Advanced Research WRF Version 4.' In: *NCAR Tech. Note NCAR/TN-556+STR*, p. 145. DOI: `10.5065/1dfh-6p97`.

Snow, C. (1954). *Formulas for Computing Capacitance and Inductance*. Circular. U.S. Government Printing Office.

SPEC (2012). *Fast CDP and Fast FSSP with Tips Designed to Reduce Shattering*. Stratton Park Engineering Company URL: *http://www.specinc.com/node/123*. Last visited 2023-08-01.

Srivastava, R. C. and J. L. Coen (1992). 'New Explicit Equations for the Accurate Calculation of the Growth and Evaporation of Hydrometeors by the Diffusion of Water Vapor'. In: *Journal of Atmospheric Sciences* 49.17, pp. 1643–1651. DOI: `10.1175/1520-0469(1992)049<1643:NEEFTA>2.0.CO;2`.

Sterzinger, Lucas J. and Adele L. Igel (2021). 'The Effects of Ice Habit on Simulated Orographic Snowfall'. In: *Journal of Hydrometeorology* 22.6, pp. 1649–1661. DOI: `https://doi.org/10.1175/JHM-D-20-0253.1`.

Stevens, R. G., K. Loewe, C. Dearden, A. Dimitrelos, A. Possner, G. K. Eirund, T. Raatikainen, A. A. Hill, B. J. Shipway, J. Wilkinson, S. Romakkaniemi, J. Tonttila, A. Laaksonen, H. Korhonen, P. Connolly, U. Lohmann, C. Hoose, A. M. L. Ekman, K. S. Carslaw and Paul R. Field (2018). 'A model intercomparison of CCN-limited tenuous clouds in the high Arctic'. In: *Atmospheric Chemistry and Physics* 18.15, pp. 11041–11071. DOI: `10.5194/acp-18-11041-2018`.

Stoelinga, M. T. (2005). *Simulated equivalent reflectivity factor as currently formulated in RIP: Description and possible improvements*. University of Washington Tech. Rep., 5 pp. [Available online at *http://citeseerx.ist.psu.edu/viewdoc/download?doi=10.1.1.522.925&rep=rep1&type=pdf*]. Last visited 2023-06-03.

Storelvmo, Trude and Ivy Tan (2015). 'The Wegener-Bergeron-Findeisen process - Its discovery and vital importance for weather and climate'. In: *Meteorologische Zeitschrift* 24, pp. 455–461.

Straka, Jerry M. and Edward R. Mansell (2005). 'A Bulk Microphysics Parameterization with Multiple Ice Precipitation Categories'. In: *Journal of Applied Meteorology* 44.4, pp. 445–466. DOI: `10.1175/JAM2211.1`.

Sulia, Kara J. and Jerry Y. Harrington (2011). 'Ice aspect ratio influences on mixed-phase clouds: Impacts on phase partitioning in parcel models'. In: *Journal of Geophysical Research: Atmospheres* 116.D21.

Sullivan, S. C., C. Hoose, A. Kiselev, T. Leisner and A. Nenes (2018). 'Initiation of secondary ice production in clouds'. In: *Atmospheric Chemistry and Physics* 18.3, pp. 1593–1610. DOI: `10.5194/acp-18-1593-2018`.

Takahashi, Tsutomu (1978). 'Riming Electrification as a Charge Generation Mechanism in Thunderstorms'. In: *Journal of the Atmospheric Sciences* 35.8, pp. 1536–1548. DOI: `10.1175/1520-0469(1978)035<1536:REAACG>2.0.CO;2`.

Thompson, Gregory, Paul R. Field, Roy M. Rasmussen and William D. Hall (2008). 'Explicit Forecasts of Winter Precipitation Using an Improved Bulk Microphysics Scheme. Part II: Implementation of a New Snow Parameterization'. In: *Monthly Weather Review* 136.12, pp. 5095–5115. DOI: `10.1175/2008MWR2387.1`.

Vergara-Temprado, Jesús, Annette K. Miltenberger, Kalli Furtado, Daniel P. Grosvenor, Ben J. Shipway, Adrian A. Hill, Jonathan M. Wilkinson, Paul R. Field, Benjamin J. Murray and Ken S. Carslaw (2018). 'Strong control of Southern Ocean cloud reflectivity by ice-nucleating particles'. In: *Proceedings of the National Academy of Sciences* 115.11, pp. 2687–2692. ISSN: 0027-8424. DOI: `10.1073/pnas.1721627115`.

Waitz, F., M. Schnaiter, T. Leisner and E. Järvinen (2021). 'PHIPS-HALO: the airborne Particle Habit Imaging and Polar Scattering probe – Part 3: Single-particle phase discrimination and particle size distribution based on the angular-scattering function'. In: *Atmospheric Measurement Techniques* 14.4, pp. 3049–3070. DOI: `10.5194/amt-14-3049-2021`. URL: `https://amt.copernicus.org/articles/14/3049/2021/`.

Westbrook, C. (2008). 'The fall speeds of sub-100 μm ice crystals'. In: *Quarterly Journal of the Royal Meteorological Society* 134.634, pp. 1243–1251. ISSN: 1477-870X. DOI: `10.1002/qj.290`.

Westbrook, C., Robin J. Hogan and Anthony J. Illingworth (2008). 'The Capacitance of Pristine Ice Crystals and Aggregate Snowflakes'. In: *Journal of the Atmospheric Sciences* 65.1, pp. 206–219. DOI: `https://doi.org/10.1175/2007JAS2315.1`.

Wikimedia Commons (2015). *Spheroid with Coordinate Axes*. URL: `https://commons.wikimedia.org/wiki/File:Ellipsoid-rot-ax.svg`.

Wisner, Chester, H. D. Orville and Carol Myers (Sept. 1972). 'A Numerical Model of a Hail-Bearing Cloud'. In: *Journal of the Atmospheric Sciences* 29.6, pp. 1160–1181.

Woolard, Edgar W. (1922). 'L. F. Richardson on Weather Prediction by Numerical Process'. In: *Monthly Weather Review* 50.2, pp. 72–74. DOI: `https://doi.org/10.1175/1520-0493(1922)50<72:LFROWP>2.0.CO;2`.

Yagi, Tsuruhei (1970). 'Measurement of the Fall Velocity of Ice Crystals Drifting in Supercooled Fog'. In: *Journal of the Meteorological Society of Japan. Ser. II* 48.4, pp. 287–292. DOI: `10.2151/jmsj1965.48.4_287`.

Yamasaki, Masanori (2013). 'A Study on the Effects of the Ice Microphysics on Tropical Cyclones'. In: *Advances in Meteorology* 2013, p. 13.

Yang, Zong-Liang and Robert E. Dickinson (1996). 'Description of the Biosphere-Atmosphere Transfer Scheme (BATS) for the Soil Moisture Workshop and evaluation of its performance'. In: *Global and Planetary Change* 13.1. Soil Moisture Simulation, pp. 117–134. ISSN: 0921-8181. DOI: `https://doi.org/10.1016/0921-8181(95)00041-0`.

Zavaleta, Jhony R. (2022). *Cloud Particle Imager (CPI)*. National Aeronautics and Space Administration (NASA) URL: *https://airbornescience.nasa.gov/instrument/CPI*. Last visited 2023-08-02.

Zelinka, Mark D., Chen Zhou and Stephen A. Klein (2016). 'Insights from a refined decomposition of cloud feedbacks'. In: *Geophysical Research Letters* 43.17, pp. 9259–9269. DOI: `https://doi.org/10.1002/2016GL069917`.

Appendices

Appendix A

Phase Relaxation Time Scale

Supersaturation originates from several microphysical and dynamical processes which each must be considered simultaneously by numerical models. The contributing terms are grouped in the *supersaturation equation* i.e. Equation 20 in Clark 1973, which must be solved each time step by the microphysics scheme. However, computing supersaturation explicitly invokes instabilities. Árnason and Brown 1971 noted that innate instabilities had been present in the cloud droplet growth equations for two decades prior, with authors often reducing the time step accordingly to achieve good results without formally identifying the constraints of instability. Árnason and Brown 1971 first formally quantified the instability by relating the time step to microphysical reaction times producing the (computational) stability constraint:

$$\delta t < 2\tau, \tag{A.1}$$

where τ is the supersaturation relaxation time scale, a variable describing the theoretical time taken for a supersaturated system to return to 100% saturation.
The time step given by Equation A.1 can be very short in circumstances where supersaturation is short lived, such as in a marginally supersaturated region with a large number of condensation or deposition sites, making it unsuitable for bulk schemes to compute (at least, historically) so an implicit/semi-analytic solution was developed to solve the saturation equation at longer time steps without generating instabilities Clark 1973; Hall 1980.

The absolute supersaturation δ is the difference between water vapour mixing ratio and the liquid saturation mixing ratio: $\delta = q - q_{\mathrm{sl}}$ Khvorostyanov and Curry 1999. The evolution of this in Eulerian form is given by Morrison and Milbrandt 2015:

$$\frac{d\delta}{dt} = A_c - \frac{\delta}{\tau},$$

where, A_c is the change in δ due to vertical motion, turbulent mixing, radiation, and the Bergeron–Findeisen process. For brevity these terms are not expanded upon here, but can be found in Hall 1980 equations 54-60. τ is the multi-phase supersaturation relaxation time scale:

$$\tau^{-1} = \tau_c^{-1} + \tau_r^{-1} + \left(1 + \frac{L_s}{c_p}\frac{dq_{\mathrm{sl}}}{dT}\right)\frac{\tau_i^{-1}}{\Gamma_i},$$

where τ_c, τ_r and τ_i are the supersaturation relaxation time scales associated with cloud droplets, rain, and ice, respectively. L_s is the latent heat of sublimation, c_p is the specific heat of air at constant pressure, and Γ_i is the psychometric correction to deposition/sublimation associated with latent heating/cooling. In general, τ is determined as follows:

$$\tau = (4\pi DNRC)^{-1},$$

where D is the diffusivity of water vapour in air, N is the number concentration of particles, R is the mean particle radius and C is the dimensionless capacitance, which determines the ability of vapour adsorption to a particle based on its geometry.

Appendix B

Proof: Moments of the Gamma Distribution

B.1 Particle Number (Zeroth Moment)

Let the number concentration N be a randomly distributed variable. We may define the probability density function of N as a gamma distribution $N \sim \text{Gam}(\alpha, \beta)$ with the following form:

$$f(x; \alpha, \beta) = N_0 x^{\alpha-1} e^{-\beta x} \{\alpha > 0, \beta > 0\},$$

where N_0 is a constant called the slope parameter and α and β are the shape parameter and rate parameter, respectively.
The total N is given by integration over all positive x of the probability density function:

$$N = \int_0^\infty f(x)dx$$

$$N = N_0 \int_0^\infty x^{\alpha-1} e^{-\beta x} dx \tag{B.1}$$

where we have moved the constant outside of the integral. To solve this we may make use of the definition of the Euler gamma function:

$$\Gamma(\delta) = \int_0^\infty t^{\delta-1} e^{-t} dt \tag{B.2}$$

which is similar to the integral in equation B.1 if we make some substitutions. Let $\delta = \alpha$

and let $t = \beta x$ and therefore $dt = \beta dx$

$$\begin{aligned}\Gamma(\alpha) &= \int_0^\infty (\beta x)^{\alpha-1} e^{-\beta x} \beta dx \\ &= \beta^\alpha \int_0^\infty x^{\alpha-1} e^{-\beta x} dx\end{aligned}$$

Therefore

$$\int_0^\infty x^{\alpha-1} e^{-\beta x} dx = \frac{\Gamma(\alpha)}{\beta^\alpha} \tag{B.3}$$

Now substitute Equation B.3 into Equation B.1

$$N = N_0 \frac{\Gamma(\alpha)}{\beta^\alpha}$$

In a population where N is known and we wish to find the parameters of the gamma distribution it is useful to rearrange for N_0

$$N_0 = N \frac{\beta^\alpha}{\Gamma(\alpha)} \tag{B.4}$$

B.2 Morrison Mass (First) Moment

To derive the mass moment of the gamma distribution we follow the same procedure as the previous section but integrate over the product of the number distribution $f(x)$ and particle mass $q(x)$.
The total Q is given by integration over all positive x:

$$Q = \int_0^\infty q(x) \cdot f(x) dx$$

$$Q = N_0 \int_0^\infty q(x) x^{\alpha-1} e^{-\beta x} dx \tag{B.5}$$

A this stage, the particle mass must be related to the dimension x using a mass-distribution hypothesis. It is common to use a power law mass dimensional relationship of the form:

$$m = cD^d \tag{B.6}$$

where D is the particle diameter. Such a relationship is a convenient choice as the parameters can be easily adjusted to accommodate cloud spectra measurements. Additionally, setting $c = \frac{\pi\rho_i}{6}$ and $d = 3$ retrieves the mass-dimensional relationship of constant density spheres:

$$\begin{aligned} m &= \frac{\pi\rho_i}{6}(2r)^3 \\ &= \frac{4\pi\rho_i}{3}r^3 \end{aligned}$$

Here we will substitute the general form equation B.6 into the integrand of equation B.5 assuming that $x \equiv D$:

$$\begin{aligned} Q &= N_0 \int_0^\infty c x^d x^{\alpha-1} e^{-\beta x} dx \\ &= N_0 c \int_0^\infty x^{\alpha+d-1} e^{-\beta x} dx \end{aligned}$$

where we have moved the constants outside of the integral. At this point we may again draw on a useful definition of the Euler gamma function:

$$\Gamma(\delta) = \int_0^\infty t^{\delta-1} e^{-t} dt$$

which is similar to the integral if we make some substitutions. Let $\delta = \alpha + d$ and let $t = \beta x$ and therefore $dt = \beta dx$

$$\begin{aligned} \Gamma(\alpha + d) &= \int_0^\infty (\beta x)^{\alpha+d-1} e^{-\beta x} \beta dx \\ &= \beta^{\alpha+d} \int_0^\infty x^{\alpha+d-1} e^{-\beta x} dx \end{aligned}$$

Therefore

$$\int_0^\infty x^{\alpha+d-1} e^{-\beta x} dx = \frac{\Gamma(\alpha + d)}{\beta^{\alpha+d}} \tag{B.7}$$

Substituting Equation B.7 into Q:

$$
\begin{aligned}
Q &= N_0 c \int_0^{\infty} x^{\alpha+d-1} e^{-\beta x} dx \\
&= N_0 c \frac{\Gamma(\alpha+d)}{\beta^{\alpha+d}}
\end{aligned}
$$

B.3 ISHMAEL Mass Moment

To derive the mass moment of the gamma distribution in ISHMAEL we follow the same procedure as the previous section and integrate over the product of the number distribution $f(x)$ and particle mass $q(x)$.
The total Q is given by integration over all positive x:

$$Q = \int_0^{\infty} q(x) \cdot f(x) dx$$

$$Q = N_0 \int_0^{\infty} q(a_i) \cdot a_i^{\alpha-1} e^{-\beta a_i} da_i \tag{B.8}$$

where we have specified that the particle dimension x to be used is the spheroid a-axis length a_i.
The mass distribution hypothesis in ISHMAEL follows from J.-P. Chen and Lamb 1994 and Harrington et al. 2013:

$$m_i = \frac{4\pi\rho_i}{3} a_i^2 c_i$$

To obtain a distribution as a function of a_i only, the c_i axis can be written as a function of the a-axis and the mean inherent growth ratio of ice δ_*

$$c_i = a_0^{1-\delta_*} a_i^{\delta_*}$$

where c_i, a_i are the axis lengths at the end of the time step and a_0 is the initial a-axis length.
By combining these equations the integrand in Equation B.8 can be completed:

$$Q = N_0 \int_0^{\infty} \frac{4\pi\rho_i}{3} a_i^2 a_0^{1-\delta_*} a_i^{\delta_*} a_i^{\alpha-1} e^{-\beta a_i} da_i \tag{B.9}$$

$$= \left[N_0 \frac{4\pi\rho_i}{3} a_0^{1-\delta_*} \right] \int_0^{\infty} a_i^{\alpha+\delta_*+1} e^{-\beta a_i} da_i \tag{B.10}$$

Recall the identity of the Euler gamma function:

$$\Gamma(\Delta) = \int_0^\infty t^{\Delta-1} e^{-t} dt$$

We will apply a substitution. Let $\Delta - 1 = \alpha + \delta_* + 1$ and let $t = \beta a_i$ then $dt = \beta da_i$. The Euler gamma can be written:

$$\Gamma(\alpha + \delta_* + 2) = \int_0^\infty (\beta a_i)^{\alpha+\delta_*+1} e^{-\beta a_i} \beta da_i$$

This can be rearranged to isolate an integral with identical form to the integral in B.10:

$$\int_0^\infty a_i^{\alpha+\delta_*+1} e^{-\beta a_i} dt = \frac{\Gamma(\alpha + \delta_* + 2)}{\beta^{\alpha+\delta_*+2}}$$

With substitution of this integral, Equation B.10 becomes:

$$Q = \left[N_0 \frac{4\pi\rho_i}{3} a_0^{1-\delta_*} \right] \frac{\Gamma(\alpha + \delta_* + 2)}{\beta^{\alpha+\delta_*+2}} \tag{B.11}$$

Appendix C

Aspect Ratio and Inherent Growth Ratio

The spheroidal aspect ratio ϕ is the ratio between the individual spheroid axes a and c such that $\phi = c/a$. J.-P. Chen and Lamb (1994) related the change in ϕ to the relative change in each axis that is incurred by a microphysical growth process:

$$\frac{dc}{da} = \delta(T)\phi,$$

where $\delta(T)$ is a function of the relative growth efficiencies of both axes (Harrington et al. 2013):

$$\delta(T) = \frac{\alpha_c}{\alpha_a}$$

Particle axial growth is driven by microphysical processes that possess unique growth efficiencies. Therefore, the inherent growth ratio may be specified for each process i.e. for deposition δ_{dep} or riming δ_{rime}. The difference in the initial and final particle axes is determined by the average inherent growth ratio across all processes δ_*, which evolves the a-axis by the following relationships:

$$a_{\mathrm{nf}} = \alpha_{\mathrm{nr}} r_{\mathrm{nf}}^{\frac{3}{2+\delta_*}} \tag{C.1}$$

$$\alpha_{\mathrm{nr}} = a_{\mathrm{ni}} r_{\mathrm{ni}}^{-\frac{3}{2+\delta_*}} \tag{C.2}$$

Where $a_{\mathrm{ni/f}}$ are the initial and final characteristic a-axis lengths, $r_{\mathrm{ni/f}}$ are the initial and final equivalent spherical axis lengths, and α_{nr} is the initial distribution of mass along a in accordance with the equivalent spherical radius.

To relate the inherent growth ratio δ_* to changes in the aspect ratio ϕ examine the δ_* equation provided by Harrington et al. (2013) (their Eq. B27):

$$\delta_* = \frac{3\log(r_{\mathrm{nf}}) - 2\log(a_{\mathrm{nf}}) - \log(a_o)}{\log(a_{\mathrm{nf}}) - \log(a_o)}, \tag{C.3}$$

this can be simplified if we suppose that $r_{\mathrm{nf}} = \gamma_{\mathrm{r}_i} a_{\mathrm{nf}}$, where γ_{r_i} determines the ratio of the equivalent spherical radius to the a-axis. When $\gamma_{\mathrm{r}_i} = 1$ the particle is spherical. When $\gamma_{\mathrm{r}_i} > 1$ the particle is prolate and when $\gamma_{\mathrm{r}_i} < 1$ the particle is oblate. Applying this substitution to Equation C.3:

$$\delta_* = \frac{3\log(\gamma_{\mathrm{r}_i})}{\log(a_{\mathrm{nf}}/a_o)} + 1$$

Then the leading term can be characterised as positive or negative:

$$\begin{aligned} &\delta_* > 1, &&\frac{3\log(\gamma_{\mathrm{r}_i})}{\log(a_{\mathrm{nf}}/a_o)} > 0 \\ &\delta_* < 1, &&\frac{3\log(\gamma_{\mathrm{r}_i})}{\log(a_{\mathrm{nf}}/a_o)} < 0 \end{aligned}$$

Recognising that $a_{\mathrm{nf}} > a_o$ the denominator is positive for all a_{nf}. Therefore the sign of the leading term is determined only by γ_{r_i}:

$$\begin{aligned} &\delta_* > 1, &&\gamma_{\mathrm{r}_i} > 1, &&(\text{Prolate}) \\ &\delta_* < 1, &&\gamma_{\mathrm{r}_i} < 1, &&(\text{Oblate}) \end{aligned}$$

Thus, if $\delta_* > 1$ then the crystal tends towards prolate, and if $\delta_* < 1$ then the crystal tends towards oblate.

To relate the inherent growth ratio to the magnitude of changes in the aspect ratio, we can combine equations C.2 and C.1:

$$a_{\mathrm{nf}} = a_{\mathrm{ni}} r_{\mathrm{ni}}^{-\frac{3}{2+\delta_*}} r_{\mathrm{nf}}^{\frac{3}{2+\delta_*}} \tag{C.4}$$

Dividing by r_{nf} we can retrieve γ_{r_i} as a function of δ_* and the relative change in equivalent spherical radius:

$$\gamma_{\mathrm{r}_i}^{-1} = \frac{a_{\mathrm{nf}}}{r_{\mathrm{nf}}} = \frac{a_{\mathrm{ni}}}{r_{\mathrm{ni}}} \left(\frac{r_{\mathrm{nf}}}{r_{\mathrm{ni}}}\right)^{\frac{3}{2+\delta_*}-1}$$

$$\gamma_{\mathrm{r}_i} = \frac{r_{\mathrm{ni}}}{a_{\mathrm{ni}}} \left(\frac{r_{\mathrm{nf}}}{r_{\mathrm{ni}}}\right)^{1-\frac{3}{2+\delta_*}}$$

Recall that δ_* is artificially bound between 0.55 and 1.3, then the exponent becomes:

$$\begin{aligned} \epsilon &= 1 - \frac{3}{2+\delta_*}, 0.55 < \delta_* < 1.3 \\ &- 0.176 < \epsilon < 0.091 \end{aligned} \tag{C.5}$$

Additionally, let $\kappa_{\mathrm{r}} = r_{\mathrm{nf}}/r_{\mathrm{ni}} \geq 1$ be the growth factor in equivalent spherical radius. Then γ_{r_i} becomes:

$$\gamma_{\mathrm{r}_i} = \frac{r_{\mathrm{ni}}}{a_{\mathrm{ni}}} \kappa_{\mathrm{r}}^{\epsilon}, \qquad -0.176 < \epsilon < 0.091$$

We may try to understand the magnitude of each term by making some appropriate assumptions. First, we may assume that the ratio of the axis lengths spans the magnitude $10^0 - 10^{-1}$, as we do not expect extreme shapes. Next, we may approximate κ_{r} by assuming that the change in axis length due to deposition is a smaller order of magnitude than the axis length itself, this is reasonable as we do not expect deposition to double an axis length within a time step, and instead apply smooth incremental changes. We can then write κ_{r} as:

$$\begin{aligned} \kappa_{\mathrm{r}} = r_{\mathrm{nf}}/r_{\mathrm{ni}} &= \frac{(r_{\mathrm{ni}} + \Delta r)}{r_{\mathrm{ni}}} \\ &= 1 + \frac{\Delta r}{r_{\mathrm{ni}}} \end{aligned}$$

Then $\kappa_{\mathrm{r}}^{\epsilon}$ can be expanded using a Taylor series:

$$\left(1 + \frac{\Delta r}{r_{\mathrm{ni}}}\right)^{\epsilon} = 1 + \epsilon \frac{\Delta r}{r_{\mathrm{ni}}} + \frac{1}{2}\left(\frac{\Delta r}{r_{\mathrm{ni}}}\right)^2 (\epsilon^2 - \epsilon) + O\left(\frac{\Delta r}{r_{\mathrm{ni}}}\right)^3 \tag{C.6}$$

Assuming a maximum order of magnitude $\frac{\Delta r}{r_{\mathrm{ni}}} \approx 1 \times 10^{-1}$:

$$\begin{aligned}
\kappa_{\mathrm{r}}^{\epsilon} &= 1 + 10^{-1}\epsilon + \frac{1}{2}10^{-2}(\epsilon^2 - \epsilon) + O\left(10^{-1}\right)^3 \\
\kappa_{\mathrm{r}}^{(9\times10^{-2})} &\approx 1 + 9\times10^{-3} + \frac{1}{2}(8\times10^{-5} - 9\times10^{-4}) \\
\kappa_{\mathrm{r}}^{(-1.8\times10^{-1})} &\approx 1 - 1.8\times10^{-2} + \frac{1}{2}(3.2\times10^{-6} + 1.8\times10^{-3})
\end{aligned}$$

Hence changes motivated by the inherent growth ratio are at least an order of magnitude smaller than the influence of the initial axes ratio. Therefore, over short time periods the ice aspect ratio is much more strongly dependent on the historical radius than on the inherent growth ratio. Whereas, over long periods of time, the inherent growth ratio drives changes in the ratio of a_n and r_n that enable it to reach parity, at which point the value of δ_* becomes much more significant. When we consider that the typical growth per time step is only fractions of the radii, it is clear that a consistent δ_* greater than 1 can coexist with $\gamma_{\mathrm{r}_i} < 1$ and thus $\delta_* < 1$. The resulting growth would be a crystal that becomes more oblate with time but at a diminishing rate until γ_{r_i} reaches parity.

Appendix D

Limits to the `getvar` Reflectivity Routine

The difference in simulated reflectivity factor when liquid skin is considered compared to when a liquid skin is not considered is termed ΔZ and is given by:

$$\Delta Z = 10\Big[\log_{10}\left(C_r(\omega(1+\delta))^{1.75} + \left(\frac{C_s}{\alpha} + \frac{C_g}{\alpha}\delta^{1.75}\right)\right) - \\ \log_{10}\left(C_r(\omega(1+\delta))^{1.75} + \left(C_s + C_g\delta^{1.75}\right)\right)\Big] \tag{D.1}$$

Where ω is the ratio of liquid to solid mass mixing ratio, δ is the ratio of graupel to snow mass mixing ratio, $\alpha = 0.224$ is a limiting constant used for solid precipitation types only. The constants C_r, C_s, and C_g contain the fixed constants associated with the reflectivity component of each hydrometeor type given in Equation G.1 i.e:

$$\begin{aligned} C_r &= \Gamma(7)\left(\frac{\rho_a}{\pi\rho_r}\right)^{1.75}\frac{1\times10^{18}}{(8\times10^{6})^{0.75}} \\ C_s &= \alpha\Gamma(7)\left(\frac{\rho_a}{\pi\rho_s}\right)^{1.75}\left(\frac{\rho_s}{\rho_w}\right)^{2}\frac{1\times10^{18}}{(2\times10^{7})^{0.75}} \\ C_g &= \alpha\Gamma(7)\left(\frac{\rho_a}{\pi\rho_g}\right)^{1.75}\left(\frac{\rho_g}{\rho_w}\right)^{2}\frac{1\times10^{18}}{(4\times10^{6})^{0.75}} \end{aligned} \tag{D.2}$$

We wish to determine the value of ΔZ in the limit that ω and δ tend to 0 and infinity. It is convenient to first simplify equation D.1:

$$\begin{aligned}\Delta Z &= 10\left[\log_{10}(a+nb) - \log_{10}(a+b)\right]\\ &= 10\left[\log_{10}\left(\frac{a+nb}{a+b}\right)\right]\\ &= 10\left[\log_{10}\left(1+\frac{n-1}{1+\frac{a}{b}}\right)\right]\end{aligned} \tag{D.3}$$

where

$$a = C_r(\omega(1+\delta))^{1.75}, \qquad b = C_s + C_g\delta^{1.75}, \qquad n = \frac{1}{\alpha}$$

For convenience, let the contents of the bracket be $\gamma = \left(1+\frac{n-1}{1+\frac{a}{b}}\right)$. the limits of ΔZ from equation D.3 can be found by evaluating the limits of a, b and γ sequentially:

$$\begin{aligned}&\lim_{\delta\to 0} b(\delta) = C_s, && \lim_{\delta\to 0} a(\omega,\delta) = C_r\omega^{1.75}, && \lim_{\omega\to 0} a(\omega,\delta) = 0\\ &\lim_{\delta\to\infty} b(\delta) = \infty, && \lim_{\delta\to\infty} a(\omega,\delta) = \infty, && \lim_{\omega\to\infty} a(\omega,\delta) = \infty\end{aligned}$$

γ takes a simple form as $\omega \to 0, \infty$:

$$\begin{aligned}\lim_{\omega\to 0}\gamma &= n\\ \lim_{\omega\to\infty}\gamma &= 1\end{aligned}$$

and finally ΔZ:

$$\begin{aligned}\lim_{\omega\to 0}\Delta Z &= 10\log_{10}(n) = 6.5\\ \lim_{\omega\to\infty}\Delta Z &= 10\log_{10}(1) = 0\end{aligned}$$

Therefore, the total possible change due to ω is 6.5 for very low ω and the lower limit is 0. Examining the limits as δ grows or decreases is slightly more complicated:

$$\lim_{\delta\to 0}\gamma = 1 + (n-1)\left(1+\frac{C_r\omega^{1.75}}{C_s}\right)^{-1}$$

$$\lim_{\delta\to\infty} \gamma = 1 + \frac{n-1}{1+\frac{\infty}{\infty}}$$

The latter equation, when $\delta \to \infty$ is indeterminate and requires a different method. We may use L'Hopital's rule to assess the limits of the derivatives:

$$\begin{aligned}\frac{a'}{b'} &= \frac{1.75C_r\omega^{1.75}(1+\delta)^{0.75}}{1.75C_g\delta^{0.75}}\\ &= \frac{C_r\omega^{1.75}}{C_g}\left(1+\frac{1}{\delta}\right)^{0.75}\end{aligned}$$

Thus the limit is readily obtained:

$$\begin{aligned}\lim_{\delta\to\infty}\frac{a'}{b'} &= \frac{C_r\omega^{1.75}}{c_g}\\ \lim_{\delta\to\infty}\gamma &= 1+(n-1)\left(1+\frac{C_r\omega^{1.75}}{C_g}\right)^{-1}\end{aligned}$$

It is evident that γ in the limit $\delta \to \infty$ takes the same form as $\gamma\ \delta \to 0$, but with a change in constant. From D.2 we find that the ratio of constants is:

$$\begin{aligned}\frac{C_r}{C_g} &= \frac{1}{\alpha}\left(\frac{\rho_w}{\rho_g}\right)^{1/4}\left(\frac{1}{2}\right)^{0.75}\\ \frac{C_r}{C_s} &= \frac{1}{\alpha}\left(\frac{\rho_w}{\rho_s}\right)^{1/4}\left(\frac{5}{2}\right)^{0.75}\end{aligned}$$

and therefore Δ_z is obtained as a function of ω:

$$\begin{aligned}\lim_{\delta\to\infty}\Delta Z &= 10\log_{10}\left[1+(n-1)\left(1+\omega^{1.75}\left(n\left(\frac{\rho_w}{\rho_g}\right)^{1/4}\left(\frac{1}{2}\right)^{0.75}\right)\right)^{-1}\right]\\ &\approx 10\log_{10}\left[1+\frac{3.46}{1+3.34\omega^{1.75}}\right]\end{aligned}$$

$$
\begin{aligned}
\lim_{\delta\to 0}\Delta Z &= 10\log_{10}\left[1+(n-1)\left(1+\omega^{1.75}\left(n\left(\frac{\rho_w}{\rho_s}\right)^{1/4}\left(\frac{5}{2}\right)^{0.75}\right)\right)^{-1}\right] \\
&\approx 10\log_{10}\left[1+\frac{3.46}{1+15.79\omega^{1.75}}\right] \qquad \text{(D.4)}
\end{aligned}
$$

The limits of ΔZ for all 4 combinations of δ and ω are readily obtained.

$$
\begin{aligned}
\lim_{\delta\to 0,\omega\to 0}\Delta Z &= 10\log_{10}(n)\approx 6.5 \\
\lim_{\delta\to 0,\omega\to\infty}\Delta Z &= 10\log_{10}(1)=0 \\
\lim_{\delta\to\infty,\omega\to 0}\Delta Z &= 10\log_{10}(n)\approx 6.5 \\
\lim_{\delta\to\infty,\omega\to\infty}\Delta Z &= 10\log_{10}(1)=0 \qquad \text{(D.5)}
\end{aligned}
$$

Appendix E

ISHMAEL Reflectivity Parameterisation for Liquid and Solid-Phase Hydrometeors

The rain reflectivity is proportional to the 6th power of diameter:

$$Z = \int_0^\infty N(D) D^6 dD \tag{E.1}$$

However, the ISHMAEL gamma distribution function is in terms of the radius:

$$Z = \int_0^\infty N(a_i) D^6 da_i \tag{E.2}$$

To complete the integrand D must be obtained as a function of a_i. This is possible using the definition of the spheroid c axis from J.-P. Chen and Lamb (1994) $c_i = a_i^{1+\delta_*} + a_0^{1-\delta*}$. Substituting this into the definition of the spheroid radius:

$$\begin{aligned} r^3 &= a_i^2 c_i \\ &= a_i^{2+\delta_*} a_0^{1-\delta*} \end{aligned}$$

To obtain the equivalent diameter, let $a_i \to 2a_i$ then:

$$\begin{aligned} D^3 &= (2a_i)^{2+\delta_*} a_0^{1-\delta*} \\ &= 2^{2+\delta_*} a_i^{2+\delta_*} a_0^{1-\delta*} \end{aligned}$$

$$D^6 = (2a_i)^{2(2+\delta_*)} a_0^{2(1-\delta*)}$$

Then equation E.2 becomes:

$$Z = \int_0^\infty N(a_i)(2a_i)^{2(2+\delta_*)} a_0^{2(1-\delta*)} da_i \tag{E.3}$$

where $N(a_i)$ is the gamma distribution function given by:

$$N(a_i) = N_0 \left(\frac{a_i}{a_n}\right)^{\nu-1} \exp\left(-\frac{a_i}{a_n}\right) \tag{E.4}$$

Combining terms:

$$Z = \frac{N_0 2^{2(2+\delta_*)} a_o^{2(1-\delta*)}}{a_n^{\nu-1}} \int_0^\infty a_i^{2(2+\delta*)+\nu-1} \exp\left(-\frac{a_i}{a_n}\right) da_i \tag{E.5}$$

This can be solved by substitution of variables using the definition of the Euler Gamma function equation B.2.

$$\Gamma(\delta) = \int_0^\infty t^{\delta-1} e^{-t} dt \qquad \{t = \frac{a_i}{a_n}, \quad dt = \frac{1}{a_n} da_i, \quad \delta = 2(2+\delta_*) + \nu\}$$

from which we obtain:

$$Z = N_0 2^{2(2+\delta_*)} a_0^{2(1-\delta_*)} a_n^{2(2+\delta_*)+1} \Gamma(\nu + 2(2 + delta_*)) \tag{E.6}$$

And substituting N_0 from equation B.4 with $\beta = 1/a_n$ and $\alpha = \nu$

$$Z = \rho_a n_i 2^{2(2+\delta_*)} a_0^{2(1-\delta_*)} a_n^{2(2+\delta_*)} \frac{\Gamma(\nu + 2(2+\delta_*))}{\Gamma(\nu)} \tag{E.7}$$

where we have used the identity $N_i = \rho_a n_i$.

Following the method Stoelinga (2005), in addition to the determination of the 6th moment of the mass distribution, the reflectivity for frozen ice particles differs from that of rain by a factor α, which originates from the dielectric factor of ice and liquid water.

Finally, the difference in radar cross section must be considered. A snow particle will have the same radar cross section as that of a solid ice sphere of equal mass. Making the comparison within the ISHMAEL framework this yields:

$$\frac{\rho_i \pi}{6} D_i^3 = \frac{4\bar{\rho}\pi}{3} r^3$$

The equation can be rearranged by converting the radius to diameter or vice versa:

$$\begin{aligned}
\frac{\rho_i \pi}{6} D_i^3 &= \frac{4\bar{\rho}\pi}{3} r^3 \\
\frac{\rho_i \pi}{6} D_i^3 &= \frac{4\bar{\rho}\pi}{3} \frac{D_s^3}{2^{2+\delta+*}}
\end{aligned}$$

therefore, the factor difference in diameter can be determined to the sixth power:

$$\frac{D_i^6}{D_s^6} = \left(\frac{6}{\pi} \frac{4\pi}{3} \frac{\bar{\rho}}{\rho_i} \frac{1}{2^{2+\delta+*}} \right)^2 \tag{E.8}$$

Multiplying E.7 by equation E.8 and α yields:

$$Z = \alpha \left(\frac{6}{\pi} \right)^2 \left(\frac{4\pi}{3} \frac{\bar{\rho} a_0^{(1-\delta_*)}}{2^{2+\delta+*}} \right)^2 \frac{\rho_a n_i}{\rho_i} (2a_n)^{2(2+\delta_*)} \frac{\Gamma(\nu + 2(2+\delta_*))}{\Gamma(\nu)} \tag{E.9}$$

Appendix F

Conventional Parameterisation of Reflectivity

Rayleigh scattering of liquid droplets is proportional to the sixth power of the droplet diameter. Therefore the simulated reflectivity factor Z can be defined by taking the sixth moment of the rain droplet size distribution:

$$Z = \int_0^\infty N(D) D^6 \, \mathrm{d}D \tag{F.1}$$

Where $N(D)$ is number concentration of droplets per unit length. Integrating over a size distribution of the form $N(D) = N_0 \exp(-\lambda D)$ yields:

$$Z_r = \Gamma(7) N_0 \lambda^{-7} \tag{F.2}$$

A solution for λ can be found from the mass moment of the distribution (see Appendix B), substituting $\alpha = 1$, $\lambda = \beta$ and using a conventional mass-diameter relation for spherical droplets $d = 3$, $c = \rho_l \pi / 6$:

$$\lambda = \left(\frac{N_0 \pi \rho_l}{q_r \rho_a} \right)^{\frac{1}{4}} \tag{F.3}$$

Two changes are made to extend this theory to frozen precipitation. Ice is innately less reflective than water by a factor equal to the ratio of their dielectric factors (Stoelinga 2005):

$$\begin{aligned} Z_s &= \frac{|K|_i^2}{|K|_l^2} Z_i \\ &\approx \frac{0.176}{0.930} Z_i \end{aligned}$$

For irregular particles, the radar cross section is the same as that of a solid sphere of ice with identical mass (Marshall and Gunn 1952). Therefore, we may derive the substitution required for the diameter as:

$$\begin{aligned} \frac{\pi \rho_i D_i^3}{6} &= \frac{\pi \rho_s D_s^3}{6} \\ D_i &= \left(\frac{\rho_s}{\rho_i}\right)^{\frac{1}{3}} D_s \end{aligned}$$

Substituting this into Equation F.1 and re-deriving the reflectivity factor returns an additional factor of $(\rho_s/\rho_i)^2$:

$$Z_s = \Gamma(7) N_0 \lambda^{-7} \left(\frac{\rho_s}{\rho_i}\right)^2 \left(\frac{|K|_i^2}{|K|_l^2}\right)$$

Following the method of Stoelinga (2005) this can be rearranged as:

$$\begin{aligned} Z_s &= \Gamma(7) N_0 \lambda^{-7} \left(\frac{\rho_s}{\rho_l}\right)^2 \left(\frac{\rho_l}{\rho_i}\right)^2 \left(\frac{|K|_i^2}{|K|_l^2}\right) \\ &= \Gamma(7) N_0 \lambda^{-7} \left(\frac{\rho_s}{\rho_l}\right)^2 \alpha_{\odot} \end{aligned} \tag{F.4}$$

Where the factor $\alpha_{\odot}$ is a constant that derives from the phase of the particle only:

$$\begin{aligned} \alpha_{\odot} &= \left(\frac{\rho_l}{\rho_i}\right)^2 \left(\frac{|K|_i^2}{|K|_l^2}\right) \\ &\approx 0.224 \end{aligned} \tag{F.5}$$

The reflectivity component of graupel is readily derived in the same way by substitution of the snow variables q_s, ρ_s to graupel variables q_g, ρ_g. Each hydrometeor component to the reflectivity can be summed to produce an equivalent reflectivity Z_e in units of $\text{m}^6\ \text{m}^{-3}$. This is converted to the standard units of $\text{mm}^6\ \text{m}^{-3}$ and provided in decibels of Z:

$$Z\,\textbf{[dBZ]} = 10 \log_{10} \left(10^{18} \left(Z_r + Z_s + Z_g\right)\right) \tag{F.6}$$

Appendix G

WRF-python Reflectivity Parameterisation

The wrf-python `getvar` source code calculates the reflectivity via the `CALCDBZ` function as follows:

```
z_e = factor_r*(rhoair*qra)**1.75/ronv**.75 +
      factor_s*(rhoair*qsn)**1.75/sonv**.75 +
      factor_g*(rhoair*qgr)**1.75/gonv**.75

dbz = 10*LOG10(z_e)
```

where terms 1–3 of `z_e` are the rain, snow, and graupel components to the equivalent reflectivity, respectively. `qra`, `qsn` and `qgr` are the rain, snow and graupel mass-mixing ratios, respectively. `ronv`$= 8 \times 10^6$, `sonv`$= 2 \times 10^7$, and `gonv`$= 4 \times 10^6$ are constant intercepts to the gamma distribution for rain, snow and graupel, respectively. Note, it is possible to modify these constants using a keyword argument, but only constant intercepts were considered in this study.

The leading factors for each term are:

```
factor_r = GAMMA_SEVEN*1.D18*(1/(PI*RHO_R))**1.75
factor_s = GAMMA_SEVEN*1.D18*(1/(PI*RHO_S))**1.75*(RHO_S/RHOWAT)**2*ALPHA
factor_g = GAMMA_SEVEN*1.D18*(1/(PI*RHO_G))**1.75*(RHO_G/RHOWAT)**2*ALPHA
```

where `RHO_R`$\equiv$`RHOWAT`$=$ 1000 kg m^{-3}, `RHO_S`$=$ 100 kg m^{-3}, `RHO_G`$=$ 400 kg m^{-3} are the assumed fixed densities of liquid water, snow, and graupel respectively. `ALPHA` = 0.224 is the constant deriving from the difference in reflectivity between liquid and frozen hydrometeors shown in F.5.

Mathematically the above is:

$$
\begin{aligned}
Z &= 10\log_{10}(Z_r + Z_s + Z_g) \\
z &= 10\log_{10}\Bigg[\\
&\left(\Gamma(7)\left(\frac{\rho_a q_r}{\pi\rho_r}\right)^{1.75}\frac{1\times10^{18}}{(\lambda_r)^{0.75}}\right) + \\
&\left(\alpha\Gamma(7)\left(\frac{\rho_a q_s}{\pi\rho_s}\right)^{1.75}\left(\frac{\rho_s}{\rho_w}\right)^{2}\frac{1\times10^{18}}{(\lambda_s)^{0.75}}\right) + \\
&\left(\alpha\Gamma(7)\left(\frac{\rho_a q_g}{\pi\rho_g}\right)^{1.75}\left(\frac{\rho_g}{\rho_w}\right)^{2}\frac{1\times10^{18}}{(\lambda_g)^{0.75}}\right)\Bigg]
\end{aligned} \tag{G.1}
$$

Which is similar to the form of Equation F.4. Each hydrometeor reflectivity component is dependent on the density and mass mixing ratio of the hydrometeor, with increases in mass increasing the reflectivity factor associated with the hydrometeor. The components of reflectivity contributed to the whole are easily compared:

$$\frac{z_s}{z_r} = \alpha\left(\frac{\rho_s}{\rho_w}\right)^{0.25}\frac{\lambda_r}{\lambda_s}\left(\frac{q_s}{q_r}\right)^{1.75} \approx 0.05\left(\frac{q_s}{q_r}\right)^{1.75} \tag{G.2}$$

Thus for parity (i.e $z_s/z_r = 1$), $q_s = 5.5\,q_r$ so 5 times as much snow is required as rain to achieve the same reflectivity factor. A similar calculation for graupel shows that:

$$\frac{z_s}{z_g} = \alpha\left(\frac{\rho_g}{\rho_w}\right)^{0.25}\frac{\lambda_r}{\lambda_g}\left(\frac{q_g}{q_r}\right)^{1.75} \approx 0.36\left(\frac{q_g}{q_r}\right)^{1.75} \tag{G.3}$$

Thus for parity (i.e $z_g/z_r = 1$), $q_g = 1.8\,q_r$. almost twice as much graupel is required as rain to achieve the same reflectivity factor. Consequently, $q_s \approx 3\,q_g$, so graupel is 3 times more reflective than snow in this framework. Of course, we note that these components aren't additive within the logarithm, but these differences indicate the tendency of the routine to output a greater reflectivity factor in cells that are biased toward rain and graupel, rather than those containing primarily snow.

Appendix H

Three Component form of the Mixed Phase Reflectivity Component

The component of mixed phase activity in the ISHMAEL reflectivity equation is $\varepsilon = Z_{\text{rain}}/Z_{\text{ice}}$. Where

$$Z_{\text{rain}} = 1 \times 10^{18} \left(\frac{\Gamma(7)\rho_a n_r}{\lambda_r^6} \right), \tag{H.1}$$

$$Z_{\text{ice}} = 1 \times 10^{18} \left[\frac{0.176}{0.93} \left(\frac{6}{\pi} \right)^2 \left(\frac{4\pi}{3} \frac{\bar{\rho}_i a_o^{1-\delta_*}}{2^{2+\delta_*}} \right)^2 \frac{\rho_a n_i}{900^2} \left(2a_{\text{ni}} \right)^{2(2+\delta_*)} \frac{\Gamma(\nu + 2(2+\delta_*))}{\Gamma(\nu)} \right] \tag{H.2}$$

To obtain a single equation of ε, it is advantageous to first simplify Z_{ice} into the product of two terms; one containing all variables and another containing only constants:

$$Z_{\text{ice}} = 1 \times 10^{18} \left[\alpha \left(\frac{8a_0}{900} \right)^2 \frac{\rho_a}{6} \right] \times \left[\left(\frac{\bar{\rho}_i a_{\text{ni}}^{2+\delta*}}{a_0^{\delta_*}} \right)^2 n_i \Gamma(8 + 2\delta_*) \right] \tag{H.3}$$

where air density is treated as a constant $\rho_a \approx 1$. Then ε is obtained by combining equations H.1 and H.3:

$$\begin{aligned} \varepsilon = \frac{Z_{\text{rain}}}{Z_{\text{ice}}} &= \frac{6\Gamma(7)(900)^2}{\pi^2 \rho_l^2 \alpha (8a_0)^2} \frac{q_r^2 a_0^{2\delta_*}}{n_r n_i (\bar{\rho}_i a_{\text{ni}}^{2+\delta*})^2 \Gamma(8 + 2\delta_*)} \\ &\approx 2.47 \times 10^{15} \frac{q_r^2 a_0^{2\delta_*}}{n_r n_i (\bar{\rho}_i a_{\text{ni}}^{2+\delta*})^2 \Gamma(8 + 2\delta_*)} \end{aligned}$$

We can simplify this conceptually by re-parameterising the ratio of raindrop number mixing ratio to ice number mixing ratio $\gamma_n = n_r/n_i$, and the ratio of raindrop mass and number mixing ratio $m_r = q_r/n_r$, which is analogous to the average raindrop mass, then:

$$\varepsilon(\delta_*, \bar{\rho_i}, a_{\mathrm{ni}}, \gamma_n, m_r) \approx [2.47 \times 10^{15}][\gamma_n m_r^2] \left[\frac{a_0^{2\delta_*}}{(\bar{\rho_i} a_{\mathrm{ni}}^{2+\delta *})^2 \Gamma(8 + 2\delta_*)} \right], \tag{H.4}$$

When the hydrometeor distribution is defined (i.e. $[\gamma_n m_r^2]$ is constant) bracket 3 in Equation H.4 becomes a constant factor whose value is defined by $\bar{\rho_i}$ and the function $F(a_{\mathrm{ni}}, \delta_*)$:

$$F(a_{\mathrm{ni}}, \delta_*) = \frac{a_0^{2\delta_*}}{(a_{\mathrm{ni}}^{2+\delta *})^2 \Gamma(8 + 2\delta_*)} \tag{H.5}$$

Which is a function of particle geometry only.

Appendix I

P3 Reflectivity Formulation

The reflectivity `diag_ze` in P3 is calculated using the following code (line

```
diag_ze  = 10*log10((ze_rain + ze_ice) 1.e+18)
```

which consists of a rain and ice component. For rain:

```
ze_rain = nr*(mu_r +6)*(mu_r +5)*(mu_r +4)(mu_r +3)*(mu_r +2)*(mu_r+1)/lamr**6
ze_rain = max(ze_rain, 1.e-22)
```

Which is:

$$\begin{aligned} Z_{\text{rain}} &= n_r(\mu_r+6)(\mu_r+5)(\mu_r+4)(\mu_r+3)(\mu_r+2)(\mu_r+1)\frac{1}{\lambda_r^6} \\ &= \frac{n_r}{\lambda_r^6}\prod_{n=1}^{6}(\mu_r+n) \end{aligned}$$

Note that $\mu_r = 0$, thus:

$$\prod_{n=1}^{6}(\mu_r+n) = \Gamma(7)$$

and lambda:

$$\lambda_r = \left(\pi\rho_w\frac{n_r}{q_r}\right)^{\frac{1}{3}}$$

Therefore combining the above the rain reflectivity component is fully defined in terms of q_r and n_r:

$$Z_{\text{rain}} = \left(\sqrt{\Gamma(7)}\frac{q_r}{n_r^{\frac{3}{2}}\pi\rho_w}\right)^2$$

Whereas for ice:

```
ze_ice      = 0.176/0.93*f1pr13*nitot *rho
ze_ice      = max(ze_ice(i,k),1.e-22)
```

Where the number concentration $N_i[\mathrm{m}^3] = \texttt{nitot} \times \texttt{rho}$. The reflectivity per crystal `f1pr13` is determined from in-scheme lookup tables that interpolate the value based on particle density and rime fraction.

```
call access_lookup_table(dumjj,dumii,dumi, 9,dum1,dum4,dum5,f1pr13)

! dums are indexes used for the ice mass and number
f1pr13    = tmp1+(dum5-real(dumjj))*(tmp2-tmp1)
tmp1      = iproc1+(dum4-real(dumii))*(gproc1-iproc1)
tmp2      = iproc1+(dum4-real(dumii))*(gproc1-iproc1)

iproc1    = itab(dumjj,dumii,dumi,index)+(dum1-real(dumi))*(itab(dumjj,dumii,
                 dumi+1,index)-itab(dumjj,dumii,dumi,index))
```

`itab` retrieves the process (in this case the process is reflectivity) for a given crystal density (jj) and rime fraction (ii). `iproc1` is an example of how this data is retrieved and averaged over a distribution with number weighted fall speed index adjustment.

We may examine the contents of the lookup table during its construction for more detail. The reflectivity constant is calculated as:

```
iproc = sum5+n0*(cs1/917.)**2*(6./pi)**2*dum**(2.*ds1+mu_i)*exp(-lam*dum)*dd
```

Where `n0` is the intercept parameter, `mu_i` is the shape parameter and `lam` is the rate or slope parameter to the standard gamma distribution. These variables are calculated based on the number normalised mass and rime fraction. `cs1` = $900\pi/6$ and `ds1` are the constant and the power in the mass dimensional relationship of ice, respectively. `dd` = 2×10^{-6} the bin width for numerical integration of ice processes (m). `dum` is the particle size in meters = `real(ii)*dd - 0.5*dd` where `ii` goes from 1 to 110000. Mathematically this is:

$$\texttt{f1pr13} = 2 \times 10^{-6} N_0 \left(\frac{900\pi}{6 \times 917}\right)^2 \left(\frac{6}{\pi}\right)^2 r^{(2d_s+\mu_i)} \exp\left(-\lambda_i r\right), \tag{I.1}$$

and therefore the ice reflectivity in P3 is:

$$\begin{aligned} Z_{\text{ice}} &= \left[2 \times 10^{-6} \frac{0.176}{0.93} \left(\frac{900\pi}{6 \times 917}\right)^2 \left(\frac{6}{\pi}\right)^2\right] \left[\frac{n_i}{\rho_a} N_0 r^{(2d_s+\mu)} \exp\left(-\lambda_i r\right)\right] \\ &\approx 3.65 \times 10^{-7} \frac{n_i}{\rho_a} N_0 r^{(2d_s+\mu_i)} \exp\left(-\lambda_i r\right) \end{aligned}$$

Where:

$$N_0 = \frac{\lambda_i^{\mu_i+1}}{\Gamma(\mu_i+1)},$$

$$Z_{\text{ice}} \approx 3.65 \times 10^{-7} \frac{n_i}{\rho_a} \frac{\lambda_i^{\mu_i+1}}{\Gamma(\mu_i+1)} r^{(2d_s+\mu_i)} \exp\left(-\lambda_i r\right),$$

and the entire formulation of reflectivity is:

$$\begin{aligned}
Z &= 10\log_{10}\left[1 \times 10^{18}\left(\left(\sqrt{\Gamma(7)}\frac{q_r}{n_r^{\frac{3}{2}}\pi\rho_w}\right)^2 + 3.65 \times 10^{-7}\frac{n_i}{\rho_a}\frac{\lambda_i^{\mu_i+1} r^{(2d_s+\mu_i)}}{\Gamma(\mu_i+1)}\exp\left(-\lambda_i r\right)\right)\right] \\
&= 10\log_{10}\left[1 \times 10^{18}(Z_{\text{rain}} + Z_{\text{ice}})\right] \\
&= 10\log_{10}\left[1 \times 10^{18}(Z_{\text{ice}}(\varepsilon+1))\right] \\
&= 10\log_{10}\left(1 \times 10^{18}\right) + \underbrace{10\log_{10}\left(Z_{\text{ice}}\right)}_{\text{A (ice)}} + \underbrace{10\log_{10}\left(\varepsilon+1\right)}_{\text{B (Mixed-Phase)}} \qquad \text{(I.2)}
\end{aligned}$$

Appendix J

Mixed-Phase Reflectivity Enhancement by a Liquid Skin

Consider the non-liquid skin formulation of reflectivity in Equation G.1. The constants can be collected to produce an equation in terms of only the mass-mixing ratio of each hydrometeor and an associated hydrometeor constant:

$$\begin{aligned} Z_1 &= 10\log_{10}\left[C_r q_r^{1.75} + C_s q_s^{1.75} + C_g q_g^{1.75}\right] \\ Z_2 &= 10\log_{10}\left[C_r q_r^{1.75} + \frac{C_s}{\alpha_\odot} q_s^{1.75} + \frac{C_g}{\alpha_\odot} q_g^{1.75}\right] \end{aligned}$$

where the removal of $\alpha_\odot$ in the liquid skin parameterisation Z_2 is accomplished by division of the hydrometeor constant C_X. Let δ be the ratio of the graupel mass-mixing ratio q_g to the snow mass mixing ratio q_s such that $q_g = \delta q_s$. Then by substitution:

$$\begin{aligned} Z_1 &= 10\log_{10}\left[C_r q_r^{1.75} + q_s^{1.75}(C_s + C_g \delta^{1.75})\right] \\ Z_2 &= 10\log_{10}\left[C_r q_r^{1.75} + q_s^{1.75}\left(\frac{C_s}{\alpha_\odot} + \frac{C_g}{\alpha_\odot}\delta^{1.75}\right)\right] \end{aligned}$$

and additionally, let ω be the ratio of liquid to solid precipitation:

$$\begin{aligned} q_r &= \omega(q_s + q_g) \\ &= \omega q_s(1+\delta) \end{aligned}$$

Then by substitution Z_1 becomes:

$$\begin{aligned}
Z_1 &= 10\log_{10}\left(q_s^{1.75}\left[C_r(\omega(1+\delta))^{1.75} + (C_s + C_g\delta^{1.75})\right]\right)\\
&= 10\left[\log_{10}\left(q_s^{1.75}\right) + \log_{10}\left(C_r(\omega(1+\delta))^{1.75} + \left(C_s + C_g\delta^{1.75}\right)\right)\right)\right]
\end{aligned}$$

and Z_2 becomes:

$$\begin{aligned}
Z_2 &= 10\log_{10}\left(q_s^{1.75}\left[C_r(\omega(1+\delta))^{1.75} + \left(\frac{C_s}{\alpha_\odot} + \frac{C_g}{\alpha_\odot}\delta^{1.75}\right)\right]\right)\\
&= 10\left[\log_{10}\left(q_s^{1.75}\right) + \log_{10}\left(C_r(\omega(1+\delta))^{1.75} + \left(\frac{C_s}{\alpha_\odot} + \frac{C_g}{\alpha_\odot}\delta^{1.75}\right)\right)\right)\right.
\end{aligned}$$

The difference in computed reflectivity ΔZ between the liquid skin and default parameterisation, can be determined by deducting Z_1 from Z_2:

$$\begin{aligned}
\Delta Z = 10\Bigg[&\log_{10}\left(C_r(\omega(1+\delta))^{1.75} + \left(\frac{C_s}{\alpha_\odot} + \frac{C_g}{\alpha_\odot}\delta^{1.75}\right)\right) -\\
&\log_{10}\left(C_r(\omega(1+\delta))^{1.75} + \left(C_s + C_g\delta^{1.75}\right)\right)\Bigg]
\end{aligned} \tag{J.1}$$

Appendix K

Review of Nucleation and Ice Field Initialisation

Nucleation of ice in clouds can occur either homogeneously or heterogeneously. Homogeneous nucleation of ice can is considered to be a primary nucleation pathway in clouds when temperatures drop below -37 °Celsius but cannot account for clouds that are often found to be partially or fully glaciated at temperatures far warmer than this threshold. To deduce the freezing rate of comparatively warmer droplets, Bigg (1953) studied the freezing of distilled droplets between -10 and -40 °C at a temperature reduction rate of 0.5 °C per minute and recorded the likelihood of freezing. Larger droplets were found to consistently freeze at temperatures above -40 °C, and smaller droplets had a smaller, but nonzero, probability of freezing too. For example, droplets larger than approximately 0.1mm consistently froze at above -30 °C. Bigg explained the discrepancy with the prevailing view at the time, that ”motes” or ”singularities” within the liquid caused freezing to initiate at warmer temperatures than expected. These particles are now understood as aerosol and heterogeneous nucleation is known to play a key role in mixed phase clouds at temperatures above -40 °C.

Many sources of aerosol are present in the atmosphere, from soot to bacteria, but only a small subsection of those can provide an efficient base for freezing. The reasons for this are unclear, initial explanations pointed to similarities between the aerosol crystal lattice and that of water, though recent studies dispute this claim. Importantly, ice nucleating particles, or INP, allow water to freeze at temperatures above the homogeneous nucleation threshold, thus accounting for glaciation.

Heterogeneous nucleation has several theorised pathways: heterogeneous deposition, condensation then freezing (or pore condensation and freezing, PCF), contact freezing, and immersion freezing. The exact importance of each mechanism is still subject to research and may depend on a variety of factors. Immersion freezing, where an INP is present within a liquid drop, accounts for the findings of Bigg and is often dubbed the primary nucleation mechanism, responsible for cloud droplet freezing across the droplet size spectrum.

Here we investigate the parametrisation of nucleation in each microphysics scheme to determine sources of discrepancy in the ice crystal nucleation rate. Additionally, the size and growth of crystals will be investigated as both factors are influential in subsequent microphysical process rates, not least graupel production.

K.1 Homogeneous Nucleation

Homogeneous nucleation is activated when ambient temperatures fall below a prescribed limit, and when cloud or rain droplets exceed a minimum mass mixing ratio. In both schemes, the mass mixing ratio and number concentration are conserved during conversion to the ice category:

$$Q_I \mathrel{+}= Q_C \tag{K.1}$$

$$N_I \mathrel{+}= N_C \tag{K.2}$$

$$Q_I \mathrel{+}= Q_R \tag{K.3}$$

$$N_I \mathrel{+}= N_R \tag{K.4}$$

Where Q_i, N_i are the mass mixing ratio and number concentration and i represents the hydrometeor species C, R, I, cloud droplets, rain droplets and ice particles, respectively.

In ISHMAEL, the threshold temperature is -35 °C, whereas in Morrison freezing occurs at slightly cooler temperatures, below -40 °C. Similarly, Morrison requires that cloud or rain droplet mass exceeds a minimum of 1×10^{-14}, but in ISHMAEL more mass is required to initiate freezing at 1×10^{-12} kg kg^{-1}.

K.2 Heterogeneous Nucleation

Heterogeneous nucleation occurs in three pathways, contact freezing, immersion freezing and deposition nucleation.

Immersion Freezing

Biggs freezing accounts for immersion or primary nucleation of cloud droplets of all sizes. For rain droplets, the formulation is identical in both ISHMAEL and Morrison:

$$Q_I \mathrel{+}= 20 \times 100\pi^2 \rho_w N_R \times \frac{e^{0.66(273.15-T)} - 1}{\lambda_R^6} \tag{K.5}$$

Where ρ_w is the density of water, 1000 kg m^{-3}, and λ_R is the slope parameter for rain.

Immersion freezing of cloud droplets is not accounted for in ISHMAEL, but is by Morrison:

$$Q_I \mathrel{+}= 100\pi^2 \rho_w \frac{N_C}{36} \frac{\Gamma(7+\kappa)}{\Gamma(1+\kappa)} \frac{e^{0.66(273.15-T)} - 1}{\lambda_C^6} \tag{K.6}$$

Where κ is the spectral shape parameter for droplets from Martin et al. 1994 and λ_c is the slope parameter for droplets.

$$\kappa = (0.0005714 \times (\frac{287.15 T N_C}{1 \times 10^6 P}) + 0.2714)^{-2} - 1 \tag{K.7}$$

Deposition Nucleation

In ISHMAEL, the DeMott et al. 2010 formulation is used to parametrise deposition nucleation which calculates the number of ice crystals nucleated by both temperature and aerosol size.

$$n_{IN,T} = a(273.16 - T)^b (n_{\text{aer},>0.5})^{(c(273.16-T)+d)} \tag{K.8}$$

Where $a = 0.0000594$, $b = 3.33$, $c = 0.0264$, $d = 0.0033$, $n_{IN,T}$ is the ice nuclei number concentration in L^{-1} at temperature T, $n_{\text{aer},>0.5}$ is the number concentration of aerosol particles with diameters larger than 0.5. In ISHMAEL, $n_{\text{aer},>0.5} = 0.03$ taken from Chagnon and Junge (1961).

n_{IN,T_k} is added directly to the ice crystal concentration and appended to the mass mixing ratio by multiplication of an average crystal mass:

$$Q_I \mathrel{+}= n_{IN,T} \times \frac{4\pi\rho_I}{3}(2 \times 10^{-6})^3 \times \Delta t \tag{K.9}$$

Where 2×10^{-6} is the initial ice radius in metres and ρ_I is the bulk ice density 920 kg m^{-3}.

In Morrison, heterogeneous deposition is handled by the Rasmussen et al. 2002 formulation by default. This requires ice saturation must be greater than 1 and the temperature less than 265.15 K (-8 °C).

The Cooper curve Cooper 1986 calculates the number of nucleated crystals based on current temperatures only, (compared to aerosol size in ISHMAEL and compared to the Meyers curve that uses supersaturation).

$$KC2 = 0.005 \times e^{(0.304*(273.15-T))} * 1000 \tag{K.10}$$

$$N_I \mathrel{+}= \frac{(KC2 - N_I - N_S - N_G)}{\Delta T} \tag{K.11}$$

$$Q_I \mathrel{+}= N_I \times M_I \tag{K.12}$$

Where M_I0 is the initial crystal mass:

$$M_I = \frac{4\pi\rho_I}{3}(1 \times 10^{-5})^3 \tag{K.13}$$

$$= 2.094 \times 10^{-12}\text{kg} \tag{K.14}$$

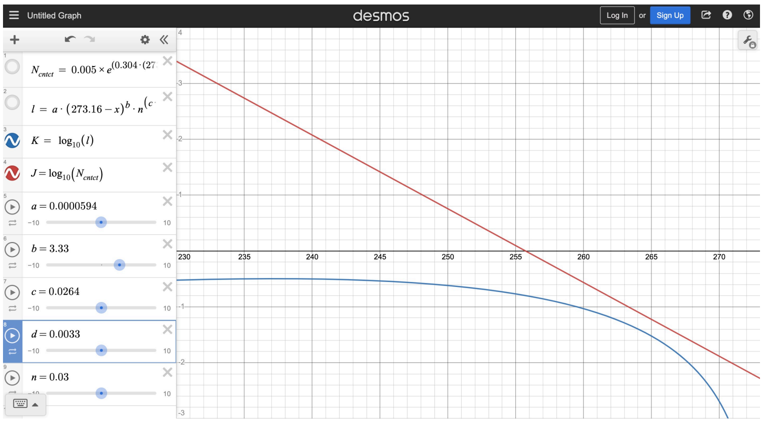

$N_{cntct} = 0.005 \times e^{(0.304\cdot(27$

$l = a\cdot(273.16-x)^b\cdot n^{(c\cdot$

$K = \log_{10}(l)$

$J = \log_{10}(N_{cntct})$

$a = 0.0000594$

$b = 3.33$

$c = 0.0264$

$d = 0.0033$

$n = 0.03$

Figure K.1. Deposition rates (L^{-1}) compared for Cooper curve (Morrison, red) and DeMott curve (ISHMAEL, blue). Y axis is $\log_{10}$ scale. Analysis produced via the Desmos Studio (2023) graphing calculator.

Contact freezing

Contact freezing is accounted for in Morrison by the Meyers et al. 1992 curve (their Equation 2.6) in a statistical approach derived from Brownian motion. The contact freezing nuclei concentrations are given as so:

$$N_{\text{contact}} = e^{(-2.80+0.262\times(273.15-T))} \tag{K.15}$$

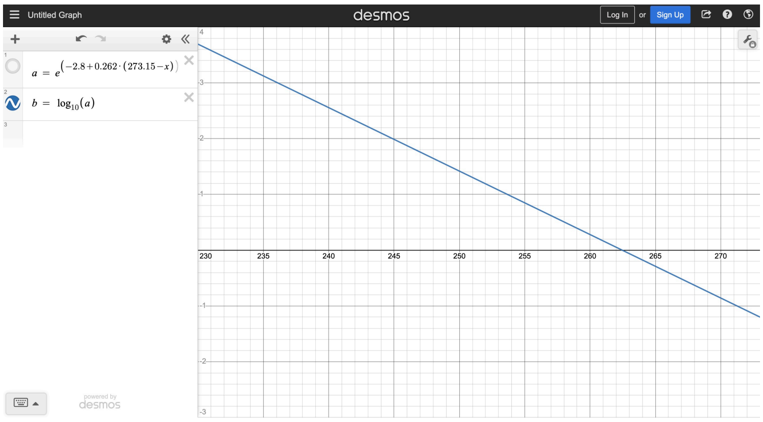

$a = e^{(-2.8+0.262\cdot(273.15-x))}$

$b = \log_{10}(a)$

Figure K.2. Number of contact nuclei (L^{-1}) used in Morrison (Meyers curve). Y axis is $\log_{10}$ scale.Analysis produced courtesy of the Desmos Studio (2023) graphing calculator.

The nuclei concentrations can then be used to determine the addition to ice:

$$Q_I \mathrel{+}= \frac{\pi^2 \rho_w D_a}{3} \times N_{\text{contact}} \times \frac{\Gamma(\kappa+5)}{\Gamma(\kappa+1)} \times \frac{N_C}{\lambda_C^4} \tag{K.16}$$

Where D_a is the diffusivity of aerosol,

Concluding Remarks

Given the compared nucleation parameterisations, some key differences can be observed:

In **homogeneous** nucleation:

- Morrison nucleates at cooler temperatures (-40°C) than ISHMAEL (-35°C).
- Morrison nucleates with smaller droplet mass mixing ratio (1×10^{-14}) than ISHMAEL $(1 \times 10^{-12}$ kg kg$^{-1})$

In **heterogeneous** nucleation:

- Immersion freezing of rain (Biggs) is identical in each scheme, but only Morrison has a Biggs formulation for cloud droplets.
- ISHMAEL has no contact nucleation. Morrison has a contact nucleation formulation that is temperature dependent. Cooler temperatures can produce an additional 10^3 of possible ice generating contact nuclei.
- Deposition is parameterised differently in each scheme. Comparison indicates that concentrations are comparable at temperatures warmer than approximately -20 °C, but lower than this Morrison can produce up to 3 orders more ice nuclei per litre.

Therefore, it is expected that Morrison is the more likely to produce ice nuclei, given the more numerous and more lucrative pathways available in the scheme. Additionally, ISHMAEL might suffer from drastically limited nucleation at warm temperatures due to dependence on deposition which occurs at typically cooler temperatures. This may be overcome by Biggs immersion freezing, but the lack of cloud droplet Biggs mechanism indicates that ISHMAEL is more dependent on rain droplet forming processes, such as coalescence, to produce ice than Morrison.

Appendix L

Morrison and ISHMAEL Microphysics Tendency Formulations

L.1 Morrison Scheme

The following is taken from Morrison et al. (2005) which states:

> *The graupel parameterisation follows that described by Ikawa and Saito (1991), Murakami (1990) and Reisner et al. (1998).*

This began a review of the graupel tendency equations in each paper to determine which is used by Morrison. All tendency equations differ slightly, with Ikawa and Saito (1991) offering the most terms in both number concentration and mixing ratio. The mixing ratio equations are listed below.

L.1.1 Referenced Tendency Equations

Murakami (1990) Tendency Equation

$$\begin{aligned}\frac{\partial Q_G}{\partial t} =& ADV(Q_G) + D(Q_G) + PR_G && \text{(L.1)}\\ &+ PG + VD_{VG} + CN_{SG} + CL_{IR} + CL_{RI} && \text{(L.2)}\\ &+ (CL_{SR} + CL_{RS})(1 - \alpha_{RS}) + FR_{RG} - ML_{GR} - SH_{GR} && \text{(L.3)}\end{aligned}$$

Where the subscripts G, S, R, V, I are graupel, snow, rain, vapour, and cloud ice. Process X_{ab} indicates a depleting and b growing.

$ADV(Q_G)$ is the advection of water.
$D(Q_G)$ is turbulent diffusion.

PR_G is graupel precipitated.
PG is the wet and dry growth of graupel by accretion.
VD_{VG} is growth or loss of graupel by vapour deposition and eevaporation (sublimation).
CN_{SG} is conversion of snow to graupel.
CL_{RI} is collection of rain by cloud ice with corresponding symmetric term.
CL_{RS} is collection of rain by snow with corresponding symmetric term.
$(1-\alpha_{RS})$ is the ratio at which collisions between rain and snow result in graupel.
FR_{RG} is freezing of rain to graupel.
ML_{GR} is melting of graupel to rain.
SH_{GR} is liquid water shedding from graupel to rain.

Ikawa and Saito (1991) Tendency Equation

$$\frac{\partial Q_G}{\partial t} = -ADV(Q_G) + D(Q_G) - P_{\text{gprc}} \tag{L.4}$$

$$+ P_{\text{gdep}} + (P_{\text{scng}} + P_{\text{g.sacw}}) + P_{\text{gacr}} + P_{\text{gacw}} + P_{\text{gaci}} + (P_{\text{iacr}} + P_{\text{raci}}) \tag{L.5}$$

$$+ (P_{\text{g.sacr}} + P_{\text{g.racs}}) + P_{\text{gfzr}} + (P_{\text{icng}} + P_{\text{g.iacw}}) - \delta P_{\text{gmlt}} \tag{L.6}$$

Where the subscripts G, S, R, V, I, W are graupel, snow, rain, vapour, cloud-ice and cloud-water. Source term P_{abcd} indicates growth of a and depletion of d during process bc.

$ADV(Q_G)$ is the advection of water.
$D(Q_G)$ is diffusion due to sub-grid-scale turbulence.
P_{gprc} is graupel precipitated.
P_{gdep} is depositional growth of graupel.
$(P_{\text{scng}}$ is snow converted to graupel.
$P_{\text{g.sacw}}$ is the generation of graupel due to accretion of cloud-water by snow.
P_{gacr} is the accretion of rain by graupel.
P_{gacw} is the accretion of cloud water by graupel.
P_{gaci} is the accretion of cloud-ice by graupel.
P_{iacr} is the accretion of rain by cloud-ice, and corresponding symmetric term.
$P_{\text{g.sacr}}$ is the generation of graupel due to accretion of rain by snow, and corresponding symmetric term.
P_{gfzr} is the freezing of rain to form graupel.
P_{icng} is cloud-ice converted to graupel.
$P_{\text{g.iacw}}$ is the generation of graupel due to accretion of cloud-water by ice.
P_{gmlt} is the melting of graupel.

Reisner et al. (1998) Tendency Equation

$$\frac{\partial(p^* Q_G)}{\partial t} = - ADV(p^* Q_G) + D(p^* Q_G) - P_{\text{gprc}} \tag{L.7}$$

$$+ p^*(P_{\text{gdep}} + P_{\text{scng}} + P_{\text{g.sacw}} + P_{\text{gacw}} + P_{\text{gacr}} + P_{\text{iacr}} + P_{\text{raci}} \tag{L.8}$$

$$+ P_{\text{g.sacr}} + P_{\text{g.racs}} + P_{\text{gfzr}} + P_{\text{icng}} + P_{\text{g.iacw}} - \delta P_{\text{gmlt}}) \tag{L.9}$$

Where the subscripts and definitions are identical to Ikawa and Saito (1991). This equation is almost identical to the Ikawa and Saito tendency equation, but includes a multiplication by p^*, which is the difference between the surface pressure and pressure at the top.This equation also does not include the term P_{gaci}, implying graupel does not accrete cloud-ice.

The equations are very similar, but verifying that each is identical requires that each term is compared individually. Instead, the tendency equation in the Morrison code was examined and compared to the three equations above.

L.1.2 In-Code Morrison Tendency Equation

The following equation is primarily taken from lines 1984 and 3196. There are no definitions in-code so this is something of a best-guess.

$$\begin{aligned} \text{QG3DTEN} =& [\text{QG3DTEN}] + \text{PRACG} + \text{PSACWG} + \text{PGSACW} \\ & + \text{PGRACS} + \text{PRDG} + \text{EPRDG} + \text{MNUCCR} + \text{PIAC} \\ & + \text{PRACI} + \text{PSACR} + \text{PGMLT} + \text{EVPMG} \end{aligned}$$

Where QG3DTEN is the previous graupel tendency at time $t - dt$.
PRACG is the accretion of rain by graupel.
PSACWG is the accretion of water droplets by graupel.
PGSACW is the graupel converted from snow accreting water droplets.
PGRACS is the graupel converted from rain collected by snow.
PRDG is graupel growth by vapour deposition.
EPRDG is graupel loss due to sublimation.
MNUCCR is ice generation by immersion.
PIACR is the accretion of rain by cloud ice, and PRACI is the symmetric term.
PSACR is the accretion of rain by snow.
PGMLT is the depletion of graupel due to melting.

EVPMG is the melting and subsequent evaporation of graupel.
The term formatting is similar to Ikawa and Saito (1991) and Reisner et al. (1998) but has 12 production terms compared to 14 and 13 respectively. Some of the above terms have references which have allowed them to be traced back to a selection of papers: Rutledge and Hobbs (1984), Ikawa and Saito (1991), Murakami (1990), Reisner et al. (1998), Y.-L. Lin et al. (1983), Morrison and Pinto (2005), Bigg (1953).

Equivalent terms, and references are listed below where available.

PRACG → P_{racs} and or P_{gacr} (Ikawa and Saito 1991) Equation 11-58
PSACWG → P_{gacw} (Reisner et al. 1998) Equation A.59
PGSACW→ $P_{\mathrm{g.sacw}}$ and or P_{scng} (Ikawa and Saito 1991) Equation 11-46
PGRACS→ $P_{\mathrm{g.racs}}$ (Ikawa and Saito 1991) Equation 11-63 and Reisner et al. (1998) Equation A.50
PRDG → P_{gdep} (Reisner et al. 1998) Equation A.36
EPRDG → -PRDG
MNUCCR → P_{gfzr} (Bigg 1953) p692 and Ikawa and Saito (1991) Equation 11-67 from Y.-L. Lin et al. (1983) Equation 45.
PIACR → P_{iacr} (Reisner et al. 1998) from Rutledge and Hobbs (1984) Equation A.7
PSACR → P_{sacr} and or P_{raci} (Ikawa and Saito 1991) Equation 11-57
PGMLT→. P_{gmlt} (Rutledge and Hobbs 1984) Equation A.18
EVPMG → Similar to 5
Leaving P_{gaci}, P_{icng}, and $P_{\mathrm{g.iacw}}$ from the Ikawa and Saito equation. all three involve cloud ice conversion to graupel. It is assumed that Morrison does not allow cloud-ice graupel relations, and instead cloud-ice grows until reaching snow, then snow converts to graupel.

L.1.3 Equation Set for Production Terms

The production terms represent equations that determine their growth or decay. The equations listed below are adapted from the Morrison code and the relevant references.

PRACG

The correct equation for PRACG is below following from the similarity of the rain and snow accretion process in Ikawa and Saito (1991) and the full derivation by Wisner et al. (1972):

$$\mathrm{PRACG} = \pi^2 E_{rg} \sqrt{(\alpha \bar{U}_r - \beta \bar{U}_g^2) + \gamma \bar{U}_g \bar{U}_r} \frac{\rho_w}{\rho} N_{r0} N_{g0} \left(\frac{5}{\lambda_g^6 \lambda_r} + \frac{2}{\lambda_g^5 \lambda_r^2} + \frac{5}{\lambda_g^4 \lambda_r^3} \right)$$

However the code erroneously has a factor of air density multiplication instead of division. This might be a bug, as explained below this term is of the order $10^0 - 10^{-1}$ which suggests that the difference between equation $X \times \rho$ and $\frac{X}{\rho}$ is $\rho^2 \sim 10^0 - 10^{-2}$ i.e. a possible underestimation. NOTE: The above correct equation is assumed in the following passage.

Where E_{rg} is the collection efficiency of rain and graupel = 1
U_r and U_g are the mass weighted mean terminal velocities of rain and graupel respectively.
α and β and γ are constants with value 1.2, 0.95 and 0.08.
ρ_w is water density, $= 997$
ρ is air density = $P\,[\text{Pa}]/(R\,[\text{J kg}^{-1}\text{ K}^{-1}] \times T\,[\text{K}])$ which has order $\simeq 10^4/(10^2 \times 10^2) \sim 10^0$
N_{r0} and N_{g0} are parameters of rain and graupel size distributions.
λ_g and λ_r are slope parameters in graupel and rain size distributions respectively.
Hence,

$$\text{PRACG}(N_r, N_g, Q_r, Q_g)$$

Scale analysis for the above terms has been conducted. The lambda terms are:

$$\lambda_r = (\frac{\pi \rho_w N_R}{Q_R})^{\frac{1}{3}} \simeq (\frac{10^0 10^2 N_R}{Q_R})^{\frac{1}{3}} \simeq (10^0)\left(\frac{N_R}{Q_R}\right)^{\frac{1}{3}}$$

$$\lambda_g = \left(\Gamma(4)\frac{(\rho_g \frac{\pi}{6})N_G}{Q_G}\right)^{\frac{1}{3}} \simeq \left(\frac{(\rho_g \pi)N_G}{Q_G}\right)^{\frac{1}{3}} \simeq (10^0)\left(\frac{N_G}{Q_G}\right)^{\frac{1}{3}}$$

Therefore:

$$\lambda_g^6 \lambda_r = \left(\frac{N_G}{Q_G}\right)^2 \left(\frac{N_R}{Q_R}\right)^{\frac{1}{3}}$$

$$\lambda_g^5 \lambda_r^2 = \left(\frac{N_G}{Q_G}\right)^{\frac{5}{3}} \left(\frac{N_R}{Q_R}\right)^{\frac{2}{3}}$$

$$\lambda_g^4 \lambda_r^3 = \left(\frac{N_G}{Q_G}\right)^{\frac{4}{3}} \left(\frac{N_R}{Q_R}\right)$$

The fall speed terms are:

$$\bar{U}_r = \frac{(\frac{\rho_{SU}}{\rho})^{0.54} A_R \Gamma(4 + B_R)}{6\lambda_R^{B_R}}$$

$$\bar{U}_g = \frac{(\frac{\rho_{SU}}{\rho})^{0.54} A_G \Gamma(4 + B_G)}{6\lambda_G^{BG}}$$

Where $A_R = 841.99667$, $B_R = 0.8$, $\rho_{SU} = 1.08369957$, $B_G = 0.37$, $A_G = 19.3$

The N size distribution parameters are:

$$N_{r0} = \frac{\lambda_r^4 Q_R}{(\pi \rho_w)} \simeq \frac{Q_R N^{\frac{1}{3}}}{10^0 10^2 Q_R^{\frac{1}{3}}} \simeq Q_R^{\frac{2}{3}} N^{\frac{1}{3}} \times 10^{-2}$$

$$N_{g0} = \frac{6\lambda_g^4 Q_G}{\Gamma(4)\rho_g \pi} \simeq \frac{((\frac{N_G}{Q_G})^{\frac{1}{3}})^4 Q_G}{10^2} \simeq \left(\frac{N_G^4}{Q_G}\right)^{\frac{1}{3}} \times 10^{-2}$$

Overall, $PRACG$ can be simplified to a proportionality relation in Q and N:

$$\begin{aligned} \text{PRACG} =& 10^1 10^0 \sqrt{(10^0 \bar{U}_r - 10^0 \bar{U}_g^2) + 10^{-1} U_g U_r} 10^3 N_{r0} N_{g0} \times \\ & \left(5 \times \left(\frac{Q_G}{N_G}\right)^2 \left(\frac{Q_R}{N_R}\right)^{\frac{1}{3}} + 2 \times \left(\frac{Q_G}{N_G}\right)^{\frac{5}{3}} \left(\frac{Q_R}{N_R}\right)^{\frac{2}{3}} + 5 \times \left(\frac{Q_G}{N_G}\right)^{\frac{4}{3}} \left(\frac{Q_R}{N_R}\right)\right) \end{aligned}$$

PSACWG

$$\text{PSACWG} = \frac{\pi a_g Q_w E_{wg} N_{o,g}}{4} \frac{\Gamma(b_g + 3)}{\lambda_g^{b_g+3}}$$

Where a_g is a constant for fall speed relationship for graupel = 19.3.
Q_w is cloud water mixing ratio.
E_{wg} is the collection efficiency for graupel collecting cloud water = 1.
$N_{o,g}$ is the slope intercept for graupel size distribution.
Γ is the gamma function.
b_g is is a constant for fall speed relationship for graupel = 0.37.
λ is the slope parameter in the graupel size distribution.
Hence,

$$\text{PSACWG}(Q_w, N_g, Q_g)$$

PGSACW

$$\text{PGSACW} = \alpha 2\Delta t \frac{3\rho_0 \pi N_{s0} (\rho Q_w)^2 E_{si}^2 a_s^2 \Gamma(2b_s + 2)}{8\rho(\rho_g - \rho_s)\lambda_s^{2b_s+2}}$$

Where α is a constant with value 1.2.
ρ_0, ρ, ρ_g and ρ_s are air density at sea level, air density, graupel density, and snow density respectively.
N_{s0} is the parameter of snow size distribution.

Q_w is the cloud water mixing ratio.
E_{sw} is the collection efficiency of snow for cloud water = 1
a_s is a fall speed constant for snow = 17
b_s is a fall speed constant for snow = 0.5 λ_s is a slope parameter in snow size distribution.
Hence,

$$\text{PGSACW}(Q_w, N_s, Q_s)$$

PGRACS

$$\text{PGRACS} = (1 - \alpha_{rs}) * \text{PRACS}$$

$$\alpha_{rs} = \frac{\rho_s^2 \left[\frac{4}{\lambda_s}\right]^6}{\rho_s^2 \left[\frac{4}{\lambda_s}\right]^6 + \rho_w^2 \left[\frac{4}{\lambda_r}\right]^6}$$

$$\text{PRACS} = \pi^2 E_{rs} \sqrt{(\alpha U_r - \beta U_s^2) + \gamma U_s U_r} \frac{\rho_s}{\rho} N_{r0} N_{s0} \left(\frac{5}{\lambda_s^6 \lambda_r} + \frac{2}{\lambda_s^5 \lambda_r^2} + \frac{5}{\lambda_s^4 \lambda_r^3} \right)$$

Where α_{rs} is the ratio for which rain-snow collision generates snow (not graupel).
ρ_s and ρ are snow density and air density.
λ_s and λ_r are slope parameters in snow and rain size distributions respectively.
E_{rs} is the collection efficiency of rain and snow = 1
U_r and U_s are the mass weighted mean terminal velocities of rain and snow respectively.
α and β and γ are constants with value 1.2, 0.95 and 0.08.
N_{r0} and N_{s0} are parameters of rain and snow size distributions.
Hence,

$$\text{PGRACS}(N_r, Q_r, N_s, Q_s)$$

PRDG

$$\text{PRDG} = \frac{2\pi N_{o,g}(S_i - 1)}{A' + B'} \left[\frac{0.78}{\lambda_g^2} + 0.31 \left(\frac{a_g \rho}{\mu} \right)^{\frac{1}{2}} \frac{\Gamma(b_g/2 + 5/2)}{\lambda_g^{b_g/2+5/2}} \right]$$

Where $N_{o,g}$ is the slope intercept in graupel size distribution.
S_i is the saturation ratio over ice.
A' and B' are the constants in Bigg's equation.
λ_g is the slope parameter in graupel size distribution.
a_g is a fall speed constant for graupel = 19.3.
ρ is the air density.
μ is the dynamic viscosity of air.
b_g is a fall speed constant for graupel = 0.37.

Hence,

$$\text{PRDG}(N_g, Q_g, Q_v)$$

EPRDG

$$\begin{gathered}\text{EPRDG} = -\text{PRDG if PRDG} < 0\\ 0 \text{ if PRDG} \geq 0\end{gathered}$$

MNUCCR

$$\text{MNUCCR} = 20\pi^2 B' N_{0r}\left(\frac{\rho_w}{\rho}\right) \times (\exp\left[A'(T_0 - T)\right] - 1)\lambda_r^{-7}$$

Where B' and A' are Bigg's constants.
N_{0r} intercept parameter of raindrop distribution.
ρ_w and ρ are density of water and air respectively.
T_0 and T are the melting temperature and in-cloud temperature.
λ_r is the slope parameter in the raindrop size distribution.
Hence,

$$\text{MNUCCR}(N_r, Q_r, T)$$

PIACR

$$\text{PIACR} = N_i E_{ir}\frac{\pi^2}{24}\rho_w N_{0r}\left(\frac{P_0}{P}\right)^{0.4}\left[\frac{a_0\Gamma(6)}{\lambda_r^6} + \frac{a_1\Gamma(7)}{\lambda_r^7} + \frac{a_2\Gamma(8)}{\lambda_r^8} + \frac{a_3\Gamma(9)}{\lambda_r^9}\right]$$

Where N_i is number concentration of cloud ice crystals.
E_{ir} is the rain and cloud ice collection efficiency = 1
ρ_w and ρ are density of water and air respectively.
N_{0r} is the intercept value in raindrop size distribution.
P_0 and P are a constant ($\approx 10^6$) and pressure respectively.
a_0 is the coefficient in polynomial fall speed relation for rain.
λ_r is the slope parameter in the raindrop size distribution.
Hence,

$$\text{PIACR}(N_i, N_r, Q_r, P)$$

PSACR

$$\text{PRACI} = \frac{\pi}{4}\rho Q_i E_{ir}\left(\frac{P_0}{P}\right)^{0.4}\left[\frac{a_0\Gamma(3)}{\lambda_r^3} + \frac{a_1\Gamma(4)}{\lambda_r^4} + \frac{a_2\Gamma(5)}{\lambda_r^5} + \frac{a_3\Gamma(6)}{\lambda_r^6}\right]$$

Where ρ is the density of air.

E_{ir} is the rain and cloud ice collection efficiency = 1

P_0 and P are a constant ($\approx 10^6$) and pressure respectively.

a_{0-3} is the coefficient in polynomial fall speed relation for rain.

λ_r is the slope parameter in the raindrop size distribution.

Hence,

$$\text{PSACR}(Q_i, N_r, Q_r)$$

PGMLT

$$\text{PGMLT} = -\frac{2\pi}{L_f}K_a(T - T_0)N_{0g}\left[\frac{0.78}{\lambda_g^2} + 0.31\left(\frac{\bar{a}\rho}{\mu}\right)^{\frac{1}{2}}\left(\frac{P_0}{P}\right)^{0.2}\frac{\Gamma(\bar{b}/2 + 5/2)}{\lambda_g^{\bar{b}/2+5/2}}\right]$$

Where L_f is the latent heat of fusion.

K_a is the thermal conductivity of air.

T_0 and T are the melting temperature and in-cloud temperature.

N_{0g} is the intercept value in graupel size distribution.

λ_g is the slope parameter in the graupel size distribution.

$\bar{a}$ and $\bar{b}$ are constants in the graupel fall speed relation 19.3 and 0.37.

ρ is the density of air.

μ is the dynamic viscosity of air.

P_0 and P are a constant ($\approx 10^6$) and pressure respectively.

Hence,

$$\text{PGMLT}(N_g, Q_g, P)$$

EVPMG

Rutledge and Hobbs (1984) Equation A19

$$\text{EVPMG} = \frac{2\pi N_{o,g}(S_i - 1)}{A' + B'}\left[\frac{0.78}{\lambda_g^2} + 0.31\left(\frac{\bar{a}\rho}{\mu}\right)^{\frac{1}{2}}\left(\frac{P_0}{P}\right)^{0.2}\frac{\Gamma(\bar{b}/2 + 5/2)}{\lambda_g^{\bar{b}/2+5/2}}\right]$$

Where $N_{o,g}$ is the slope intercept in graupel size distribution.

S_i is the saturation ratio over ice.

A' and B' are the constants in Bigg's equation.
λ_g is the slope parameter in graupel size distribution.
$\bar{a}$ and $\bar{b}$ are constants in the graupel fall speed relation 19.3 and 0.37.
ρ is the air density.
μ is the dynamic viscosity of air.
Hence,

$$\text{EVPMG}(N_g, Q_g, P)$$

Complete Morrison Graupel Tendency Dependencies

$$\text{QG3DTEN}(N_g, Q_g, N_r, Q_r, N_i, Q_i, Q_s, N_s, Q_v, Q_w, T, P)$$

L.2 ISHMAEL Scheme

The ISHMAEL scheme has no graupel category. Instead, only 3 ice categories exist; columnar or planar nucleated ice, and aggregates. Graupel is then classified by the qualities of the ice: effective density ρ_I, aspect ratio ϕ_I, ice mass-weighted fall speed ν_{t_I}. Therefore to understand the growth of graupel, one needs to understand the growth of the ice variables.

L.2.1 Fall Speed

Fall speed vt_I is denoted as the variable `DIAG_VMI3D_1/2/3`. In calculations of the 1d grid the variable used is `vmi1d(ICE1/2/3, k)`, and then switched to `vtrmi1` on line 2632.

Taken from Harrington et al. (2013) Equation B36:

$$vt_I = \frac{N_{\text{Re}}(a_n)\eta_a}{\rho_a L(a_n)} \frac{\Gamma(\nu + b_n b_m - b_l + 2 + \delta_*)}{\Gamma(\nu + 2 + \delta_*)}$$

Where,

$$N_{\text{Re}} = a_m X^{b_m} = a_m x_n^{b_m} a^{b_n b_m}$$

with a_m and b_m provided as best fit coefficients in Mitchell (1996).
X is the Best number.
$x_n = x_B(4/3)[(\pi\rho_i\alpha_* a_l^2)/\alpha_*\pi]$
$x_B = \frac{2(\rho_i - \rho_) g \rho_a q_e^{3/4}}{\rho_i \eta_a^2}$ NOTE x_B is included in x_n in the code.
q_e is the projected area of the crystal onto a spheroid.
η_a is the dynamic viscosity.
L is an appropriate particle length scale:

$L = 2a$ for plates
$L = 2\sqrt{(ac)}$ for columns
$L = 2r$ for a sphere.
ρ_a is the density of air.
ν is the distribution shape parameter.
$b_n = \delta_* + 2 + 2b_l - b_a$
$b_l = 1$ for plate-like crystals and $b_l = (\delta_* + 2)/3$ for columnar crystals.
$a_l = 2$ for plate-like crystals and $a_l = 2\alpha_*^{1/3}$ for columnar crystals.
$\alpha_* = a_0^{1-\delta_*}$
b_a is Best fall speed constant.
δ_* is a time average of the inherent growth ratio over the particle growth history, also described in J.-P. Chen and Lamb (1994). This is usually fixed in bulk models but can evolve in ISHMAEL. Is a function of a_n and c_n.

a_n is the characteristic a-axis length that is related to the mean a-axis length (see Harrington et al. (2013) section 3e):

$$a_n(t) = \frac{\rho_a}{\nu N_i} A(t)$$

Where N_i is number concentration. A is the projected area of the spheroid given in Sulia and Harrington (2011).
Hence v has the dependencies:

$$vt_I = vt_I(\rho_i, c_n, a_n)$$

L.2.2 Effective Density

Effective density ρ_I is denoted as the variable `DIAG_RHOPO3D_1/2/3`. In calculations of the 1d grid the variable used is `rhopo1d(ICE1/2/3, k)`. The evolution of density comes from a particle density ρ_i and an additional accumulated mass with density ρ_{rime} amongst other processes. *rhobar* is modified by several processes, and is therefore a function of several variables. These are:

$$\rho_i = \rho_i(\mathtt{q}_i, \mathtt{prd}(cc), \mathtt{rhodepout}, \mathtt{prd}(cc), \mathtt{rhorimeout}(cc), \mathtt{qmlt}, \mathtt{nucfrac})$$

where:
$\mathtt{q}_i$ is ice mass mixing ratio
`prd` is vapour growth rate
`rhodepout` is the ice effective density from deposition
`prd` is riming growth rate $= (\mathtt{iwcfr} - \mathtt{iwci}) * \mathtt{i}_{\mathtt{rhoair}}(k) * \mathtt{i}_{dt}$
`qmlt` is the mass melting rate

Temperature Range (°C)	*rimec1*
-5 > T ≥ -10	$\beta_{T_l} \times (0.0066 - 0.012) + 0.012$
-10 > T ≥ -15	$\beta_{T_l} \times (0.005 - 0.0066) + 0.0066$
-15 > T ≥ -20	$\beta_{T_l} \times (0.004 - 0.005) + 0.005$
-20 > T ≥ -30	$\beta_{T_l} \times (0.0036 - 0.004) + 0.004$
-30 > T	0.0036

Table L.1. Parameterised relationship between temperature (°C) and cloud-ice rime density (kg m^{-3}) featured in the ISHMAEL scheme, described by (Jensen et al. 2017) and adapted from measurement by Macklin (1962). The parameter β_{T_l} is a function of temperature shown in Equation L.2.2.

`nucfrac` is ice added through nucleation
`rhorimeout` is the ice effective density from riming
Many of these terms will be described in the equation set.

ρ_{rime} is derived from Macklin (1962) (their Figure 6) which gives ρ_{rime} as a function of particle radius and impact velocity. ISHMAEL calculates an average value of $r_l v_0$ over the riming rate, and interpolates this to ambient air temperature. This is calculated for rain and cloud-water in look-up tables, `itabr` and `itab` respectively, read once in the `jensen_ISHMAEL_init` subroutine.

Further examination of the ISHMAEL code shows that the variable `rhopold(ICE1/2/3, k)` is set equal to `rhobar(cc)` on line 2618. `rhobar(cc)` is a function of `rhorimeout(cc)` (Line 1892), which includes the Macklin parameterisation, specifically defined in lines 1286:

$$\texttt{rhorimeout} = \texttt{rhobar} \times \frac{vi}{vfr} + \left(\texttt{gdentotal} * \left(1 - \frac{vi}{vfr}\right)\right)$$

Where $gdentotal$ is the total rime density from ice-cloud-water ice-rain interactions. This is a function of the riming rate `rimesum(`$n_i, n_c/n_r$`)` as well as `gdenavgr` (rain) and `gdenavg` (cloud-water) defined as:

$$\texttt{gdenavgr}(cc) = (1000. * (0.8 * \text{tanh}(rimec1 * qi\_qr\_nrd(cc)/qi\_qr\_nrm(cc)) + 0.1))$$

On line 1247 and

$$\texttt{gdenavg}(cc) = (1000. * (0.8 * \text{tanh}(\texttt{rimec1} * qi\_qc\_nrd(cc)/qi\_qc\_nrm(cc)) + 0.1))$$

on line 1202.
`qi_qr_nrd` is related to the normalised rime density for rain-ice interactions.
`qi_qr_nrm` is the normalised riming rate.
`qi_qc_nrd` is related to the normalised rime density for cloud water-ice interactions.
`qi_qc_nrm` is the normalised riming rate.
and `rimec1` is the ice density parameterised from Macklin (1962).

$$\beta_{T_L} = \frac{abs((T - T_0)) - T_l)}{T_l - T_h} \tag{L.10}$$

T = ambient air temperature (K).
$T_0 = 273.15K$ temperature at 0°C
T_l = Lower temperature limit absolute magnitude
T_h = higher temperature limit absolute magnitude

L.2.3 Aspect Ratio

Aspect ratio ϕ_I is denoted as the variable `DIAG_PHII3D_1/2/3`. In calculations of the 1d grid the variable used is `phii1d(ICE1/2/3, k)`. Line 2617 states:

$$phii1d = cni(cc)/ani(cc) \times gamma\_tab(gi) \times i\_gammnu$$

cni(cc) = characteristic c-axis size of ice.
ani(cc)= characteristic a-axis size of ice.
$cni = ci/ni$ and $ani = ai/ni$ grows as dictated by the production rates, where ni is the ice number mixing ratio. $ai = a^2c$ is the ice mixing ratio, and $ci = c^2a$
gamma_tab(gi)= is a tabulated gamma function, where *gi* is the index for the gamma(NU) lookup.
$gi(gamma\_arg(NU = 4, deltastr)$.
$i\_gammnu = 1/\Gamma(\nu) = 1/6$ due to $NU = 4$
$deltastr(cc) = log(cni(cc)) - log(ao))/(log(ani(cc)) - log(ao))$
Where ao is the ISHMAEL parameter $\alpha_* = a_0^{1-\delta_*} = 0.1 \times 10^{-6}$

Hence, the multiplying factor is a probability density function given by the general form:

$$PDF = \frac{X^{\nu-1}e^{-\nu}}{\Gamma(\nu)}$$

but more specifically, from Harrington et al. (2013)

$$n(a) = \frac{N_i}{\Gamma(\nu)} \left(\frac{a}{a_n}\right)^{\nu-1} \frac{1}{a_n} \exp\left(-\frac{a}{a_n}\right)$$

Where $X = \frac{a}{a_n} = ani$, and ν is the shape parameter. Comparing to the conventional gamma distribution cited in Heymsfield et al. (2002):

$$N = N_{0\Gamma} D^{\mu} e^{-\lambda_\Gamma D}$$

Then,

$$N_{0\Gamma} \equiv \frac{N_i}{\Gamma(\nu)a_n}$$
$$D \equiv \left(\frac{a}{a_n}\right)$$
$$\mu \equiv (\nu - 1)$$
$$\lambda_\Gamma \equiv 1$$

So the population shape distribution is determined by a single size spectrum and radius. So all dependencies can be summarised by the following:

$$phii1d = phii1d(c_i, n_i, a_i)$$

where the dependent parameters may belong to functions (Gamma, Log..).

L.2.4 Equation Set for Production Terms

ISHMAEL uses growth equations for ice that result in bulk changes to the variables ϕ_I, ρ_{rime} and vt_I via their dependencies $(ci, ni, ai, r_l, v_0, T,)$.

For a single ice-particle, the mass tendency equation has a general from for several processes (e.g. vapour growth, riming and melting), that is:

$$\left.\frac{dm_i}{dt}\right|_x = \rho_x \left.\frac{dV_i}{dt}\right|_x$$

Where x is the process, V_i is the ice particle volume, ρ_x is the growth density (the mass added by growth process x, distinct from the ice particle density ρ_i). ρ_x is described later, i.e. as ρ_{rime} and $\rho_{\text{deposition}}$.

To describe the axial growth rates, J.-P. Chen and Lamb (1994) is used, which relates a_i and c_i during vapour growth:

$$\left.\frac{dc_i}{da_i}\right|_{\text{dep}} = \delta_{\text{dep}}(T)\phi_i$$

Where δ_{dep} is the inherent growth ratio derived from laboratory measurements.

$$\text{Crystal Shape Tendency} = \begin{cases} \text{Prolate}, & \text{if } \delta_{\text{dep}} > 1 \\ \text{Oblate}, & \text{if } \delta_{\text{dep}} < 1 \\ \text{Constant } \phi, & \text{if } \delta_{\text{dep}} = 1 \end{cases}$$

This can be expanded to all processes if δ_x is correctly parameterised for each. The change in aspect ratio can be linked to volume by:

$$\frac{d\phi_i}{\phi_i} = \left(\frac{\delta_x - 1}{\delta_x + 2}\right) \frac{dV_i}{V_i}$$

This framework for single ice particles is expanded to the bulk scheme ISHMAEL. To remove the potential loss of variation between ice species, two ices are generated at the nucleation stage as planar or columnar, allowing the coexistence of two ice species in a grid cell. These ices are however free to evolve between oblate or prolate over time. A third ice species, aggregates, are distinct from ices 1 and 2 in order to preserve the ice qualities which are changed drastically during aggregation.

To conserve ice shape between transport, volume mixing ratios are calculated. These, along with mass mixing ratios, present conserved quantities during grid cell interchange.

The modified gamma function is used to model the particle population, and is a function of a-axis length only due to the relation:

$$c_i = a_0^{1-\delta_*} a_i^{\delta_*}$$

That relates a and c. a_0 is the initial (nucleation) size, and δ_* is the average of various δ_x that cause shape evolution. This relation allows the mass mixing ratio and volume mixing ratio to be entirely linked. i.e.

$$q_i = \frac{1}{\rho_a} \int_0^\infty m_i(a_i, c_i) n(a_i) da$$

$$m_i = \rho_i \frac{4}{3} \pi a_i^2 c_i$$

$$n(a) = \frac{N_i}{\Gamma(\nu)} \left(\frac{a_i}{a_n}\right)^{\nu-1} \frac{1}{a_n} \exp\left(-\frac{a_i}{a_n}\right)$$

Hence with substitution of the above equations:

$$q_i = \frac{1}{\rho_a} \int_0^\infty [\rho_i \frac{4}{3} \pi a_i^2 (a_0^{1-\delta_*} a_i^{\delta_*})][\frac{N_i}{\Gamma(\nu)} \left(\frac{a_i}{a_n}\right)^{\nu-1} \frac{1}{a_n} \exp\left(-\frac{a_i}{a_n}\right)]da$$

leading to

$$q_i = \rho_i \frac{N_i}{\rho_a} \frac{4}{3} \pi a_0^{1-\delta_*} \frac{1}{\Gamma(\nu)} \int_0^\infty [a_i^2 (a_i^{\delta_*})][\left(\frac{a_i}{a_n}\right)^{\nu-1} \frac{1}{a_n} \exp\left(-\frac{a_i}{a_n}\right)]da$$

Recall the definition of the Gamma function:

$$\Gamma(\nu) = \int_0^\infty x^{\nu-1} e^{-x} dx$$

In this case:

$$\Gamma(\nu+2+\delta_*) = \int_0^\infty x^{\nu+1+\delta_*} e^{-x} dx$$

Finally:

$$q_i = \rho_i \frac{N_i}{\rho_a} [(4/3)\pi a_0^{1-\delta_*} a_n^{2+\delta_*}] \frac{\Gamma(\nu+2+\delta_*)}{\Gamma(\nu)}$$

This the mass is related to axis size in a similar manner to conventional $m - D$ relationships, but in this case has environmental evolution. Earlier stated equations for ice particles can be expanded to the bulk population:

$$\frac{dc_n}{da_n} = \delta_x \frac{c_n}{a_n}$$

and

$$c_n = a_0^{1-\delta_*} a_n^{\delta_*}$$

Thus the two volume relations can be stated:

$$\vartheta_I = \frac{N_I}{\rho_a} a_n^2 c_n$$

$$\psi_I = \frac{N_I}{\rho_a} a_n c_n^2$$

Conserved quantities in advection are $q_I(t), n_I(t), \vartheta_I, \psi_I$ which are used to calculate $a_n(t), c_n(t)$ and $\delta_*(t)$.

L.2.5 Ice microphysical process rates

Vapour deposition and Sublimation

The change to the mass mixing ratio due to deposition or sublimation is:

$$\frac{dq_I}{dt_{\text{dep}}} = \frac{1}{\rho_a} \int_0^\infty 4\pi C_i G_i s_i n(a_i) da_i = \frac{N_I}{\rho_a} 4\pi C_i G_i s_i$$

C_i is the distribution averaged capacitance
G_i is an *effective* diffusion coefficient for vapour diffusion, thermal conduction and ventilation.

s_i is the ice supersaturation.
Number loss is:

$$\frac{dN_I}{dt_{\text{sub}}} = \frac{w_{\text{sub}}}{\Delta t} N_I$$

The weighting function w_x weights the mass loss with density changes.

Riming

The total bulk riming rate is employed when ices have a fall speed exceeding the droplets'. Following from Jensen and Harrington (2015b).

$$\frac{dq_I}{dt_{\text{rime}}} = \frac{1}{\rho_a} \sum_i \left. \frac{dm_r}{dt} \right|_i N_i = \frac{1}{\rho_a} \sum_i \left(\sum_l E_{il} A_g |v_i - v_l| m_l n_l \right)$$

E_{il} is the collision efficiency from Jensen and Harrington (2015b) Equation 6
A_g geometrical cross sectional area for collision
v_i is the ice particle fall speed.
v_l is the liquid drop fall speed
m_l is the mass of liquid.
n_l is the number concentration of liquid drops
N_i the number concentration of ice particles in bin i
In this case, δ_{rime} is parameterised such that riming allows oblate ice to evolve towards an aspect ratio of 0.8 found in observations, and prolate ice the inverse of this 1.25. During wet growth, there is no axial growth and water is assumed to grow the mass mixing ratio. Once this ice reaches the set density of bulk ice, soaking ceases and axial growth occurs.

Melting

Equations for melt-rate are largely based on work by Lamb and Verlinde (2011) Equation 8.85 which reads:

$$\frac{dm}{dt} = 4\pi f_h k_{T,\text{air}} r_p (T_\infty - T_{\text{sfc}}) + 4\pi l_v f_v D_v r_p (\rho_{v,\infty} - \rho_{v,\text{sfc}})$$

and integrated in the form by Kong and Yau (1997):

$$ML_{ir} = \frac{2\pi}{\rho L_f} \left[\rho L_v D_f (q_v - q_{v,s_0}) + K(T - T_0) \right] A_i N_t \left(\frac{6\rho q_i}{\pi \rho_i N_t} \frac{\Gamma(2+\kappa)}{\Gamma(1+\kappa)} \right)^{1/3}$$

There is no current theory of melting, but it is assumed that as particles melt, water pools towards the centre making the particle more isometric and dense, resulting in a fall speed increase.

Nucleation

Deposition nucleation, contact freezing and immersion freezing of cloud droplets is taken from DeMott et al. (2010):

$$n_{IN,T_k} = a(273.16 - T_k)^b (n_{\text{aer},0.5})^{(c(273.16 - T_k)+d)}$$

Where the nucleation rate n_{IN,T_k} is a function of cloud temperature T_k, and the number concentration of sufficiently large aerosol particles $n_{\text{aer},0.5}$. The constants a, b, c, d are fit to data.

Immersion Freezing comes from Bigg (1953) as shown in Morrison `MNUCCR`.

Appendix M

Figures of Reflectivity Components in the ISHMAEL scheme

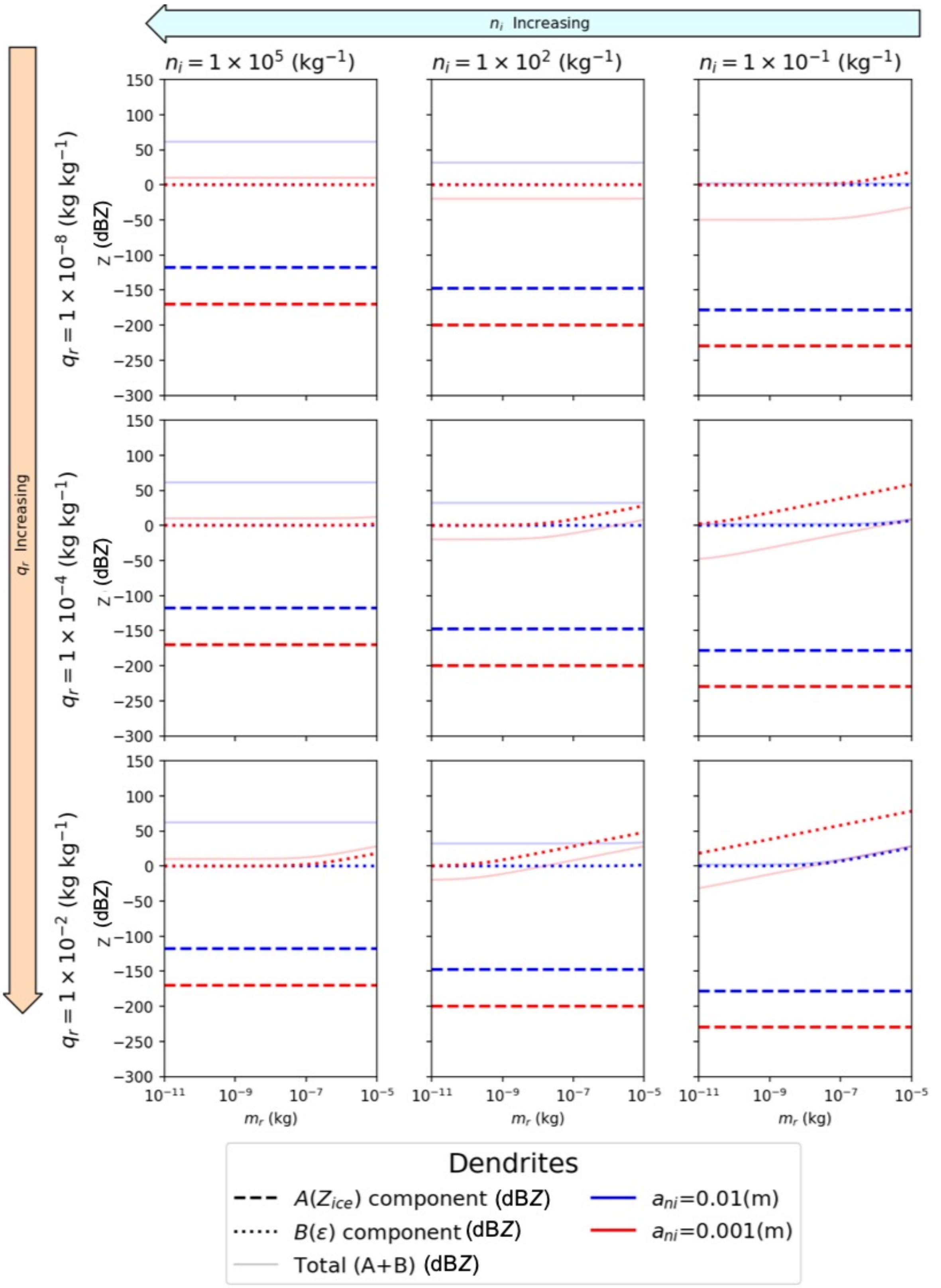

Figure M.1. Reflectivity components A and B (see Equation 6.8) and their summation (multiplied by 10) the total reflectivity Z_{total} (dBZ) versus the average rain droplet mass m_r (kg) for dendrites ($\delta_* = 0.6$, $\bar{\rho} = 100$). Terms A, B and the total are shown by dashed, dotted, and translucent lines. Components are plotted for three values of the ice number concentration n_i (kg^{-1}): 1×10^5, 1×10^2, 1×10^{-1} in columns 1–3, respectively, and three values of ice mass mixing ratio q_r (kg kg^{-1}): 1×10^{-8}, 1×10^{-4}, 1×10^{-2} in rows 1–3, respectively.

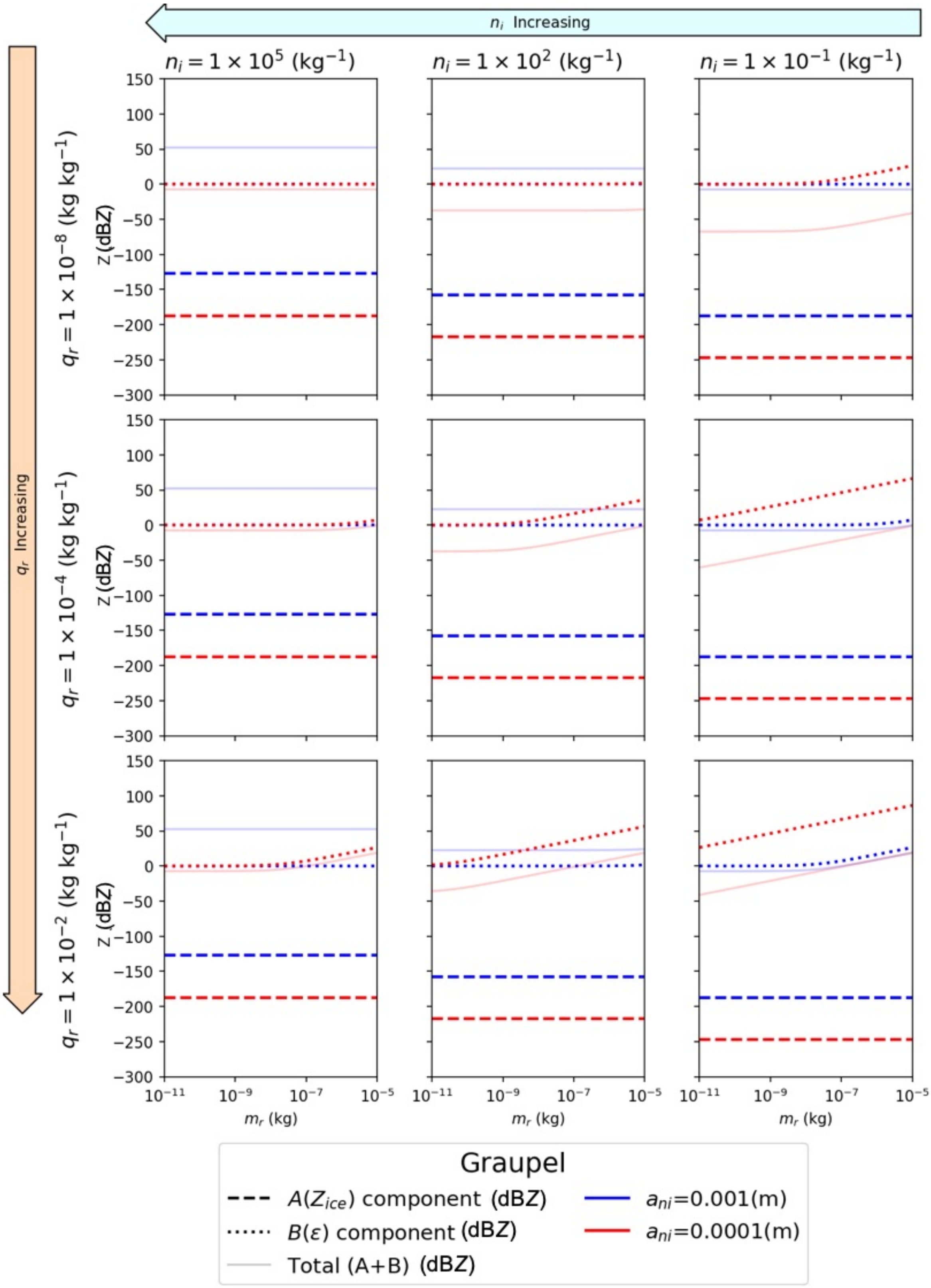

Figure M.2. Reflectivity components, and the total reflectivity Z_{total} (dBZ) versus the average rain droplet mass m_r (kg) ($\delta_* = 1$, $\bar{\rho} = 400$) as in Figure M.1 for graupel hydrometeors.

Appendix N

Total Reflectivity Analysis for Unrimed and Partially Rimed Crystals

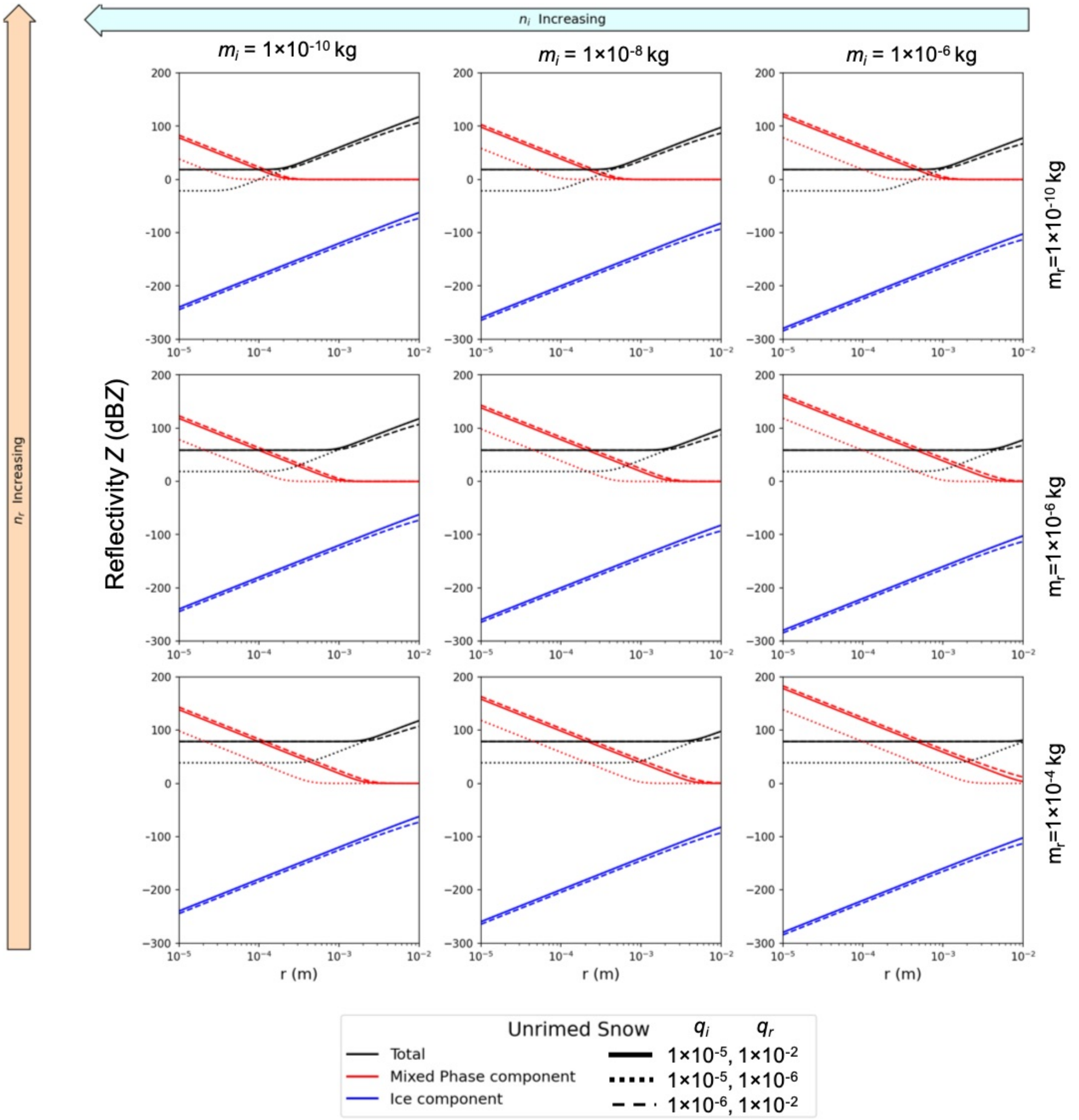

Figure N.1. Total reflectivity Z (dBZ, black), ice reflectivity component A (dBZ, blue), and mixed-phase reflectivity component B (dBZ, red) as shown in Equation 6.15 versus average ice particle radius r (m) for unrimed snow. Average crystal mass $m_i = 1 \times 10^{-10}$, 1×10^{-8}, 1×10^{-6} kg in columns 1–3, respectively. Average raindrop mass $m_r = 1 \times 10^{-10}$, 1×10^{-6}, 1×10^{-4} kg in rows 1–3, respectively. Three sets of fixed ice mass mixing ratio q_i and rain mass mixing ratio q_r are shown with differing line styles; base state $q_i = 1 \times 10^{-5}$, $q_r = 1 \times 10^{-2}$, decreased ice $q_i = 1 \times 10^{-6}$, $q_r = 1 \times 10^{-2}$ and decreased rain $q_i = 1 \times 10^{-5}$, $q_r = 1 \times 10^{-6}$ shown by solid, dashed, and dotted lines, respectively.

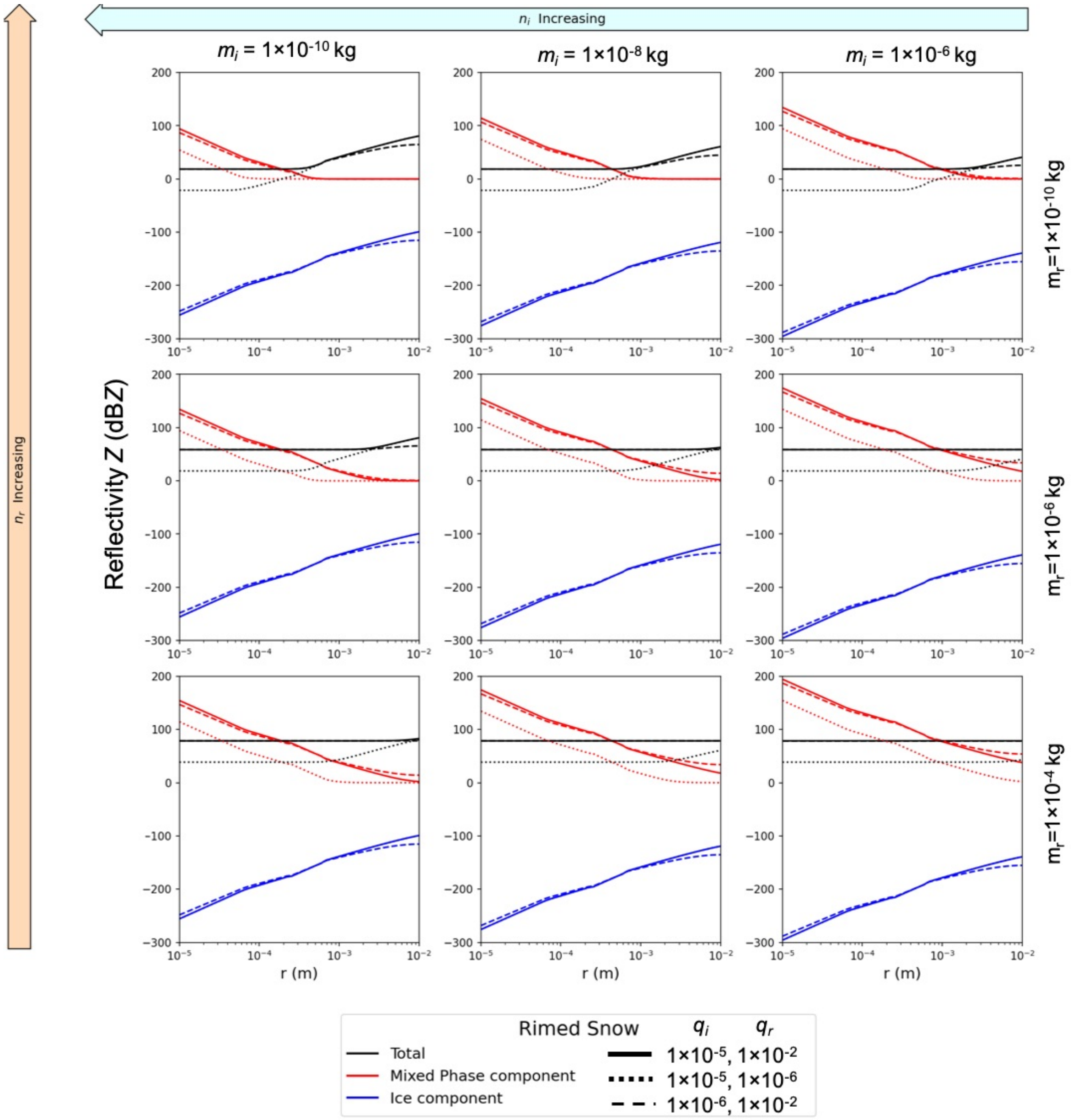

Figure N.2. Total reflectivity Z (dBZ, black), ice reflectivity component A (dBZ, blue), and mixed-phase reflectivity component B (dBZ, red) as shown in Equation 6.15 versus average ice particle radius r (m) for partially rimed snow. See Figure N.1 for description.

Appendix O

PHIPS Algorithm for the Analysis of Ice Habit Imagery

The Particle Habit Imaging and Polar Scattering (PHIPS) probe is a particularly useful resource in this case because it provides particle geometric information such as crystal dimension, habit and porosity that are not often obtained *in situ* for extra tropical cyclones. This is particularly useful for the evaluation of the ISHMAEL scheme, which predicts ice crystal aspect ratio explicitly. However, to conduct any comparative analysis the PHIPS data sets must be processed into a more useful quantitative format. In its raw form, each image per pair shows a near-opaque ice crystal silhouette set against a grey background as shown in Figure O.1. Additionally, the crystal images were found to contain numerous artefacts that complicated their processing. For example, blurred ice-particles when a second crystal intercepted the lens' focal point, or ice crystals that were only partially in frame. Given the size of the data set per case, manual analysis of each image pair was impractical. Instead, computational methods were developed to process the images in a feasible timescale.

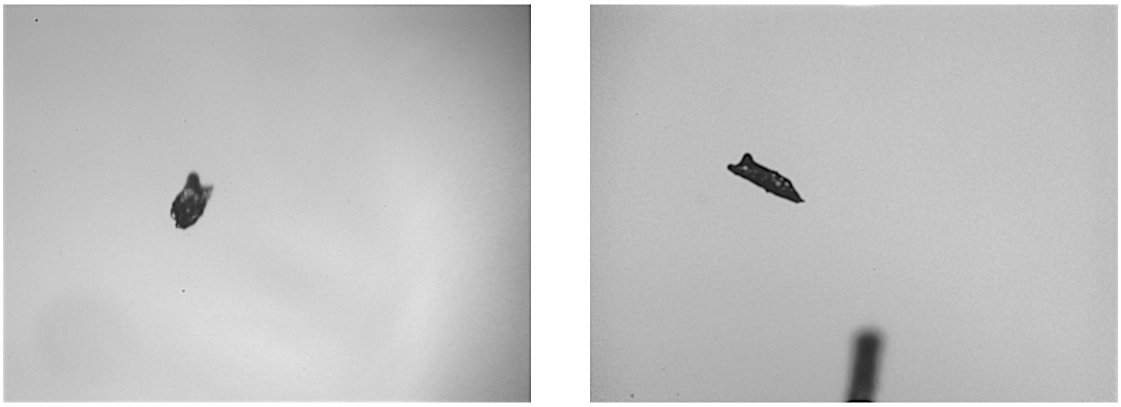

(a) Crystal Image 1 of 2

(b) Crystal Image 2 of 2

Figure O.1. Two PHIPS images (one image pair) of a single ice crystal (dark) from two lenses separated by an angle of 120°.

Post Processing Methodology

The aims of post-processing PHIPS data were to obtain the crystal dimensions in the template of a standard ellipsoid so that the axes were comparable to the ISHMAEL parameterisation of habit. It was necessary then to first determine an appropriate type of ellipsoid (i.e. *oblate* or *prolate*) that would best match the photographed crystal. Then, the spheroid could be resized to appropriately capture the crystal surface area. With a best-fit ellipsoid fully defined, further information could be prognosed such as the maximum dimensional length and the aspect ratio. These features were desirable to retrieve as they are variables produced by the ISHMAEL scheme. Importantly, this methodology does not consider habit, not only because building and verifying the script's accuracy in this regard would be a complex task, but because the ISHMAEL scheme cannot produce ice-habits in the conventional sense so this information was not required. The computational logic of post processing is as follows:

1. Read-in

The post processing script takes two directories as arguments, each corresponding to an angle. The script first checks the images to identify incomplete pairs and returns a list of viable pairs for further processing. At this stage, the crystals take on the appearance of near-opaque silhouettes and no error checking of the image has been undertaken to remove artefacts. Figure O.2 shows an example image pair corresponding to one crystal separated by 120 degrees. Two possible errors (at the users discretion) are visible, blurring of the crystal as it leaves the lens' focus, and intersection of the image boundary, which might conceal important geometric information.

2. Crystal Area Identification

In both of the loaded images (Figure O.2) ice crystals may be separated from the background by the gradient of the colour scale. For example, the crystal edge exhibits a sharp change in colour that can be used to separate the edge from the relatively light, grey background. However, note that the colours are not precisely defined. In Figure O.2 the ice crystal and background are actually an assortment of many shades of grey of differing darkness. For some crystals, the difference in colour may be relatively small so the crystal area is identified using a relative colour difference with variable tolerance chosen by the user. This allows for *strict* or *lenient* crystal area identification.

Once the crystal area is identified it is stored as a binary array in the image coordinate system. The binary array for the example crystal is plotted in Figure O.3. Note that crystal

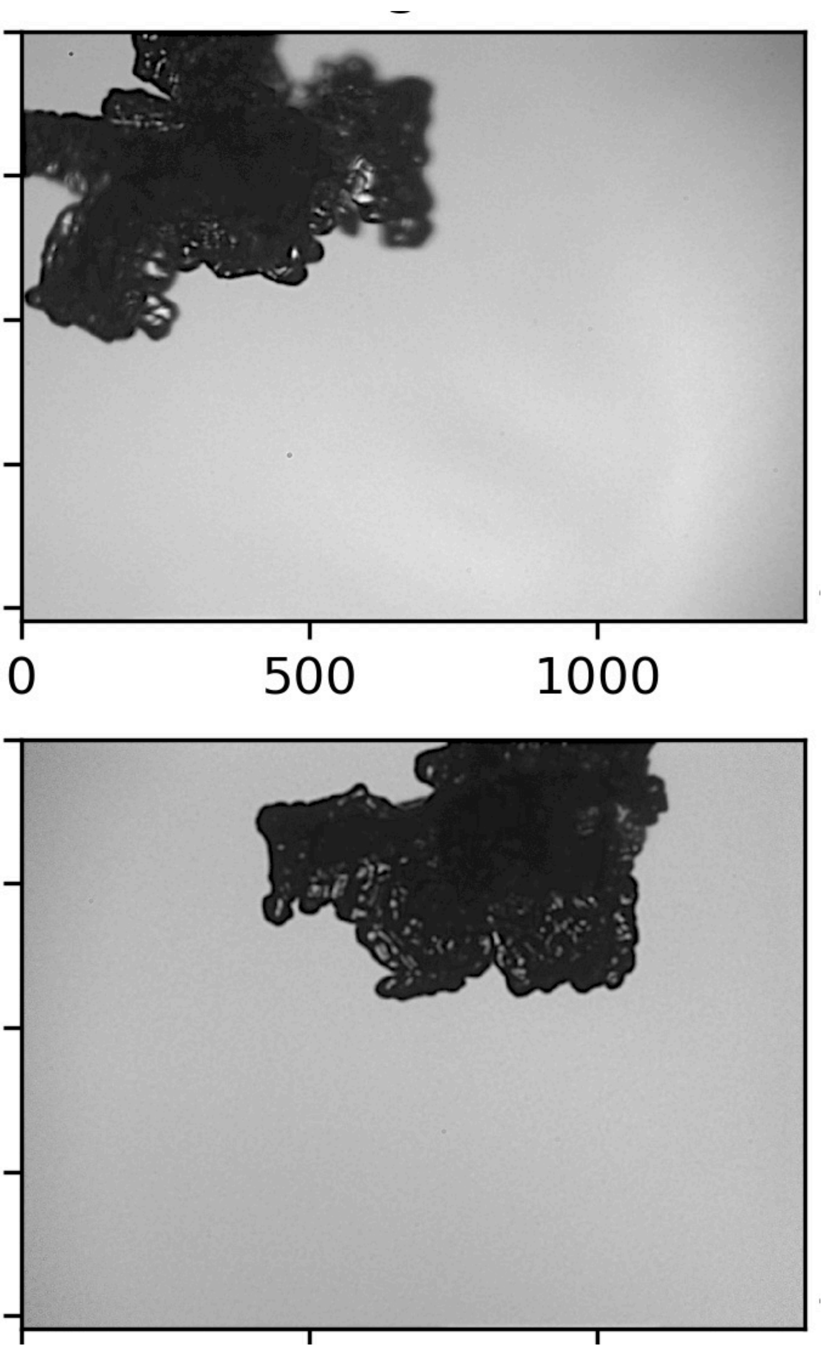

Figure O.2. Example image-pair read in by the post processing script during Step 1. The crystal image may contain artefacts or other unwanted features at this stage. The crystal is identifiable by a near-opaque silhouette but exhibits blurring and intersection with the image boundary.

pores are conserved during the area mapping if they are clear or translucent, which allows for subsequent measurements of porosity. This is an interesting feature of the post-processing method for possible future use, but in this case computational estimations of porosity were not explicitly considered.

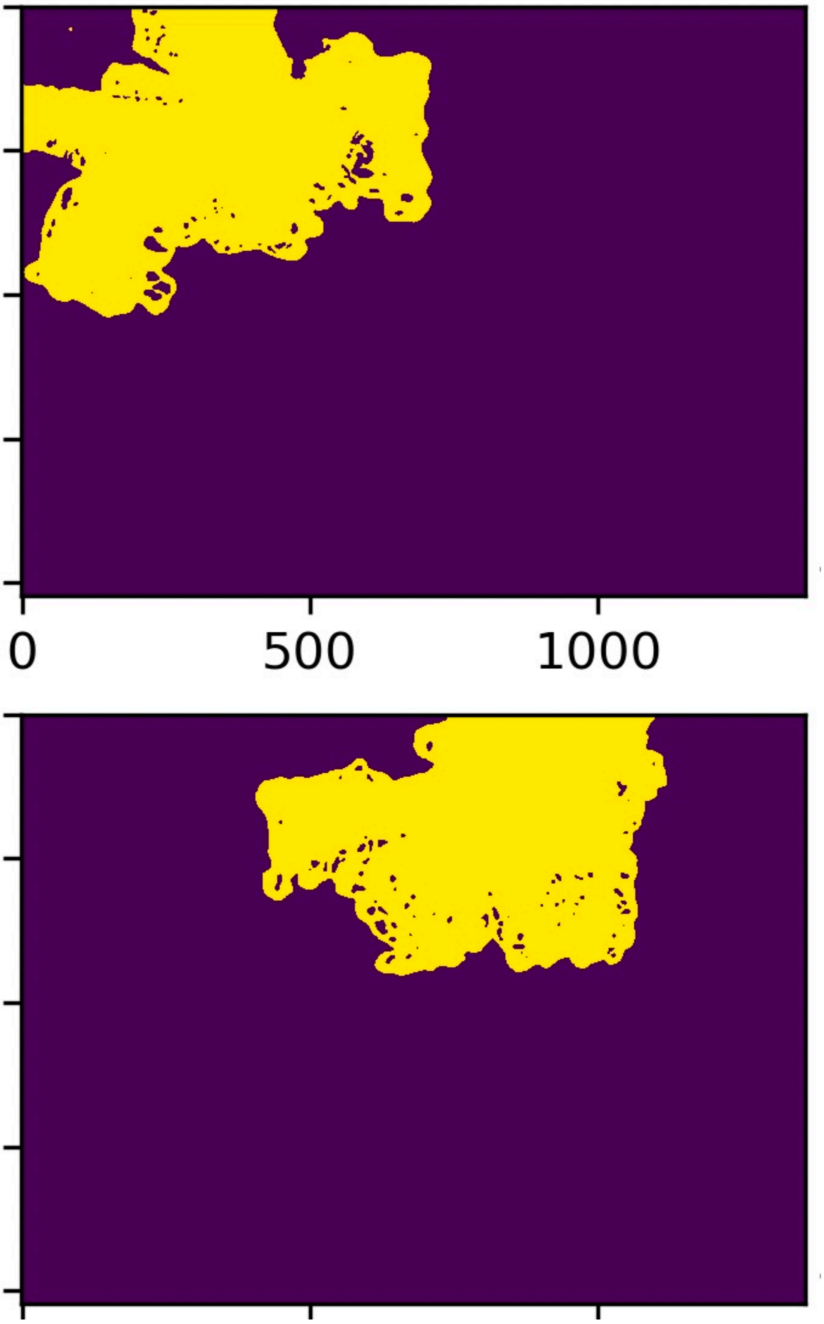

Figure O.3. Example image-pair as in Figure O.2 after crystal-surface mapping has been applied (Step 2). The output data-field is a binary array (i.e. crystal=1, background =0) plotted here where the crystal area is mapped in yellow.

3. Crystal Boundary Identification

Using the crystal-area array, the coordinates of the crystal edge points can be identified. This is a required step to reproduce variables such as maximum dimension or axial lengths that are mathematically defined between edge points. At this stage, additional processing is required to ensure that the crystal area array is operating as expected. For example, if more than one crystal is found in the image (see Figure O.1) then Step 2 may identify it as viable crystal area. This raises errors because the simultaneous computation of boundaries is generally non-trivial but in any case, it is advantageous to remove artefacts from the images before harvesting data.

A subroutine of the post processing script identifies if more than one crystal is present in the binary array and the script removes all but the largest crystal. This method was chosen because artefacts, such as splinters, droplets fragments are often smaller than the intended target of the photograph. Additionally, large crystals that were not the intended target of PHIPPS tend to substantially intersect the image frame, and are therefore removed in Step 4.

In the hierarchical structure of crystal identification, the deciding factor for whether a crystal is the intended PHIPS target is if the ice particle can be readily identified in the second, rotated image. A check is performed to ensure that the crystal in image one is therefore located at the expected x and y coordinates in image 2.

4. Check Image Viability

In some cases only part of the full crystal is photographed, this can happen when PHIPS is triggered but the crystal is too large for the frame or not centred in frame. In these cases, proceeding haphazardly could yield incorrect or misleading results. For example, a crystal that intersects the frame edge may have a large particle axis outside the image boundaries, and so a maximum dimension calculated within the frame would be inaccurate. At this stage, the programme determines if the crystal overlaps the image border in either of the image-pair panels. If it does, then the script determines if the size of the overlap is small enough that we can assume the majority of the crystal is in-frame. For example, the crystal shown in Figure O.4 has an overlapping boundary at the top of the frame. In this step, the total length of the intersected frame segment is determined and compared to the overall geometry of the crystal boundaries. The user sets the tolerance for the maximum permissible frame length relative to the in-frame crystal dimension. In Figure O.4 the total maximum length is much larger than the intersected length of the image frame, so the analysis proceeds with the given boundary. This method is chosen because very large ice crystal features are deemed unlikely to occur when normal to a thin ice width. We note that this method is likely to hold for plates, but may be unreliable for columnar ice. Therefore the option of a user-tolerance is provided.

5. Fit Ellipse

Using the coordinates of the boundary points for each image, an ellipse is fitted that maximises the area within the contours whilst preserving the approximate dimensions (Lag-

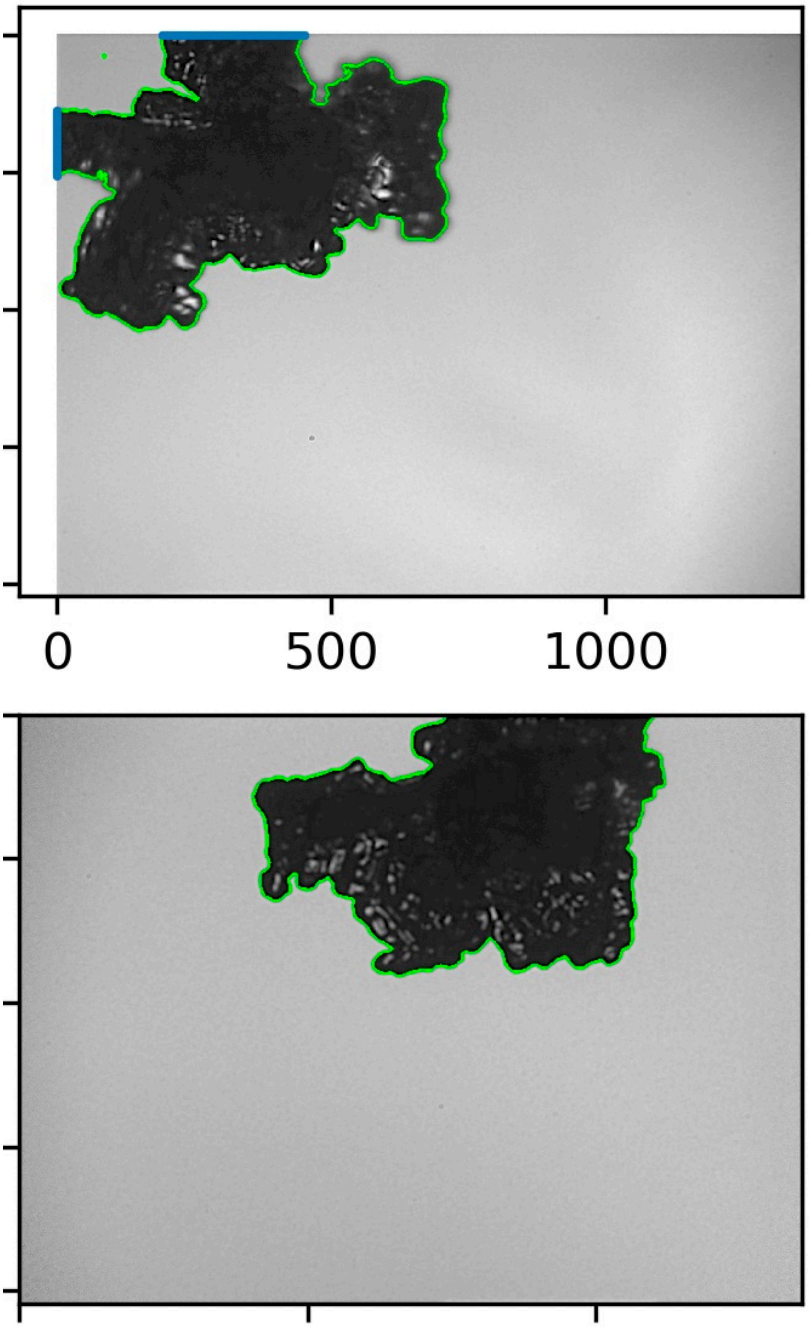

Figure O.4. The boundary of the crystal edge is established in Step 3 from the predetermined crystal surface area (Step 2). The computed crystal borders are shown in green.

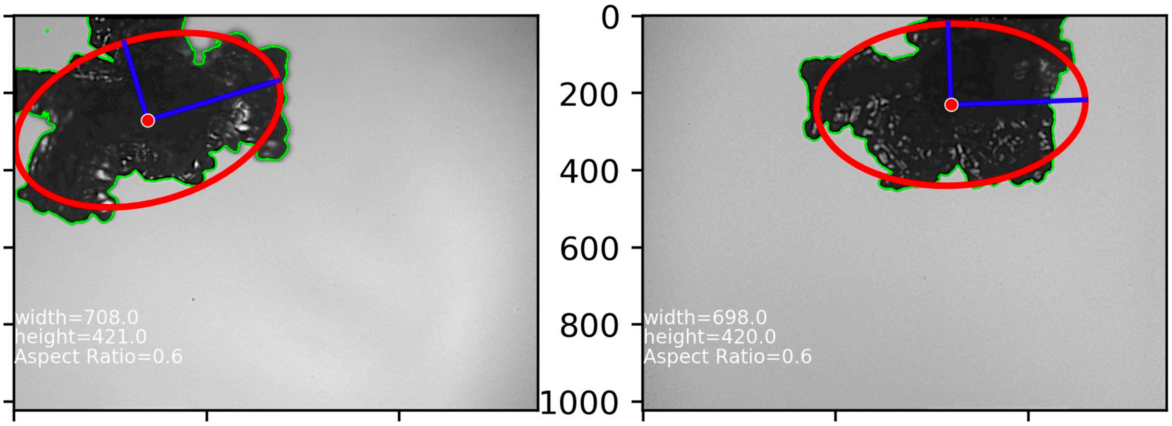

Figure O.5. Example crystal with previously computed boundary (green). The maximum dimension of the boundary and its normal length are used to compute an ellipse (red) that conserves these quantities. The ellipse axes can be used to approximate the maximum dimension.

rangian maximisation method). This method tends obtains an ellipse that appropriately approximates the width and height of the crystal. Figure O.5 shows how an ellipse is placed across each imaged ice crystal cross section, that preserves the maximum dimension and its normal dimension. This process is applied independently to both ice crystal images and is an effective way to determine the maximum crystal dimension.

Inferred Three-Dimensional Geometry

The retrieval of maximum dimension from the ellipse axes in Figure O.5 is a reasonable first approximation but it is important to note that crystal images show only a two-dimensional cross section of a three dimensional object. It is possible, if not likely, that the crystal maximum dimension is not normal to the image plane but instead, lies at an angle to it. This would reduce the perceived dimension and bias the analysis. To improve the approximation of crystal geometry, an additional step is required to approximate the 2-D image in three dimensions. We note that it is not possible to upscale the dimensions beyond the two given by the PHIPS crystal images, but the angular displacement of both crystal images can allow the user to infer three-dimensional properties of the ice.

Consider the two fitted ellipses for the example ice in Figure O.5. These may be interpreted as two slices of an ellipsoid on two planes separated by an angle displacement of 120 °. While the full dimension along $\hat{z}$ cannot be accurately known, we can use assumptions to infer the proportions of the ellipsoid. For example, by allowing the ellipsoid to preserve its dimensions under rotation. These assumptions allow the script to output the dimensions of a three dimensional ellipsoid that is intersected by the two ellipsoids along their respective planes. This data is considered final and is written to file.

The assumptions used to infer ellipsoid properties are difficult to verify, as an ellipsoid of

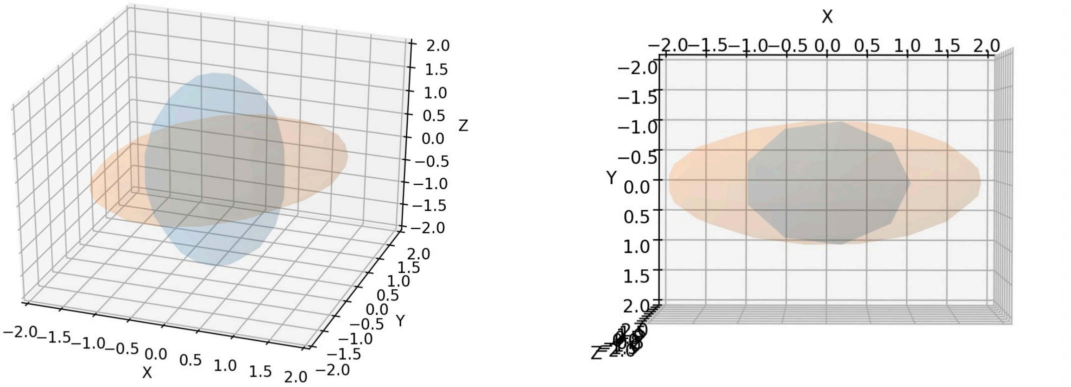

(a) Ellipses in 3D projection

(b) 2. As in (a) but rotated to the X-Y plane

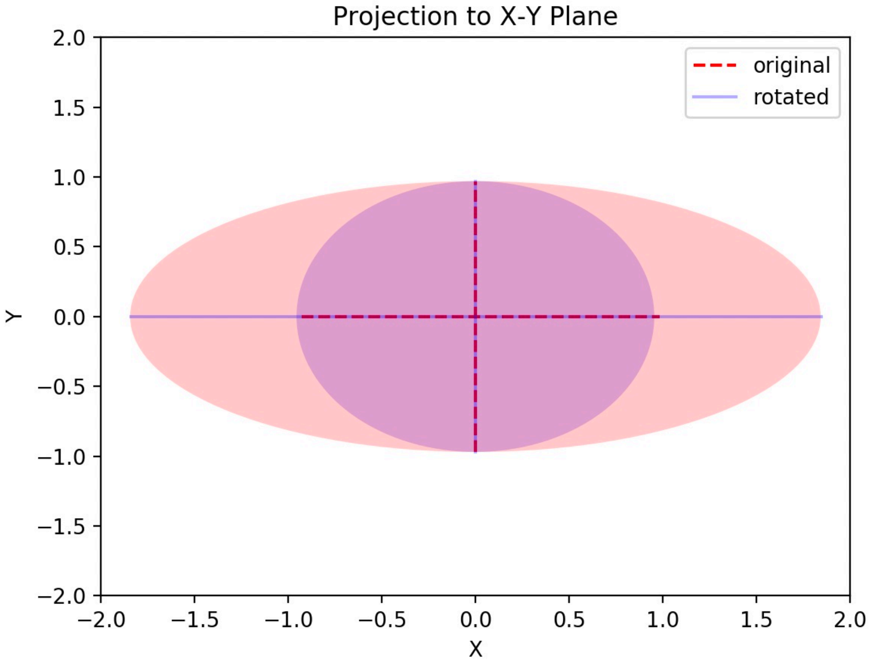

(c) Two dimensional projection of (b) onto the X-Y plane

Figure O.6. Three dimensional inferred properties of two 2-dimensional images separated by an angle of 120 degrees in the third dimension. (a) Two ellipsoids based on the boundary contours of the 2-dimensional images are represented at their relative angle. (b) identical ellipsoids as in (a) but with the viewing plane reoriented to the X-Y plane. (c) The projection of the ellipsoids in (b) against a two-dimensional plane (the projected area)

any spatial dimension could be imaged from an infinite number of angles. So to verify the assumptions and the validity of the output data, a second program was written to plot the planar ellipses and their governing ellipsoid in three dimensions. The program enabled an ellipsoid of any type (prolate, oblate, spherical) to be plotted at any orientation relative to the x-y plane, and for its projection against the x-y plane to be obtained. The projection data, height, width and aspect ratio were then output to confirm the assumptions. An example of this process is shown in Figure O.6.

Rotations of the model ellipsoids shown in Figure O.6 are used to determine the projected area of the governing ellipsoid in two dimensions. Figure O.7 shows how the rotation of the ellipsoid in three dimensional space affects the properties of the projected two-dimensional area. In panel (a) a prolate ellipsoid with radial length 1 in $\hat{x}$ and $\hat{y}$ and a radius of 2 along $\hat{z}$ is rotated about 180 degrees. Correspondingly, the aspect ratio of the two-dimensional projection changes from spherical to oblate and then back to spherical, but the height in the z-axis does not change. In panel (b) the length of the $\hat{z}$-parallel radius is 4 times larger, this results in a very oblate two-dimensional projection for smaller rotations.

Figure O.7 suggests that particles with more extreme aspect ratios are statistically more likely to project an extreme aspect ratio in two dimensions than their less extreme counterparts. Or rather, the maximum projected aspect ratio is maintained for a larger rotational interval for crystals with more extreme three-dimensional aspect ratios. In a physical measurement context, this bias causes crystals with relatively extreme aspect ratios to be captured in greater apparent frequency, and similarly crystals with less extreme aspect ratios will be mischaracterised as having a more spherical aspect ratio in greater frequency. Therefore, probability distributions of the aspect ratio variable are likely to be enhanced at the extreme ends and close to one, but suppressed between these intervals. For ice crystal habits, needles, long columnar crystals, or flat plates are very likely to exhibit an accurate two-dimensional projection and will therefore will appear to be very common, weakly oblate or prolate particles such as graupel or aggregates will appear to be less common, and near-spherical particles will be increased accordingly. Such an effect was identified by Jiang et al. (2017) who noted that oblate aggregates have a preferential projected aspect ratio that artificially inflated their true aspect ratios. This had caused aggregates to be incorrectly diagnosed as having erroneously large average aspects ratios. We pose that it may be possible to statistically re-balance the aspect ratio distribution with consideration of this bias, but analysis in this regard was not pursued during this study.

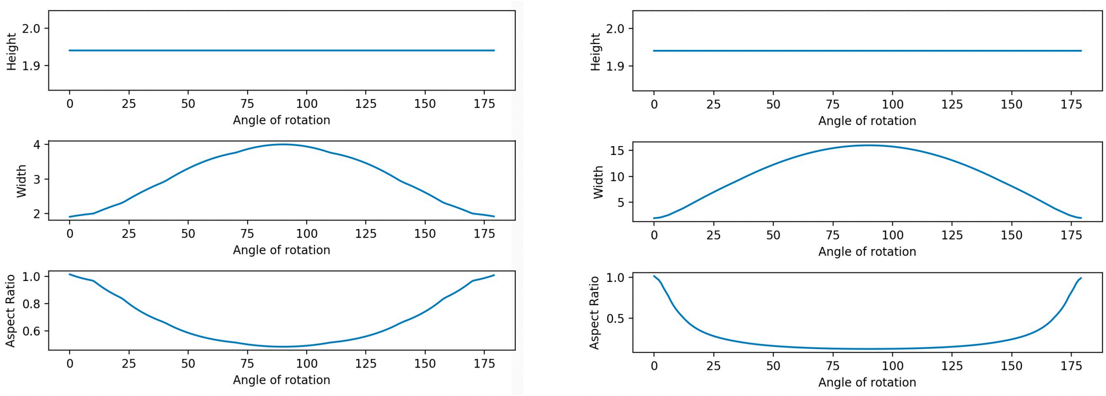

(a) Rz = 2

(b) Rz = 8

Figure O.7. Height, width and aspect ratio variations of the two-dimensional projected area of a prolate ellipsoid during rotation. In panel (a) the prolate ellipsoid has z-parallel axis length equal to 2. In panel (b) the z-parallel axis length is equal to 8. In both cases the x and y-parallel axes have unit length.

Appendix P

Initialisation and Operation of the WRF Model

Resource	URL	Notes
CSF3 homepage	`http://ri.itservices.manchester.ac.uk/csf3/`	Login, loading modules etc.
CSF3 HPC Pool	`http://ri.itservices.manchester.ac.uk/csf3/hpc-pool/`	Help specific to the HPC
WRF source code	`https://www2.mmm.ucar.edu/wrf/users/download/get_sources_new.php`	`git clone` links, static data etc.
Real Meteorological Data	`https://rda.ucar.edu/`	Useful data resource for several key data sets (GFS, ERA). Free with sign up
WRF Manuals	`https://www2.mmm.ucar.edu/wrf/users/docs/user_guide_V3/contents.html`	Up to version 3.9, however much of the content remains unchanged.
Namelist best practices	`https://www2.mmm.ucar.edu/wrf/users/namelist_best_prac_wps.html`	Useful when understanding namelist options
WRF installation guide	`https://www2.mmm.ucar.edu/wrf/OnLineTutorial/compilation_tutorial.php`	The page that first taught me WRF compilation. Note that content related to libraries is not applicable to the CSF3.
Visualising WRF domains	`https://wolfscie.wordpress.com/2017/10/05/visualizing-wrf-domain/`	A useful python script to visualise your domain, available via Github. The programme is similar to ncview, but the latter is graphical and difficult to run via SSH.
The WRF Users Forum	`https://forum.wrfforum.com/index.php`	*The* place to find solutions and request help. Likely where you will be redirected from a google search.

Table P.1. Useful links and resources for users of the WRF model or the University of Manchester CSF

The Weather Research and Forecasting Model *WRF* is a mesoscale numerical model capable of simulating weather phenomena for both research and forecasting. WRF is one of the most used weather models worldwide with users spanning 160 countries. The broad appeal of WRF is three-fold: first, the model is centrally supported by its developers, primarily the National Center for Atmospheric Research (NCAR). Second, the model is free and available to researchers worldwide regardless of nationality. And third, the model is highly customisable with little programming knowledge required. Consequently, WRF appeals to a wide audience and has lent itself to fair scientific scrutiny and evaluation, which have only spurred its development. For example, various parametrisation schemes have been developed by the community, published and then included with the WRF standard distribution so that other users may test and utilise them.

CSF3

The CSF3 is a high performance computing (HPC) cluster comprising 9700 cores and 68 GPU units funded by the accumulated contributions of research groups across the University of Manchester. Additionally, a HPC pool comprising 4800 cores is available for select projects that require a large number of cores for parallel execution. The HPC pool is ideal for WRF simulations as WRF is computationally intensive and runs more quickly when many cores are used in parallel.

The CSF3 is a shared resource, and therefore has some rules and customs that enable fair usage for all. The resource is managed by IT services, who should be contacted in the first instance regarding questions of hardware.

Remote Access

Using an internet connection, commands can be sent from the local terminal to a remote server and executed there. In fact, we may log into a remote server and operate its hardware in our terminal, as if we were accessing that hardware locally. This process is called remote access. By logging into the remote system, we can issue commands using the computational power its hardware provides.

```
MyLocalPrompt:Documents$ ssh MyUsername@RemoteServer
> Password?
************
> ------------------------------------------
> Welcome to the Remote Server!
> ------------------------------------------

MyRemotePrompt:$ ls
```

```
>   Remote_Folder1    Remote_Folder2
```

Listing P.1. Login to a Remote Server

In the above example, the user logs into a remote server using SSH. The server requests a passcode for entry and the user subsequently types this in, here illustrated as asterisks (*). However, please note that it is common for password input to show no visual cue. The server then greets the user with an entry message if succesful, and the prompt changes to reflect the new location in the remote system. Finally, the user issues the `ls` command. The remote server returns the directories and files in the remote location. This is the method you will use to login to the CSF.

Linux and Mac default terminal applications are usually capable of an immediate login. If you are running Windows the process is more complicated, see this link for help getting set-up: `http://ri.itservices.manchester.ac.uk/csf3/getting-started/connecting/windows/`. Open a line of communication between your local machine and the CSF with secure shell (SSH) login from your local computer using the login details given to you.

Login is performed using SSH and the user's specific login details. The server asks for a password but the terminal does not indicate when a letter is being typed for security purposes. After entering the password and pressing `RETURN/ENTER` the CSF shows a welcome message and the noticeboard. It is clear that the location is now within the CSF as the prompt contains `[CSF3]`.

Using The CSF3

At log in users are resident on the *Login Node*. This is a small, shared resource that can be used only for small tasks such as writing code, moving files, and issuing BASH commands. As this is a shared resource, you should be careful not to abuse the login node. For example, running WRF on the login node would consume significant resources, likely causing the CSF login to be slow, frozen or inoperable for other users. Therefore, do not run large jobs on the login node.

To ensure fair use, the majority of the CSF's resources are not directly accessible but managed by a batch system that chooses which jobs will run first according to several factors i.e total resources requested and recent usage history. If your job is not granted immediate access it will be placed in a queue. A WRF job may be queued for up to two days during busy periods but more often it will begin within a day.

Batch submission is handled by the `qsub` command, which takes a plain-text file as argument. For ease the file can have the extension *jobscript* although this is not mandatory. The jobscript file requests a set number of cores to run a process, loads modules, confirms the users identity and provides commands to run. When running WRF, we will specify the number of cores to run in parallel and a single command will execute the wrf.exe programme.

P.1 Building WRF & WPS

Git Clone the WRF Source Code

WRF consists of two components, the WRF pre-processing system (WPS) and the WRF model (WRF).

To retrieve the source code, follow this link: `https://www2.mmm.ucar.edu/wrf/users/download/get_sources_new.php` to a download page where two methods are listed. We will use `git` to download a copy of the latest model which can be updated later. `git` is a useful version control software that effectively stores and updates code as you write it.

To use git the CSF requires some us to load some modules. Modules are pre-installed programmes that we can load to assist us.

```
 MyRemotePrompt:$ module search git
 >  apps/git/2.19.0/gcc-4.8.5
 > services/git
 > tools/bintools/git-lfs/2.8.0
 > tools/gcc/git/2.24.0
 > More apps/versions may also be available by first doing: 'module load apps/bioinf'
 > If module names are repeated, show detailed version info using:
 > module --long search git

MyRemotePrompt:$ module load tools/env/proxy
MyRemotePrompt:$ module load apps/git/2.19.0
> apps/git/2.19.0/gcc-4.8.5
> | -- libs/gcc/system
> |    * --> OK
> |
> OK
```

Listing P.2. Loading the git modules

First, I have searched the CSF for modules that include git and the CSF has returned several hits which it thinks may be relevant. The correct module to load begins with `apps/git...`. I load this module using the command `load` followed by the module path. Additionally, as git is communicating with an external server it requires a proxy. Further information can be found at `http://ri.itservices.manchester.ac.uk/csf3/software/tools/git/`.

Now we can clone into the git repositories. The location is given at the website above.

```
MyRemotePrompt:$ ls
>
MyRemotePrompt:$ time git clone https://github.com/wrf-model/WPS
> Cloning into 'WPS'...
> remote: Enumerating objects: 6456, done.
 ...
 ...
> real  0m6.756s
...

MyRemotePrompt:$ time git clone https://github.com/wrf-model/WRF
> Cloning into 'WRF'...
> remote: Enumerating objects: 60853, done.
...
...
> real  6m16.655s
...
MyRemotePrompt:$ ls
> WPS   WRF
```

Listing P.3. Loading the git module

Where I have used the command `time` to additionally output the time taken for each `clone`. To download WPS takes less than 10 seconds and WRF less than 10 minutes.

WPS and WRF contain all of the written code that defines the model. The majority of this code is written in Fortran, which unlike python, is not a pre-compiled language. This means that the code must be repackaged into a form that a computer can read, this stage is called compilation. The result of compilation will be new files called executables, which are essentially an efficient and unmodifiable translation of the code to machine language. Executables have the benefit of being easy to run (self-contained) and extremely computationally efficient. The downsides are that they are unreadable in raw format, and any changes you wish to make to the source code will require a complete re-compilation of the model to produce new executables.

Download, Transfer, and Uncompress the Static Geography Data

Before we proceed to compilation, the WRF model requires additional files. The first are the mandatory static geography files, which contain the (generally) unchanging properties of our planet, namely topography and land use categories. These can be downloaded to your local computer by clicking ”Download Highest Resolution of each Mandatory Field” at this link: `https://www2.mmm.ucar.edu/wrf/users/download/get_sources_wps_geog.html`. NOTE: The compressed file is 2.6 GB and 29 GB uncompressed. Do not uncompress on your local machine.

The downloaded tar file will be named `geog.tar.gz` or similar, the next step will be to send this file from our local machine to the CSF. To do this we will use the Secure Copy Protocol (SCP) that should be installed on your local terminal. SCP is capable of copying large files between a local and remote machine with a transfer rate largely limited by the speed of your internet connection. General use of the command is as follows:

```
MyLocalPrompt:$ ls
> send_me.txt
MyLocalPrompt:$ scp send_me.txt username@RemoteMachine:/remote/directory/of_choice/
MyLocalPrompt:$ ls
> send_me.txt
MyLocalPrompt:$ ssh MyUsername@RemoteServer
MyRemotePrompt:$ ls /remote/directory/of_choice/
> send_me.txt
```

Listing P.4. Using SCP

Using the above steps, transfer the tar file via scp to the `Build_WRF` directory. Ensure that you use your specific remote login for CSF3.

Once the file has been sent, you can uncompress it with `gunzip` and `tar`. This will produce all files within a directory called `geog`. You MUST rename this directory to `WPS_GEOG` for it to be found by geogrid.exe.

```
MyRemotePrompt:Build_WRF:$ ls
> geog.tar.gz
MyRemotePrompt:Build_WRF:$ gunzip geog.tar.gz
MyRemotePrompt:Build_WRF:$ tar -xf geog.tar
MyRemotePrompt:Build_WRF:$ ls
> geog/
MyRemotePrompt:Build_WRF:$ mv geog WPS_GEOG
MyRemotePrompt:Build_WRF:$ ls
> WPS_GEOG
```

Listing P.5. Decompress and rename the static geography files

Obtain Real-World Input Data

WRF requires some knowledge of the real-world conditions in order to compute the progression of the atmospheric variables. This is provided by input data that can span many meteorological variables, formats and time periods making this the least standardised and most tricky step when running WRF. In this example we will use ECMWF ERA5 reanalysis data as it is easy to download and is a high quality data resource for future simulations.

We must provide WRF with data for each time period we wish to simulate. Furthermore, WRF requires a set of specific variables to run that can be found by examining the contents of a Vtable. Whilst we can download data directly from the ECMWF database, in this case it will be easier to use the ucar RDA.

The data sets can be found here `https://rda.ucar.edu/datasets/ds633.0/` and will require you to register in order to access. The time taken for registration to be accepted is approximately 1-2 days. Once you have access, click Data Access this will show all possible products in several formats. We will require pressure level analysis in grib format so for this option choose Web File Format > Faceted Browse and narrow the data set to a time period of your choosing and tick the boxes matching those required by the Vtable. Once complete, click continue to be directed to file links. Tick all boxes, and generate a unix script that will download them.

Repeat this process for the relevant data of surface analysis. Both surface and pressure level data are required for WRF to run.

On the CSF we will store the data in a separate folder called DATA within `Build_WRF/`. Make this directory and enter it. Then, create a new text file and insert the unix script. You will need to modify the script with your password. Make the script executable with chmod and run in the current directory. NOTE: You are accessing external data to the CSF, so a proxy must be loaded.

Compile WRF

We will now begin to compile the model, beginning with WRF so change into the `WRF/` folder. WRF requires several libraries to run, but many of these are already installed on the CSF3. Therefore, we simply need to load them and set some shell variables so that the WRF MAKEFILE can locate them:

First set the variables:

```
MyRemotePrompt: Build_WRF/WRF$ export CC=gcc
MyRemotePrompt: Build_WRF/WRF$ export CXX=g++
MyRemotePrompt: Build_WRF/WRF$ export FC=gfortran
MyRemotePrompt: Build_WRF/WRF$ export FCFLAGS=-m64
MyRemotePrompt: Build_WRF/WRF$ export F77=gfortran
MyRemotePrompt: Build_WRF/WRF$ export FFLAGS=-m64

MyRemotePrompt:$ echo $F77
> gfortran
\end{{lstlisting}

Next, load the modules

\begin{lstlisting}[language=BASH]
```

```
MyRemotePrompt: Build_WRF/WRF$ module load compilers/gcc/system
MyRemotePrompt: Build_WRF/WRF$ module load libs/gcc/netcdf/4.6.2
MyRemotePrompt: Build_WRF/WRF$ module load mpi/gcc/openmpi/4.0.1
MyRemotePrompt: Build_WRF/WRF$ module load libs/gcc/jasper/2.0.14
MyRemotePrompt: Build_WRF/WRF$ module load libs/gcc/libpng/1.6.36
\end{{lstlisting}

And finally, export some additional variables as a consequence of loading these libraries

\begin{lstlisting}[language=BASH]
MyRemotePrompt: Build_WRF/WRF$ export NETCDF=$NETCDFDIR
MyRemotePrompt: Build_WRF/WRF$ export JASPERINC=$JASPERINCLUDE
MyRemotePrompt: Build_WRF/WRF$ export WRFIO_NCD_LARGE_FILE_SUPPORT=1
MyRemotePrompt: Build_WRF/WRF$ export MPI_LIB=
\end{{lstlisting}

Within WRF are three executables ready to be run. We will first run \texttt{clean} and  \texttt{configure} as follows:
\begin{lstlisting}[language=BASH]
MyRemotePrompt: Build_WRF/WRF$ ./clean
MyRemotePrompt: Build_WRF/WRF$ ./configure
> ...
>  32. (serial)  33. (smpar)  34. (dmpar)  35. (dm+sm)   GNU (gfortran/gcc)
MyRemotePrompt: Build_WRF/WRF$ 34
>Compile for nesting? (1=basic, 2=preset moves, 3=vortex following) [default 1]:
MyRemotePrompt: Build_WRF/WRF$ 1
> ...
> Configuration complete!
```

Configure offers many options for compilation. In my experience the easiest to work with is GNU, with which would like to choose the dmpar option (34). Next, a nesting option is offered. Usually, basic is the correct choice. If after selecting these options `Configuration complate` is not returned, do not proceed with any further steps. You must correct the issue at this stage. Additionally, check for the presence of a `configure.wrf` file:

```
MyRemotePrompt: Build_WRF/WRF$ ls *.wrf
> configure.wrf
```

Finally we will issue the compile command. We wish to run a real case, i.e. a weather event that has happened in reality, not an idealised case. For this we will choose to compile with `em_real`:

```
MyRemotePrompt: Build_WRF/WRF$./compile em_real >& log.compile
```

> tells the terminal to divert any output to a file, log.compile, whilst the ampersand & forces the process to run in the background, giving us control whilst the process runs. If you wish to see the text being written to the file, you might use the `tail` command with flag `-f`. Typ-

ically compiling WRF can take around 10 minutes on the CSF. If the process finishes in less time than this, it is likely that it has encountered an error. To check for errors, examine the log.compile file after completion:

```
MyRemotePrompt: Build_WRF/WRF$ vi log.compile

/Error

> ... (Returns line matching keyword search) ...

[CTRL+C]

MyRemotePrompt: Build_WRF/WRF$ tail log.compile
> ...
> Executables successfully built
> ...
```

If at the bottom of the log.compile file a message states ”Executables successfully built” then you can proceed. To double check these executables you can examine the main/ folder:

```
MyRemotePrompt: Build_WRF/WRF$ ls main/*.exe
> run/ndown.exe  run/real.exe  run/tc.exe  run/wrf.exe
```

Compile WPS

Once WRF is compiled we can repeat the process for WPS. NOTE: The order is significant, do not proceed if WRF is not properly compiled.

```
./clean
./configure
./compile >& log.compile
```

Choose the matching serial option for the gfortran processor. Make sure it does not say `NO_GRIB2`. This will produce three executables in the geogrid, ungrib and metgrid folders. You may also check the log.compile file for any Errors.

P.2 Running WRF and WPS

Now that WPS is compiled we can begin to process our data and build a grid. Controlling the function of WPS is done within the namelist.wps file. Information regarding these settings can be found here: `https://www2.mmm.ucar.edu/wrf/users/namelist_best_prac_wps.html`. The time interval for the data we downloaded, the dates of your simulation and the domains should all be present here before running executeables.

Choosing a Domain

The domain is difficult to build from the namelist file, so there are several tools available to visualise this prior to running WPS. An installation of WRF to your local machine will provide ncview, a useful programme that quickly plots domains and variables. Additionally, GRIDVIEW can quickly produce an image from the domains. Unfortunately, the remote installation of WRF makes using these programs difficult due to the lack of graphical interface.

To overcome this issue, a python program can be run in a remote jupyter notebook that will help us to visualise this domain. The code can be found by git cloning into `https://github.com/lucas-uw/WRF-tools.git` and more information can be found from the *Visualising WRF Domains* link in Table P.1. You can find more information about starting a jupyter notebook from the CSF3 homepage.

Now that we can see our domains as we build them, we can consider their shape and number. It is good practice to keep your domains square, or as close to square as possible. You may also wish to simulate more than one domain at higher spatial or temporal resolution. This is called nesting. In the namelist, nested domains settings are placed in additional columns to the right of existing domains. You should be careful to ensure that one third of the parent domain is left between the nested domain edge and the parent domain edge.

When we eventually run WRF, the domain will be split into tiles that are divided amongst the processors. A poor choice of domain grid number at this stage will produce errors later, when the processes cannot be neatly divided amongst tiles. We must therefore consider the number of cores we will use later on. When running on the HPC pool we have access to a minimum of 128 cores up to a maximum of 1028, in 32 core groupings.

Suppose we specify 128 cores for a square parent domain: `e_we = 150, e_sn = 150` then WRF will likely split the processes amongst the two closest divisors of the core count, i.e 8x16 patches. Thus our patches will be `18.75 x 9.375` or `9.375 x 19.75` multiples of the grid. It is generally a good idea, and more efficient for WRF to disperse even numbers of grids amongst the cores and for those patches to be close together in number. A better optimisation of the grids would be to consider using 192 cores, which should produce 12 x 16 patches, already much closer in size. Then consider grid numbers which are nicely divided by these: i.e. `e_we = 156, e_sn = 160` this should allow WRF to divide each patch into 13 x 10 grid-sized tiles.

Additionally, suppose I produce a nested domain with grid ratio of 3, this means that each of my nested grids is a third the size of the parent. I might choose `e_we = 240, e_sn = 240` to produce 20 x 15 grid-sized patches. However, `e_we` must be one greater than an integer multiple of the `parent_grid_ratio` of 3, and $(240 - 1)/3 = 79.7$. This rule supercedes the efficiency of the processors. Instead, I should choose `e_we = 160, e_sn = 160`, producing patches: `13.3 x 10` meeting the criterion and giving WRF an easier job of dividing the processors.

In my example, I have set the WPS namelist as follows

```
&share
 wrf_core = 'ARW',
 max_dom = 2,
 start_date = '2011-07-01_00:00:00','2011-07-01_00:00:00',
 end_date   = '2011-07-03_00:00:00','2011-07-03_00:00:00',
 interval_seconds = 3600
/

&geogrid
 parent_id         =   1,   1,
 parent_grid_ratio =   1,   3,
 i_parent_start    =   1,  45,
 j_parent_start    =   1,  50,
 e_we              =  156, 160,
 e_sn              =  160, 160,
 geog_data_res = 'default','default',
 dx = 15000,
 dy = 15000,
 map_proj = 'lambert',
 ref_lat   =  55.688,
 ref_lon   = 12.584,
 truelat1  =  70.0,
 truelat2  =  40.0,
 stand_lon = 12.584,
 geog_data_path = '/mnt/iusers01/fatpou01/sees01/t08073jc/Build_WRF/WPS_GEOG/'
/

&ungrib
 out_format = 'WPS',
 prefix = 'FILE',
/

&metgrid
 fg_name = 'FILE'
/
```

Figure P.1 shows the domain checked with the python programme, I see that a nest has been set up over Copenhagen.

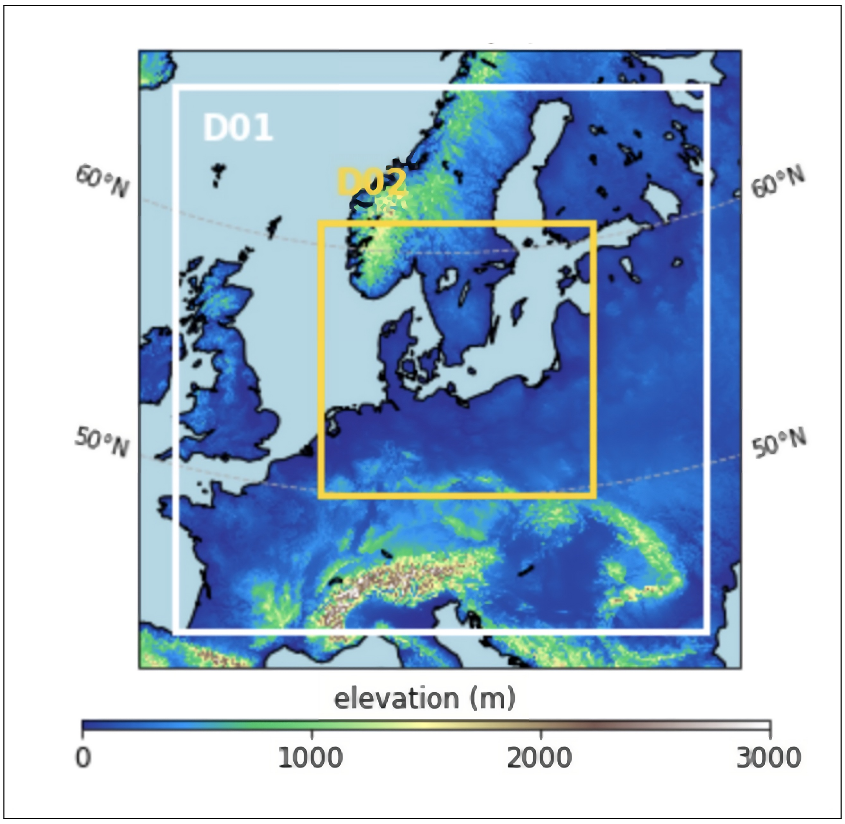

Figure P.1. Spatial locations of two WRF domains set up as detailed in the test run example. Domain 1 (D01, parent) indicated by white bounding box. Domain 2 (D02, nested) indicated by yellow box. Plotted variable is elevation (m) of the terrain within the domains.

Running WPS

Once you have made changes to the namelist, run geogrid to produce the grid for our simulation:

```
./geogrid.exe >& log.geogrid
```

Check that a `geo_em.d0` has been created for each domain. Next, we will link the input data that we downloaded.:

```
 ./link_grib.csh path_where_you_placed_GFS_files
```

WRF requires a table that connects the variables in our input data to the variables WRF expects. This is different for each data set (and for non-standard data sets, you may have to create your own table). Fortunately, a GFS table is already available in the Vtable directory included with WPS. We will use a soft link to connect this table to a standard variable `Vtable`:

```
ln -sf ungrib/Variable_Tables/Vtable.GFS Vtable
```

Now that we have linked our data and constructed our grid, we can begin to unpack that data. The ungrib programme takes a grib file and transfers it to an intermediate file format that is easier to work with. Running the ungrib executable should take 10 minutes on the CSF.

```
./ungrib.exe
```

Check that a `FILE` file has been created for each time period. Finally, we will interpolate to our geogrid using metgrid:

```
./metgrid.exe >& log.metgrid
```

This should result in a `met_em` file for each time period and domain. Now that our data has been interpolated to the grid boundaries we can begin a simulation. First, enter the `WRF` directory and navigate to the `run/` directory. We will use this directory as a base to perform the simulation.

Running WRF

Edit the wrf namelist file to match the options of the previous WPS namelist. At this stage you can also choose to modify any parameterisation schemes. We will stick with a well tested set of parameterisations given by setting the `physics_suite` option as `CONUS`. Leave all parametrisation options as -1 unless you are aware of a particular parameterisation scheme you wish to simulate.

We then need to link our metgrid files so that WRF can find them. Use the following command from within the `run/` directory to create soft links to each `met_em` file:

```
ln -sf ../../WPS/met_em* .
```

Check that the links have been generated. We can now begin to move our files over to scratch. Remember, we cannot run WRF on the login node, but must request resources from the HPC. All executables to be run on the HPC must be located in the scratch space, which provides high read/write speed memory and increased (short-term) memory capacity.

```
cd ~/scratch
mkdir TEST_RUN
cd TEST_RUN
```

Now copy the files over using the path to the run/ directory:

```
cp -rL /MY/PATH/TO/Build_WRF/WRF/run .
```

the L flag ensures that links within this directory (i.e. our metgrid files) are preserved correctly. You should find that the run directory has been copied to scratch.

While metgrid horizontally interpolated our data to the grid, real.exe vertically interpolates this data to vertical levels. This is in effect the last stage before WRF can be considered primed to go. We will submit the real.exe as a jobscript. Open a new file called `real.jobscript` and insert the following code:

```
#!/bin/bash --login
#$ -cwd
#$ -pe smp.pe 4
module load libs/gcc/netcdf/4.6.2
module load mpi/gcc/openmpi/4.0.1
rm rsl.error.* rsl.out.*
mpirun -np 4 ./real.exe
```

The third line indicates that we will run this job in parallel on 4 cores. We must also resupply the modules as the script will run in a new shell environment. Finally we tell MPI to run the real executeable on 4 cores.

Save the file, and submit it to the batch system. This should take a few minutes. Check that the process has run correctly by examining the contents of the `run` directory. You should see a `wrf_bdy_d01` file and `wrfinput_d0` files for each domain. Additionally, check the jobscript's `rsl.out` files for a successful completion message.

Finally, WRF is ready to run. Create a jobscript to run WRF by opening a new text file called wrf.jobscript and inserting the following text:

```
#!/bin/bash --login
#$ -cwd
#$ -pe hpc.pe CORE_COUNT
#$ -P MY_HPC_CODE
module load mpi/gcc/openmpi/4.0.1
module load libs/gcc/netcdf/4.6.2
rm rsl.error.* rsl.out.*
mpirun -np CORE_COUNT ./wrf.exe
```

You will need to replace `MY_HPC_CODE` with your personal access code that should have been sent to you with your application. Additionally, you will need to replace `CORE_COUNT` with the number of cores you wish to request. The HPC is for jobs using at least 128 cores and extending up to 1024 but remember your job will queue for less time when you request fewer cores. Generally, you should aim to make domains integer multiples of the number of cores if possible.

Submit your WRF job using qsub, you can keep an eye on it with qstat which will indicate if your job is still in the queue (`qw`) or running (`r`). You can check the current computed time of the simulation by examining the rsl.out files.

When the job is finished, the RSL files will display a successful completion message. You should also have `wrf_out` NetCDF files for each domain and time period.

Appendix Q

Comparison of Loading Efficiency for WRF Analysis

Introduction

Loading WRF-out variables for analysis is often a problematic task for several reasons. To those with coding experience, the process initially requires a little research and then, once a method is obtained, regular refining of the method to ensure it is efficient and flexible. For those with less coding experience, the process can be dumbfounding and disheartening. Coming up to speed may take many weeks and that's time that could certainly be spent more productively. This document will briefly explain some common issues when loading WRF variables, describe some methods to overcome them, and draw some conclusions based on comparisons.

Common Issues

NetCDF

At first glance, the format of the WRF out files is not obvious but they are in NetCDF format; this is somewhat surprising given the complex dance required to avoid NetCDF at the pre-processing stage, i.e. the *Gribbing* and *un-Gribbing* of files. NetCDF is an efficient file format for the storage and loading of large (1 GB to 100s GB) data sets.

The NetCDF format can be a confusing data format for newcomers to understand due to its all-in-one packaging of multiple variables and their meta-data, not to mention the n-dimensional variable structure. To access a variable, first load the NetCDF file as a data frame, this allows the metadata to be accessed without physically loading all of the contained variables into memory. The metadata may contain useful information such as the date and time period of the simulation, as well as the variables contained within the file.

Each variable will also have its own metadata, which may have important features or notes including physical units.

Once a variable has been determined by the user it can be extracted for all indices, or a subsection of its dimensions. This stage is important as loading into memory is time intensive for large files and loading multiple variables can quickly use all of the available memory. Memory constraints and loading time are discussed in in later sections.

Once extracted, the user may choose to convert to a more convenient format such as a numpy array or xarray. This will allow for some fast analysis and provide access to the modules array tools. Experience with matrices may help the user to better understand the format of arrays and the possibilities for analysis, as well as some techniques that are useful for loading, like concatenating and collapsing dimensions. The user should be aware that conversion to numpy arrays will strip the meta data, and while this is often not a problem, very occasionally the meta data will be required for some functions, for example `metpy` functions require `unit` meta data.

How to visualise NetCDF for WRF

For the specific case of WRF-out data the easiest way to understand the file structure is by imagining a Rubik's Cube as in Figure Q.1, where the coloured cubes represent grid cells and the entire cube represents the domain at time step t. Thus, indexing the NetCDF file in one dimension is akin to choosing a line of coloured tiles and indexing in two dimensions is akin to selecting a cube face that can be rotated. Importantly, indexing in three dimensions extracts a cube of data at a model time step, and thus the variable is a collection of these cubes for each time step of the history interval. Imagining the data in this way helps to relate the file-dimensions to a tangible physical example that is also an accurate representation of the simulated domain. It also serves to appropriately separate time steps from each other, which can help during the analysis stage.

For most WRF variables, 4 dimensions is all that will be required to understand the data. In some cases, such as orthogonal winds computed by `getvar`, the variables are bundled together into 5 dimensions. In these cases, a simple approach is to imagine the 5th dimension as a directory containing n variables, and then return to the Rubik's cubes example above.

Multiple WRF files

Most users will output WRF data into multiple WRF output files to disperse the memory in a more manageable way. Consequently, accessing the entire data requires rebuilding from multiple NetCDF files in post-processing. Rather than loading multiple entire datasets into

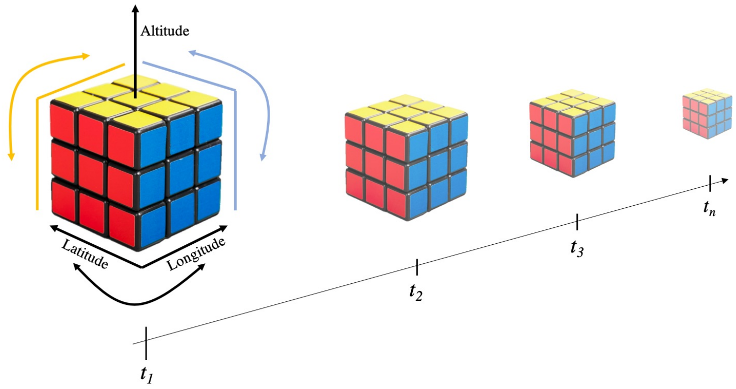

Figure Q.1. Graphical aid for the interpretation of NetCDF file structures adapted from Russell (2018). Single variables within a NetCDF data mirror the three-dimensional WRF domain structure which is compared to a Rubiks cube. Multiple Rubiks cubes represent the compartmentalisation of spatial data across the fourth time dimension at time step t_x.

memory, a more efficient method is to extract a variable from individual output files, perform the analysis to obtain the result for this subset, and then stitch together the result. For example, imagine that we wish to derive a mass-weighted timeseries of the mass-mixing ratio variable that is split over 24 hourly WRF output files. Extracting the mass-mixing ratio from each file, loading into memory, and stitching these together into a single array before performing analysis is a memory-intensive methodology. Instead, by loading and analysing the hourly periods individually, the user need only access enough memory for a single hours worth of data plus the stored result (which for a timeseries is negligible). This example serves to illustrate the considerable time savings that can be achieved by planning a data-efficiency strategy into the analysis, rather than viewing loading and analysis as two very separate processes in the analysis workflow.

WRF restarts

WRF restarts are a great way to save time when your simulation crashes unexpectedly as they enable the user to pickup a new simulation from the output of the last wrf restart file. The frequency of WRF restart files can be specified in the namelist settings, though it is important not to produce restart files too frequently as the files have considerable size and write times, which may increase computation time. A technical caveat when using restart files is that the filename format will refer to the time of restart, which may diverge from the typical format of other output files. Users should ensure that they cater to this in their analysis, especially if automated loading functions form part of the workflow.

`numpy.where()`

When manipulating numpy arrays, a fantastic tool is numpy's `where`, which can quickly filter through an array based on a conditional statement. I have found that the output array can be larger in size than the input, this is due to the routine initialising an empty numpy array in memory with 64 bit precision. Therefore, regardless of the actual data, np.where will request the same amount of memory, if not more memory, than the array to be analysed. The problem is twofold, since the initialised array and the input array coexist, requiring available memory for both arrays. To overcome this issue, the user may either convert the precision of the array to be analysed, or convert the precision of the np.where output array after the fact. The choice of method pertains to whether the user can tolerate the loss of precision before or after the analysis.

Saving Arrays

Simple and fast methods exist to save numpy arrays to physical memory and re-load them at a later time. This is can form a useful part of the analysis methodology if, for example, part of the intermediary analysis requires arrays that take a long time to produce. By saving these arrays, the user may save time in future analyses that are repeated, or allow for time-consuming analysis to be returned to at a later date. Note that, as previously mentoned, it is convenient to convert the array to a reduced precision form prior to saving, so as to reduce physical memory usage, as well as read and write times.

Overview of Methods

In this chapter we will illustrate some common problems when loading a WRF file by using an example load-case. Suppose that we wish to understand the relationship between 90th percentile reflectivity and rain mass mixing ratio throughout a simulation. We must execute the following steps:

1. Load the NetCDF data set for time period *T*
2. Extract the variable *QRAIN*
3. Compute the variable *refl* using `wrf.getvar`
4. perform some analysis using `np.where`
5. save the array for later use

In addition to the steps outlined above, we should consider that the analysis is conducted for time period T only, and thus we must repeat the analysis for further time periods or extract the data for multiple time periods and then perform a single analysis run. This use case is relatively simple.

Loading NetCDF and Extracting a Variable

A WRF-OUT file can be loaded in python using the NetCDF4 module like so:

```python
import netcdf4 as nc

#Define File Location
wd = "/mnt/eps01-rds/Schultz-WeatherSim/Schultz-Carter-WeatherSim/"
directory = "ISHMAEL/19_09_2021/run/"
Domain = 1

#Load as NetCDF
ncfile = dataset(wd+directory+"wrfout_d0"+str(Domain)+"_2013-02-08_00:00:00", "r")

```

The ncfile itself does not take up much memory, instead it provides a look into the file by providing headers and metadata. Loading a variable from the data frame takes much more time as the data is unpacked into system memory for easy access.

```python
Rain = ncfile['QRAIN'][:]
```

One should be aware that variables can be very large and rapidly consume memory, especially if working on a local machine. For example:

```python
#get the dimensions
print('Rain has dimensions:', thisrain.shape)
  > Rain has dimensions: (48, 90, 255, 255)

#get bit size in memory
print(type(Rain[0,0,0,0]))
  > <class 'numpy.float32'>

#total size in GB
print('{:.2f}'.format(np.product(Rain.shape)*32/(8*(1024**3))), 'GB')
  > 1.05 GB
```

A relatively small variable with shape $(48, 90, 255, 255)$ has $48\times90\times255\times255 = 2.8\times10^8$ datapoints stored as 32 bit floats, this equates to approximately 1 GB of data. Thus, increasing the resolution, loading multiple time periods, and multiple variables will rapidly add up.

You should also consider that loading gigabytes of data can be time consuming. In this example, the QRAIN variable took 7.4 seconds to load, but this provides only a quarter of the total simulation data so loading all the data will require approximately 30 seconds.

Imagine that we wish to load both mass and number concentrations for 6 hydrometeor categories in three microphysics schemes. That's $2 \times 6 \times 3 = 48$ variables, and accounting for the entire simulation, $48 \times 4 = 192$ variable arrays. For the array given in the example above, that's 192 GB of storage, and almost 24 minutes of loading time. This also assumes the loading time is consistent, and the NetCDF WRFOUT files take negligible time and storage. We should also consider that the load time does not scale proportionally with array size.

Let's quickly examine the load time for NetCDF files and their variables for a range of sizes. Figure Q.2 shows the load times for 150 NetCDF files and the `QRAIN` variable in each. The domain approximately corresponds to file size as increasingly nested domains have greater resolution and thus more data points.

For NetCDF files, regardless of domain the total memory is of the order $\sim$KB and consequently, the load time is extremely small, less than half a second in all cases. There is not necessarily correlation between domain and file size, which is expected behaviour as the loaded NetCDF file provides metadata that is largely consistent for all domains. For variables, there is a clear relationship between the size of the loaded variable and the time required to load it. With increasing size, the time taken to load a variable grows linearly at approximately 4 times the variable size in Gigabytes. From this we may conclude that variables in high resolution domains require the greatest times to load and therefore provide the greatest opportunity for speed up.

We should also consider that the loading time might change as memory is used up. Figure Q.3 shows the loading time of NetCDF files and the QRAIN array for a given amount of memory already in use prior to loading. To produce this figure, a random sample of 100 WRFOUT files and QRAIN variables of varying domain were loaded and measured for the time taken to achieve load. The variables were stored in memory recursively. We find that the time taken to load is often longer when more variables are stored in memory for a given file size, this is indicated by generally lighter shades towards the right side of the figure than on the left for a given file size or row of data points. This relationship is inconsistent and marginal, for example the time difference spans a few seconds for the largest files and only a fraction of a second for the smallest. Nonetheless, this memory throttling is important to consider when loading multiple variables.

It is clear then, that the bottleneck in loading will arise when loading variables not NetCDF files. Additionally, we should aim to conserve as much memory as possible, load only the

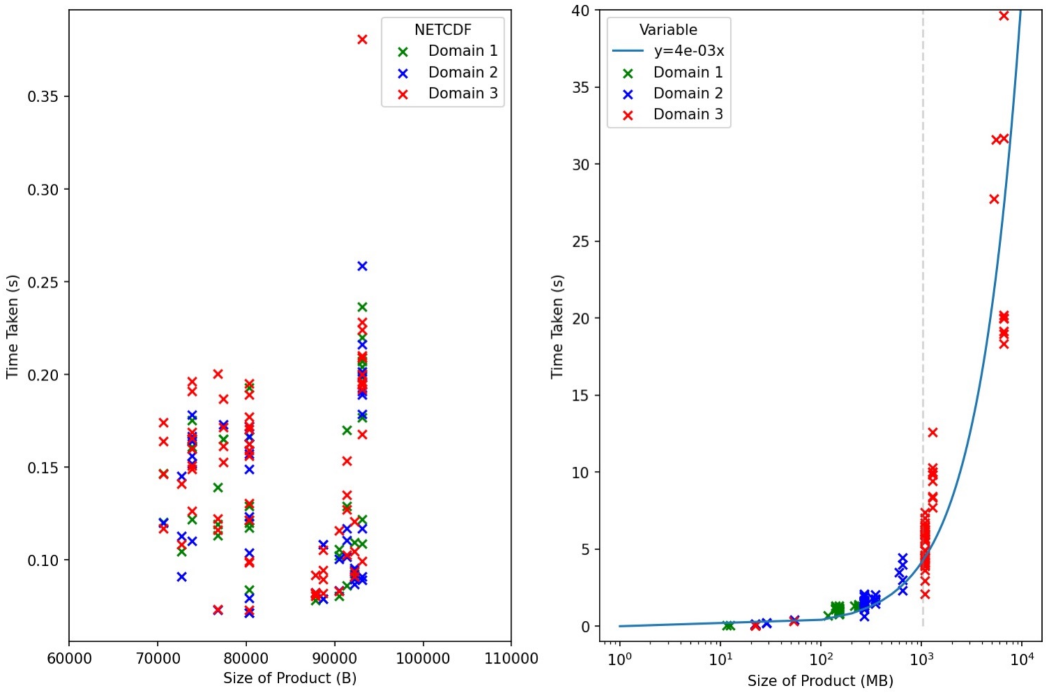

Figure Q.2. Comparison of loading times (s) for left: NetCDF files and right: NetCDF variables, of multiple file size. Loaded files correspond to Part II case one simulated domains one (green, 20 km), two (blue, 4 km), and three (red, 800 m). An exponential function with form shown in Figure legend is fit to NetCDF variables (blue, right)

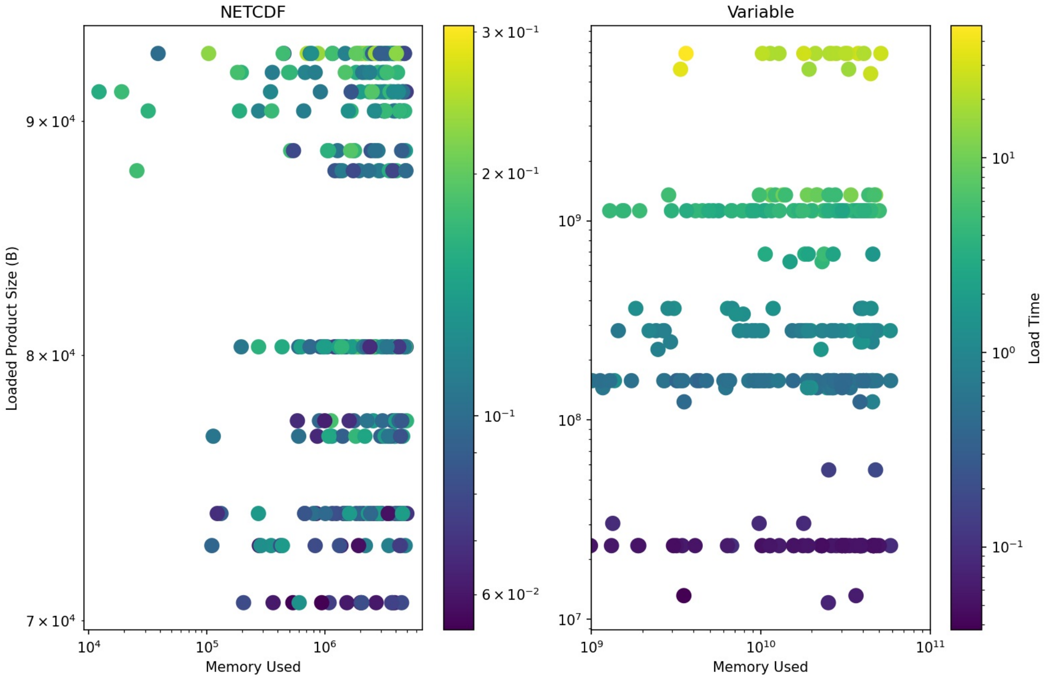

Figure Q.3. Load time (s, shaded) for a NetCDF file (left) and QRAIN variable (right) as a function of the loaded file or variable size (y-axis) and the system memory (Bytes) already in use during loading (x-axis).

variables that we require, and remove them as soon as they're no longer needed.

Using `wrf.getvar`

Let's suppose that we wish to obtain the reflectivity. We can load a WRF-OUT file as above, but the reflectivity is not a standard output variable for our microphysics scheme. To overcome this we can do some post processing to obtain the reflectivity from the variables that we do have available. Such functionality is provided by the WRF-python module via `wrf.getvar`. A variable name can be provided to this function and it will use internal libraries to calculate it from an input NetCDF file. This function adds an additional layer of computation and is thus more time intensive than loading a variable from the NetCDF file directly. The time taken will depend on the complexity of the calculation required to compute the variable in question:

```
 start=time.time()
dbz = wrf.getvar(ncfile, "dbz", timeidx=wrf.ALL_TIMES)
end=time.time()
dbz_time = end-start

start=time.time()
p   = wrf.getvar(ncfile, 'p', timeidx=wrf.ALL_TIMES)
end=time.time()
p_time = end-start

print(dbz_time, p_time)
  > 109.43,  8.56

```

So in this case, the reflectivity takes almost 2 minutes to load, whilst the pressure takes only 8 seconds. For variables that aren't standard, `getvar` is the fastest method and so little can be done to reduce the time taken.

A second advantage of `getvar` is that it can be used to load NetCDF variables too. This flexible approach comes at a very small cost, for example:

```
start=time.time()
snow1 = wrf.getvar(ncfile, "QRAIN", timeidx=wrf.ALL_TIMES)
end=time.time()
getvar_time = end-start

start=time.time()
snow2 = ncfile['QRAIN'][:]
end=time.time()
standard_time = end-start

print(getvar_time, standard_time)
  > 2.80     2.82

```

So when building a generalised loading method, using getvar allows for much greater flexibility without compromising on the loading time.

Performing Analysis with `np.where`

Let's suppose we wish to determine the 90th percentile of the rain mass mixing ratio, this can be achieved easily with `np.where`, which can filter through array elements based on some criteria.

```
prcnt_90_rain = np.where(rain >= np.percentile(rain[rain>0], 90), rain, 0)

```

`np.where` is fast and efficient making it extremely useful for dealing with arrays. It can be used to confirm conditions, for example lets find where the 90th percentile mass mixing ratios are and signify them with a 1, otherwise 0:

```
where_is_90 = np.where(prcnt_90_rain > 0, 1, 0)
```

However, when we check the array sizes:

```
 Rain : 1.05 GB
 prcnt_90_rain : 1.05 GB
where_is_90    : 2.09 GB
```

So, our array containing only ones and zeros is somehow twice as large as our original array! The reason for this is that numpy stores the data in the same precision as the input criteria:

```
print(*[str(type(x[0,0,0,0]))+'\n' for x in [prcnt_90_rain, rain, where_is_90]])

 <class 'numpy.float32'>
 <class 'numpy.float32'>
 <class 'numpy.int64'>

```

WRFOUT variable data is saved as a 32bit float for maximum compatibility and efficiency in FORTRAN, whereas I am running python on a 64 bit system and so the integer 1 is saved in 64 bit precision. I have highlighted this feature as it can quickly cause memory to increase if you're not careful to specify a dtype to numpy. Figure Q.4 shows the memory usage for the rain array with conversion to a variety of dtypes. We see that the memory grows as $y = \frac{A_0}{8}x$ where x is the datatype in bits, A_0 is the total number of datapoints in the input array and y is in bytes.

Manual conversion is possible and encouraged so long as you understand the dtype you are converting to and how it may affect the data. Suppose we convert the rain array to 64 bit and 16 bit for comparisons:

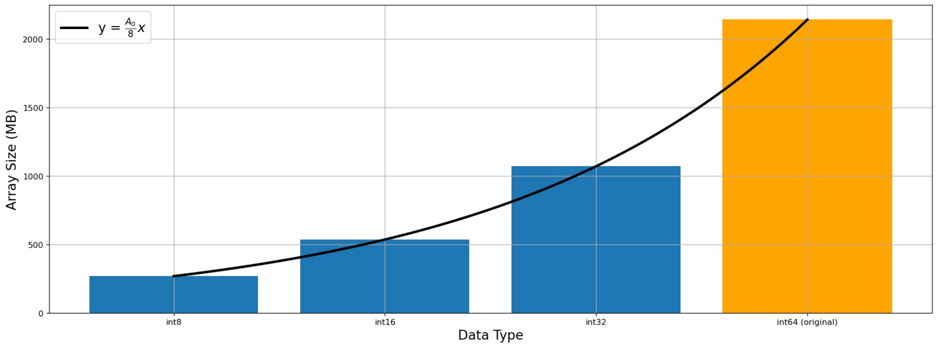

Figure Q.4. Variation of NetCDF variable system memory usage (MB) versus a variety of common datatype formats. As standard, variables are loaded as int64 type (orange) but can be converted to less precise data types (blue) during analysis. The function $y = \frac{A_0}{8}x$ is given in black, where x is the size of the datatype precision in bits (i.e. the suffix). A_0 is the total number of data points in the input array.

```
test_array = rain.copy()

#convert the test array to 64 bit
test_64   = np.ndarray.astype(test_array, np.float64)
print(test_64.dtype, rain.dtype, (rain==test_64).all())

#convert the test array to 16 bit
test_16   = np.ndarray.astype(test_array, np.float16)
print(test_16.dtype, rain.dtype, (rain==test_16).all())

> float32 float32 True
> float64 float32 True
> float16 float32 False

```

Increasing the precision does not affect the accuracy of the stored variables, however, decreasing the precision does:

```
 different =  np.where(test_16 != rain, rain, 0)

#show the largest example difference
indices = np.where(different == np.amax(different[different!=0]))
inds = tuple([i[0] for i in indices])

print(rain[inds], test_16[inds])

> 0.000108071195,  0.00010806
```

Thus the decimal places have been adjusted and we have lost some potentially important precision. Its not all doom and gloom though, lets try the same with our filtered array:

```
test_array = where_is_90.copy()

#convert the test array to 8 bit
```

```
test_8   = np.ndarray.astype(test_array, np.int8)
print(test_8.dtype, where_is_90.dtype, (where_is_90==test_8).all())

> int8 int64 True

print(int(test_8.nbytes/(1024**2)), 'MB', int(where_is_90.nbytes/(1024**2)),'MB')

> 267 MB 2143 MB
```

Because the stored values are integers we don't lose accuracy by converting to 8 bit, but we make considerable memory savings of 1.82 GB, which is an 87% reduction on the original array. It is important to note that when conducting analysis with arrays spanning multiple datatypes, `numpy` will use the datatype with the greatest precision. However, we still gain the benefits of reduced loading time. Using the example above where the array A (MB) has load time $T = 0.004 \times A$, we might expect to save almost 90% of the load time. In real terms this is around 7.5 seconds, but the benefit is greater for larger arrays. For example:

```
#make a massive 64 bit array
BIG = np.ones((192, 90, 600, 600))
print(gigs(BIG), BIG.dtype)

> 46.35 GB, float64

#convert to int8 format
test_8   = np.ndarray.astype(test_array, np.int8)
print(gigs(test_8 ), test_8 .dtype)

> 5.79 GB, int8

#show the time saving
test_8_mb, BIG_mb = int(test_8.nbytes/(1024**2)), int(BIG.nbytes/(1024**2))
print(int(0.004*(BIG_mb-test_8_mb)), 's')

> 166 s
```

Thus we could save 3 and half minutes in loading, and around 40 GB in memory by converting the array before saving it.

Loading Multiple Variables

You might save considerable time by placing the above steps into a loading function that will load all NetCDF files, load the required variable from each file and concatenate at the end. We can use getvar to load variables in a flexible way, but a second method exists to load multiple variables from multiple ncfiles called `wrf.extract_vars`. Thus, the following method:

```
#Method 1
for var in varlist:

  for ncfiles in ncfilelist:
    dum = wrf.getvar(ncfile5, str(var), timeidx=wrf.ALL_TIMES)
    if ncfiles == ncfiles[-1]:

      #Must add a time dimension to the last file
      dum = np.expand_dims(dum, axis = 0)

    dumlist.append(dum)
        DUM  = wrf.to_np(np.concatenate(dumlist, axis=0))
  outdict[var] = DUM
```

can be simplified using:

```
#Method 2
DUM = wrf.extract_vars(ncfilelist, timeidx=wrf.ALL_TIMES,  varnames=varlist)
```

Not only is this more condensed and far simpler to understand, but there are tangible time savings to be made across multiple variables when using the `wrf.extract_vars` routine. Figure Q.5 shows the time saved by using method 2 for a list of N variables. The domain, indicated by differing colours shown in the figure legend, are related to the variable size in memory, with each domain d approximately correlating to $\sim\ 1 \times 10^d$ MB. The average time savings increase with both the size of each variable and the total number of variables to be loaded. For example, loading one or two small files with method 2 can shave around 1 second but the same method used when loading 5 variables of gigabyte-scale size can save 10-15 seconds. Although not explicitly measured here, methods that load multiple (>6) very large (> 10 GB) variables could save tens of minutes in loading time using this method.

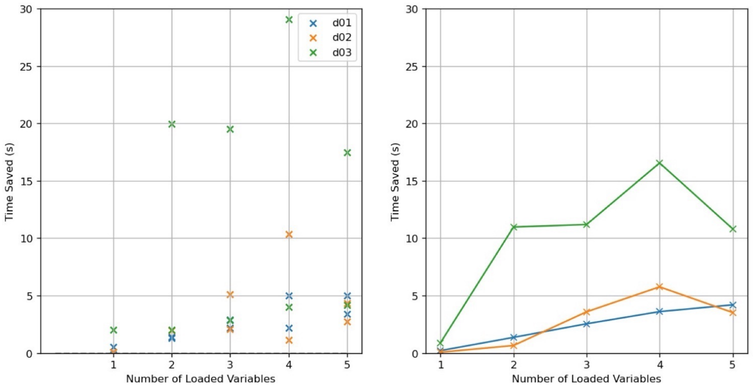

Figure Q.5. Time saved (s) when using a late-stage concatenation method on NetCDF variables. Domains 1–3 (i.e. d01–do3) represent increasing array sizes in system memory. Left: variables loaded from Part II case study. Right: variables loaded from Part III case study one.

Chunking

The above method is the most convenient way to load a full variable for analysis, for example, we load the 'QRAIN' and 'QICE' variables for all time points in the simulation, do some joint analysis with each array, and finally produce a plot. However, this method is generally problematic for loading many large variables due to the considerable overheads of the stored arrays in system memory. For example, examining Method 1 the memory in use at any one time is

$$\begin{aligned} M &= \texttt{dumlist+ dum +DUM+ outdict} \\ &= \texttt{N(dum)+ dum +N(dum)+ N(dum)} \\ &= (3N+1)\texttt{dum} \end{aligned}$$

where we have expanded each variable and approximated the size of a container by its contents ignoring overheads. N is the number of ncfiles in the ncfilelist. This method is inefficient for loading a large number N_v of variables, as the scaling goes as:

$$M \approx 6N_L\texttt{DUM} + N_v\texttt{(3N+1)dum} \tag{Q.1}$$

where N_L is the amount of variables loaded to that point. Suppose we load a 10 variables with total size 1 GB spread over 6 ncfiles, then we would accumulate $10 \times 19 \times 1/6 = 190/6 = 31$ GB of overhead per variable, when we reach the 10th variable, we have 9 stored in memory already resulting in an additional 9 GB of memory, thus overall we require peak memory of 40 GB. Quite a considerable increase for a total variables combined size of only 10 GB.

To get around this, one might choose to clear system memory of old variables on the fly using `del VAR` and `gc.collect()`, but we remain limited by the total system memory if it is exceeded by the combined size of all variables to be loaded.

A solution to this is 'chunking' the data. This is when the user loads only a small fraction of the data (such as a vertical column, time step or other array subset), conducts the analysis on it, stores the results of the analysis, and repeats. This method is much less memory intensive, but can be slower due to the repetition of loading variables multiple times for each chunk.

Appendix R

Determination of Mass Weighted Variables

R.1 Mass Weighting of a Single Variable in *n* Dimensions

The mass weighting of a variable V with N elements and corresponding masses M with an equal number of elements is:

$$V = \{v_1, v_2 ... v_N\}\ , M = \{m_1, m_2 ... m_N\}$$

$$V_w = v_1 \times \frac{m_1}{m_T} + v_2 \times \frac{m_2}{m_T} + ... v_n \times \frac{m_N}{m_T}$$

Where,

$$m_T = \sum_{i=0}^{N} m_i$$

This can be represented as a function:

$$V_w = \sum_{i=0}^{N} f(v_i, m_i)$$

Where:

$$f(v, m) = v_i \times \frac{m_i}{\sum_{i=0}^{N} m_i}$$

Expanding this definition for n-dimensional variables of total number N:

$$V_w = \sum_{\mathbf{i}=0}^{N} f(\mathbf{v}_i, \mathbf{m}_i)$$

Where,

$$\mathbf{v} = v_{a,b...n}$$

$$\mathbf{m} = m_{a,b...n}$$

This fully defines the P3 scheme with one ice and one snow category. For the three dimensional case of a square area across a set time period:

$$V_w = \sum_{\mathbf{i}=0}^{N} \mathbf{v}_i \times \frac{\mathbf{m}_i}{\sum_{i=0}^{N} \mathbf{m}_i}$$

Where,

$$\mathbf{v} = v_{x,y,t}$$
$$\mathbf{m} = m_{x,y,t}$$

R.2 Mass Weighting of Multiple Variables in *n* Dimensions

ISHMAEL simulates 3 ice categories that we wish to combine into one value. Here we consider K variables V_a ... V_K with corresponding mass sets M_a ... M_K:

$$\begin{aligned}
V_a &= \{v_{a,1}, v_{a,2}, ...v_{a,N}\}, M = \{m_{a,1}, m_{a,2}, ...m_{a,N},\} \\
V_b &= \{v_{b,1}, v_{b,2}, ...v_{b,N}\}, M = \{m_{b,1}, m_{b,2}, ...m_{b,N},\} \\
&\vdots \\
V_K &= \{v_{K,1}, v_{K,2}, ...v_{K,N}\}, M = \{m_{K,1}, m_{K,2}, ...m_{K,N},\}
\end{aligned}$$

The mass weighting of K variable sets with N elements is:

$$\begin{aligned}
V_w = v_{a,1} &\times \frac{m_{a,1}}{m_T} + v_{a,2} \times \frac{m_{a,1}}{m_T} + ...v_{a,N} \times \frac{m_{a,N}}{m_T} + \\
&\vdots \\
v_{K,1} &\times \frac{m_{K,1}}{m_T} + v_{K,2} \times \frac{m_{K,1}}{m_T} + ...v_{K,N} \times \frac{m_{K,N}}{m_T}
\end{aligned}$$

Where,

$$m_T = \sum_{i=0}^{N} m_{a,i} + ... m_{K,N}$$

This can be represented as a function of K n-dimensional variables over N elements:

$$V_w = \sum_{\mathbf{i}=0}^{N} f(\mathbf{v}_{a,i}, \mathbf{m}_{a,i}, ... \mathbf{v}_{K,N}, \mathbf{m}_{K,N})$$

Where:

$$f(v_0, m_0, \ldots v_K, m_K) = \sum_{j=0}^{K} v_j \times \frac{m_j}{\sum_{i=0}^{N} \sum_{j=0}^{K} m_{ij}}$$

Appendix S

Evaluation of IMPACTS Data Sets

Table S.1. Review of available measurement data products for an IMPACTS storm (see Table 2.1). Information pertains to storm case one (Part III). Data product indicates the equipment used to retrieve measurement data. Full data product names can be found in the abbreviations and acronyms section. Available indicates whether the data was available to download at the onset of Part III analysis. Type lists the variables obtained by the measurement equipment.

Product	Avail.	Size	Location	Type	Notes
AMPR	Y	27 MB	In air	Brightness temperature	
AVAPSn	N	-	-		
ASOS	Y	40 K	ground	Surface temperature, dew point, precipitation, wind direction, wind speed, wind gust, sea level pressure, and the observed weather code	
APU	Y	1-2 MB	In air	Precipitation amount, precipitation rate, reflectivity in Rayleigh regime, liquid water content, drop diameter, and drop concentration	ASCI see documentation for headers
CPL	Y	800 MB	In air	Back-scatter coefficient, Lidar depolarisation ratio, layer top/base height, layer type, particulate extinction coefficient, ice water content, and layer-/cumulative optical depth data	HDF5 format
CRS	N				
CosMIR	Y	8 MB	In air	Brightness temperature	

Continued on next page

Table S.1 – continued from previous page

Product	**Available**	**Size**	**Location**	**Type**	**Notes**
ER-2 navigation	Y	2 MB		Typical navigation data (e.g., date, time, latitude/longitude, and altitude) it also contains outside meteorological parameters such as wind speed, wind direction, and temperature	
ER-2 EXRAD	N			Radar reflectivity and Doppler velocity	
GOES	Y	> 1MB	Satellite	Single reflective band radiance products	
HIWRAP	N				
NEXRAD (i.e. KOKX)	Y	> 1MB	Radar	Radar reflectivity, radial velocity, spectrum width, differential reflectivity, differential phase, and cross correlation ratio	
LIP	Y			Electrical field measurements	ASCII .txt format
Mobile UIUC Soundings	Y	24 K		Vertical profiles of atmospheric temperature, relative humidity, pressure, wind speed, and wind direction	Rawinsonde
NPOL	Y	3 MB		Radar reflectivity, differential reflectivity, specific differential phase, differential phase, co-polar correlation, and Doppler velocity images	
NCAR Particle Probes	Y	>10 MB		Particle Size Distributions	Multiple probes

Continued on next page

Table S.1 – continued from previous page

Product	Available	Size	Location	Type	Notes
NCSU soundings	N			Vertical profiles of atmospheric temperature, relative humidity, pressure, wind speed, and wind direction	North Carolina state university
New York State Mesonet	Y			Temperature, wind, wind direction, mean sea level pressure, precipitation, and snow depth measurements, as well as profiler Doppler LiDAR and Microwave Radiometer (MWR) measurements	Browse only
NEXRAD Mosaic East	Y	20 MB		Radar reflectivity, radial velocity, spectrum width, differential reflectivity, differential phase, and cross correlation ratio	
NEXRAD Mosaic Mid west	Y	22 MB		Radar reflectivity, radial velocity, spectrum width, differential reflectivity, differential phase, and cross correlation ratio	
NOAA Soundings	Y	7 K	M	Wind direction, dew point temperature, geopotential height, mixing ratio, atmospheric pressure, relative humidity, wind speed, temperature, potential temperature, equivalent potential temperature, virtual potential temperature measurements and Radiosonde	

Continued on next page

Table S.1 – continued from previous page

Product	Available	Size	Location	Type	Notes
P-3 Meteorological and Navigation Data	Y	4.7 MB		GPS positioning and trajectory data, aircraft orientation, and atmospheric state measurements of temperature, pressure, water vapour, and horizontal winds	
PHIPS	Y			Particle shape, size, and habit	.PNG images
SBU Ceilometers	Y		M	Cloud height / base	
SBU Doppler LiDAR	Y		M	Wind	
KASPR	Y	50MB	M	Reflectivity, mean velocity, spectrum width, linear depolarisation ratio, differential reflectivity, differential phase, specific differential phase, co-polarised correlation coefficient, and signal-to-noise ratio	
SBU Meteorological Station	Y	2.4	M	Temperature, dew point, relative humidity, absolute humidity, mixing ratio, air pressure, wind speed, and wind direction	
SBU Micro Rain Radar 2	Y	122 Mb	M	Reflectivity, Doppler velocity, signal-to-noise ratio, spectral width, droplet size, Liquid Water Content, melting layer, drop size distribution, rain attenuation, rain rate, and radial velocity	
SBU Mobile Soundings	Y	200 K		Temperature, humidity, height, and horizontal wind direction and speed	

Continued on next page

Table S.1 – continued from previous page

Product	Available	Size	Location	Type	Notes
SBU Parsivel	Y	5 MB	M	Particle size distribution, fall speed, radar reflectivity and precipitation rate	
SBU Pluvio Precipitation Gauge	Y	163 K		Precipitation intensity and precipitation accumulation	.CSV
TAMMS	Y	37 MB	In air	Wind speed, wind direction, and cross wind speed	
2DVD	Y	100 M		Size, equivalent diameter, fall speed, oblateness, cross-sectional area of raindrops, particle concentration, total number of drops, total drop concentration, liquid water content, rain rate, reflectivity, and rain event characteristics	.txt
MRR2	N			Reflectivity, Doppler velocity, signal-to-noise ratio, spectral width, droplet size, Liquid Water Content, melting layer, drop size distribution, rain attenuation, rain rate, and radial velocity	
UAlbany Parsivel	N			Particle size distribution, fall speed, radar reflectivity and precipitation rate	
UND Cloud microphysics	N			Cloud particle measurements	